CORA Cork Open Research Archive
Cartlann Taighde Oscailte Chorcaí

Title	Design, fabrication and characterisation of components for microfluidic enzymatic biofuel cells
Authors	Żygowska, Monika
Publication date	2014
Original Citation	Żygowska, M. 2014. Design, fabrication and characterisation of components for microfluidic enzymatic biofuel cells. PhD Thesis, University College Cork.
Type of publication	Doctoral thesis
Rights	© 2014, Monika Żygowska. - http://creativecommons.org/licenses/by-nc-nd/3.0/
Download date	2026-11-04 06:53:41
Item downloaded from	https://hdl.handle.net/10468/1912



UCC
University College Cork, Ireland
Coláiste na hOllscoile Corcaigh

Design, fabrication and characterisation of components for microfluidic enzymatic biofuel cells

Monika Żygowska Eng. M.Sc.



National University of Ireland, Cork

A thesis submitted for the degree of

DOCTOR OF PHILOSOPHY

Department of Chemistry
University College Cork
Microsystems Centre
Tyndall National Institute

Research supervisor:	Dr. Grégoire Herzog
Co-supervisor:	Dr. Vladimir Ogurtsov
Head of Department:	Prof. Martyn Pemble

April 2014

By its nature, every endeavour employing the scientific method requires a significant amount of effort. This thesis is no different but the privilege of contributing to the body of human knowledge easily justifies the toil involved.

I certify that this thesis is my own work and that I have not obtained a degree from University College Cork or from any other university on the basis of the work submitted in this thesis.

Monika Żygowska

To my Family, whose love and support were the driving force throughout the Ph.D. process and all the years of my education.

ACKNOWLEDGMENTS

First and foremost, I would like to acknowledge my supervisors, Dr. Grégoire Herzog and Dr. Vladimir Ogurtsov for providing me with the opportunity to continue my research in the life sciences. Thank you for introducing me into the field of biofuel cells and teaching me how to be an independent researcher. I appreciate you taking me on as a Ph.D. student in the first place. I am very grateful to Dr. Ogurtsov for his input in the modelling work, the challenging discussions on electrical circuits and imparting general engineering wisdom. I wish to acknowledge his leadership in the LSI team and his efforts in maintaining the integrity of the group and continuity of the interdisciplinary research. Thank you for looking after me and Azura, for securing the much needed funding and for help you provided anytime we needed it. I would also like to acknowledge Dr. James Rohan, for making a significant contribution in that matter, for providing me with the opportunity to continue my research in microfluidics and nanomaterial deposition.

I wish to sincerely thank Dr. Alan O'Riordan for voluntarily taking on a role of my mentor. His radiant enthusiasm, guidance and practical advice, preserved the oddments of hope in completing this Ph.D. work. Special thanks to Dr. Peter O'Brien for much appreciated advice on the fabrication of microfluidic devices, the support and constructive talks on the importance of design specification.

I extend my gratitude to the Central Fabrication Facility staff for the fabrication of the platforms for my microfluidic prototypes, their invaluable advice on the design and machining of high quality custom parts and devices.

Thank you to IT for their help and assistance in all sorts of technical problems, granting me the access to various software packages and sorting out all my PC woes.

In the course of my Ph.D., I have been fortunate enough to encounter many great researchers and wonderful people who deserve a special mention. Dr. Anita Hamilton, The Saviour Electrochemist, who joined the Tyndall community when one was badly needed. Thank you for helping me with everything and putting up with me throughout the hard

time of the write-up period. Dr. Ray Duffy, thank you for advice on thesis and paper writing and precious life tips. Dr. Veronika Urbanova, a postdoc at the time of my secondment, thanks to whom the challenging sol-gel experience was much more enjoyable and bearable.

Special mention to Azura Said and Ilias Chlis for their companionship, kindness and sharing the long working hours spent at Tyndall. Our vibrant exchange of goodies and energetic treats kept the right glucose levels throughout the night and put a final knot on our great friendship. Azura, thank you for lifting up my spirits when work was not going well (most of the time), motivating me and helping us to push each other's limits further than we could have ever expected. You have been like a sister to me.

Thanks to Kasia & Nicola, Clare & Pierre, Farzan & Lida, Aga, Anushka, Maryam 'Shirin', Shelly, Eddie, Padraic, Mark and Jan for sharing the happy and sad moments, building scientific discussions, multicultural food contests and for being the best Emergency Viva Support Group one could imagine. A special mention goes to the PGC members - Anna, Conor, Evan, Gangotri and Tuhin. You guys are a wonderful circle of friends that I can always rely on.

I wish to dedicate this work to my family: to Mum, Dad and babcia Helenka, who have always had complete faith in me and believed in my abilities more than I ever did myself. Thank you for all the years of unwavering support, the unconditional love, the cherished memories and all the virtues I learnt from you. It has not been easy at times but I could always rely on you. Very special thank you to my beloved Dad, the greatest role model of all and the person I attribute all my life accomplishments to. You taught me to always give the best of myself and follow my dreams. You showed me the value of hard work, dedication and compassion. Without you I would not be who and where I am at the moment. I hope I make you proud Dad. Thanks to my sister, Marta, for keeping me down to earth in those rare moments when I thought I was the brighter child.

To Neil and Mary Daly, for their love, continuous support and always treating me like one of their own. Thank you for saving me from lonely walks home in the rain and the dark, making sure I was safe and sound, for Sunday dinners and my very first Christmas turkey and ham.

Last but not least, I would like to thank my boyfriend Aidan, for the most amazing years of my life and for keeping me sane at times of despair and hopelessness. You have been my twin soul and my dearest friend. Thank you for your absolute faith in me, encouragement to try new things and pushing me to constantly challenge myself. If not for

you, I would probably still detest mathematical modelling and would be petrified by deep water. Paradoxically, thank you for tearing the first draft of my work apart and helping me put together the best thesis I could have ever written. I would have not been able to come this far without your love, patience and support.

Niniejszą rozprawę doktorską dedykuję mojej rodzinie: najdroższym rodzicom, Iwonie i Grzegorzu; siostrze Marcie i najukochańszej pod słońcem babci Helenie. Zarówno ta praca jak i cały mój dotychczasowy dorobek naukowy jest Waszą zasługą. To Wy nauczyliście mnie, że warto walczyć o marzenia i nie zrażać się przeszkodami, bo dobre rzeczy nie przychodzą do tych którzy biernie oczekują, ale tych, którzy aktywnie wspomagają swój los.

Dziękuję Wam za bezinteresowną miłość, nieustanne wsparcie i wiarę w moje możliwości, niejednokrotnie sielniejszą niż moja własne przekonania. To Wam zawdzięczam determinację, pracowitość i przeświadczenie, że nawet najtrudniejsze szlaki są osiągalne i najwyższe szczyty są w zasięgu ręki.

Kochanemu Tacie dziękuję za pomoc w dokonaniu życiowego wyboru, za pokazanie mi, że ciężka praca, oddanie i dedykacja są najlepszą drogą do sukcesu.

Monika

ABSTRACT

The concept of a biofuel cell takes inspiration from the natural capability of biological systems to catalyse the conversion of organic matter with a subsequent release of electrical energy. Enzymatic biofuel cells are intended to mimic the processes occurring in nature in a more controlled and efficient manner. Traditional fuel cells rely on the use of toxic catalysts and are often not easily miniaturizable making them unsuitable as implantable power sources. Biofuel cells however use highly selective protein catalysts and renewable fuels. As energy consumption becomes a global issue, they emerge as important tools for energy generation.

The microfluidic platforms developed are intended to maximize the amount of electrical energy extracted from renewable fuels which are naturally abundant in the environment and in biological fluids. Combining microfabrication processes, chemical modification and biological surface patterning these devices are promising candidates for micro-power sources for future life science and electronic applications.

This thesis considered four main aspects of a biofuel cell research. Firstly, concept of a miniature compartmentalized enzymatic biofuel cell utilizing simple fuels and operating in static conditions is verified and proves the feasibility of enzyme catalysis in energy conversion processes.

Secondly, electrode and microfluidic channel study was performed through theoretical investigations of the flow and catalytic reactions which also improved understanding of the enzyme kinetics in the cell.

Next, microfluidic devices were fabricated from cost-effective and disposable polymer materials, using the state-of-the-art micro-processing technologies. Integration of the individual components is difficult and multiple techniques to overcome these problems have been investigated. Electrochemical characterization of gold electrodes modified with Nanoporous Gold Structures is also performed.

Finally, two strategies for enzyme patterning and encapsulation are discussed. Several protein catalysts have been effectively immobilized on the surface of commercial and microfabricated electrodes by electrochemically assisted deposition in sol-gel and poly-(*o*-phenylenediamine) polymer matrices and characterised with confirmed catalytic activity.

TABLE OF CONTENTS

Declaration ..... **ii**

Acknowledgements ..... **v**

Abstract ..... **ix**

1. ***Introduction*** 1
1.1. Biofuel cells - emerging renewable energy sources 1
1.2. Objectives of this work 39
1.3. Bibliography 42

2. Experimental procedures **49**
2.1. Chemical and biological reagents 49
2.2. The electrochemical set-up 49
2.3. Instrumentation 58
2.4. Glassware, compounds and reagents 58
2.5. Electrode cleaning procedures 59
2.6. Electrochemical measurements 62
2.7. Materials for cell components 65
2.8. Fabrication of gold and platinum electrodes 66
2.9. Electrodeposition of NPG structures 67
2.10. Microfluidic channel - design and fabrication 68
2.11. Sol-gel encapsulation of enzymes 72
2.12. Enzyme encapsulation in *o*-phenylenediamine 74
2.13. Preparation of Zeonor electrodes 77
2.14. Solutions for electrode modification 77
2.15. Buffered solutions for enzyme testing 79
2.16. Redox solutions for enzyme testing 81
2.17. Bibliography 83

3. Miniature enzymatic biofuel cell **85**
3.1. Introduction 85
3.2. Cell development and characterization 93
3.3. Results and discussion 102
3.4. Conclusions 115
3.5. Bibliography 117

4. Modelling and optimization studies..... 119
4.1. Introduction 119
4.2. Theory of the microfluidic enzymatic cell 123
4.3. Velocity of the flow and electrode geometry 130
4.4. Modelling of the enzyme kinetics 142
4.5. Conclusions 169
4.6. Bibliography 173

5. Microfluidic devices with integrated electrodes 177
5.1. Introduction 177
5.2. Review of microfabrication technologies 178
5.3. Microfluidics in device fabrication 189
5.4. Electrode design and fabrication 197
5.5. Electrochemistry of Zeonor electrodes 205
5.6. Electrode modification with NPG 213
5.7. Microfluidic channel - design and fabrication 225
5.8. Assembly of microfluidic devices 236
5.9. Conclusions 244
5.10. Bibliography 250

6. Immobilization of enzymes catalysts 251
6.1. Introduction 251
6.2. Enzyme immobilization strategies 252
6.3. Selected methods of catalyst encapsulation 257
6.4. Materials and methods 273
6.5. Results and discussion 286
6.6. Enzymatic biofuel cell in static conditions 333
6.7. Conclusions 339
6.8. Bibliography 344

7. Conclusions and future work 353
7.1. Bibliography 359

Publication list 361

Appendices

A. Methods of electrochemical characterization 365

B. Microfabrication technology 387

C. Mathematica code.....413

CHAPTER I

INTRODUCTION TO BIOFUEL CELL RESEARCH

Without energy life would be extinguished instantaneously, and the cellular fabric would collapse

Albert-Szent Gyorgi

1.1. Biofuel cells - emerging renewable energy sources.

1.1.1. Alternative power supply.

Consumption and production of energy, which still rely primarily on combustion of fossil fuels, have a severe impact on world economics and ecology. As the global energy demand per annum has been continuously increasing, the contemporary dependence on traditional fuels is no longer sustainable due to limited natural resources, growing atmospheric pollution and global warming repercussions [1]. In the times of a constant increase of the rate of annual energy consumption, a growing depletion of traditional fossil fuels supply and environmental issues associated with the traditional methods of energy generation and consumption, alternative energy sources became an urgent research theme. Electrochemical energy production is currently under serious consideration as a more sustainable and environmentally friendly alternative energy/power source. Among three main types of electrochemical systems for energy conversion and storage, the most recognized are batteries and fuel cells [2].

Fig. 1.1 compares some of the existing alternative energy sources with respect to the power that can be drawn from the device. As can be seen from the diagram, the amount of energy, which can be extracted from the biofuel cells is within μW and mW range. This is several orders of magnitude less than the lowest power derived from a traditional fuel cell. Due to the biocompatible and environmentally friendly nature of

biological cells, these devices can be however successfully employed as the green micro-power energy sources, where fuel cells cannot be applied.

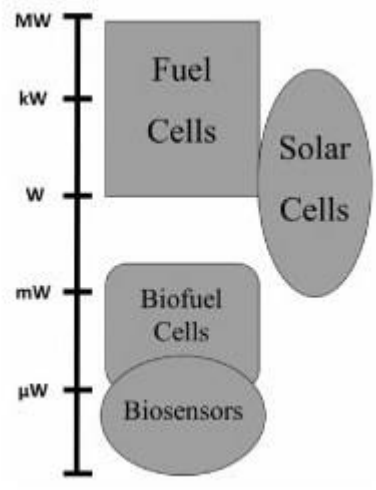


Fig. 1.1. Diagram of the power range delivered by some of the alternative energy producing systems [3], based on the information provided in ref. [4].

Fuel cells have been utilized for their power-generating abilities as early as in 1839 however they were first applied for commercial use in 1955 by the General Electric Corporation, known these days as a joint venture with Plug Power under a common name, GE Fuel Cell Systems (GEFCS). Forgotten and re-emerged after a period of inactivity, fuel cells are now a vibrant subject of extensive research focused on energy production. All fuel cells have the same major components: a cathode and an anode immersed in a mutual electrolyte solution. The technology is based on the conversion of chemical energy from highly energetic fuels into electrical energy via redox reactions occurring at the electrode/electrolyte interface. In the cell, the anode breaks down the substrate by oxidizing it into electrons and ions. The electrons are subsequently transferred to the cathode, where the reaction of reduction takes place, generating waste products, such as water. The electrolyte solution is necessary to facilitate the flow of ions, while the electron transfer is carried by an external circuit. The fuel itself is also necessary to drive forward the chemical reaction that produces the current, and hence generates the power. While the most common substrate used is hydrogen, various other fuels have been investigated, such as organic solvents (methanol, ethanol) [5]. Vast majority of conventional fuel cells utilize hydrogen or methanol, forming water and carbon dioxide as reaction by-products. While CO_2 is by nature a harmless gas, H_2 used to produce energy gives rise to a number of

safety issues related with its transport and storage. Furthermore, many substrates employed in fuel cell studies include substances generated as a result of petroleum combustion. For these reasons, the imperative demand for alternative power sources has been urgently recognized, with numerous efforts being made towards the development of energy harvesting devices capable of operating in physiological conditions without the prerequisite for frequent recharging.

It should be noted that the request for alternative energy sources corresponds particularly to micro-power systems, where due to the exponentially growing number of microscale devices requiring a prolonged operation time without the power source replacement, this demand is even more urgent. In this light, small scale medical devices, primarily miniaturized implants such as pacemakers; insulin pumps; nano-robots for accurate delivery of drugs and health monitoring systems, has focused the commercial attention on micro-power sources, with a special consideration of biofuel cells [1]. Among various different fuel cell categories, biologically driven devices employing microbial or purely enzymatic systems soon became one of the most appealing avenues that have ever diverged from the original design solution. The principle behind the operation of biological cells relies on the conversion of chemical energy naturally present in organic substrates into electrical energy, via the catalytic capabilities of stand-alone or cell contained enzymes.

The significant upsurge in the research and development of biologically driven power sources has been attributed to a number of key factors. Enzymes and biofuels are renewable energy sources that are sustainable and have the potential to limit environmental impact from the corresponding power devices. This is in contrast with more traditional energy carriers, which are fossil fuels and organic solvents, both non-renewable and potentially harmful to the environment. Due to their ability to utilize glucose and oxygen abundant in blood, biofuel cells can be potentially implanted in a human body and power *in vivo* miniaturized devices such as pacemakers, hearing aids, insulin pumps, etc. This would be feasible since fuel, oxidant, and by-products of the catalytic reactions are harmless and often biologically endogenous.

Furthermore, unlike in the case of non-renewable noble metal catalysts, scaling up the use of biological species in enzymatic or microbial cells yields in reduced production costs, while facilitating improved relative substrate turn over.

Fig. 1.2 is a juxtaposition of the micro-scale enzyme-based biofuel cells with the existing batteries in terms of their specific energy density [6]. The benefits of

microcell/MEMS-based devices have been attributed to advanced microfabrication technologies capable of producing and packaging of layered structure systems, a key factor affecting the enhanced utilization of the fuel.

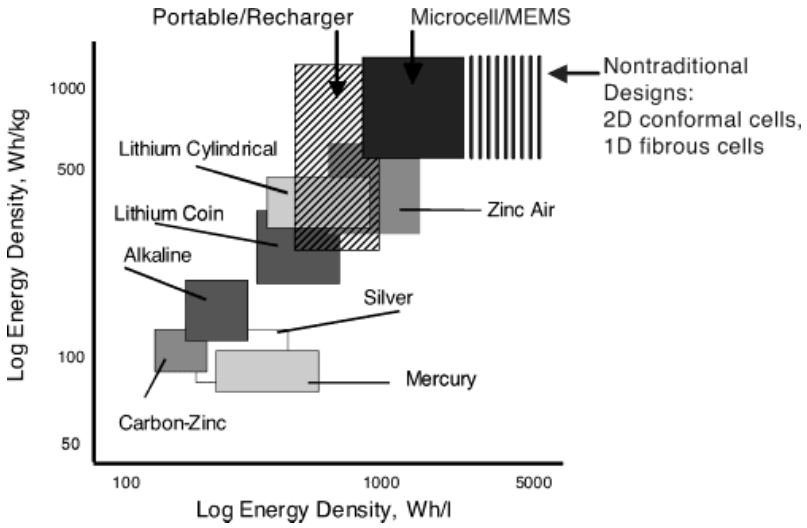


Fig. 1.2. Graphical representation of the energy densities provided by traditional batteries and juxtaposed with enzymatic biofuel cell solutions [6].

A) Applications of fuel cells.

Initial market opportunities for biofuel cells are most likely to be where there is a need for large amounts of energy and low power demands [7]. This is due to the ability of biofuel cells to achieve high efficiencies of fuel oxidation, reflected by substantial energy densities, but lower power densities due to inferior catalytic activity, as compared to metal catalysts of conventional fuel cells. Biofuel cells can be employed as an *in vivo* power sources for implantable medical devices, such as pacemakers, micro-drug pumps, deep brain stimulators or integrated, disposable and subcutaneously introduced glucose monitoring sensor-transmitters [8]. An existing market where biofuel cells could be ideally suited to provide increased performance as a power supply is *wireless sensor network*s (WSN) [9]. Applications of WSN are ranging from residential home automation and commercial building developments to industrial monitoring, control and military use.

Ability to utilize high energy density fuels such as variety of sugars and alcohols, which cannot be utilized by conventional metal catalysts, enables biofuel cells to address

markets and applications that traditional fuel cells cannot reach. Abundance of organic compounds in waste water, especially high concentrations of industrial by-products (e.g. cellulose, glycerol, ethanol) offers easily accessible and highly sustainable fuels for enzyme-based energy production. Enzymatic removal of the organic pollutants supports the conventional chemical systems and can form the basis of waste water treatment plants combined with the energy production from the biological matter present in sewage.

1.1.2. Microbial and enzymatic biofuel cells.

Biofuel cells are a division of conventional fuel cells that employ the nature of enzyme catalysts to carry out biochemical reactions in order to provide electrical energy. Due to a broad diversity of biological species capable of utilizing a wide number of alternative fuel sources, these energy harvesting systems are of immense consideration as by their nature they are renewable, environmentally friendly and self-sustainable.

Depending on the origin of the biocatalyst used, biofuel cells can be classified into three categories: enzymatic, microbial and mitochondrion based cells.

Although mitochondria have been long considered the powerhouse of the cells, the concept of employing these cellular structures as biocatalysts for the energy conversion is relatively recent. The intermediate biofuel cell group employing organelles, has been reported by Arechederra and co-workers only in 2008 [10] and has not yet gained its complete attention. Nonetheless, a promising performance of these biological entities has been continually reported by Minteer *et al.* [10-12] with a potential insight into a number of new applications and alternative fuels [13].

In spite of the advantages of mitochondrion in the energy production scheme, the two most recurrently investigated power cells are still based on the catalytic activities of enzymes and whole microorganisms. Enzymatic biofuel cells (EBFC) are defined as systems, which employ specific enzyme molecules, isolated from their natural cellular environment and used for all or at least part of their operational strategy. Microbial systems (MBFC) on the other hand utilize whole cells and the energy conversion is driven by the enzymes contained in their natural biological setting. Although MBFC are generally more efficient in overall fuel conversion, due to the presence of assorted enzyme contents, EBFC provide much higher current and power densities with respect to specific biochemical reactions. Complete multi-step breakdown of organic fuels into CO_2 and H_2O,

while naturally obtained by microbial cells, is also achievable in the purely enzymatic systems provided that an appropriate combination and cascading of catalysts have been employed [14, 15]. In this regards, EBFCs are of particular importance for the practical implementation in the efficient energy generation.

Regardless of the source of the catalyst, the active component needs to be confined on the electrode surface in order to achieve sufficient electrical connection between the two half-cells.

1.1.3. Advantages of enzymatic biofuel cells.

Among all the novel nature - derived and biomimetic power sources, energy conversion based on electrochemical processes, has gained the highest consideration. Three major types of electrochemical systems for energy conversion include batteries, fuel cells and supercapacitors [2]. Although their energy storage and conversion mechanisms differ, certain electrochemical similarities in between remain.

Since the majority of currently existing batteries and fuel cells require reactive and often corrosive or toxic elements with their size being controlled by a number of large components, the final dimensions are typically much larger than any sensor of functional analytical packaging (e.g. sensor-on-chip or lab-on-chip). In the light of this, a strategic need for miniature power sources integrated on disposable and implantable electronic subsystems exists for life sciences (e.g. biomedical), electronic or environmental applications [6].

Enzymatic biofuel cells are unique in comparison with their traditional energy harvesting ancestors (e.g. batteries) in a number of ways. Biofuel cells replace expensive precious metal catalysts with low cost, renewable enzymes for the catalysis of redox-reactions [16], offering significant economic advantage over traditional fuel cells. The chemical reactions in these cells are driven by abundant bio-fuels and highly selective biological species, enabling the implementation of these enzyme powered devices in variety of diverse applications.

Environmentally ample substrates utilized by biofuel cells, such as alcohols and carbohydrates, are typically of high theoretical energy and, as such, can potentially provide substantial power outputs. As most of available fuels are biogenic, the consumption and production cycles are considered to be carbon neutral, self-sustainable

and hence unlimited in practice. These features offer great advantage over conventional cells, which are reliant on limited endogenic mass supply and frequently toxic catalysts, where the by-products of the conversion in some cases are environmental pollutants.

The ability of biofuel cells to metabolize carbohydrates and molecular oxygen has been the driving force, which have sparked the idea of implantable power sources. The abundant presence of glucose and O_2 in bodily fluids supported by excellent biocompatibility of often tissue-specific catalysts enables the implementation of enzymatic biofuel cells in a human body and their application as power sources for e.g. pacemakers.

Wide range of available enzymes with diverse biological functions and high catalytic activities superior to that of platinum, allow the operation in various working conditions, at mild temperature (20 - 40ºC) and physiological pH. Substrate specificity eliminates the prerequisite for fuel purification enabling efficient conversion directly from the bulk solution without the risk of side-product formation. Furthermore, the ability of enzymes to catalyze very specific reactions, in general, disregards the existing expensive polymer electrolyte membranes and allows a 'one-pot' operation without the need to separate the anolyte and catholyte processes. Elimination of the separating element reduces the size of the cell and enables further miniaturization.

Unlike microbial biofuel cells, enzyme-powered devices do not require nutrients or biomass acclimation and the electrochemical processes can be controlled in a more accurate manner. Moreover, the enzymatic BFCs generally produce higher power output densities and can be easier scaled down to a miniaturized format. Due to the natural rules governing the life cycle of any microorganism, microbial fuel cells require an initial transitory period, where the cells grow and adapt to the experimental conditions and applied electron transport scheme. As the enzymatic biofuel cells utilize purified biological catalysts, isolated from their respective cellular environment, these systems do not require any pre-conditioning and as a result exhibit much faster response to the external stimuli (e.g. substrate).

In addition, with the current knowledge of material sciences and the availability of diverse polymer materials, components of the enzymatic biofuel cells can be fabricated from cheap and disposable plastic substrates, significantly reducing the manufacturing costs.

1.1.4. The operating principles of an enzyme driven biofuel cell.

According to a broad definition by Bullen *et al*. [4], biofuel cells are characterized as "devices capable of directly transforming chemical to electrical energy via electrochemical reactions involving biochemical pathways." Direct electrochemical conversion of species is highly desirable in the energy production scheme as it prevents thermodynamic limitations associated with the traditional combustion of fuels [17].

The operational principle of biofuel cells, in general, relies on a transformation of biochemical potential energy embedded in organic molecules into an electrical energy [6]. In the case of enzymatic biofuel cells, the process is carried out by two distinct catalysts, immobilized on the surface of metal or carbon electrodes, both of them possessing redox properties. In order to complete the reaction, the oxidation of fuel in the anodic compartment needs to be coupled with the reduction of the oxidant on the cathodic side of the cell. As the overall process incorporates two consecutive but dissimilar electrochemical steps, a pair of often unrelated biological species, catalysing the desired reactions needs to be employed. The oxidation of a highly energetic fuel, occurring at the anode, supplies the cathode with electrons for the enzymatic reduction of a given oxidant [18].

While the redox reactions are electronically separated within the system in order to force the electron flow through an external circuit, the ions generated as a result of the substrate oxidation are free to diffuse across the anodic and cathodic compartments (Fig. 1.3). Unrestricted ionic transfer within the cell maintains the overall charge balance and completes the electronic circuit [3].

Enzymatic biofuel cells, which are the scope of this Ph.D. work, can utilize a wide range of catalysts, dependent on the substrates used (Tab. 1.1 & Tab. 1.2).

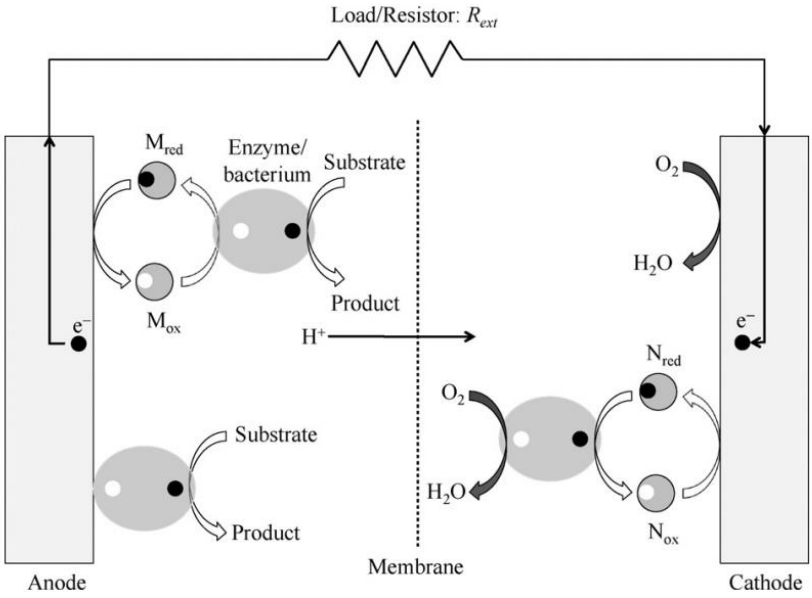


Fig. 1.3. Schematic of an enzymatic/microbial biofuel cell [17].

Tab. 1.1. List of oxidants and respective enzymes typically used for enzymatic biofuel cells. Required co-factors and half-cell reactions are also presented [18].

Oxidant	Enzyme	Metal/ Co-factor	Half-cell Reaction
oxygen	laccase, EC 1.10.3.2	Cu	$O_2 + 4H^+ + 4e^- \rightarrow 2H_2O$
	bilirubin oxidase, EC 1.3.3.5	Cu	see above
	cytochrome oxidase, EC 1.9.3.1	Cu, Fe / heme	see above
	cytochrome c, -	Fe / heme	-
hydrogen peroxide	microperoxidase-11, -	Fe / heme	$H_2O_2 + 2H^+ + 2e^- \rightarrow 2H_2O$
	horseradish peroxidase, EC 1.11.1.7	Fe / heme	see above
	(glucose, GOx) microperoxidase-8, -	Fe / heme	see above
cumene peroxide	microperoxidase-11, -	Fe / heme	$C_9H_{12}O_2 + 2H^+ + 2e^- \rightarrow C_9H_{12}O + H_2O$

Tab. 1.2. Summary of fuels and corresponding biological catalysts typically used for enzymatic biofuel cells together with their co-factors and half-cell reactions [18].

Fuel	Enzyme	Co-factor	Half-Cell Reaction	Natural Acceptor
glucose	glucose oxidase, EC 1.1.3.4	FAD	glucose → glucono-1,5-lactone + $2H^+ + 2e^-$	O_2
	glucose dehydrogenase, EC 1.1.1.47	NAD	see above	NAD
	glucose dehydrogenase, EC 1.1.5.2	PQQ	see above	quinone
	cellobiose dehydrogenase, EC 1.1.99.18	FAD, heme	see above	acceptor
fructose	fructose dehydrogenase, EC 1.1.99.11	FAD, heme	fructose → 5-dehydrofructose + $2H^+ + 2e^-$	acceptor
cellobiose	cellobiose dehydrogenase, EC 1.1.99.18	FAD, heme	cellobiose → cellobiono-1,5-lactone + $2H^+ + 2e^-$	acceptor
lactose	cellobiose dehydrogenase, EC 1.1.99.18	FAD, heme	lactose → 4-O-(galactopyranosyl)-glucono-1,5-lactone + $2H^+ + 2e^-$	acceptor
methanol	alcohol dehydrogenase*, EC 1.1.1.1	NAD	alcohol → aldehyde + $2H^+ + 2e^-$	NAD
	aldehyde dehydrogenase*, EC 1.2.1.5	NAD	aldehyde + H_2O → acid + $2H^+ + 2e^-$	NAD
	formate dehydrogenase*, EC 1.2.1.2	NAD	formate → CO_2 + $2H^+ + 2e^-$	NAD
	alcohol dehydrogenase, EC 1.1.99.8	PQQ, heme	alcohol → aldehyde + $2H^+ + 2e^-$	acceptor
ethanol	alcohol dehydrogenase*, EC 1.1.1.1	NAD	see above	see above
	aldehyde dehydrogenase*, EC 1.2.1.5	NAD	see above	see above
	alcohol dehydrogenase, EC 1.1.99.8	PQQ, heme	see above	see above
glycerol	alcohol dehydrogenase*, -	PQQ, heme	alcohol → aldehyde + $2H^+ + 2e^-$	-
	aldehyde dehydrogenase*, -	PQQ, heme	aldehyde + H_2O → acid + + $2H^+ + 2e^-$	-
	oxalate oxidase*, EC 1.2.3.4	FAD, Mn	oxalate → $2CO_2$ + $2H^+ + 2e^-$	O_2
pyruvate	pyruvate dehydrogenase*, EC 1.2.4.1	NAD	pyruvate + CoA→ acetylCoA + $2H^+ + 2e^-$	NAD
hydrogen	membrane-bound hydrogenase, -	-	H_2 → $2H^+ + 2e^-$	-

*enzymes taking part in complete fuel oxidation

The most frequently employed anodic enzymes are mostly reliant on glucose (glucose oxidase [19-21], glucose dehydrogenase [22, 23], cellobiose dehydrogenase [24, 25]) and ethanol (alcohol dehydrogenase) [26-29] with infrequent reports on lactate (lactate oxidase and dehydrogenase [15]) and glycerol (alcohol and aldehyde dehydrogenase [30]). A number of authors considered the use of even less common hydrogen (hydrogenase [31]) and various intermediates of the citric acid cycle (Krebs cycle) as anodic fuels for the oxidation half-reaction (pyruvate dehydrogenase, citrate synthase, fumarase and malate dehydrogenase [11, 15, 32]). The most common cathodic enzymes include laccase [33-35] and bilirubin oxidase [36-38] for electroreduction of molecular oxygen and a promising application of horseradish peroxidase [39] for H_2O_2 conversion.

In order to complete the oxidation/reduction cycle and collect the current generated as a result of the catalytic reactions, efficient electrical connection between the enzyme's active center and the underlying electrode needs to be established. This can be obtained by

direct (DET) electron transfer, whereby the electrons are exchanged directly between the enzyme and the electrode surface or via mediated transport (MET), which requires small redox molecules capable of shuttling the electrons between the two (Fig. 1.4)

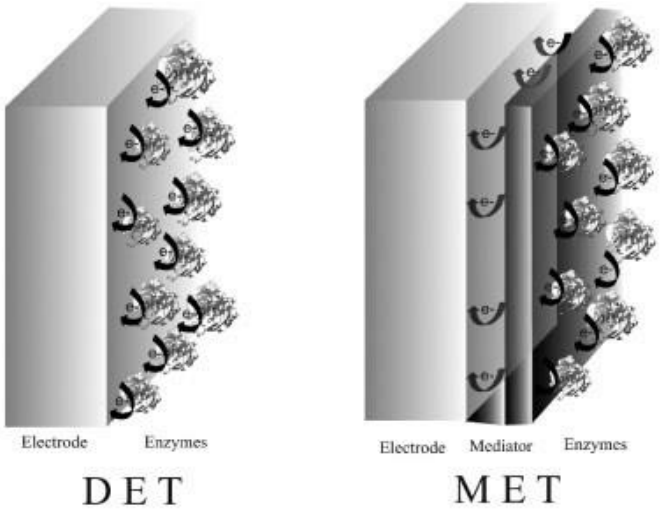


Fig. 1.4. Direct (DET) and mediated (MET) electron transfer mechanisms between the catalyst and the electrode surface in enzymatic biofuel cells [3].

Considering that the catalytic center of most enzymes is buried deeply in the cavities created by the 3D structures of these biomolecules, direct electron transfer is typically not feasible [40, 41] and an auxiliary species, which is enzyme specific, is required in order to achieve the electrical contact (MET) [42]. For instance, anodic oxidation of glucose by GOX often incorporates ferrocene monocarboxylic acid, ferrocenemethanol or pyrroquinoline quinone (PQQ) as e^- shuttling molecules [43]. Mediators are redox reagents, which facilitate the electron transfer between the active component and the electrode. The electrons generated as a result of the enzymatic fuel oxidation are conveyed to the mediator, reducing it to $M1_{red}$. Regeneration of the molecule to its initial oxidized state ($M1_{ox}$) occurs at the anode, where the mediator releases the e^- for consecutive transport to the cathode (through the external circuit). The cathodic mediator temporarily accepts the electrons ($M2_{ox} \rightarrow M2_{red}$) before it shuttles them further to the enzyme for the electro-reduction of the oxidant. The coupled reduction/re-oxidation cycle relies on the ability of the redox mediator to diffuse between two enzymes, which impose certain constraints on maintaining the species in close proximity of both, the catalyst and the electrode surface (Fig. 1.5).

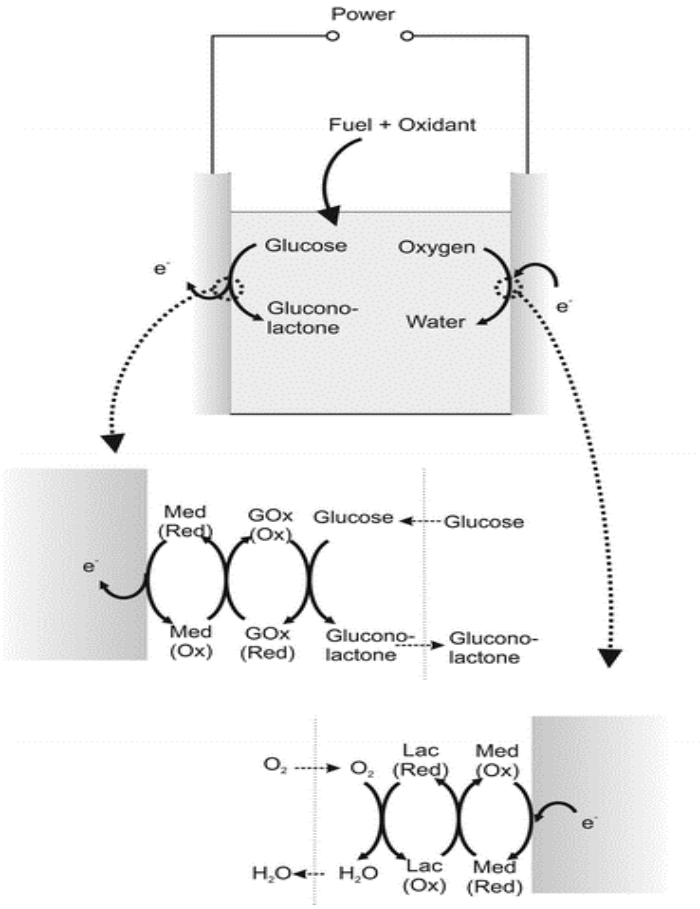


Fig. 1.5. Schematic of an electron transfer mechanism in a glucose/oxygen biofuel cell [44].

Despite the clear distinction between the direct and mediated electron mechanisms, certain systems utilizing a mixture of redox polymers, carbon nanotubes or non-diffusive mediators, which are confined along with the enzyme at the electrode vicinity, can be considered as both DET and MET. Some reported biofuel cell solutions have been categorized on the basis of materials and methods applied in the electrode preparation, with the most prominent being the apoenzyme approach or immobilization in redox polymers and in the presence of various nanostructure elements [45, 46].

The operating principle of a biofuel cell can be, in general, defined by a number of parameters with the short circuit, I_{SC} (current at 0 V), the Open Circuit Potential (OCP) and the cell voltage (E_{cell}) being the prime determinants of the cell performance. In principle, the E_{cell} for a biofuel cell is independent of the current drawn and is understood as a difference in the thermodynamic potentials between the cathode and anode (ΔE_c-E_a), known as the theoretical reversible cell voltage for the overall reaction. In practice, this

value is; however, reliant on a number of factors and can be significantly decreased due to the overpotential ($\Delta\eta$) related to the slow electron transfer at the electrodes, ohmic drop ($\sum\Omega$) reflected by the overall resistance of the system components e.g. membrane, supporting electrolyte and the electrode degradation and wear out effects, as well as concentration losses (Δ£) [3]. In the steady-state condition, and provided spatially distributed reactants, the cell voltage can be approximated by Eq. 1.1.

$$E_{cell} = \Delta_{E_c - E_a} - \Delta\eta - \sum\Omega - \Delta£ \qquad \text{Eq. 1.1}$$

The ΔE_c-E_a can be estimated from the Gibbs free energy change (ΔG) for the reactions occurring at the anode and cathode.

In their comprehensive discussion, Clauwaert and co-workers [47] report three major losses which contribute to the overall overvoltage of the cell: activation overpotentials, ohmic losses and concentration related mass-transport overpotentials. Graphical representation of the potential losses in an operating cell is depicted in Fig. 1.6, adopted from a review by Osman [17]. As illustrated in Fig. 1.6, the activation or charge losses, which are associated with the energy barrier between the mediator/enzyme and the electrode couple, dominate typically at low current values. In principle, the activation losses can be effectively minimized by improving the electrode surface area or by optimizing the overall catalysis and the operating conditions, such as the temperature and the pH of the working buffers. An estimate value of the activation overpotentials can be in theory obtained provided that the reaction rates at the two electrodes are known (e.g. Butler-Volmer reaction). At higher current density, Ohmic losses ($\sum\Omega$) occur. These are reliant on the ionic and electronic resistance to charge transport across numerous cellular components, including the contribution from electrical contacts, current collectors, electrodes, membranes and the interface in between them. The $\sum\Omega$ can be calculated from Ohm's law as a function of the resistivity ρ_i and the thickness l_i of each component i at a generated current density j ($j \sum_i \rho_i l_i$). While the resistivity of the solution can be reduced by altering its composition (without compromising the activity of the enzyme catalyst), the ohmic losses can be minimized by: implementing a higher conductance membrane, decreasing the gap between the electrodes and by establishing a good connection between the individual components [17]. Mass transfer losses, encountered at relatively high current densities (Fig. 1.6) are typically reflected by large concentration gradients,

dominating at the electrode/bulk interface. Component $\Delta\pounds$ is negligible in well-mixed solutions obtained by continuous stirring and recirculation or in air-breathing cathodes, promoting efficient diffusion of O_2.

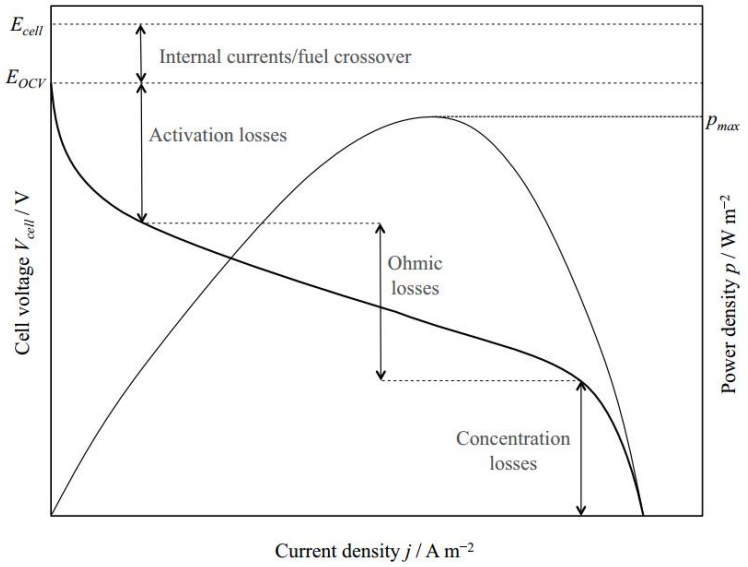


Fig. 1.6. The cell voltage and the power output of an operating biofuel cell as a function of the current density. Typical losses of the cell voltage with the estimated range of the current density at which they occur [17].

The relationship between the actual and theoretical cell voltage depicted in Eq.1.1 provides useful information about the enzymatic electrode. In general, wider thermodynamic potential windows (E_c - E_a), reflected by higher Open Circuit Potential (OCP, the cell voltage at zero-current) values, facilitate improved performance of the biofuel cell and as such have become one of the main determinants of the bioelectrodes composition. Biofuel cells with high OCP and overall reduced resistivity, providing higher current and power outputs, are hence the scope of contemporary research on commercial prototypes.

As the prime function of any existing biofuel cell is energy generation, the essential parameter defining its performance is the power (P) that can be extracted from the device as a result of enzymatic reactions generating electrons. While the power output of the conventional fuel cells is in the orders of mW to kW, the enzymatic biofuel cells operate at much lower power values (μW-mW) and as such are suitable for microelectronic applications.

Another critical measure of the biofuel cell operability is the coulombic efficiency, referred to as the ratio of coulombs produced as a result of the anodic fuel oxidation to the

hypothetical maximum of generated coulombs provided the complete substrate conversion (x 100 %) [48]. Reduced coulombic efficiency can be attributed to several factors, including: alternative reactions which do not lead to current production, mass build-up or fuel and oxidant cross-over, a phenomenon typically encountered in membrane-less configurations [47].

As the magnitude of the operating voltage is dictated by the potential difference at which the oxidation and reduction occur in the cell, the upper limit of the E_{cell} of the enzymatic biofuel cell is determined by the formal potentials of both catalysts and mediators (MET only).

In mediated electron transfer, where additional redox species are required in order to facilitate the electron transport to/from the electrode surface, undesirable thermodynamic losses are recurrently encountered and need to be accounted for. This is due to the fact that the $E_{mediator}$ is typically shifted from that of the catalytic center (E_{enzyme}) to enable the electron exchange. Nevertheless, provided sufficiently large mediator concentrations, the current drawn in MET systems can be relatively high [49].

1.1.5. Cell design and composition.

Classical solution to enzymatic biofuel cell design relies on a two chamber configuration with a permselective membrane separating the areas of the anolyte and catholyte reactions. A pair of enzymes, capable of catalyzing the oxidation-reduction reactions is introduced in the vicinity of the electrodes in a form of a buffered suspension with the mediator or by co-immobilizing the species at the electrochemically active surface. Depending on the origin of the associated redox cofactor or the type of the electrical communication (direct or mediated), the oxidoreductase family can be subdivided into three main groups [50]. The first includes PQQ-dependent dehydrogenases (e.g. alcohol, glucose and glycerol dehydrogenase), which although are structurally dissimilar, all require multiple metal centers and the PQQ coenzyme (Fig. 1.7) tightly attached to the enzyme active site [17].

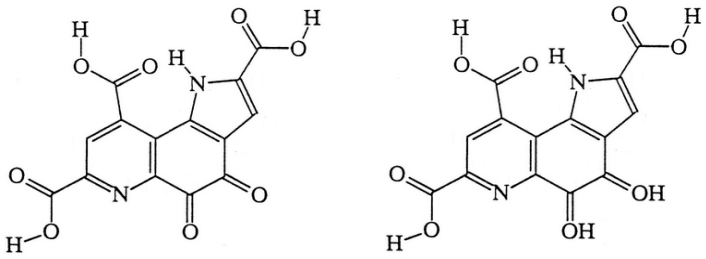


Fig. 1.7. Structure of the oxidized PQQ (left) and reduced $PQQH_2$ (right) forms of the PQQ cofactor (from www.Examine.com).

The second most prominent group consists of catalysts operating in the presence of diffusible and loosely bound nicotinamide adenine dinucleotide (NAD^+/NADH) or its phosphorylated equivalent ($NADP^+$/ NADPH), such as alcohol and glucose dehydrogenases. High mobility of the cofactor enables a certain time lag in the electron transfer to the electrode, particularly relevant in flow-through systems, when the catalytic center of the enzyme may no longer be available locally. In order to confine the protein within the electrode area by e.g. covalent attachment, a certain degree of flexibility must be retained to facilitate reversible movement of the cofactor between the enzyme and the acceptor of the electrons. Fig. 1.8 depicts the structures of the oxidized and reduced nicotinamide cofactors.

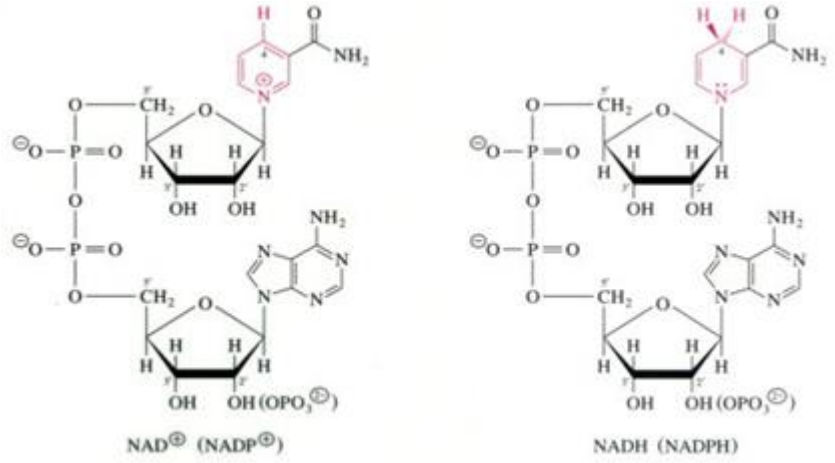


Fig. 1.8. Structure of the oxidized (NAD^+/$NADP^+$) and reduced (NADH/NADPH) nicotinamide cofactors (from web.campbell.edu).

The third and the last group incorporates catalysts dependent on the redox properties of the flavin adenine di- ($FAD/FADH_2$) and mononucleotide ($FMN/FMNH_2$) as shown in Fig. 1.9.

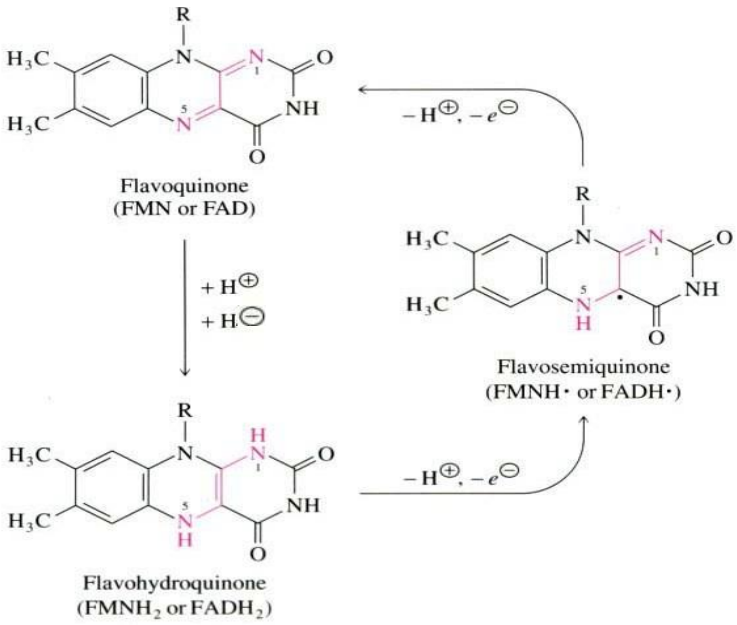


Fig. 1.9. Possible oxidation forms of flavin derived cofactors, FMN and FAD (from web.campbell.edu).

FAD and FMN redox cofactors are buried in the protein structure of the enzyme (e.g. GOX) preventing an easy access to the electrons. Although the redox potential of FAD at GOX's catalytic site is negative in aqueous solutions and can, in principle, be successfully used for DET on the anode, systems employing the enzyme are typically based on mediated electron transfer or a mixed mechanism using nanostructure elements [51].

Conversely, the cathodes of biofuel cells usually incorporate multicopper oxidases, capable of a four-electron reduction of the oxidant (O_2) to water. Typical examples include laccase [52, 53], bilirubin oxidase [54]. While the first requires slightly acidic environment, BOX exhibits the maximum operational activity in neutral or slightly alkaline solutions. Microperoxidase [55] and horseradish peroxidase [56] have also been used as cathodic enzymes.

Numerous reports have suggested that the removal of the physical separator can significantly reduce the internal resistance simultaneously increasing the power and current outputs from the cell. In addition, the single compartment design can facilitate

device miniaturization and reduction of fabrication related costs, offering an attractive strategy in biofuel cell development. Design simplification is possible due to the intrinsic selective nature of enzyme catalysts and diverse immobilization procedures, enabling stable encapsulation of species without compromising their biological activity. The membrane-less approach requires however a careful consideration, in order to minimize potentially low coulombic efficiencies, due to the fuel and oxidant cross-over effects.

Enzyme immobilization techniques

Since the vast majority of biological catalysts are only active for a limited period of time, when free in the solution (up to 7h), immobilization on the electrode surface prolongs their lifetime and operability and allow for a controlled orientation with respect to the electrochemical element.

While the employed immobilization strategy depends strongly on a number of factors, the optimum technique relies, in general, on the individual properties of the incorporated species, their compatibility with the used matrix and the attachment method, the magnitude of the interaction with the support and the ultimate application. Regardless of the method used, the immobilized biomolecules need to be able to retain their native structure and biological activity and must not leach during the operation of the biofuel cells.

The classical division of enzyme immobilization strategies into chemical and physical approaches is depicted in Fig. 1.10, obtained from a recent article published by Taher [57]. Adsorption of catalysts is the most common and straightforward immobilization method. It can be performed in mild conditions, by simple dropcoating of the liquid suspension of the enzyme. However, due to the weak bonds, the stability of adsorbed layer is rather poor and often results in desorption. Covalent bonding of molecules, while very robust and providing short response time; is, in general, an irreversible method, which can potentially produce random and non-uniform species orientation. Cross-linking, is an example of a chemical carrier-free immobilization method, which relies on the use of a secondary cross-linker molecule (e.g. glutaraldehyde). Although this technique is simple and provides improved stability of incorporated proteins, it is difficult to control and often results in large diffusional barriers,

leading to decreased activity of the catalysts. As stated by Hartmann and Jung [58], cross-linking protocol can be a time-consuming and labor intensive procedure, which requires high purity of incorporated proteins. Physical encapsulation or entrapment of catalysts within a biocompatible matrix are one of the most recurrently employed immobilization methods as they enable incorporation of several diverse biomolecules within the same polymer or gel host. The prime disadvantage of the techniques is the potential diffusion barrier between the fuel and the catalytic center, possible leakage of the catalyst and the prerequisite of relatively high monomer concentrations. Additionally as the entrapment requires the polymerization step, the synthesis of the enzyme-polymer composite is restricted by the catalyst dependency on the temperature, pH and the tolerance to various solvents. Example of encapsulation is electropolymerization of species in sol-gel.

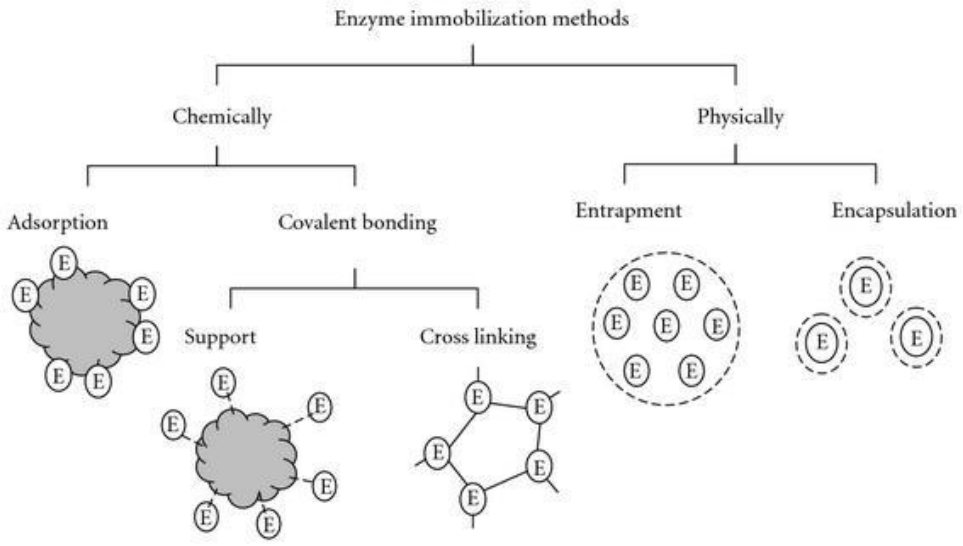


Fig. 1.10.Traditional separation of enzyme immobilization methods into chemical and physical routes [57].

The more contemporary approach to catalyst immobilization is reliant on the type of support used and as such distinguishes: binding to the electrode, cross-linking (support-free method) and encapsulation (Fig. 1.11).

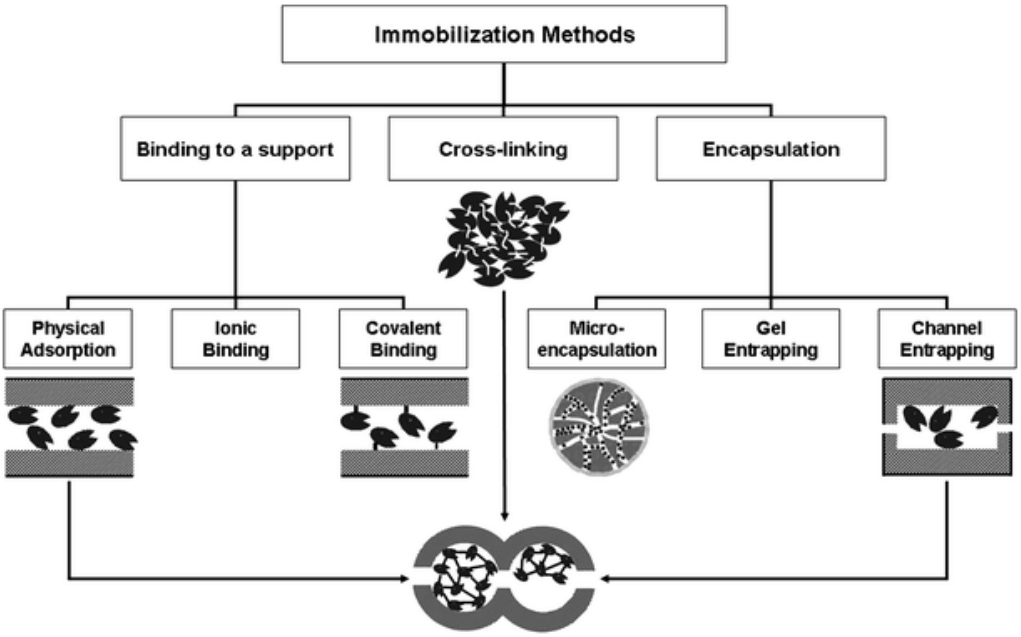


Fig. 1.11.Current division of immobilization techniques based on origin of the support [58].

While each immobilization methodology, bears certain advantages and disadvantages, comparison of various techniques is often difficult, as the assessment of the method is typically made with respect to a free enzyme, not to alternative immobilization approaches [55]. The employed strategy needs to be therefore adapted to the individual properties of the biological species, the source of the carrier used and the ultimate, desired application.

1.1.6. Review of the current state of knowledge.

The amount of attention dedicated to enzymatic biofuel cells is growing very rapidly due to recent advances, which makes their practical applications even more promising. The main strategic scheme relies on the design of biologically driven devices. This approach is capable of utilizing high concentrations of fuels and their complete oxidation to carbon dioxide, leading to significant increase of the cell energy density. In

this regards, miniaturized membrane-less, on-chip BFCs operating in physiological conditions for prolonged periods of time, are of particular interest.

A) Historical account on the biofuel cell development.

Ever since Galvani first discovered the connection between a twitching leg of a frog and the applied electrical current [59], the electrochemical connotation of many biological pathways have been extensively studied and applied in energy oriented research. It soon became apparent that since the electrical action can prompt a biological reaction, the opposite is, in many cases, also possible and the natural biochemical processes can generate electricity upon appropriate stimulation. This would indicate that, in principle, any energy rich biological material (e.g. lactose from cheese industry) can be employed as a fuel for a power source [60].

The first fuel cell, commonly known as "Grove cell" was reported by Sir William R. Grove in 1839, who used a hydrogen anode and oxygen cathode in order to generate electrical current [61]. One of the earliest applications of the energy-harvesting properties of *E.coli* was demonstrated at the University of Durham, by Michael Cresse Potter in 1910 [62]. The author showed that by placing a platinum electrode in a bacterial culture, a difference in potential could be recorded. The work by Potter was further continued by Cohen, at the University of Cambridge, whose research led to the development of what is known nowadays as microbial fuel cells. By connecting a number of half-cells in series, he was able to generate potentials as high as 35 Volts [63]. The true revolution in the biofuel cell development is however dated back to the fall of 1950s and the beginning of 1960s, when the USA government launched a space program, which employed microbial fuel cells as advanced tools for waste disposal treatment in space shuttles. The concept of microorganism based systems has been widely applied since the early 1970s [64, 65] and improved in 1980s, when several research groups suggested that electron transfer mediators can significantly ameliorate the power output [66-68]. Growing awareness of the toxicity and instability of certain redox species diverted the attention to mediator-less microbial biofuel cells, capable of direct electrical contact with the electrode. Early generation of these devices emerged at the end of the 20^{th} century as a technology for waste water treatment and generation of electrical current [69, 70]. Microorganisms used for direct electrocatalysis (e.g. *Shewanella, Geobacter, Rhodoferax*) have been found to be

able to transfer the electrons directly through the cellular membrane with high coulombic efficiency and stability [71, 72].

B) Evolution of enzymatic biofuel cells.

The first account on an enzymatic biofuel cell, utilizing a stand-alone catalyst purified from its cellular medium, has been reported in 1964 by Yahiro and Kimble [73]. The authors employed glucose oxidase, alcohol dehydrogenase and amino acid oxidase in order to construct three different catalytic systems. When studied the performance of each cell, the highest open circuit potential of 350 mV has been recorded for GOX with the lowest output from alcohol dehydrogenase. The driving force behind this discovery was a prospective application of enzyme-driven cells as power sources for medical implants, capable of utilizing organic matter present in physiological fluids. Following their initial discovery, a continuous progress has been made towards the improvement of the power density, operational stability [74, 75] and life time of the enzyme catalysts. Since the energy derived from the enzymatic biofuel cells was still significantly lower than the requirements of typical commercial demands, emphasis on particular micro-applications (e.g. implantable medical devices [6]) has been considered instead. Additionally, due to the poor electron transfer efficiencies and low intrinsic stability of certain biological species, research interest in the late 1960s focused on the electrocatalytic properties of bare metallic electrodes in the enzyme-free biofuel oxidation. At that time, the majority of work investigated the use of platinum in the electrochemical conversion of glucose and other natural metabolites. Despite numerous attempts, the recurring inability of metals to complete the oxidation of biofuels along with electrode passivation problems occurring at low temperatures abolished further research in the area.

After a few years of dormancy, the resurgence in the research activity on enzymatic biofuel cells has been made through investigation of methanol oxidation by alcohol dehydrogenase. The study continued until the end of 1990s and led to a revolutionary discovery by Palmore and Whitesides [76], who reported complete oxidation of MeOH to CO_2 via a cascade of dehydrogenase enzymes: alcohol, formaldehyde and formate. Although the breakthrough did not spark further research on methanol specifically, the finding of Palmore and Whitesides, reinforced by later work by Adam Heller *et al.* on glucose oxidase bioanodes, revitalized the interest in the area of enzymatic

biofuel cells [77]. Heller's variation of the methanol biofuel cell, which employed wiring the GOX to the anode through redox Os polymers, extended the operational time of the enzyme from 8 hours to up to 10 days as compared to the design proposed by Palmore. Following the initial promising results, Heller and co-workers directed their efforts towards the application of biofuel cells in the small electronic devices [78], demonstrating as the first authors that the enzymes immobilized on the anode and cathode can effectively operate in a compartment-less format [79].

One of the earliest functional enzymatic biofuel cells, which did not use glucose, utilized a pyrroloquinoline quinone (PQQ)-modified gold anode and a microperoxidase-11 (MP-11)-functionalized gold cathode [55]. The cell operated based on 1,4-dihydronicotinamide adenine nucleotide (NADH) and hydrogen peroxide, as respective anodic and cathodic fuel and oxidant. While the electrode area was not indicated, the maximum electrical power extracted from the device was 8 μW at an external load of 3 kΩ.

A novel glucose/O_2 biofuel cell was developed soon afterwards neglecting the separation between the electrode compartments. The catalytic system on the anode and cathode consisted of reconstituted enzyme monolayers, glucose oxidase and cytochrome c/ cytochrome oxidase couple. Further major advance in the design of enzyme driven devices was the fabrication of an electroswitchable and tunable biofuel cell based on biocatalysed oxidation of glucose [80]. Implementation of a copper based polyacrylic acid polymer and its ability to change the conductivity depending on the redox state of Cu enabled controlled performance of the biofuel cell alternating between the ON and OFF modes. The authors did not specify the area of the electrode; however, a maximum power of 4.3 μW was drawn from the cell at an external load of 1 kΩ. Similarly, an enzyme based biofuel cell with a pH-switchable oxygen electrode utilizing Boolean logic gates (AND/OR) was reported relatively recently by Hao and co-workers. Electrochemical activity of the cathode was reliant on the current pH value of the solution and hence regulated the magnitude of biochemical reactions occurring in the system [81].

The use of genetically engineered protein catalysts has been first proposed and reported by Yuhashi and co-workers in 2005 [82]. The authors demonstrated a range of synthesized mutants of glucose dehydrogenase with stabilities and overall activity greatly exceeding the characteristics featured by wild-time enzyme. Interestingly, some of the

modified catalysts were capable of withstanding high operational temperatures of up to 70 ºC. When the engineered GDHs were immobilized onto carbon anodes and combined with BOX/carbon cathodes, the power density extracted from the constructed biofuel cell was in the order of 17.6 μW cm^{-2}. Although this value is comparable to the output obtained from the wild-type enzyme, the assembly was found to have an operating lifetime of up to 152 h, which is six time longer than what can be achieved for an unmodified glucose dehydrogenase.

In the early 2000s, Mano and co-workers reported a ground-breaking approach to implantable biofuel cell solution [79]. The authors demonstrated successful power generation from a living plant, driven by the simplicity of the employed method and the minimalistic design. The device was comprised of anodic glucose and cathodic bilirubin oxidases, electrically wired to the electrodes in a form of cross-linked electrostatic adducts with Os polymers (Fig. 1.12).

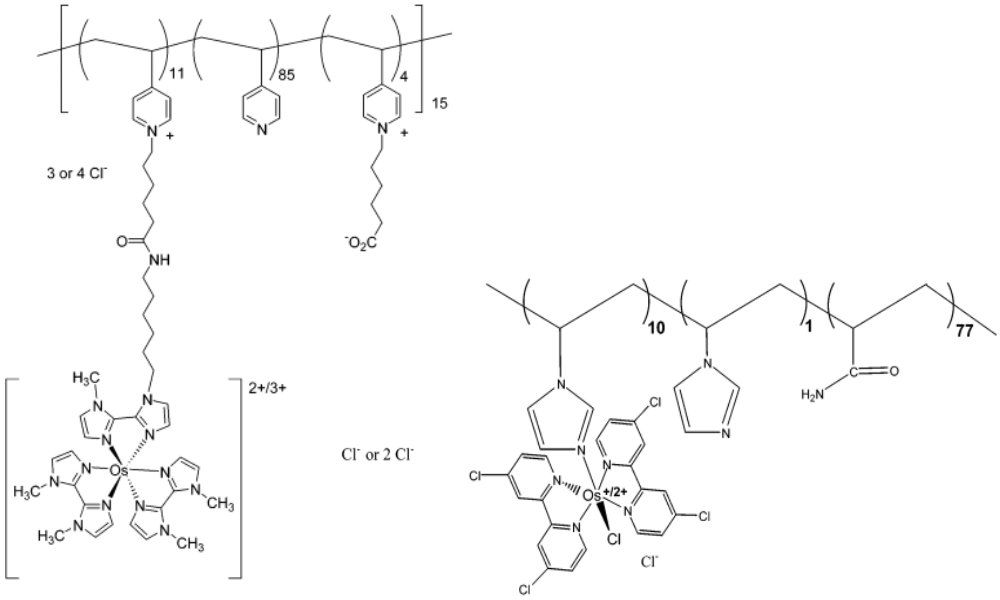


Fig. 1.12. Structures of the anodic (left) and cathodic (right) Os polymers used by Mano to electrically wire GOX and BOX to the electrodes [79].

The constructed biofuel cell generated power density of an astonishing 430 μW cm^{-2} at an operating potential of 0.52 V, when inserted in a grape [79].

One of the first microfluidic platforms for mediated glucose oxidation has been fabricated by Togo and co-workers at the Kyoto University [83]. The cell was composed

of a vitamin K_3-modified poly-L-lysine polymer for the catalytic regeneration of NADH co-factor in the presence of an enzyme, diaphorase (Dp). PLL-VK_3 and Dp were co-immobilised on the surface of the anode and subsequently coated with NAD^+-dependent glucose dehydrogenase (GDH). Addition of a carbon black (Ketjenblack, KB) into the PLL/VK_3/Dp/GDH layer considerably extended the effective surface area of the electrode and consequentially improved the efficiency of biochemical conversions. The glucose/oxygen biofuel cell operated in flowing conditions, at a rate of 1 mL min^{-1}, and reached a maximum power density of 32 μW cm^{-2} at 0.29 V when 5 mM glucose and 1 mM NAD^+ were present in the buffer (pH 7.0). The authors reported a 50 % decline in the power and current efficiencies following an 18 h continuous operation, presumably associated with the swelling of the enzymatic layer. Fig. 1.13 illustrates the design of the microfluidic biofuel cell constructed by Togo *et al*. and comprised of a PDMS flow channel and a glass slide with patterned electrodes.

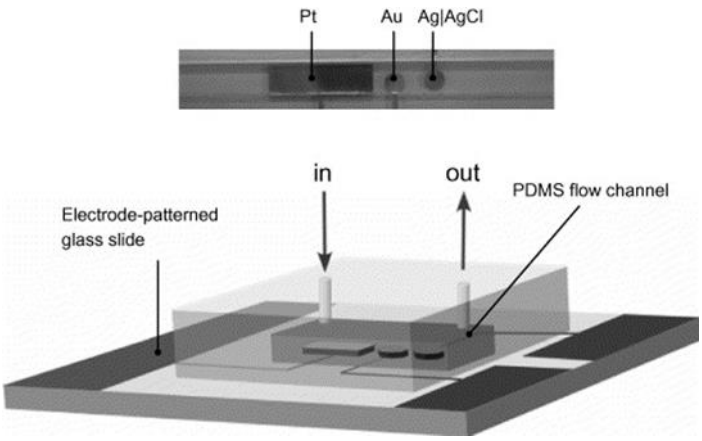


Fig. 1.13. Schematic of the microfluidic cell employed by Togo [83].

Further advancement in the non-compartmentalized, miniaturized approach to the enzymatic biofuel cell design has been reported by Coman and co-workers [84]. The authors proposed a membrane-, mediator- and cofactor-less glucose and O_2 utilizing cell, based on a direct bioelectrocatalysis by cellobiose dehydrogenase (CDH) and laccase as the anodic and cathodic enzymes, accordingly (Fig. 1.14).

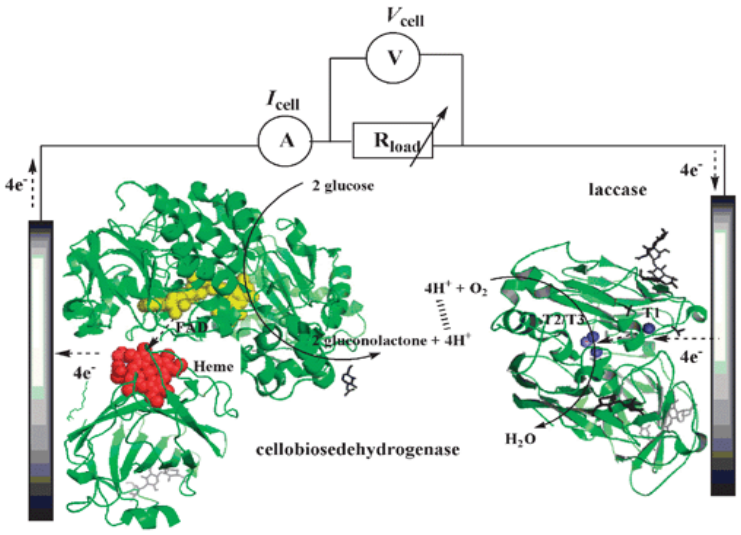


Fig. 1.14. Membrane-, mediator- and cofactor-less enzymatic biofuel cell utilizing CDH and laccase, constructed by Coman and co-workers [84].

The open circuit potential of 0.73 V, the maximum power density of 5 μW cm^{-2} obtained at 0.5 V cell voltage and an estimated half-life of more than 38 h have been demonstrated.

A novel needle-based miniature enzymatic biofuel cell generating power from biofluids abundant in living organisms have been recently demonstrated by a group of Miyake [85]. The assembled device was composed of four needle anodes and an air-breathing carbon based cathode for the electrochemical oxidation of fructose and the electroreduction of oxygen (Fig. 1.15). The maximum power of 26.5 μW (115 μW cm^{-2}) has been extracted from the cell at a potential of 0.34 V, when operating in a raw grape. A light-emitting diode (LED), connected to the device, acted as an indicator of the sugar levels. Although the power generated from the grape was lower than previously reported by Mano [79], the fuel cell exhibited prolonged operability and stability. The electrodes were further coated with a layer of 2-methacryloyloxyethyl phosphorylcholine (MPC)-polymer, an anti-clotting agent, and implanted in a rabbit's ear in order to study the power generated from blood glucose.

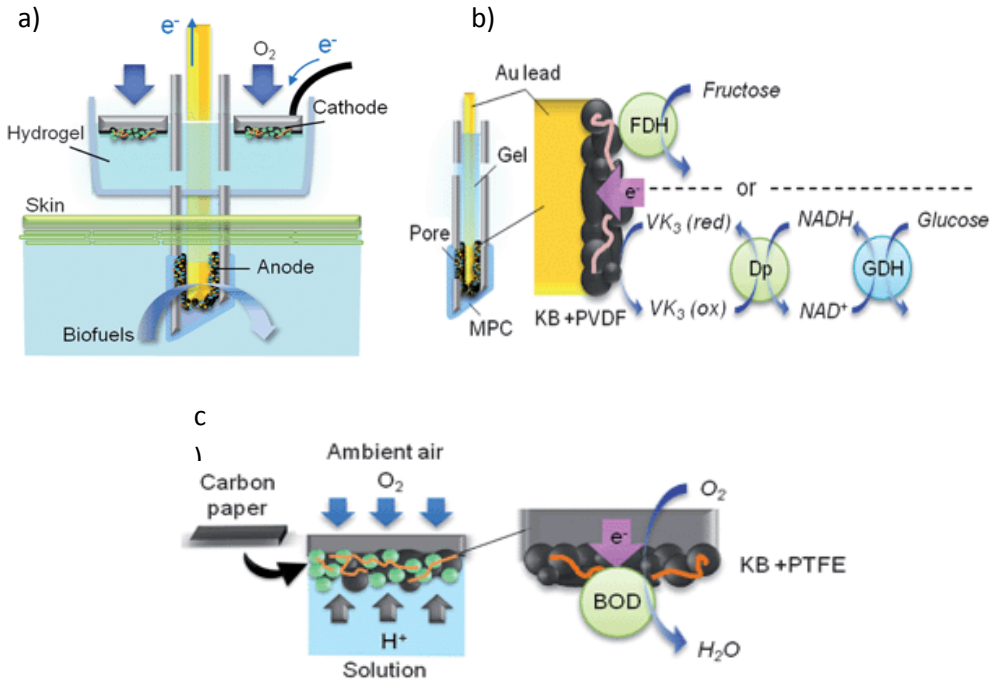


Fig. 1.15 (a) Schematic of a needle based enzymatic biofuel cell designed for power generation in living organisms; (b) Graphical representation of the biochemical oxidation of fructose and glucose at the needle anodes; (c) Diagram of O_2 reduction at the enzymatic air-breathing cathode [85].

In the past few years, the unremitting attention and considerable efforts devoted to enzyme-driven power sources has brought the research on enzymatic biofuel cells into a new era of cutting-edge applications and ground-breaking design solutions. In 2012, Falk and co-workers [86] pioneered a three-dimensional, microscale enzymatic biofuel cell producing electrical energy from human lachrymal liquid (tears). The reported electronic contact lens was composed of gold nanostructured microelectrodes coated with cellobiose dehydrogenase and bilirubin oxidase as corresponding anodic and cathodic bioelements (Fig. 1.16). Although the constructed glucose/O_2 biofuel cell feeding on human tears produced relatively low power density of 1 μW cm^{-2} at a cell voltage of 0.5 V, the operational half-time reached 20 h.

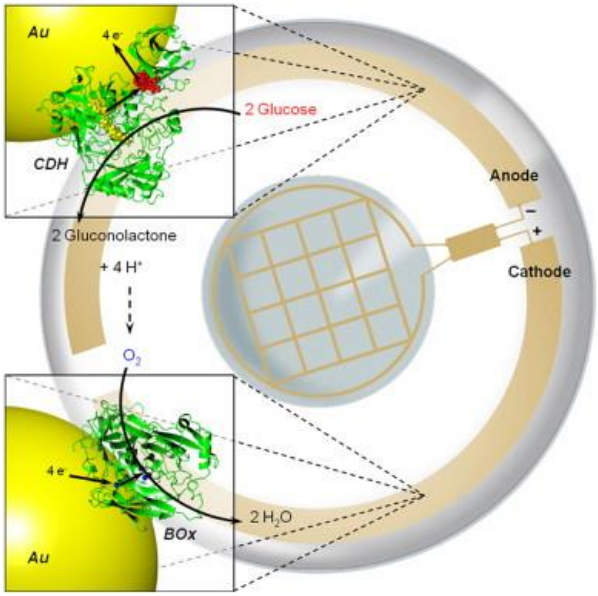


Fig. 1.16. Graphical representation of the electronic contact lens with internal biofuel cell, able to operate using glucose and oxygen present in human tears; reported in [86].

Simultaneously, a group led by Evgen Katz successfully demonstrated the potential of activating the electrical and electronic devices by employing the energy generated in living organisms. The authors reported construction of a biofuel cell integrated in batteries and operating *in vivo* in clams [87]. The electrodes of these devices were composed of compressed carbon nanotubes (CNTs) providing direct, mediator-less bioelectrocatalysis by anodic PQQ-glucose dehydrogenase and cathodic laccase. The "electrified" molluscs were able to produce sustainable energy from their physiological glucose and oxygen stores. Various battery configurations of unspecified surface areas generated power and current of up to 37 μW and 300 μA respectively. The clam-cells were connected to a capacitor, which upon charging to 240 mV, provided 28.8 mJ of accumulated electrical energy.

A novel approach to the fabrication of miniature enzymatic cells has been lately proposed by Haneda and co-workers [88], who used nanoengineered carbon fabric sheets (CF) stacked with agarose film, in order to produce flexible and highly efficient biofuel cell. The constructed fructose/O_2 device operated based on catalytic properties of fructose dehydrogenase (FDH) and bilirubin oxidase (BOX), as shown in Fig. 1.17. Modification of CF with multiwalled carbon nanotubes (MWCNTs for anode) and additional

application of Ketjenblack on carbon strips (cathode) yield approximately 2 mA cm^{-2} of current and 550 μW cm^{-2} of power densities, at a voltage of 0.4V.

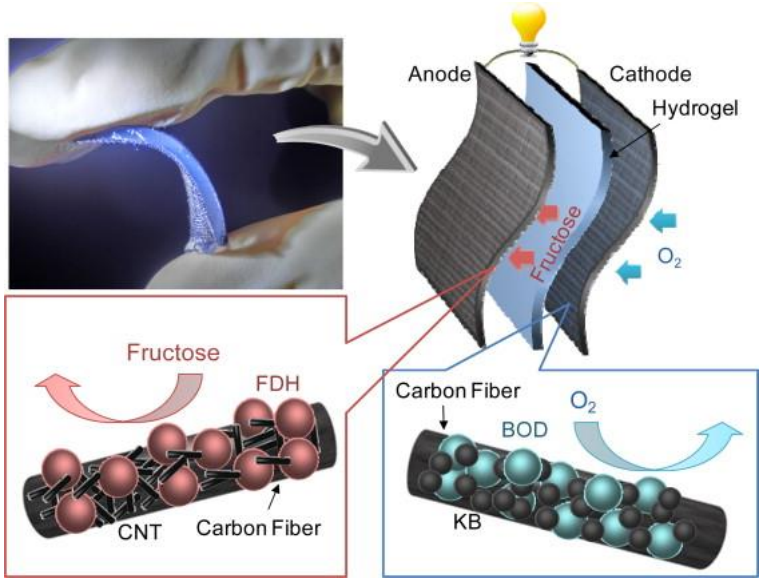


Fig. 1.17. Sheet-shaped fructose/O_2 biofuel cell constructed from FDH and BOX modified carbon fabric electrodes [88].

In the past year, the concept of biofuel cell devices implanted in living organisms has gained new dimensions. With inevitable use of higher organized biological structures as "living batteries" the long anticipated application of enzymatic systems as biocompatible human implants will soon become tangible.

Recent state-of-the-art work by MacVittie and co-workers [89] demonstrated enzyme-based biofuel cells operating in two biotic configurations, in a lobster and as an active component of a fluidic system mimicking the circulation of blood in humans (Fig. 1.18). The cell employed PQQ-dependent glucose dehydrogenase for anodic oxidation of glucose and cathodic electroreduction of oxygen by laccase, immobilized on buckypaper conductive material. As reported by the authors, the operational voltage of the devices was 1.2 V and the amount of energy generated from two lobsters with implanted biofuel cells arranged in series, was sufficient to power an electrical watch. The complex fluidic system, imitating human physiological conditions, was composed of five cells filled with human serum containing normal or pathological levels of glucose. Once connected in series, the biofuel cells generated electrical energy sufficient to power a pacemaker at a cell voltage of 3 V. While the lobster model demonstrates an enzymatic system with future

military and environmental monitoring purposes, the battery based on the serum illustrates palpable prospects for implantable medical devices harvesting the electricity from a human body.

The evolution of the enzymatic biofuel cell research throughout the century, since their first appearance in 1911 is schematically illustrated in Fig. 1.19. As can be seen, the current direction in the biofuel cell development is strongly influenced by the recent advances in the area of nanotechnology.

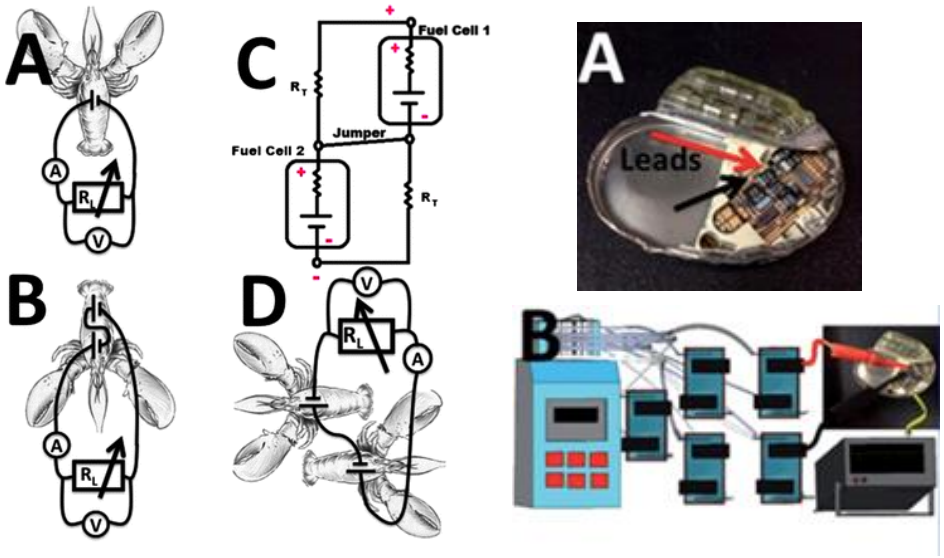


Fig. 1.18. (Left) A cartoon representing different wiring of the electrodes implanted in the lobster: single anode and cathode (A); double set of electrodes (B); the electrical current corresponding to scheme (B) and two pairs of biocatalytic electrodes connected in series and implanted into two different lobsters; (Right) The open pacemaker with removed battery (A) and the schematic of an experimental setup with five biofuel cells electrically connected in series and powering the pacemaker [89].

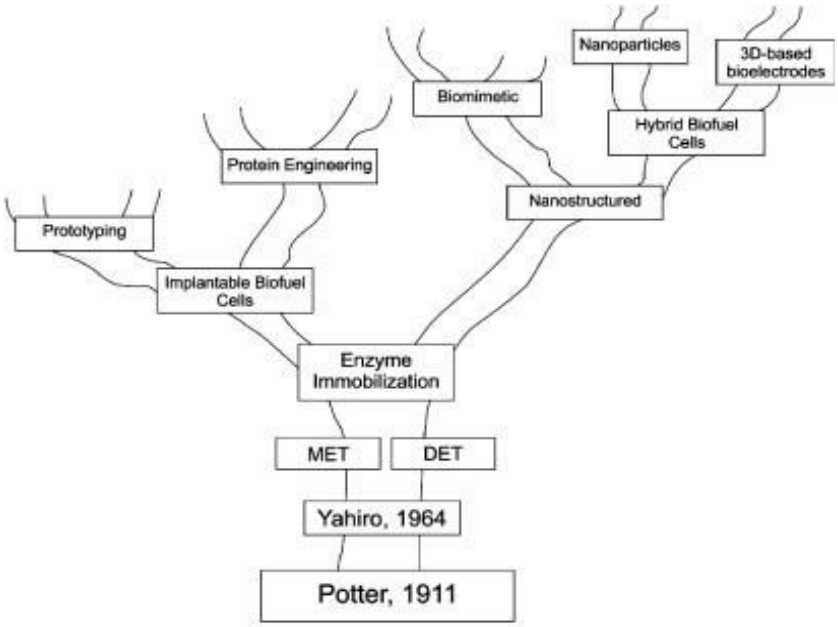


Fig. 1.19. A diagram representing the natural progression of enzymatic biofuel cells according to [3].

Tab.1.3 illustrates major landmarks in the development of enzymatic biofuel cells in the past decade. As indicated, rapid advancement of the materials and methods employed in enzymatic biofuel cells, gradually replaced conventional electrode substrates such as gold, platinum and carbon, with biocompatible conducting polymer hosts capable of efficient electron transfer. Furthermore, the continuous strive to improve the performance of the devices, has led to the enhanced implementation of numerous conductive mesoporous materials with high surface areas (e.g. nanoparticles, nanofibers, nanocomposite electrodes). One of the most recent advances in enzymatic biofuel cells is the application of single- and multi-walled carbon nanotubes, exhibiting excellent electrical properties. According to certain sources densely packed systems of enzyme and mediator catalysts biofunctionalized on the carbon-fiber electrodes retain biological activity and can lead to power densities of up to 1.69 mW cm^{-2} at 0.3 V [90]. With the evolution of the approach to enzymatic biofuel cell, prevailing use of traditional mediators has been gradually substituted by mediated electron transport between the enzyme and the electrode with the use of redox polymers and re-constituted catalysts.

Tab. 1.3. Major developmental milestones for enzymatic biofuel cell research in the past decade [1].

Fuel	Enzyme	Electrode	Electron transfer	OCV (V)	Current density ($\mu A\ cm^{-2}$)	Reference
Glucose/ O_2	GOx/laccase	Carbon fiber electrodes	MET	0.8	64	Chen et al. (2001)
Glucose/ O_2	GOx/BOx	Carbon fiber electrodes	MET	0.84	432	Mano et al. (2002)
Glucose/ O_2	GDH/BOx	Glassy carbon disc electrodes	MET	0.44	58	Tsujimura et al. (2002)
Glucose/ O_2	GOx/COx	Gold electrodes coated with Cu	MET	0.12	4.3	Katz & Willner (2003)
Glucose/ O_2	GOx/BOx	Carbon fiber electrodes	MET	0.68	50	Kim et al. (2003)
Glucose/ O_2	GOx/BOx	Carbon fiber electrodes	MET	0.8	440	Mano et al. (2003)
Glucose/ O_2	GOx/BOx	Carbon fiber electrodes	MET	0.63	244	Mano & Heller (2003)
Glucose/ O_2	GOx/laccase	Carbon fiber electrodes	MET	1.0	350	Heller (2004)
EtOH to CH_3CHO to CH_3COOH	ADH, ADH +AldDH, formaldehyde dehydroge-nase + FDH	Carbon coated with poly(methylene)	MET	0.62	1160	Akers et al. (2005)
Glucose/ O_2	PLL-VK3 / PDMS	Pt	MET	0.55	130	Togo et al. (2007)
Ethanol/H_2O_2	QH-ADH/AOx	Pt	DET	0.24	30	Ramanavicius et al. (2008)
Glucose/ O_2	GDH/PDMS	Pt	DET	0.80	11000	Sakai et al. (2009)
Glucose/ O_2	GOx/laccase	Silicon/ SWNTs	DET	N/A	30	Wang et al. (2009)
Glucose/ O_2	GOx/laccase	Au/SWNTs	DET	0.46	960	Lee et al. (2010)
Glucose/ O_2	PQQ-GDH/BOD	Au/MWNTs substrates	DET	0.60	200	Tanne et al. (2010)
Glucose/O_2	GDH/NB	Glass carbon/ SWNTs	DET	0.35	100	Saleh et al. (2011)

C) Innovative miniature biofuel cells.

With the emerging demand for miniature power supplies for biomedical and electronic applications, micro-scale power systems employing biological catalysts have been under growing consideration for the past decade. The prime reason for the successful candidacy of implantable BFCs is the viable possibility of these devices to substitute

traditional batteries as long-term and self-sustainable power sources, which do not require frequent replacement. Since the successful application of energy-harvesting systems in biomedicine relies on their miniaturization potential, scaling down of the devices has been the main driving force in the contemporary biofuel cell research.

With the current microfabrication technologies and expanding area of microfluidic studies, existing miniature biofuel cells offer significant advances over original design solutions, primarily due to large surface areas to volume ratio, fast response time, enhanced efficiencies and the ability to establish laminar flows. Photolithography, etching, polymer molding or metal deposition [91, 92], are only sample techniques commonly employed in small-scale manufacturing processes enabling the fabrication of highly efficient and long-term power sources operating in a micro-scale format.

- **Micro-scale enzymatic biofuel cells.**

The first functional miniature enzymatic biofuel cell utilizing glucose and O_2 has been demonstrated by Chen and co-workers [77] in 2001. The device was comprised of two 7 μm in diameter and 2 cm long catalyst coated carbon fibers and operated at ambient temperature in an aqueous solution at pH 5.0. The reported electrode areas were 60 fold smaller than those of the smallest prevailing methanol fuel cell and 180 times reduced in size as compared to the minutest biofuel cell at the time. The recorded power density of the biofuel cell was 64 μW cm^{-2} and 137 μW cm^{-2} at 23 ºC and 37 ºC respectively. The observed dependence of the power density on the temperature reflects the thermodynamic behavior of the enzyme catalysts. These results indicated a 5 fold increase in the highest power density ever generated from an enzymatic biofuel cell, which is sufficient to operate small-power consuming CMOS. The following year, Mano *et al.* [93] developed a carbon fiber based micro-scale enzymatic biofuel cell working in physiological conditions. The assembly generated 0.9 J of electrical energy with 1.7 C of a passed charge during a week of a sustainable operation. Based on their initial success, the authors reported a successful development of a miniature single-compartment enzymatic biofuel cell utilizing glucose and oxygen extracted *in vivo* from a grape [79]. The cell produced 2.4 μW at 0.52 V, the amount of power required to operate low-voltage CMOS/SIMOX integrated circuits. The performance of the implant was later improved by increasing the operating voltage to 0.78 V, at pH 5.0 and temperature of 37 ºC. In 2004, a group led by Soukharev [94] developed

a compartmentless glucose/O_2 enzymatic biofuel cell incorporating an innovative cathode, functioning at 0.88 V, the highest cell voltage ever reported for a miniature fuel cell. Improved electron transfer properties have been achieved by cross-linking the laccase to the carbon cathode through a layer of hydrated and conducting hydrogel polymer. Later report on a micro-scale biofuel cell based on glucose and O_2 by Li and co-workers [95] employed single walled carbon nanotube (SWCNT) coated carbon fiber microelectrodes with a power density of 58 μW cm^{-2} at a cell voltage of 0.4 V. 25 % and 50 % power decline have been recorded, following 24 h and 48 h continuous operation with an external 1 MΩ load accordingly.

In an effort to further miniaturize the cell, a number of research groups have demonstrated the use of versatile fabrication methods based on a carbon-micromechanical (C-MEMS) 3D technology.

- **Carbon-MEMS processing of microelectrodes.**

Since the current drawn from the cell is reliant on the active surface area, the electrode dimensions and patterning determine the overall power output. Classical two-dimensional approach to electrode fabrication implies a system of planar anodes and cathodes, typically arranged in parallel and separated by a liquid electrolyte [1]. The C-MEMS fabrication technology emerged in the area of enzymatic biofuel cells relatively recently as a process for manufacturing of carbon based devices with highly complex 3D microelectrode structures (Fig.1.20).

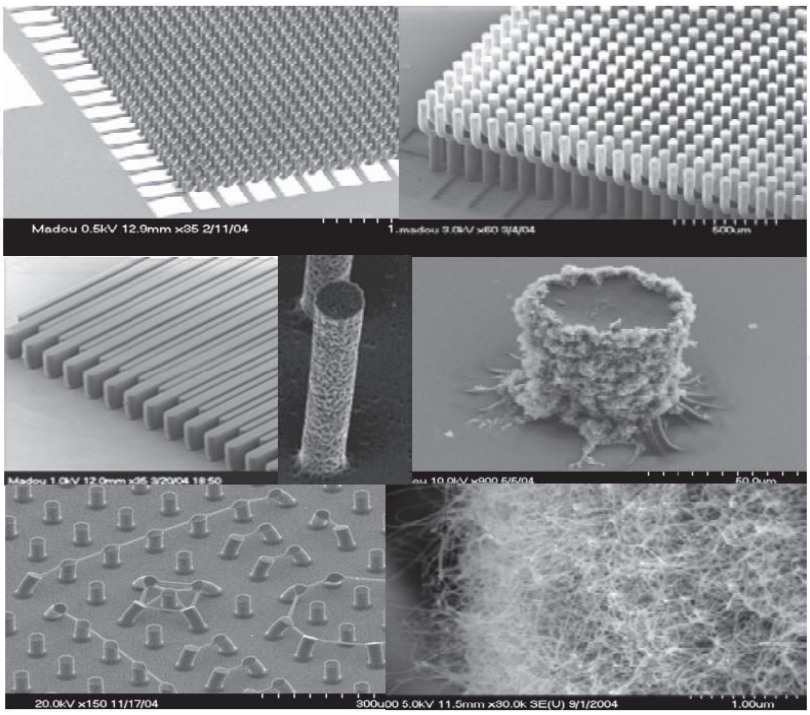


Fig.1.20. SEM micrographs of diverse carbon architectures obtained via C-MEMS [1].

A general diagram of the C-MEMS manufacturing technology is depicted in Fig.1.21. The process involves four subsequent fabrication steps: photoresist coating, patterning and development and ultimately the conversion of the organic polymer (negative or positive resist) into a pyrolytic carbon [96]. The microelectromechanical technology developed originally for powering MEMS and small electronic devices provides high surface area 3D structures which have been successfully employed in the fabrication of electrodes for enzymatic biofuel cells [97].

The use of C-MEMS interdigitated electrodes have been reported lately by Song *et al.* [98] in their work on glucose/O_2 powered enzymatic biofuel cell. According to a more recent report by Madou and co-workers [99], micropatterned carbon electrodes obtained using MEMS strategy, can be successfully functionalized with a catalytic multilayer of enzyme and amine linked redox species (Fig.1.22). Although the technique enables precise control of the feature dimensions, the essential pyrolytic step renders the electrode surface less responsive, thus requiring additional activation by e.g. reactive hydrogel layer [99].

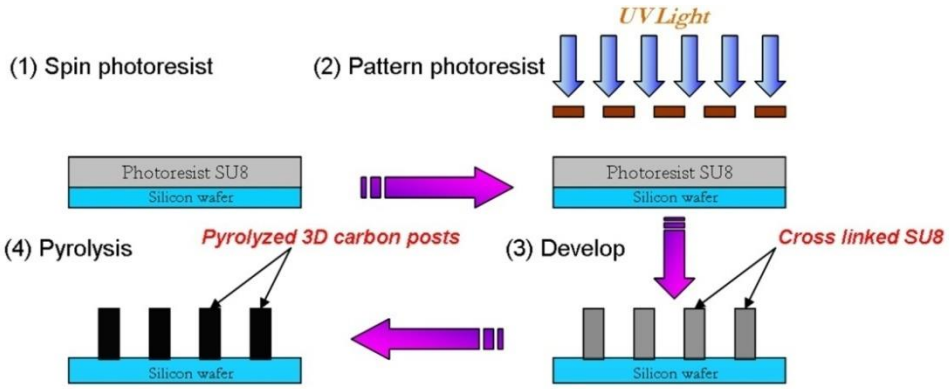


Fig.1.21. Schematic of a typical C-MEMS process [1].

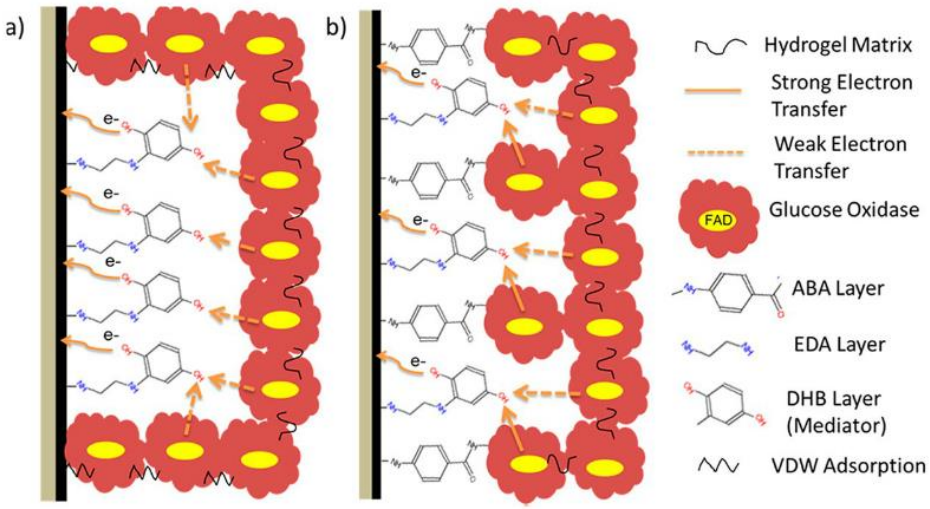


Fig.1.22. Illustration of the C-MEMS fabricated electrodes functionalized with a hydrogel layer of GOX and mediator species a) covalent attachment of the mediator to the electrode; b) mediator and the enzyme co-attached to the micropatterned carbon surface.

A comprehensive discussion on the miniaturized enzymatic biofuel has been proposed by Yang *et al.* as part of the extensive review on biological and electrochemical fuel cells in general [100].

1.1.7. Challenges associated with enzyme-driven cells.

Despite the numerous advantages and potential applications of enzymatic biofuel cells, several key factors need to be considered in order to obtain a practical device. Since the vast majority of enzymes are proteins whose three-dimensional structure is sustained primarily by weak electrostatic interactions, hydrogen bonds and hydrophobic attraction, suitable chemical environment needs to be introduced in order to reinforce and maintain their catalytic functions.

The main challenges in the development of enzyme-based systems are related to the longevity and activity of the protein catalysts, which although highly efficient and substrate-specific, exhibit rather limited life-time in the solution.

The short life-span of the enzymes, which affects the long-term operability of the cell, is attributed to its reduced stability in the experimental environment. Diminished biological functions yield low electron exchange rates between the enzyme active center and the electrode surface and therefore result in small current and power densities, which are the prime shortcomings of various biofuel cell designs [101]. Numerous efforts have been made to address these limitations, in order to improve the performance of the cells [85, 102]. Although the inherent lifetime of the enzymes is in the order of few hours, stable immobilization of the catalyst and relevant storage conditions can significantly extend the longevity of the species [42]. As reported by Moore *et al.* [103], following the encapsulation of dehydrogenase enzyme in tetrabutylammonium bromide modified Nafion membrane, the half-life of the catalyst increased to over 45 days, while in its free form in solution the activity was only recorded for up to 8 h. While the confinement of the enzyme can, in principle, prolong its operability, certain materials and immobilization methods result in restricted electron transfer rates and limited enzyme loading.

Sustainable electrical contact between the enzyme active center and the electrode is another fundamental requirement for successful bioelectrocatalysis and a critical point in the development of enzymatic biofuel cells.

Recent advancement in nanobiocatalysis, offers the possibility to overcome these challenges by introducing a number of highly porous and multifunctional nanostructures as suitable hosts for enzyme immobilization. These include nano-particles, -tubes, -rods or mesoporous materials.

Ever recurring obstacles in the biofuel cell reactions are the mass transfer limitations associated with: 1) the diffusion of fuel or oxidant to the active center of the enzyme; 2) mediated (MET) or direct (DET) electron transport between the catalyst and the electrode and 3) proton exchange across the anolyte and catholyte compartments. As in traditional chemical fuel cells, high resistance of the working solution (or the individual device components) to the mass transfer produces a concentration gradient between the bulk and the site, where the catalysis occurs, typically at the electrode. The resultant built up of products`` slows down the enzymatic reaction and causes electrode polarization [101]. While the performance of porous materials is significantly limited in static environment, operation in flowing conditions should, in principle, facilitate the fuel turn-over and prevent mass transfer limitations associated with small dimensions of the featured electrodes. Correspondingly, application of patterned designs or the introduction of mechanical stirring should alleviate these restrictions.

Certain mediators employed in the electron transfer chain, such as osmium functionalized polymers, have been considered toxic and unsuitable for *in vivo* and on a large scale applications [6]. Osmium metals and compounds have been frequently used in the enzyme studies due to their excellent redox properties, good stability and rich chemistry. While Os itself has been reported rather harmless, in its compact tetroxide form, it is a strong oxidizer and is defined as 'highly toxic' in the USA and 'very toxic' according to the European Union legislation.

Apart from the alleged toxicity of certain mediators, high molecular weight redox molecules often suffer from mass transfer limitations, in particular when incorporated as a part of polymer matrices. While the apparent diffusion coefficient of small size mediators is 10^{-6} ~ 10^{-5} cm^2 s^{-1}, the typical value for generic redox polymers is approximately 3 orders of magnitude lower (10^{-9} ~ 10^{-8} cm^2 s^{-1}). This problem can be however alleviated through a careful design of the materials, for instance by increasing the length of the spacer between the redox center and the polymer backbone [104] or by grafting the active sites onto the polymer bulk.

One of the major shortcomings in the development of enzymatic biofuel cells is the power density, typically measured as the amount of power generated by a single unit of the electrode surface area. Alternatively, the density can be given per volume or weight of the cell. As high enzyme loading will, in principle, yield in amplified current densities, the

corresponding power output from the device should also be increased. Since the majority of enzymes operate at potentials lower than 1 V and the upper limit of current density of 0.2 mA cm^{-2}, the maximum theoretical power that can be extracted from the cell is correspondingly lower than 0.2 mW cm^{-2} [101].These findings have been first suggested by Willner and co-workers in 1996 [105], who studied a randomly packed monolayer of reconstituted GOX immobilized on a surface of flat gold electrode. The maximum current density of a 0.2 mA cm^{-2} was calculated based on the enzyme loading of 1.7 x 10^{-12} mol cm^{-2} (determined by the physical size of the enzyme) and the assumption that all GOX molecules are active in the solution and exhibit a typical substrate turnover of 600 s^{-1}. As glucose oxidase has been long considered one of the most efficient oxidoreductases, the estimated current and power output from other, less effective catalysts, is expected to be much lower [101].

Recent efforts have been dedicated to improve the performance of the enzymatic electrodes by increasing the catalyst concentration in a number of ways. Several research groups [72, 106] have concurrently demonstrated that application of multiple enzyme layers not only facilitates enhanced species loading but also positively influences the performance of the biofuel cell in general, resulting in a two-fold increase in the power density as compared to the prevailing electrode designs.

With emerging tools for nanostructured biocatalysis, gradual introduction of genetically engineered protein catalysts with improved properties and the discovery of novel bioactive species, solution to the aforementioned challenges can be soon envisaged. It has been foreseen, that with the current rate of the advancement in the energy harvesting technologies, continuously driven by economic and environmental applications, biofuel cell research will ultimately be able to meet the commercial demands. To support that statement, Naryanan and Valdez [107], suggested that biofuel cells generating powers of more than 1 mA cm^{-2} may have been already sufficient as cellular phone chargers.

1.2. Objectives of the work.

The prime incentive of this Ph.D. work was a growing demand for efficient and environmentally friendly micro-power sources capable of harvesting energy from the abundant organic matter present in the nature. Extensive research in the field of enzymatic

biofuel cells has led to a significant progress in the area; however, a number of limitations associated with prevailing solutions still exist. In addition to the main parameters defining the performance of any energy harvesting device, such as, the current and power efficiencies; the prime improvements are required with respect to considerable size and structural complexity of the fuel cell design, toxicity of certain reagents, poor stability and longevity of biological catalysts and limited operability of the devices. In order for the biofuel cells to meet the anticipated commercial applications, the associated shortcomings need to be resolved in an effective and cost-efficient manner. In this light, the development of innovative components and attractive electroanalytical methods for the construction of enzymatic biofuel cells with improved performances, were the driving force behind this research work.

The feasibility of a biofuel cell functioning in a macroscopic configuration, reported by a number of authors and demonstrated experimentally in Chapter III, instigated the research towards its micro-scale equivalent. As such, prime efforts have been dedicated towards the development of miniaturized biofuel cell components which could ultimately be assembled in a microfluidic format and successfully operate in physiological or environmental samples.

The investigation carried out as part of this Ph.D. work focused on three major aspects of the enzymatic biofuel cell research.

Mathematical modelling has been employed in order to study the effects of various physical, catalytic and electrochemical parameters on the behaviour of the microscopic flow and the kinetics of the enzymatic reactions (Chapter IV). The purpose of the theoretical studies was to provide recommendation on the optimum design of the microfluidic channels and the electrode geometries, as well as the paramount operational conditions based on predicted catalytic and electrochemical behaviour of the cell.

Majority of the prevailing biofuel cell models reported up to date offer limited architectural solutions and lack in the quality and reproducibility of fabricated devices. In this light, the recommendations obtained from the theoretical studies were further realised in the design of innovative microfluidic platforms for future enzymatic biofuel cells, using the state-of-the-art micro-manufacturing technologies, available at the Tyndall National Institute. The employed fabrication processes provided high precision of generated components, at a nano-scale accuracy, and enabled the use of cost-effective and disposable polymers. The additional investigation of various assembly approaches, offers a practical solution in the development of microfluidic devices for energy harvesting purposes. A

comprehensive description of the cell designs, the applied microfabrication processess and the electrochemical characterization of the in-house produced electrodes, are reported in Chapter V. The functionalization of the electrodes with robust and inert nanoporous gold structures, undertaken as part of Chapter V, suggested promising alternative to conventional surface methods and viable improvement in the fuel cell parameters, e.g. current and power efficiencies.

The investigation of suitable host matrices and enzyme immobilization strategies, essential for the functionality of any biofuel cell is presented in Chapter VI. The most promising methods have been selected and the stable encapsulation and successful catalysis have been demonstrated for a number of biological species confined on both, commercial and in-house microfabricated electrodes. Preliminary characterization of miniature cells in static conditions provides prospective application of proposed fabrication and electrochemical solutions in a fluidic format.

1.3. Bibliography.

1. Song, Y., V. Penmatsa, and C. Wang. *Recent development of miniaturized enzymatic biofuel cell*. in *Proc. of SPIE Vol*. 2011.
2. Winter, M. and R.J. Brodd, *What Are Batteries, Fuel Cells, and Supercapacitors?(Chem. Rev. 2003, 104, 4245-4269. Published on the Web 09/28/2004.).* Chemical Reviews, 2005. **105**(3): p. 1021-1021.
3. Aquino Neto, S. and A.R. De Andrade, *New energy sources: the enzymatic biofuel cell.* Journal of the Brazilian Chemical Society, 2013. **24**(12): p. 1891-1912.
4. Bullen, R.A., et al., *Biofuel cells and their development.* Biosensors and Bioelectronics, 2006. **21**(11): p. 2015-2045.
5. Cracknell, J.A., K.A. Vincent, and F.A. Armstrong, *Enzymes as working or inspirational electrocatalysts for fuel cells and electrolysis.* Chemical Reviews, 2008. **108**(7): p. 2439-2461.
6. Calabrese Barton, S., J. Gallaway, and P. Atanassov, *Enzymatic biofuel cells for implantable and microscale devices.* Chemical Reviews, 2004. **104**(10): p. 4867-4886.
7. Gellett, W., et al., *Biofuel cells for portable power.* Electroanalysis, 2010. **22**(7-8): p. 727-731.
8. Higgins, S.R., et al., *Hybrid biofuel cell: microbial fuel cell with an enzymatic air-breathing cathode.* ACS Catalysis, 2011. **1**(9): p. 994-997.
9. Endo, H., et al., *Wireless enzyme sensor system for real-time monitoring of blood glucose levels in fish.* Biosensors and Bioelectronics, 2009. **24**(5): p. 1417-1423.
10. Arechederra, R. and S.D. Minteer, *Organelle-based biofuel cells: Immobilized mitochondria on carbon paper electrodes.* Electrochimica Acta, 2008. **53**(23): p. 6698-6703.
11. Sokic-Lazic, D. and S.D. Minteer, *Pyruvate/air enzymatic biofuel cell capable of complete oxidation.* Electrochemical and Solid-State Letters, 2009. **12**(9): p. F26-F28.
12. Arechederra, R.L., K. Boehm, and S.D. Minteer, *Mitochondrial bioelectrocatalysis for biofuel cell applications.* Electrochimica Acta, 2009. **54**(28): p. 7268-7273.
13. Bhatnagar, D., et al., *Mitochondrial biofuel cells: expanding fuel diversity to amino acids.* Physical Chemistry Chemical Physics, 2011. **13**(1): p. 86-92.
14. Sokic-Lazic, D., et al., *Oxidation of biofuels: fuel diversity and effectiveness of fuel oxidation through multiple enzyme cascades.* Electroanalysis, 2010. **22**(7-8): p. 757-764.
15. Sokic-Lazic, D., A.R. de Andrade, and S.D. Minteer, *Utilization of enzyme cascades for complete oxidation of lactate in an enzymatic biofuel cell.* Electrochimica Acta, 2011. **56**(28): p. 10772-10775.
16. Atanassov, P., et al., *Enzymatic biofuel cells.* Interface-Electrochemical Society, 2007. **16**(2): p. 28-31.
17. Osman, M., A. Shah, and F. Walsh, *Recent progress and continuing challenges in bio-fuel cells. Part I: Enzymatic cells.* Biosensors and Bioelectronics, 2011. **26**(7): p. 3087-3102.
18. Ivanov, I., T. Vidaković-Koch, and K. Sundmacher, *Recent Advances in Enzymatic Fuel Cells: Experiments and Modeling.* Energies, 2010. **3**(4): p. 803-846.
19. Ivnitski, D., et al., *Glucose oxidase anode for biofuel cell based on direct electron transfer.* Electrochemistry Communications, 2006. **8**(8): p. 1204-1210.

20. Reuillard, B., et al., *High power enzymatic biofuel cell based on naphthoquinone-mediated oxidation of glucose by glucose oxidase in a carbon nanotube 3D matrix.* Phys. Chem., 2013. **15**(14): p. 4892-4896.
21. Shim, J., G.-Y. Kim, and S.-H. Moon, *Covalent co-immobilization of glucose oxidase and ferrocenedicarboxylic acid for an enzymatic biofuel cell.* Journal of Electroanalytical Chemistry, 2011. **653**(1): p. 14-20.
22. Zafar, M.N., et al., *Characterization of different FAD-dependent glucose dehydrogenases for possible use in glucose-based biosensors and biofuel cells.* Analytical and bioanalytical chemistry, 2012. **402**(6): p. 2069-2077.
23. Miyake, T., et al., *Biofuel cell anode: NAD^+/glucose dehydrogenase-coimmobilized ketjenblack electrode.* Chemical Physics Letters, 2009. **480**(1): p. 123-126.
24. Shao, M., et al., *A low-potential glucose biofuel cell anode based on a toluidine blue modified redox polymer and the flavodehydrogenase domain of cellobiose dehydrogenase.* Electrochemistry Communications, 2013.
25. Salaj-Kosla, U., et al., *Mediated electron transfer of cellobiose dehydrogenase and glucose oxidase at osmium polymer-modified nanoporous gold electrodes.* Analytical and bioanalytical chemistry, 2012: p. 1-8.
26. Deng, L., et al., *A membraneless biofuel cell powered by ethanol and alcoholic beverage.* Biosensors and Bioelectronics, 2010. **26**(1): p. 70-73.
27. Fenga, P., et al., *Multiwalled Carbon Nanotubes to Improve Ethanol/Air Biofuel Cells.* Electrochimica Acta, 2013.
28. Forti, J., et al., *Development of novel bioanodes for ethanol biofuel cell using PAMAM dendrimers as matrix for enzyme immobilization.* Biosensors and Bioelectronics, 2011. **26**(5): p. 2675-2679.
29. Ramanavicius, A., A. Kausaite, and A. Ramanaviciene, *Enzymatic biofuel cell based on anode and cathode powered by ethanol.* Biosensors and Bioelectronics, 2008. **24**(4): p. 761-766.
30. Arechederra, R.L., B.L. Treu, and S.D. Minteer, *Development of glycerol/O_2 biofuel cell.* Journal of Power Sources, 2007. **173**(1): p. 156-161.
31. Rüdiger, O., et al., *Enzymatic Anodes for Hydrogen Fuel Cells based on Covalent Attachment of Ni-Fe Hydrogenases and Direct Electron Transfer to SAM-Modified Gold Electrodes.* Electroanalysis, 2010. **22**(7-8): p. 776-783.
32. Narváez Villarrubia, C.W., et al., *Methylene green electrodeposited on SWNTs-based "bucky" papers for NADH and l-malate oxidation.* ACS Applied Materials & Interfaces, 2011. **3**(7): p. 2402-2409.
33. Kavanagh, P., et al., *Performance of a glucose/O2 enzymatic biofuel cell containing a mediated Melanocarpus albomyces laccase cathode in a physiological buffer.* Fuel Cells, 2009. **9**(1): p. 79-84.
34. Brunel, L., et al., *Oxygen transport through laccase biocathodes for a membrane-less glucose/ O_2 biofuel cell.* Electrochemistry Communications, 2007. **9**(2): p. 331-336.
35. González-Guerrero, M.J., et al., *Rapid Prototyping of a Membraneless Glucose/O_2 Microfluidic Enzymatic Biofuel Cells using Pyrolyzed Photoresist Film Electrodes.* Lab Chip, 2013.
36. Filip, J., et al., *Electrochemistry of bilirubin oxidase and its use in preparation of a low cost enzymatic biofuel cell based on a renewable composite binder chitosan.* Electrochimica Acta, 2012.

37. Jose, M.V., et al. *Carbon Nanotube Coated Electrospun Gold Fiber for Mediatorless Enzymatic Biofuel Cell Application*. in *Meeting Abstracts*. 2012. The Electrochemical Society.
38. Liu, C., et al., *Membraneless enzymatic biofuel cells based on graphene nanosheets.* Biosensors and Bioelectronics, 2010. **25**(7): p. 1829-1833.
39. Jia, W., et al., *Glucose Oxidase/Horseradish Peroxidase Co-immobilized at a CNT-Modified Graphite Electrode: Towards Potentially Implantable Biocathodes.* Chemistry-A European Journal, 2012. **18**(10): p. 2783-2786.
40. Sucheta, A., et al., *Reversible electrochemistry of fumarate reductase immobilized on an electrode surface. Direct voltammetric observations of redox centers and their participation in rapid catalytic electron transport.* Biochemistry, 1993. **32**(20): p. 5455-5465.
41. Ferapontova, E.E., T. Ruzgas, and L. Gorton, *Direct electron transfer of heme-and molybdopterin cofactor-containing chicken liver sulfite oxidase on alkanethiol-modified gold electrodes.* Analytical Chemistry, 2003. **75**(18): p. 4841-4850.
42. Moehlenbrock, M.J. and S.D. Minteer, *Extended lifetime biofuel cells.* Chemical Society Reviews, 2008. **37**(6): p. 1188-1196.
43. Harper, A. and M.R. Anderson, *Electrochemical glucose sensors—developments using electrostatic assembly and carbon nanotubes for biosensor construction.* Sensors, 2010. **10**(9): p. 8248-8274.
44. Caruana, D.J. and S. Howorka, *Biosensors and biofuel cells with engineered proteins.* Molecular BioSystems, 2010. **6**(9): p. 1548-1556.
45. Willner, I., et al., *Integrated Enzyme-Based Biofuel Cells–A Review.* Fuel Cells, 2009. **9**(1): p. 7-24.
46. Sarma, A.K., et al., *Recent advances in material science for developing enzyme electrodes.* Biosensors and Bioelectronics, 2009. **24**(8): p. 2313-2322.
47. Clauwaert, P., et al., *Minimizing losses in bio-electrochemical systems: the road to applications.* Applied Microbiology and Biotechnology, 2008. **79**(6): p. 901-913.
48. Liu, H., S. Cheng, and B.E. Logan, *Power generation in fed-batch microbial fuel cells as a function of ionic strength, temperature, and reactor configuration.* Environmental Science & Technology, 2005. **39**(14): p. 5488-5493.
49. Kamitaka, Y., et al., *Fructose/dioxygen biofuel cell based on direct electron transfer-type bioelectrocatalysis.* Physical Chemistry Chemical Physics, 2007. **9**(15): p. 1793-1801.
50. Heller, A., *Electrical connection of enzyme redox centers to electrodes.* The Journal of Physical Chemistry, 1992. **96**(9): p. 3579-3587.
51. Zayats, M., et al., *Reconstitution of apo-glucose dehydrogenase on pyrroloquinoline quinone-functionalized Au nanoparticles yields an electrically contacted biocatalyst.* Journal of the American Chemical Society, 2005. **127**(35): p. 12400-12406.
52. Palys, B., A. Bokun, and J. Rogalski, *Poly- o-phenylenediamine as redox mediator for laccase.* Electrochimica Acta, 2007. **52**(24): p. 7075-7082.
53. Barrière, F., P. Kavanagh, and D. Leech, *A laccase–glucose oxidase biofuel cell prototype operating in a physiological buffer.* Electrochimica Acta, 2006. **51**(24): p. 5187-5192.
54. Tsujimura, S., et al., *Bioelectrocatalytic reduction of dioxygen to water at neutral pH using bilirubin oxidase as an enzyme and 2, 2'-azinobis (3-ethylbenzothiazolin-6-sulfonate) as an electron transfer mediator.* Journal of Electroanalytical Chemistry, 2001. **496**(1): p. 69-75.

55. Willner, I., G. Arad, and E. Katz, *A biofuel cell based on pyrroloquinoline quinone and microperoxidase-11 monolayer-functionalized electrodes.* Bioelectrochemistry and Bioenergetics, 1998. **44**(2): p. 209-214.
56. Pizzariello, A., M. Stred'ansky, and S. Miertuš, *A glucose/hydrogen peroxide biofuel cell that uses oxidase and peroxidase as catalysts by composite bulk-modified bioelectrodes based on a solid binding matrix.* Bioelectrochemistry, 2002. **56**(1): p. 99-105.
57. Taher, H., et al., *A review of enzymatic transesterification of microalgal oil-based biodiesel using supercritical technology.* Enzyme Research, 2011. **2011**.
58. Hartmann, M. and D. Jung, *Biocatalysis with enzymes immobilized on mesoporous hosts: the status quo and future trends.* Journal of Materials Chemistry, 2010. **20**(5): p. 844-857.
59. Galvani, L., *DeViribus Electricitatis In Motu Musculari Commentarius. English translation by RM Green (1953), Cambridge, E*, 1791, Licht Publisher.
60. Davis, F. and S.P. Higson, *Biofuel cells—recent advances and applications.* Biosensors and Bioelectronics, 2007. **22**(7): p. 1224-1235.
61. Appleby, A., *From Sir William Grove to today: fuel cells and the future.* Journal of Power Sources, 1990. **29**(1): p. 3-11.
62. Potter, M. *On the difference of potential due to the vital activity of microorganisms*. Proc. Univ. Durham Phil. Soc. 1910.
63. Cohen, B., *The bacterial culture as an electrical half-cell.* J. Bacteriol., 1931. **21**(1): p. 18-19.
64. Suzuki, S., et al., *Biochemical energy conversion using immobilized whole cells of Clostridium butyricum.* Biochimie, 1980. **62**(5): p. 353-358.
65. Karube, I., et al., *Microbial electrode BOX sensors.* Biotechnology and Bioengineering, 1977. **19**(10): p. 1535-1547.
66. Roller, S.D., et al., *Electron-transfer coupling in microbial fuel cells: 1. comparison of redox-mediator reduction rates and respiratory rates of bacteria.* Journal of Chemical Technology and Biotechnology. Biotechnology, 1984. **34**(1): p. 3-12.
67. Delaney, G.M., et al., *Electron-transfer coupling in microbial fuel cells. 2. performance of fuel cells containing selected microorganism—mediator—substrate combinations.* Journal of Chemical Technology and Biotechnology. Biotechnology, 1984. **34**(1): p. 13-27.
68. Vega, C.A. and I. Fernández, *Mediating effect of ferric chelate compounds in microbial fuel cells with Lactobacillus plantarum, Streptococcus lactis, and Erwinia dissolvens.* Bioelectrochemistry and Bioenergetics, 1987. **17**(2): p. 217-222.
69. Kim, B.-H., et al., *Direct electrode reaction of Fe (III)-reducing bacterium, Shewanella putrefaciens.* Journal of Microbiology and Biotechnology, 1999. **9**(2): p. 127-131.
70. Chaudhuri, S.K. and D.R. Lovley, *Electricity generation by direct oxidation of glucose in mediatorless microbial fuel cells.* Nature Biotechnology, 2003. **21**(10): p. 1229-1232.
71. Min, B., S. Cheng, and B.E. Logan, *Electricity generation using membrane and salt bridge microbial fuel cells.* Water Research, 2005. **39**(9): p. 1675-1686.
72. Schröder, U., J. Nießen, and F. Scholz, *A generation of microbial fuel cells with current outputs boosted by more than one order of magnitude.* Angewandte Chemie International Edition, 2003. **42**(25): p. 2880-2883.

73. Yahiro, A., S. Lee, and D. Kimble, *Bioelectrochemistry: I. Enzyme utilizing bio-fuel cell studies.* Biochimica et Biophysica Acta (BBA)-Specialized Section on Biophysical Subjects, 1964. **88**(2): p. 375-383.
74. Palmore, G.T.R. and G.M. Whitesides, *Microbial and enzymatic biofuel cells.* Enzymatic conversion of biomass for fuels production, 1994. **566**: p. 271-290.
75. Govil, G. and A. Saran, *Biochemical fuel cells.* J. Indian Chem Soc, 1982. **59**(11-12): p. 1226-1228.
76. Palmore, G.T.R., et al., *A methanol/dioxygen biofuel cell that uses NAD^+-dependent dehydrogenases as catalysts: application of an electro-enzymatic method to regenerate nicotinamide adenine dinucleotide at low overpotentials.* Journal of Electroanalytical Chemistry, 1998. **443**(1): p. 155-161.
77. Chen, T., et al., *A miniature biofuel cell.* Journal of the American Chemical Society, 2001. **123**(35): p. 8630-8631.
78. Heller, A., *Miniature biofuel cells.* Physical Chemistry Chemical Physics, 2004. **6**(2): p. 209-216.
79. Mano, N., F. Mao, and A. Heller, *Characteristics of a miniature compartment-less glucose-O_2 biofuel cell and its operation in a living plant.* Journal of the American Chemical Society, 2003. **125**(21): p. 6588-6594.
80. Katz, E. and I. Willner, *A biofuel cell with electrochemically switchable and tunable power output.* Journal of the American Chemical Society, 2003. **125**(22): p. 6803-6813.
81. Hao Yu, E. and K. Scott, *Enzymatic biofuel cells—fabrication of enzyme electrodes.* Energies, 2010. **3**(1): p. 23-42.
82. Yuhashi, N., et al., *Development of a novel glucose enzyme fuel cell system employing protein engineered PQQ glucose dehydrogenase.* Biosensors and Bioelectronics, 2005. **20**(10): p. 2145-2150.
83. Togo, M., et al., *An enzyme-based microfluidic biofuel cell using vitamin K_3-mediated glucose oxidation.* Electrochimica Acta, 2007. **52**(14): p. 4669-4674.
84. Coman, V., et al., *A membrane-, mediator-, cofactor-less glucose/oxygen biofuel cell.* Physical Chemistry Chemical Physics, 2008. **10**(40): p. 6093-6096.
85. Miyake, T., et al., *Enzymatic biofuel cells designed for direct power generation from biofluids in living organisms.* Energy & Environmental Science, 2011. **4**(12): p. 5008-5012.
86. Falk, M., et al., *Biofuel cell as a power source for electronic contact lenses.* Biosensors and Bioelectronics, 2012. **37**(1): p. 38-45.
87. Szczupak, A., et al., *Living battery–biofuel cells operating in vivo in clams.* Energy & Environmental Science, 2012. **5**(10): p. 8891-8895.
88. Haneda, K., et al., *Sheet-shaped biofuel cell constructed from enzyme-modified nanoengineered carbon fabric.* Electrochimica Acta, 2012. **82**: p. 175-178.
89. MacVittie, K., et al., *From "cyborg" lobsters to a pacemaker powered by implantable biofuel cells.* Energy & Environmental Science, 2013. **6**(1): p. 81-86.
90. Sakai, H., et al., *A high-power glucose/oxygen biofuel cell operating under quiescent conditions.* Energy & Environmental Science, 2009. **2**(1): p. 133-138.
91. Kjeang, E., N. Djilali, and D. Sinton, *Microfluidic fuel cells: A review.* Journal of Power Sources, 2009. **186**(2): p. 353-369.
92. wook Lee, J. and E. Kjeang, *A perspective on microfluidic biofuel cells.* Biomicrofluidics, 2010. **4**: p. 041301.
93. Mano, N., F. Mao, and A. Heller, *A miniature biofuel cell operating in a physiological buffer.* Journal of the American Chemical Society, 2002. **124**(44): p. 12962-12963.

94. Soukharev, V., N. Mano, and A. Heller, *A four-electron O_2-electroreduction biocatalyst superior to platinum and a biofuel cell operating at 0.88 V.* Journal of the American Chemical Society, 2004. **126**(27): p. 8368-8369.
95. Li, X., et al., *A Miniature glucose/O_2 biofuel cell with single-walled carbon nanotubes-modified carbon fiber microelectrodes as the substrate.* Electrochemistry Communications, 2008. **10**(6): p. 851-854.
96. Yuan, L., et al., *Nano-structured Sn O_2-carbon composites obtained by in situ spray pyrolysis method as anodes in lithium batteries.* Journal of Power Sources, 2005. **146**(1): p. 180-184.
97. Bisht, G., et al., *Novel Carbon Micro Electrode Array Platform for Enzyme Based Micro Biofuel Cell. www.mmadou.eng.uci.edu*
98. Song, Y. and C. Wang. *A Miniature Glucose/Oxygen Biofuel Cell based on C-MEMS Interdigitated Electrode Arrays*. in *Meeting Abstracts*. 2011. The Electrochemical Society.
99. Bisht, G.S., et al., *Diffusion-Free Mediator Based Miniature Biofuel Cell Anode Fabricated on a Carbon-MEMS Electrode.* Langmuir, 2012. **28**(39): p. 14055-14064.
100. Yang, J., et al., *Miniaturized biological and electrochemical fuel cells: challenges and applications.* Phys. Chem., 2013. **15**: p. 14147-14161
101. Kim, J., H. Jia, and P. Wang, *Challenges in biocatalysis for enzyme-based biofuel cells.* Biotechnology Advances, 2006. **24**(3): p. 296-308.
102. Fischback, M.B., et al., *Miniature biofuel cells with improved stability under continuous operation.* Electroanalysis, 2006. **18**(19-20): p. 2016-2022.
103. Moore, C.M., et al., *Improving the environment for immobilized dehydrogenase enzymes by modifying Nafion with tetraalkylammonium bromides.* Biomacromolecules, 2004. **5**(4): p. 1241-1247.
104. Mao, F., N. Mano, and A. Heller, *Long tethers binding redox centers to polymer backbones enhance electron transport in enzyme "wiring" hydrogels.* Journal of the American Chemical Society, 2003. **125**(16): p. 4951-4957.
105. Willner, I., et al., *Electrical wiring of glucose oxidase by reconstitution of FAD-modified monolayers assembled onto Au-electrodes.* Journal of the American Chemical Society, 1996. **118**(42): p. 10321-10322.
106. Winder, R., *Alcoholic fuel.* Chemistry and Industry, 2003(17): p. 15.
107. Narayanan, S., et al., *Handbook of Fuel Cells—Fundamentals.* Technology and Applications, 2003. **4**: p. 1133.

CHAPTER II

EXPERIMENTAL PROCEDURES

Progress in science depends on new techniques, new discoveries, and new ideas, probably in that order.

Sydney Brenner

2.1. Chemicals and Biological Reagents.

All reagents used for the purpose of this thesis are listed in an alphabetical order in Tab. 2.1 and Tab. 2.2. All chemicals and biological species are of analytical grade (95 % at least) and were used without further purification. All solutions were prepared fresh prior to any experimental work using nano-pure water with a resistivity of 18.2 MΩ cm from ELGA Ltd.

2.2. The electrochemical setup.

All electrochemical measurements require a working set-up where the reaction can occur. The integral part of the electrochemical work station is an electrochemical cell with two or three electrodes. The cell is connected to a potentiostat which controls the potential applied to the working electrode and measures the current being produced as a result of an electrochemical reaction. In order to collect the data, the potentiostat is connected to a computer, which can operate the required electrochemical software. To reduce electromagnetic noise, which could potentially interfere with the results obtained, the electrochemical cell is predominatingly placed in a Faraday cage while the measurement is being taken (Fig.2.1). For the purpose of this research all electrochemical studies were performed using a CH Instrument Potentiostat hardware version CHI 660B or CHI 620B (IJ Cambria, Burry Port, Wales, UK).

Tab. 2.1. List of chemical reagents and their suppliers.

Chemical reagent	Supplier	CAS No.
ABTS [2, 2'-azino-bis (3-ethylbenzothiazoline-6-sulphonic acid)]	Sigma-Aldrich	30931-67-0
Acetone	Sigma-Aldrich	67-64-1
D-(+)-Glucose, ≥ 95 %	Sigma-Aldrich	50-99-7
D-Sorbitol, 98 %	Sigma-Aldrich	50-70-4
Chitosan, medium molecular weight	Sigma-Aldrich	9012-76-4
Ethanol	Sigma-Aldrich	67-17-5
FDM [1,1- Ferrocene dimethanol]	Sigma-Aldrich	1291-48-1
FCA [Ferrocene monocarboxylic acid]	Fluka	1271-42-7
GPS [3-(Glycidyloxypropyl) trimethoxysilane], 98 %	Sigma-Aldrich	2530-83-8
Heptane, anhydrous, 99 %	Sigma-Aldrich	142-82-5
Isopropyl alcohol, ≥ 99.7 %	Sigma-Aldrich	67-63-0
Methanol	Sigma-Aldrich	67-63-0
MPTMS [(3-Mercaptopropyl) trimethoxysilane], 95 %	Sigma-Aldrich	4420-74-0
NAD^+ [β - Nicotinamide Adenine Dinucleotide]	Sigma-Aldrich	53-84-9
Nitric acid, 70 %	Sigma-Aldrich	7697-37-2
o-Phenylenediamine	Sigma-Aldrich	95-54-5
PBS [Phosphate Buffered Saline]	Sigma-Aldrich	-
PDDA [Poly (diallyldimethylammonium chloride)]	Sigma-Aldrich	26062-79-3
PDMS [Polydimethylsiloxane] Sylgard®184 Silicon elastomer kit	Dow Corning	8050-81-5
PEI [Polyethyleneimine]	Fluka	9002-98-6
Potassium chloride	Sigma-Aldrich	7447-40-7
Potassium dicyanoaurate (I)	Sigma-Aldrich	13967-50-5
Potassium dicyanoargentate	Sigma-Aldrich	506-61-6
Potassium ferricyanide (III)	Sigma-Aldrich	13746-66-2
Prime coat adhesive (92-023)	Ellsworth Adhesives	-

	Ltd/Dow Corning	
Prussian Blue [Iron(III) ferrocyanide]	Sigma-Aldrich	14038-43-8
Sodium hydroxide	Fluka	1310-73-2
Sodium L-lactate	Sigma-Aldrich	867-56-1
Sodium phosphate dibasic, ≥ 99 %	Sigma-Aldrich	7558-79-4
Sodium phosphate monobasic, ≥ 99 %	Sigma-Aldrich	7558-80-7
Sodium sulphate	Fluka/Riedel-de-Haën	7757-82-6
Sulfuric acid, 95-98 %	Sigma-Aldrich	7664-93-9
TEOS [Tetraethyl orthosilicate], ≥ 99 %	Alfa Aesar	78-10-4
TMOS [Tetramethyl orthosilicate], 98%	Alfa Aesar	681-84-5
Tris [Tris (hydroxymethyl) aminomethane], ≥ 99.8 %	Sigma- Aldrich	77-86-1

Tab. 2.2. List of enzymes and their suppliers.

Biological species	**Supplier**	**CAS No.**
Bilirubin oxidase from *Myrothecium verrucaria*	Sigma-Aldrich	80619-01-8
Diaphorase from *Bacillus stearothermophilus*	Unitika	-
D-Sorbitol dehydrogenase from *Gluconobacter oxydans*	Amano Enzyme Inc.	-
Glucose oxidase from *Aspergillus niger*	Genzyme	-
Laccase from *Trametes versicolor*	Sigma-Aldrich	80497-15-3
Lactate oxidase from *Pediococcus sp.*	Sigma-Aldrich	9028-72-2

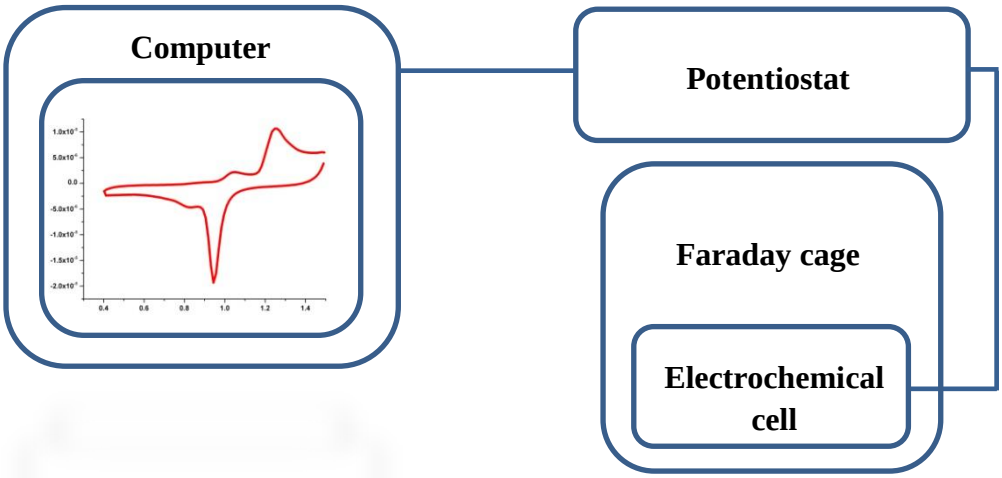


Fig. 2.1. Experimental set-up for the electrochemical measurements.

In general, we can distinguish two types of electrochemical cells: *electrolytic* and *galvanic.* Any devices, which convert chemical energy into electrical energy such as biofuel cells, are considered to be *galvanic cells* and these are the research scope of this Ph.D. dissertation. In this type of devices the enzymatic reaction in a half-cell is carried out by protein catalysts as soon as the relevant potential is applied to the electrode (as described in Appendix A).

The electrochemical measurements, unless stated otherwise, were conducted using a standard three-electrode system comprised of working (WE), also known as the *indicator electrode*; counter (CE) and reference (RE) electrodes. Each of the electrodes plays a particular role in the electrochemical cell. The electrochemical reaction accompanied by the corresponding WE current takes place at the interface between the working electrode and the supporting electrolyte, while the CE supplies the electrons to the reaction at the working electrode. The RE provides a stable electrochemical potential used as a reference level for the application of the stimulation potential to the WE.

A three-electrode cell set up is by far the most common system used in electrochemistry. As shown in Fig. 2.2, the current flows between the WE and CE, while the potential difference is applied between the working and reference electrode and set to be equal to the value specified by the user. This configuration allows the potential across the electrochemical interface at the WE to be controlled with respect to the RE. Due to the

physical separation of the WE and RE in solution, some ohmic losses exist (*Uncompensated resistance*). These can be partially compensated for by using a capillary that brings the two electrodes close together. Since miniscule current flows into the reference electrode, a very small voltage drop across the capillary is generated, fixing the potential at the end of it to a value, which is very close to the actual potential of the RE.

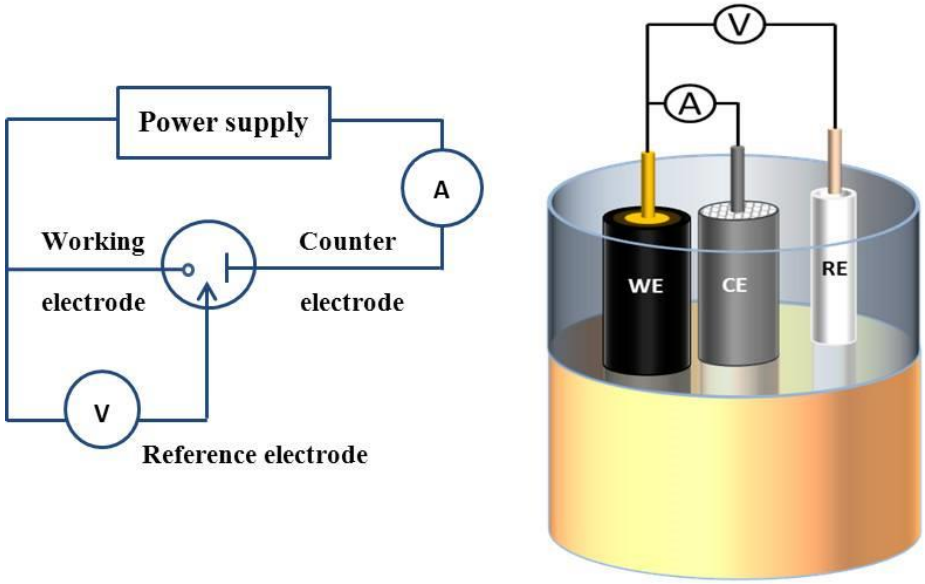


Fig. 2.2. Diagrams representing the three- electrode electrochemical system.

Two-electrode cells are often used to measure small current values, when the simplification of the set-up is a key factor. Here, the counter and reference electrodes are usually merged together, Fig. 2.3 [1].

Potential across the cell involves the contributions from the interface between the counter electrode and the electrolyte as well as from the electrolyte itself. The two electrode configuration is often employed when one is interested in the behavior of the cell as a whole and when a precise control of the potential across the WE is not crucial. Two-electrode system is frequently employed in the energy harvesting and storing devices, such as, batteries and fuel cells. Additionally, this configuration is also widely used in electrochemical impedance measurements at frequencies higher than 100 kHz [1]

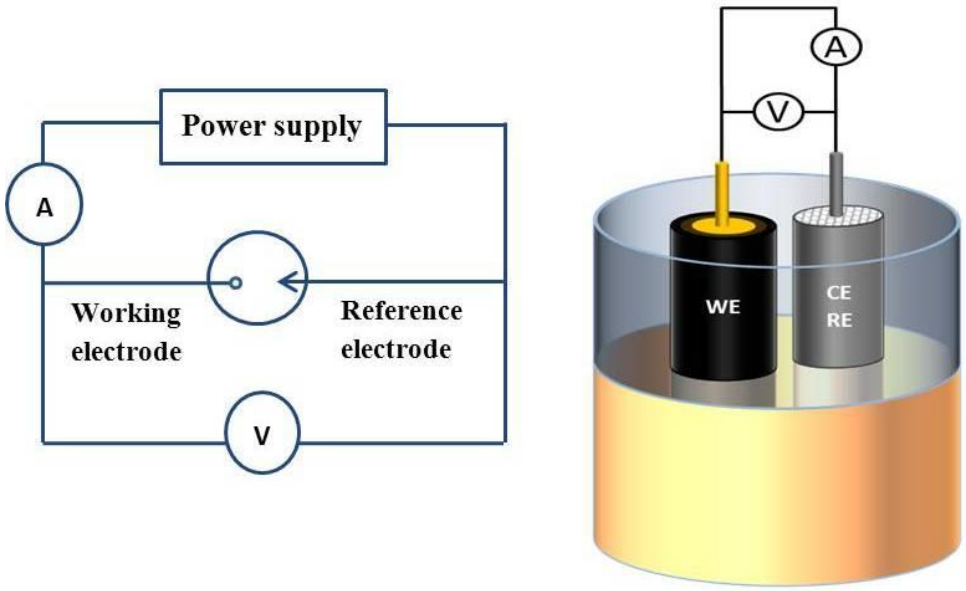


Fig. 2.3. Diagrams representing the two-electrode electrochemical system.

Working electrodes by definition can be metals or semiconductors and they can exist in a solid or liquid form. The same concerns the counter and reference electrodes; however, these need to be chemically inert and must not interfere with the reactions occurring at the working electrode.

Working Electrode

The working electrode is the interface at which the reaction of interest occurs in the electrochemical cell. In bioelectrochemistry, it is usually the reduction or oxidation of biological species being studied. Depending on the application, a variety of metal and carbon based materials are used as working electrodes provided that they are conductive, chemically stable and reactive towards the species analyzed. Common working electrodes consist of noble metals (gold or platinum) or carbon materials (glassy carbon, graphite, carbon paste). The size and the shape of the working electrodes also vary and they depend greatly on the particular application. For many decades commercial macro size disc/probe shaped electrodes, often coated with a blanket of an insulating epoxy, have been predominating in electrochemical studies. With the recent trend towards device miniaturization and emerging novel applications a new era of microfabricated (screen printing, soft lithography etc.) electrodes has arisen in the electroanalytic measurements in

the past years. New generation of electrodes provides increased sensitivity to the electroactive species under investigation and improved electron transfer properties, making them ideal candidates to study the electrochemistry of biomolecules, in particular enzymes and cells. Commercial disc electrodes are; however, a point of reference when studying the behavior of unknown species. They are still frequently used for standard electrochemical protocols, as well characterized and with a highly reproducible response. A variety of commercial macro electrodes were used for the purpose of this research. The majority of results presented in the following chapters were obtained using three types of working disc electrodes: gold (Au), platinum (Pt) and glassy carbon (GC). The diameter of gold and platinum was 2 mm and the glassy carbon – 5 mm, resulting in the electrode surface areas of 7.07×10^{-2} cm^2 and 19.64×10^{-2} cm^2 respectively.

Electrodes microfabricated in due course of this PhD research were obtained by electroplating a thin layer of Au and Pt (100 nm thick) as anodes and cathodes for the biofuel cell respectively. The underlying titanium coating (20 nm thick) acted as an adhesive for the prevailing metal. A number of electrode layouts with various size and electrode numbers were investigated in the study. Micro-electrodes were then appropriately modified with enzyme containing polymer based films and gold nanostructures (NPG).

Reference electrode (RE)

The potential of the working electrode is always given with respect to the reference, implying that the transfer of electrons within the WE is observed or controlled within a specified range. The reference electrode has a constant make up and a fixed and well-known potential that should not vary with the potential applied to the working electrode. An ideal reference maintains a constant potential regardless of whether it operates as the anode or cathode and irrespective of the current that is driven through the cell. This means that any fluctuations in the electrochemical cell correspond to the changes at the working electrode only. To fulfill these requirements the RE must provide a constant supply of all the species involved in the reference electrode reaction with their activity being constant at all times. The reference electrode must also be chemically stable, robust and unaffected by the evaporation processes that may occur when used discontinuously. High stability of the reference electrode is usually achieved by a redox system (buffered or

saturated) composed of constant concentrations of all species involved in the reference reactions.

For the purpose of this research Ag|AgCl|KCl, 3M KCl (CH Instruments, IJ Cambria, Burry Port, Wales, UK) was used as RE (Fig. 2.4).

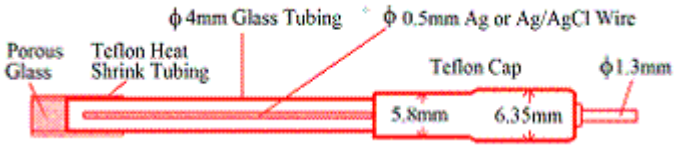


Fig. 2.4. Schematic of a reference electrode (from www.ijcambria.com).

The electrode is comprised of a silver wire covered in AgCl and immersed in a 3 M KCl solution confined in glass tubing. The bottom end of the electrode is sealed with porous glass cap that provides the contact point with the solution during the electrochemical measurement.

The Ag|AgCl|KCl reference electrode half-reaction is given by Eq. 2.1 and it generates a potential of E^0 = 0.22 V vs. the standard hydrogen electrode.

$$AgCl + e^- \rightleftarrows Ag + Cl^- \qquad Eq.\ 2.1$$

Counter electrode (CE)

Counter is the electrode that is used to close the current circuit in an electrochemical cell. In the three-electrode set up the auxiliary electrode provides the current necessary for the reaction at the working electrode to take place. By applying more negative potentials to the working electrode, the energy of electrons raises resulting in a flow of electrical charge from the electrode to solution, provided by the counter as so called *reductive current*. Likewise, imposing more positive potential will cause the flow of electrons from the solution towards the electrode, giving rise to an *oxidative current* [1]. The critical potentials at which these processes occur are dependent on the *formal potentials* (E^0) of the electroactive species and are very important when studying the electrochemistry of enzyme modified electrodes. CE also minimizes the impact of any

inaccuracies that can arise from the cell resistance when controlling the potential. In the process of choosing the CE it is important to take into consideration the fact that some electrodes electrolyze in the solution forming products that can potentially interfere with the electrochemical processes under investigation. Nevertheless, the electrochemical properties of the majority of counter electrodes usually have little or no influence on the behavior of the working electrode and as such the CE can in most instances be of any source desired. One existing requirement for the CE is that the surface area of the counter has to be significantly greater than the working electrode counterpart in order to prevent the kinetic limitations of the reaction at the WE. In voltammetric studies the counter electrode is typically made of an inert material such as Pt (wire, mesh or a coil), Au or carbon and usually does not participate in the electrochemical reaction itself. The counter electrode used in this study is a Pt coil, also from CH Instruments (IJ Cambria, Burry Port, Wales, UK). Commercial electrodes used in this study are pictured in Fig. 2.5.

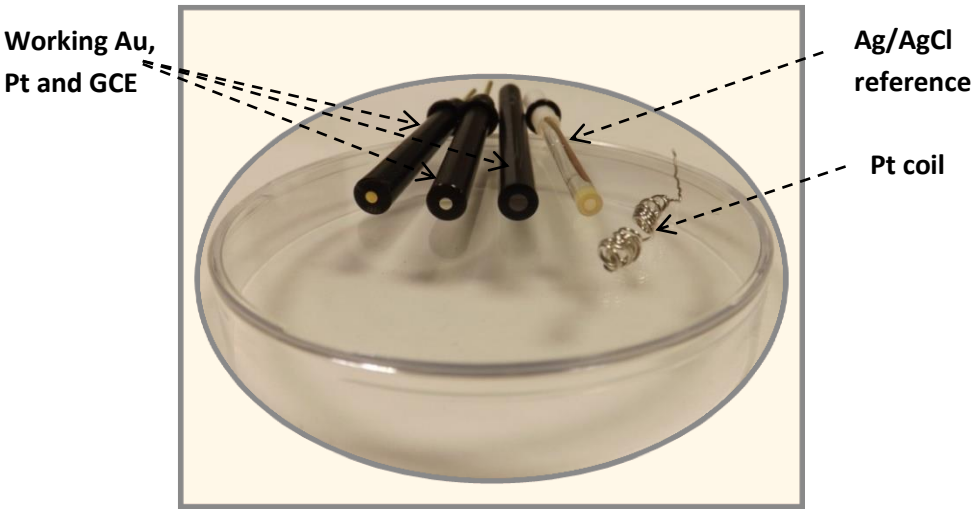


Fig. 2.5. Disc gold, platinum and glassy carbon working electrodes, Ag/AgCl (in 3 M KCl internal electrolyte) reference and platinum coil counter used for electrochemical studies.

2.3. Instrumentation.

The cleaning of microfabricated electrodes was performed using oxygen plasma asher (Harrick Plasma, New York, USA). Surface properties of bare and thin film modified electrodes were investigated through contact angle measurements using *DataPhysics* Contact Angle System OCA Instruments (Germany). Visual characterization of the samples was carried out by scanning electron microscope (Quanta 650 FEG, FEI, Oregon USA) and a high-resolution optical microscope (Nikon America Inc.). Features hot-embossed in Zeonor were investigated using SEM and Tencor measurements (Tencor Alphastep 200 system, CAE, USA). The preliminary experiments in flowing conditions were performed using a syringe pump (KD Scientific, USA). Homogeneity of samples and solutions was obtained using a sonicator (UltraWave, UK). Buffered substrate and mediator solutions were pre-warmed in a Heareas oven (Cruinn Diagnostics Ltd, Dublin, Ireland) to a desirable temperature prior to any measurements of catalytic activity of the enzymes used.

2.4. Glassware, chemical compounds and biological reagents.

Glassware was thoroughly washed with Dekon 90 (Decon Laboratories Ltd., East Essex, UK), rinsed with copious amounts of de-ionized water and small amounts of IPA following which they were dried under the stream of nitrogen.

Pt coil electrode was cleaned by immersing it in 70 % nitric acid overnight prior to any measurement.

Chemicals used for this study were purchased from the following suppliers: Sigma-Aldrich/Fluka (Ireland, Ltd Dublin), Alfa Aesar GmbH & Co KG (Karlsruhe, Germany) and Ellsworth Adhesives Ltd (Germany). Enzyme catalysts were obtained from Genzyme (Ireland, Ltd Waterford) and Sigma-Aldrich (Ireland, Ltd Dublin. D-Sorbitol dehydrogenase from *Gluconobacter oxydans* was kindly donated by the Amano Enzyme Inc. (Japan). All enzymes and cofactors were used without further purification.

Zeonor chips (1 mm thickness, 100 piece packaging) were purchased from the *microfluidic ChipShop* GmbH (Jena, Germany).

Phosphate and acetate buffers were prepared on a monthly basis using appropriate salt and acid solutions in DI in respective v/v ratio. Buffers were autoclaved and stored at 4 ºC while not in use.

Solutions for the modification of the electrode surface and samples containing substrates and mediators for the enzymes were prepared fresh before any measurement and electrode functionalization.

Sterile autoclaved tips, disposable Eppendorfs and plastic containers were used when preparing enzyme solutions.

2.5. Electrode cleaning procedures.

Electrode cleaning is a crucial procedure which should be performed prior to any electrochemical measurements, in particular when working on the surface modification of the electrode material. In general, most cleaning protocols involve multiple consecutive mechanical and electrochemical steps to ascertain complete removal of contaminants of any source (organic and inorganic). Mechanical cleaning relies on polishing the electrode surface with either diamond paste or alumina powder suspended in water. Solid metal or carbon based electrodes, where the active electrode component is contained in a non-metal coating (e.g. disc electrodes) are resilient to physical damage during the mechanical step. The electrodes with thin layers of metals, fabricated in-house by deposition techniques, cannot be however cleaned mechanically. Depending on the robustness of the electrodes, often determined by the thickness of the metal and the underlying adhesive layers, electrochemical cleaning or oxygen plasma treatment may need to be applied exclusively.

Electrochemical cleaning

Wet, electrochemical treatments typically employ the use of H_2SO_4 either in a form of a mixture with H_2O_2 (Piranha solution) or by electrochemical potential cycling in 1 M acid solutions. Piranha solution is a highly corrosive and strong oxidizing agent and is used only routinely when other less aggressive cleaning methods fail. Piranha is employed frequently to clean microelectrodes as it successfully removes most organic residues at a nano scale and hydroxylates the surface making it more hydrophilic. Electrochemical cleaning in H_2SO_4 is performed by cycling the electrode potential over a range of values at

a fixed scan rate, until repeatable voltammograms are obtained (usually 100–200 cycles). Cleaning of Au surfaces typically requires a potential of 0.4 V to 1.6 V vs. Ag/AgCl to be applied to the electrode, while the potential window for Pt is not as broad (-0.2 V to 1.3 V vs. Ag/AgCl).

Plasma treatment

A mild alternative to acid treatment is plasma cleaning. Plasma is a partially ionized gas composed of ions, radicals and neutral molecules that removes organic impurities and contaminants from the material surface and introduces additional polar groups improving its hydrophilic properties. Unlike Piranha it does not employ strong oxidizing chemicals. The joint cleaning agent in this case is a UV light generated in the plasma and reactive oxygen species. The UV breaks down organic contaminants and Low Molecular Weight Molecules (LMWM), which in turn bind to oxygen generating water and CO_2. Plasma treatment leaves the surface "grafted" with polar functional groups that can be functionalized with various reactive species in the surface modification step (Fig. 2.6).

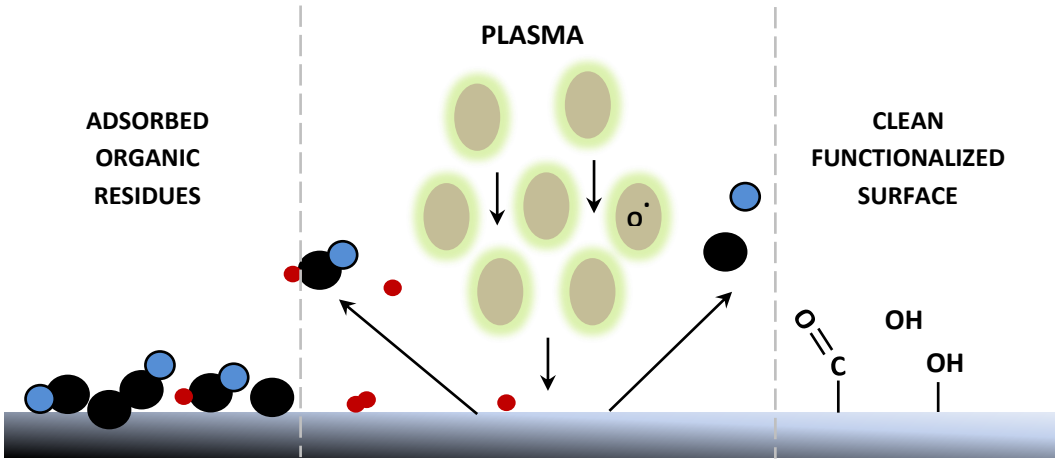


Fig. 2.6.General schematic of a plasma cleaning process.

Whether or not the plasma treatment has been successful can be further assessed by contact angle measurements. Compared to traditional wet methods, plasma offers an attractive alternative to time consuming and labor intensive cleaning procedures (Tab. 2.3).

Tab. 2.3. Comparison of plasma cleaning and wet chemical cleaning.

Plasma Cleaning	Wet Chemical Cleaning
Process controlled by adjusting the power, pressure, gas type, cleaning time	Processes dependent on the nature of chemical reagents, their concentration, potential applied, processing time
Majority of gases used for plasma generation are non-toxic	Most of the inorganic acids and organic solvents are harmful and pose danger
User friendly, no special training required	Require experience in handling the chemicals
In successful cleaning no organic residues remain	Organic contaminants may exist which may require further cleaning steps
No waste as gaseous by-products are harmless	Large volumes of liquid organic waste requiring specialized treatment and a subject to safety regulations

Plasma treatment improves the wettability and hydrophilic properties of the surface under investigation, therefore can be used as a bonding technique for variety of materials (e.g. PDMS, glass). The role of plasma activation in the substrate assembly has been discussed in Chapter V.

2.5.1. Cleaning protocol for commercial disc electrodes.

For the purpose of this research, cleaning of all disc electrodes involved polishing with alumina powder of decreasing particle size (1 µm; 0.3 µm; 0.05 µm), followed by sonication in a 1:1 mixture (v/v) of absolute EtOH and DI water to remove any remaining alumina powder. This procedure was repeated twice and the electrodes were rinsed with DI water and dried in a stream of nitrogen. Following the initial polishing step, electrodes were exposed to oxygen plasma (power set to high, pressure of approximately 900 milliTorr) for a period of 20 min after which they were carefully rinsed with DI water and IPA alternately. The final cleaning step involved potential cycling in 1 M sulfuric acid until a stable response was obtained. As for most electrochemical measurements, the

treated electrode was used as the working electrode and platinum coil was the counter. All polarization plots are given with respect to Ag/AgCl as the reference. Potential ranges for cleaning of gold and platinum were as follows: 0.4 V and 1.6 V for Au and -0.2 V to 1.3 V for Pt.

2.5.2. Cleaning procedure for electrodes microfabricated on Zeonor.

Electrodes on Zeonor substrates were fabricated by metal deposition and for that reason they were not suitable for mechanical polishing as each cleaning cycle can induce thin films of metal to peel off damaging the electrode. Au and Pt electrodes on polymer were first cleaned in the oxygen plasma at high power and approximately 900 milliTorr of pressure. Plasma treatment was repeated three times, following each cycle the electrode was rinsed with copious amounts of DI and IPA and dried in a stream of nitrogen. Electrodes were then cleaned electrochemically in 1 M H_2SO_4 for a period of approximately 3 h.

2.6. Electrochemical measurements.

Electrochemical studies were conducted in a cell placed in a Faraday cage and connected to a potentiostat. The Faraday cage is an important part of an electrochemical set up as it minimizes electromagnetic noise that could potentially interfere with the measurement. The electronic hardware was connected to a personal computer via external interface, enabling a complete control over the parameters applied in the study. Depending on the application a two- or a three-electrode configuration has been used, in each the electrodes were connected to the potentiostat with the aid of “crocodile clips”.

Fig. 2.7 and Fig. 2.8 illustrate a typical set-up employed during the electroanalysis with three- and two-electrode systems, respectively.

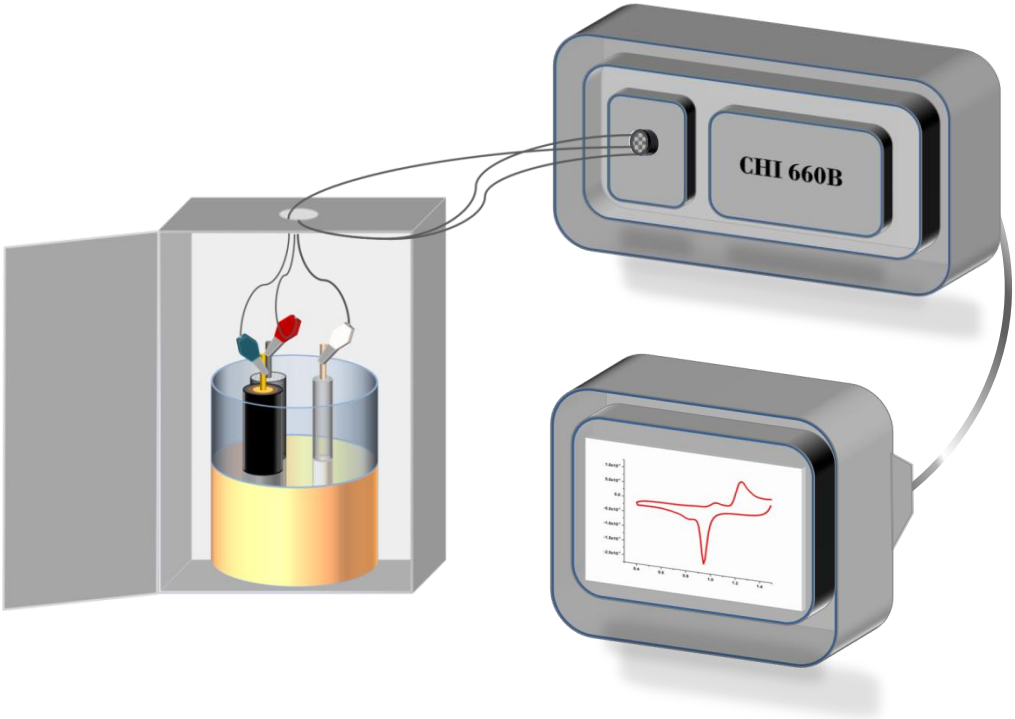


Fig. 2.7. Schematic representing the three-electrode set-up composed of the electrochemical cell, potentiostat and personalized computer.

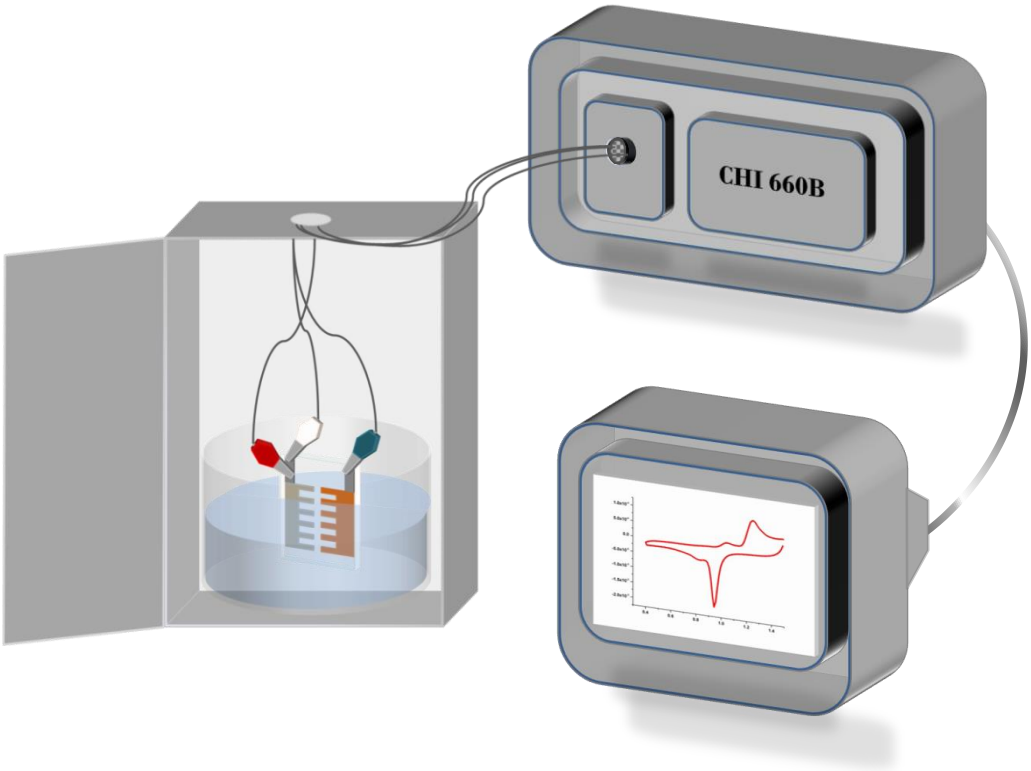


Fig. 2.8. Graphical representation of the two-electrode configuration composed of the electrochemical cell, potentiostat and personalized computer.

The surface modification and the electrochemical characterization of the electrodes on Zeonor substrates alone were performed using a custom-made holder, depicted in Fig. 2.9, fabricated in the Mechanical Workshop at the University of Lorraine in Nancy, France.

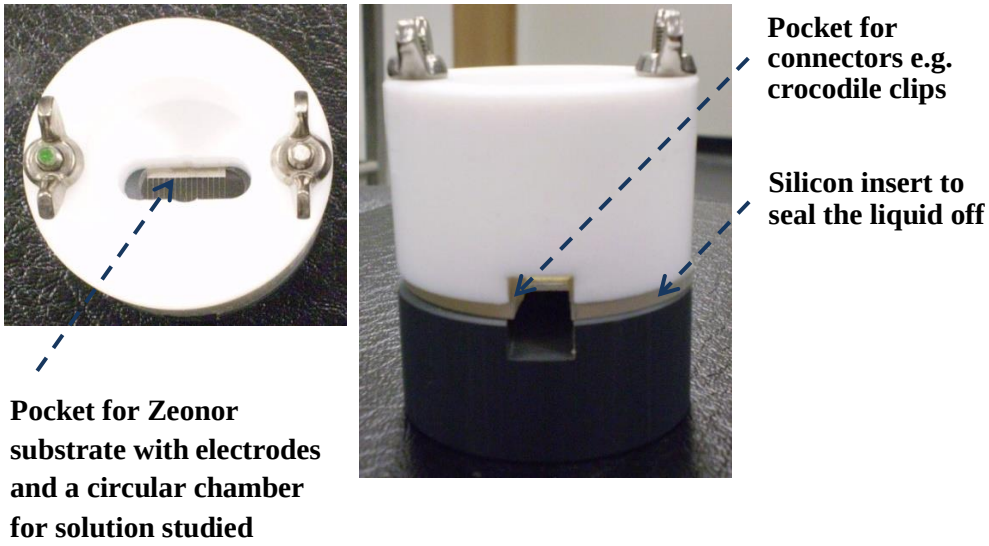


Fig. 2.9. Holder used for the modification and electrochemical testing of microfabricated electrodes.

The holder is comprised of two main components separated by a water tight insert and held in place by metal screws. The design includes a bottom compartment accommodating the microfluidic chip with electrodes and a pocket for connectors, as well as a top part containing a solution chamber.

The experiments with assembled microfluidic devices, conducted mainly in static conditions, employed a microfluidic holder, depicted in Fig. 2.10. The clamp was comprised of a bottom unit accommodating the electrodes patterned in Zeonor and the top part bearing the channel.

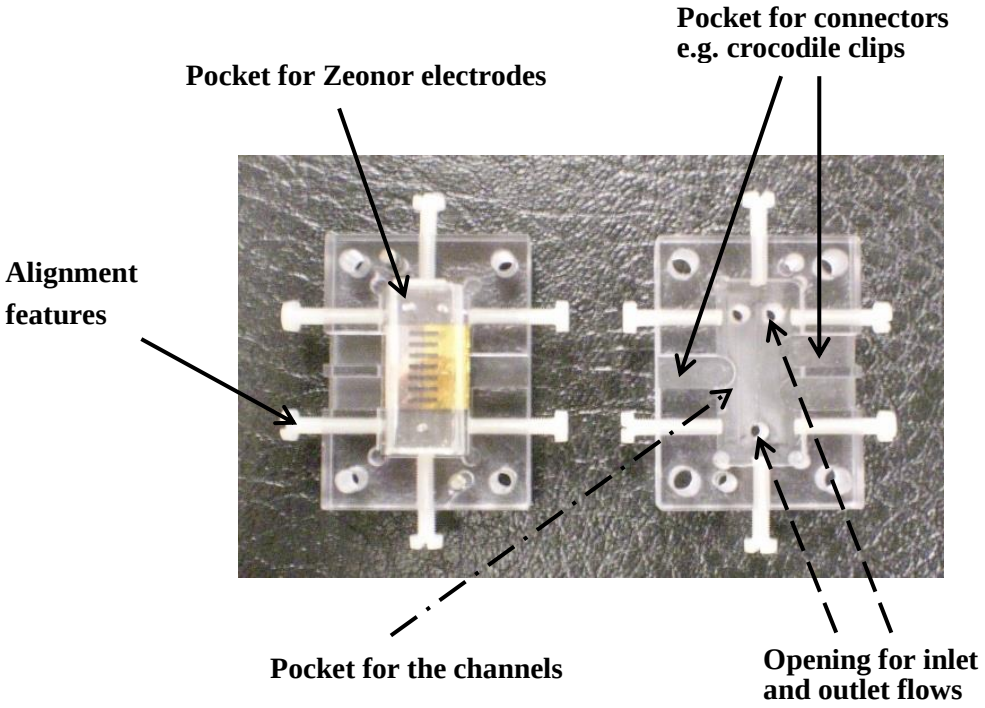


Fig. 2.10.Fabricated microfluidic holder for electrochemical measurements of electrodes on a chip intended for static and flowing conditions.

2.7. Material choice for the electrode and channel substrates.

Indium thin oxide (ITO) has been initially considered as the material of choice for the electrode compartments. Nevertheless preliminary studies with ITO indicated a significant loss of the material integrity and electrical properties during the metal evaporation step. This has been attributed to incompatible thermal conditions in the reaction chamber, caused by severe overheating. In this view, ITO was substituted with gold and platinum. Cyclo-Olefin-Polymer (COP), Zeonor, was selected as the support material for the fabrication of the electrodes, predominantly due to its suitable physicochemical and mechanical properties [2]. Polydimethylsiloxane (PDMS) was employed as the source substrate for the channel patterning, as described in Chapter V.

2.8. Microfabrication of gold and platinum electrodes.

Gold anodes and platinum cathodes have been microfabricated in the Central Fabrication Facility (CFF) at the Tyndall National Institute, according to the processes described in Chapter V. The electrodes were prepared by a *UV-photolithographic lift-off* technique during which the metals were patterned onto a Zeonor substrate. A thin coating (20 nm) of titanium has been applied as an adhesive layer, in order to obtain high quality adherence of Au and Pt to the polymer. For gold anodes, a layer of Pt was additionally incorporated in between Ti and Au, preventing the diffusion of Au towards the adhesive. Gold and platinum were deposited in two separate lithographic steps; therefore two individual photomasks were required. The thickness of Au and Pt layers was 100 nm. The considered electrode designs and the corresponding microfabrication process are discussed in detail in Chapter V.

2.8.1 Preparation of the masks for the electrode patterning.

Chrome-on-Glass (COG) masks for the microfabrication of gold and platinum electrodes (Fig. 2.11) were designed in the Central Fabrication Facility of the Tyndall National Institute using *Mentor Graphics IC Station* software. Manufacturing of the COG masters was carried out by Compugraphics Intl. Ltd (Scotland). Detail protocol for the preparation of COG masks can be found in Appendix C.

2.8.2. Microfabrication of gold and platinum electrodes.

Deposition of gold anodes and platinum cathodes was performed in two consecutive steps of a *UV- photolithographic lift off* process. Two separate photomasks have been employed. Following the e-beam assisted evaporation of platinum; gold has been electrosputtered in the same fabrication run to ensure good adhesion of the metal to the Zeonor substrate. Comprehensive description of the fabrication procedure, supported with relevant diagrams is enclosed in Chapter V of this thesis.

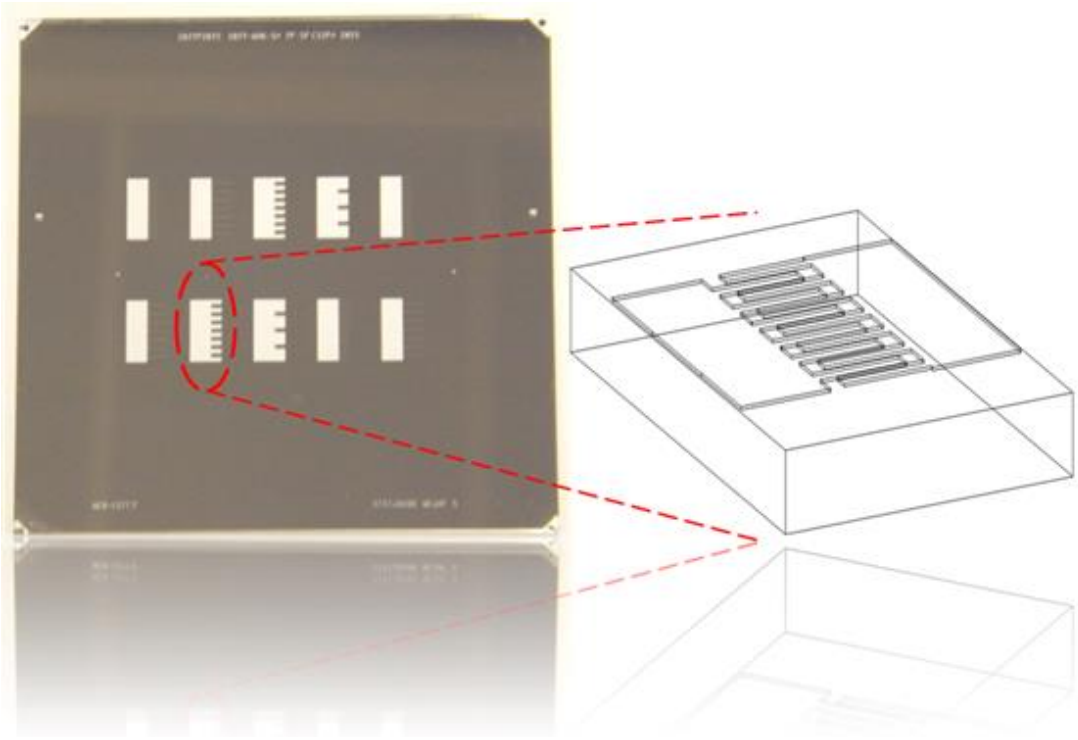


Fig. 2.11. Chrome-on-Glass photomasks for the fabrication of the on-chip electrodes.

2.9. Electrochemically assisted deposition of Nanoporous Gold Structures.

Modification of Au electrodes with Nanoporous Gold Structures has been carried out, as described in Chapter V, according to a protocol in ref. [3]. Metal alloys for the NPG were obtained from alkaline solutions of $KAu(CN)_2$ and $KAg(CN)_2$ in Na_2CO_3. Deposition of gold and silver composites was followed by an Ag dealloying step, resulting in a formation of a porous network of gold nanostructures at the electrode surface. Electrochemical modification of gold electrodes microfabricated on Zeonor was performed using Ag/AgCl and Pt/Ti gauze as the reference and counter electrodes, respectively. The presence of the NPG deposit was confirmed by cyclic voltammetry measurements in 1 M NaOH. The structure was visualised by the SEM. Fig. 2.12 represents NPG deposit on gold [3] obtained with molar ratio of 0.18:0.82 Au to Ag.

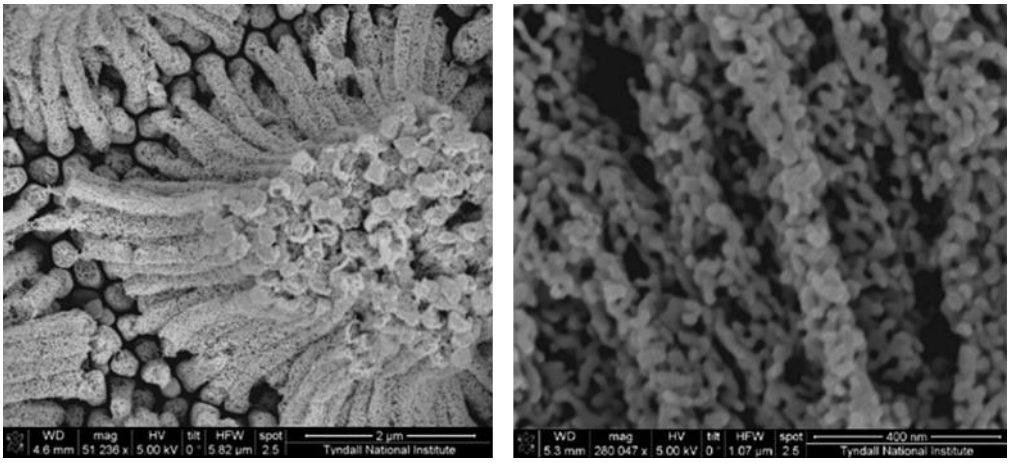


Fig. 2.12. SEM image of the NPG wire-array taken from [3].

2.10. Design and fabrication of microfluidic channels.

Fabrication of microfluidic channels required an accurate design of the photolithographic masks. Chrome-on-Glass (COG) master templates carrying the micro-features were designed on the basis of theoretical studies of the fluid flow and the reaction kinetics in the channels. COG masks laid the foundation for the fabrication of silicon stamps which were later used for a direct transfer of the patterns onto the polymer substrates. Microfluidic channels in Zeonor have been produced using a hot-embossing technique under conditions of elevated temperature and applied pressure. Channel patterns in PDMS have been obtained by simple casting of the liquid polymer onto the silicon master followed by thermal curing of the assembly. The comprehensive description of the COG mask fabrication is enclosed in Appendix B.

2.10.1. COG masks for the microfluidic channels.

Design of the photomasks for microfluidic channels (Fig. 2.13) was prepared in the Central Fabrication Facility at the Tyndall National Institute using *Mentor Graphics IC Station* software. Chrome on Glass (COG) templates were provided by Compugraphics Intl. Ltd in Scotland, where they were prepared by chemically etching the metal pattern unexposed to UV light, as discussed in Appendix B.

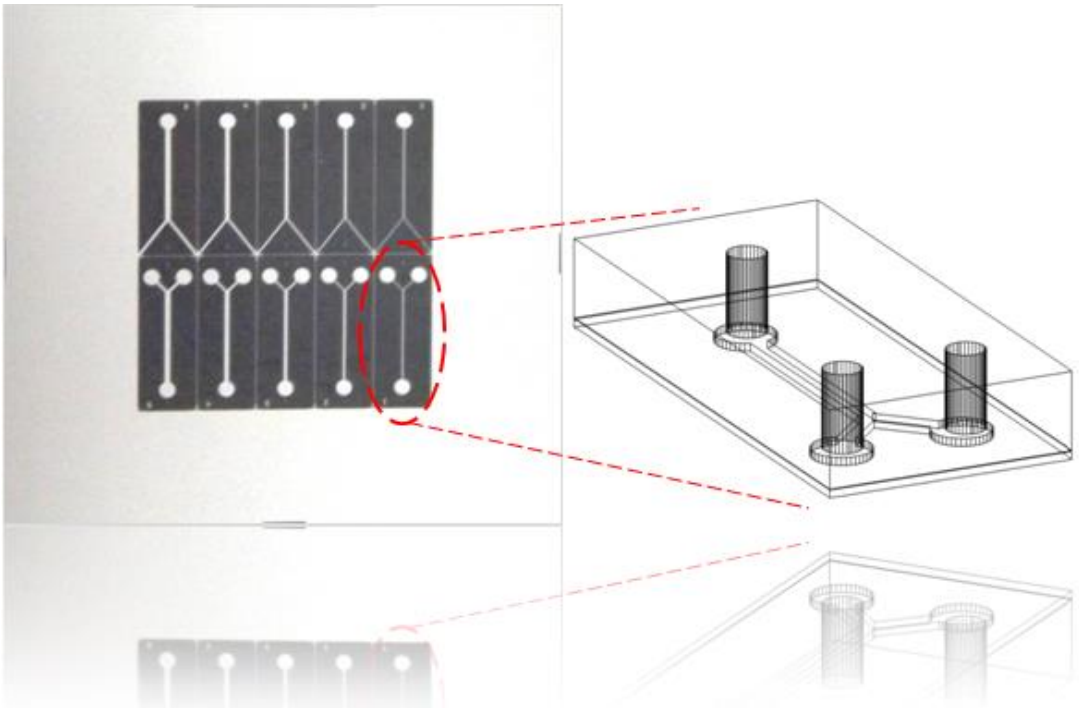


Fig. 2.13. Chrome-on-Glass photomasks for the fabrication of microfluidic channel.

2.10.2. Silicon stamps for the microfluidic channels.

Stamps for the channels were prepared by a Deep Reactive Ion Etch (DRIE) of silicon in a mixture of gases (dry etch). The profile and size of the features obtained are precisely controlled by the design of the mask that has been used. Combination of a low pressure and strong electrical field disrupts the atomic structures forming highly energetic ions, which in turn bombard the surface of the silicon nearly vertically, effectively etching the underlying material. Silicon etch is typically carried out in the presence of sulfur hexafluoride [SF_6], as the main reactive component of the plasma. DRIE is part of a multi-phase fabrication process reported in detail in Chapter V. Main steps involve: (i) coating the silicon wafer with a layer of a photoresist; (ii) exposing the surface to UV light through an appropriate photomask; (iii) deep reactive ion etch of the silicon and the removal of the remaining resist. Prior to any treatment, the substrate undergoes a thorough cleaning procedure.

2.10.3. Channel preparation in Zeonor and PDMS.

Silicon stamps for channel imprinting were cleaned thoroughly with IPA and DI water and dried in a stream of nitrogen. Patterning in Zeonor involved aligning the polymer substrate and the master in a hot-embosser and applying elevated temperature and mechanical pressure for a defined period of time. Under certain conditions the polymer reaches its glass transition point and conforms to the features on the stamp. Subsequent cooling preserves the embossed channel patterns in the polymer structure even after mask removal. Channel profiles were then evaluated by SEM and Tencor measurements.

Channel molding in PDMS was carried out by simply casting a degassed, liquid elastomer mixture containing the base and the catalytic agent onto the silicon stamp and curing it in the oven until set. Solid PDMS was then separated from the master template revealing the features of the channel. The channel body was removed from the bulk PDMS; the inlet entries and flow outlet point were pierced with a metal hollow rod of Ø 2 mm, as shown schematically in Fig. 2.14. Silicon master was retrieved and after cleaning was used for further casting.

Description of the hot-embossing and casting protocols is enclosed in Chapter V of this thesis.

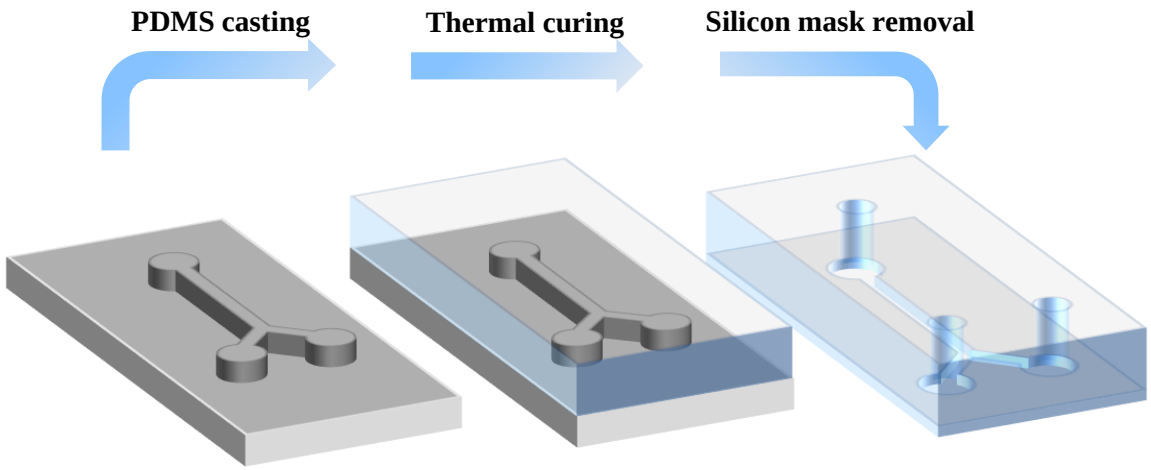


Fig. 2.14. Schematic representation of the channel molding in PDMS.

Plasma activation of PDMS channels

Following casting and prior to device assembly, PDMS surface was treated in the oxygen plasma (Fig. 2.15), rinsed with copious amounts of IPA and DI water and blow-dried in the stream of nitrogen. Exposure to plasma introduces hydrophilic functional groups and enables PDMS attachment to other materials.

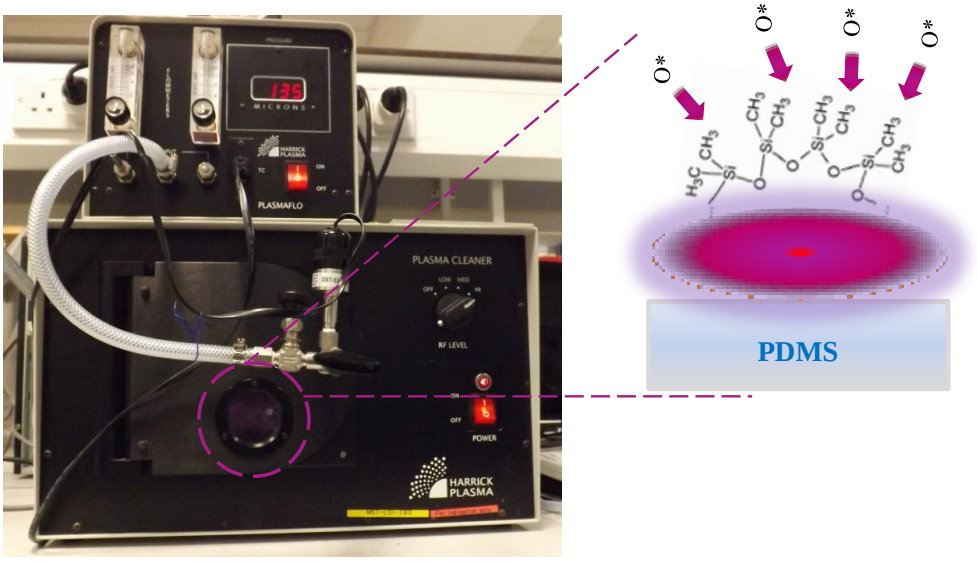


Fig. 2.15. Activation of the PDMS surface in the oxygen plasma.

2.10.4. PDMS bonding to Zeonor.

PDMS to Zeonor bonding was successful in the presence of an Adhesive Prime Coat [4] diluted in heptane to a 10 % volume. The solution was sparsely applied on the PDMS avoiding the channel areas and activated in the oxygen plasma at low pressure and high power readings. Immediately after exposure, the substrates were brought together in a firm grip and the assembly was dried overnight at the room temperature.

2.11. Sol-gel entrapment of the enzyme catalysts.

Sol-gel encapsulation of D-Sorbitol dehydrogenase (from *Gluconobacter oxydans*) and bilirubin oxidase (from *Myrothecium verrucaria*) was carried out from an alkaline solution of 0.25 M tetraethyl-orthosilicate (TEOS), as reported in [5]. The electrochemical characterization of enzyme-modified electrodes was performed by measuring cyclic voltammetry response in a three-electrode system composed of the working disc electrode (Au, Pt or GCE), Pt disc counter and Ag/AgCl (3 M KCl internal electrolyte) reference. Electrodes were connected to an Autolab PGSTAT-12 potentiostat (Metrohm Autolab B.V, Netherlands) and the measurement was monitored by the General Purpose Electrochemical System software (GPES).

Prior to surface treatment, WE was scrupulously polished with alumina powder (Ø 0.05 µm), rinsed with deionized water and dried with a tissue paper. The schematic of the on-chip sol-gel encapsulation of enzymes is depicted in Fig. 2.16.

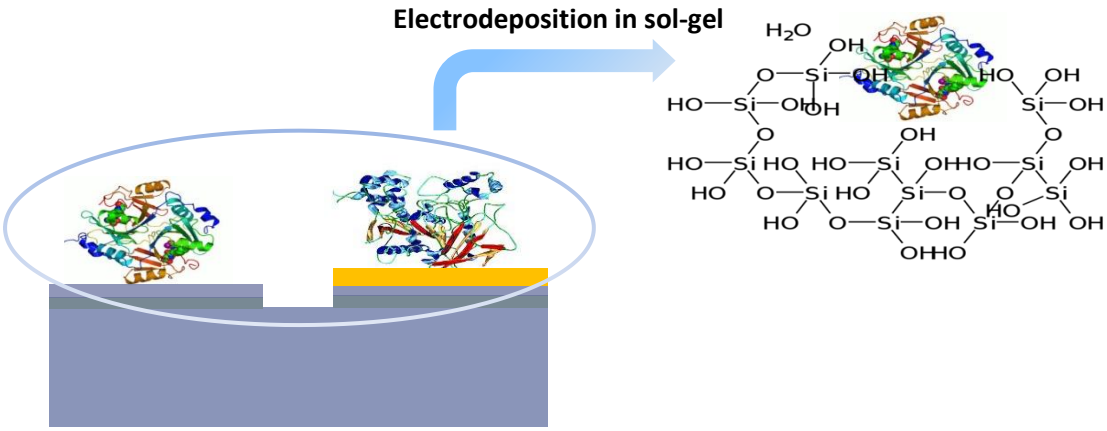


Fig. 2.16. Sol-gel encapsulation of the enzyme catalysts on the on-chip electrodes.

2.11.1. Electrodeposition of DSDH in sol-gel.

The solution for the sol-gel electrodeposition of D-Sorbitol dehydrogenase was composed of 0.25 M TEOS; poly (diallyldimethylammonium chloride) (PDDA); the enzyme, DSDH (aliquot of the 10 mg mL^{-1} stock); diaphorase (stock concentration of 5 mg mL^{-1}); NAD^+ - GPS and polyethyleneimine (PEI, 10 % in DI water, pH 9), as described in Chapter VI. 200 µL of the silica based mixture was coated on the electrode

and a constant potential of -1.2 V was applied to the working electrode for 60 s. Following the electroplating, the deposit was carefully rinsed with deionized water, excess moisture was removed with a tissue paper and the electrode was left to mature at room temperature for 2 h.

Activity of DSDH modified films was studied electrochemically in 0.1 M Tris-HCl buffer, pH 7.5, in the presence of the mediator, 0.1 mM ferrocenedimethanol (FDM) and the substrate for DSDH, D-Sorbitol (2 mM - 8 mM).

2.11.2. Sol-gel entrapment of BOX.

The encapsulation of BOX in sol-gel was carried out from a solution containing 0.25 M TEOS matrix, aliquot of enzyme (from 10 mg mL^{-1} stock in deionized H_2O) and osmium polymer acting as the mediator. Polyethyleneimine (PEI, 10 % in DI water, pH 9) was added to stabilize the interaction between the negatively charged bilirubin oxidase and the cationic polymer. The mixture was drop-coated onto the electrode and left at room temperature to polymerize for a period of 2 h. Catalytic response of BOX to atmospheric oxygen was studied using cyclic voltammetry measurements in 0.1 M Phosphate Buffered Saline (PBS). Deaerated buffers were obtained by purging the solutions with N_2 for 40 min. Oxygen was provided to the enzyme by leaving the solution exposed to air for 30 min. Attempts to electrodeposit bilirubin oxidase, according to the procedure enclosed in section 2.11.1 (presence of PEI and PDDA, -1.2 V for 60 s), have also been undertaken. This method was however not successful in supporting the enzyme's catalytic activity.

2.11.3. Surface modification of Au electrode.

To improve the attachment of the silica films to gold surfaces, Au electrode was pre-treated with (3-Mercaptopropyl) trimethoxysilane (MPTMS) monolayer, as shown in Fig. 2.17. Modification of gold surface was carried out by drop-coating an aliquot of 20 mM MPTMS in EtOH onto the electrode and incubating it with the solution for 20 minutes [6]. Following the treatment, the surface of gold was rinsed with water and ethanol mixture (1:1 v/v) and the electrode was immediately used for the electrodeposition of BOX in sol-gel.

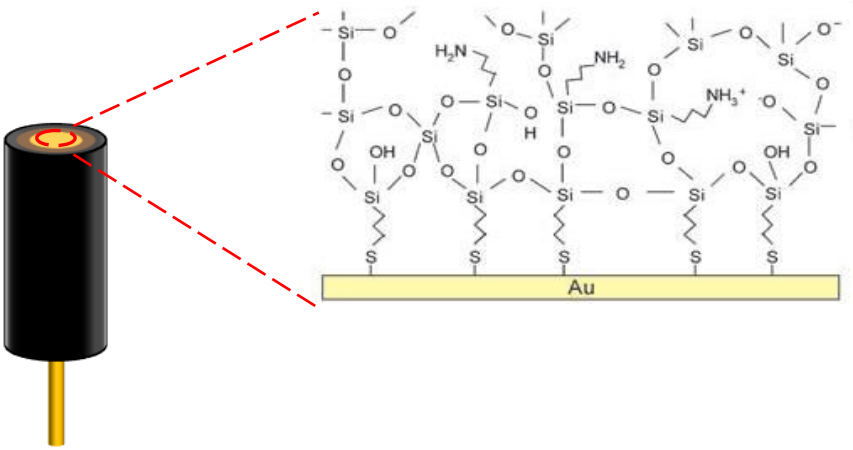


Fig. 2.17. Modification of gold disc electrode with MPTMS.

2.12. Electrodeposition of enzymes in *o*-phenylenediamine.

The electrodeposition of enzymes in *o*-phenylenediamine was carried out from buffered solutions containing 10 mM and 5 mM *o*-PD, according to the methods described by Wang *et al*. [7] and Rogalski [8]. Glucose oxidase (from *Aspergillus niger*) was deposited on the gold electrode amperometrically, by applying a constant positive potential of 0.75 V for a period of 20 min. For the encapsulation of laccase (from *Trametes versicolor*), the platinum working electrode was cycled between -0.5 V to 0.9 V for 40 sweeps (20 cycles), at 20 mV s^{-1} scan rate. Immobilization of lactate oxidase (from *Pediococcus sp.)* was carried out from 5 mM *o*-PD buffered solution by applying a constant potential of 0.65 V for 20 min, as reported by Wang *et al*. [9]. All potentials were recorded with respect to Ag/AgCl electrode (3 M KCl as internal electrolyte). Application of a certain potential (or a potential window) results in the polymerization of *o*-phenylenediamine and if present, subsequent encapsulation of the enzyme molecules within a growing chain of the polymer (Fig. 2.18). Prior to the electrodeposition, enzyme mixtures with *o*-phenylenediamine were purged with nitrogen for 20 min to remove the oxygen. Solutions containing glucose oxidase were additionally supplemented with 5 mM of sodium sulfite to minimize the electron scavenging properties of oxygen.

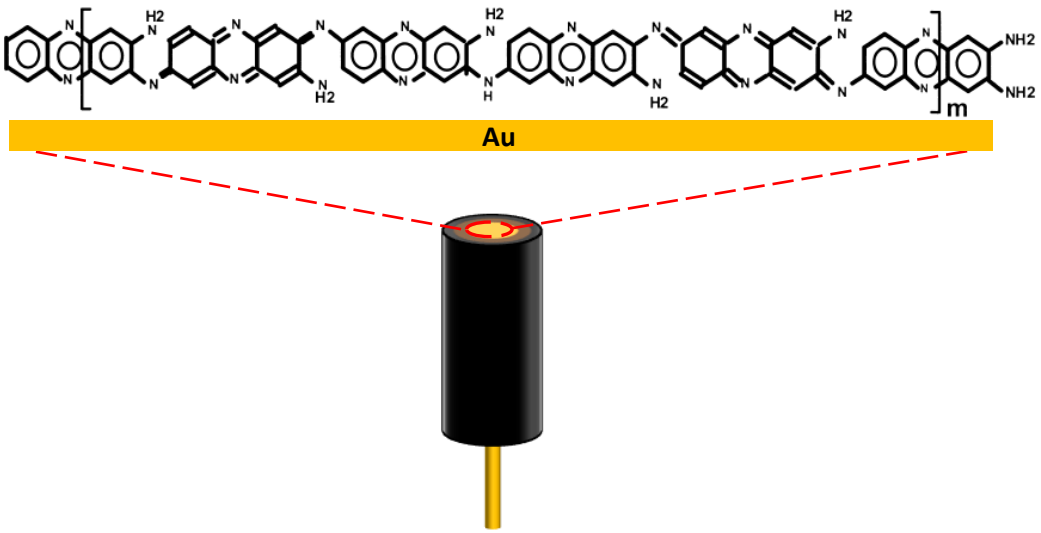


Fig. 2.18. Modification of electrode with poly o-phenylenediamine.

2.12.1. Entrapment of glucose oxidase.

Electrochemically assisted encapsulation of 10 mg mL^{-1} GOX in *o*-phenylenediamine matrix was carried out, according to the protocol reported in [7], as described in Chapter VI. A potential of 0.75 V was applied for a period of 20 min to allow the polymerization of *o*-PD and subsequent gradual growth of the GOX functionalized polymer film. Following the deposition, the electrode was carefully rinsed with deionized water and the excess moisture was removed with a tissue paper. Immediately after surface modification, the catalytic activity of GOX was studied in 0.1 M phosphate buffer, pH 7.4, in a presence of ferrocenecarboxylic acid and glucose as the mediator and substrate for the enzyme, respectively. The solution for the electrodeposition contained sodium sulfite and was additionally purged with nitrogen for 20 min, prior to the surface modification to remove oxygen. Three-electrode system was composed of a gold disc as a working electrode (Ø 2 mm), a Pt coil counter and an Ag/AgCl reference immersed in 3 M KCl internal electrolyte. For the on-chip electrodes Au was used as the WE and Pt acted as both CE and RE. Electrochemical signal was monitored by a CHI 660B potentiostat. When not in use, GOX - modified electrodes were stored in the buffer (pH 7.4) at 4 ºC.

2.12.2. Encapsulation of laccase.

The electrodeposition of 0.1 mg mL^{-1} laccase in *o*-phenylenediamine was carried out as described in [8]. The electrochemical polymerization of *o*-PD and subsequent incorporation of laccase molecules into the polymerized film is triggered by cycling the potential of the working electrode between -0.5 and 0.9 V for approximately 20 min. Following the deposition, the electrode was carefully rinsed with deionized water and dried with a tissue paper. Likewise for the encapsulation of glucose oxidase, two- and three-electrode systems were used depending on the type of the electrode being modified, with Pt (Ø 2 mm) as the WE. Prior to the electroplating, the solution was purged with nitrogen for 20 min. Immediately after modification the catalytic activity of the enzyme was monitored in 0.1 M phosphate buffer pH 6.0 solutions in the presence and absence of hydroquinone and oxygen as the mediator and substrate, respectively. When not in use, laccase biofunctionalized electrodes were stored in the buffer (pH 6.0) at 4 ºC.

2.12.3. Electropolymerization of lactate oxidase.

The electropolymerization of LOX in *o*-PD was carried out, as described by Wang *et al*. [9], from an oxygen free solution containing of *o*-phenylenediamine in 0.05 M phosphate buffer, pH 7.4. Electropolymerization from an enzyme-polymer suspension was performed by applying a constant potential of 0.65 V for 20 min in a three-electrode system. Prior to the deposition, the solution for electrode modification was purged with nitrogen for 20 min to remove the interfering oxygen. Following encapsulation, the LOX functionalized electrode was carefully rinsed with deionized water and stored in the buffer (pH 7.4) at 4 ºC, when not in use. Catalytic activity of lactate oxidase was measured indirectly by studying the amount of hydrogen peroxide formed as a result of L-lactate conversion.

To improve the electrode sensitivity to hydrogen peroxide detection, Iron (III) ferrocyanide (Prussian Blue) was deposited on the working electrode as the supporting layer, according to the protocol described in ref. [10]. Following the electrochemical and thermal activation of PB, LOX/*o*-PD film was electrodeposited as the succeeding layer.

2.13. Preparation of the electrodes microfabricated on Zeonor for electrochemical studies.

In this Ph.D. work, gold and platinum electrodes were microfabricated on Zeonor substrates using a *UV-lithographic lift off* technique. As described previously, this process requires the use of a photoresist, which needs to be further removed using a mixture of organic and inorganic solvents.

Photoresist Removal

Prior to any electrochemical measurements, the electrodes fabricated on Zeonor substrate were diced in the Central Fabrication Facility of the Tyndall National Institute. A protective layer of a positive photoresist, Microposit S18130 (Shipley, UK), was applied on each wafer before dicing to shield the metal patterns from the mechanical stress. Once diced, the polymer slides were chemically treated to remove the residual photoresist layer. Cleaning process involved immersing the chips for 5 min each in boiling acetone, 1, 2-dichloroethane, IPA and DI water consecutively. The procedure was repeated twice following which the electrodes were washed thoroughly with deionised water and dried with nitrogen. Zeonor substrates were stored in a closed container when not in use.

2.14. Solutions for the electrode modification.

2.14.1. Solution for the electrodeposition of GOX in *o*-PD.

Solutions of 10 mM *o*-phenylenediamine and 5 mM of sodium sulfite were prepared by dissolving 0.011 g of *o*-PD and 0.0063 g of Na_2SO_3 in 0.1 M phosphate buffer, pH 7.4. Directly before the electrodeposition, 100 mg of GOX was added to a final concentration of the enzyme of 10 mg mL^{-1}.

2.14.2. Solution for the encapsulation of laccase in *o*-PD.

Solutions of 5 mM *o*-phenylenediamine and 5 mM of sodium sulfite were prepared by dissolving 0.0055 g *o*-PD in 0.1 M phosphate buffer, pH 6. Directly before the electrodeposition, 1 mg of laccase was added to a final enzyme concentration of 0.1 mg mL^{-1}.

2.14.3. Solution for the electrodeposition of LOX in *o*-PD.

Solutions of 5 mM *o*-phenylenediamine were prepared by dissolving 0.0055 g of *o*-PD and 0.0063 g of Na_2SO_3 in 0.05 M phosphate buffer, pH 7.4. Directly before the electrodeposition, 100 µL aliquot of LOX (0.1 mg mL^{-1}) was added to a final concentration of the enzyme of 0.005 mg mL^{-1}.

2.14.4. Solution for the electrodeposition of PB.

Solutions of 4 mM Prussian blue (PB) in 0.1 M KCl and HCl were prepared by dissolving 0.0687 g of PB and 0.372 g of KCl in 0.1M HCl [9]. 0.1 M HCl was made by taking a 5 mL aliquot of 1 M hydrochloric acid stock and diluting it with deionized water to a 50 mL volume.

2.14.5. Preparation of the sol-gel from 1.5 M TeOS stock solution.

1.062 g of tetraethyl-orthosilicate (TEOS) was mixed with 1 mL of deionized water and 1.25 mL 0.01 M HCl. Sol-gel precursor was vigorously stirred for 12 h at room temperature.

2.14.6. Preparation of the NAD^+ - GPS for DSDH encapsulation sol-gel.

25 mg of NAD^+ was combined with 37.5 mg of GPS and 400 µL of Tris-HCl, pH 7.5. The mixture was stirred for 12 h in RT.

2.14.7. Solution for the sol-gel electrodeposition of BOX.

20 µL of 0.25 M TEOS (1:6 dilution of 1.5 M stock) was combined with 10 µL BOX (10 mg mL^{-1} in deionized H_20), 5 µL of Os polymer and 2.5 µL of polyethyleneimine (PEI, 10 % in DI water, pH 9).

2.14.8. Solution for the sol-gel electrodeposition of DSDH.

70 µL of 0.25 M TEOS was mixed with 30 µL of poly -diallyldimethylammonium chloride (PDDA); 70 µL of D-Sorbitol dehydrogenase (DSDH, 10 mg mL^{-1}); 40 µL of diaphorase (DI, 5 mg mL^{-1}); 50 µL of NAD^+-GPS and 40 µL of polyethyleneimine (PEI, 10 % in DI water, pH 9). It has been shown that the order at which the individual components are added, different than described above, negatively affects the quality of the sol-gel deposit and the catalytic activity of DSDH.

2.15. Preparation of buffered solutions for enzyme testing.

2.15.1. Preparation of 0.01 M Phosphate buffered saline (PBS), pH 7.4.

Phosphate buffered saline solution, also known as PBS, was prepared according to the protocol recommended by the supplier, Sigma-Aldrich. 1 tablet of PBS was dissolved in 200 mL of ultrapure water (DI water) yielding 0.01 M phosphate buffer, 0.0027 M KCl

and 0.137 M NaCl, pH 7.4, at 25 ºC. PBS solution was prepared on a monthly basis, autoclaved (15 min cycle at 122 ºC) and stored at 4 ºC when not in use.

2.15.2. Preparation of 0.2 M Phosphate buffer stock solutions.

0.1 M phosphate buffers, pH 6 and pH 7.4, were prepared by mixing appropriate volumes of 0.2 M Sodium phosphate monobasic (NaH_2PO_4) and 0.2 M Sodium phosphate dibasic (Na_2HPO_4) stock solutions.

A stock solution of 0.2 M Sodium phosphate monobasic was obtained by dissolving 12 g of NaH_2PO_4 powder in 0.5 L of deionized water. Solution was sonicated, autoclaved (15 min cycle at 122 ºC) and stored at 4 ºC when not in use.

0.2 M Sodium phosphate dibasic was prepared by taking 14.20 g of NaH_2PO_4 powder and making it up with deionized water to 0.5 L volume. Solution was sonicated, autoclaved (15 min cycle at 122 ºC) and stored at 4 ºC when not in use.

2.15.3. Preparation of 0.1 M Phosphate buffer pH 7.4.

In order to make 0.1 M Phosphate buffer pH 7.4, 44 mL of the acid (NaH_2PO_4) were added to 156 mL of the base (Na_2HPO_4) and the volume was brought up to 400 mL with deionized water. Phosphate buffer pH 7.4 solution was prepared on a monthly basis, autoclaved and stored at 4 ºC when not in use.

2.15.4. Preparation of 0.1M Phosphate buffer pH 6.0.

0.1 M Phosphate buffer pH 6 was made by adding 175.4 mL of the acid (NaH_2PO_4) to 24.6 mL of the base (Na_2HPO_4) and bringing the volume to 400 mL with deionized water. Phosphate buffer pH 6 solution was prepared on a monthly basis, autoclaved and stored at 4 ºC when not in use.

2.15.5. Preparation of 0.05 M Phosphate buffer pH 7.4.

In order to prepare 0.05 M Phosphate buffer pH 7.4, 0.54 g of Na_2HPO_4 and 0.144 g of NaH_2PO_4 were dissolved in 0.4 L of DI water. Solution was sonicated, autoclaved and stored at 4 ºC when not in use.

2.15.6. Preparation of 0.1 M Acetate buffer pH 4.5.

0.1 M Acetate buffer pH 4.5 was made by dissolving 0.8204 g of anhydrous sodium acetate (CH_3COONa) in a mixture of 10.64 mL of acetic acid (CH_3COOH) and 89.36 mL of DI water. The buffer was stored for a month at 4 ºC when not being used.

2.16. Preparation of redox solutions for enzymatic testing.

7 mM of ferrocenecarboxylic acid (FCA) and 50 mM glucose in 0.1 M phosphate buffer pH 7.4 was prepared weekly in order to study the electrochemistry of glucose oxidase. The solution was made by weighing out 0.45 g of D-(+)-Glucose and 0.081 g of ferrocenecarboxylic acid and dissolving the powders in 50 mL of the supporting buffered electrolyte. The mixture was left in the sonicator for approximately 20 min to ensure complete dissolution of FCA.

The electrochemical response of laccase was investigated in a solution of 3 mM Quinone (Q) in 0.1 M phosphate buffer, pH 6.0. A stock of 50 mL was prepared weekly by dissolving 0.0165 g of Q in the supporting buffer. Oxygen was provided from a (BOC Gasses Ireland Ltd) cylinder by purging the contained solution with O_2 directly through a Teflon tubing for 40 min. Aerated buffers were obtained by incubating the solution in the stream of nitrogen for the same period of time.

To measure the catalytic activity of D-Sorbitol dehydrogenase in sol-gel, solutions of 0.1 mM ferrocenedimethanol (FDM) in 0.1 M Tris-HCl containing increasing concentrations of D - Sorbitol (2 mM - 8 mM) were prepared. 0.5 L of 0.1 M Tris-HCl buffer stock was prepared by dissolving 6.057 g of a Tris base in 0.3 L of deionized water and titrated with 1 M HCl, until pH 9.0 was reached. Following the pH adjustment, the

solution was transferred into a clean conical flask and DI water was added to a final volume of 0.5 L. Solution of 0.1 mM FDM was made by weighing out 1.08 mg of ferrocenedimethanol powder and dissolving it in 50 mL of previously prepared 0.1 M Tris-HCl buffer. Solutions of D-Sorbitol (2 mM, 4 mM, 6 mM and 8 mM) were obtained by taking 7.3 mg, 0.015 g, 0.022 g and 0.03 g of the substrate respectively and dissolving in 20 mL of 0.1 mM FDM in 0.1 M Tris-HCl buffer.

For the electrochemistry of bilirubin oxidase modified sol-gel films, 0.5 mM solutions of 2, 2′- Azino-bis (3-ethylbenzothiazoline-6-sulfonic acid) diammonium salt (ABTS) was prepared in 0.1 M PBS pH 7.4 by weighing out 5.5 mg of the ABTS powder and adding it to 20 mL of the PBS buffer.

The catalytic activity of lactate oxidase functionalized PB/*o*-PD electrode was studied in a 0.05 M phosphate buffer pH 7.4 in the presence of increasing concentrations of the substrate, sodium L-lactate (2 mM – 6 mM). 10 mM stock solution of lactate was prepared by dissolving 0.011 g of the crystalline powder in 10 mL of the supporting buffer. Subsequent aliquots of the stock were then added to the phosphate buffer to obtain a desired final concentration of the lactate [9].

The electrochemical characterization of gold and platinum electrodes microfabricated on Zeonor was carried out from a solution of 5 mM potassium ferricyanide $K_3[Fe(CN)_6]$ in 0.1 M PBS buffer, pH 7.4. Ferricyanide was prepared from 0.033 g of $[Fe(CN)_6]^{3-}$ and brought up to a volume of 20 mL.

2.17. Bibliography.

1. Bard, A. and L. Faulkner, *Methods involving forced convection—hydrodynamic methods.* Electrochemical Methods—Fundamentals and Applications, John Wiley & Sons, Inc. 2001: p. 331-367.
2. Tsao, C., et al., *Low temperature bonding of PMMA and COC microfluidic substrates using UV/ozone surface treatment.* Lab on a Chip, 2007. **7**(4): p. 499-505.
3. Nagle, L.C. and J.F. Rohan, *Nanoporous gold anode catalyst for direct borohydride fuel cell.* International Journal of Hydrogen Energy, 2011. **36**(16): p. 10319-10326.
4. Kim, L., et al., *A practical guide to microfluidic perfusion culture of adherent mammalian cells.* Lab on a Chip, 2007. **7**(6): p. 681-694.
5. Wang, Z., et al., *Electrochemically assisted deposition of sol–gel bio-composite with co-immobilized dehydrogenase and diaphorase.* Electrochimica Acta, 2011. **56**(25): p. 9032-9040.
6. Sibottier, E., et al., *Factors affecting the preparation and properties of electrodeposited silica thin films functionalized with amine or thiol groups.* Langmuir, 2006. **22**(20): p. 8366-8373.
7. Windmiller, J.R., et al., *Bicomponent Microneedle Array Biosensor for Minimally-Invasive Glutamate Monitoring.* Electroanalysis, 2011. **23**(10): p. 2302-2309.
8. Palys, B., A. Bokun, and J. Rogalski, *Poly-o-phenylenediamine as redox mediator for laccase.* Electrochimica Acta, 2007. **52**(24): p. 7075-7082.
9. Dempsey, E., J. Wang, and M.R. Smyth, *Electropolymerised o-phenylenediamine film as means of immobilising lactate oxidase for a L-lactate biosensor.* Talanta, 1993. **40**(3): p. 445-451.
10. Karyakin, A.A. and E.E. Karyakina, *Prussian Blue-based artificial peroxidase as a transducer for hydrogen peroxide detection. Application to biosensors.* Sensors and Actuators B: Chemical, 1999. **57**(1): p. 268-273.

CHAPTER III
MINIATURE ENZYMATIC BIOFUEL CELL OPERATING IN STATIC CONDITIONS

In science, the credit goes to the man who convinces the world, not to the man to whom the idea first occurs.

Sir Francis Darwin

3.1. Introduction.

3.1.1. Main objectives and approach imperatives.

The aim of this chapter was to investigate the design, feasibility, and the characteristics of a small scale enzymatic biofuel cell, operating in a static environment under ambient conditions, compatible with the requirements of the implantable micro-power sources. The expected outcome of this study was to obtain an experimental definition of the main directions, leading to the improved biofuel cell performance. Simplicity of the proposed design, rudimentary preparation methodology and prevalence of structural and biological components of the cell were the key factors under consideration. Commercial and easily accessible gold and platinum disc electrodes have been selected as integral constituents of the design. Immobilization of enzyme catalysts has been performed via drop-coating technique and the quality and stability of adhered films investigated. Membrane type and material source were also explored for efficient separation of catholyte and anolyte half-cell compartments. Operability of the constructed prototype has been examined in buffered solutions, in the presence of respective enzymatic substrates and electron mediating species. Enhancement of the cell performance through the implementation of enzyme molecules has been studied and compared to a non-

enzymatic design approach. Characterization of the miniature enzymatic biofuel cell and its individual constituents has been carried out in static conditions employing basic electrochemical techniques, such as, cyclic voltammetry and chronoamperometry.

The work carried out as part of this chapter was dedicated to the determination of the feasibility of an enzymatic biofuel cell operating in a basic configuration. In a microfluidic biofuel cell, all the fundamental components are housed in a single microstructured device, which exploits the laminar fluid flow in a channel to essentially create two half-cells. Due to the laminar regime, electrolyte cross-talk is minimized and maintains the biofuel cell functional without the use of a membrane.

3.1.2. State-of-the-art on enzymatic biofuel cell development.

Enzymatic biofuel cells are unique in comparison to their traditional fuel cell predecessors in that the catalytic reactions employ environmentally friendly and biocompatible protein molecules, which are directly immobilized on the electrodes via physical or chemical interactions with various functional surface groups. Conventional fuel cells, such as, polymer-electrolyte, solid oxide or direct-methanol systems [1] rely on costly noble metal catalysts and operate on reformed fossil fuels [2]. In order to successfully carry out their functions, a number of components are required (Tab. 3.1), which contribute to the complexity and large size of proceeding devices. Implementation of highly selective enzyme catalysts eliminates the separation prerequisite and reduces the size of biofuel cells by a factor of ~100, compared to the dimensions of the smallest battery or the fuel cell produced to date [3]. Implantable enzymatic biofuel cells benefit from bodily glucose sources, therefore the reservoir for the fuel storage and the corresponding delivery systems are not necessary. Likewise, due to oxygen present abundantly in all tissues and organs, the air breathing membrane of the cathode compartment is typically not required.

In traditional fuel cells and batteries, strongly acidic or basic electrolytes and volatile, often toxic reactants transformed at high temperatures are confined and sealed in a case, typically made of stainless steel. Conversely, biofuel cells mimic innocuous processes occurring in nature and therefore, can operate in mild physiological conditions, in the presence of natural biological fuels and oxidants. Since the products formed as a

result of catalytic conversions are non-toxic and environmentally friendly, the case and the corresponding seal are obsolete.

Tab. 3.1. Structural components of the conventional and enzymatic fuel cells.

Conventional fuel cells	Enzyme "wired" biofuel cells
Case	-
Case seal	-
Membrane	-
Ion conducting electrolyte e.g. phosphoric acid	-
Anode	Anode
Cathode	Cathode
Plumbing to anode/cathode compartment	-

To successfully separate the anolyte and catholyte solutions and prevent the species cross-over, a membrane is typically employed in conventional fuel cells. This is of a particular importance when one of the electrodes is composed of platinum or if a redox mediator is present in either compartment, which can diffuse across the interface and interfere with the counterpart reaction. The implementation of the membrane prevents undesirable reactions by blocking the transfer of either fuel or O_2. The separator conducts the flow of ions formed on the anode to the cathodic chamber, while inhibiting the electron transfer across the interface and forcing the generated current through the external circuit.

The use of compartment-separating membranes can be successfully omitted in the enzymatic biofuel cells where the anodic and cathodic reactions are not carried out by noble metals but by selective protein catalysts. Biological cells can operate as a single unit containing both the fuel and oxidant, provided that the anodic and cathodic redox mediators cannot be regenerated by opposing enzymes or upon cross- reactions, which would significantly reduce the power output. Both issues can be however, resolved by subsequent immobilization of the catalyst and the mediator species on the electrode surface.

Traditional enzymatic biofuel cells were comprised of an anode and cathode separated by a membrane allowing for a discriminate transport of ions between the anolyte and catholyte buffered solutions. The majority of early glucose/O_2 biofuel cells contained a platinum group metal catalyst and required the use of a membrane in order to prevent electrode fouling by products of glucose electrooxidation. Implementation of an enzymatic couple which could selectively catalyse redox reactions was a first milestone leading to a membrane-less approach.

In 1999, Katz and co-workers demonstrated for the first time a separator-free, single chamber biofuel cell incorporating two enzyme catalysts "wired" to the underlying electrodes using bioengineering technique [4]. The cell was composed of a surface reconstituted apo- glucose oxidase on pyrroloquinoline quinone (PQQ)-Flavin Adenine Dinucleotide (FAD) monolayer and cytochrome c functionalized cytochrome c oxidase modified Au disc electrodes (Fig. 3.1). The catalytic activity of glucose oxidase (GOX) and cytochrome oxidase (COD) were recorded in 1 mM glucose electrolyte solution saturated with air.

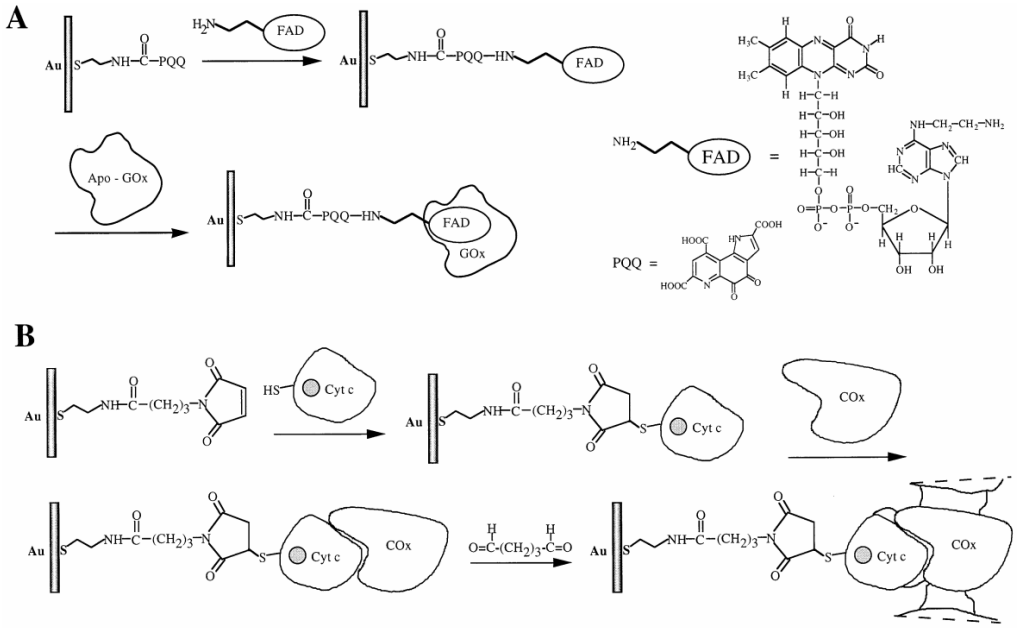


Fig. 3.1. Apo-glucose oxidase functionalized bioanode and cytochrome c oxidase cathode of the first membrane-free, single chamber enzymatic biofuel cell constructed by Katz and co-workers [4].

The cell operated at 60 mV and generated a power density of as little as 4 μW cm^{-2}. The diminutive voltage and very low power output effectively prevented device

miniaturization. For the cell to be considered in any biomedical applications, the active area would need to be approximately 1 cm^2, which would not be compatible with the size of the rest of the system.

The very first successful miniaturization of the enzymatic biofuel cell was reported in 2001, by a group led by Adam Heller [3]. The cell consisted of carbon fibers (Ø 7 μm) as anodes and cathodes for the enzymatic consumption of glucose and oxygen. The electrode material was functionalized with glucose oxidase and laccase catalysts, immobilized in appropriate polymer matrices for efficient conversion of the fuel and the oxidant. The redox supports used to attach the enzymes were carefully chosen so that undesirable electrooxidation or reduction of opposing species would not take place [5, 6]. Due to high sensitivity of laccase to neutral and basic environments, as well as the negative influence of Cl^- on its biological function [7-9], the cell operated in a chloride-free citrate buffer at pH 5. Implementation of conductive polymer coatings enabled the electron transport between the carbon surface and the active site without the mediator prerequisite and eliminated the need for a membrane [3]. Application of multiple polymer layers increased the power output to 140 μW cm^{-2} at 0.4 V, with the current densities of 1 mA cm^{-2} and 5 mA cm^{-2} for the anode and cathode, accordingly.

Improvement to Heller's strategy was proposed by Tsujimura and co-workers in 2001 [5]. The group produced a membrane-less enzymatic biofuel cell utilizing bilirubin oxidase and glucose dehydrogenase, cross-linked to osmium polymer functions and immobilized on glassy carbon disc electrodes. The prototype was capable of an efficient electrocatalysis under neutral pH and in the presence of chloride ions. The maximum power density of 58 μW cm^{-2} was obtained at 0.19 V. This particular study proved successful operation of a membrane-less biofuel cell in physiological buffer solutions.

In 2005, Ramanavicius reported the use of alcohol dehydrogenase from *Gluconobacter sp.* and glucose oxidase (*Aspergillus niger*) coupled with microperoxidase from horse heart (MP-8) as respective anodic and cathodic catalysts [10]. The constructed single-chamber biofuel cell was composed of graphite disc electrodes (Ø 3 mm) functionalized with enzymes adsorbed in the presence of glutaraldehyde. The cell exhibited an operational half-life of 2.5 days and a maximum open circuit potential of 270 mV when surplus concentrations of ethanol and glucose were present (> 2 mM), however the power output of the cell was not specified by the authors.

Kamitaka and co-workers [11] reported a single-unit, separator-free biofuel cell utilizing fructose dehydrogenase (FDH) from *Gluconobacter sp.* and laccase from

Trametes sp. for electrochemical conversion of fructose and oxygen. The cell consisted of a carbon paper anode modified with FDH adsorbed on Ketjen black (KB) and carbon aerogel cathode with attached multicopper oxidase. The maximum power density of 850 μW cm^{-2} was obtained at a potential of 0.41 V under stirring conditions. Highest recorded current output was 2.8 mA cm^{-2}.

More recently, Wang and co-workers [12] demonstrated the use of porous silicon (pSi) substrates for the immobilization of glucose oxidase and laccase, as anodic and cathodic catalysts of a membrane-less and mediator-free biofuel cell. Prior to the enzyme attachment, the silicon matrix was functionalized with single walled carbon nanotubes (SWCNs) by chemical vapour deposition (CVD) or electrophoretic deposition on gold-coated pSi. The cell operated in phosphate buffer solution at neutral pH. While the maximum power density derived from the cell was low (1.38 μW cm^{-2}) and a half-life of 24 hours was recorded, relatively simple architectural design indorsed future optimization.

The possibility of employing graphene nanosheets as viable candidates for biofuel cell electrode materials was demonstrated in 2010 by Li *et al.* [13]. The authors described the use of sol-gel matrix deposited on gold plate electrodes for the encapsulation of glucose and bilirubin oxidase enzymes. The anode and cathode were then brought together in a self-designed Teflon holder and the performance of the resulting cell was studied in an air saturated PBS buffer (pH 7.4) solution containing 100 mM glucose. The maximum power density of approximately 24.3 ± 4 μW cm^{-2} and a half-life of 7 days were reported.

In 2011, a group under Michael J. Cooney [14] constructed a macroscopic hybrid lactate/air biofuel cell composed of a microbial anode and an enzymatic air-breathing cathode. The cell utilized *Shewanella* MR1 incorporated in a chitosan-carbon nanotube matrix and a teflonized carbon black with adsorbed laccase (Fig. 3.2). The open circuit potential of 1 V and a power density of 26 μW cm^{-3} were reported.

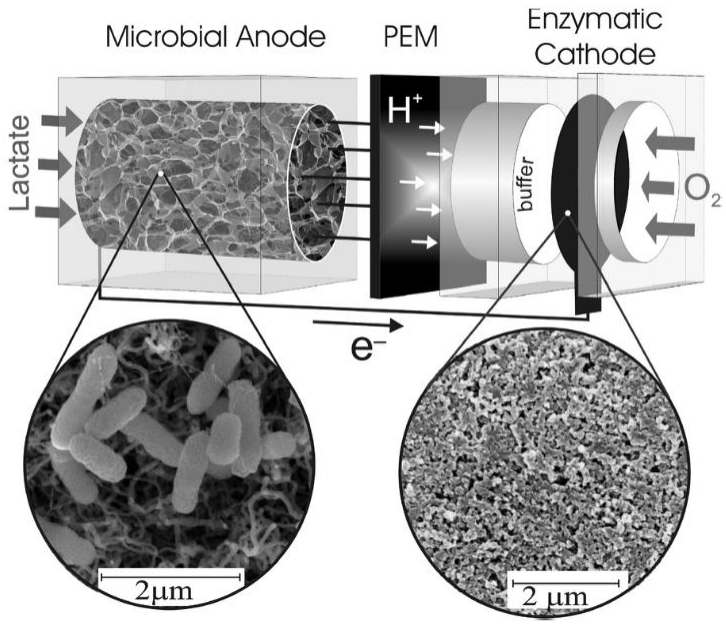


Fig. 3.2. Hybrid lactate/air biofuel cell composed of a microbial anode and gas-diffusion cathode [14].

One of the core objectives of the enzymatic biofuel cell research is to provide a neat design solution, which would enable a long-term operation of a functional cell in continuous regime. The first flow-through platforms proposed in 2011 by Plamen Atanassov and co-workers [15, 16], were composed of a system of multiple electrodes connected by plumbing elements and confined by padding structures (Fig. 3.3). The cell consisted of an air-breathing carbon and nickel mesh cathode functionalized with laccase (*Trametes versicolor sp*.) and a NAD^+- dependent alcohol dehydrogenase (*Saccharomycescerevisiae sp*.) modified reticulated vitreous carbon (RVC) anode of a defined porosity. The innovative configuration of the cell enabled individual studies of anode and cathode, prior to the measurements of the complete biofuel cell. The maximum power density of 26 μW cm^{-2} was reported at 0.372 V.

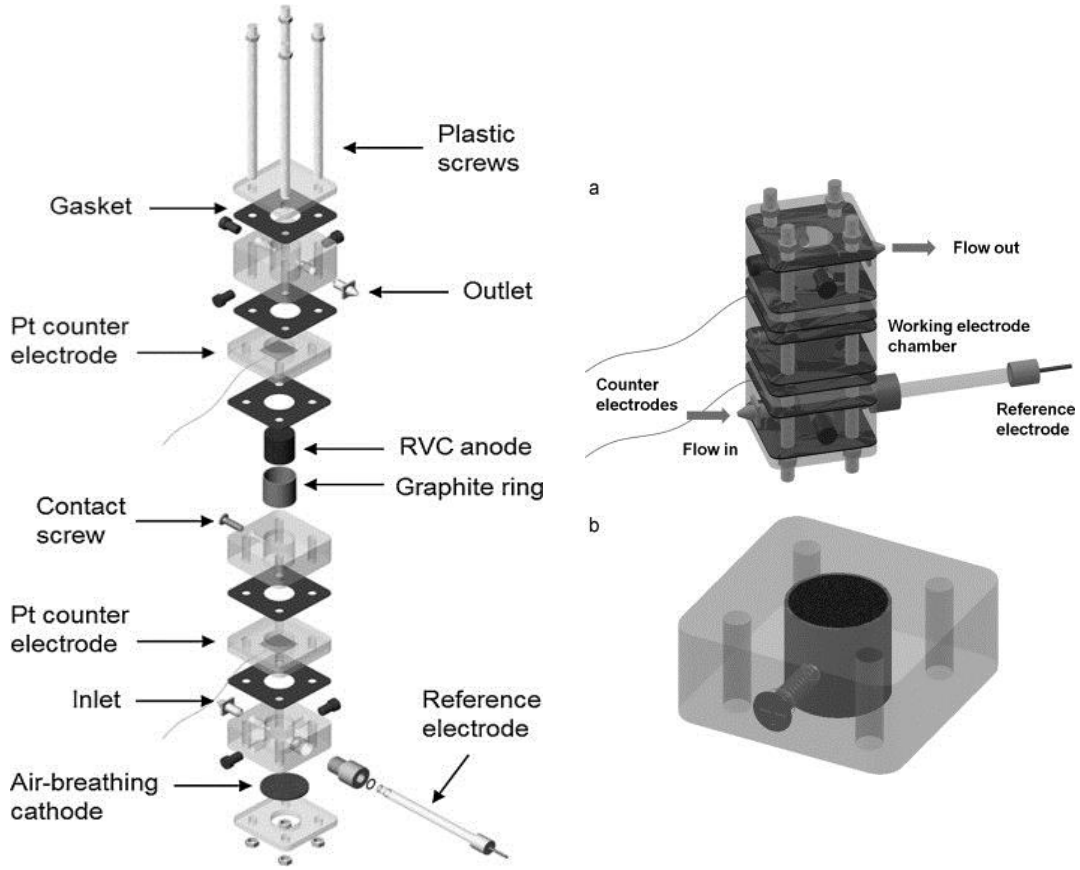


Fig. 3.3. Schematics of flow-through biofuel cells utilizing NAD+ dependent dehydrogenase enzymes (left and right images) [15, 16] and laccase (left image) [15].

Recently, Mano and co-workers [17] developed a novel three-dimensional biofuel cell employing glucose oxidase from *Aspergillus niger* and bilirubin oxidase (*Trachiderma tsunodae)* for a direct electrooxidation of glucose and mediated reduction of oxygen. Protein catalysts were immobilized on highly porous carbonaceous foam electrodes on glassy carbon supports. The maximum power density of 202 μW cm^{-2} was reported at a potential of 0.4 V.

Very few enzymatic biofuel cells operating in a microfluidic environment have been reported up to date, most of which are accessible as patents [18, 19] and not openly available to the public. The majority of published accounts on the application of microfluidic systems employ the same basic design, use a limited number of catalysts and fuels and are restricted to two core materials: PDMS and glass. The mainstream approach undertaken by various research groups, is to study the conversion of glucose and O_2 in glucose oxidase and laccase functionalized cells composed of simple geometries of gold or

carbon patterned electrodes and Y-shape channels embedded in PDMS [20-22]. Currently, one of the highest power densities of 110 $\mu W\ cm^{-2}$ was extracted from the microfluidic cell operating at 0.3 V [21, 22]; however, that is still not sufficient for a number of desirable applications. Novel design of microfluidic platforms for enzymatic biofuel cell, incorporating a variety of electrode and channel designs, has been therefore proposed as part of this Ph.D. thesis and is discussed in detail in the following chapters.

3.2. Development & investigation of the enzymatic biofuel cell.

Two main experimental set-ups were employed in the development and the characterization of the miniature enzymatic biofuel cell proposed as part of this chapter. The first configuration was a simple electrochemical cell with a three-electrode system which has been used for fundamental electrochemical measurements of stand-alone bare and enzyme modified electrodes. Gold or platinum discs have been employed as working electrodes, with a platinum wire auxiliary, and an Ag/AgCl (in 3M KCl supporting electrolyte) reference electrode.

Following the characterization of the individual components, an in-house built prototype of the enzymatic biofuel cell was constructed in a two-electrode configuration, with a gold counter and reference anode and platinum disc cathode used as working electrode.

3.2.1. Components of the fuel cell and their integration.

The preliminary design and operation of a miniature enzymatic biofuel cell, constructed as part of this chapter, were based on research previously reported in the area of biological power sources.

The cell consisted of two compartments separated by a semi-porous silicon membrane. Gold disc (Ø 2 mm) anode located in a bottom half of the cell acted as both reference and counter electrodes, while the platinum disc (Ø 2 mm) cathode situated in the upper chamber was connected as the working electrode. Platinum and glassy carbon materials were also investigated as anodes. The cathoyte solution was composed of 50 mM 2,2'-azino-bis-3-ethylbenzothiazoline-6-sulphonic acid (ABTS) in acetate buffer, pH

4.6. The anolyte consisted of 20 mM glucose, 5 mM ferricyanide $K_3Fe(CN)_6$ in 0.1M phosphate buffer at pH 7.

Glucose oxidase from *Aspergillus niger* and laccase from *Trametes versicolor* have been selected as the anodic and cathodic catalysts for the assembly of the enzymatic biofuel cell. Glucose oxidase (GOX) is a dimeric oxidoreductase capable of catalyzing the oxidation of glucose to gluconolactone and hydrogen peroxide. The enzyme is highly suited for immobilization at the anode due to its well established characteristics and inherent oxidative properties. Laccase has been chosen as the cathodic enzyme due to its ability to selectively reduce molecular oxygen to water. Both enzymes have been extensively employed in the area of catalytic investigations involving the biofuel cell and biosensor studies. General abundance and relatively robust nature enable their easy manipulation and allow their implementation in various life science applications.

The immobilization of biomolecules has been achieved by applying a 20 µL aliquot of the enzyme suspension to the electrode and drying it by RT evaporation for 1 h. Following drop-casting, the modified electrodes were immersed in the appropriate buffered solutions containing respective substrate and mediator. The electrodes were held in Eppendorf tubes adjusted to accommodate the anodic and cathodic counterparts. A small capillary tube has been used to act as a salt bridge, typically employed in galvanic cells to form a connection between the oxidation and reduction half-cells. Although glucose oxidase and laccase are suitable for the required redox reactions at the respective electrodes, they are not compatible when coexisting in a single solution for several reasons. The optimal pH for glucose oxidase is approximately 7.0, while the maximum activity of laccase is observed at pH 4.6. In addition, dissolved O_2, while being a desirable substrate at the cathode, interferes with electrooxidation of glucose catalyzed on the anode. O_2 intercepts electrons from the anode by acting as a competitive substrate for glucose oxidase. This results in the attenuation of the electron flow and an overall decrease in delivered power by up to 50 % as reported by Zebda [21]. To prevent the negative influence of molecular oxygen and eliminate fuel and oxidant mixing, a series of insulating semi-porous silicon based membranes have been investigated, as means to isolate the two half-reactions taking place in the biofuel cell. The selected membranes were initially employed at the Tyndall National Institute in a bioanalytical detection of charged oligopeptides [23], where they have demonstrated excellent ion transfer properties. Fig. 3.4 depicts Scanning Electron Micrographs of two representative micro-

and nanoporous silicon based membranes used in the assembly of the enzymatic biofuel cell constructed as part of this chapter.

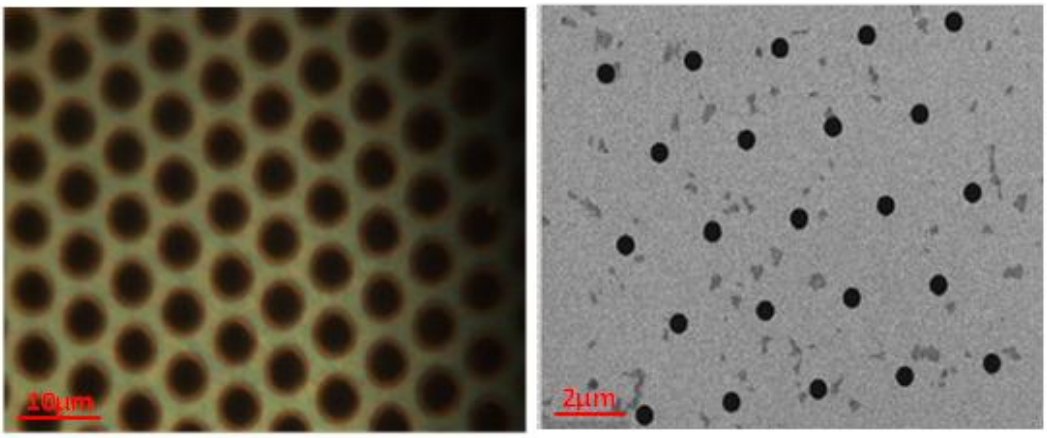


Fig. 3.4 SEM micrographs of porous membranes microfabricated at the Tyndall National Institute: (left) array of 2900 pores of Ø 5 µm; (right) array of 120 pores of Ø 500 nm.

The membranes were attached to the end of a glass capillary using a biocompatible silicon epoxy and dried at room temperature overnight. Prior to membrane attachment, the capillary surface was thoroughly polished on a wet sand paper until smooth, sonicated in an acetone bath for 20 mins, rinsed with copious amount of deionized water and dried in a nitrogen stream. The membranes were treated in oxygen plasma for 5 mins at 900 mTorr pressure and high power settings, in order to remove any residual organic debris. Following the exposure they were rinsed with IPA and deionized water and dried in nitrogen flow. A thin layer of the silicone adhesive was applied on the surface with the aid of a small brush; the membrane was carefully placed on the capillary using tweezers and pressed against the glue for a few seconds. The epoxy was left to dry in ambient temperature overnight. Once set, the semi-porous capillary was placed in the upper Eppendorf vial effectively separating the enzymes and their supporting electrolyte solutions.

GOX catalyzed electrooxidation of glucose on the anode produces gluconolactone, H^+ and e^-. Generated protons are conducted through a permselective membrane towards the cathode where they participate in a catalytic reduction of oxygen to water. Due to an insulating nature of the membrane the electrons are forced through an external circuit and are detected as current. Highly electronegative O_2 and $[Fe(CN)_6^3]^-$,when mutually present in the anolyte solution, will naturally compete for the electrons generated as a result of

glucose electrooxidation. In order to prevent the negative influence of molecular oxygen and to eliminate potential current and power losses, the bottom compartment of the cell was equipped with a nitrogen line, providing a constant supply of N_2 to the anolyte. A schematic diagram of the miniature enzymatic biofuel cell set-up is illustrated in Fig. 3.5.

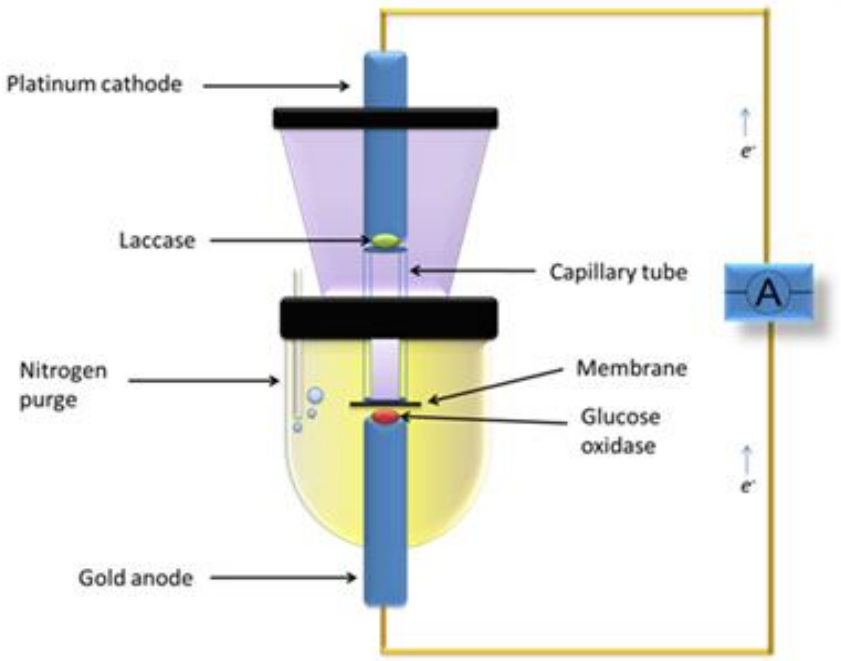


Fig. 3.5. Schematic of the miniature enzymatic glucose/ air biofuel cell incorporating glucose oxidase and laccase catalysts and a semi-porous membrane separating the anolyte and catholyte solutions and conducting the electron flow through the external circuit is indicated.

The half-cell reactions catalyzed at anode and cathode are summarized in Fig.3.6. As illustrated, two redox molecules have been introduced as anodic and cathodic mediators to ensure efficient electron transfer between the enzyme active site and the electrode surface. Potassium ferricyanide $K_3Fe(CN)_6$ has been employed to support the electrooxidation of glucose on the anode and 2,2'-azino-bis-3-ethylbenzothiazoline-6-sulphonic acid (ABTS) has been the mediator of choice for oxygen reduction at the cathode.

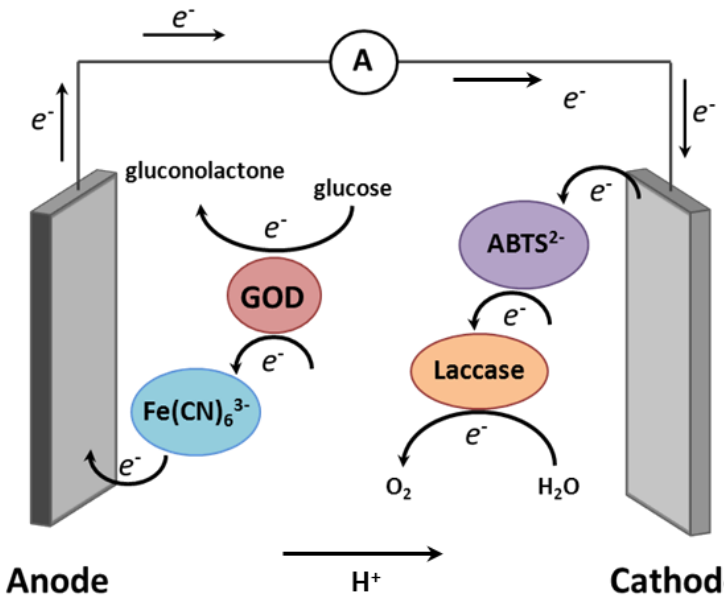


Fig. 3.6. Half–cell reactions of the glucose/O_2 enzymatic biofuel cell. Electrons generated from the electrooxidation of glucose are transported through $Fe(CN)_6^{3-}$ to the anode and shuttled to cathode for reduction of molecular oxygen. Electron flow is promoted via a cathodic mediator ($ABTS^{2-}$) transferring e^- to laccase.

The molecular structures of $K_3Fe(CN)_6$ and ABTS are represented in Fig. 3.7.

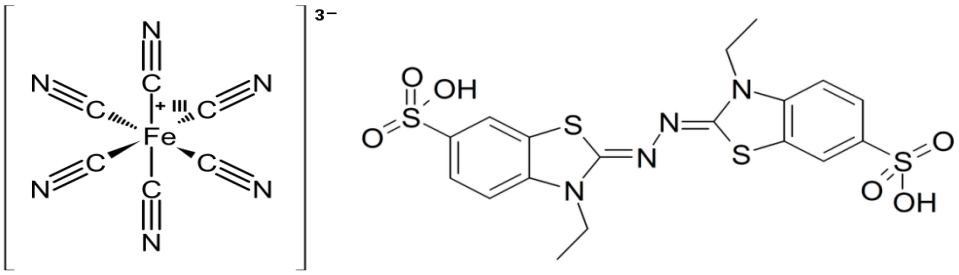


Fig. 3.7. Chemical structures of anodic and cathodic mediator molecules: $Fe(CN)_6^{3-}$ (left) and 2,2'-azino-bis(3-ethylbenzothiazoline-6-sulphonic acid), ABTS (right).

To isolate the half-cells, several nm and μm in diameter semi-porous silicon membranes, varying in the number of pores, have been investigated. The predominant function of the membrane was to prevent the undesired diffusion of molecular oxygen to

the anodic compartment and to conduct proton ions across to the cathode while enforcing the electron flow between the electrodes through an external circuit.

Two main types of membranes microfabricated in the Silicon Fabrication Facility of the Tyndall National Institute have been under investigation. 150 and 500 nm pore membranes with 390 pores each were manufactured from silicon wafers pre-coated with Si_3N_4 using optical lithography and etching techniques. 5 μm pores (with 120 and 2900 pores) were produced via Deep Reactive Ion Etching (DRIE) of silicon. In both processes, a 525 μm thick silicon support was used as the underlying material. Nano- and micro-fabrication routes employed the same orientation of the silicon wafer substrate (<100>) and analogous process-flows. Due to the highest pore density and size, the majority of experiments undertaken as part of this research scope were conducted utilizing micropore arrays (Ø 5 μm) with a total number of 2900 pores. The potential use of the remaining micro-and nanoporous membranes has also been evaluated; however, due to expected greater diffusion rate of protons through the film of the largest pore concentration, the former has been selected for the final design of the biofuel cell.

3.2.2. Fabrication of the silicon membranes.

While the porous membranes discussed in this section were designed specifically for the purpose of bioanalytical detection with electrochemical methods [23-25], they can be similarly applied in the catalytic studies using biofuel cells.

Fabrication of silicon-nitride membranes

Nanopores have been fabricated in a 100 nm layer of silicon nitride (Si_3N_4) deposited on a silicon wafer. Pad-Oxide (35 nm) coating was thermally adsorbed between pure Si and Si_3N_4 and acted as a stress relief agent. A layer of an electron-beam resist was coated onto silicon nitride and the nanopore arrays were patterned via electron-beam lithography. Nano-size openings were formed using a standard magnetic zero-resonant etch protocol in a mixture of fluorocarbon gases (CF_4 and CHF_3). A layer of protective ProTEK B3 polymer film (Brewer Science, Montana, USA) was spun coated onto the front-side of the wafer to protect the membrane during the last fabrication steps. The back-side was etched using PERIE nitride-on-oxide etch, 10:1 HF and KOH baths. Exposure of

a 100 Si wafer to a concentrated solution of potassium hydroxide resulted in a selective etch along the plane of the silicon crystal, at a 54.7 ºC and at a rate of 1 µm min^{-1}. The ultimate removal of the protective polymer coating in an appropriate solvent stripper (ProTEK Remover 100) and O_2 plasma exposure to remove any potential debris were the final steps in the fabrication of nanoporous membranes (Fig. 3.8).

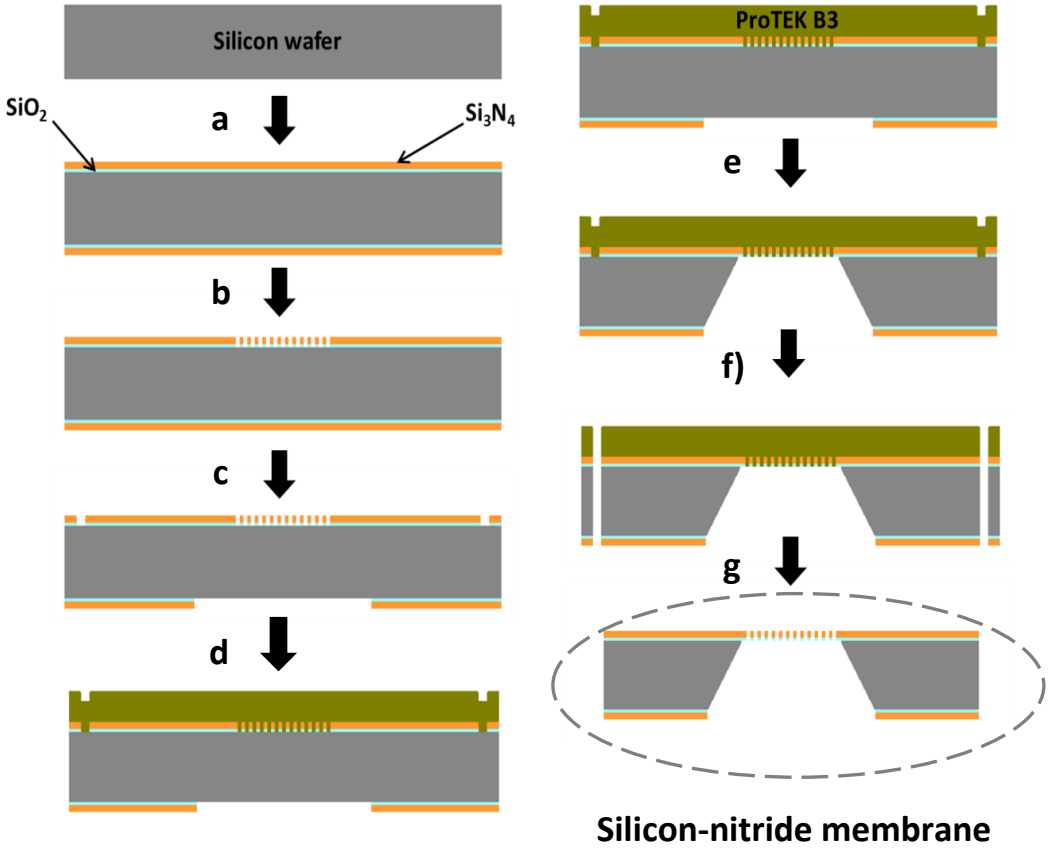


Fig. 3.8. Fabrication flow of the nanoscopic pore arrays in Si_3N_4. A) thermal oxidation (SiO_2) and LPCVD of Si_3N_4; b) E-beam patterning and dry-etch of nanopores through SiO_2 and Si_3N_4; c) dry-etch and wet-etch (10:1) through SiO_2 and Si_3N_4; d) application of ProTEK B3 protective layer onto front-side of the wafer; e) crystalline selective back-to-front etch of silicon in KOH bath; f) chip dicing; g) removal of ProTEK B3 polymer in solvent stripper and O_2 plasma clean.

Fabrication of porous silicon membranes

Porous silicon membranes have been produced in silicon wafers thermally oxidized, in order to form a hard-mask layer of silicon oxide (SiO_2). The openings were generated using a standard dry-etch protocol into SiO_2, in a mixture of gases (CF_4 and CHF_3). A layer of Si_3N_4 was then applied on front- and back-side of the wafer using Low Pressure Chemical Vapor Deposition (LPCVD) to protect the underlying SiO_2 during a subsequent KOH wet-etch of the membrane. Patterning of back side openings for succeeding dry-etch of Si_3N_4 + SiO_2 hard masks was carried out using optical lithography technique. Bulk silicon substrate located directly under the membrane area was etched in a potassium hydroxide bath up to a residual thickness of 100 μm and the layer of silicon nitride was removed in hot concentrated phosphoric acid. Micropore arrays were manufactured via Deep Reactive Ion Etch (DRIE) of front silicon bulk to a final depth of 100 μm. In order to prevent etch-through causing diffusion of helium maintaining a constant cooling temperature across the wafer, 5 μm of aluminum layer was applied at the back-side of the wafer. The final fabrication steps involved removal of Al etch-stop coating and SiO_2 hard mask using wet-etch technique (Fig. 3.9).

3.2.3. Characterization of a miniature enzymatic biofuel cell in static conditions.

In order to obtain baseline current values, the electrochemical response of bare gold and platinum disc electrodes has been investigated prior to enzyme immobilization. Glassy carbon and platinum have also been considered as potential electrode materials for the bioanode. Due to the favorable response of redox species on Au and the ease of patterning the metal microelectrodes on chip, gold has been selected as the ultimate active support for GOX. Platinum has been chosen as the electrode for the biocathode. As previously, other materials were under investigation; however, due to the metal's superior ability to sequester molecular oxygen and reduce it to water, Pt has been chosen for further assembly in the biofuel cell. This was due to the fact that if the immobilization of the enzyme has not been successful, the bare metal could have been used as a natural catalyst for O_2 reduction.

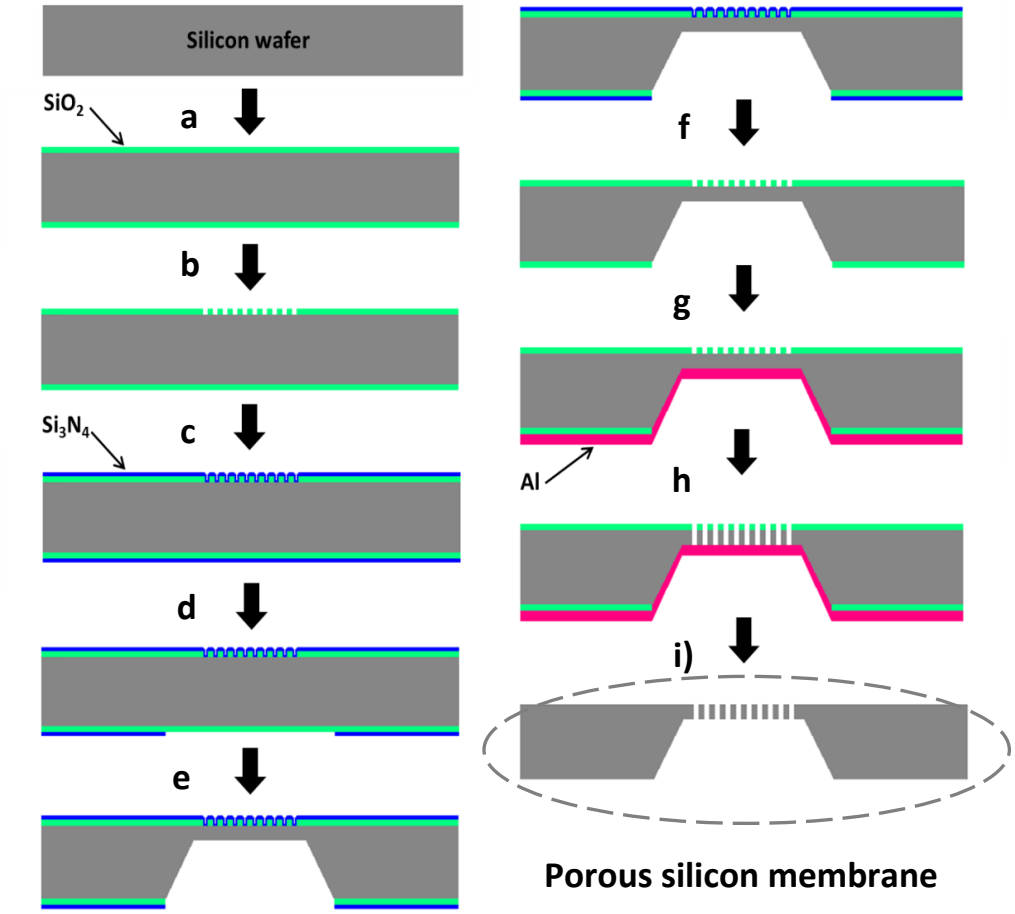


Fig. 3.9. Fabrication flow of the pore arrays in Si. a) thermal oxidation of 1µm SiO_2 b) dry-etch of nanopores in SiO_2; c) LPCVD of Si_3N_4; d) optical lithography to pattern the openings for KOH wet-eth at the back of the wafer; e) KOH back-to-front etch of underlying silicon up to 100 µm; f)removal of Si_3N_4 in hot concentrated phosphoric acid; g) spin-coating of aluminium layer on the back-side of the wafer as a stop-etch; h) DRIE of pores through SiO_2 and silicon; i)wet-etch removal of Al and SiO_2 hard mask.

The electrodes have been thoroughly cleaned, according to the protocol enclosed in Chapter II. The procedure involved mechanical polishing with alumina suspensions in deionized water (alumina particle size of 1 µm, 0.05 µm and 0.3 µm), sonication in EtOH and DI H_2O bath (1:1 v/v) for 20 mins and the electrochemical cycling of the electrode within a certain potential range in a fresh solution of 1 M H_2SO_4 for approximately 3 h.

The characterization of gold and platinum has been carried out using cyclic voltammetry measurements in appropriate buffer solutions containing the respective redox

species. The setup was composed of a three electrode system containing Au or Pt working electrodes, Pt wire auxiliary and Ag/AgCl reference in 3 M KCl supporting electrolyte.

Following the initial studies on the bare electrodes, glucose oxidase and laccase have been immobilized on gold and platinum accordingly, by evaporation from the enzyme aliquot using a simple casting method. 20 µL of 8 mg mL^{-1} GOX and 1 mg mL^{-1} laccase in respective buffer solutions were drop-coated onto gold and platinum electrodes and left to dry for 1 h.

3.3. Results and discussion.

The electrochemical response of both catalysts has been studied using cyclic voltammetry measurements in buffered solutions containing substrate and mediator molecules. The influence of the square root of the scan rate on the produced current has been investigated and the diffusion coefficients of $K_3Fe(CN)_6$ and ABTS have been calculated using the Randles-Sevčik formula. The open circuit potential of the enzyme modified electrodes has also been recorded and compared to the readings obtained for bare Au and Pt. The OCP measurements of the assembled biofuel cell were obtained and the electrochemical performance has been evaluated based on the current and power output. An increased open circuit potential is an indicator of enhanced power capabilities of a cell. The current density at various potentials applied to the biofuel cell has been measured using chronoamperometry. Power density has been calculated by multiplying the applied voltage and the current density from the obtained polarization curves. Resulting power vs. potential dependency provided useful information on the optimal operational cell voltage and the power density that can be drawn from the cell.

The response of a bare gold electrode has been measured in a 0.1 M phosphate buffer, pH 7.0, containing 20 mM glucose and 5 mM $K_3Fe(CN)_6$. The electrochemical signal of the substrate and mediator has been recorded for variety of scan rates (Fig. 3.10) and the shape of the behavior investigated to determine the reaction limiting factors.

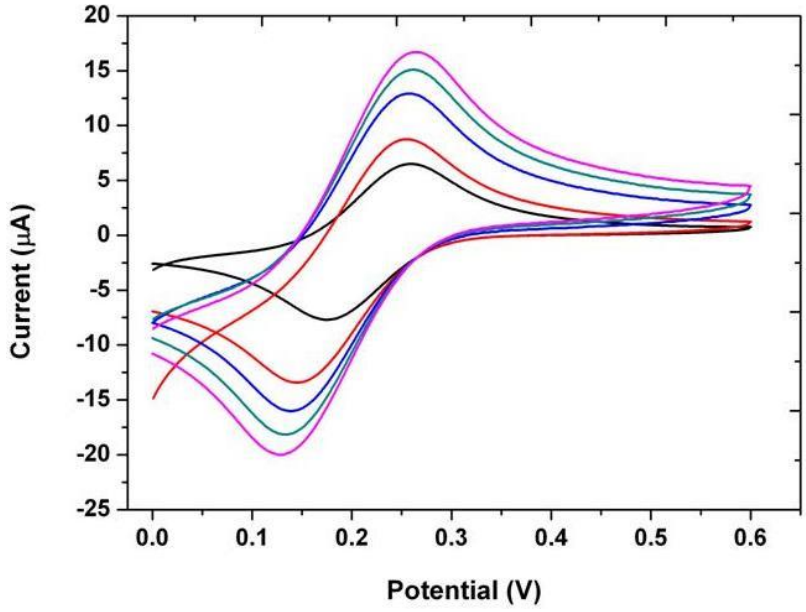


Fig. 3.10 CV of bare gold disc electrode in 20 mM glucose, 5 mM $K_3Fe(CN)_6$ in 0.1 M phosphate buffer pH 7.0. Dependency of the peak current on increasing scan rate: 10 mV s^{-1} (black line); 20 mV s^{-1} (red line); 30 mV s^{-1} (blue line); 40 mV s^{-1} (green line); 50 mV s^{-1} (magenta line). Potential recorded vs. Ag/AgCl (3 M KCl).

As illustrated in Fig. 3.10, cyclic voltammograms of bare gold in 0.1 M phosphate buffer, pH 7.0, containing 20 mM glucose and 5 mM $K_3Fe(CN)_6$ confirmed a diffusion-dependent response of ferricyanide, typically expected on macroelectrodes. The increased current values were recorded for higher scan rates and a characteristic diffusional shape of both redox peaks indicated a linear influx of $Fe(CN)_6^{3-}$ to the electrode surface and current limitations due to the mass transfer restrictions. These observations suggest that the reaction kinetics is faster than the diffusion of species. The distorted shape of the cyclic voltammogram at more negative potential values is due to the improper choice of the starting potential, forcing the oxidation of $Fe(CN)_6^{3-}$ species, as opposed to their initial reduction by cycling the potential from 0.6 V back to 0 V.

As discussed in Appendix A, the reversibility of the redox system is, by convention, determined based on the potential difference (ΔE) between the oxidation and reduction peaks. For a reaction to be reversible, ΔE in a single electron transfer process should be approximately 59 mV and independent of the scan rate used. As indicated in Fig. 3.10, the oxidative and reductive peak voltage for ferricyanide recorded at 0.01 V s^{-1} scan rate were 0.259 V and 0.173 V respectively. The resulting voltage difference in this

case was 86 mV, which is higher than the hypothetical ΔE expected in theory for a reversible process. This dissimilarity may be due to unaccounted resistance of the solution.

The influence of the square root of the scan rate on the oxidation peak current has also been investigated and is illustrated in Fig. 3.11. The presence of an intercept is most likely associated with the incorrect choice of the starting potential for the CV measurement.

The linear dependency of the oxidation peak current, i_p on the square root of the applied scan rate, $v^{1/2}$, depicted in Fig. 3.11, suggests that the response of ferricyanide on bare gold electrode can be mass transport limited.

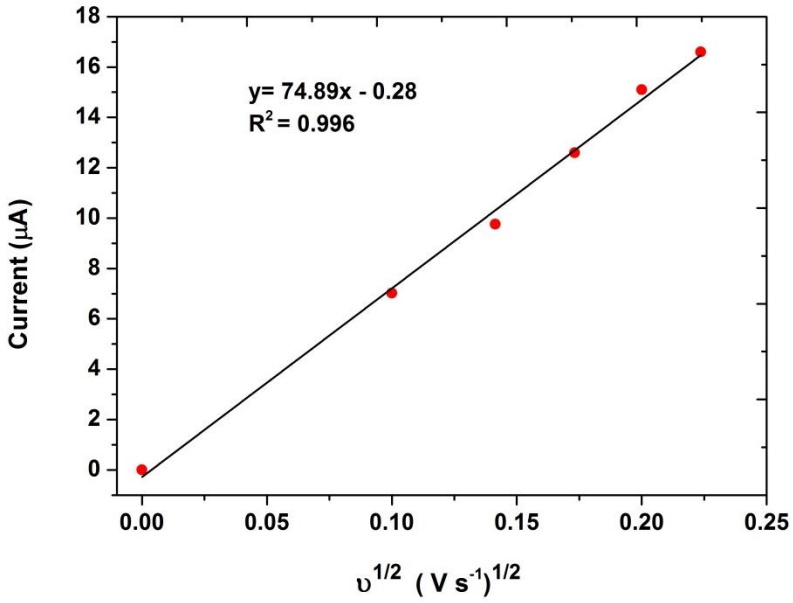


Fig. 3.11. Dependency of the maximum oxidation current (i_p) on the square root of the scan rate ($v^{1/2}$). Response of 5 mM $K_3Fe(CN)_6$ in 0.1 M phosphate buffer pH 7.0 on Au disc electrode.

Based on the slope of the oxidation current dependency on the $v^{1/2}$ and the assumption of the reversibility of the ferricyanide redox reaction, the diffusion coefficient of $K_3Fe(CN)_6$ has been determined (Eq. 3.2) using the transformed Randles-Sevčik equation (Eq. 3.1).

$$D_{ferricyanide} = \left(\frac{slope}{2.69\ x\ 10^5 A c_o}\right)^2 \qquad Eq.\ 3.1$$

Where,

$$slope = 74.89\ x\ 10^{-6}\ \frac{A}{Vs^{-1}};\quad A = 0.032\ cm^2\ ;\ c_0 = 5\ x\ 10^{-6}\ mol\ cm^{-3}$$

$$D_{ferricyanide} = \left(\frac{74.89\ x\ 10^{-6}}{(2.69\ x\ 10^5)\ (0.032)(5x10^{-6})}\right)^2 \qquad Eq.\ 3.2$$

$$D_{ferricyanide} = 3.03\ x\ 10^{-6} \pm 1.2\ x\ 10^{-7}\ cm^2 s^{-1}$$

Diffusion coefficient of ferricyanide ($D_{ferricyanide}$), determined from Randles-Sevčik formula (Eq. 3.1) based on the slope of the i_p vs. $v^{1/2}$ line gave a value of $3.03 \times 10^{-6} \pm 1.52\ x\ 10^{-7}$ cm^2 s^{-1}. This is in an acceptable agreement with the theoretical 7.6×10^{-6} cm^2 s^{-1} correspondent for ferricyanide, as reported in [26, 27]. The observed discrepancy is due to the presence of the intercept on the i_p vs. $v^{1/2}$, which is followed from the improper potential start.

The electrochemical signal of a bare platinum electrode has been recorded in an aerated 0.1 M acetate buffer, pH 4.6, containing 50 mM ABTS (Fig. 3.12). Cyclic voltammetry of the electrode at increasing scan rates was performed to determine whether the ion transfer to the platinum surface is a diffusion-controlled process.

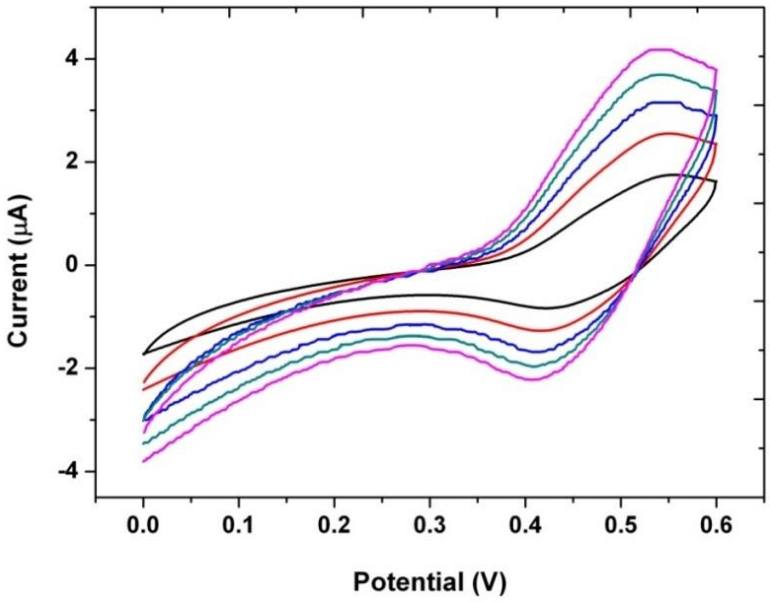


Fig. 3.12. CV of bare platinum disc electrode in 50 mM ABTS in 0.1 M acetate buffer pH 4.6. Dependency of the peak current on increasing scan rate: 10 mV s^{-1} (black line); 20 mV s^{-1} (red line); 30 mV s^{-1} (blue line); 40 mV s^{-1} (green line); 50 mV s^{-1} (magenta line). Potential recorded vs. Ag/AgCl (3 M KCl).

In a similar manner to $K_3Fe(CN)_6$, the electrochemistry of 50 mM ABTS on platinum electrode indicated enhanced current values corresponding to increased scan rates (Fig. 3.12) suggesting that the response of the mediator may be diffusion-controlled.

The potential of the oxidation and reduction peaks for ABTS recorded at 0.01 V s^{-1} were 0.54 V and 0.435 V, accordingly. The calculated ΔE was determined as 105 mV, which is nearly twice the theoretical value of 59 mV for a single electron transfer process. The recorded discrepancy may be attributed to the impeded electron transfer in the solution due to the nature of the buffer and employed experimental conditions (e.g. pH and temperature).

In order to confirm the limiting effect of diffusion on the overall rate of redox processes, the square root of the scan rate has been plotted against the oxidation peak current as shown in Fig. 3.13.

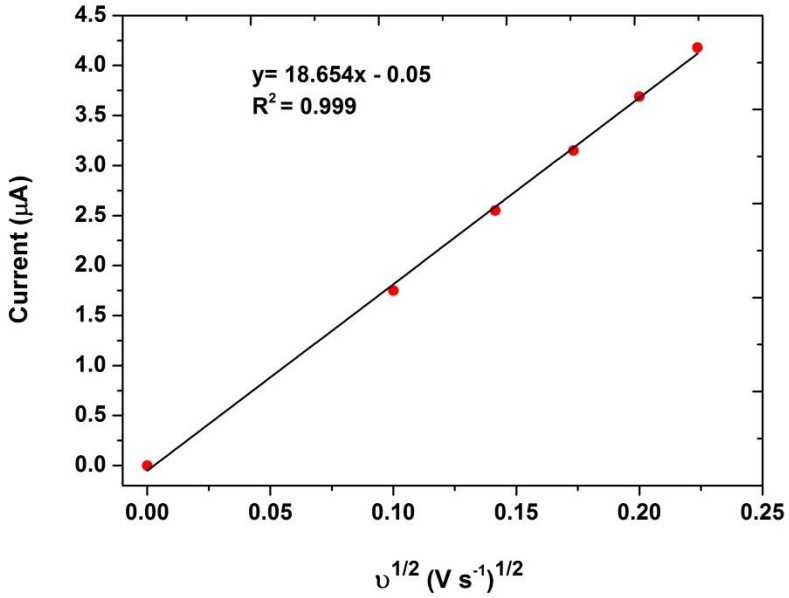


Fig. 3.13. Linear relationship of the peak current and the square root of the scan rate for 50 mM ABTS in 0.1 M acetate buffer pH 4.6 on bare Pt disc electrode.

A linear dependency of the oxidation peak current, i_p on the square root of the scan rate, $v^{1/2}$ (Fig. 3.13) suggested that the reaction is governed by the diffusion of ABTS species to the electrode surface, however the large peak separation indicated additionally a slow electron transfer and to certain extent, kinetic limitations.

The diffusion coefficient of ABTS has been calculated as shown in Eq. 3.3 using the transformed Randles-Sevčik equation (Eq. 3.1), under the assumption of the reversibility of the ABTS redox reaction. Here:

$$slope = 18.654\ x\ 10^{-6}\ \frac{A}{Vs^{-1}};\ A = 0.032\ cm^2;\ c_0 = 5\ x\ 10^{-5}\ mol\ cm^{-3}$$

$$D_{ABTS} = \left(\frac{18.654\ x\ 10^{-6}}{(2.69\ x\ 10^5)(0.032)(5x10^{-5})}\right)^2 \qquad Eq.\ 3.3$$

$$D_{ABTS} = 1.88\ x\ 10^{-6} \pm 6.6\ x\ 10^{-8} cm^2\ s^{-1}$$

Diffusion coefficient of ABTS (D_{ABTS}) calculated from the slope of the linear relationship of the i_p and $v^{1/2}$ gave $1.88\ x\ 10^{-6} \pm 6.6\ x\ 10^{-8}\ cm^2\ s^{-1}$. This is in a

good agreement with the expected literature equivalent of $3.2 \times 10^{-6} cm^2\ s^{-1}$ [28] for ABTS.

The electrochemical response of glucose oxidase modified gold disc electrode has been studied in 0.1 M phosphate buffer pH 7.0 in the presence of 20 mM glucose and 5 mM $K_3Fe(CN)_6$ in. The solution has been purged with nitrogen for 20 mins, prior to the measurement, to remove the interfering oxygen. The enzymatic activity of GOX has been then compared to the signal of plain Au recorded in identical working conditions (Fig. 3.14).

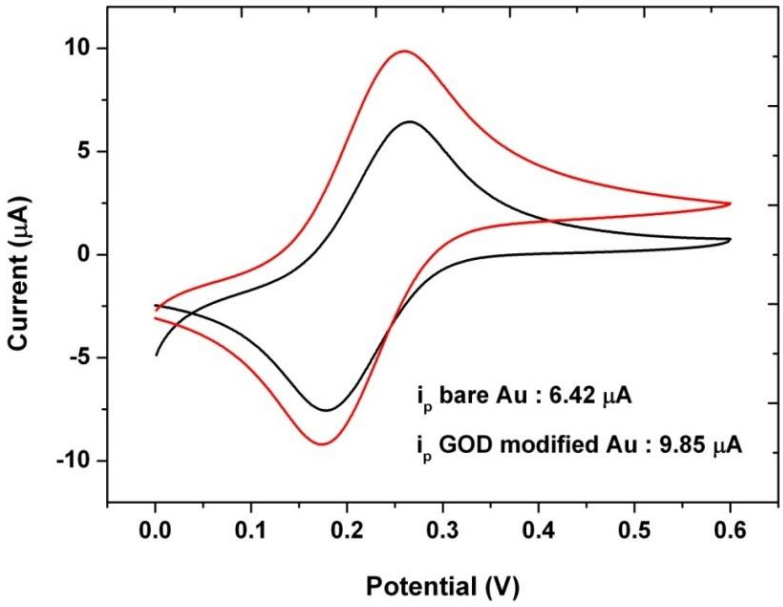


Fig. 3.14. CV of gold in 20 mM glucose and 5 mM $K_3Fe(CN)_6$ in 0.1 M phosphate buffer pH 7.0. Response of bare Au (black line) and GOX modified electrode (red line); scan rate of 10 mV s^{-1}. Potential recorded vs. Ag/AgCl (3 M KCl).

As previously, the distorted shape of the CV response of bare Au electrode at more negative potential values is due to the improper choice of the starting potential, forcing the oxidation of $Fe(CN)_6^{3-}$ species, as opposed to their initial reduction by cycling the potential from 0.6 V back to 0 V.

The electrooxidation of glucose by glucose oxidase has been catalyzed in the presence of a mediator molecule, $K_3Fe(CN)_6$. The reaction scheme is illustrated in Eq. 3.4.

$$\mathbf{Glucose_{(red)} + GOX_{(ox)} \rightarrow gluconolactone_{(ox)} + GOX_{(red)} + 2H^+}$$
$$\mathbf{GOX_{(red)} + 2\ Fe(CN)_6^{3-}{}_{(ox)} \rightarrow GOX_{(ox)} + 2\ Fe(CN)_6^{4-}{}_{(red)}} \qquad Eq.3.4$$

The oxidation peak currents of GOX modified gold electrode and bare Au, recorded in 20 mM glucose and 5 mM $K_3Fe(CN)_6$ in the supporting phosphate buffer, (pH 7.0), have been recorded at 9.85 ± 0.29 µA and 6.42 ± 0.19 µA respectively. The aforementioned findings suggest that biofunctionalisation of the electrode by physical immobilization of glucose oxidase (drop-coating) results in an enhanced catalysis of glucose electrooxidation as compared to the intrinsic activity of bare metal.

The electroreduction of molecular oxygen catalyzed by laccase immobilized on platinum disc electrode has been examined in aerated 0.1 M acetate buffer solution at pH 4.6 in the presence of 50 mM ABTS. Prior to the measurement, the buffer has been exposed to the air for 20 mins to ensure sufficient amount of oxygen present. The current output was then compared to the signal of plain Pt (Fig. 3.15).

As can be seen from Fig. 3.15, the peak currents for the electrochemical reduction of molecular oxygen by laccase functionalized Pt and bare metal electrode have been recorded as -1.83 ± 0.06 µA and -0.80 ± 0.02 µA respectively. While this change may suggest the electroactivity of laccase towards O_2 reduction, the wholesale shift in the CV curve suggests the effect of the bulk conversion of ABTS to its oxidized form rather at the start of the experiment, rather than an evidence for electrocatalysis of the reaction on the CV timescale

Again, the atypical shape of the CV response on Pt electrode at more negative potential values is caused by an improper choice of the starting potential, where the oxidation of $Fe(CN)_6^{3-}$ species is preceded by their initial reduction if the potential was cycled from 0.6 V back to 0 V.

Successful catalysis of the enzymatic reduction of molecular oxygen into water by laccase in the presence of ABTS as the mediator would follow the reaction defined by Eq. 3.5.

$$\mathbf{4\ ABTS^{2-}_{(red)} + laccase_{(ox)} \rightarrow 4\ ABTS^{-}_{(ox)} + laccase_{(red)}}$$
$$\mathbf{4\ H^{+} + laccase_{(red)} + O_{2\,(ox)} \rightarrow laccase_{(ox)} + 2\ H_2O_{(red)}} \qquad Eq.\ 3.5$$

The successful catalysis by GOX and laccase adsorbed on gold and platinum electrodes suggests that they can be effectively employed as bioanode and biocathode

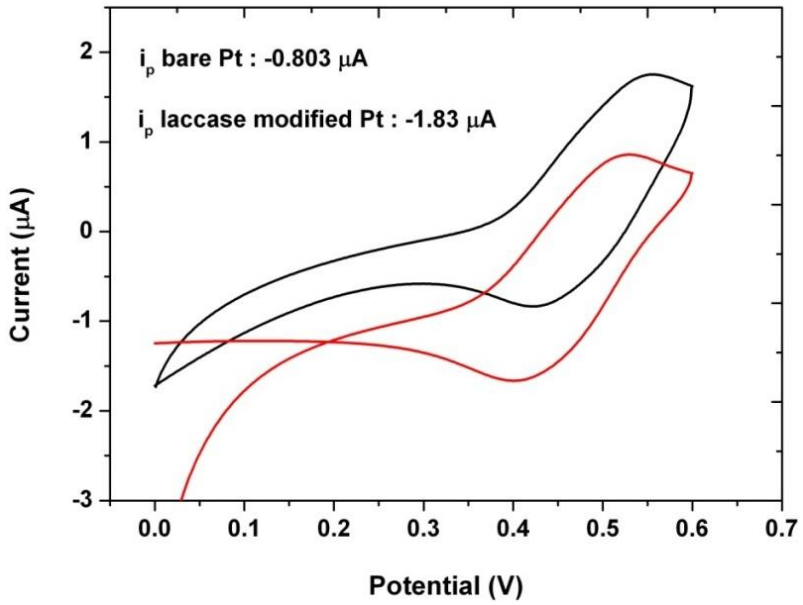


Fig. 3.15. Cyclic voltammogram of platinum in response to oxygen measured in 50 mM ABTS, 0.1M acetate buffer pH 4.6. Response of bare Pt (black line) and laccase modified Pt electrode (red line) at a scan rate of 10 mV s^{-1}. Potential vs. Ag/AgCl.

systems in enzymatic biofuel cell applications, in static and potentially in microfluidic configurations.

The open circuit potentials (OCP) for plain and enzyme modified electrodes have been recorded in respective buffer solutions (Fig. 3.16), in order to measure the potential driving force for the investigated enzymatic reactions. 20 mM glucose and 5 mM $K_3Fe(CN)_6$ phosphate buffer at pH 7.0 has been used for OCP measurements of gold and gold modified electrode, while the activity of bare and laccase functionalized platinum have been evaluated in 50 mM ABTS in aerated 0.1 M acetate buffer pH 4.6.

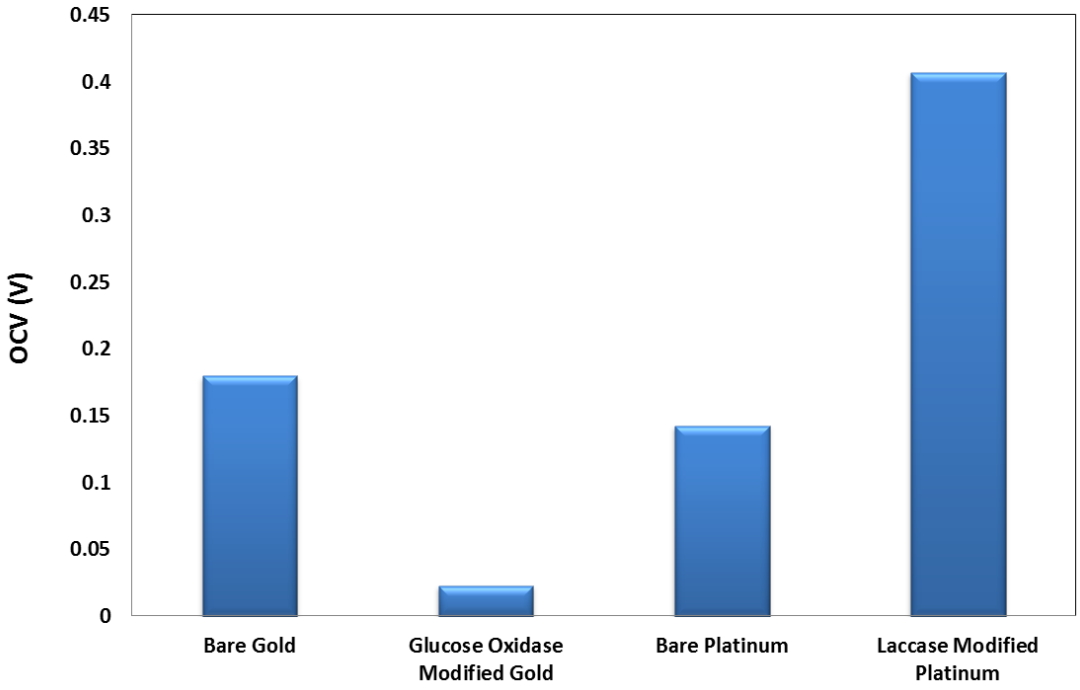


Fig. 3.16. Comparison of OCP values recorded for bare and enzyme modified electrodes in respective buffer solutions containing the substrate and mediator molecules. Bare Au- 0.18 V; GOX modified Au- 0.34 V; bare Pt- 0.14 V; laccase modified Pt -0.41 V. OCP recorded vs. Ag/AgCl (3 M KCl).

The open circuit potential measurements of enzyme modified electrodes confirmed increased OCP values as compared to bare gold and platinum (Fig. 3.16). The OCP increase for GOX/Au and laccase/Pt are indicators of much greater performance of the enzymatic half-cells.

The classical approach to the biofuel cell design requires the use of a membrane to isolate the divergent half-cell processes occurring in the reaction system, in order for both catalysts to accomplish their biological functions without any loss of their enzymatic activity. In due course of this research work, a number of biofuel cell configurations employing various microfabricated SiO_2 and Si_3N_4 semi-porous membranes have been investigated. The use of commercially available Nafion perfluorinated film has also been studied, due to its well established characteristics and suitable proton conductivity. The effects of the porosity and the source of the separation material on the cell performance have been determined.

The performance of an assembled enzymatic biofuel cell, developed as part of this Ph.D. work, operating in substrate and mediator supplemented buffer solutions under

static conditions, has been therefore investigated with a number of porous silicon membranes and the OCP values have been recorded (Fig. 3.17).

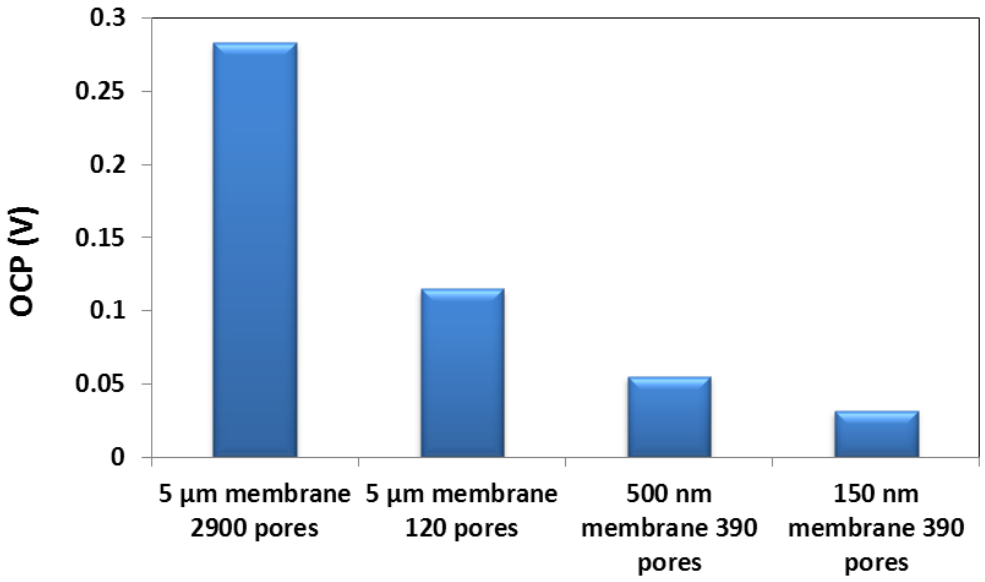


Fig. 3.17. OCP values for a glucose/oxygen enzymatic biofuel cell operating in static conditions utilizing a semi-porous insulating membrane to isolate the anolyte and catholyte compartments. Ø 5µm, 2900 pores- 0.28 V; Ø 5µm, 120 pores- 0.12 V; Ø 500 nm, 390 pores- 0.06 V; Ø 150 nm, 390 pores- 0.03 V. OCP vs. Ag/AgCl.

OCP readings of a fully assembled enzymatic biofuel cell operating in working buffer solutions have shown the correlation between the porosity of the membrane and the measured potential (Fig. 3.17). The OCP value for the highest porosity silicon membrane (2900 pores of Ø 5 µm diameter each) has been greater than that for 120 pores of Ø 5 µm. Moreover, the open circuit potential of the former showed dramatic increases when compared to Ø 500 nm 390 and Ø 150 nm, 390 pore arrays. The fundamental explanation supporting these findings is the fact that Ø 5µm 2900 pore array provides the highest surface area available for the mass transfer of hydrogen protons across the anode and cathode interface. H^+ generated from the electrooxidation of glucose is further utilized by laccase in the catalytic process of oxygen reduction. Higher proton influx gives rise to greater O_2 turnover, which completes the catalytic cycle and in turn results in a higher driving force for the enzymatic reactions within the cell.

The OCP of the enzymatic biofuel cell incorporating GOX and laccase catalysts has been compared to its non-enzymatic equivalent operating in the same working buffer solutions (Fig. 3.18). For the purpose of this study, the membrane of the highest porosity (Ø 5 µm, 2900 pores) has been employed.

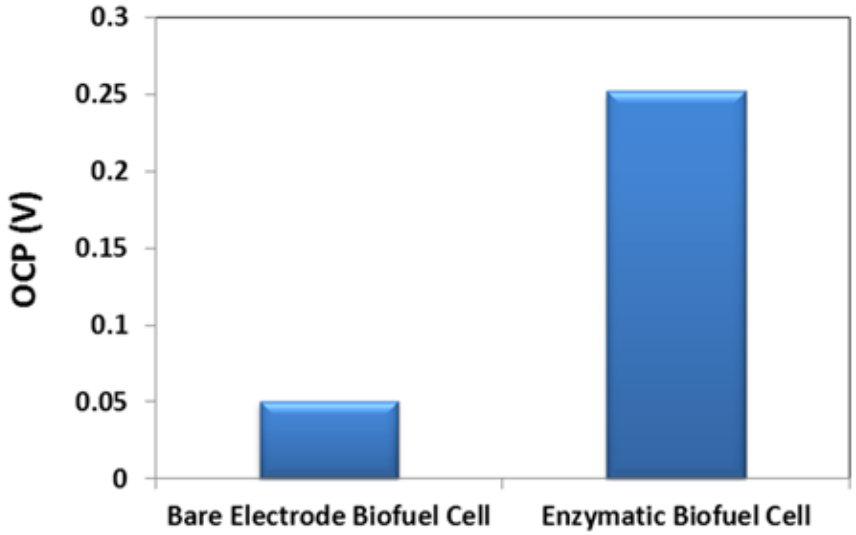


Fig. 3.18. OCP values for a biofuel cell operating in static conditions, non-enzymatic configuration (0.05 V) and GOX/laccase cell (0.283 V). Ø 5 µm, 2900 pore membrane has been used to separate the anodic and cathodic compartments. OCP recorded vs. Ag/AgCl (3 M KCl).

The OCP measurements have been confirmed by chronoamperometric studies investigating the polarization curves of fully assembled enzymatic biofuel cells operating in working solutions under static conditions. The current produced as a result of the enzymatic electrocatalysis has been recorded at various potentials and normalized by the surface area of the electrodes (Fig. 3.19), yielding the current density (µA cm^2).

As illustrated in Fig. 3.19, the constructed prototype exhibited a characteristic polarization trend of the current drop with increased voltage when utilizing the highest porosity membrane (2900 and diameter of Ø 5µm). The dependency of the current on the applied potential for the Nafion film also seemed to have a linear tendency; however, the current output was significantly lower. The use of other silicon membranes drastically attenuated the performance of the cell. While the response in the presence of Ø 150 nm,

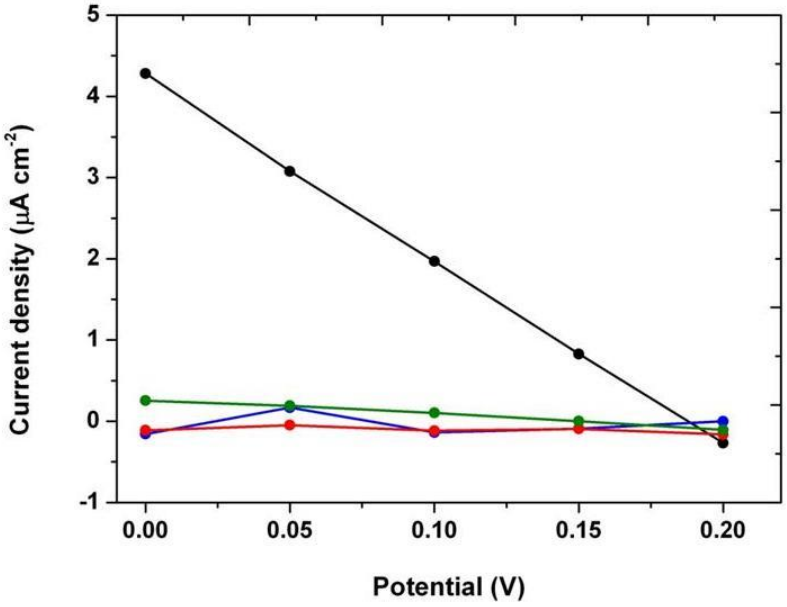


Fig. 3.19. Polarization curve for glucose/air miniature enzymatic biofuel cell utilizing GOX and laccase as anodic and cathodic catalysts; separation of the anolyte (oxygen-free 20 mM glucose, 5 mM $K_3Fe(CN)_6$ 0.1 M phosphate buffer pH 7.4) and the catholyte solution (50 mM ABTS 0.1 M acetate buffer pH 4.6 exposed to air for 20 mins) has been obtained with the aid of various membranes: Ø 5 μm, 2900 pores in SiO_2 (black line); Nafion perfluorinated (green line); Ø 150 nm, 390 pores in Si_3N_4 (red line); Ø 5 μm, 120 pores in SiO_2 (blue line). Potential recorded vs. Ag/AgCl (3 M KCl).

390 pores in Si_3N_4 varied only slightly, the current values for Ø 5 μm, 120 pore array fluctuated in what appears to be a random manner. The unexpected behavior of the microporous film might have been due to a blockage accidentally introduced at the membrane preparation step or a capillary action that prevented the fluid flow through the pores. The negative values of the current density obtained in the case of Ø 150 nm, 390 pores in Si_3N_4 and Ø 5 μm, 120 pores in SiO_2 membranes are most likely the result of an internal bias in the cell due to the pH difference between the anodic and cathodic compartments.

The investigation of various silicon based membranes as potential separation materials for the anodic and cathodic compartments revealed promising results for microporous array films. While many proceeding biofuel cells employ Nafion films due to their durability, efficient proton conductivity and well characterized properties, in the light of the aforementioned results, the use of highly porous silicon membranes for the

assembly of miniature EBFC is however favored where higher current and power output is required.

The power density of the constructed biofuel cell has been calculated for the highest porosity SiO_2 membrane and Nafion separator based on obtained current density values and the applied voltage, as presented in Fig. 3.20.

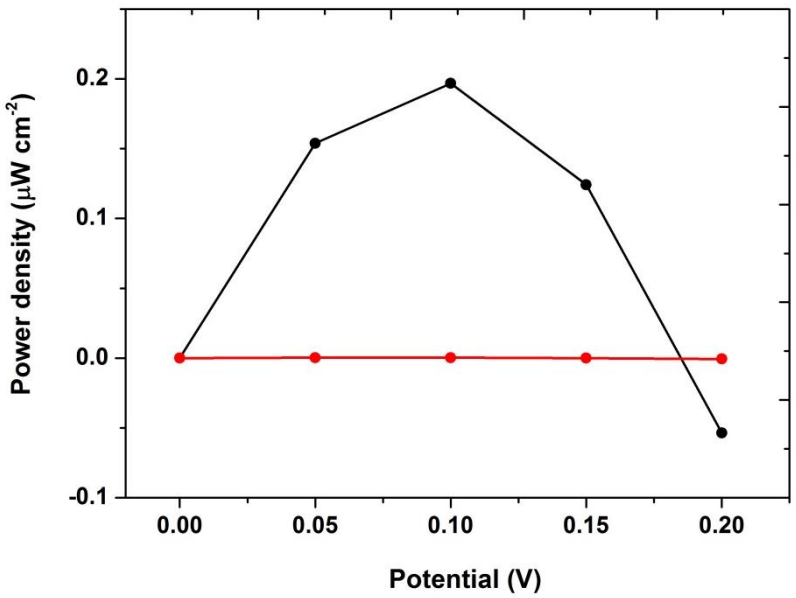


Fig. 3.20. Power density for glucose/air miniature enzymatic biofuel cell utilizing GOX and laccase as anodic and cathodic catalysts; 20 mM glucose, 5 mM $K_3Fe(CN)_6$ in 0.1 M phosphate buffer pH 7.4 anolyte solution and 50 mM ABTS 0.1 M acetate buffer pH 4.6 exposed to air for 20 mins as the catholyte separated by various membranes. Ø 5 μm, 2900 pores in SiO_2 (black curve); Nafion perfluorinated (red line). Potential recorded vs. Ag/AgCl (3 M KCl).

A distinctive bell-like shape of the power curve has been obtained when the enzymatic cell operated in the presence of the highest pore density membrane. The maximum power of 0.197 μW cm^{-2}, recorded at 0.1 V, corresponds to performance of the constructed prototype greater than that reported for some existing biofuel cells [20].

3.4. Conclusions.

Rapid and continuous development of the architecture and operational methodology of the enzymatic biofuel cells have led to a significant improvement in the

power and energy efficiencies. Substantial advantage has been contributed to a membrane-free approach and invention of an air-breathing cathode, leading to a single chamber design and a higher substrate turnovers. Nevertheless, for many applications, further enhancement in the device performance is still required. In order to employ enzymatic biofuel cells for electronic applications, high energy density fuels such as glycerol or ethanol are required. Issues related to the fouling of active surfaces and loss of enzymatic activities of biomolecules could be resolved by incorporating highly catalytic carbon electrode materials. In depth modelling studies encompassing mass transport, diffusion of species and reaction kinetics can greatly contribute to the current understanding of the bioelectrochemical reactions governed by enzyme catalysts. Carefully corroborated mathematical models can not only deliver useful information on the expected kinetic behaviour of the cell, but also accelerate the development of practical systems by providing theoretical background on device optimization.

The rudimentary cell design proposed in this chapter enables conversion of glucose and oxygen in a very simple static configuration, employing commercially available and extensively explored enzyme catalysts, glucose oxidase and laccase. The electrochemical characterization of the assembled miniature biofuel cell revealed the current and powered densities of 1.97 $\mu A\ cm^{-2}$ and 0.197 $\mu W\ cm^{-2}$ which are greater than values obtained and published for some of the prevailing biofuel cell solutions [20, 29].

The feasibility of a miniature enzymatic biofuel cell has been investigated in the prospects of transposing the design into an enzyme driven device operating in a microfluidic regime. The application of glucose oxidase and laccase as catalysts for glucose and oxygen conversion significantly increased the current and power densities of the constructed cell. Further optimization of the enzyme concentration and immobilization technique as well as the configuration and the working format of the cell are required. The findings presented in this chapter have been used as a supporting platform for the design and fabrication of microfluidic devices with potential prospects as biocompatible or environmental power sources.

3.5. Bibliography.

1. Larminie, J., A. Dicks, and M.S. McDonald, *Fuel cell systems explained*. Vol. 2. 2003: Wiley Chichester.
2. Osman, M., A. Shah, and F. Walsh, *Recent progress and continuing challenges in bio-fuel cells. Part I: Enzymatic cells.* Biosensors and Bioelectronics, 2011. **26**(7): p. 3087-3102.
3. Chen, T., et al., *A miniature biofuel cell.* Journal of the American Chemical Society, 2001. **123**(35): p. 8630-8631.
4. Katz, E., I. Willner, and A.B. Kotlyar, *A non-compartmentalized glucose/O_2 biofuel cell by bioengineered electrode surfaces.* Journal of Electroanalytical Chemistry, 1999. **479**(1): p. 64-68.
5. Tsujimura, S., K. Kano, and T. Ikeda, *Glucose/O_2 Biofuel Cell Operating at Physiological Conditions.* Electrochemistry Tokyo, 2002. **70**(12): p. 940-942.
6. Binyamin, G. and A. Heller, *Stabilization of wired glucose oxidase anodes rotating at 1000 rpm at 37 C.* Journal of the Electrochemical Society, 1999. **146**(8): p. 2965-2967.
7. Barton, S.C., et al., *Electroreduction of O_2 to water at 0.6 V (SHE) at pH 7 on the 'wired' Pleurotus ostreatus laccase cathode.* Biosensors and Bioelectronics, 2002. **17**(11): p. 1071-1074.
8. Barton, S.C., et al., *Electroreduction of O_2 to water on the "wired" laccase cathode.* The Journal of Physical Chemistry B, 2001. **105**(47): p. 11917-11921.
9. Barton, S.C., et al., *The "Wired" laccase cathode: high current density electroreduction of O2 to water at + 0.7 V (NHE) at pH 5.* Journal of the American Chemical Society, 2001. **123**(24): p. 5802-5803.
10. Ramanavicius, A., A. Kausaite, and A. Ramanaviciene, *Biofuel cell based on direct bioelectrocatalysis*. Biosensors and Bioelectronics, 2005. **20**(10): p. 1962-1967.
11. Kamitaka, Y., et al., *Fructose/dioxygen biofuel cell based on direct electron transfer-type bioelectrocatalysis.* Physical Chemistry Chemical Physics, 2007. **9**(15): p. 1793-1801.
12. Wang, S.C., et al., *Membrane-less and mediator-free enzymatic biofuel cell using carbon nanotube/porous silicon electrodes.* Electrochemistry Communications, 2009. **11**(1): p. 34-37.
13. Liu, C., et al., *Membraneless enzymatic biofuel cells based on graphene nanosheets.* Biosensors and Bioelectronics, 2010. **25**(7): p. 1829-1833.
14. Higgins, S.R., et al., *Hybrid biofuel cell: microbial fuel cell with an enzymatic air-breathing cathode.* ACS catalysis, 2011. **1**(9): p. 994-997.
15. Rincón, R.A., et al., *Enzymatic fuel cells: Integrating flow-through anode and air-breathing cathode into a membrane-less biofuel cell design.* Biosensors and Bioelectronics, 2011. **27**(1): p. 132-136.
16. Rincón, R.A., et al., *Flow-through 3D biofuel cell anode for NAD^+ dependent enzymes.* Electrochimica Acta, 2011. **56**(5): p. 2503-2509.
17. Flexer, V., et al., *A novel three-dimensional macrocellular carbonaceous biofuel cell.* Phys. Chem., 2013. **15**(17): p. 6437-6445.
18. Kenis, P.J., A. Wieckowski, and E.R. Choban, *Membraneless electrochemical cell and microfluidic device without pH constraint*, 2009, US 7635530 B2.
19. Minteer, S.D., R.S. Martin, and C.M. Moore, *Microfluidic biofuel cell*, 2010, WO 2005096430 A1.

20. Beneyton, T., et al., *Membraneless glucose/O_2 microfluidic biofuel cells using covalently bound enzymes.* Chemical Communications, 2013. **49**(11): p. 1094-1096.
21. Zebda, A., et al., *Electrochemical performance of a glucose/oxygen microfluidic biofuel cell.* Journal of Power Sources, 2009. **193**(2): p. 602-606.
22. Zebda, A., et al., *A microfluidic glucose biofuel cell to generate micropower from enzymes at ambient temperature.* Electrochemistry Communications, 2009. **11**(3): p. 592-595.
23. Scanlon, M.D., G. Herzog, and D.W. Arrigan, *Electrochemical detection of oligopeptides at silicon-fabricated micro-liquid/liquid interfaces.* Analytical Chemistry, 2008. **80**(15): p. 5743-5749.
24. Strutwolf, J., M.D. Scanlon, and D.W. Arrigan, *Electrochemical ion transfer across liquid/liquid interfaces confined within solid-state micropore arrays–simulations and experiments.* Analyst, 2009. **134**(1): p. 148-158.
25. Berduque, A., R. Zazpe, and D.W. Arrigan, *Electrochemical detection of dopamine using arrays of liquid–liquid micro-interfaces created within micromachined silicon membranes.* Analytica Chimica Acta, 2008. **611**(2): p. 156-162.
26. Stackelberg, M.V., M. Pilgram, and V. Toome, *Bestimmung von diffusionskoeffizienten einiger ionen in wäbriger lösung in gegenwart von fremdelektrolyten. I.* Z. Elektrochem, 1953. **57**: p. 342-350.
27. Gooding, J., V. Praig, and E. Hall, *Platinum-catalyzed enzyme electrodes immobilized on gold using self-assembled layers.* Analytical Chemistry, 1998. **70**(11): p. 2396-2402.
28. Tsujimura, S., et al., *Bioelectrocatalytic reduction of dioxygen to water at neutral pH using bilirubin oxidase as an enzyme and 2, 2'-azinobis (3-ethylbenzothiazolin-6-sulfonate) as an electron transfer mediator.* Journal of Electroanalytical Chemistry, 2001. **496**(1): p. 69-75.
29. Coman, V., et al., *A membrane-, mediator-, cofactor-less glucose/oxygen biofuel cell.* Physical Chemistry Chemical Physics, 2008. **10**(40): p. 6093-6096.

CHAPTER IV

MODELLING AND OPTIMIZATION STUDIES

I don't demand that a theory correspond to reality because I don't know what reality is. All I'm concerned with is that the theory should predict the results of experiment.

Stephen Hawking

The final truth about a phenomenon resides in the mathematical description of it. As long as there is no imperfection in this, our knowledge of the phenomenon is complete.

Sir James Jeans

4.1. Introduction.

While the field of enzymatic electrodes for electrochemical biosensors is relatively well established [1, 2], the investigations into enzyme-driven biofuel cells are still at a relatively early stage of development. As the reactions are complex and, in some aspects, not fully understood it means that most articles on enzymatic reactions and biofuel cells in the literature assume simplifications of the system [3]. It is believed that models of electrochemical cells, such as the polymer electrolyte membrane fuel cells (PEM) and batteries, can act as suitable prototypes for the design of their biofuel cell analogs [4]. A comprehensive review on the electrodes for sensing purposes and their significant overlap with those employed in fuel cell applications has been reported by Bartlett and co-workers [5].

Analysis of enzymatic biofuel cells reported to date mainly use well-known Michaelis – Menten expressions, discussed later in this chapter, supported by the material balance and mass transport conditions [6-8]. This method is generally accepted as the best description of enzyme kinetics provided a non-allosteric character of the biological catalyst (unresponsive to effector molecules). Other less frequently reported approaches

include metabolic control [9] and statistical analysis [10]. Cell performances are typically analyzed using the current-voltage response under various operational conditions. Studies with additional focus on the optimization of the electrode configuration, fuel/oxidant composition [10], substrate utilization efficiency [6] and mass transport or kinetic limitations of the catalytic system [11] have also been performed. Computational analysis of the influence of the electrode and channel geometry in membraneless microfluidic biofuel cells has also been reported by a few research groups [12-15].

Depending on the mechanism of the electron transfer between the enzyme and the electrode surface, direct (DET) and mediated (MET) strategies can be considered. While direct electron transfer has a pure form of Michaelis – Menten kinetics, the MET incorporates an additional e^- shuttling molecule i.e. according to a two – substrate ping – pong mechanism. The majority of catalysts employed in biological cells demonstrate MET.

Numerous enzymatic configurations have been considered in the literature, where the mediator and the catalyst were both free to diffuse across the membrane, or at least one of them has been immobilized at the electrode surface providing a direct oxidation of the enzyme at the electrode plane. As a general rule, for catalytic systems with co-immobilized mediator and enzyme molecules, the diffusion coefficient of reactants corresponds to the diffusion of the charge, rather than a physical movement of the species through the matrix [1].

Different catalytic species have characteristic rate constants, which govern the rates of production and dissociation of the enzyme-substrate complexes, formed transiently during the reaction. The first theoretical simulations of an enzymatic microstructured biofuel cell was published by Kjeang and co-workers in 2006 in their study on catalyzed conversion of methanol fuel [6]. In order to optimize a three-step oxidation of the alcohol, the group examined various enzyme patterning strategies including spatially – distributed or uniformly mixed along the electrode plane. High fuel utilization was calculated at low velocities of the flow and the reaction was kinetically controlled implying that system performance could be improved using catalytic species with faster rate constants.

Estimates for these rates can be made by fitting theoretically generated cyclic voltammograms to experiment data as demonstrated in 2008 by Gallaway and co-workers in their one-dimensional numeric description of O_2 reduction by laccase/Os-hydrogel modified electrodes [16]. The authors noted that the computed rate coefficients for the

laccase - oxygen reaction were lower when the catalyst was free in solution that when immobilized in the hydrogel.

The following year, Tamaki et al. [17] proposed a model of GDH catalyzed oxidation of glucose on high surface area carbon electrodes coated with a layer of redox polymer. As indicated from their studies on varying the diffusion coefficient of charge through the polymer, the apparent electron diffusion is not a rate limiting step for the overall enzyme kinetics. According to the authors, current densities of up to 0.1 A cm^{-2} could be potentially obtained at high surface area carbon black electrodes, provided increased catalyst loading and accelerated turnover rates [17].

One potential limitation of biofuel cell performance is an unequal utilization of the anodic and cathodic substrates with the slower half-cell governing the current production rate. This is usually attributed to difficulties achieving solutions which maintain a high level of O_2 saturation. Modelling the effect of the O_2 mass transport on the overall performance of a microfluidic catalytic system has been explored by Bedekar *et al.,* where a decline in the oxygen levels at the electrode regions located further along the channel was recorded. [18]. This limits the length of the channel allowed for a given flow rate unless multiple oxidant inlets are used. Research into the effects of the oxygen model has been later expanded by Glykys *et al*. who considered a GOX and laccase based biofuel cell incorporating Osmium functionalized electrodes [9]. Provided sufficiently high levels of the mediator, various O_2 concentrations had been found to have no effect on the kinetics of the catalysts. Additionally, the simulations revealed that under some conditions the fuel cell performance was governed solely by the operation of the anode.

Recent work published by Osman and Shah were on models of a device incorporating glucose based anodes (GDH [7] and GOX [8]) and an air-breathing cathode separated by a Nafion membrane based on a Michaelis – Menten reaction mechanism. The distribution of the enzyme concentration and the values of electrochemical rate constants for the mediator and oxygen reactions were determined by fitting experimental current-voltage curves. Steady state polarization curves were in a very good agreement with the empirical data but the dynamical response did not match as well. Enzyme poisoning in the presence of dissolved oxygen, prediction of the anode and cathode over-potentials and the dependency of the cell performance on the local pH of the anolyte solution were also discussed. The electrical output of the cell was found to be strongly dependent on the mass transport limitations associated with the mediator species [8].

Considering the above results altogether, it is clear that the exact mechanisms underlying the reaction are not understood at a fundamental level in terms of how the enzyme reaction occurs and the effects of changing operational conditions can only be observed at a macroscopic level. Depending on the exact cell design, species concentrations, electrode shape and even external factors like the ambient temperature, which affects the enzyme activity, any component of the system could be the rate limiting factor.

Overall, the work in this chapter is performed in order to inform subsequent device design for maximum performance as well as to gain understanding of the catalytic processes occurring in enzymatic systems. In addition to knowledge gained from the literature, custom simulation work is performed and a framework for further studies is constructed.

First, the basic principles of the enzymatic microfluidic biofuel cell are described including some of the novel aspects of this design. Next, the behavior of the flow is studied for various velocities using Computational Fluid Dynamics in order to improve the separation between the fuel and oxidant species feeding the reaction. Using the mass transport of a simple fuel (glucose) and its consumption via simulated redox reactions, different electrode geometries and channel dimensions are assessed in terms of the optimum fuel utilization. Desired flow properties include minimal mixing between the anolyte and catholyte compartments to prevent enzyme denaturing due to differing optimum pH levels in each flow and fuel utilization along the entire length for the maximum efficiencies.

Collectively, accounts on microbial [19-21] and enzymatic [1, 6-8, 16, 17, 22-24] biofuel cells explain a significant amount of the bioelectrochemical processes occurring at the electrodes but a comprehensive understanding is still lacking. Although Osman and Shah's papers [7, 8] investigated the fluid flow and factors potentially limiting the enzyme kinetics, the transitory enzyme-substrate and enzyme-mediator complexes were not. To date, the only model which accounts for any transitory complex is that reported by Wu *et al.* [25] although that work only includes the enzyme-substrate complex and omits the enzyme-mediator. The authors employed a potential-step method in order to evaluate the dynamic processes occurring in an anodic half-cell. The numerical analysis demonstrated that at higher potential values, the reaction rates dominated the diffusion effects and that the electrochemical processes were limited by the mass transfer of species.

Finally, a modified Michaelis – Menten type system which includes both enzyme complexes is investigated with a view to understanding the operational mechanisms of the biofuel cell and to understanding the effect of the complexes on the reaction dynamics. Both limited fuel and diffusion supported reactions are considered and the effect of catalytic rate constants, the membrane thickness and the bulk concentration are all studied. Simulated cyclic voltammograms are used to state some general design rules for the reaction portion of the fuel cell

As the general understanding of the devices in the biofuel cell community increases, more integrated models will be reported which consider all of the competing effects, including enzyme chemistries [26], new methods, materials and electrode designs. The complex nature of such a system will prevent simple conclusions being drawn so that simplified and approximate systems will always be useful.

4.2. Fundamentals of the microfluidic enzymatic biofuel cell.

The microfluidic cell under investigation is comprised of two main structural components: the microfluidic channel for the supply and distribution of the fuel and oxidant streams and the metal electrodes located at the bottom of the flow geometry used for the catalytic conversion of provided species (Fig. 4.1). Here, the fuel (on the anode) and oxidant (on the cathode) solutions are delivered to the cell through separate inlets, flow through the channel in a laminar manner without mixing and are withdrawn from the cell through a common outlet point. The bottom of the channel is patterned with gold anodes and platinum cathodes coated with a polymer film incorporating enzyme molecules for the catalytic oxidation and reduction of the provided fuel and oxidant, accordingly (Fig. 4.2).

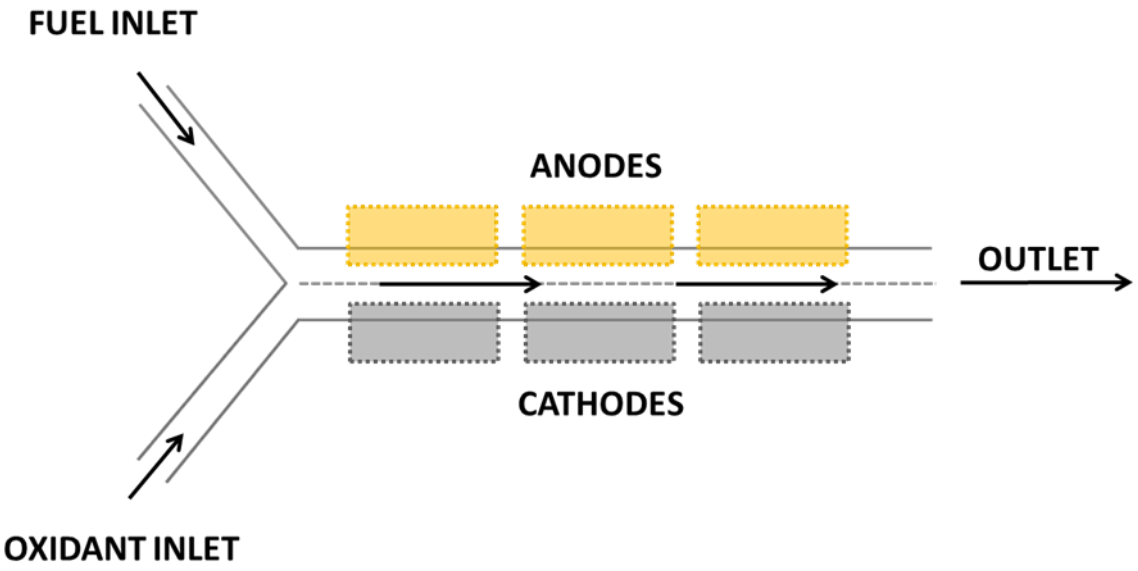


Fig. 4.1. Schematic of the microfluidic cell composed of the flow channel and two types of metal electrodes patterned at the bottom of the microfluidic geometry: anodes for the catalytic oxidation of the fuel and cathodes for the enzymatic reduction of the oxidant

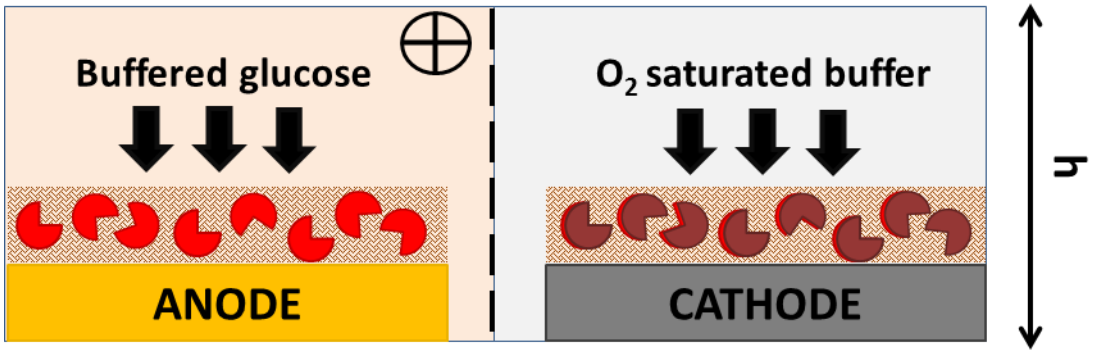


Fig. 4.2. Schematic of the channel cross-section representing the polymer film with immobilized enzyme molecules and the diffusion of glucose and O_2 towards the surface of the anode and cathode, accordingly. The direction of the fluid flow away from the reader is indicated by a cross in a circle; h represents the height of the channel cavity.

In principle, the polymer layer can be selectively deposited on the electrode surface following the assembly of the cell. This could be achieved in a process, known as electrodeposition, whereby filling the channel with a solution of an appropriate electroactive monomer and applying a suitable potential, a polymer coating of a controllable thickness is formed selectively at the electrode. The catalyst present in the

initial solution becomes incorporated in the polymer matrix and co-deposited at the electrode. As the process can be carried out in flowing conditions, any excess or unused catalysts can be recycled and employed in the deposition in subsequent devices. In this study, buffered glucose and oxygen saturated solutions have been considered as the simplest case of the anolyte and catholyte substrates, respectively. Both solutions flow in parallel to the electrode film, however glucose and oxygen carried by the fluids are able to diffuse in a perpendicular direction, towards the enzymatic layers. Once the species reach the vicinity of the electrodes they are converted by the protein catalysts immobilized at the metal surfaces. The species generated as a result of the enzymatic reactions are washed away by the motion of the fluid and are collected as waste at the channel outlet. The applied fuel flow prevents the built up of the reaction product and its potential role in the feedback inhibition of the enzyme. In order to avoid confusion, a distinction must be made between the two common uses of the term *membrane*. Regarding this microfluidic cell, *membrane* refers to a polymer layer which immobilizes the catalysts at the electrode surface. In other works it is a name given to a physical separation between the fuel and oxidant solutions.

Since various enzyme catalysts require different optimum working conditions (i.e. pH, ionic strength, temp.), fluid cross-over could result in enzyme denaturation and therefore, the isolation of the anodic and cathodic solutions is often essential to maintain their activity. As membraneless designs lack a physical separation of the fuel and the oxidant streams, an undesirable mixing of species can occur across the fluid interface. In this regards, one of the key features of this microfluidic system is its ability to maintain the laminar regime and minimized mixing of the adjacent flows. One of the parameters affecting this is the design of the channel inlet, due to its effect on the laminarity of the flow introduced into the channel. In principle, parallel supply of the fuel and oxidant should provide the least turbulent entry and hence the most efficient separation of the fluids in the channel. Nevertheless, in order to provide the solutions to the channel, a feeding system needs to be established. In the laboratory conditions, the fluid and oxidant streams for microfluidic cells are traditionally provided by a pump via two separate syringes connected to the channel inlets through Teflon tubing, as shown in Fig. 4.3. As the typical diameter of the tubing is 1.6 mm, in order to accommodate two individual connections, a separation of the inlet points is essential from the practical perspective. In this light, the modelling approach reported in the literature focusses primarily on two main

geometries of the channel inlets: classical Y [27] and the less recurring T-shape [28]. Since the T-shaped channel design was reported to aid microfluidic mixing [29], the Y geometry was selected for a practical reason of maintaining the laminar flow of the fluids. The chosen separation of the inlets was a compromise between the ideal parallel inflow of species at 0 ° and the technical requisite for the tubing connections. Fig. 4.4 demonstrates impeded mixing of glucose (fuel) and plain buffer (oxidant) solutions in the proposed geometry of the Y-shaped channel. In the study the fuel was provided only to the anodic compartment, indicated in red, (plain buffer in the cathodic component) and the evolution of the flow along the channel length was studied in order to assess the degree of cross-stream mixing. The widths of the main body of the channel and the inlets were 200 μm and 100 μm accordingly. The concentration of the anolyte glucose was assumed to be 2 mM, while the amount of the substrate in the catholyte solution was 0 mM (indicated in blue). The velocity of the modelled flow was 1.3 mm s^{-1}.

Since the model is composed of two relatively autonomous units, the investigation of the fluid flow in the channel and the enzymatic reactions at the electrodes can be performed independently of each other. Two studies have been investigated in this section: the analysis of the velocity of the flow in the channel and the electrode geometry (number, distribution and dimensions of the electrodes). Since the considered cell does not have a physical membrane separating the fuel and oxidant solutions, the emphasis of this work was to find flow rates, which would facilitate a laminar flow between the streams and therefore limited mixing of species. Additionally, as the device is intended to act as a biofuel cell the studies of various electrode geometries are expected to provide a recommendation of the metal design resulting in a maximum fuel efficiency.

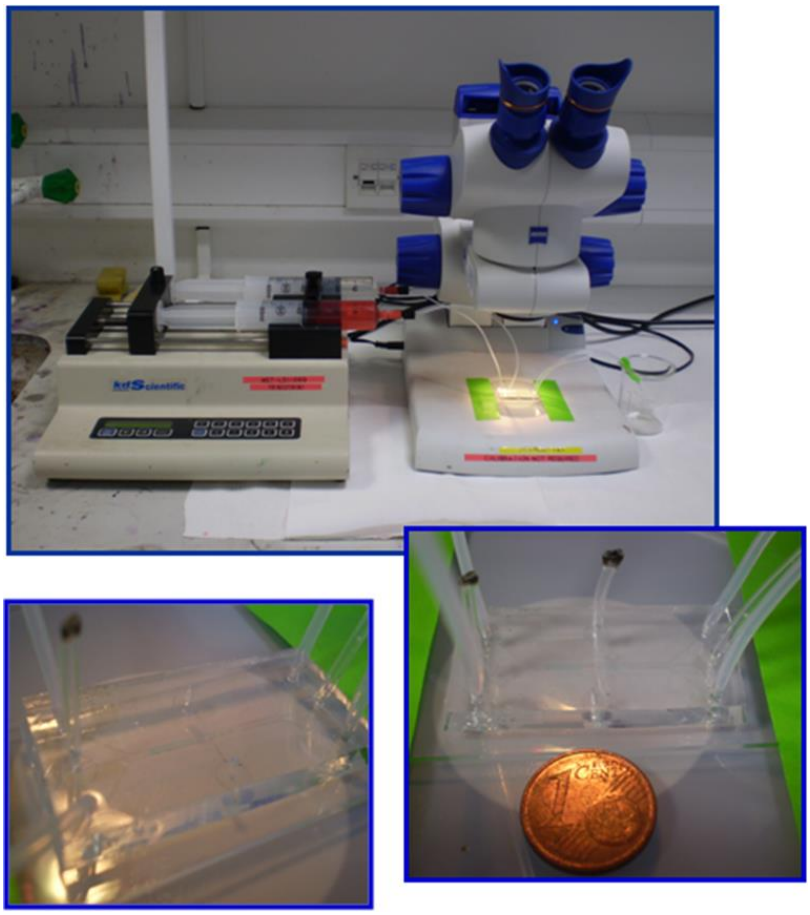


Fig. 4.3. Images representing the microfluidic cell connected to the pump system supplying the fuel and oxidant solutions. For visualization purposes two different fluids were pictured: plain transparent buffer and an aqueous solution supplemented with a red dye. The required use of tubings determines the minimal separation of the inlet entries.

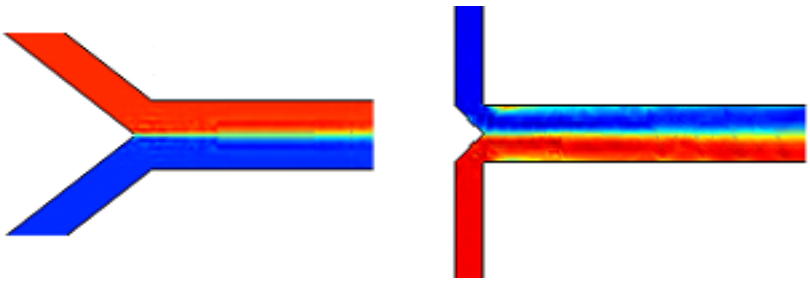


Fig. 4.4. Effective separation of the fuel and oxidant solutions in a Y-shaped channel geometry. Width of the channel: w = 200 µm, the velocity of the flow: u = 1.3 mm s^{-1} and glucose concentration [Glucose] = 2 mM (red stream). Indicated in blue is a zero concentration of glucose in the catholyte compartment.

The simulations were performed using commercial computing software, COMSOL *Multiphysics*. COMSOL is a numerical solver, which relies on a finite element analysis (FEM) of a given system described by a series of applicable partial differential equations (PDEs). Under (FEM), the three-dimensional geometry of the model is subdivided into a limited number of spatial elements in a process called meshing. The set of PDEs, which governs the entire system, is solved independently in each mesh element and the influence of neighboring spatial components is taken into account at the shared elemental boundaries. The condition at the mesh boundaries continuously updates until no change in time is observed and the system reaches its steady-state. Fig. 4.5 illustrates a schematic meshed channel and electrode geometry. In general, smaller features require finer mesh elements and yields in higher resolutions and more accurate results of the modelling. Finer mesh, although typically preferred in simulations, leads to extended computational times, due to higher number of required calculations.

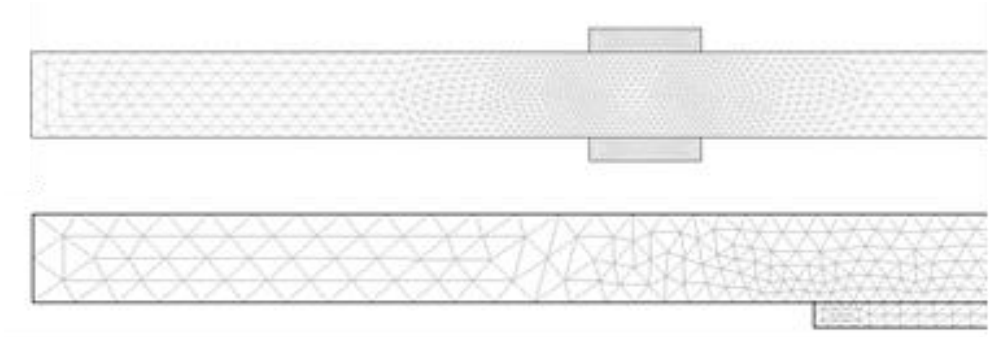


Fig. 4.5. Graphical representation of sample mesh sizes: fine (top) and coarse (bottom) used in the COMSOL modelling of small and larger features accordingly.

In a classical micro-scale environment the bodily forces are dominated by the surface tension and the fluid is considered incompressible, indicating no change of volume with applied pressure or stress [30]. In that case, the velocity field can be calculated using two partial differential equations, Incompressible Navier-Stokes (Eq. 4.1) and continuity (Eq. 4.2), at their steady-states [28].

$$\rho(\boldsymbol{u}\cdot\nabla)\boldsymbol{u} = \nabla\cdot[-p\boldsymbol{I} + \eta(\nabla\boldsymbol{u} + (\nabla\boldsymbol{u})^T)] \qquad Eq.\ 4.1$$

$$\nabla\cdot\boldsymbol{u} = 0 \qquad Eq.\ 4.2$$

Here, ρ and η denote the density (kg m^{-3}) and viscosity of the fluid (Pa s), u is the velocity of the flow (m s^{-1}), p stands for the pressure (Pa), T and I are respective transposed and identity matrices.

Depending on the origin of the reacting species carried by the fluid motion, the flow can be solved on two ways. If a change in solute concentration does not affect the density and viscosity of the fluid, as is in the considered case, Incompressible Navier-Stokes and mass balance equations can be solved consecutively. However, when the viscosity depends on the concentration of molecules, typically in solutions containing larger species, an adaptive correction term [31] needs to be implemented in the original formula.

The velocity field, previously determined by Incompressible Navier-Stokes equation, can be employed in the modelling of the mass transport phenomena in the micro-scale domain. As discussed in Appendix A, the transport of species within the microfluidic channel occurs by means of convection and diffusion [32], with the latter being essential for the replacement of the substrates consumed by the reaction at the vicinity of the electrodes and occurring in a direction transverse to the flow.

If, as in our case, the concentrations of reactants are sufficiently low, the interactions between different solute species can be disregarded and diffusion rates are assumed to be linearly proportional to the concentration gradients. In general, the fluidic system under consideration is assumed to be isothermal and the differences in pressure are not large enough to influence the diffusion coefficients of investigated species. Based on the assumption of constant concentrations and diffusion coefficients, the distribution of the fuel and oxidant can be described by Fick's law:

$$-\nabla \cdot (-\boldsymbol{D}\nabla c + c\boldsymbol{u}) = 0 \qquad Eq.\ 4.3$$

Here, D denotes the diffusion coefficient (m^2 s^{-1}); c represents the local concentration of the reactants (mol m^{-3}) and u is the velocity of the flow (m s^{-1}).

In the model, a number of relevant boundary conditions were applied to the walls of the simulated domain. These incorporated: a constant velocity of the flow at the channel inlets; an assumption of a natural discharge of the outlet to the atmospheric pressure (no external force applied) and a no-flow of the fuel through the channel walls, constricting the fluid motion within the main body of the channel only (Eq. 4.4). Additionally, the

presence of the electrodes at the bottom of the channel was assumed negligible in the fluid motion and hence the flow of the fuel and oxidant has been set to continue into the electrode subdomains. The symmetry boundary has been applied at the horizontal plane, defining the top and bottom of the flow channel, implying that a velocity component in the direction normal to the surface equals zero (Eq. 4.5).

$$n \cdot \boldsymbol{u} = 0 \qquad Eq.\ 4.4$$

$$t \cdot\ n(\nabla \boldsymbol{u} + (\nabla \boldsymbol{u})^T)\ \boldsymbol{u} = 0 \qquad Eq.\ 4.5$$

Here, t = time (s), u refers to the velocity of the flow (m s^{-1}), n is a direction normal to the plane.

A uniform concentration, c_0, has been applied at the channel inlets with a convective flux condition being assumed at the outlet (no external force applied) (Eq. 4.6). In addition, an insulation boundary condition (Eq. 4.7) has been assumed at the channel walls, confining the transport of species solely to the channel cavity.

$$(-\boldsymbol{D}\nabla c) \cdot n = 0 \qquad Eq.\ 4.6$$

$$(-\boldsymbol{D}\nabla c + c\boldsymbol{u}) \cdot n = 0 \qquad Eq.\ 4.7$$

4.3. Investigation of the velocity of the flow and the electrode geometry.

The classical Y-shaped design channel considered in this study was defined by five parameters: the length of the main body (L) and the inlets (l), the angle between the fuel and oxidant entry points (α), the height (h) of the channel (Fig. 4.4) and the width (w) of the flow geometry, as shown in Fig. 4.6. For the purpose of this work, L and l were selected to be 15 mm and 1.5 mm respectively, h was fixed at 150 μm. These values were based on the practical limitations of the fabrication processes and the requirement for small scale features. This is due to the fact that smaller structures require lower pumping pressure in order to introduce the fluids into the geometry and to maintain the velocity of the flow. While only two w values were considered theoretically (w = 200 μm and w =

600 μm), a number of channel geometries with varying widths (200 μm -1000 μm) has been fabricated, as discussed in Chapter V, and were investigated experimentally.

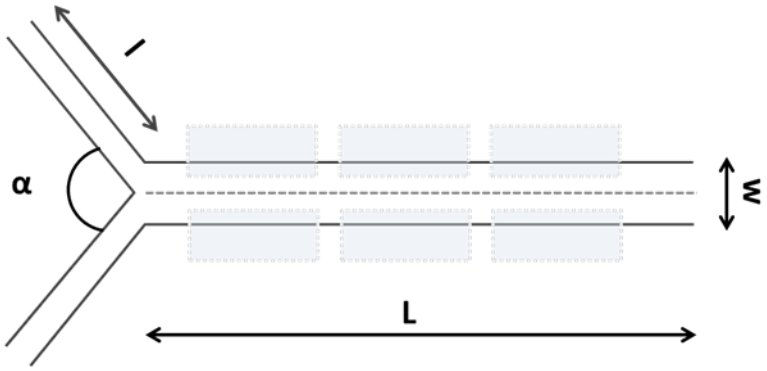


Fig. 4.6. Geometry of the microfluidic channel considered in the study, where L and l indicate lengths of the main body and the inlets, w is the width and α is the angle between the entry points. The height of the channel is not indicated on the diagram.

This section considered two fundamental studies of the microfluidic cell. The demonstration of a laminar flow in a channel of w = 200 μm and studies of the effect of various fluid velocities on the degree of internal mixing are presented at first. Second part of this work focused on the investigation of diverse electrode geometries on the fuel consumption within the channel and aimed to determine the metal design, which would facilitate the maximum efficiency of the cell.

4.3.1. Velocity of the flow.

The influence of the flow velocity, u, on the distribution of glucose and oxygen solutions within the channel has been investigated using parameters enclosed in Tab. 4.1. Since the considered cell is intended to act as a platforms for future generation of biofuel cells, the concentrations of the fuel and oxidant employed in the study have been obtained from the literature and were based on the physiological values reported in blood [33, 34]. The velocities selected for oxygen were higher than for glucose, due to its faster diffusion coefficient, facilitating increased degree of cross-over and internal mixing. Since the concentrations of the considered species were relatively low and both solutions were buffers (aqueous based), the physicochemical parameters of the fluids were assumed to be the same as for pure water. As the model assumed diluted fuel and oxidant, the viscosity

and density of the corresponding anolyte and catholyte solutions were taken to be unaffected by the glucose and O_2 levels and hence have been fixed at constant values. The diffusion coefficients for glucose [35] and O_2 [36, 37] in aqueous samples have been obtained from the literature.

Tab. 4.1. Numerical values of the parameters used in the simulation of the mass-transport of species in the microfluidic channel.

Parameters of the flow			
[Glucose]	**1 – 5 mM**	**$u_{glucose}$**	**0.5 - 1.4 mm s^{-1}**
$D_{glucose}$	**6.9 x 10^{-10} m^2 s^{-1}**	**u_{oxygen}**	**1 - 10 mm s^{-1}**
[O_2]	**1 - 2.9 mM**	**Inlet pressure**	**2 Pa**
D_{oxygen}	**1.7 x 10^{-9} m^2 s^{-1}**	**Channel width (w)**	**200 , 600 μm**
Density	**1000 kg m^{-3}**	**Channel height (h)**	**150 μm**
Viscosity	**0.001 Pa s**	**Channel length (L)**	**15 mm**

The influence of the velocity of the flow on the distribution of species at the channel cross-section was studied for 1 mM oxygen and is illustrated in Fig. 4.7 a) and b). In the model, two buffered solutions were simultaneously supplied to the channel via separate inlets: O_2 saturated catholyte (left channel compartment) and plain anolyte buffer (right side of the geometry). Two input velocities were considered: 1.5 mm s^{-1}, as shown in Fig. 4.7 a), and 10 mm s^{-1}, depicted in Fig. 4.7 b). The flow of both streams was predicted based on the simulation results and the distribution of oxygen was analysed at the mid-point of the channel length (L= 7.5 mm) and demonstrated for half the height of the channel (h = 75 μm). As the presence of the electrodes does not contribute significantly to the motion of the fluid, the effect of the anodes and cathodes patterned at the bottom of the channel on the flow was not taken into account in this study. The semi-parabolic distribution of O_2 in the cathodic stream is due to the cross-section obtained for half of the channel height.

As can be seen from Fig. 4.7, increased velocities of the flow provide better separation of the oxidant and fuel streams by reducing the time at which the species occupy the channel locally and hence minimizing the degree of mixing. This is in contrast with larger cross-over effect observed at a slower flow rate.

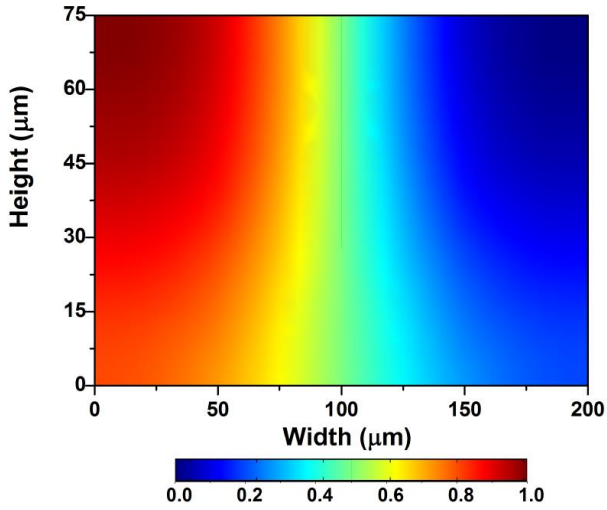


Fig. 4.7 a) Distribution of O_2 in a 200 μm channel, at a 1.5 mm s^{-1} velocity, represented at the cross-section of its geometry at L=7.5 mm.

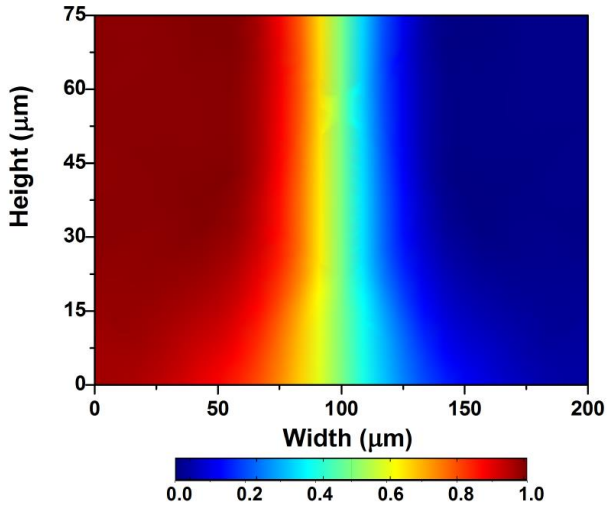


Fig. 4.7 b) Distribution of O_2 in a 200 μm channel, at a 10 mm s^{-1} velocity, represented at the cross-section of its geometry at L=7.5 mm.

The influence of the velocity and the input glucose concentration supplied to the anodic inlet of the channel, on the distribution of the substrate within the flow geometry have been evaluated by plotting the concentration profile of glucose computed at a channel cross-section taken at L= 10 mm (10 mm along the length) and at h = 75 μm. Fig. 4.8 illustrates the internal mixing at various u, when 2.5 mM was initially provided to the channel. The effect of various $[Glucose]_{Inlet}$ and a constant velocity of 1 mm s^{-1} is illustrated in Fig. 4.9. The position 100 μm on the x-axis indicates the mid-point of the channel where a theoretical interface between the anodic and cathodic compartments exists.

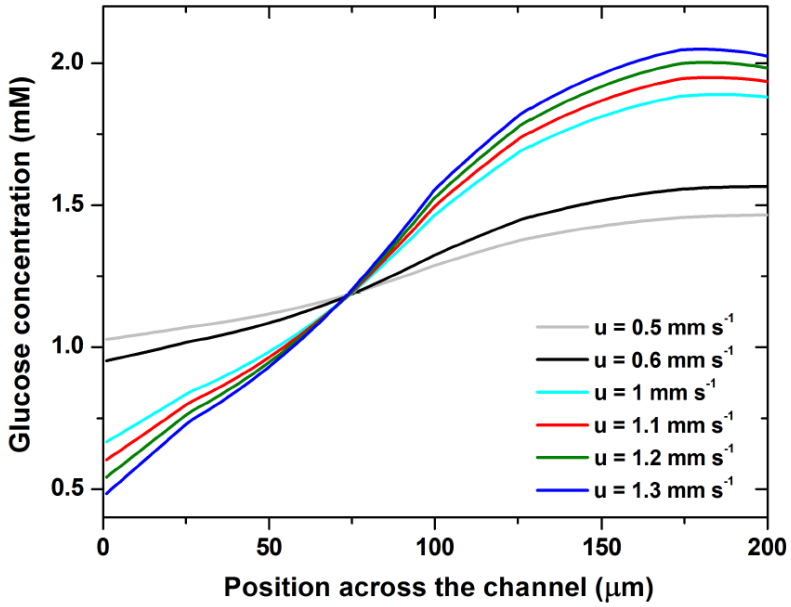


Fig. 4.8. The influence of the velocity of the flow on the distribution of glucose across the channel at L=10 mm. $[Glucose]_{Inlet}$ = 2.5 mM;

Spatial distribution of glucose, depicted in Fig. 4.8, confirms the previous statement that lower velocities of the flow resulted in faster mixing of the anolyte and catholyte solutions, while higher rates of the fuel transport provide accelerated movement of particles in the direction of the flow, minimizing the diffusion effect across the channel width. The lack of symmetry about the mid-point of the channel is most likely due to a flux boundary condition generating a non-zero gradient at x = 0.

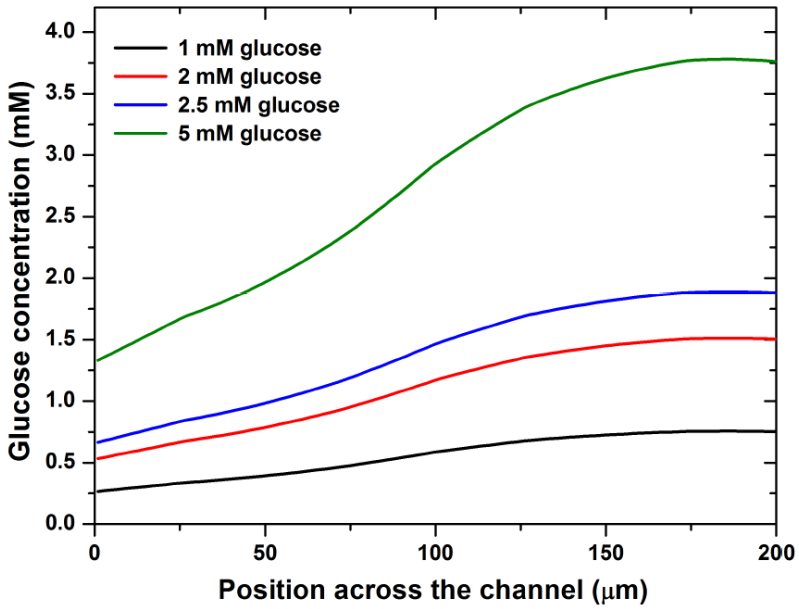


Fig. 4.9. Dependency of the [Glucose]$_{Inlet}$ on the concentration profile of the species at 1 mm s^{-1} velocity.

As demonstrated in Fig. 4.9., 5 mM glucose although yielded in overall greater concentration of species in the cathodic compartment of the cell, demonstrated lower mixing (29 %) than when 1 mM concentration of fuel was initially supplied to the channel (33 %). This result suggests the dependency of the mixing rate on the input [Glucose]$_{Inlet}$ and needs to be accounted for when optimizing the cross-over effects. As previously, the non-zero gradient at x = 0 is due to a flux boundary condition, resulting in the material possibly being lost across x= 0.

The evolution of the spatial profile of glucose along the flow geometry has been studied for 3 mM input concentration and at u = 1.3 mm s^{-1}. The profiles of the fuel taken at fixed points across the channel are plotted in Fig. 4.10. As previously, position 100 μm on the x-axis signifies the mid-point of the channel separating the anolyte (right) and the catholyte compartments (left).

Studies of the concentration of the substrate as a function of the distance from the inlet (Fig. 4.10) demonstrate that at given parameters of the model the distribution of glucose further down the channel shows increased mixing effect between the oxidant and fuel solutions. The onset of the cross-over is detectable as early as at L= 2 mm, with a near complete homogeneity of both flows obtained at the offset of the channel (L = 14 mm).

This suggests that in order to further minimize the magnitude of mixing, increased velocity should be investigated. Since the position 100 µm signifies the mid-point of the channel separating the anolyte and catholyte compartments, thus exactly this location can be recommended as the minimum distance for the electrode positioning in the bio-fuel cell. As in Fig. 4.8, the lack of symmetry about the mid-point of the channel is most likely due to the flux boundary condition resulting in a non-zero gradient at x = 0.

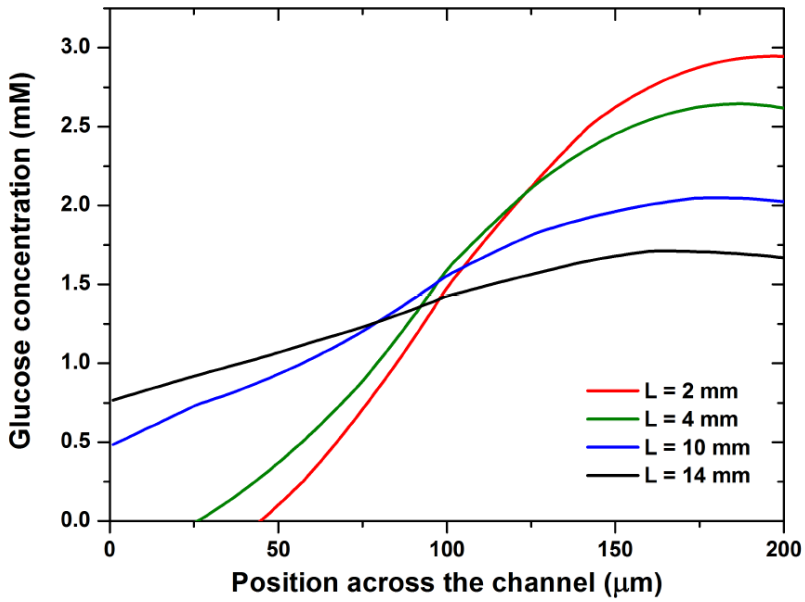


Fig. 4. 10. Distribution of glucose at different cross-sections of the channel evaluated for $[Glucose]_{Inlet}$ *= 3 mM, u = 1.3 mm* s^{-1}.

4.3.2. Electrode geometry.

The rate of consumption of the fuel and oxidant in a microfluidic biofuel cell determines the generated current and power outputs and hence the overall electrical performance of the device. Since the energy conversion occurring within the channel of projected cells is catalyzed by enzymes immobilized at the electrodes, the geometry and the spatial distribution of the anodes and cathodes patterned at the bottom of the flow channel is of particular importance. This is due to the fact that the efficiency of the biochemical reactions is dependent on the surface area available to the catalyst (enzyme load) and the sufficient diffusion of the substrate towards the electrode.

Theoretical investigation of the fuel and oxidant consumption at the electrodes provides the distribution profiles for both species within the microfluidic channel and enables further optimization of the geometry of the cell (e.g. electrode design) and parameters associated with the fluid motion e.g. velocity of the flow.

In order to understand the influence of the electrode layout on the species consumption in the microfluidic channel, two main designs have been considered: single electrode geometry, presented in Fig. 4.11 a), and an electrode composed of a series of regularly distributed active elements, as shown in Fig. 4.11 b). Physical separation of the anodes and cathodes enables independent studies of the fuel and oxidant reactions.

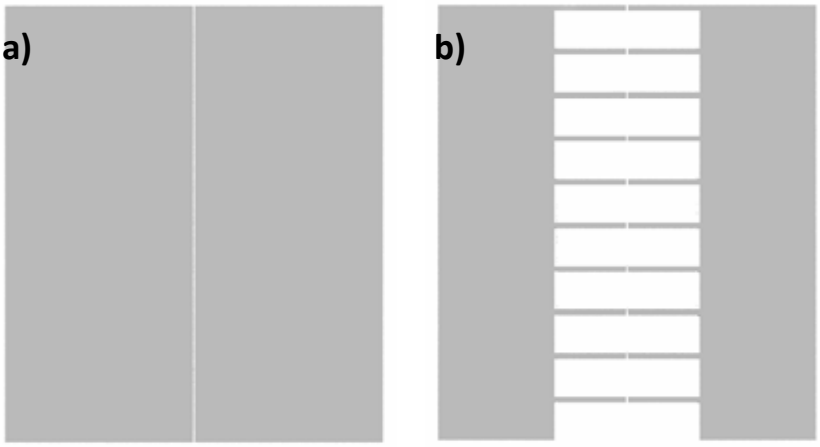


Fig. 4.11. Schematic illustration of the main electrode layouts considered in the study: a) single and b) dispersed. The gap within the geometry indicates a physical separation of the anodes and cathodes.

For simplification, initial studies of the catalytic reactions within the microchannel did not consider the presence of the enzyme and assumed the process was solely governed by the diffusion of species. The model applied a hypothetical condition of a maximum species turnover, indicated by a zero concentration of the substrate at the electrodes. This implied that the moment the fuel or oxidant reached the active surface it was entirely consumed by the reaction. This assumption simplified the computations; however it can only be applicable in an ideal scenario, where the reaction rate is independent of the enzyme properties and governed by a fast transport of species to the electrode surface. In real life applications, the catalysis, while still dependent on the diffusive mass transport of the substrates, obeys the principles of enzyme kinetics and thus often leads to an

incomplete substrate conversion. In this case the concentration of species at the electrodes is typically greater than zero. While the scope of this work is to obtain a catalytic system, which is not limited by the electrode design, the consideration of the ideal kinetics is useful in this case.

In order to study the influence of the electrode geometry on the efficiency of the fuel and oxidant conversion, the model had to be additionally supplemented with a system of initial and boundary conditions, schematically depicted in Fig. 4.12.

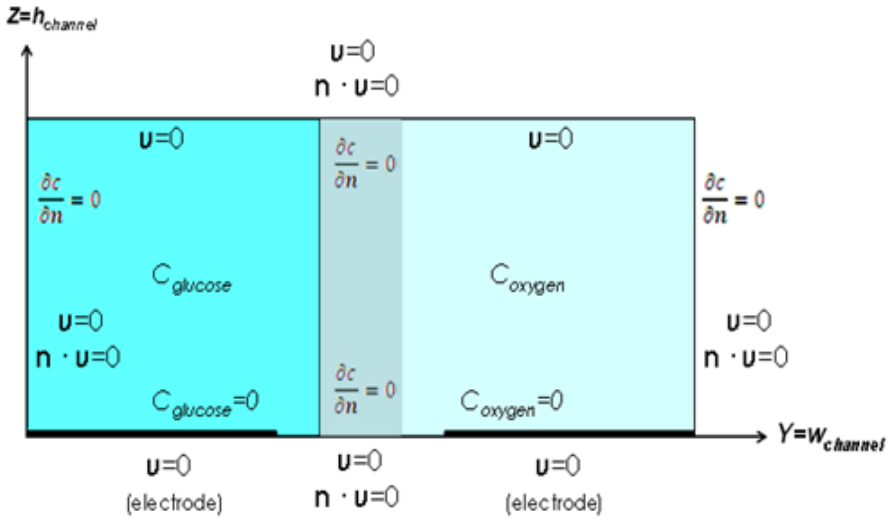


Fig. 4.12. Boundary conditions employed for the simulations of the fuel and oxidant consumption within the channel. Assumption of the zero-substrate concentration at the electrodes applies.

Theoretical investigation of the two hypothetical electrode designs, illustrated in Fig. 4.11, has been carried out for glucose solution supplied to the channel at a velocity of 1.3 mm s^{-1} and the computed two dimensional concentration profiles of the fuel have been presented in Fig. 4.13. The concentration of glucose applied in the study was 2.5 mM.

The simulation studies indicated that a single electrode allocated at the bottom of the flow channel, as shown in Fig. 4.13 a), results in an accelerated consumption of glucose and a progressive development of a depletion layer along the length of the geometry, indicated by a gradual diminution of the red band (glucose). Provided the presence of the enzyme immobilized at the electrode, the catalyst allocated in the farther

parts of the microfluidic channel would in that case be deprived of the fresh supply of the substrate and the biological potential of the species would not be optimally utilized.

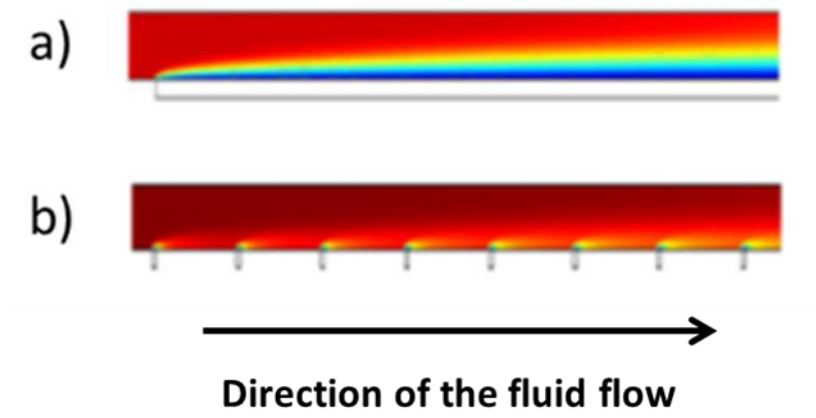


Fig. 4.13. Glucose concentration profiles for two electrode design patterned at the bottom of the flow channels: a) single electrode and b) electrode broken down into series of regularly distributed smaller features. [Glucose]$_{Inlet}$ = 2.5 mM, u = 1.3 mm s^{-1}. [Glucose] = 2.5 mM (deep red) and [Glucose] = 0 mM (deep blue).

This suggests that the analysed design would be most applicable for high concentrations of the species, in the case where the efficiency of the reaction is not restricted by the level of the fuel or oxidant and where the maximized total current and power is required. This is particularly relevant when the substrate is continuously replenished or provided into the channel through multiple inlet points. Conversely, higher density of electrode patterning, illustrated in Fig. 4.13 b), yields in slower glucose consumption, due to smaller dimensions of the features. Spatial distribution of the electrodes at the bottom of the channel separates the adjacent reactions and the inter-electrode distance minimizes the potential overlap of the diffusion layers. The reactive species can easily access the gap between the electrodes and enter the reaction zone in a more efficient manner, therefore resulting in a better distribution of the fuel along the flow geometry, hence providing improved current and power densities. The investigated discrete distribution of the electrodes can have a prospective application in the energy harvesting from physiological samples, where the organic fuels and oxidants are present in limited concentrations and the reaction rate is limited by the amount of available species.

For highly concentrated fuels and oxidants, which are ideal candidates for the substrates utilized in biofuel cells, a double-electrode configuration has been evaluated, as presented in Fig. 4.14 b), in order to study the effect of the additional reaction surface on the distribution profile within the channel. The model assumed the presence of two continuous electrodes, top and bottom, located in a 600 μm wide flow channel. Concentration of glucose supplied at the inlet was 5 mM and the modelled velocity of the fluid was set to 0.8 mm s^{-1}. As, in general, wider geometries maintain the laminar flow of fluids at lower flow rates, smaller u was assumed in this study, considered three times higher w of the channel. The investigation of a single-electrode geometry has been presented in Fig. 4.14 a) for comparison.

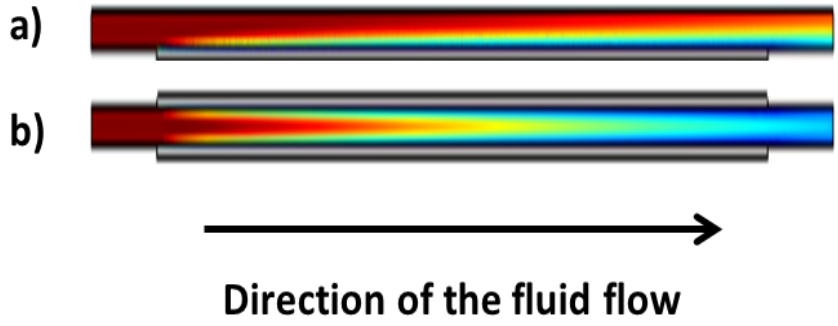


Fig. 4.14. Concentration profiles for glucose in a microfluidic channel of a width of 600 μm and height = 150 μm for: a) single and b) double electrode layouts. $[Glucose]_{Inlet}$ *= 5mM, u = 0.8 mm* s^{-1}*. [Glucose] = 5 mM (deep red), [Glucose] = 0 mM (deep blue).*

As corroborated from the theoretical investigations, the double-electrode configuration, presented in Fig. 4.14 b), triggers accelerated glucose consumption and leads to an almost immediate depletion of the substrate at the electrode onset, indicated by the increase in the blue band. These results are in agreement with the pervious simulations and suggest the potential application of the top and bottom geometry in the utilization of highly concentrated fuels. Additionally, the length of the electrode geometry needs to be optimized with respect to the enhanced catalytic rate and is expected to be shorter than what is required for a single electrode design, enabling device miniaturization.

The influence of the flow rate and the channel dimensions on the rate of consumption of species by the reactions at the electrodes has been studied in 3D physical

models incorporating a discrete electrode patterning at the bottom of the flow channel. The choice of the geometry was determined by the fact that inter-electrode distance provides better distribution of the species (Fig. 4.13) and that the majority of fuels and oxidants obtained from physiological samples are characterized by limited concentrations of the substrates. The study was based on the investigation of a 1 mM glucose stream in the anolyte compartment of a microfluidic channel at 150 µm height and 600 µm width appropriately. Plain buffer, with a zero glucose concentration has been assumed as the cathodic component. The inter-electrode gap was set to 50 µm and the velocity of the modelled flow was assumed to be 1 mm s^{-1}. The distribution profiles of glucose computed from the model have been presented at two channel cross-sections for half of the channel height (h = 75 µm), at the onset (L = 5 mm) and at the end (L = 11 mm) of the geometry, as depicted in Fig. 4.15 a) and Fig.4.15 b) respectively.

The diminishing concentration of the fuel in the remote parts of the channel, shown in Fig. 4.15 b) is indicative of a progressive consumption of glucose by the reaction at the electrodes distributed along the channel. Furthermore, a higher degree of cross-stream mixing can be detected at L = 11 mm as compared to L = 5 mm, as the fuel is given more time to diffuse to the cathodic compartment of the modelled design. In the light of these results, in order to improve the separation of the oxidant and fuel in a studied 15 mm long channel, greater distance between the electrodes and higher velocity of the flow need to be implemented. This is in agreement with the previous study on the channel design, where a suggested electrode location was 100 µm apart and a low degree of mixing was obtained at u = 1.3 mm s^{-1} (Fig. 4.8). The semi-parabolic distribution of glucose in the anodic stream is due to the cross-section demonstrated for half of the channel height.

Based on these simulation results and as presented in Chapter V, 100 µm was selected as the distance between the anodes and cathodes for all electrode geometries fabricated in the course of this Ph.D. work.

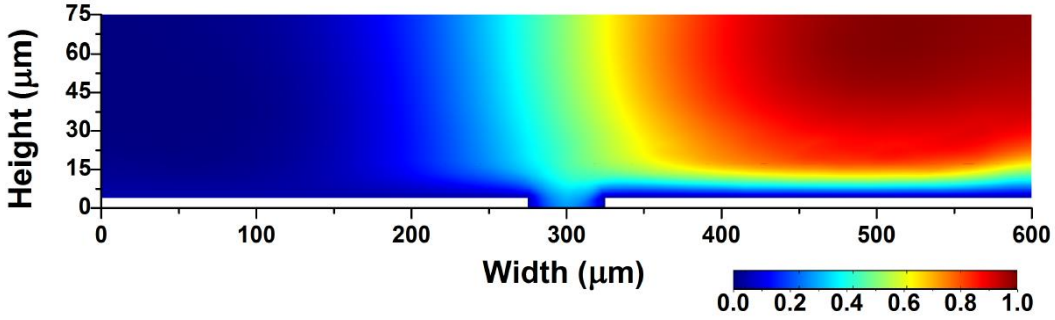


Fig. 4.15 a) Concentration profile for glucose at the electrode located 5 mm into the microfluidic channel of a width of 600 μm and height of 150 μm. $[Glucose]_{Inlet}$ = 5 mM, u = 1 mm s^{-1}. A scale bar for glucose concentration (mM) is given in the inset.

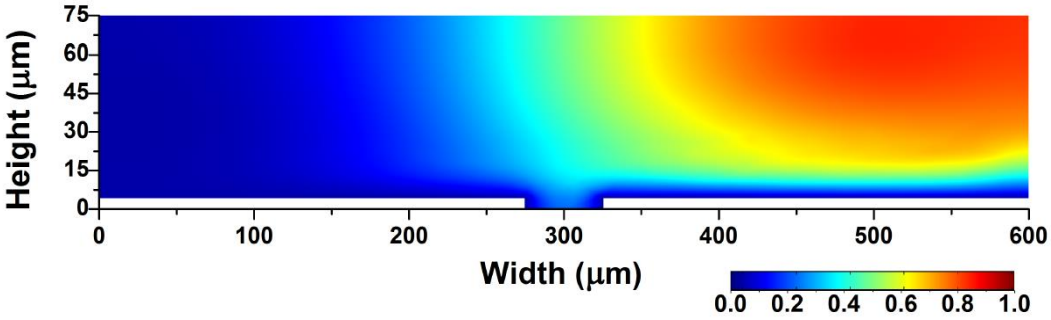


Fig. 4.15 b) Concentration profile for glucose at the electrode located 11 mm into the microfluidic channel of a width of 600 μm and height of 150 μm, 1 mm s^{-1} velocity. $[Glucose]_{Inlet}$ = 1 mM, u = 1 mm s^{-1}. A scale bar for glucose concentration (mM) is given in the inset.

4.4. Modelling of the enzyme kinetics.

In this section, the enzyme kinetics of two relevant systems was considered: the isolated and diffusion-controlled catalysis. The objective of this work was to increase the understanding and aid experimental interpretation of the reaction within the enzymatic membrane of the functional biofuel cell. Unlike the reaction system considered in section 4.3, where a zero-concentration of the substrate was assumed at the electrodes, the application of the enzyme kinetics would enable more accurate representation of the dynamics in the polymer layer.

To begin, it was necessary to construct a system of differential equations, which correctly describes the occurring dynamics. Then, with appropriate boundary conditions, the isolated system which does not feature substrate replenishment was investigated. Different stages of the reaction were identified and discusses as well as the effect of the variation of the catalytic constants, k_{cat} and k_m. Finally, the complete diffusion-supported system was considered including the effect of the membrane thickness and the

concentration of the bulk substrate. Computed cyclic voltammetry data was employed to identify the cell performance.

System rate equations

The physical model of the catalytic layer was composed of two distinct elements: a redox polymer membrane of a thickness w coated onto a solid electrode of a length L (Fig. 4.16).

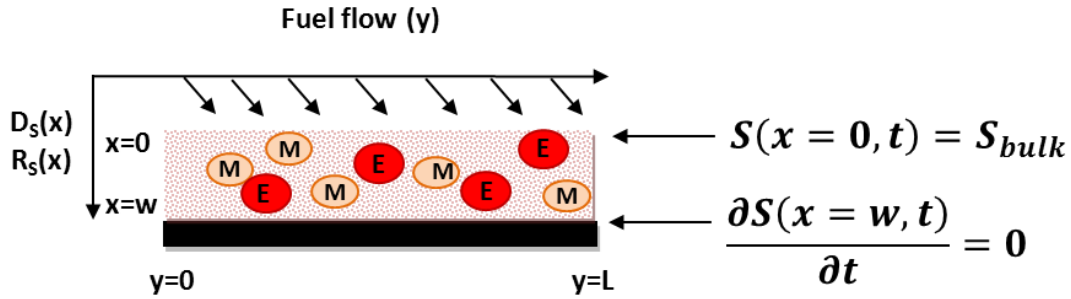


Fig. 4.16. Schematic of the reaction layer including the initial boundary conditions used for modelling purposes. Here, M-mediator; E-enzyme; w is the thickness of the polymer coating and L is the length of the electrode; D_s and R_s denote the respective diffusion and reaction of the substrate within the catalytic layer.

The polymer layer contained immobilized enzyme (E) and mediator (M) species for the catalytic conversion of the given fuel. The substrate in the fluid flow diffuses into the membrane where, in the presence of the enzyme and mediator, a catalytic reaction occurs. The electrons liberated as a result of the fuel oxidation are collected at the electrode and measured as current. However, the enzyme and mediator molecules are physically entrapped in the polymer matrix and not free to disperse within the membrane. While E and M are immobilized in the film, they can change their redox state through electron hopping. This was modelled as diffusion following the method reported by Bartlett [1]. Since ES and EM are complexes rather than oxidized or reduced forms of individual species, this type of conversion is not possible and therefore, they are considered to be non-diffusive.

In reality, the biofuel cell is three-dimensional and is described by three spatial coordinates: x, y and z. The vertical ordinate, x, is the direction across the membrane, y is

the direction parallel to the electrode but perpendicular to the flow and z is in the direction along the electrode. Using symmetry arguments, the problem can be reduced to one spatial dimension, x. Due to a sufficiently fast flow rate and suitable electrode geometry, complete substrate replenishment is assumed to be achieved all the way along the channel and across the electrode. In this case, each species is considered a function of only a single spatial ordinate, x, and a temporal coordinate, t, S → S (x, t). The rate of change of all reactants can be considered as the sum of all the diffusion and reaction effects.

$$\frac{\partial S(x,t)}{\partial t} = diffusion(x,t) + reaction(x,t) \qquad Eq.\ 4.8$$

As the diffusion of species is driven by the concentration gradients, it can be modelled via the second order spatial derivative term:

$$diffusion\ (x,t) = D\frac{\partial^2 S(x,t)}{\partial x^2} \qquad Eq.\ 4.9$$

Here, the constant of proportionality is termed the diffusion constant and is a property of each reactant.

Considering the reaction illustrated in Fig. 4.16, a set of modified Michaelis-Menten rate equations was identified. Since in its classical form, Michaelis-Menten reaction scheme considers direct catalysis only, the system of equations was modified by two additional expressions, accounting for the presence of the mediator (Eq. 4.10- Eq. 4.12).

$$[S] + [E_{ox}] \underset{k_{ES-}}{\overset{k_{ES+}}{\rightleftharpoons}} [ES] \xrightarrow{k_{cat}} [E_{red}] + [P] \qquad Eq.\ 4.10$$

$$[E_{red}] + [M_{ox}] \underset{k_{EM-}}{\overset{k_{EM+}}{\rightleftharpoons}} [EM] \xrightarrow{k_m} [E_{ox}] + [M_{red}] \qquad Eq.\ 4.11$$

$$[M_{red}] \underset{k_e}{\overset{k_e}{\rightleftharpoons}} ne + [M_{ox}] \qquad Eq.\ 4.12$$

Here, [S] is the amount of the substrate available for the reaction; $[E_{ox}]$, $[E_{red}]$, $[M_{ox}]$ and $[M_{red}]$ are the concentrations of the oxidized and reduced forms of the enzyme and mediator respectively; [ES] and [EM] are the quantities of the enzyme-substrate and

enzyme-mediator complexes; and [P] is the amount of product formed in the reaction. The k_{ES+} / k_{ES-} and k_{EM+} / k_{EM-} are the catalytic constants determining the rates of formation/dissociation of the ES and EM complexes from/to the corresponding substrates E_{ox} and M_{ox}; k_{cat} and k_m signify the rates at which the enzymatic complexes decompose to the respective products E_{red} and M_{red}; k_e is the rate of electron transfer for the M_{red}/M_{ox} redox couple.

In the modified Michaelis – Menten scheme, the oxidized form of the enzyme, E_{ox}, reacts with the substrate, S, to generate the transient enzyme-substrate complex, ES, which further decomposes into the reduced form of the catalyst, E_{red}, and the product, P, as illustrated in Eq. 4.10. The oxidized mediator regenerates the active form of the enzyme, E_{ox}, and consequently produces reduced M_{red} (Eq. 4.11). The mediator species is ultimately re-oxidized at the electrode generating current and recycled for subsequent redox reactions, as seen in Eq. 4.12. While the formation of the enzyme-substrate, ES, and enzyme-mediator, EM, complexes is reversible, the dissociation of complexes is an irreversible step (Eq. 4.10 and Eq. 4.11).

Based on the Michaelis-Menten mechanism, the rate of change of any species can be given by the sum of the individual rates of consumption and generation within the entire system, as shown in Eq. 4.13.

$$reaction = generation - consumption \qquad Eq.\ 4.13$$

For instance, the substrate is consumed at a rate proportional to the concentrations of E_{ox} and S and is regenerated at a rate proportional to the concentration of ES. Following from this, the reaction term for the substrate can be written as:

$$\frac{d[S_{reaction}]}{dt} = k_{ES-}[ES] - k_{ES+}[S][E_{ox}] \qquad Eq.\ 4.14$$

Similar arguments can be applied to all reactants and therefore using Eq. 4.8 it was possible to construct a set of second order partial differential equations, which adequately describe the enzyme kinetics occurring within the polymer membrane:

$$\frac{d[S]}{dt} = D_S \frac{\partial^2 S(x,t)}{\partial x^2} + k_{ES-}[ES] - k_{ES+}[S][E_{ox}] \qquad Eq.\ 4.15$$

$$\frac{d[ES]}{dt} = k_{ES+}[S][E_{ox}] - (k_{ES-} + k_{cat})[ES] \qquad Eq.\ 4.16$$

$$\frac{d[E_{ox}]}{dt} = D_e \frac{\partial^2 E_{ox}(x,t)}{\partial x^2} + k_{ES-}[ES] - k_{ES+}[S][E_{ox}] + k_m[EM] \qquad Eq.\ 4.17$$

$$\frac{d[E_{red}]}{dt} = D_e \frac{\partial^2 E_{red}(x,t)}{\partial x^2} + k_{cat}[ES] - k_{EM+}[E_{red}][M_{ox}] + k_{EM-}[EM] \qquad Eq.\ 4.18$$

$$\frac{d[M_{ox}]}{dt} = D_e \frac{\partial^2 M_{ox}(x,t)}{\partial x^2} + k_{EM-}[EM] - k_{EM+}[E_{red}][M_{ox}] + \mathbf{k_e[M_{red}]} \qquad Eq.\ 4.19$$

$$\frac{d[EM]}{dt} = k_{EM+}[E_{red}][M_{ox}] - (k_{EM-} + k_m)\,[EM] \qquad Eq.\ 4.20$$

$$\frac{d[M_{red}]}{dt} = D_e \frac{\partial^2 M_{red}(x,t)}{\partial x^2} + k_m[EM] - \mathbf{k_e[M_{red}]} \qquad Eq.\ 4.21$$

$$\frac{d[P]}{dt} = D_P \frac{\partial^2 P(x,t)}{\partial x^2} + k_{cat}[ES] \qquad Eq.\ 4.22$$

In this system of equations square brackets indicate concentrations of the individual components. A special note should be made of the bold $\mathbf{k_e[M_{red}]}$ terms in Eq. 4.19 and Eq. 4.21 which simulate the oxidation of the mediator. By rights these do not exist for the full diffusion controlled equations and *are not included* in those calculations. For the isolated system considered in this section there is no electrode boundary condition so these terms need to be added to re-oxidize the mediator after the dissociation of the EM complex.

Implicit in these equations is the conservation of the total concentrations of the enzyme and mediator species, divided between free and complex bound forms. That is:

$$[E_{ox}] + [E_{red}] + [EM] + [\mathrm{ES}] = [E_O] \qquad Eq.\ 4.23$$

$$[M_{ox}] + [M_{red}] + [EM] = [M_O] \qquad Eq.\ 4.24$$

Where $[E_0]$ and $[M_0]$ denote total initial concentrations of the enzyme and mediator species.

The system of equations described above has to be solved simultaneously to generate concentration profiles for the individual components of the catalytic system. Due to the high level of complexity and non-linearity, no analytical solutions were found

therefore, numerical integration techniques were employed. In particular, the Wolfram *Mathematica* computer algebra system was used, although other alternatives, such as, Matlab would have been equally appropriate. *Mathematica* code to solve this system and to perform related calculations was established in conjunction with Dr. Aidan Daly of Dept. of Physics and the Tyndall National Institute, University College Cork and is enclosed in Appendix C.

Using parameters appropriate to glucose, two distinct scenarios were considered, namely an isolated and a diffusion-supported reaction. In the isolated system the substrate was supplied only once, leading to the ultimate termination of the reaction, due to the substrate exhaustion. The diffusion-controlled configuration assumed a continuous replenishment of the fuel. There, the substrate constantly diffused from the bulk into the membrane, allowing the reaction to reach a dynamic equilibrium.

4.4.1. Isolated catalytic system.

In the isolated system, the supply of the substrate to the reaction was not replenished, so that the catalysis would eventually terminate, due to the exhaustion of the fuel. This helps to identify different stages of the reaction and to understand the enzyme kinetics. This scenario was studied using Eq. 4.15 – Eq. 4.22 with the diffusion constants for all reactants set to zero, so that the spatial dependence of all species vanishes i.e. S (x, t) $\rightarrow$ S (t) and the system is reduced to a set of ordinary differential equations related to a hypothetical, isolated point within the membrane.

The various parameters employed in the simulations are presented in Tab. 4.2. The catalytic constants governing the rate of glucose consumption were appropriate for glucose oxidase operating at 27 °C [38]. The total concentrations of the enzyme and mediator species were much lower than the initial amount of the substrate (3.3 %), a condition typically employed in the experimental work.

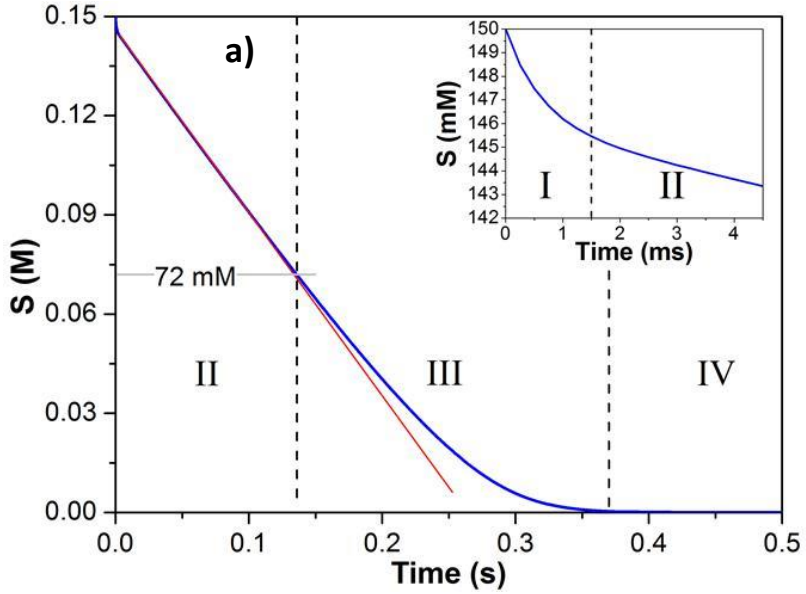
At time t = 0, [S] = [S_0] and the concentrations of the oxidized system components, [E_{ox}] and [M_{ox}], are equal to the total amount of the enzyme and mediator used in the study. The quantity of the remaining reactants is assumed to be zero. These initial conditions are presented in Tab. 4.3.

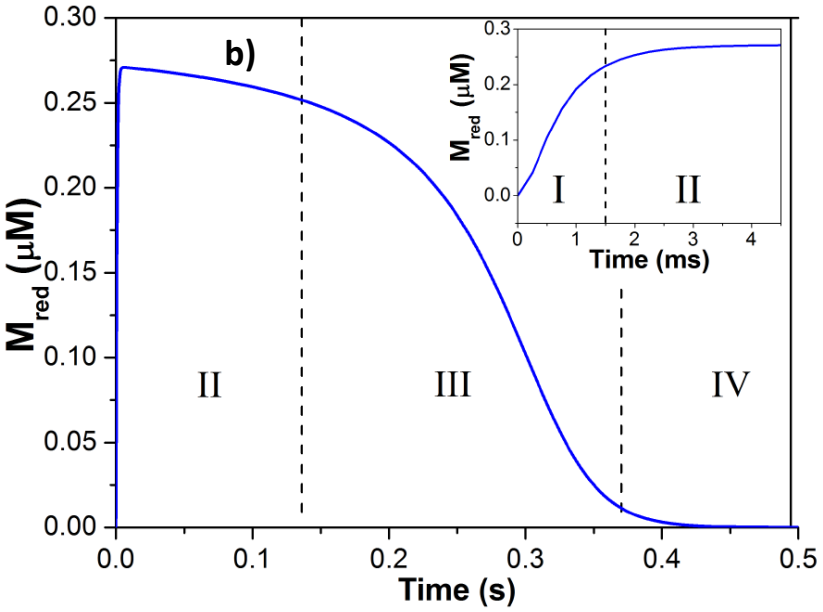
Tab. 4.2 Parameters used in the theoretical investigation of the enzyme kinetics in the isolated system.

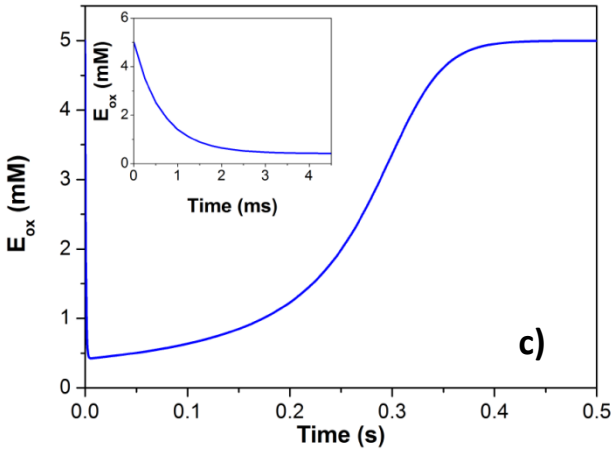
Simulation parameters			
k_{ES+}	**10000 M^{-1} s^{-1}**	k_{EM+}	**2.1 x 10^6 M^{-1} s^{-1}**
k_{ES-}	**400 s^{-1}**	k_m	**1150 s^{-1}**
k_{cat}	**5000 s^{-1}**	k_e	**2.075 x 10^6 s^{-1}**
k_{EM-}	**8.4 x 10^4 s^{-1}**		

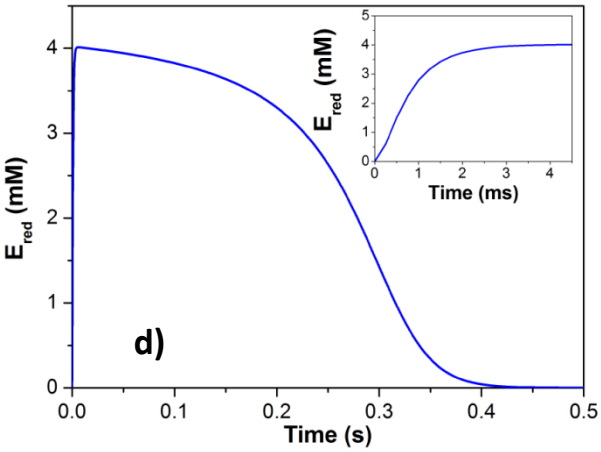
Tab. 4.3. Initial conditions for the isolated system.

Initial conditions	
[S] (0) = [S_0] = 150 mM	**[M_{red}] (0) = 0 mM**
[E_{ox}] (0)= [E_0] = 5 mM	**[ES] (0) = 0 mM**
[M_{ox}] (0) = [M_0] = 5 mM	**[EM] (0) = 0 mM**
[E_{red}] (0) = 0 mM	**[P] (0) = 0 mM**


a)
S (M)
Time (s)
72 mM
II
III
IV
S (mM)
Time (ms)
I
II


b)
M_red (µM)
Time (s)
II
III
IV
M_red (µM)
Time (ms)
I
II


c)
E_ox (mM)
Time (s)
E_ox (mM)
Time (ms)


d)
E_red (mM)
Time (s)
E_red (mM)
Time (ms)

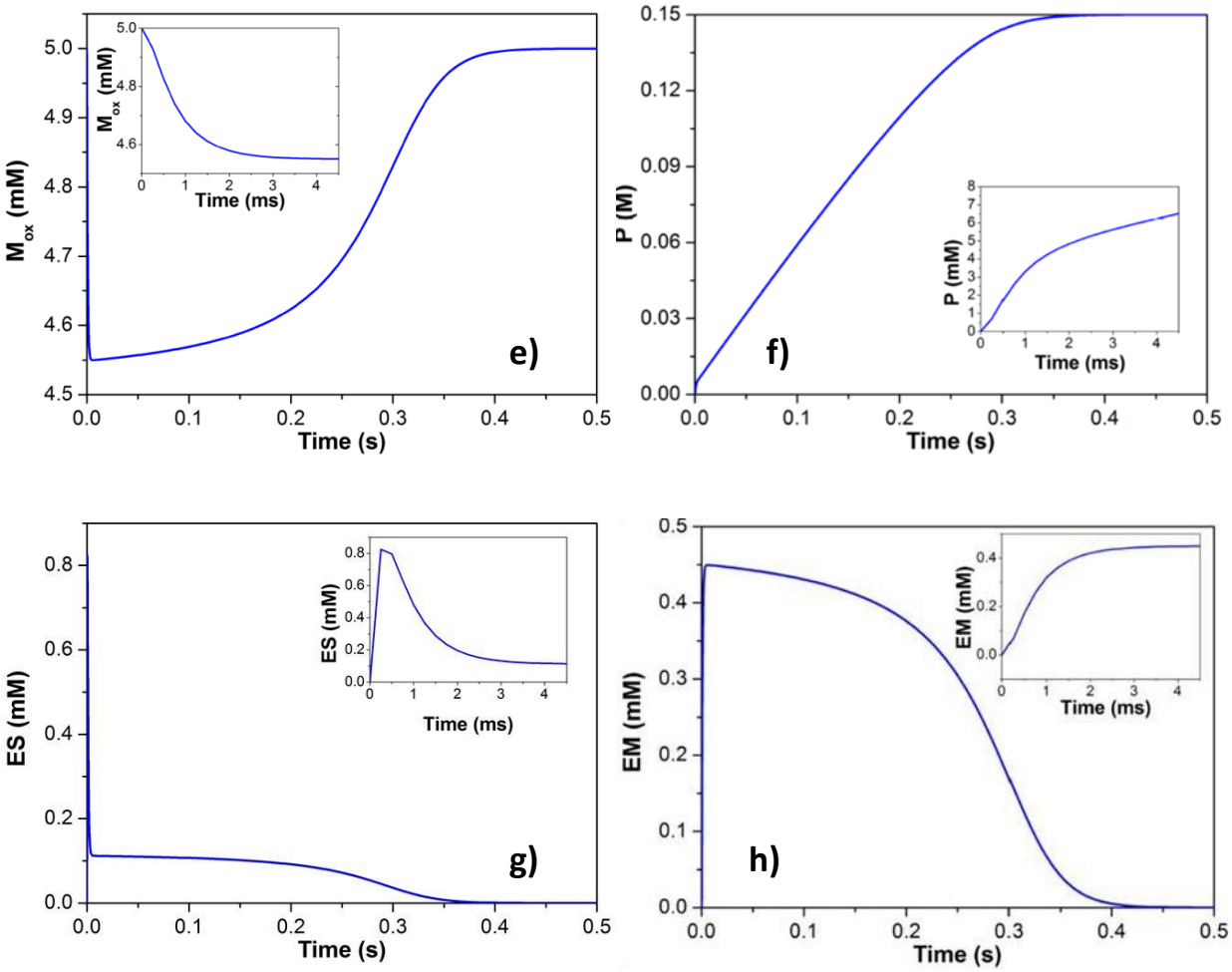


Fig. 4.17. Time dependency of the concentrations of species in an isolated system for a) substrate, b) reduced mediator, c) oxidized enzyme, d) reduced enzyme, e) oxidized mediator, f) product, g) enzyme-substrate complex, h) enzyme-mediator complex.

The time evolution of the species concentrations are shown in Fig. 4.17. The computed time dependent concentration profiles for S and M_{red} are shown in Fig. 4.17 a) and Fig. 4.17 b). Four distinct regions can be identified in these curves: initial catalysis (I), sustained catalysis (II), the turn-off stage (III) and the reaction termination (IV). These zones can be identified for all the species but are only highlighted for the substrate and the reduced mediator. At the reaction onset, when the enzyme and mediator molecules are solely in their active oxidation forms, the catalysis progresses rapidly, once the substrate is provided at t = 0. This is indicated by a sharp drop in the concentrations of S, E_{ox} and M_{ox} within the first 5 ms accompanied by a corresponding increase in P, E_{red} and $M_{red,}$ see region I in the insets of Fig. 4.17.

Considering Fig. 4.17 a) between 1 ms and 2 ms there is a change of slope from approx. -4400 mM s^{-1} to approx. -500 mM s^{-1}, indicating a slowing down in the rate of consumption of S. This occurs as in I E_{ox} is yet unsaturated and every molecule of S, which wishes to bind to any oxidized enzyme can do so. Once all of the initially available E_{ox} is bound to the substrate the reaction slows down as the substrate waits for E_{ox} to regenerate by shuttling the electrons to M_{ox}. Such a mechanism is supported by noting that at -4400 mM s^{-1} approximately 3.5 mM of S and correspondingly of E_{ox} is consumed in the first 0.8 ms of the reaction. This tends to the entire available amount of E_{ox} = 5 mM by 1.5 ms. The region of slower reaction is that of sustained catalysis (II), where the reaction rate is dependent on the entire system through E_{ox} regeneration and not just the quick binding of the substrate to the free oxidized enzyme. The observation of a constant decrease in [S], coupled with a review of Eq. 4.15, suggests that [S] x [E_{ox}], which is a dominant term in that expression, must be approximately constant. Indeed, the flat shape of the [S] x [E_{ox}] curve in this region verifies this statement, Fig. 4.18.

The amount of generated product matches the consumed substrate, due to a 1:1 conversion ratio. Regarding the remaining species, a quasi-steady state is attained during this phase, as the concentration of S is sufficient to generate ES at a rate faster than it is decomposing into P and E_{red}. Considering Eq. 4.25 it is clear that

$$[S] > (k_{ES-} + k_{cat}) \frac{[ES]}{k_{ES+}[E_{ox}]} \qquad Eq.\ 4.25$$

is required for net ES generation. Using quasi-steady state estimates of [ES] = 0.1 mM and [E_{ox}] = 0.75 mM, [S] = 72 mM is calculated as the minimum substrate concentration necessary to satisfy this condition. This occurs after 0.13 s. Once [S] drops below this level, the reaction begins to slow down and region III, turn-off, is entered. Over the next 0.25 s the ever reducing concentration of S leads to the reaction tapering off gently until the substrate is completely depleted. As the process requires a finite time to occur, it takes another 0.025 s before the catalysis is complete and the reaction is terminated (IV).

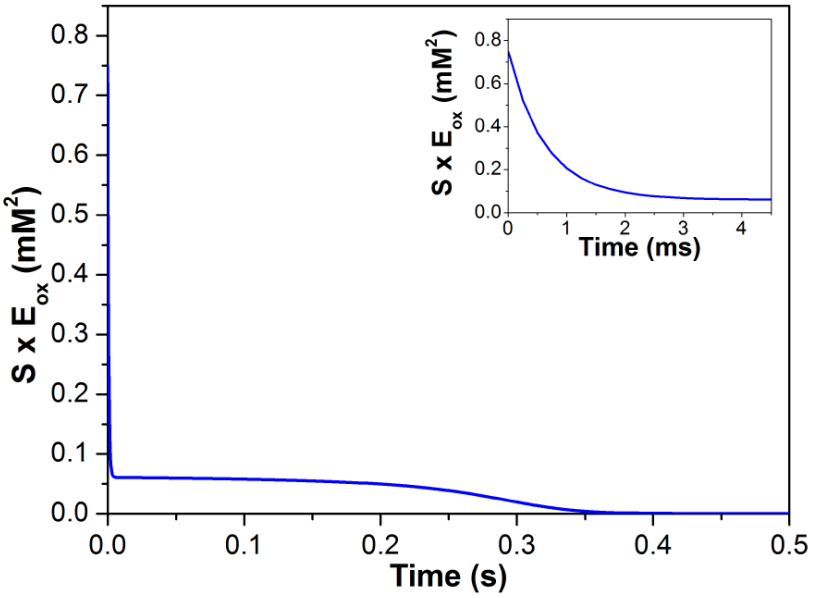


Fig. 4.18. Time dependency of the S and E_{ox} couple computed for an isolated system.

The shapes of the time profiles are dependent on the initial concentrations and the catalytic properties of the enzymes. In order to analyze the effect of some of these properties on the reaction, the concentration profiles of S and M_{red} have been computed for several values of k_{cat} and k_m. These constants are characteristics of particular enzymes and govern the rates of the limiting steps of the reaction (dissociation of the respective ES and EM complexes) and can thus provide useful insights into the kinetics. Despite the common place use of enzymes in catalytic studies, accurately determining the individual rate constants is difficult. Therefore, this study investigated the qualitative effect of k_m and k_{cat} variation rather than providing quantitative data. All other rate coefficients were fixed, according to Tab. 4.2. The calculated time dependencies with k_m = 1150 s^{-1}, are presented in Fig. 4.19 and Fig. 4.20. Overall, increasing the magnitude of these constants, results in an earlier termination of the reaction. This is to be expected, as k_m and k_{cat} govern the rate limiting steps of the enzyme kinetics. Looking at Fig. 4.19, the slower depletion of S is limited by the availability of E_{ox}. This is because a significant portion of the enzyme is bound as ES. The low k_{cat} value means a slow generation of E_{red}. There is excess oxidized mediator available to convert the reduced enzyme back to E_{ox}. However, if only a small minority of the mediator exists in its reduced form, a low electrode current will be recorded, as verified in Fig. 4.19 b), where small values of k_{cat} give low peak concentrations of M_{red} compared to high k_{cat}. For values of $_{kcat}$ above 5000 s^{-1} no change in

the time dependency is observed. This indicates that the ES decomposition is no longer having any sort of rate limiting effect and S is not entirely consumed before 0.4 s.

By fixing the value of k_{cat} at 5000 s^{-1} and varying k_m, earlier reaction terminations can be computed, as seen in Fig. 4.20. In fact, for k_m greater than 1500 s^{-1} all the reactions finish prior to 0.375 s, indicating its role as a limiting rate for values of k_{cat} higher than 2000 s^{-1}. According to Fig. 4.20 b), large peak concentrations of M_{red} are calculated, demonstrating the possibility of high peak currents at the electrode.

Potentially, enzymes with sufficiently fast catalytic constants, could lead to a system limited by the electron transfer rate at the electrode, k_e. This study concludes that catalysts with large k_m and k_{cat} would be most suitable for this fuel cell application, in particular, when the substrate is continuously replenished.

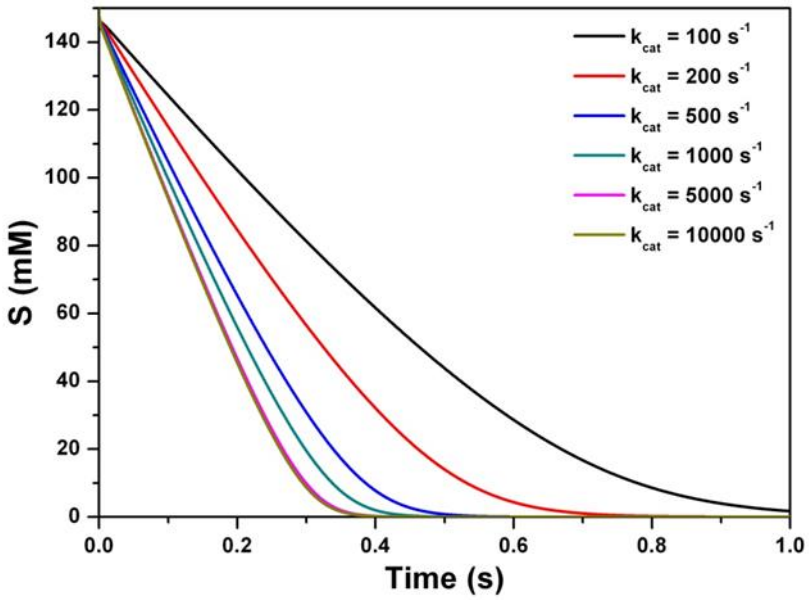


Fig. 4.19 a) Substrate concentration as a function of time for k_m = 1150 s^{-1} and different k_{cat}.

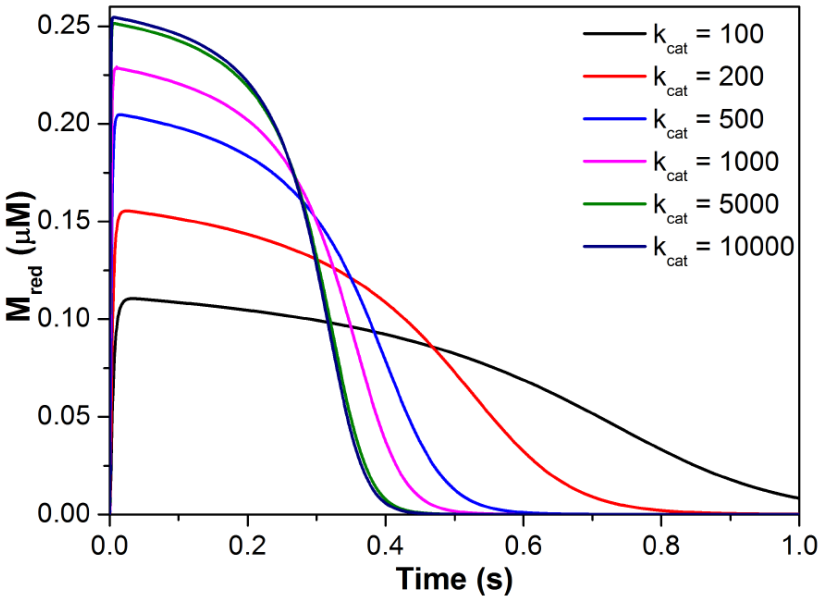


Fig. 4.19 b) Concentration of reduced mediator as a function of time for k_m= 1150 s^{-1} and different k_{cat}.

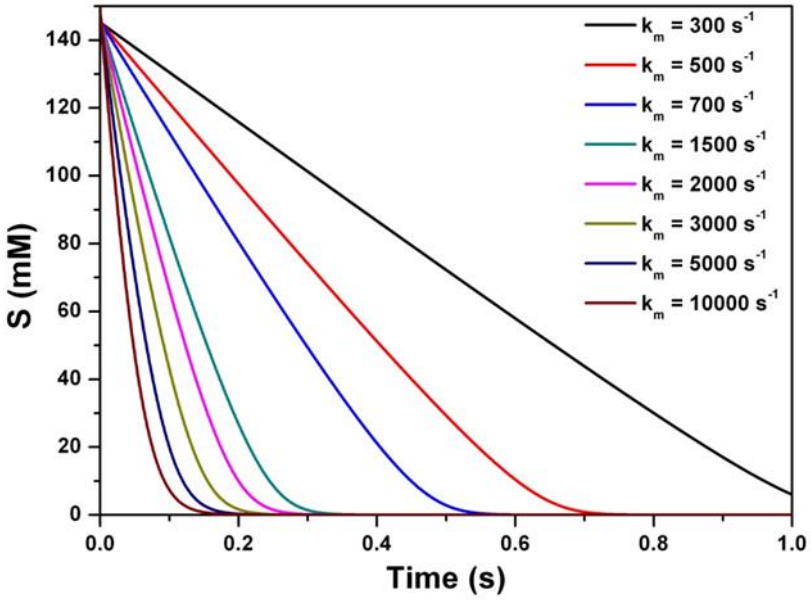


Fig.4.20 a) Substrate concentration as a function of time for k_{cat} = 5000 s^{-1} and different k_m.

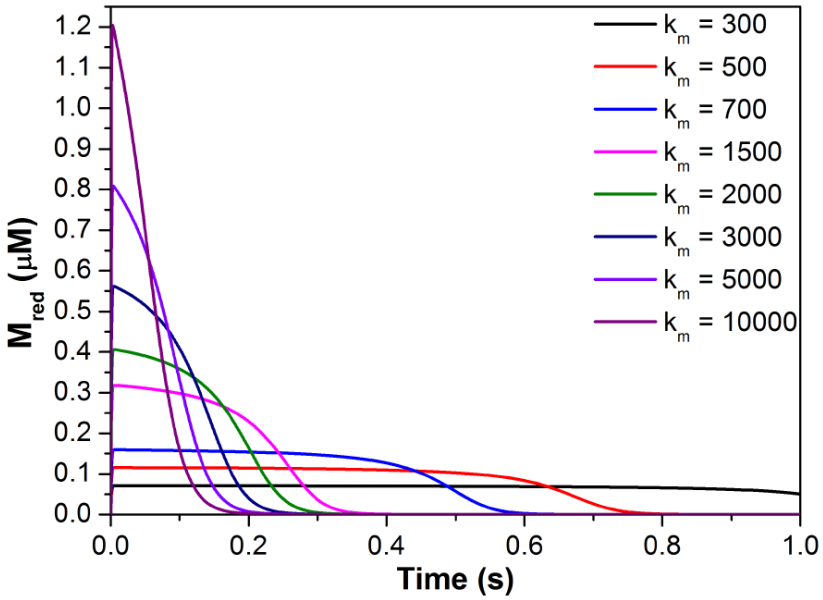


Fig.4.20 b) Concentration of reduced mediator as a function of time for k_{cat} of 5000 s^{-1} and different k_m.

4.4.2. Diffusion-controlled enzyme kinetics.

In order to support a continuous current flow, the enzymatic biofuel cell uses microfluidics to constantly deliver the substrate to the surface of the polymer layer. The transport of reactants from the bulk solution occurs by diffusion of species across the membrane, driven by concentration gradients. It is assumed that the flow is sufficient to maintain a given concentration of the substrate at the membrane, termed S_{bulk}. Using Eq. 4.15 – Eq. 4.22 with appropriate boundary conditions, the spatial distribution of the various reaction species has been studied. In this section, the time evolution of reactants starting from a spatially homogenous state was calculated including cyclic voltammetry curves (CV), which were used to gauge the performance of the enzymatic electrode. Additionally, S_{bulk} and the membrane thickness were varied to help understand the relationship between the diffusion and reaction effects occurring within the membrane.

The simulation constants used here are the same as in Tab. 4.2. In addition to the parameters required for the isolated system, values for the diffusion coefficients as well as the half-cell potentials, E_{cell} and E_{formal}, are needed. These correspond to the half-cell oxidation potential and the formal half-cell oxidation potential in standard conditions, further discussed in Appendix A, and were selected based on related experimental work.

The ratio of the concentrations of the redox couple reacting at the electrode is set by these potentials. In mediated catalysis, provided the reversibility of the $M_{red} \rightleftarrows M_{ox}$ kinetics, the electron transfer at the electrode is carried out by the mediator and therefore, the concentrations of the oxidized and reduced forms of M can be can be calculated via the Nernst equation [2]:

$$E_{cell} = E_{formal} + \frac{RT}{nF} \ln \frac{[M_{ox}]}{[M_{red}]} \qquad Eq.\ 4.26$$

Where R is the universal gas constant (8.314 J mol^{-1} K^{-1}), T is the temperature expressed in K, n represents the number of electrons exchanged in the reaction and F is the Faraday constant (96485 C mol^{-1}). For clarity, $\frac{RT}{nF}$ is denoted as a constant *N*.

In general, diffusion of species in a physical membrane is restricted relative to their transport in solution. A number of D_S values have been reported for glucose in various polymer matrices. The diffusion coefficient used here was selected on the basis experimental work on glucose in a polyacrylamide gel [39] although the model is not specific to any particular polymer matrix. Additionally, due to high structural similarity of glucose and gluconolactone, the diffusion coefficients for the substrate and the reaction product were assumed to be equal. All of the discussed parameters are presented in Tab. 4.4.

Tab. 4.4. Parameters for the diffusion-supported enzymatic system [39].

Constants (unit)		**Constants (unit)**	
D_S	**2.7 x 10^{-5} m^2 s^{-1}**	**E_{cell}**	**0.6 V**
D_e	**4 x 10^{-4} m^2 s^{-1}**	**E_{formal}**	**0.33 V**
D_P	**2.7 x 10^{-5} m^2 s^{-1}**	$\boldsymbol{N = \frac{RT}{nF}}$	**0.0591 V**
D_{EM} and D_{ES}	**0 m^2 s^{-1}**	**Membrane thickness**	**5 mm**

As the system of partial differential equations is second order in x and first order in t, two spatial boundary conditions and one temporal initial condition are required for each of the reactants except for the complexes, which do not have diffusion terms. The values of all reagents are therefore either specified at the polymer/bulk interface and the electrode surface or else are assigned a no-flux boundary condition. The catalytic layer was considered to be pre-occupied by the oxidized forms of the catalyst ($[E_{ox}] = E_0$, $[E_{red}] = 0$) and mediator ($[M_{ox}] = M_0$, $[M_{red}] = 0$) and to be fully saturated with the substrate i.e. $[S] = S_{bulk}$. In this pre-reaction stage, the enzyme complexes [ES] and [EM] have not been formed yet.

The no-flux for all time condition at the electrode, defined as zero spatial gradient across the boundary, indicates the boundary is impermeable. This may be obvious at the electrode surface but it applies also on the polymer/bulk interface, as there is no diffusion of reactants except for the substrate across that boundary, due to the immobilization. Recall, due to the fast flow approximation, the substrate concentration is considered to be always equal to S_{bulk}.

As illustrated in Tab. 4.5, the concentrations of $[M_{red}]$ and $[M_{ox}]$ at the electrode surface are governed by the transformed Nernst equation and have been defined as $\frac{[M_0]}{1+e^{\frac{E_{cell}-E_{formal}}{N}}}$ and $\frac{[M_0]}{1+e^{\frac{E_{formal}-E_{cell}}{N}}}$ respectively. This means that at high potentials where $e^{\frac{E_{cell}-E_{formal}}{N}} \gg 1$ and $e^{\frac{E_{formal}-E_{cell}}{N}} \ll 1$, $[M_{red}] \cong 0$ and $[M_{ox}] \cong M_0$ respectively.

Since experimentally the reactions are characterized by cyclic voltammetry, the operation of the theoretical half-cell should be measured in a similar manner. The magnitude of the current can be determined from the rate of the $M_{red} \rightarrow M_{ox}$ conversions at the electrode. Alternatively, the substrate flux to the layer can be assumed equivalent to the current generation, as reported previously by Bartlett *et al.* [2]. This is true as the entire system operates on a one to one ratio, so that counting the number of substrate molecules entering the membrane in the steady-state must equal the number of electrons liberated at the electrode. Mathematically, the flux of S, j_S, is given by Eq. 4.27.

Tab. 4.5. Initial & boundary conditions for the diffusion-supported kinetics.

Initial conditions	**Boundary conditions at x = 0 (membrane) and x = w (electrode)**
$[\mathbf{S}](\mathbf{x},\mathbf{0}) = \mathbf{S_{bulk}} = \mathbf{150\ mM}$	$[\mathbf{S}](\mathbf{0},\mathbf{t}) = \mathbf{S}_{bulk}$ $\frac{\partial \mathbf{S}(\mathbf{w},\mathbf{t})}{\partial \mathbf{x}} = \mathbf{0\ mM\ mm^{-1}}$
$[\mathbf{E_{ox}}](\mathbf{x},\mathbf{0}) = \mathbf{E_0} = \mathbf{5\ mM}$	$\frac{\partial E_{ox}(\mathbf{0},\mathbf{t})}{\partial \mathbf{x}} = \mathbf{0\ mM\ mm^{-1}}$ $\frac{\partial E_{ox}(\mathbf{w},\mathbf{t})}{\partial \mathbf{x}} = \mathbf{0\ mM\ mm^{-1}}$
$[\mathbf{M_{ox}}](\mathbf{x},\mathbf{0}) = \mathbf{M_0} = \mathbf{5\ mM}$	$\frac{\partial \mathbf{M_{ox}}(\mathbf{0},\mathbf{t})}{\partial \mathbf{x}} = \mathbf{0\ mM\ mm^{-1}}$ $[\mathbf{M_{ox}}](\mathbf{w},\mathbf{t}) = \frac{\mathbf{M_0}}{\mathbf{1} + \mathbf{e}^{\frac{\mathbf{E_{formal}} - \mathbf{E_{cell}}}{N}}}$
$[\mathbf{E_{red}}](\mathbf{x},\mathbf{0}) = \mathbf{0\ mM}$	$\frac{\partial \mathbf{E}_{red}(\mathbf{0},\mathbf{t})}{\partial \mathbf{x}} = \mathbf{0\ mM\ mm^{-1}}$ $\frac{\partial \mathbf{E}_{red}(\mathbf{w},\mathbf{t})}{\partial \mathbf{x}} = \mathbf{0\ \ mM\ mm^{-1}}$
$[\mathbf{M_{red}}](\mathbf{x},\mathbf{0}) = \mathbf{0\ mM}$	$\frac{\partial \mathbf{M}_{red}(\mathbf{0},\mathbf{t})}{\partial \mathbf{x}} = \mathbf{0\ mM\ mm^{-1}}$ $[\mathbf{M_{red}}](\mathbf{w},\mathbf{t}) = \frac{\mathbf{M_0}}{\mathbf{1} + \mathbf{e}^{\frac{\mathbf{E_{cell}} - \mathbf{E_{formal}}}{N}}}$
$[\mathbf{ES}](\mathbf{x},\mathbf{0}) = \mathbf{0\ mM}$	-
$[\mathbf{EM}](\mathbf{x},\mathbf{0}) = \mathbf{0\ mM}$	-
$[\mathbf{P}](\mathbf{x},\mathbf{0}) = \mathbf{0\ mM}$	$\frac{\partial \mathbf{P}(\mathbf{0},\mathbf{t})}{\partial \mathbf{x}} = \mathbf{0\ mM\ mm^{-1}}$ $\frac{\partial \mathbf{P}(\mathbf{w},\mathbf{t})}{\partial \mathbf{x}} = \mathbf{0\ mM\ mm^{-1}}$

$$j_S = D_S \left.\frac{d[S]}{dx}\right|_{x=0} \qquad Eq.\ 4.27$$

According to Bartlett and co-workers, in a non-immobilized catalytic system the observed current is typically smaller than the substrate flux, due to the concentration losses associated with the partition of the mediator across the polymer/bulk boundary [2]. If, as here, the mediator molecules are immobilized and cannot discharge into the solution, the assumption that the flux of the substrate equals the current is valid. Another condition on this assumption is that the diffusion must be sufficient to maintain a substrate concentration at the electrode, such that M_{red} can reach the value set through the Nernst equation.

The rate equations with the boundary conditions discussed were solved using Wolfram *Mathematica* and three dimensional time and spatial dependent concentration profiles across the membrane were computed. These solutions, although obtained for all reactants, are only presented for the substrate (Fig. 4.21) and the reduced mediator (Fig. 4.22). In the plots, 0 mm corresponds to the plane of the enzyme-mediator membrane, in direct contact with the fluid flow, and 5 mm indicates the electrode surface. For these initial conditions, the system reaches a steady-state after approximately 1 s.

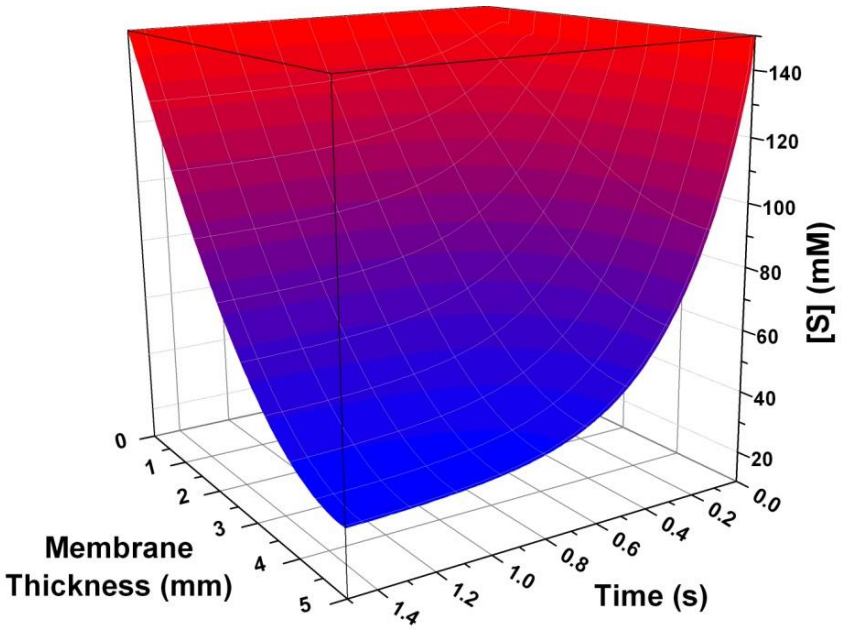


Fig. 4.21. Evolution of the concentration profile of the substrate across the enzyme-mediator layer computed for the diffusion-supported model.

In Fig. 4.21, the highest concentration of the fuel is found at the polymer boundary (0 mm), as expected from the boundary conditions. The initial concentration of S right across the membrane is saturated at 150 mM. As the substrate depletion appears to occur mainly at the electrode, [S] is quickly consumed in this region. It is however noted that, the concentration near the electrode, never reaches zero as the diffusion from the bulk is sufficient to feed the reaction faster than it is being consumed. After approximately 1 s, the competing diffusion and reaction forces have reached a state, where neither has ceased operation but are balanced in such a way, so that the reaction can proceed indefinitely without the change in concentration profile across the membrane. The magnitude of the gradient is governed by the catalytic rates and diffusion constants for the species involved in the reaction. For the parameters used here, the diffusion forces are large enough to feed the reaction all the way across the membrane without saturating. To a first approximation, [S] varies nearly linearly across the film from 100 mM at the bulk to around 40 mM at the electrode. More accurately, the concentration profile flattens out slightly at the electrode proximity.

Due to the immobilization and lack of external replenishment, the spatial gradient in [M_{red}] can be attributed exclusively to catalytic conversions and internal diffusion effects, Fig. 4.22. Initially, there is no M_{red} anywhere in the membrane but the steady-state profile shown is achieved very quickly, in less than 0.5 s (inset of Fig. 4.22). The concentration of M_{red} at the electrode is not zero but it is fixed at 0.05 mM by the half-cell potentials in the boundary condition for the electrode. Near the bulk, [M_{red}] is high as the large [S] binds to E_{ox} eventually producing high concentrations of reduced mediator. A higher concentration of M_{red} is expected at the bulk, as the gradients driving the diffusion of [M_{ox}] decreases across the membrane. In reality, due to the immobilization, the high concentration of M_{red} at the membrane can be explained as the rate of oxidation through electron hopping reduces with distance from the electrode.

Based on the above theory, the potential dependent current response of the diffusion-supported reaction system has been evaluated and is plotted in Fig. 4.23.
The CV output has been calculated for potentials between -1 V and + 1.5 V for scan rates between 10 and 500 mV s^{-1}. Note that this is current rather than current density as the model doesn't include a parameter for the area of the electrode hence the density could not be estimated.

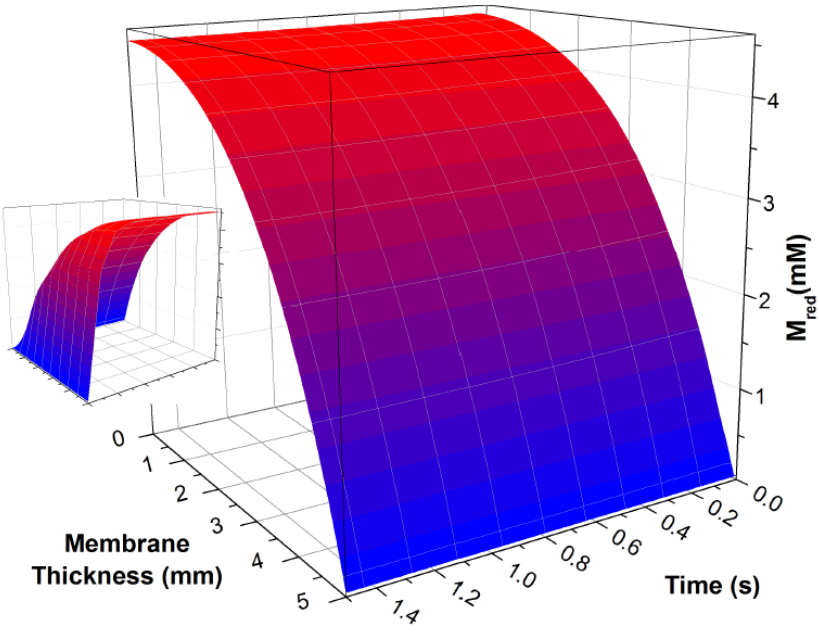


Fig. 4.22. Evolution of the concentration profile of the mediator across the enzyme-mediator layer computed for the diffusion-supported model.

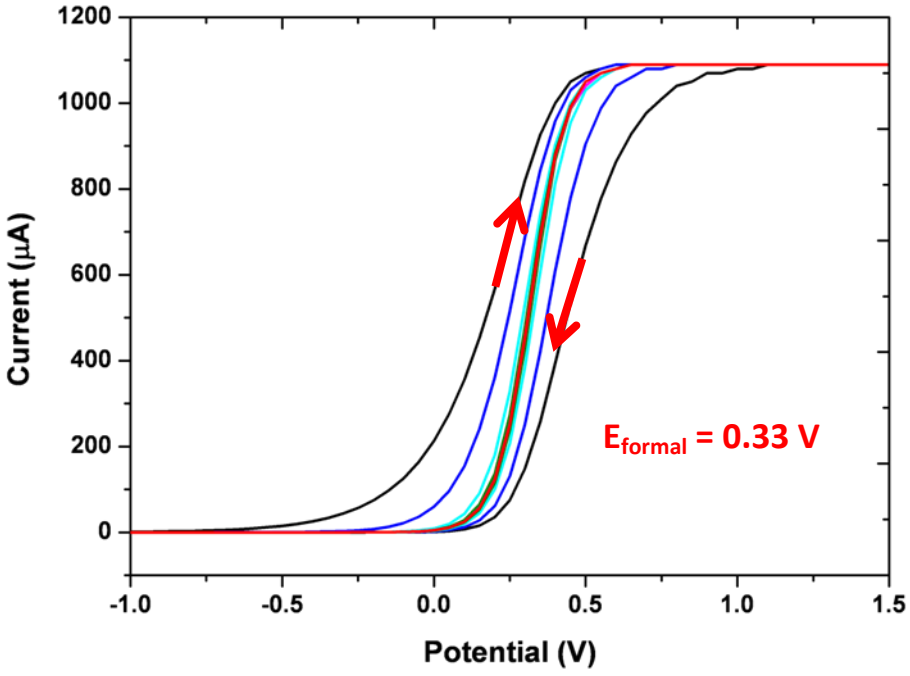


Fig. 4.23. Cyclic voltammograms for the simulated system for multiple scan rates: 500 mV s^{-1} (black line); 200 mV s^{-1} (navy blue line); 100 mV s^{-1} (cyan line); 50 mV s^{-1} (green line); 20 mV s^{-1} (red line) and 10 mV s^{-1} (magenta line).

As can be seen from Fig. 4.23, the maximum current at all cases is the same indicating that the process is not limited by diffusion of the mediator approximated by $D_{electron}$ but rather by the employed catalytic constants. At low scan rates the forward and reverse sweeps display a very close separation, while for faster scans the curves begin to separate noticeably. This phenomenon is essentially a time lag effect, as at a fast scan rate, the system has to adjust to a larger potential change in the same amount of time before the new current is measured. Observation of Fig. 4.23 shows that, in both sweep directions, the current recorded at a given potential for a fast scan rate matches that of a previous potential at a slower scan rate. At a high enough potential, the current for the slow scan rate stops changing, as the $[M_{red}]$ boundary condition reaches $[M_0]$. This allows the response at fast scan rates to catch up, which is why the limiting current is the same in all cases. Further evidence of this is given by the fact that the difference between the fast and slow scan rates increases with the change in the potential from that which attains the limiting current for the slow sweep rate.

Since the substrate diffusion is driven by concentration gradients, varying the thickness of the membrane is expected to have a significant effect on the spatial distribution of the reactants in the catalytic layer. As the thickness of the polymer coating can be controlled by the conditions of the electrochemical process (e.g. applied potential, deposition time) and varies depending on a particular use, the influence of the film thickness on the substrate and reduced mediator has been studied. The results, presented in Fig. 4.24 and Fig. 4.25, show the steady-state (for each thickness) concentration profiles of S and M_{red} for membrane widths between 0.2 mm and 25 mm. Two graphs for each reactant are needed, due to the differences in scales.

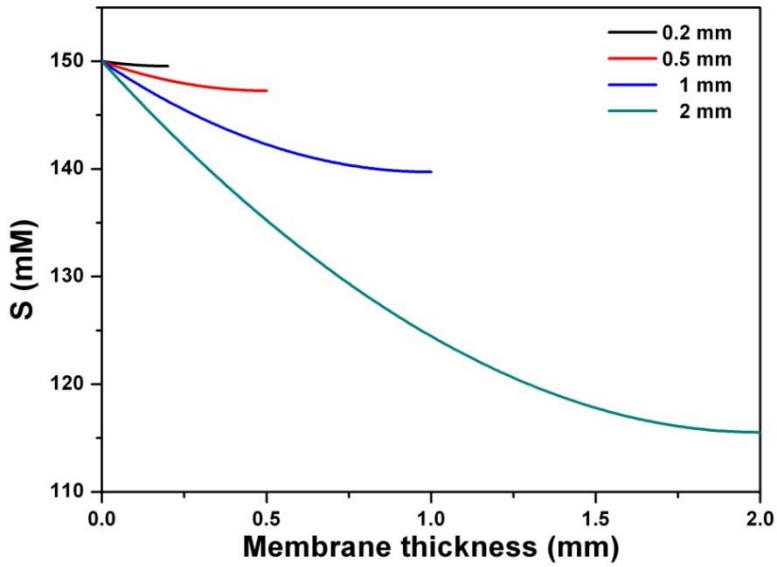


Fig. 4.24 a) Distribution of the substrate across the membrane for thicknesses between 0.2 mm and 2 mm for a diffusion-supported catalytic system.

As seen in Fig. 4.24 a), thin enzymatic films (thickness less than 0.5 mm) result in a nearly linear steady state distribution of S across the membrane, due to a close proximity to the bulk solution and diffusion effects dominating the reaction. Increasing the thickness of the polymer layer to 5 mm yields a semi-hyperbolic distribution of S, as discussed in Fig. 4.21. The substrate concentration at the electrode drops with increasing thickness up until 10 mm. At larger thicknesses, the value of the substrate plateaus at 30 mM for the parameters used here, Fig. 4.24 b). Overlying the curves for thicknesses of 10, 15 and 25 mm, aligned at the electrode plane, illustrates the similar shape of each profile in that region. For the 5 mm nearest to the electrode an almost identical shape is calculated each time, however further away the curves begin to diverge. From this, it can be concluded that the reaction is dominant in the 5 mm near the electrode but its influence decreases beyond that.

Similar behaviour has been reported for reduced mediator, where thinner membranes result in a small gradient of M_{red}, as shown in Fig. 4.25 a), due to a greater availability of the electron donating substrate and fast catalysis. The distribution of M_{red} within thin polymer coatings has a semi-parabolic shape and a higher peak concentration

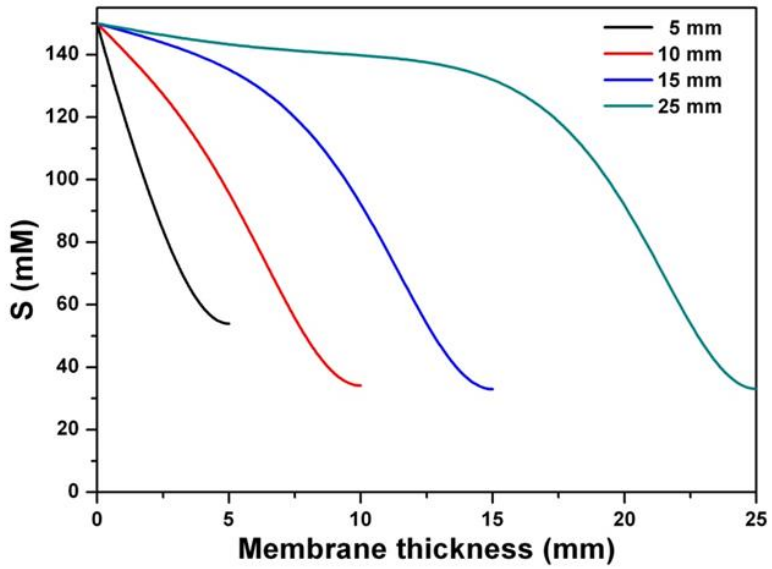


Fig. 4.24 b) Distribution of the substrate across the membrane for thicknesses between 5 mm and 25 mm for a diffusion-supported catalytic system.

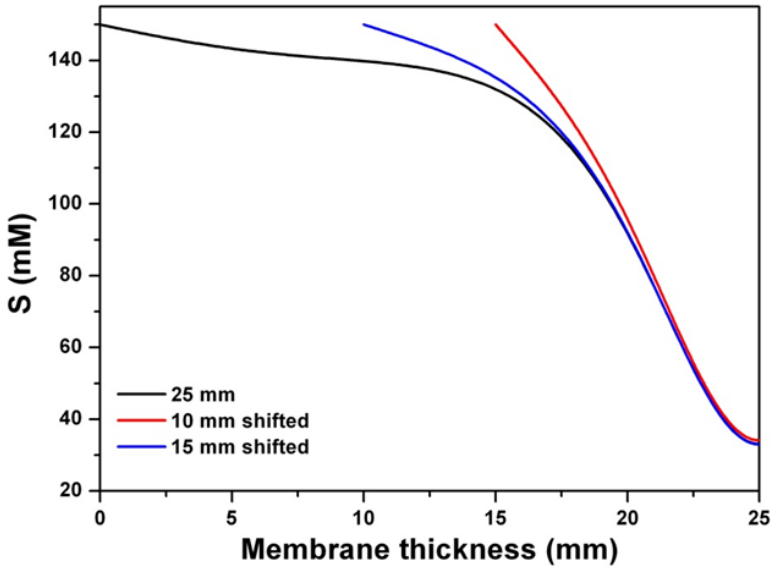


Fig. 4.24 c) Steady-state concentration profiles for 10, 15 and 25 mm membrane thicknesses aligned at the electrode plane. The similar responses near the electrode indicate that the reaction is dominant in that region.

at the membrane, as the effects of the reaction reduce with increasing distance from the electrode. For thicknesses greater than 10 mm, this peak value saturates at the total available mediator (5mM). M_{red} remains saturated at M_0 to within 5 mm of the electrode, in agreement with the conclusions drawn from Fig. 4.24 c). Near the electrode, [M_{red}] reduces smoothly to the concentration set by the potential applied at the boundary through the Nernst equation.

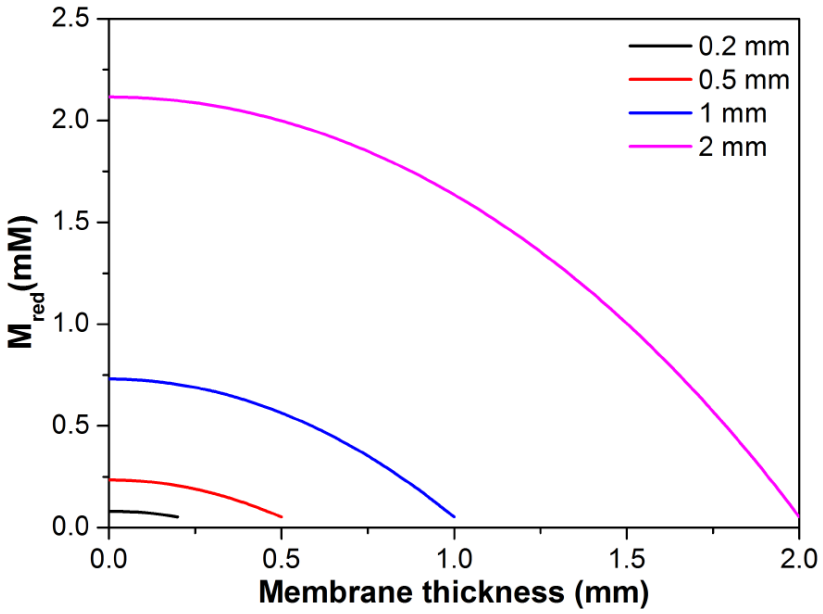


Fig. 4.25 a) Distribution of the reduced mediator across the membrane for thicknesses between 0.2 mm and 2 mm for a diffusion-supported catalytic system.

The effect of the membrane thickness on the magnitude of the oxidation current is presented in Fig 4.26. Note that this is current rather than current density as the model doesn't include a parameter for the area of the electrode hence the density could not be estimated. The output recorded from the oxidation peak currents of the CV curves at a 200 mV s^{-1} scan rate, increases with membrane thickness reaching a maximum for these parameters at a value of 5 mm. Further increase in the polymer thickness results in a decline in the observed current. Combining the peak current at a membrane thickness of 5 mm and recalling the saturation effects shown in Fig. 4.24 b) and Fig. 4.25 b), a design rule for the half-cell can be suggested. That is, taking the diffusion into account, the membrane should not be so thick that the observed saturation occurs.

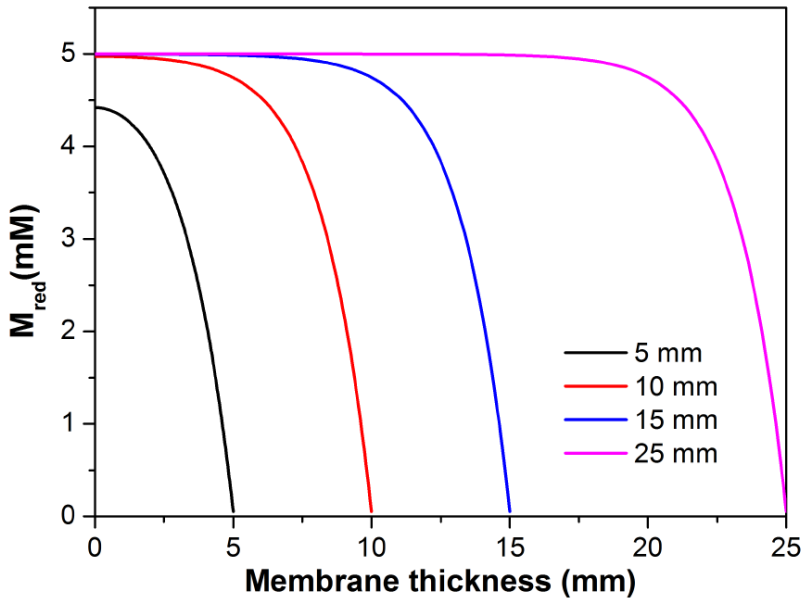


Fig. 4.25 b) Distribution of the reduced mediator across the membrane for thicknesses between 5 mm and 25 mm for a diffusion-supported catalytic system.

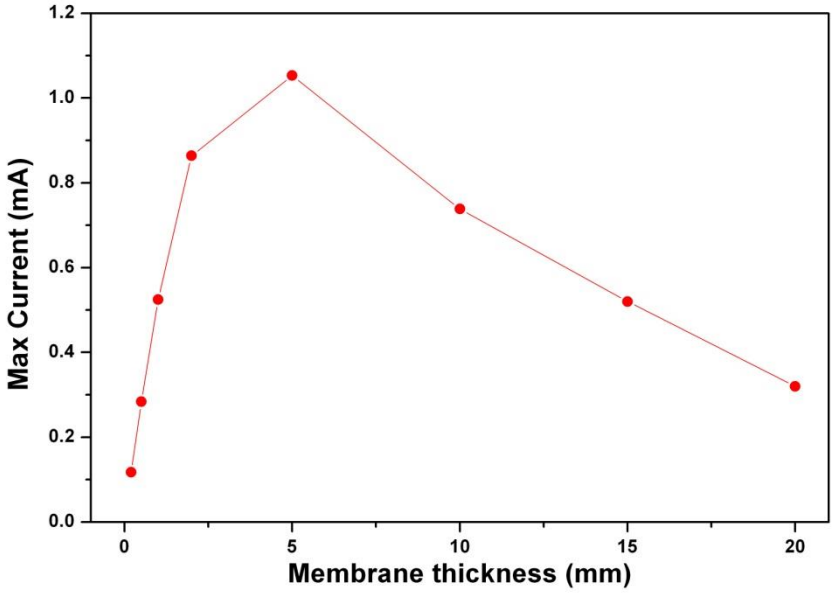


Fig. 4.26. Dependency of the maximum oxidation peak current on the thickness of the membrane. Values have been recorded for 150 mM substrate and at 200 mV s^{-1}.

The influence of S_{bulk} on the steady-state of the reaction has also been studied. Two dimensional distribution profiles of S and M_{red} for various [S_{bulk}] are presented in Fig. 4.27 and Fig. 4.28 respectively. In particular, concentration values of 1 mM, 5 mM, 10 mM, 25 mM, 50 mM, 75 mM, 100 mM and 150 mM were used and the thickness of the membrane was fixed at 5 mm. All other system conditions were as noted in Tab. 4.5 and Tab. 4.4.

At low values of S_{bulk} the concentration of the substrate near the electrode is zero. In fact, for these parameters, S_{bulk} needs to be greater than 50 mM, before a non-zero substrate concentration is recorded at the electrode. With regards to M_{red}, as seen in Fig. 4.28, dilute fuels result in low concentrations of reduced mediator across the film. For S_{bulk} greater than 75 mM, [M_{red}] in proximity to the membrane tends towards saturation levels. This appears to be less than [M_0], approximately 4.5 mM. Of course, for all S_{bulk}, M_{red} at the electrode is fixed by the Nernst boundary condition, as previously noted.

The concentration of the substrate at the electrode surface has been recorded for various [S_{bulk}] and plotted in Fig. 4.29.

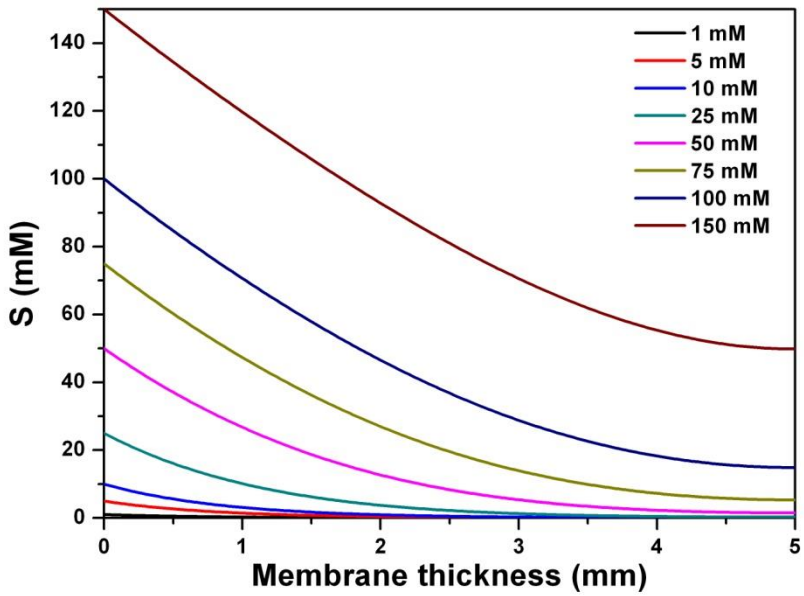


Fig.4.27. Steady-state distribution profiles of S at the membrane cross-section for various initial substrate concentrations [S_{bulk}].

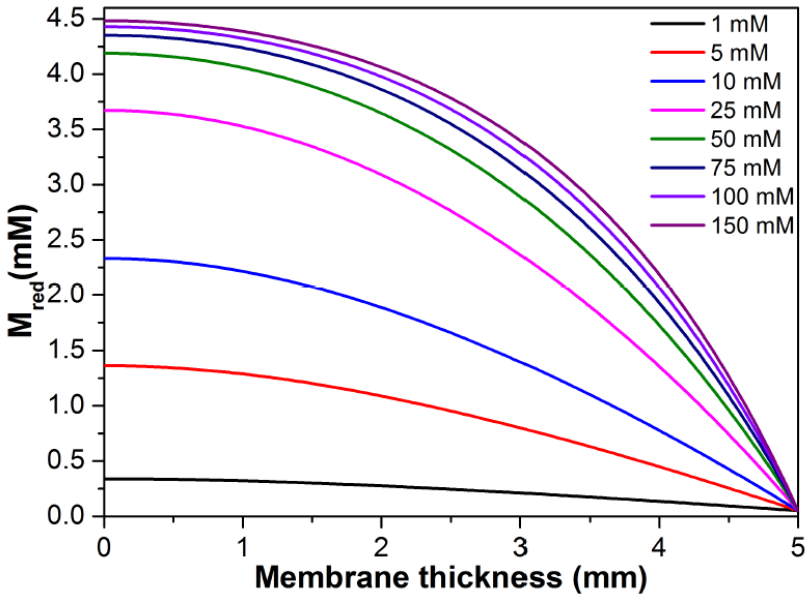


Fig. 4.28. Steady-state distribution profiles of [M_{red}] across the membrane for various initial substrate concentrations [S_{bulk}].

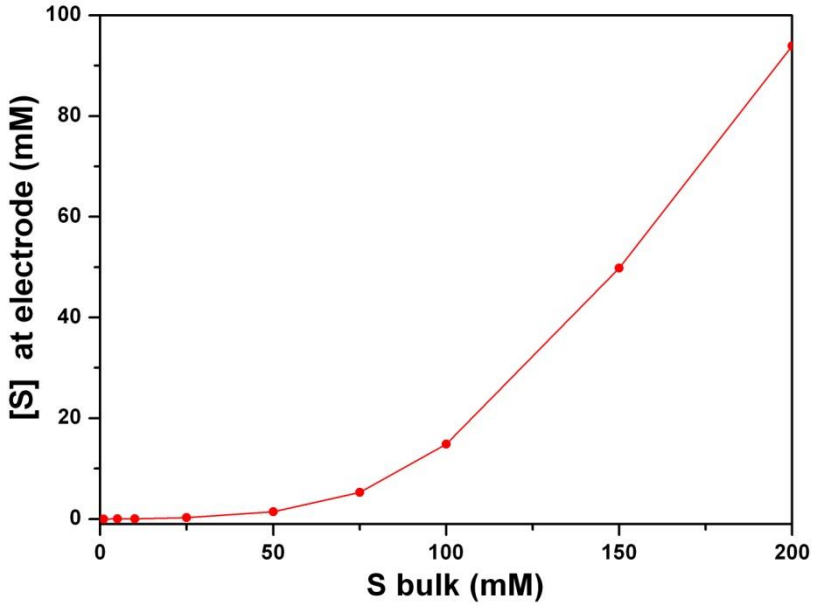


Fig. 4.29. The steady-state concentration of the substrate at the electrode as a function of [S_{bulk}].

Once S_{bulk} is sufficient to maintain a non-zero substrate concentration at the electrode, an approximately linear increase in [S] is observed. For the considered values, the [S] at the electrode is always less than [S_{bulk}] but eventually it will saturate to the input substrate concentration.

The CV responses for the various [S_{bulk}] were calculated for a constant scan rate of 200 mV s^{-1} and are presented in Fig. 4.30. Again these plots are labelled as current and not current density as the model used does not feature a parameter related to the area of the electrodes. Even at a bulk concentration of only 1 mM, where no substrate is recorded at the electrode, a non-zero output current is calculated. With increasing S_{bulk}, the limiting current begins to saturate. For each bulk concentration, the saturation current is reached at a potential between 0.9 V and 1 V. The exception being [S_{bulk}] = 1 mM, where this phenomenon occurs at 0.25 V.

For clarity, the maximum current at each [S_{bulk}] is plotted in Fig. 4.31, showing saturation around 1.1 mA for the parameters used. This suggests that the availability of the fuel is no longer a limiting factor for the reaction. In terms of the biofuel cell design, these results suggest that higher concentrations of the input substrate are desirable, as that the performance is not limited by the substrate availability and rather by enzyme kinetics.

As previously, Fig. 4.30 and Fig. 4.31 represent current rather than current density since the model doesn't include a parameter for the area of the electrode.

4.5. Conclusions.

This chapter aimed to use some of the available software tools to theoretically investigate the biofuel cell which would be constructed as part of this work. In particular, there were two main topics which were focused upon: the physical design of the micro channel and an understanding of the reaction within the membrane. The outcome of all results influenced the later device design and fabrication as well as assisting in experimental interpretation.

First, finite element method simulations of the flow in the channel were used to verify that the proposed design exhibited only a limited mixing between the fluids entering

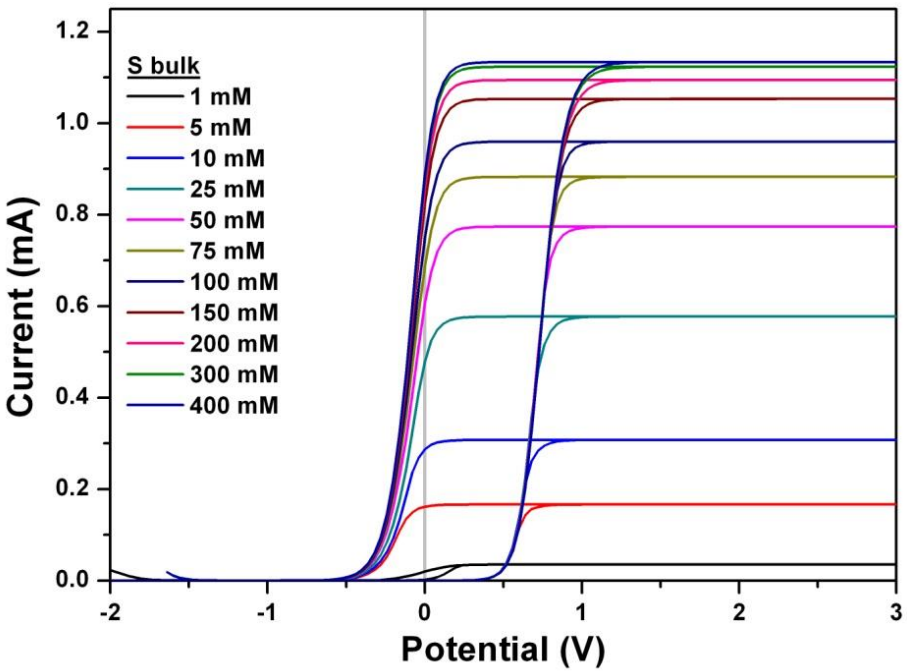


Fig. 4.30. Cyclic voltammograms of the catalytic system for various [S_{bulk}].

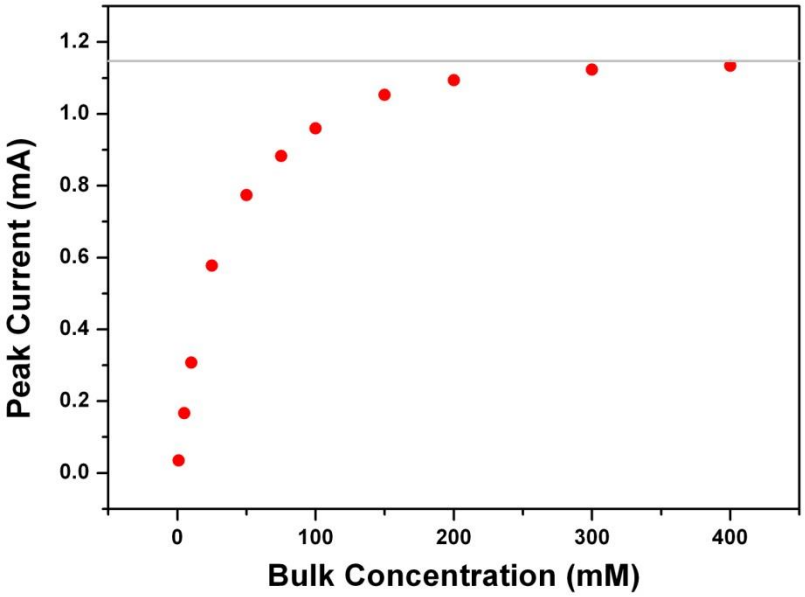


Fig. 4.31. Dependency of the oxidation peak current on the concentration of the bulk substrate.

the main body of the channel through the two inlets. Calculations at different flow rates and channel widths verified that higher speed flows in general exhibit a laminar flow and limited mixing. Shorter channels would achieve the same effect by reducing the time available for mixing between the constituent flows. The shape of the electrodes along the bottom of the channel was then considered. While previously reported microscale biofuel cells use a continuous macro-electrode, an alternative approach examined in the thesis employed a single electrode split into a multiple smaller elements with intervening gaps similar to a haircomb. Both a single, continuous electrode and a spatially distributed electrode were determined to be good choices for the electrode design. As the membrane could also be deposited on the side walls of the electrodes, the surface area of the densely packed distributed electrodes could potentially be much larger than the planar electrode. On this basis, it was decided that distributed electrodes, rather than single, continuous electrodes, would be fabricated in the real devices. Determining the most efficient design, in terms of current generation from the reaction, would require an optimization of the surface area, flow rate and channel dimensions. Such a study is beyond the scope of this thesis. The work here is intended as a foundation and starting point for a more comprehensive study. A three dimensional design with densely packed distributed electrodes on the top, bottom and side walls would be an avenue worth exploring from this regard.

Second, the kinetics of the reaction occurring within in the polymer layer on top of the electrode were investigated based on a set of eight 2^{nd} order partial differential equations formulated by a modified Michaelis-Menten analysis of the system. Due to the complexity and highly coupled nature of this system it can be difficult to draw direct conclusions about how a given parameter influences the dynamics. To start, a reaction where only a finite amount of substrate is available is simulated. This system is easier to understand and the effects of changes in the rate constants are more directly observed. A study of k_{cat} and k_m showed that increasing either constant quicken the reaction rate and that the dissociation of the complexes can be rate limiting steps. Four phases in this reaction have been identified: initial catalysis, sustainable catalysis, the turn-off stage and the reaction termination. At each stage, different kinetics are observed as the relative abundances of the substrate and other reactants change.

Calculations of the steady state of the diffusion supported system revealed spatial concentration gradients of the species across the polymer membrane. These gradients are

the result of the competition between reaction and diffusion forces. Cyclic Voltammetry curves at different scan rates were produced to help understand experimental results and the response of the system to a changing potential. Following studies on the effect of the membrane thickness and the bulk concentration, some design rules for the optimum CV performance biofuel cell were suggested.

The work in this chapter is, essentially, the creation of a framework within which the operation of biofuel cells could be investigated prior to fabrication. Unfortunately, this is framework is not yet fully integrated. The modelling of the flow and of the reaction is done using separate software. In the future, an accurate description of the kinetics should be combined with the flow model so that the concentrations across the entire channel, the membrane and at the electrode could be studied for different geometries. Making the rate constants dependent on the applied potential would be another realistic improvement.

4.5. Bibliography.

1. Ivanov, I., T. Vidaković-Koch, and K. Sundmacher, *Recent Advances in Enzymatic Fuel Cells: Experiments and Modeling.* Energies, 2010. **3**(4): p. 803-846.
2. Bartlett, P.N. and K.F.E. Pratt, *Theoretical treatment of diffusion and kinetics in amperometric immobilized enzyme electrodes Part I: Redox mediator entrapped within the film.* Journal of Electroanalytical Chemistry, 1995. **397**(1–2): p. 61-78.
3. Flexer, V., et al., *Relaxation and Simplex mathematical algorithms applied to the study of steady-state electrochemical responses of immobilized enzyme biosensors: Comparison with experiments.* Journal of Electroanalytical Chemistry, 2008. **616**(1–2): p. 87-98.
4. Shah, A., T. Ralph, and F. Walsh, *Modeling and simulation of the degradation of perfluorinated ion-exchange membranes in PEM fuel cells.* Journal of the Electrochemical Society, 2009. **156**(4): p. B465-B484.
5. Bartlett, P.N., et al., *Modelling Biosensor Responses*, in *Bioelectrochemistry* 2008, John Wiley & Sons, Inc. p. 267-325.
6. Gallaway, J.W. and S.A. Calabrese Barton, *Kinetics of redox polymer-mediated enzyme electrodes.* Journal of the American Chemical Society, 2008. **130**(26): p. 8527-8536.
7. Tamaki, T., T. Ito, and T. Yamaguchi, *Modelling of Reaction and Diffusion Processes in a High-surface-area Biofuel Cell Electrode Made of Redox Polymer-grafted Carbon.* Fuel Cells, 2009. **9**(1): p. 37-43.
8. Bullen, R.A., et al., *Biofuel cells and their development.* Biosensors and Bioelectronics, 2006. **21**(11): p. 2015-2045.
9. Kjeang, E., D. Sinton, and D. Harrington, *Strategic enzyme patterning for microfluidic biofuel cells.* Journal of Power Sources, 2006. **158**(1): p. 1-12.
10. Osman, M., A. Shah, and R. Wills, *Detailed Mathematical Model of an Enzymatic Fuel Cell.* Journal of the Electrochemical Society, 2013. **160**(8): p. F806-F814.
11. Osman, M., et al., *Mathematical modelling of an enzymatic fuel cell with an air-breathing cathode.* Electrochimica Acta, 2013. **112**: p. 386-393.
12. Glykys, D.J. and S. Banta, *Metabolic control analysis of an enzymatic biofuel cell.* Biotechnology and bioengineering, 2009. **102**(6): p. 1624-1635.
13. Jeon, S.W., et al., *Optimization of cell conditions for enzymatic fuel cell using statistical analysis.* Journal of Industrial and Engineering Chemistry, 2008. **14**(3): p. 338-343.
14. Krishnamurthy, D., et al., *Computational modeling of microfluidic fuel cells with flow-through porous electrodes.* Journal of Power Sources, 2011. **196**(23): p. 10019-10031.
15. Bedekar, A., et al., *Oxygen limitation in microfluidic biofuel cells.* Chemical Engineering Communications, 2007. **195**(3): p. 256-266.
16. Chan, D.-S., D.-J. Dai, and H.-S. Wu, *Dynamic Modeling of Anode Function in Enzyme-Based Biofuel Cells Using High Mediator Concentration.* Energies, 2012. **5**(7): p. 2524-2544.
17. Zebda, A., et al., *Membraneless microchannel glucose biofuel cell with improved electrical performances.* Sensors and Actuators B: Chemical, 2010. **149**(1): p. 44-50.
18. Bazylak, A., D. Sinton, and N. Djilali, *Improved fuel utilization in microfluidic fuel cells: A computational study.* Journal of Power Sources, 2005. **143**(1): p. 57-66.

19. Yoon, S.K., G.W. Fichtl, and P.J. Kenis, *Active control of the depletion boundary layers in microfluidic electrochemical reactors.* Lab on a Chip, 2006. **6**(12): p. 1516-1524.
20. Ebrahimi Khabbazi, A., A. Richards, and M. Hoorfar, *Numerical study of the effect of the channel and electrode geometry on the performance of microfluidic fuel cells.* Journal of Power Sources, 2010. **195**(24): p. 8141-8151.
21. Picioreanu, C., et al., *Model based evaluation of the effect of pH and electrode geometry on microbial fuel cell performance.* Bioelectrochemistry, 2010. **78**(1): p. 8-24.
22. Picioreanu, C., et al., *Modelling microbial fuel cells with suspended cells and added electron transfer mediator.* Journal of Applied Electrochemistry, 2010. **40**(1): p. 151-162.
23. Picioreanu, C., et al., *A computational model for biofilm-based microbial fuel cells.* Water Research, 2007. **41**(13): p. 2921-2940.
24. Kar, P., et al., *Simulation of multistep enzyme-catalyzed methanol oxidation in biofuel cells.* Journal of the Electrochemical Society, 2011. **158**(5): p. B580-B586.
25. Martens, N. and E.A. Hall, *Model for an immobilized oxidase enzyme electrode in the presence of two oxidants.* Analytical chemistry, 1994. **66**(17): p. 2763-2770.
26. Kano, K. and T. Ikeda, *Fundamentals and practices of mediated bioelectrocatalysis.* Analytical Sciences, 2000. **16**(10): p. 1013-1022.
27. Choban, E.R., et al., *Microfluidic fuel cell based on laminar flow.* Journal of Power Sources, 2004. **128**(1): p. 54-60.
28. Kamholz, A.E., et al., *Quantitative analysis of molecular interaction in a microfluidic channel: the T-sensor.* Analytical Chemistry, 1999. **71**(23): p. 5340-5347.
29. Johnson, T.J., D. Ross, and L.E. Locascio, *Rapid microfluidic mixing.* Analytical Chemistry, 2002. **74**(1): p. 45-51.
30. Stone, H.A., A.D. Stroock, and A. Ajdari, *Engineering flows in small devices: microfluidics toward a lab-on-a-chip.* Annu. Rev. Fluid Mech., 2004. **36**: p. 381-411.
31. Ervin, V., W. Layton, and J. Maubach, *Adaptive defect-correction methods for viscous incompressible flow problems.* SIAM Journal on Numerical Analysis, 2000. **37**(4): p. 1165-1185.
32. Hartmann, C. and L. Sasso, *Convection–diffusion in microchannels*, 2007, Internal report, DTU, Lyngby.
33. Van de Ven-Lucassen, I. and P. Kerkhof, *Diffusion coefficients of ternary mixtures of water, glucose, and dilute ethanol, methanol, or acetone by the Taylor dispersion method.* Journal of Chemical & Engineering Data, 1999. **44**(1): p. 93-97.
34. Wilke, C. and P. Chang, *Correlation of diffusion coefficients in dilute solutions.* AIChE Journal, 1955. **1**(2): p. 264-270.
35. Jamnongwong, M., et al., *Experimental study of oxygen diffusion coefficients in clean water containing salt, glucose or surfactant: Consequences on the liquid-side mass transfer coefficients.* Chemical Engineering Journal, 2010. **165**(3): p. 758-768.
36. Gibson, Q.H., B.E. Swoboda, and V. Massey, *Kinetics and mechanism of action of glucose oxidase.* Journal of Biological Chemistry, 1964. **239**(11): p. 3927-3934.
37. Segel, I.H., *Enzyme kinetics* 1993: Wiley New York.

38. Malitesta, C., et al., *Glucose fast-response amperometric sensor based on glucose oxidase immobilized in an electropolymerized poly (o-phenylenediamine) film.* Analytical Chemistry, 1990. **62**(24): p. 2735-2740.
39. Aoki, A. and A. Heller, *Electron diffusion coefficients in hydrogels formed of cross-linked redox polymers.* The Journal of Physical Chemistry, 1993. **97**(42): p. 11014-11019.

CHAPTER V

DESIGN AND FABRICATION OF MICROFLUIDIC DEVICES WITH INTEGRATED ELECTRODES

Discovery consists of looking at the same thing as everyone else and thinking something different

Albert-Szent Gyorgi

5.1. Introduction.

Chapter V of this thesis discusses the work underlying the design and development of microfluidic platforms with incorporated electrodes. A detailed description of the selected fabrication processes is preceded with a literature review of the emerging manufacturing technologies and the material evaluation. The principles and advantages of the microfluidic approach in the design consideration are also included.

5.1.1. Main objectives.

The main objective of this chapter was to design and fabricate novel microfluidic devices that could be successfully employed in enzymatic biofuel cell applications. Many device approaches have been considered up to date, majority of which involving non-automated, time consuming and labor intensive fabrication of highly complex and multiple-component systems for enzymatic electrocatalysis [1]. System miniaturization supported by simplicity and high precision of device manufacturing were the driving force for this research work. The microfluidic approach undertaken in the course of this Ph.D. work enables significant reduction of the feature size due to the membrane-free structure and high cost-efficiency of the device fabrication. Low power consumption and small volumes of analyte used in microfluidic designs allow efficient operation of the cell and utilization of the fuel at high surface area-to-volume ratio, enabling detailed investigation

of the physicochemical effects in the micro-domain. Low-cost, non-toxic and easily micromachined polymer materials were the primary criteria of the material choice for device fabrication.

Excellent manufacturing standards of the Silicon and the Central Fabrication Facilities (CFF) at the Tyndall National Institute provided state-of-the-art microfabrication techniques.

This chapter describes the design considerations, material choice and the fabrication of the device components, followed by the proposed assembly of the microfluidic platforms. The electrochemical characterization of microfabricated electrodes and a selected method of chemical modification of gold surface are also presented. A general introduction into the rapid development of microfabrication technologies and the current state-of-the-art is also presented.

5.2. Literature review on fabrication technology.

The following section discusses the evolution of fabrication technologies and considers the properties and potential applications of diverse structural materials.

5.2.1. Material comparison.

Successful fabrication and efficient operation of microfluidic devices depend strongly on the type of material that has been used on the manufacturing step. Substrate properties of the highest importance for microfluidic applications include the optical characteristics of the material, its molecular adsorption, surface charge and machinability [2].

The beginning of microfluidic studies dates back to late 1990s. At that time all devices were fabricated from either silicon or glass using photolithography and etching techniques [3]. Although nowadays processing in glass is significantly less extensive than in the past, silicon is still commonly used as a material for microfabrication.

Silicon is widely used as a natural semiconductor in electronics industry. Due to its exceptional mechanical properties and well established machining technologies, it can be employed in microfabrication of highly complex networks of circuits and miniscule

features for biochemical systems. Nevertheless the lack of optical transparency does not elect it as a candidate of choice for optical detection systems which are usually based on microscopic techniques. Glass on the other hand is among the few solids that transmit the visible light and as such traditionally forms the basics of virtually all optical systems [4]. For this reason it is particularly suitable for fabrication of micro-devices for optical detection. Glass components exhibit superior dielectric properties; they are thermally stable, chemically inert and can easily form seals with metals and ceramics. For that reason, glass has been successfully employed in microelectronic industry and for applications requiring high-temperatures. Due to its good chemical and mechanical stability, glass has been used for the fabrication of biosensors and biofuel cells. Nevertheless, its low porosity and lack of permittivity do not suit cell culture very well. In a similar manner to silicon, glass for microfabrication is also supplied as a wafer and it is available in a variety of structural compositions (quartz, fused silica, borosilicate glass etc.). Despite the abundance and well defined properties, a number of manufacturing challenges have been associated with silicon and glass [5]. The processing of these two materials is relatively expensive, labour intensive and prone to particle contamination, therefore it requires clean-room environment. Soft materials (e.g. polymers) on the other hand, are easy to manufacture and hence emerged as an excellent alternative rapidly replacing the use of silicon and glass in certain applications.

Polymer materials have been the emerging substrates for microfluidic devices primarily due to their low cost, widespread availability and ease at which they can be employed in the manufacturing procedures, particularly when compared to glass or silicon. Wide range of available polymer substrates enable to choose the material with properties that are most suitable for a particular application. Depending on the processing, different parameters may be crucial when considering the material of choice. For instance, glass transition temperature and the thermal expansion coefficient are two most fundamental substrate characteristics affecting the successful hot-embossing and injection molding techniques [2]. The glass transition of a polymer occurs when the amount of heat provided is sufficient to alter the physical appearance of the polymer from its rigid glassy form to a soft un-melted state. The Glass Transition Temperature (GTT) should not be miconcepted for a Melt Temperature (TM), which is usually much higher and causes the polymer to flow. Most polymers can be characterized by GTT and TM parameters; however, the majority of thermoplastics and highly cross-linked polymer substrates do not undergo

melting but they remain soft and decompose at very high temperatures. Thermal expansion coefficient on the other hand relates the degree of volume change with respect to the unit change in temperature. Polymer imprinting at room temperature requires very low hardness and significant degree of flexibility and it is usually not considered in microfluidic applications due to the risk of unexpected pattern un-molding. Instead, soft lithography methods are frequently applied and these require the ability of the polymer to maintain its original shape and dimensions after the fabrication step. Different polymer materials exhibit a variety of surface charges, which can have profound effect on the electroosmotic flow in the channel and device assembly. Channel characteristics are determined by intrinsic properties of the polymer but can also be modified by a fabrication process. For instance, features imprinted thermally by laser ablation or at room temperature will have much higher surface charge density than those obtained in the same material using hot-embossing [6, 7]. Surface charge can also be modulated by hydrolysis or plasma treatment [8]. In general, properties such as electroosmotic flow or charge density and its location are dependent on the following key factors: the polymer material, fabrication procedure and type of the surface treatment. Regardless of the particular application, the majority of materials for microfluidic device fabrication need to be chemically inert, transparent and permeable to gasses. Biomedical industry and research encompassing biosensing or cell culture, in particular, require polymer materials to be also biocompatible.

Up-to-date, three types of polymeric materials have been frequently employed for prototyping of microfluidic devices [9]:

- Photodefinable polymers, such as SU-8, which although they have been well recognized and widely used in microelectronics, were not a subject of this Ph.D. work, due to the intricacy and elevated costs of the fabrication process (e.g. UV-curing in the presence of a photo mask);

- Thermoplastic materials e.g. poly-methylmethacrylate (PMMA) and Cyclo-Olefin-Copolymers (COC) are routinely employed materials, due to their excellent optical properties, moldability and low water intake;

- Elastomers, among which the most popular is poly-dimethylsiloxane (PDMS), which exhibit excellent moldability and simplicity of device fabrication.

PDMS is by far the most ubiquitous organic silicon-based polymer used in microfluidics. It is 50 times cheaper than silicon and features a wide range of attractive properties. It is non-toxic, transparent at optical wavelengths (240 nm-1100 nm) and displays outstanding gas permeability which makes it an ideal candidate for cell culture cultivation [10], enzyme based assays and biomedical applications. The ability to permeate gas has been frequently used to sustain cells and microorganisms inoculated in PDMS interiors [11]. PDMS possesses unique flexural and dielectric strength and compressibility as well as the usability over a wide range of temperatures. Furthermore, it is biocompatible and can be applied together with enzymes or microbial cells, without posing any risk to their intrinsic biological functions.

PDMS devices are usually prepared by a low temperature hydrosilation of the polymer substrate induced by a platinum-based curing agent. Curing time is adjustable with temperature and can take up to 5 h. PDMS structures can be easily obtained via replica mold techniques, by simply casting the liquid polymer onto the patterned stamp and curing the assembly at elevated temperature. Once cross-linked, PDMS becomes an elastomeric material with a high degree of flexibility (Young's modulus of 750 kPa). This and a low surface energy (20 erg cm^{-2}) allow PDMS to conform to surfaces in a reversible manner and facilitate easy release from molds after patterning [2]. Upon surface treatment, polydimethylsiloxane can however form irreversible seals with glass and other polymer substrates. The presence of reactive silanol groups (Si-OH) formed when exposing PDMS to oxygen plasma not only provides efficient bonding to other materials but also creates a site for chemical modification of PDMS surface. Silanol functions can participate in a number of condensation reactions with silyl chloride, hydroxyl and carboxyl groups etc. At pH higher than 3.0, Si-OH groups can however dissociate into $Si\text{-}O^-$ and H^+ forming a negative charge on the surface. If a positive surface charge is required, PDMS can be successfully coated with a positive polymer, such as polybrene. High flexibility (adjustable with the ratio of base to the curing agent) and reversible deformability of PDMS allows the patterning of highly integrated systems of features (channels, valves, pumps etc.), often at a micron size scale. When compared to many plastics commonly used in microfabrication, PDMS exhibits very low auto-fluorescence facilitating visual observation of microchannel contents using microscopic techniques. Despite the advantages of PDMS, the material absorbs water and solvent vapours, which can result in swelling and a loss of substrate clarity. Due to its hydrophobic nature, PDMS can capture

and release non-polar molecules from poorly cross-linked substrate affecting the composition of the solution under investigation. As reported by [12], the undesired swelling in organic solvents has been the reasoning behind the restricted operability of PDMS-based microfluidic devices in various hydrocarbon solutions (e.g. acetone, hexane, toluene). For these reasons, currently any applications involving the use of organic solvents are based on original glass and silicon systems. In order to expand the use of microfluidic devices, a new generation of elastomer materials that would combine the attractive properties of polydimethylsiloxane and the ability to use organic solvents needs to be urgently explored.

As PDMS is mainly suitable for prototyping in academic research, most commercially used fabrication processes (e.g. metal deposition) require other polymer substrates for microfluidic device manufacturing. These materials are predominantly transparent thermoplastics and they come in a form of microfluidic chips and wafers of different dimensions. Thermoplastics can be successfully used for applications involving aqueous and mildly acidic or basic solutions but they poorly tolerate concentrated acids and bases, aromatics, ketones and halogenated hydrocarbons. Most frequently used thermoplastic polymers include PMMA (Polymethylmetacrylate), PC (Polycarbonate) and PS (Polystyrene), Topas and Zeonor.

PMMA, also known as Plexiglas or acrylic glass, is a polymer of methylmethacrylate. Because its fundamental monomer is an ester of acrylate, the carbonyl group can be successfully employed for chemical modification of the PMMA surface. Polymethylmethacrylate is commonly used as a lightweight or shatter-resistant substitute to glass. Microfluidic devices made of PMMA can be effectively used in aqueous solutions, in the presence of aldehydes, amines and oils however they cannot withstand alcohols, esters, aromatic components or highly concentrated solutions of acids and bases.

Polystyrene (PS), is one of the most routinely used materials in life sciences primarily due to its enhanced chemical stability and relatively low price. It is an aromatic polymer of styrene and unlike other thermoplastics it can resist certain alcohols (e.g. ethylene, butyl), organic acids and hydrogen oxides. PS is poorly permeable to gasses and vapours and has a low melting point, making it unsuitable for high temperature applications. As other polymers used in microfluidics, it comes in a solid wafer form but it can also be produced as foam.

Topas and Zeonor are of particular importance in microfluidics due to their excellent optical properties, residual permeability to water vapours and very low capacity for the absorption of water. They are nonpolar, thermoplastic polymers of a non-crystalline structure. In addition, they are resistant to polar organic solvents and can be used for applications involving acetone or isopropanol, frequently used in life sciences. Unlike other thermoplastics, Topas and Zeonor are not suitable for oil and lipid industry.

Polycarbonate (PC), unlike Zeonor or Topas, displays enhanced hydrophilic properties and as such shows much better filling behaviour of the channels which is a key requirement when working with flow-through devices. Compared to PMMA, it exhibits a higher Glass Transition Temperature and can be used for applications requiring high temperatures e.g. PCR. The main challenge related to PC is its high autofluorescence, which prevents it from being used for optical detection systems. Similar to other polymers, polycarbonate cannot be used in the presence of strong acids or bases, aromatics, ketones or halogenated hydrocarbons.

Apart from common thermoplastics, many microfluidic devices use polymers doped with a number of certain additives. These materials, known as plastics, can incorporate a wide range of components including fillers (e.g. calcium carbonate), plasticizers (e.g. dioctyl phthalate), stabilizers (heat or UV; salicylates) or antioxidants (e.g. amines) that influence their shelf-life and fabrication process. Ceramics (e.g. alumina, Al_2O_3) also have been used extensively as substrates in microelectronics packaging [13].

Table 5.1 illustrates the physicochemical properties of the main group of materials used for the fabrication of microfluidic devices [11].

Tab. 5.1. Main materials used for the fabrication of microfluidic systems and their properties [11].

Materials	Properties relevant to microfluidic systems for biological applications					
	Fabrication technique	Visible light transmittance	Autoclavable	Water diffusion coefficient x 10^{9} /m^{2} s^{-1}	Gas permeability x 10^{9} /cm^{3} (cm^{2} s cm Hg)$^{-1}$	Young's Modulus/GPa
PDMS	Soft lithography	Clear	Yes	3-6	N_2 : 280 CO_2 : 340 O_2 : 600	3.6 x 10^{-4} – 8.7 x 10^{-4}
Silicon	Micro-electronics fabrication	Opaque	Yes	N/A	N/A	165
Glass	Micro-electronics fabrication	Clear	Yes	N/A	N/A	63-73
PMMA	Hot-embossing, injection-molding, laser photoablation	Clear	Yes	0.002	N_2 : 0.039 CO_2 : 0.78 O_2 : 0.23	3.3
Zeonor	Hot-embossing, injection - molding	Clear	Yes	N/A	N/A	2.1

With the diversity of available structural materials, the choice of the substrate appropriate for a particular application is based on the individual characteristics of the component and its suitability for a selected fabrication process. The physicochemical properties of the end product (e.g. degree of optical transparency, robustness), the cost and the accessibility of micromachining and molding technologies are typical determinants of the material selection.

5.2.2. State-of-the-art of the fabrication processes.

By the end of 1990s, the majority of microfluidic devices were still manufactured in glass. Very few fabrication protocols report the use of alternative materials such as plastics, metals or ceramics [2]. Any records of prototypes micromachined in polymer substrates were published as patents and they were not available to the public. Relatively high material and processing costs alongside a poor yield rate made silicon unappealing as a material for the fabrication of disposable microfluidic devices. Since mid-1990s, microfabrication technology has been moving towards polymer substrates whose manufacturing is less time consuming and of low cost. The group of VerLee from Abbott Laboratories was one of the first to report a microfluidic system entirely made of plastic components [14, 15]. The device consisted of a complete channel network micromachined with a milling tool controlled by a personalized computer. Despite this great achievement, the smallest feature was still in the order of a size of a traditional capillary tube. An expanding market for polymer based substrates started at the end of the XX th century, when high-profile companies began investing in the development of innovative microfluidic technologies. Growing expertise and continuous development in the area of microfabrication in the late 1990s gave rise to a number of highly progressive micromachining technologies that could produce features of dimensions smaller within the range of 15-30 μm.

Nowadays, fabrication of microfluidic devices is still based on technologies developed for the Integrated Circuit (IC) industry and, as such, enables processing of numerous identical devices at a low expenditure and a large scale. Basic technologies established for the Integrated Circuit include the deposition of thin films (by evaporation or sputtering), the 3D structuring of the devices (by wet and dry etching techniques) and back-end processing (dicing, wiring and packaging). Fabrication of microfluidic devices

arose from these techniques to finally develop as an independent research field. As discussed before, depending on the applications, different materials can be considered for the fabrication of the microfluidic devices (e.g. silicon, glass, plastic).

Patterning of microchannels in polymer substrates was simultaneously reported for the first time at the end of 1990s [16, 17]. The very first fabrication approaches employed the use of wires as stamps to transfer desired features onto plastic materials [15]. Nowadays, hot-embossing and imprinting methods utilize high-precision stamps micromachined in silicon or metal. Both materials can withstand elevated temperatures and rapid changes of fabrication conditions and, as such, can be repeatedly used for a large number of fabrication cycles. Unlike hot-embossing and imprinting, injection molding can create much more complex three-dimensional structures, which become embedded in the substrate directly at the molding step.

Fabrication of microfluidic channels using injection molding was first described by a research group based in ACLARA [18]. Since then the method had been widely employed for reproducible prototyping of micro-scale features in a variety of plastic substrates [19]. The most significant impact on the development of microfluidic platforms has been associated with the introduction of soft lithography techniques, as described in ref. [20]. In this method the stamp is not exposed to the elevated pressure and heat conditions and therefore can be made of softer materials, such as photoresists. A natural improvement of the process led to an application of soft lithography in the fabrication of three-dimensional microfluidic devices [21] and has been the most frequent method used for elastomer patterning ever since. In 1997, a group directed by Roberts introduced a microfabrication method, known as laser photoablation [22]. In this process, a pulsed UV light source is used to disturb the structure of the polymer substrate and to pattern the feature of microchannel. A number of other fabrication techniques has emerged throughout the years, such as low energy e-beam etching (IBE) [23] or UV-patterning of photoresist (e.g. SU-8). Tab. 5.2 summarizes and compares the main fabrication technologies in terms of their processing characteristics and associated costs.

Tab. 5.2. Comparison of the main microfabrication techniques [2].

Technology	Geometry choice	Min. feature size	Height	Aspect ratio	Lifetime	Cost	Availability
Wet silicon etch	-	+	**0**	-	+	+	++
Dry silicon etch	+	++	+	+	-	**0**	++
Optical lithography	+	++	+	**0**	+	**0**	**0**
Laser ablation	++	+	+	+	+	-	-
Mechanical micromachining	+	**0**	+	**0**	++	-	-

The vast majority of microfluidic fuel cells reported up to date have been made on glass slides, with patterned platinum or gold electrodes and an overlaying microfluidic PDMS channel network. Traditional fuel cells are complex and costly systems, requiring a number of components elevating their processing intricacy and related costs [24]. To be fully operative they need both an anode and a cathode together with their corresponding compartments; as well as a case, a membrane and a conducting electrolyte. Some of these necessary elements can undergo miniaturization steps only to some extent or not at all. This fabrication process although suitable for laboratory based research is not appropriate for a large scale production, where high degree of automation and low manufacturing costs are key requirements. In this light, cheap and easy to fabricate plastic chips seem to be an appealing alternative to the classical approach using glass or silicon substrates. Additionally, replacing expensive patterning of noble metal electrodes by more economically-friendly conducting carbon materials would significantly lower manufacturing expenses and the complexity of the microfluidic systems. Substituting the platinum cathode with an oxygen reducing enzyme-based biocathode, together with a bioanode for the oxidation of glucose, would effectively eliminate the use of precious metal catalysts in the microfluidic environment. The implementation of selective biological catalysts, such as, enzymes or microbial cells leads to an overall simplification

of the fuel cell structure. Due to the discriminating nature of biomolecules towards particular substrates, anodic and cathodic compartments no longer have to be separated by an internal partition. These innovative designs of plastic microfluidic chips would help to overcome problems related with the diffusion layer thickness at the interface between anodic and cathodic compartments of the cell as well as the issues associated with the depletion of the fuel in the microfluidic channel. Furthermore, miniaturization of the biofuel cells and their fabrication using plastic materials would enable stacking of several chips together, in order to reduce the total volume occupied by the system. Application of biological entities supported by the laminar flow of fuels in microfluidic environment enables the development of a membrane-free fuel cell, where all separating barriers become obsolete [25].

Laminar flow has already been implemented in fuel cell research. In some applications though, a third solution had to be introduced isolating the anodic and cathodic streams feeding the electrodes [26]. The role of the additional flow was to act as a membrane dividing the remaining two streams and preventing the diffusion of species between the compartments. Theoretical studies on the influence of the microchannel and electrodes geometries on the overall microfluidic performance of the cell had also been investigated. It has been shown that the thickness of the depletion layer might be an issue for the fuel utilization [27] and by splitting the electrodes into a series of smaller counterparts, we can prevent the growth of the diffusion layer and improve greatly the efficiency of the biofuel cell. The majority of ongoing research on enzymatic biofuel cells reported up to date, are composed of a simple platinum cathode for the oxygen reduction and a biofunctionalized anode for the fuel oxidation [28]. Modelling studies; however, have proven that the performance of a microfluidic device depends significantly on the reaction rate [29] and thus patterning of both electrodes with enzyme catalysts would lead to an improved fuel consumption.

Current advances in the area of enzymatic biofuel cells incorporate the use of non-typical material alternatives, such as, photocurable “Liquid Teflon” [3] and fabrics. A very simple concept on how to fabricate a low-cost and easy to operate microfluidic biofuel cell has been developed by a research group in Monash University, Australia [30]. The authors used a dewaxed, plasma treated cotton thread together with a polymer film to create three-dimensional microfluidic devices for diagnostic applications. Tsujimura et al. [31] reported recently a high performance paper-based biofuel cell with porous carbon

electrodes. The cell was composed of layers of a Japanese paper printed with porous carbon ink as a matrix for enzyme encapsulation. Fig. 5.1 illustrates schematically the mainstream designs that have been used for biofuel cell applications in the past few years [29].

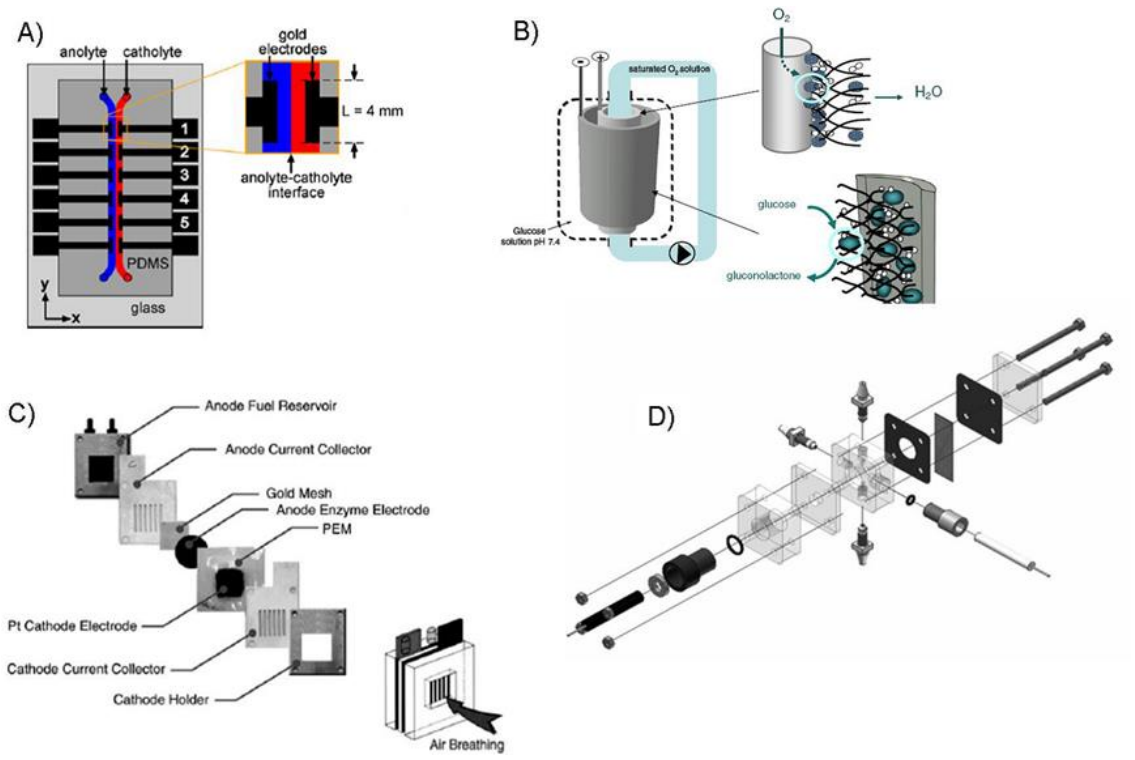


Fig. 5.1. Schematic representation of the types of biofuel cell devices available up to date [29] (A) microfluidic and (B) concentric cells; (C) miniature platforms with an enzymatic anode and an air-breathing Pt cathode; (D) standardized modular stack cell designs.

5.3. Application of microfluidics in device fabrication.

The following section of Chapter V introduces the principles of microfluidics and discusses its application in the fabrication of miniature devices for electrochemical studies, with a particular emphasis on enzymatic biofuel cells. Section 5.3.1 explicitly discusses the design and material composition for the fabrication of microfluidic platforms, developed in due course of this Ph.D. work.

Fundamentals and advantages of microfluidics

Microfluidics is a multidisciplinary field intersecting engineering, physics, chemistry, microtechnology and biotechnology, with a practical application in the design of microscale systems, in which a controlled transport of measurable fuel quantities can be implemented. It emerged in the early 1980s, as a result of shared efforts towards the development of miniature implantable devices for biomedical applications, such as, microflow sensors, micropumps and microwalves. Since its advent, the area of microfluidics gained remarkable consideration within the first decade and has been continuously attracting research attention ever since. Fig. 5.2 represents rapid increase in the number of ISI articles published per year in the area of microfluidic studies between the years 1990 and 2010, following the early appearance of a functional micro-scale device.

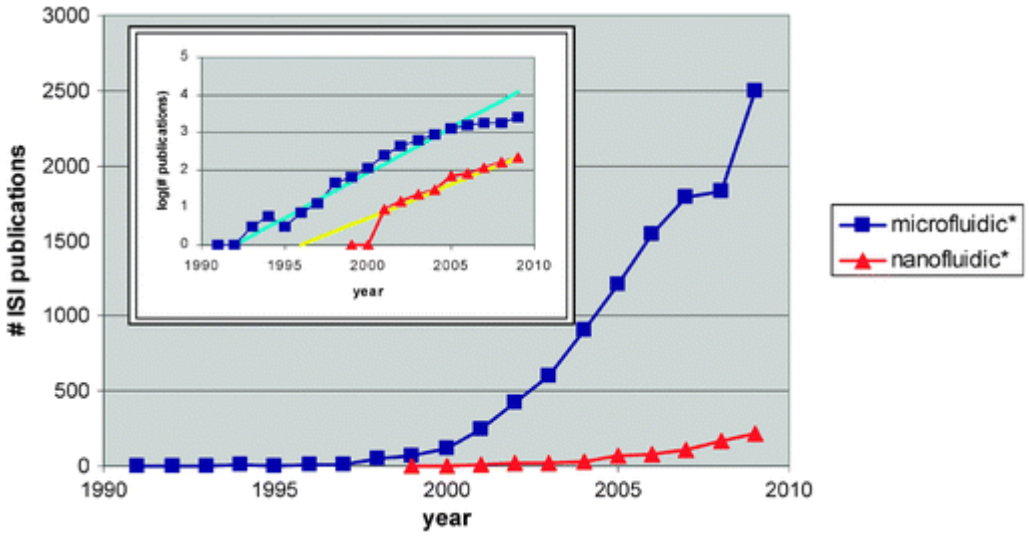


Fig. 5.2. Increased number of micro- and nanofluidic-related ISI journal publications between 1990 and 2010 [32].

Initially, microfluidics was considered a part of the MEMS technology employing infrastructure and technologies established in microelectronics [25]. Although the fabrication of microflow sensors, microvalves and pumps dominated the early stage in the

field throughout the 80s, a revolutionary work by Manz and co-workers demonstrated in 1989, suggested that the prime research applications of microfluidics lie in life sciences and chemistry [33]. Its introduction into the biochemical field led to the development of novel research disciplines dealing with mass transport phenomena in fluidic systems on microscale lengths, known as 'Bio-MEMS', 'MEMS-fluidics' and 'biomicrofluidics' [34].

The main advantage of microfluidics relies on the ability to utilize scaling laws for unique, microscopic effects and improved performance of corresponding devices. This is due to the miniscule volumes of fluid the device can handle, leading to reduced pathways of numerous biochemical and chemical reactions [35].

Unlike the conventional macroscopic flow based on continuum hypotheses, in micro-scale devices the fluid mechanics is governed by a transitional behaviour of both the continuum and molecular-dominated regime. Exploration of the distinctive fluid dynamics associated with miniaturized systems, such as electrokinetic pumping, surface tension-driven flows or electromagnetic forces, while they have no real bearing on the behaviour of the macroscopic flow, offers significant advantages over mechanical principles, once applied to a micro-scale systems. As the term *micro-* refers to the microscopic quantity of the fluid, rather than the fluidic system itself, while miniaturization of the system is essential in various applications, it is not a prerequisite in microfluidics. Therefore, regardless of the size of the surrounding environment and the material from which the device was fabricated, only the space where the fluid is physically confined requires miniaturization. This allows the changes in fluid behaviour to be attributed exclusively to the small size scale of the fuel, in principle, not associated with any particular length measure. Fig. 5.3 compares the size of a typical microfluidic device with the dimensions of common biological particles.

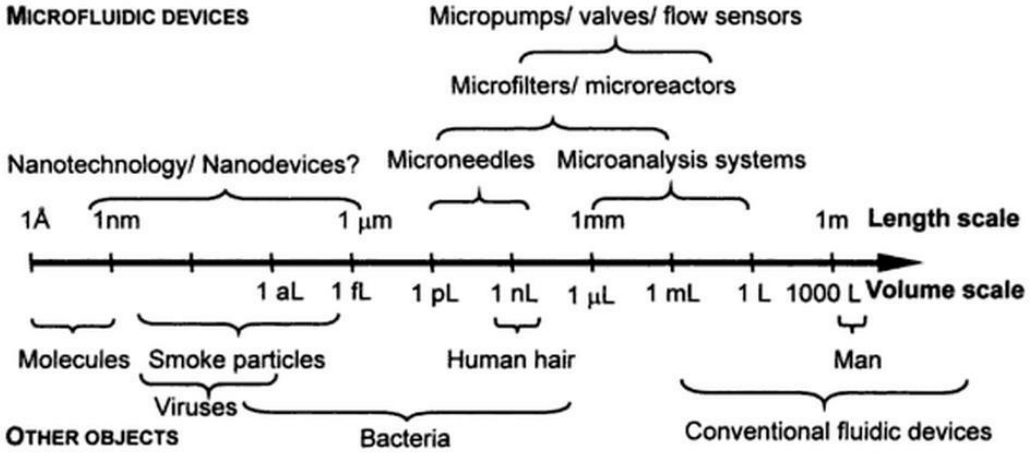


Fig. 5.3. Size characteristics of a typical microfluidic device as compared to commonly known abiotic particles and living structures [36].

In traditional fluid mechanics, the flow pattern is determined by dimensionless Reynolds (Re) numbers, with low values corresponding to a laminar regime and high Re for turbulent behaviour. Laminar flow, where the viscous forces are dominant and the fluid motion is considered smooth and constant, is the characteristic feature of any microfluidic design and enables high surface area to volume ratios and an accurate control of the force fields applied [37].

In the classical laminar regime, the fuel and oxidant flow in parallel to each other, side-by-side, without mixing (Fig. 5.4). Under these conditions, both electrodes remain in contact with their respective solutions during the energy conversion [38].

The only means of molecular transfer between the adjacent streams is diffusion, which is dependent on the natural dispersion of individual species and the parameters associated with the flow: the dimensions of the channel under investigation and the applied flow rate (Fig. 5.5). The depletion zones, generated at the vicinity of the electrodes as a result of fuel/oxidant consumption, can be predicted from the modelling studies and their magnitude controlled by the choice of the channel design and a flow rate couple.

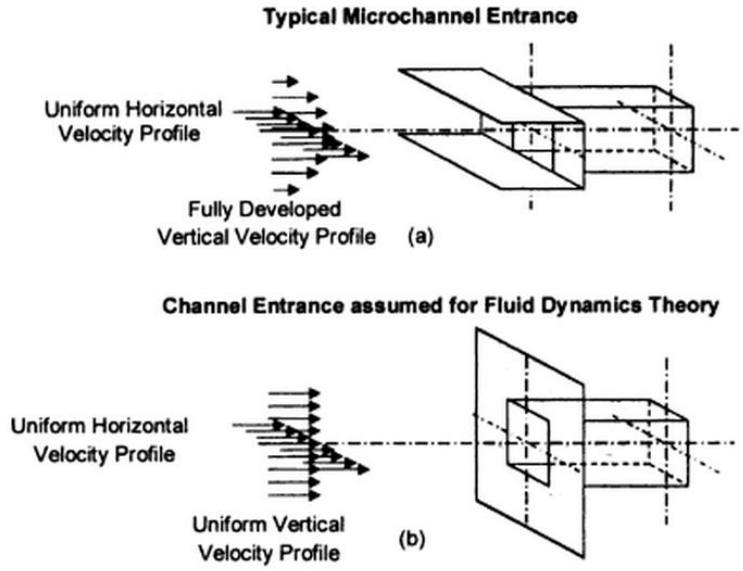


Fig. 5.4. Comparison of the fluid entrance in a typical macroscopic channel geometry (b) and a microscopic entry due to the planar microfabrication (a) [36].

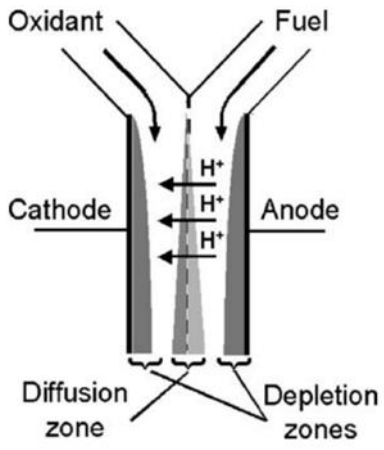


Fig. 5.5. Schematic of a laminar flow of fuel and oxidant in a microfluidic channel of a membraneless biofuel cell. The regions of the fuel/oxidant diffusional cross-over and the depletion zones are indicated [39].

Since the performance of an electrochemical microfluidic device is reliant on the interplay between the mass transport of species and the kinetics of the catalytic reactions, the essential requirement in the biofuel cell development is a comprehensive understanding of the underlying fluid behaviour and reaction characteristics. In carefully designed and optimized microfluidic systems, the depleted regions trigger mass transfer of the fuel and oxidant from the bulk layers, replenishing the locally exhausted species with fresh substrates at a relevant rate [38].

Several experimental studies on microfluidic systems for biofuel cell applications indicated that repeated withdrawing and infusion of the fuel and oxidant to the electrode surface can significantly reduce the depletion layer. This approach however requires relatively high pumping power for the fuel delivery [38]. Alternative strategies which rely on passive control of mixing by alternating the shape of the microchannel also require high external power inputs [40, 41].

The fabrication of miniature enzymatic biofuel cells can greatly benefit from the advantages of microfluidics. Since the Reynolds number for most microfluidic channels is typically less than 1, no convective mixing of fluids occurs and as such the conventional compartmentalization prerequisite becomes obsolete (Fig. 5.6). As discussed previously, the only force of mass transfer in a direction transverse to the flow is diffusion. Therefore, the fuel can be provided to the enzymes immobilized on the electrodes in a laminar manner, where all of the fluid particles move in paths parallel to the overall flow direction, suggesting that the two solutions will be flowing without mixing. The high surface area to volume ratio ensures that the fuel intake by the enzyme is maximised. Likewise, a possibility to model mass transport and reactions occurring in the fluids due to well-defined laminar flow phenomena exists [42].

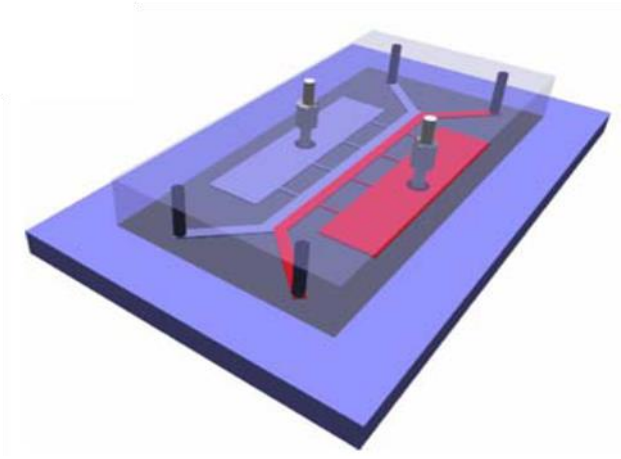


Fig. 5.6. Membraneless microfluidic device fabricated at the Central Fabrication Facility of the Tyndall National Institute. Generic schematic of two aqueous streams flowing in the micro-scale channel.

The implementation of microfluidics has a significant impact on electrochemical analysis and catalytic studies [43], similar to one that integrated circuits had on computers and electronics. Microscopic flow effects, unique to microfluidic systems, alongside with bio- and chemical reactions occurring on a miniature scale as well as innovative fluid measurement techniques for micro-flows utilizing in situ miniaturized instruments, has led to an expansion of emerging applications in chemistry and bioengineering. A mass market

of cost-effective and disposable microfluidic substitutes for non-reusable expensive systems can revolutionize instrumental business and is the driving force behind the extensive research in the area. Reduced quantities of required fluids facilitate rapid analysis of biological and chemical materials investigated in a number of assays, enabling parallel testing and enhancing the screening throughput [44-47].

5.3.1. Microfluidic devices for enzymatic biofuel cells.

Microfluidic devices, envisaged in this Ph.D. work, are comprised of two polymer units: bottom component carrying patterned Au and Pt electrodes and a top part bearing a microfluidic channel with two separate inlet points for the individual supply of the fuel and oxidant. The top and bottom structural elements are later assembled in a water tight seal, in order to contain the supplied fluids (Fig. 5.7). The solutions are provided through Teflon tubings inserted in the openings of the channel inlets and once passed through the channel, they are collected at the outlet. The proposed design is intended to act as a platform for the development and characterization of the enzymatic biofuel cells in a microfluidic format. In the projected device, the micropatterned gold and platinum electrodes are employed as anodes and cathodes for the oxidation and reduction of the given fuel and oxidant, accordingly. The investigation of the catalytic reactions within the channel setting is conducted via electrochemical measurements and is suitable for the analysis in static and flowing conditions. The choice of optically transparent Zeonor and PDMS materials has been determined by the requirement of visual investigation of the fluid flow in the channel of the fabricated devices.

The following section contains a comprehensive description of the design and selected methods for the fabrication of the physical components of the cell. The electrochemical characterization of the fabricated electrodes and the investigation of diverse assembly techniques have also been discussed.

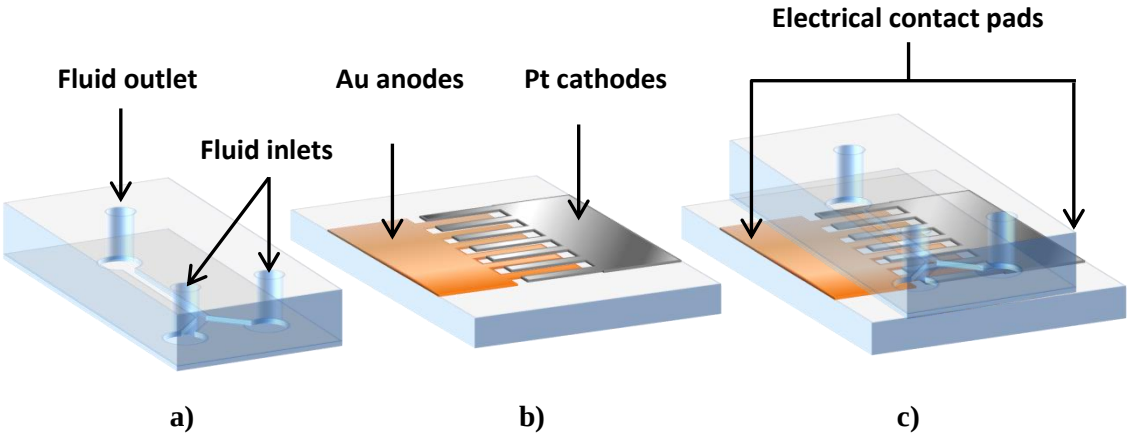


Fig. 5.7. Schematic of the microfluidic device proposed as part of this Ph.D. work; a) top component with a microfluidic channel; b) bottom unit with patterned electrodes (Au anodes and Pt cathodes); c) assembled device.

5.3.2. Material choice for electrode and channel substrates.

Indium tin oxide (ITO) was originally considered as the source material for the patterning of electrodes. ITO displays excellent optical transparency, high electrical conductivity, and a wide potential window. Therefore, it is a promising candidate for microfluidic applications, where the simultaneous electrochemical analysis and a visual detection of the laminar flow are typical requirements [48]. Despite its suitable properties, the deposition of ITO can be problematic as it is an ion-assisted evaporation process and leads to overheating of the reaction chamber. As a result, plastic is distorted inducing cracks in the ITO layer and leading to loss of conductivity. For that reason ITO was substituted with gold and platinum deposited on a Cyclo-Olefin-Polymer (COP), Zeonor, mainly due to its high transparency and low auto-fluorescence over a broad range of spectrum [49] . Due to low binding affinity between Zeonor substrates, channels were later fabricated in Polydimethylsiloxane (PDMS).

5.4. Design and fabrication of metal electrodes.

5.4.1. Layouts of the metal patterning.

Four electrode geometries have been considered in the design and fabrication of the anodes and cathodes of the biofuel cells (Fig. 5.8 and Fig. 5.9), in order to obtain the optimum utilization of the species in various fuel and oxidant solutions. Two main approaches have been undertaken: the design of micro- and macroelectrodes, with the potential application for the low and high concentrations of species, accordingly. While the number and the dimensions of Au and Pt features vary between individual designs, the length of the metal pattern (15 mm) and the distance between the anodes and cathodes, with the exception of design 1 bearing interdigitated electrodes, is fixed at 100 μm. Each design contains 4 mm wide continuous metal pads for the establishment of the electrical connection with the potentiostat during the electrochemical measurements. Tab. 5.3 summarizes the corresponding dimensions of the electrode features for designs 1 - 4.

Fig. 5.8 illustrates designs 1 and 2 of the microelectrode patterns, including an interdigitated layout (design 1). The micro-size anodes and cathodes have been envisaged to efficiently utilize diluted fuels, due to the high influx of species to the electrode.

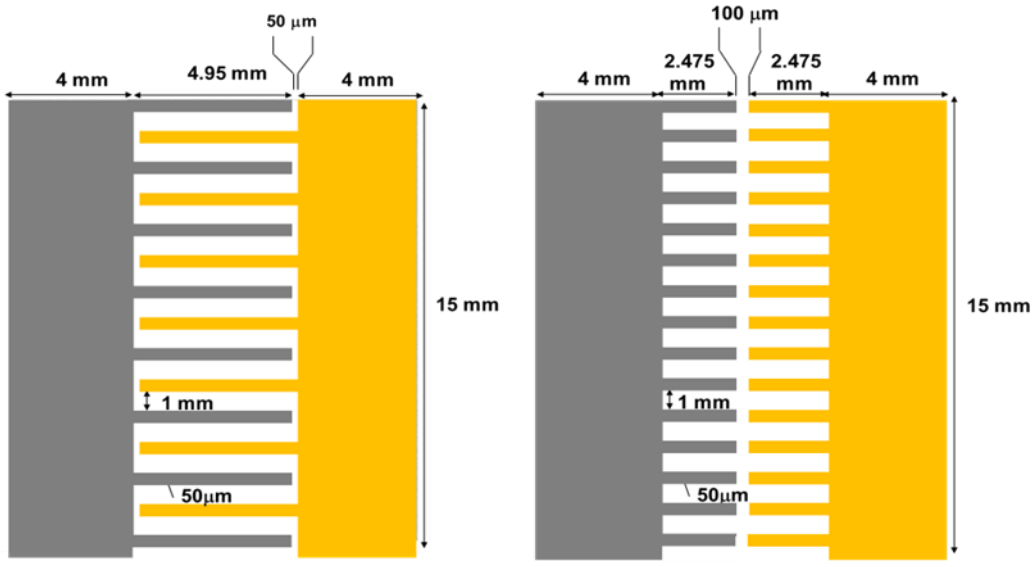


Fig. 5.8. Designs 1 (left) and 2 (right) of the microelectrode geometries. The length of the metal pattern is 15 mm; the width of the connection pads is 4 mm.

Fig. 5.9 represents the macroelectrode features of designs 3 and 4. The macro-size anodes and cathodes have been predicted to be more suitable for high concentration of species, due to the greater surface areas as compared to designs 1 and 2.

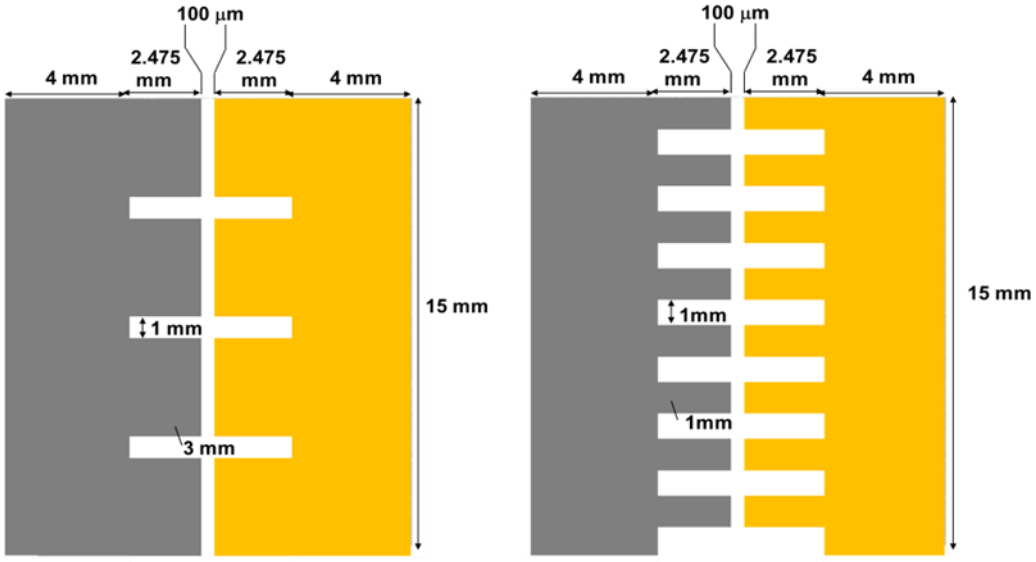


Fig. 5.9. Designs 3 (left) and 4 (right) of the macroelectrode layouts. The length of the metal pattern is 15 mm; the width of the connection pads is 4 mm.

Tab. 5.3. Dimensions of the electrode patterns for designs 1-4.

	Microelectrodes		***Macroelectrodes***	
Electrode Parameters	**Design 1**	**Design 2**	**Design 3**	**Design 4**
Number	7 Au & 8 Pt	15 Au & 15 Pt	4 Au & 4 Pt	8 Au & 8 Pt
Width	4.95 mm	2.475 mm	2.475 mm	2.475 mm
Thickness	50 µm	50 µm	3 mm	1mm
Inter-electrode distance	1 mm	1 mm	1 mm	1 mm
Anode and cathode separation	50 µm	100 µm	100 µm	100 µm
Pattern length	15 mm	15 mm	15 mm	15mm

5.4.2. Microfabrication of gold anodes and platinum cathodes.

Gold anodes and platinum cathodes have been microfabricated in the Central Fabrication Facility (CFF) of the Tyndall National Institute. The electrodes were prepared by a *UV-photolithographic lift-off* process, during which the metals were patterned onto a Zeonor substrate. A thin coating (20 nm) of titanium has been applied as an adhesive layer, in order to obtain high quality adherence of Au and Pt to the polymer. For gold anodes, a layer of Pt was additionally incorporated in between Ti and Au to act as a diffusion barrier for Au. The thickness of gold and platinum layers was 100 nm for all electrode designs. As discussed previously, two main layouts of the metal patterns have been considered in this study, micro-design 1 & 2 and macroelectrodes (designs 3 & 4), illustrated schematically in Fig. 5.10.

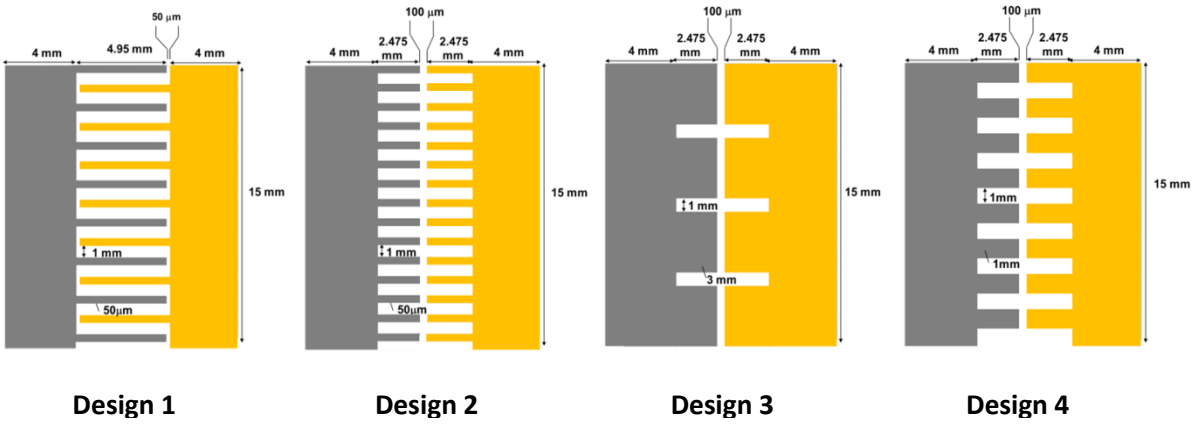


Fig. 5.10. Layouts of Au and Pt electrodes fabricated at the Tyndall National Institute including designs 1 & 2 of the microelectrodes (left) and designs 3 & 4 of the macro-patterns (right).

Gold and platinum were deposited in two separate lithographic steps using Chrome-on-Glass (COG) photomasks, outsourced by Compugraphics Intl. Ltd (Scotland). The processing of the masks for Au and Pt has been discussed in detail in Appendix B.

Processing of gold and platinum electrodes is schematically illustrated in Fig. 5.11.

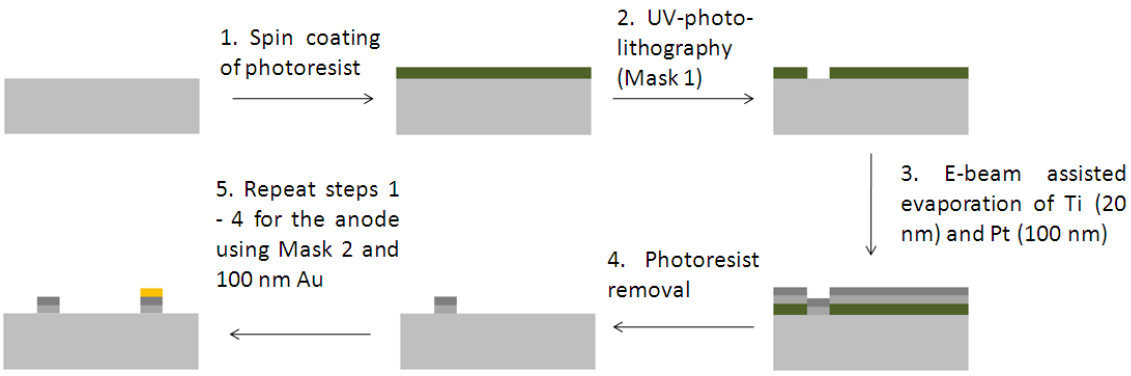


Fig. 5.11. Deposition of platinum and gold electrodes via the E-beam assisted evaporation with an adhesive layer of Ti.

The deposition involved coating the Zeonor substrate with a layer of a photosensitive emulsion (resist) promoting the transfer of a desired electrode pattern from a transparent mask onto the polymer. Masks for photolithography are typically clear glass plates with metal (usually chromium) features. Placing the mask over the surface of a photoresist and exposing the assembly to a UV light changes its properties and allows further dissolution (for negative resist) or etching (positive resist) in a developer solution (Fig. 5.12).

In the consecutive steps, a thin coating (20 nm) of titanium and a layer of Pt (100 nm) are deposited via E-beam assisted evaporation of the metals. The remaining, underlying photoresist is removed and the processing steps are repeated for gold anodes during the same fabrication run (Fig. 5.13). This is a technical requirement, as breaking down the vacuum to evacuate the chamber prior to the next fabrication cycle would significantly reduce the adherence of Au and Pt thin films.

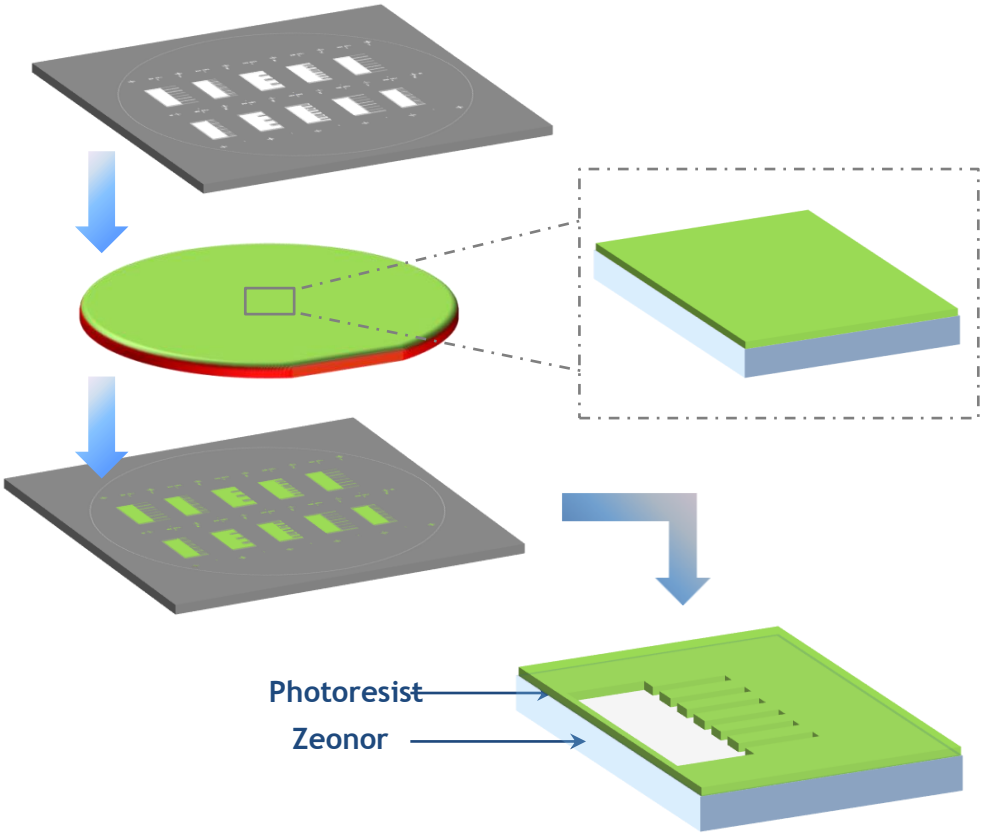


Fig. 5.12. Patterning of the photoresist with UV light.

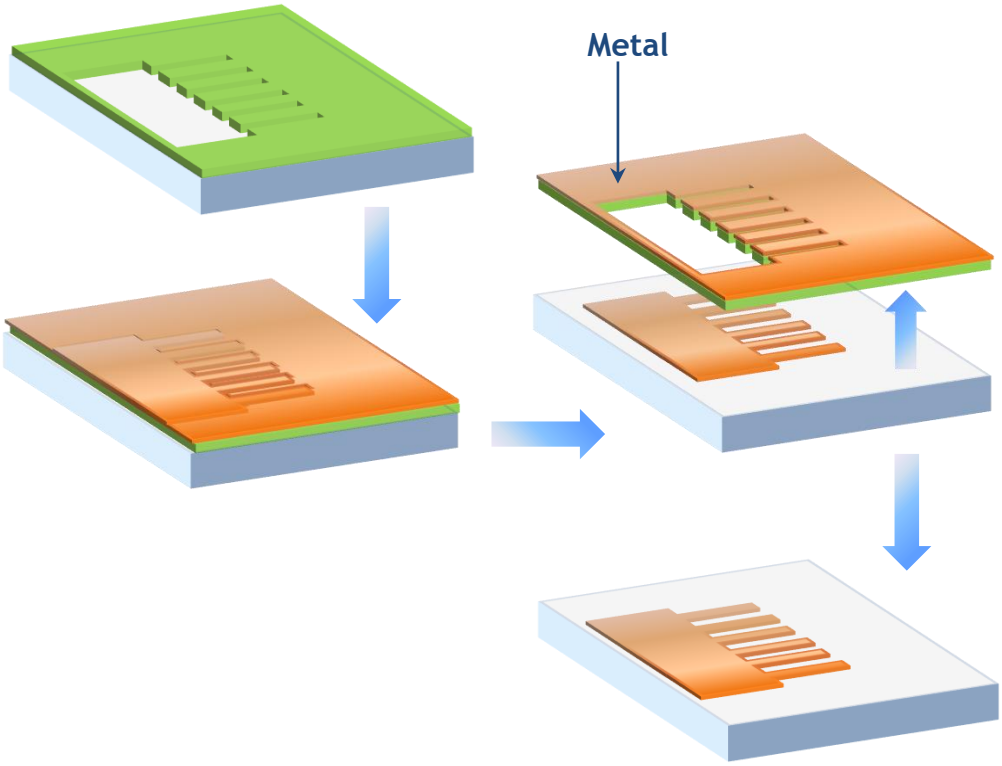


Fig. 5.13. E-beam assisted deposition of the metal followed by the removal of the resist.

For this particular application, Zeonor wafers were pre-treated in the oxygen plasma cleaner at 50 W for 3 min to promote good adhesion of the photoresist. Following plasma exposure, Zeonor was coated with PMGI SF11 Lift-off resist (MicroChem Corp., MA, USA) using a Laurell spin coater at 3000 rpm (Laurell Technologies Corp., USA) and hot-baked at 115 ºC for 6 min. A layer of Microposit S1813 imaging photoresist (Shipley, UK) was then spun coated at 4000 rpm and hotplate baked at 115 ºC for 2 min. Resist treated wafers were later exposed to UV light through the photomask in Karl Suss MA1006 mask aligner (SUSS Micro Tec, USA) for 7 s (exposure dose ~70 mJ cm^{-2}). Samples were developed in Microposit MF319 developer (Shipley, UK) for 2 min, rinsed with deionized water and blow-dried with nitrogen. To provide good metal adhesion wafers were oven baked at 90 ºC for 30 min. Samples were loaded into a FC200 e-beam evaporator (Temescal, USA) and the chamber was pumped to a pressure below 5 x 10^{-7} Torr. The deposition by evaporation was carried out in a 20:100 nm ratio of Ti to Pt and the excess metal was lifted off in a bath of Microposit R1165 resist stripper (Shipley, UK). The electrodes were rinsed in running deionized water and blow-dried in a stream of nitrogen. The same reaction steps applied in the deposition of the counterpart gold metal (Fig. 5.14)

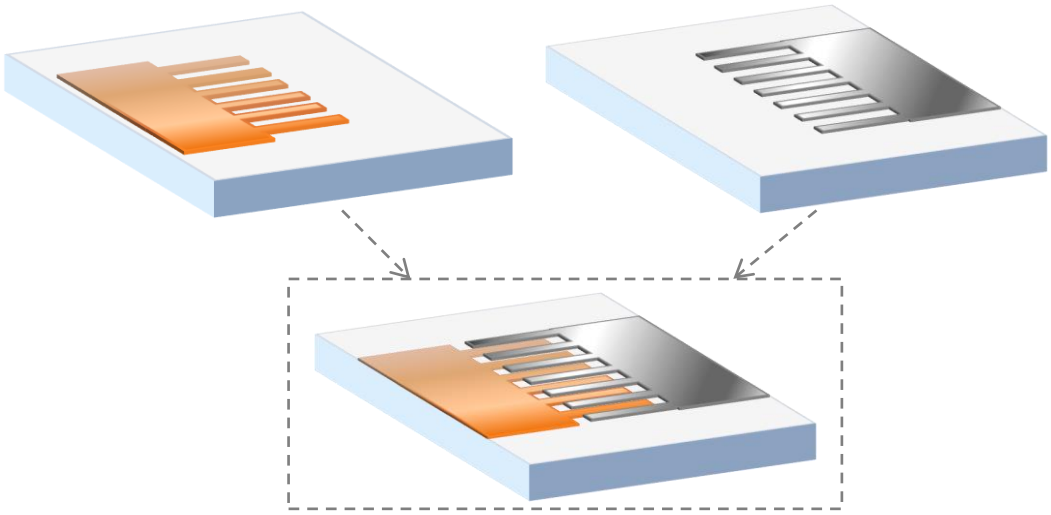


Fig. 5.14. Schematic representation of electrodes on Zeonor substrates, Au anodes indicated in orange and Pt cathodes in grey.

Following the metal deposition, Zeonor wafers were diced in the Packaging Lab of the Tyndall National Institute, using a Disco DAD3350 Automatic Dicing saw (Disco

Corporation, Japan). Once diced, the electrodes were visually investigated using a high resolution optical microscope to confirm the absence of any potential fabrication flaws (Fig. 5.15).

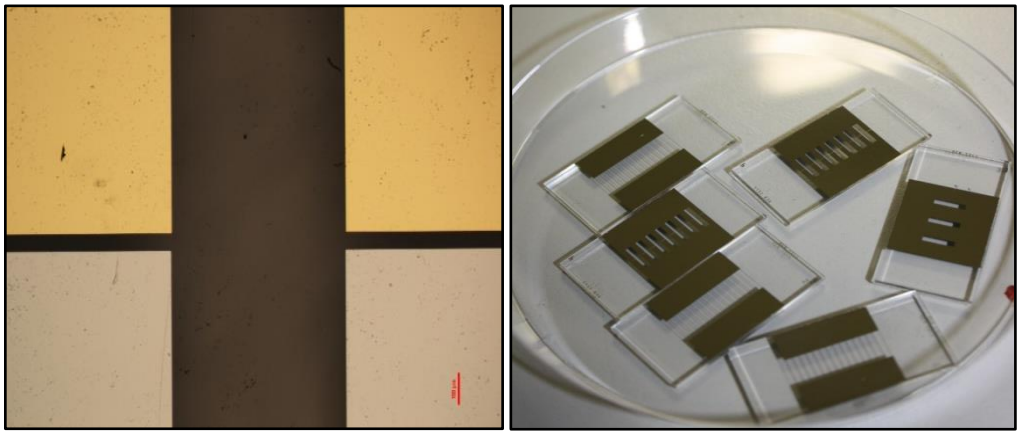


Fig. 5.15. Microscopic images of Au (yellow) and Pt (pale) electrodes for design 3 (left); different electrode layouts on Zeonor after dicing.

5.4.3. Challenges associated with the electrode fabrication.

The main issue related with the E-beam deposition of gold and platinum electrodes was the adhesion of the metals to the Zeonor substrate. The initial batch of the samples fabricated in the facilities of the Tyndall National Institute exhibited very low mechanical stability, was prone to scratching and detachment at the dicing step of the wafer processing, which is shown in Fig. 5.16. In addition, it has been observed that gold was much less adherent to Zeonor than platinum, suggesting that an additional adhesive layer might be required.

Further, visual inspection of the electrode under the microscope revealed the presence of undesired features (Fig. 5.17).

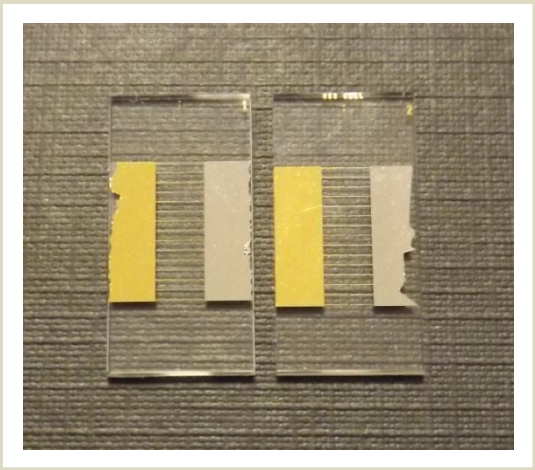


Fig. 5.16. Image of gold and platinum electrodes deposited on Zeonor substrates. Poor adhesion of both metals leads to material peeling off.

The potential reason for the initial fabrication issues was most likely the fact that Zeonor substrate has never before been used for the deposition of metals in any research carried out within the Tyndall National Institute. Glass or silicon would be the usual substrates for the patterning of Au and Pt and, as such, the optimization of working conditions was required. After the adjustment of the reaction conditions and application of a thick layer of the photoresist prior to dicing, the subsequent batch of the electrodes was much more robust and less susceptible to damage. Additionally, when depositing gold, a supplementary layer of platinum was plated underneath to act as a diffusion barrier and to prevent penetration of Au towards titanium. This adjustment significantly enhanced the adhesion between gold and the polymer substrate.

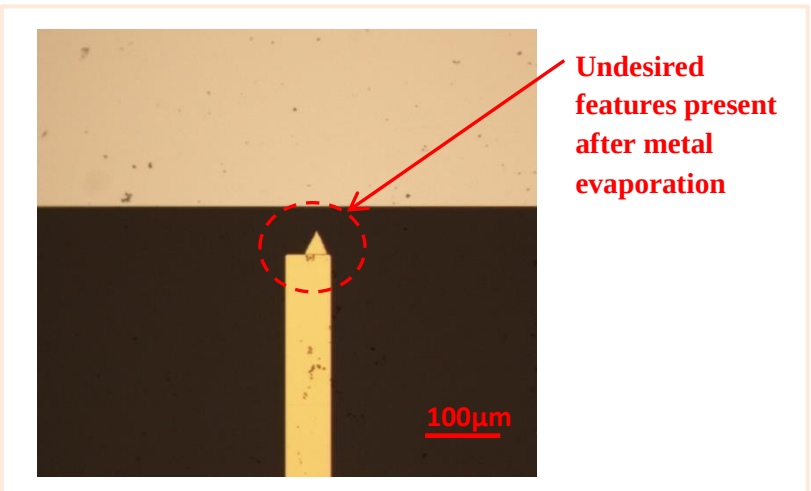


Fig. 5.17. Image of gold electrodes (design 1) obtained with a high resolution Nikon microscope. Metal evaporation resulted in unspecific electrode features.

5.5. Electrochemical characterization of electrodes patterned on Zeonor.

Electrochemical characterization of microfabricated gold anodes and platinum cathodes has been carried out in static conditions in the presence of redox reactive species.

Response of 5 mM potassium ferricyanide [$K_3Fe(CN)_6$] has been studied in 0.01 M PBS pH 7.4 solutions via cyclic voltammetry measurements. Prior to any experimental work, Zeonor chips were thoroughly cleaned in the oxygen plasma (3 cycles of 1 min at the pressure of 900 mT and high power settings), rinsed with IPA and deionized water and dried in the nitrogen stream. Following drying, the electrodes were chemically cleaned in 1 M H_2SO_4 for 3 h to remove any residual organic contaminants. Fresh solutions of the ferricyanide in PBS buffer were prepared directly before the measurements. The electrochemical set up was comprised of a two-electrode on-chip system connected to a CHI 660B potentiostat instrument via crocodile clips. In order to prevent metal damage, the electrical connection was initially established using copper tape sealed to the Pt and Au electrodes on the microfluidic chip. A number of inconveniencies have been however related to this solution, involving primarily the need to remove the conductive adhesive during the cleaning step causing gradual disintegration of the underlying metal layer. Moreover, in order to establish an intimate contact with the electrode multiple point connections had to be introduced by pressing the tape against the metal surface using the tip of a needle. Therefore the ultimate setup involved a direct connection of crocodile clips to the electrodes on the Zeonor chips.

The electrochemical response of electrodes microfabricated in Zeonor has been investigated under operational conditions of the biofuel cell. The cyclic voltammetry signal of both Au and Pt has been studied in static conditions in the presence of 5 mM $K_3Fe(CN)_6$ in 0.01 M Phosphate buffer saline (PBS). The response has been recorded for three electrode designs at variety of scan rates and the resulting current has been measured. CV profiles recorded at a single scan rate have been analyzed to confirm the differences in the current generated by various electrode layouts. In order to mimic the electrochemistry of ferricyanide on metals in the device configuration, the electrodes have been previously assembled with various designs of the microfluidic channels embossed in PDMS. The shape of the electrochemical signal has been evaluated and the dependency of

the current on the square root of the scan rate has been determined. The difference in the oxidation and reduction potential peaks has been determined at 0.01 V s^{-1} scan rate and the reversibility of the redox system has been discussed at the end of the chapter. Electrical connection has been established through crocodile clips directly clipped to metals deposited on the Zeonor polymer. The reaction potential has been controlled using a CHI 660B instrument. The influence of the electrode active area has been investigated with respect to the current output and the shape of the electrochemical signal of ferricyanide. The electrochemically active surface areas of the electrodes have been calculated from the Randles-Sevcik formula and compared with the theoretical equivalents derived based on the assembly, provided an ideal alignment of the channel and electrode components.

5.5.1. Results and discussion.

The electrochemical response of 5 mM $K_3Fe(CN)_6$ in 0.01 M PBS on gold has been evaluated for designs 2, 3 and 4 of the metal electrodes as an assembly with selected PDMS channel layouts. The theoretical areas of the active metals are presented in Tab. 5.4. The CV signals have been recorded at a single scan rate, 50 mV s^{-1}, (Fig. 5.18) in order to evaluate the differences in the current scale obtained for various electrode geometries.

Cyclic voltammetry measurements of 5 mM $K_3Fe(CN)_6$ studied on Au electrodes microfabricated on Zeonor substrate, indicate a significant difference in the electrochemical signal for various electrode designs. As can be seen from Fig. 5.18, the current generated as a result of the ferricyanide reactions increases substantially with the theoretical surface area of gold exposed to the redox solution. A sigmoidal steady-state shape of response for Au layout 2, typical for a microelectrode design, is compared with a peak characteristics obtained for macro-design 3, which is indicative of a diffusion-controlled process. A slight peak shaped response is observed for design 4, suggesting a linear diffusion consistent with the macro-dimensions of the electrode. The origin of the additional oxidation peak at 0.35 V is the electrode contamination with organic impurities, which were retained at the metal surface following the oxygen plasma and chemical cleaning steps. Since the electrodes were re-assembled with a number of channel designs

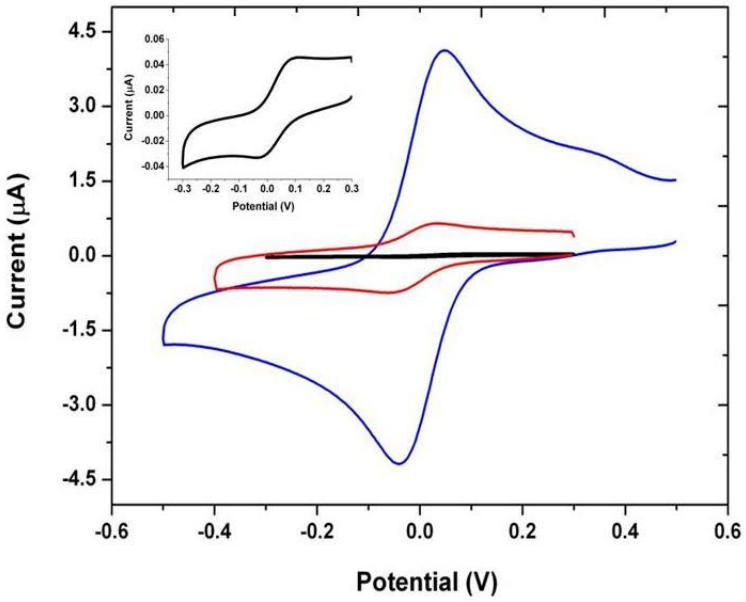


Fig. 5.18. Cyclic voltammetry of 5 mM $K_3Fe(CN)_6$ in 0.01 M PBS recorded on Au.: design 2 (black curve), design 3 (blue curve) and design 4 (red curve). Scan rate of 50 mV s^{-1}. Included in the inset is a magnification of the response for design 2. Potential recorded vs. Ag/AgCl (3 M KCl).

Tab. 5.4. Summary of the investigated electrode and channel assemblies, including the resulting theoretical areas of the electrodes.

	Design 2	***Design 3***	***Design 4***
Electrode metal	Au	Au	Au
Channel layout	3	4	5
Electrode area	0.19 mm^2	4.2 mm^2	3.6 mm^2

Tab. 5.5. Summary of the investigated electrode and channel assemblies, including the resulting theoretical areas of the electrodes.

	Design 2	***Design 3***	***Design 4***
Electrode metal	Au	Pt	Au
Channel layout	3	4	5
Electrode area	0.19 mm^2	4.2 mm^2	3.6 mm^2

and re-tested for characterization purposes, these are most likely PDMS residues remained at the electrode after device detachment.

Fig. 5.19 represents cyclic voltammetry responses of 5 mM $K_3Fe(CN)_6$ in 0.01 M PBS, measured at variety of scan rates using the channel and electrode assemblies as reported in Tab. 5.4. The schematics of the investigated electrode geometries and the resulting theoretical surface areas of the electrodes exposed to the redox solution (Tab. 5.5) are also presented.

Cyclic voltammetry of platinum design 3, Fig. 5.19 B), and gold design 4, Fig. 5.19 C), macroelectrodes studied in 0.01 M PBS pH 7.0 in the presence of 5 mM $K_3Fe(CN)_6$ confirmed a diffusion dependent response of ferricyanide. Increased current values were recorded for higher scan rates with a characteristic diffusive shape of the electrochemical signal demonstrating a linear influx of $Fe(CN)_6^{3-}$ to the electrode surface. This suggests that current limitations occur due to the concentration gradient indicating that the redox reaction is governed by species diffusion rather than limited kinetics of the electron transfer. The highest current output has been obtained for Pt design 3, which is consistent with the largest surface area of the metal. Planar diffusion, characteristic for macroelectrodes, provides low mass transport of species and, as such, is suitable for high concentrations of fuel.

CV response of gold design 2, Fig. 5.19 A), represented a sigmoidal shape of the electrochemical signal indicating a radial diffusion of species. The sigmoidal shape of the voltammogram obtained for microelectrodes design 2 is consistent with the expected hemispherical influx of ferricyanide to the electrode of microscopic dimension, where the rate of diffusion is equivalent to the rate at which the electron transfer occurs. Microelectrodes of design 2 can provide high mass transport of species and as such are suitable for low concentrations of fuel, however this design leads to relatively low current output as compared with the macroelectrode layouts 3 and 4.

The reversibility of the redox system has been studied at 0.01 V s^{-1} scan rate and determined based on the potential difference (ΔE) between the oxidation and reduction peaks. The respective ΔE for designs 3, ΔE = 94 ± 3.7 mV (oxidation and reduction peak voltage of 0.03 V and -0.07 V) and 4, ΔE = 87 ± 2.6 mV, (oxidation and reduction peak voltage of 0.04 V and -0.05 V) have been found in a better

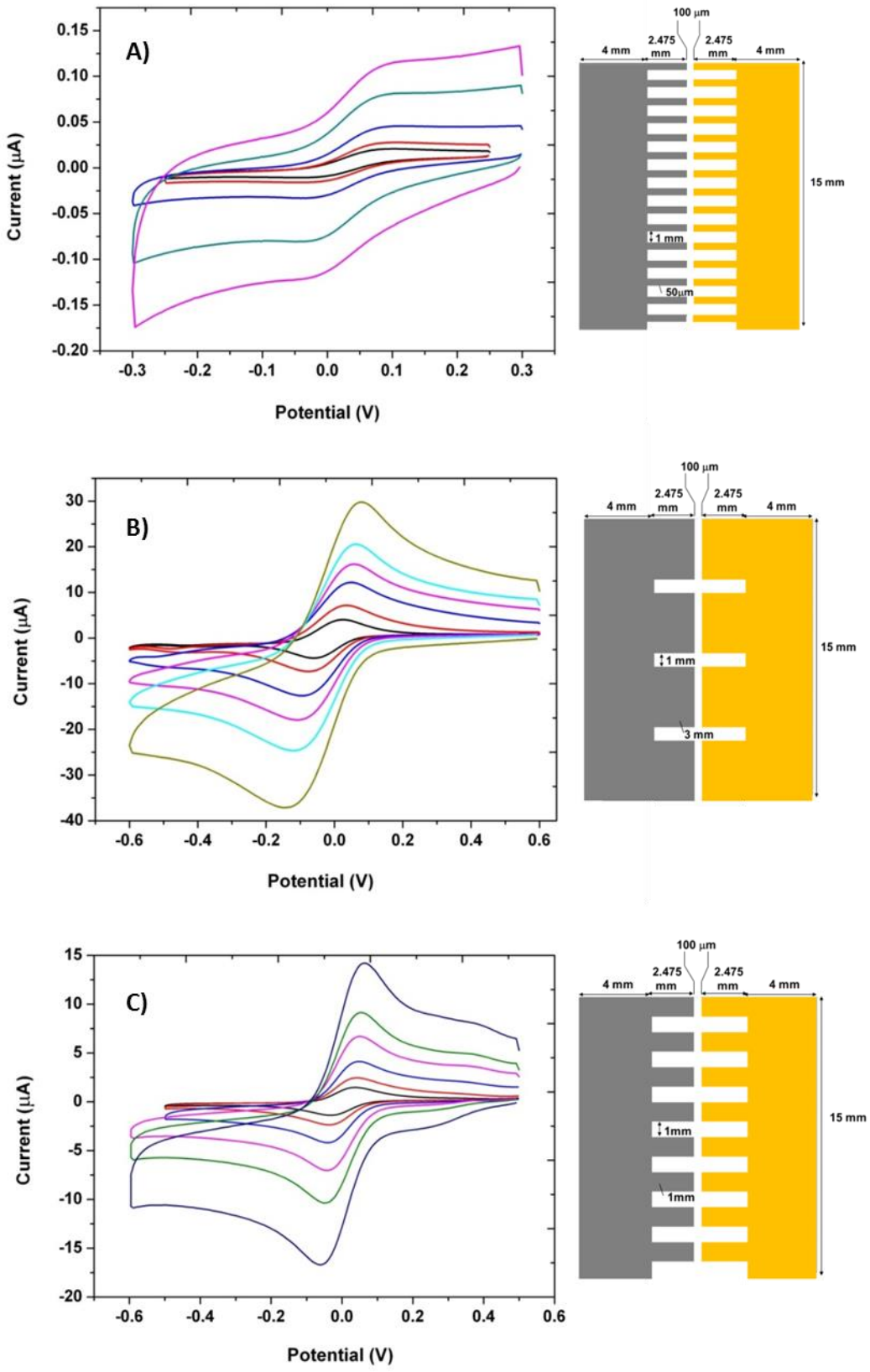


Fig. 5.19. Cyclic Voltammetry of 5 mM $K_3Fe(CN)_6$ in 0.01M PBS on metal electrodes assembled with PDMS channels. A) Au design 2 of the electrode and design 5 of the microfluidic channel. Scan rates of 10 mV s^{-1} (black line), 20 mV s^{-1} (red line), 50 mV s^{-1} (blue line), 100 mV s^{-} (green line), 200 mV s^{-1} (magenta line; B) Pt design 3 of the electrode and design 4 of the channel. Scan rates of 10 mV s^{-1} (black line), 20 mV s^{-1} (red

line), 50 mV s^{-1} (blue line), 100 mV s^{-1}(magenta line), 200 mV s^{-1} (cyan line) and 500 mV s^{-1} (green line); C) Au design 4 of the electrode layout and microfluidic channel design 5. Scan rates of 10 mV s^{-1}(black line), 20 mV s^{-1}(red line), 50 mV s^{-1} (blue line), 100 mV s^{-1}(magenta line), 200 mV s^{-1}(green line) and 500 mV s^{-1} (navy line). Potential recorded vs. Ag/AgCl.

accordance to the theoretical single electron transfer requirement (ΔE = 59 mV) than in the case of microelectrodes design 2, ΔE = 99 mV (oxidation and reduction peak voltage of 0.09 V and -0.01 V). This has been attributed to an unaccounted resistance of the redox solution, where the IR drop should be less significant at lower current values.

The dependency of the limiting current, taken as the oxidation peak (i_p) of $K_3Fe(CN)_6$, on the square root of the scan rate used ($v^{1/2}$) has been investigated for all three designs and is depicted in Fig. 5.20.

As shown in Fig. 5.20, a linear dependency of the limiting current i_p on the applied $v^{1/2}$ has been obtained for all electrode layouts. This is consistent with the diffusion-controlled redox processes occurring at the macroelectrodes, design 3 and 4. A nearly constant value of current for Au electrode design 2, represented by a very small slope of the I vs. $v^{1/2}$ line is consistent with a typical response for a microband design. Here, the current should be independent of the square root of the scan rate used, suggesting that the reaction at the microelectrode is not limited by the mass transport of species. Small variation in the current recorded in Fig. 5.20 a) are however indicative of a residual dependency of the response on the mass transport of species. As discussed previously, this may be due to the overlap of the diffusion layers between the adjacent electrodes, separated only by a distance of 1 mm. In addition, a quasi-steady state is also reached with microband electrode design, which could also explain the observed dependency of the current on the applied scan rate.

The experimental active surface areas of the electrodes have been calculated for all three designs from the equation of the i_p vs. $v^{1/2}$ slope, according to Eq. 5.1, based on the reported value of the diffusion coefficient for ferricyanide $7.6\ x\ 10^{-6}\ cm^2\ s^{-1}$ [50, 51].

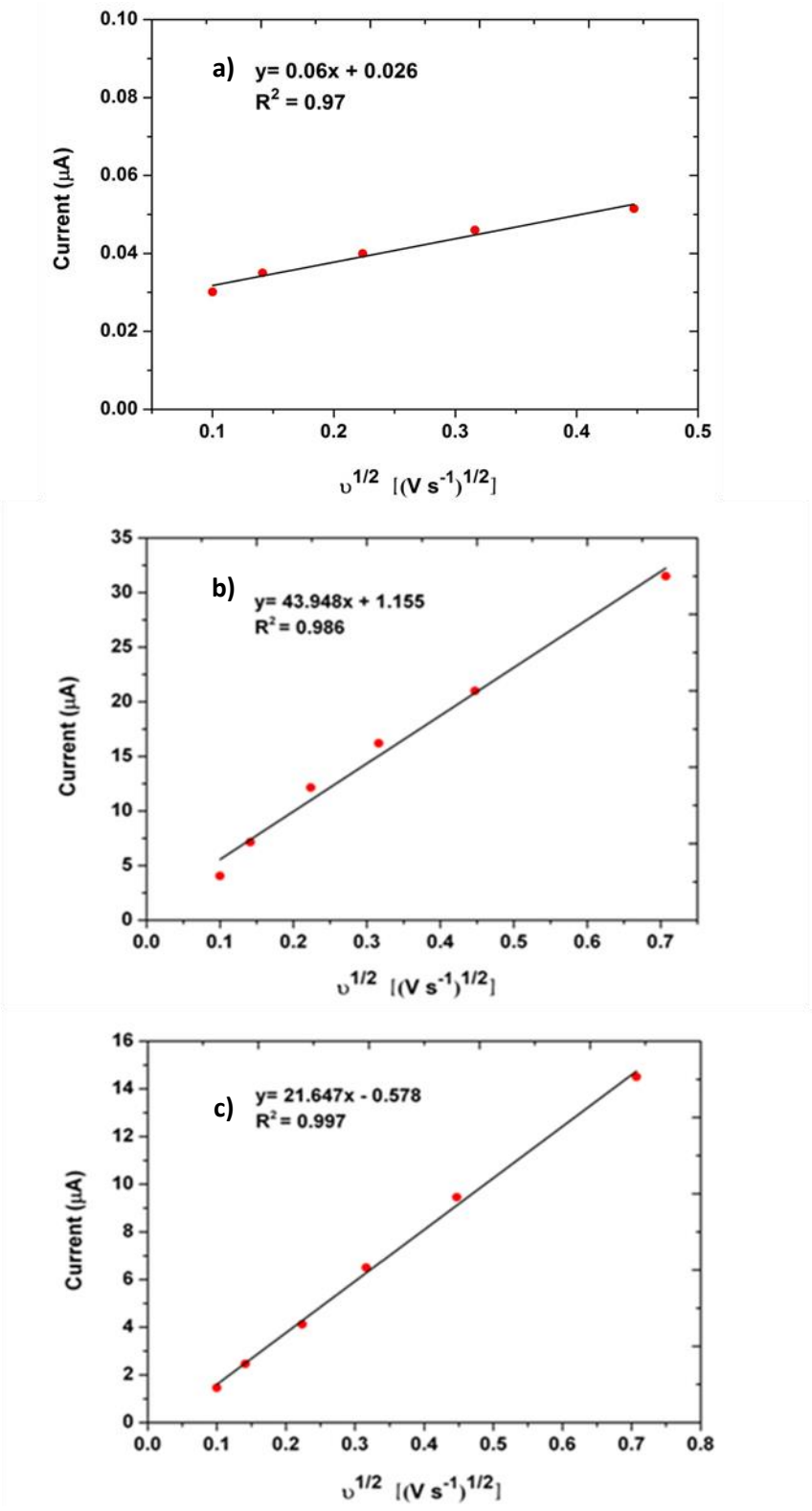


Fig. 5.20. Oxidation peak current values as a function of the square root of the scan rate, recorded for 5 mM $K_3Fe(CN)_6$ in 0.01 M phosphate buffer saline pH 7.0. a) Au design 2, channel layout 3; b) Pt design 3, channel design 4; c) Au design 4, channel layout 5.

them with the expected, theoretical areas. Eq. 5.2 represents sample calculations for Au design 2.

$$A = \frac{slope}{(2.69\ x\ 10^5)n^{3/2}c_o D^{1/2}} \qquad Eq.\ 5.1$$

Here,

$$slope = 0.06\ x\ 10^{-6}\ \frac{A}{\sqrt{Vs^{-1}}};\ n = 1;\ D = 7.6\ x\ 10^{-6}\ cm^2\ s^{-1}$$

$$c_o = 5\ x\ 10^{-6}\ mol\ cm^{-3}$$

$$A = \frac{0.06\ x\ 10^{-6}}{(2.69\ x\ 10^5)(1)^{3/2}(5\ x\ 10^{-6})\ (7.6\ x\ 10^{-6})^{1/2}} \qquad Eq.\ 5.2$$

$$A = \ 0.006\ cm^2$$

Tab. 5.6. Experimental electrode areas calculated from the Randles-Sevčik equation.

	Design 2	***Design 3***	***Design 4***
Metal layout	Au	Pt	Au
Experimental electrode area	0.006 cm^2	4.29 cm^2	2.11 cm^2
Theoretical electrode area	0.002 cm^2	0.042 cm^2	0.036 cm^2

As illustrated in Tab. 5.6, the electrode areas calculated from the slope for designs 3 and 4 are two orders of magnitude higher than the predicted values. In comparison, the difference between the experimental and theoretical values obtained for design 2 is only a factor of 3. This is primarily due to the inhibited diffusion of ferricyanide to the electrodes, caused by a gradual evaporation of the solution from the channel and decreased mobility of the species throughout the measurement. Additional sources of discrepancies include the alignment imprecision associated with the manual assembly of the channel and

electrode compartments. Furthermore, the reported theoretical values correspond to the 2D geometries of the electrodes and do not account for the height (100 nm) of the metal features, due to the negligible dimension. The side planes of the electrodes are however exposed to the redox solution and contribute to the produced current output.

5.6. Modification of gold electrodes with Nanoporous Gold Structures.

In order to improve the electrochemical response of the bare electrodes, the metal catalysts employed in the energy harvesting applications are often altered to adjust their surface properties to a particular catalytic task.

In the course of this Ph.D. gold electrodes microfabricated on Zeonor substrates, were chemically modified to increase the active surface area of the metal and to facilitate stable immobilization of the enzyme species and enhanced biological response, resulting in a prolonged and improved performance of the intended biofuel cells. Although a number of strategies have been considered for this particular research task (e.g. the use of gold nanoparticles), Nanoporous Gold Structures (NPG) were believed to be the most suitable for the modification purpose. NPG approach has been selected, due to high porosity and chemical inertness of their structures, offering good prospects for the efficient and stabilizing environment for the enzyme chemistry. Additionally, unlike alternative modification techniques, the formation of NPG is a simple two-step protocol and does not require lengthy and advanced preparation procedures or intensive labour.

NPG, among varied electrode materials, exhibit a number of desirable features, which distinguish them from other surface treatment routes and make them highly suitable for the electrochemical measurements in mild conditions. Unlike other integral surface catalysts, such as, platinum and palladium, Nanoporous Gold Structures remain active and entirely selective at low temperatures and therefore, can be successfully employed for the electrochemical studies under a range of conditions [52, 53]. It has been demonstrated that NPG are resistant to thermal stress and high oxidation and in contrary to extensively used gold nanoparticles do not aggregate in oxidative and thermally challenging environment [54].

As reported in the literature, gold nano-deposits demonstrate high intrinsic density, excellent conductivity and a large surface area and have been frequently reported as

matrices for catalyst immobilization [55]. Increased surface areas, supported by excellent electrochemical and electrocatalytic properties of NPG modified electrodes, can effectively supplement the intrinsic biological functions of the enzymes employed in biofuel cells. The porosity of generated features is easily tunable by controlling the composition of the modifying solution. The size of gold pores can range from as little as few nm to a few μm and the generated structures are of high chemical purity. Due to adjustable dimensions of generated porous features, gold nanostructures can be applied for immobilization of different sized biomolecules and therefore can be used for diverse biological applications. As compared to other surface modification techniques, such as, the sol-gel, the formation of NPG is highly reproducible and unaffected by slight alterations in the ionic strength and pH of the supporting solution. In general, NPG modified electrodes are prepared from commercially available or in-house made gold and silver alloys by chemically etching of the deposits in concentrated nitric acid solutions.

In the light of discussed advantages of the NPG electrode modification methods, the Au macroelectrodes, fabricated on Zeonor substrates, have been electrochemically treated, in order to grow the NPG features leading to increased surfaces of the active area. In order to confirm improved electron-transfer properties of the modified electrodes, the response of bare gold microfabricated on Zeonor substrates has also been investigated.

The NPG structures, obtained as part of this Ph.D. chapter, were produced according to a protocol from ref. [56]. Two electrode layouts have been used for the modification purpose, design 3 and design 4 of the electrode design. Prior to the surface treatment, the metals were exposed the oxygen plasma and chemically cleaned in 1 M H_2SO_4 cleaned, following the two-step protocol enclosed in Chapter II.

The electrodeposition of gold nanostructures was carried out from a solution containing 20 mM KAu (CN) $_2$ and 100 mM KAg (CN) $_2$ in a molar ratio of $Au_{0.18}$: $Ag_{0.82}$ in 250 mM Na_2CO_3, pH 13, as a supporting electrolyte. The electrochemical set up consisted of a three electrode system with Ag/AgCl and high surface area Pt coated Ti gauze as reference and counter respectively. The potential of the working electrode was controlled by a CHI 660B instrument. Prior to the surface treatment, all solutions were purged with nitrogen for 20 min, in order to remove the interfering presence of oxygen. Deposition was carried out at room temperature, by applying a constant potential of -1.2 V for 600 s at a rate of film growth of 20 nm min^{-1}.

The influence of the composition of gold and silver alloy on the morphology and porosity of generated NPG has been investigated by Searson and co-workers [57] and it has been proven that solution containing the selected $Au_{0.18}$: $Ag_{0.82}$ molar ratio results in the formation of the shortest ligaments (20-30 nm long) and the highest surface area upon dealloying in 30 % nitric acid [57].

5.6.1. Results and discussion.

Prior to the deposition of NPG, a CV response in 1 M NaOH has been measured for the bare Au electrode by sweeping the potential from -1.6 to 0 V vs. Ag/AgCl at 10 mV s^{-1} scan rate. The electrochemical signal in NaOH has been further recorded following the deposition, indicating the presence of Au and Ag metal oxide reduction peaks at potential values of 0 V and 0.3 V vs. Ag/AgCl accordingly (Fig. 5.21) and was compared with the behavior of bare gold.

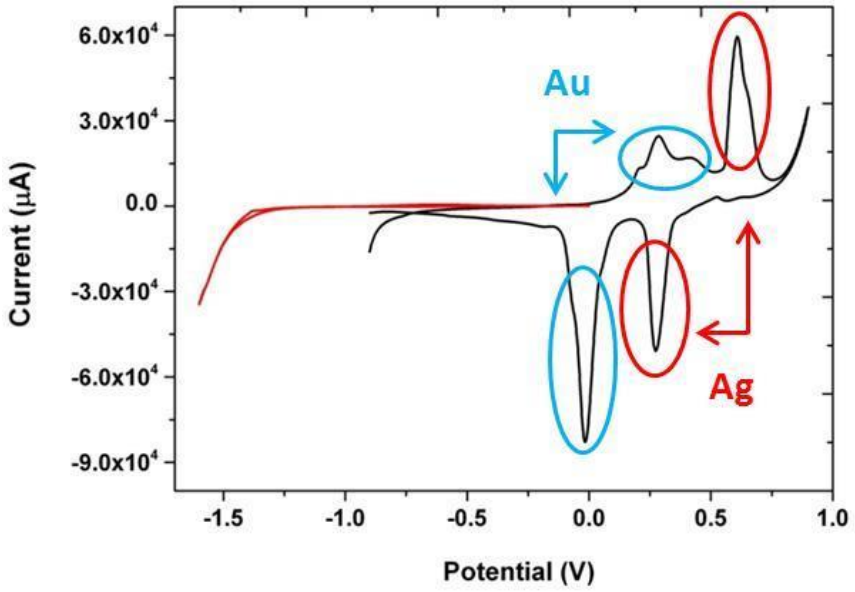


Fig. 5.21. Electrochemical response in 1 M NaOH vs. Ag/AgCl for: a) bare Au electrode, design 4; b) $Au_{0.18}Ag_{0.82}$ alloy on gold design 4, reduction and oxidation peaks for Au were recorded at 0 V and 0.3 V respectively; redox behavior of Ag is indicated at 0.3 V (reduction) and 0.6 V (oxidation). Deposition potential: -1.2 V, deposition time: 600 s. Scan rate of 10 mV s^{-1}.

Cyclic voltammetry measurements of bare and AuAg modified gold electrodes confirmed successful deposition of the alloy layer, as denoted in Fig. 5.21. The incubation of the resulting deposit in 30 % nitric acid has led to an expected gradual removal of the silver, corresponding to a steady reduction in the observable oxidation and reduction peaks for Ag. Complete dealloying has been obtained after approximately 90 min of the acid treatment.

Following the successful generation of gold and silver alloy composite, the Ag component was chemically etched by submerging the modified electrode in 30 % nitric acid for 90 min according to the protocol described in [58]. A gradual desertion of the peak for silver oxide has been recorded by CV measurements in 1 M NaOH until complete removal of Ag has been observed (Fig. 5.22) resulting in a highly porous nano-gold framework.

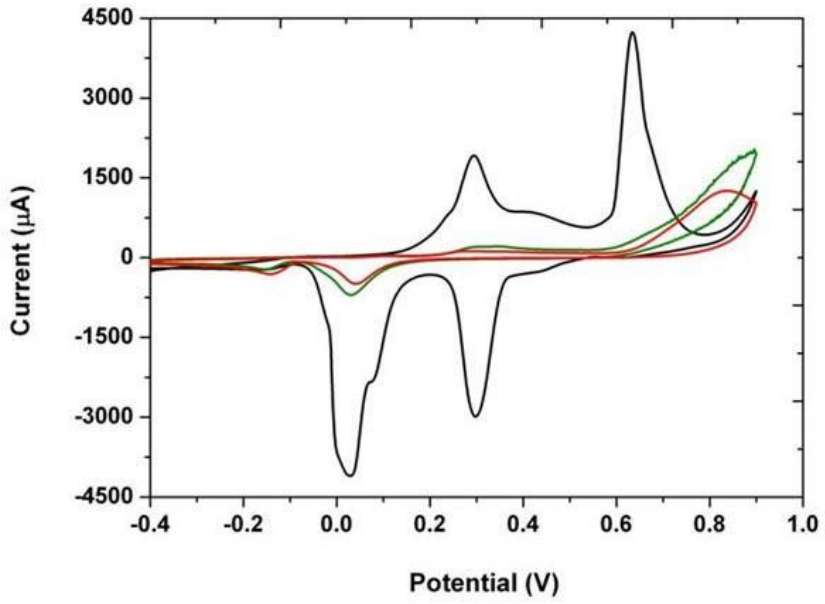


Fig. 5.22. CV scan of AuAg modified gold electrode in 1 M NaOH recorded vs. Ag/AgCl directly after the alloy deposition (black line) and upon dealloying in 30 % HNO_3: 30 min (red line); 90 min (green line). Scan rate: 10 mV s^{-1}. Chemical etch of the less noble metal results in a gradual loss of the electrochemical signal of Ag triggering atomic rearrangement of Au layer.

Dissolution of silver during the chemical etch of silver was additionally confirmed by the measurements of the ratio of the oxidation charge peaks for Ag to Au. Each cycle represents a 10 min incubation of the alloy coated gold in 30 % HNO_3. As the amount of charge passing through the metal is directly proportional to the quantity of the alloy deposit on the surface, decrease in the Ag/Au ratio with an increasing number of dealloying steps are an indication of a successful etch (Fig. 5.23.). In the case of generated NPG deposits, 9 cycles of 10 min acid treatment have been found optimum to remove the silver component.

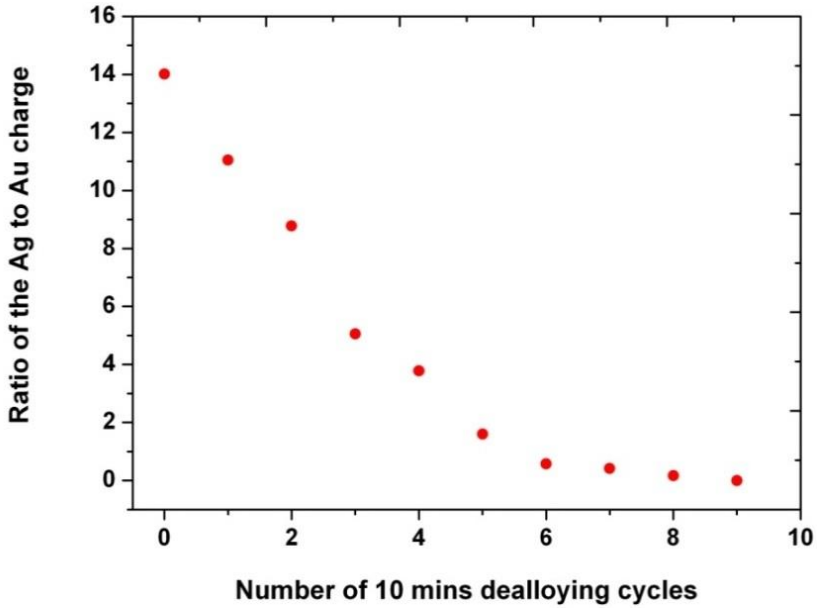


Fig. 5.23. Ratio of the oxidative charge for Ag and Au with respect to the number of dealloying cycles. Each cycle represents a 10 min treatment in 30 % HNO_3.

Scanning Electron Microscopy measurements confirmed the presence of a porous NPG network deposited on Au electrodes (Fig. 5.24). High resolution SEM micrographs of Nanoporous Gold revealed a compact network of highly porous deposits, composed of randomly oriented gold ligaments with high step density. The thickness of the resulting NPG layer was measured to 200 nm and controlled by the conditions and duration of the deposition step.

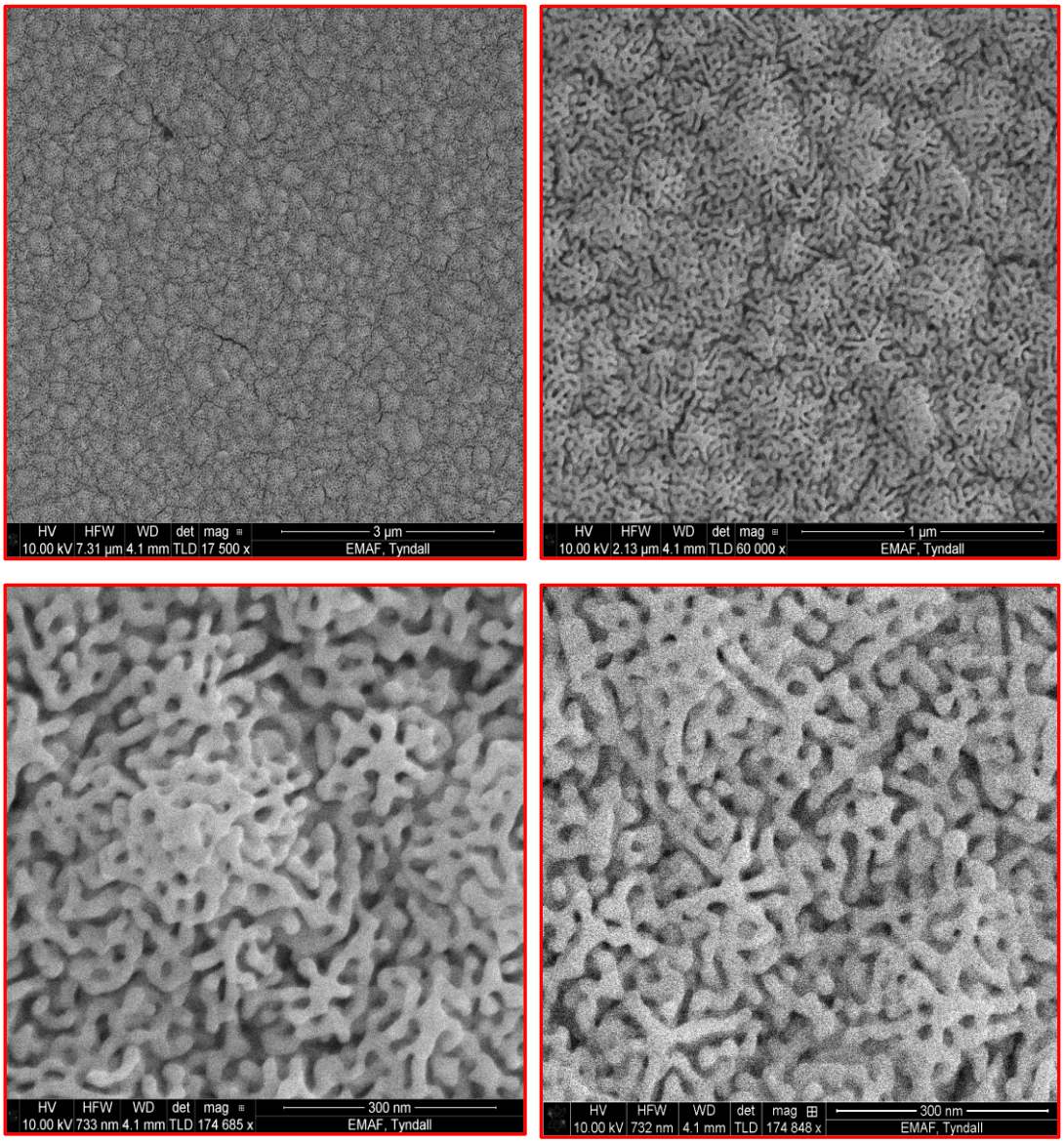


Fig. 5.24. High resolution SEM micrographs of NPG structures on Au electrodes, design 4 shortly after dealloying; taken at the Tyndall National Institute; magnification of 17 500 (top left); 60 000 x (top right); and 175 000 x (bottom row);

The electrochemical signal of NPG modified electrodes have been studied for designs 3 and 4 of the metal layouts and compared to the response of bare gold electrode. The electrochemical set up was composed of a three electrode system comprised of microfabricated Au WE, Pt as CE and Ag/AgCl as RE respectively as illustrated in Fig. 5.25. Potential of the working electrode was controlled by CHI 660B potentiostat.

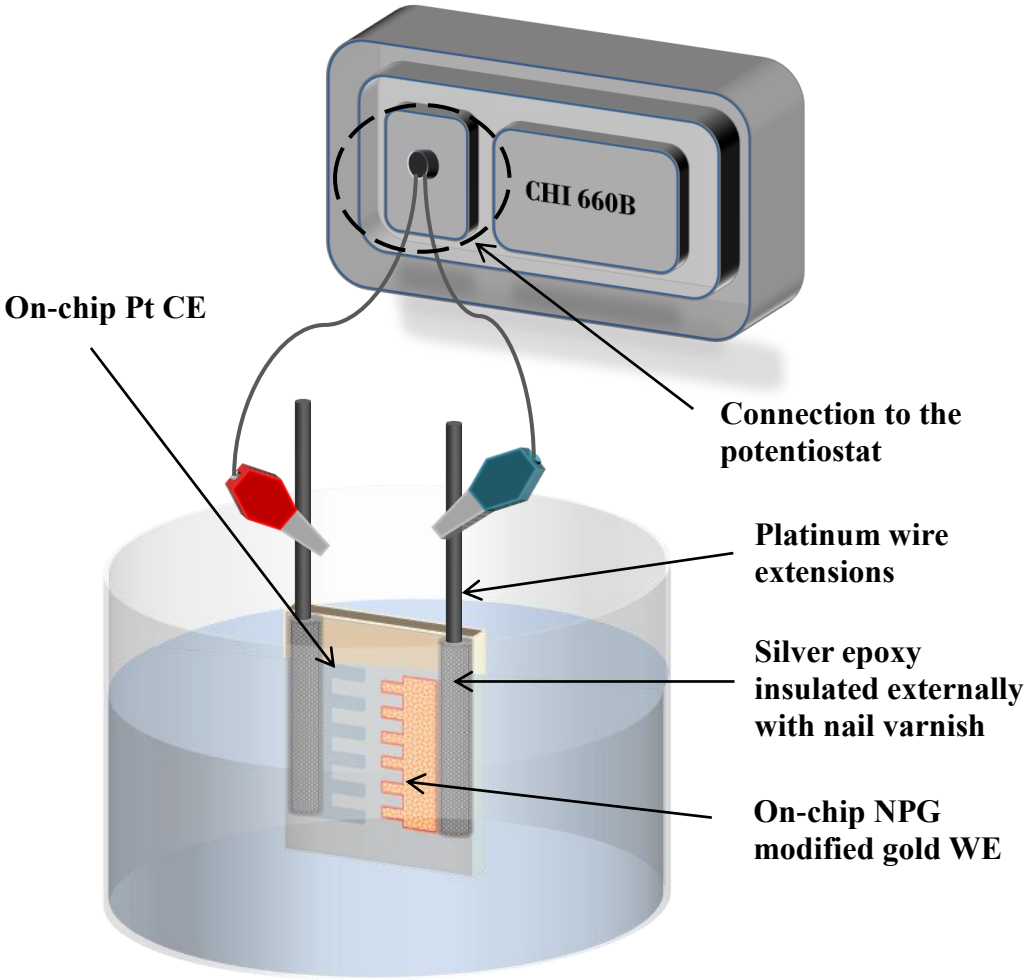


Fig. 5.25. Diagram of the electrochemical set-up for the characterization of plain and NPG modified electrodes in 0.1 M H_2SO_4 and in 0.01 M PBS buffered solutions. Not shown on the image is the external Ag/AgCl reference electrode.

Characterization of plain and NPG gold metals has been carried out in static conditions using Cyclic Voltammetry measurements in 0.1 M H_2SO_4 and various 0.01 M PBS based solutions.

The electrochemical response of NPG modified electrodes, design 3, and was first recorded in 0.1 M H_2SO_4 and compared with the signal of plain gold electrode as shown in Fig. 5.26.

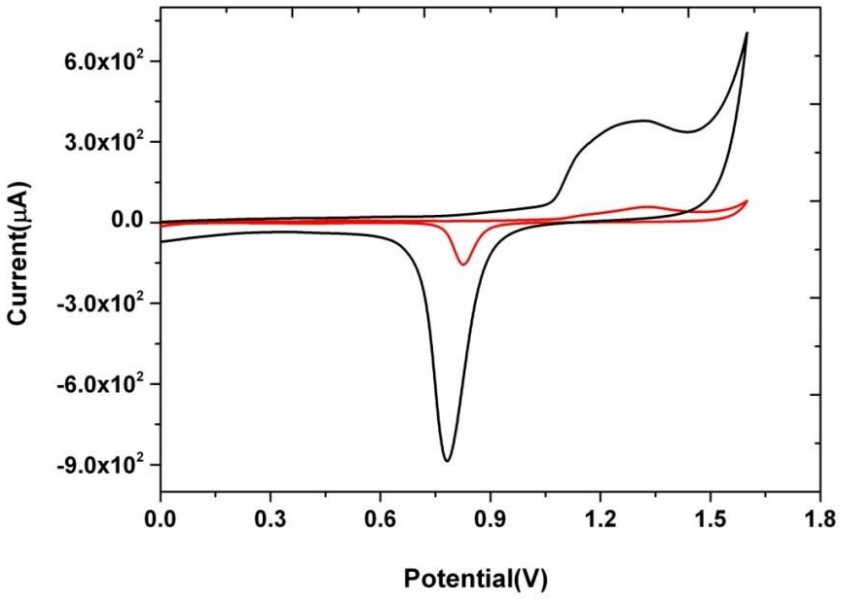


Fig. 5.26. CV of plain (red line) and NPG modified (black line) on-chip electrodes, design 3, in 0.1M H_2SO_4, recorded vs. Ag/AgCl. Scan rate: 10mV s^{-1}

As can be seen from Fig. 5.26, the modification of gold with NPG structures resulted in a 60 % increase in the reduction and oxidation peak currents when measuring the signal in 0.1M H_2SO_4, indicating enhanced area of the electroactive metal surface. The improved response of NPG to the reactive species has been attributed to higher step densities and a larger number of active sites as compared to planar Au electrodes. Due to lower bond coordination numbers and favorable steric and electronic properties, gold nanostructures can provide adsorption sites suitable for variety of reagents [56]. It has been recently proven that the behavior of NPG active layer promotes prolonged residence time for certain species [59, 60].

Based on the average reduction peak of gold oxide in 1 M H_2SO_4 recorded at a scan rate of 0.05 mV s^{-1}, theoretical ($A_{geometric}$) and electrochemical ($A_{electrochem}$) surface areas of bare and NPG gold have been obtained for designs 3 and 4 of the electrode layouts. Calculations of the electrochemically active surfaces were based on the assumption that the amount of charge generated by cm^2 of Au electrode is 3.90 x 10^{-4} C [61]. Consequently, the roughness factors $f_r = \frac{A_{electrochem}}{A_{geometric}}$ for planar and NPG gold electrodes have been attained and the ratio between the two values was obtained for both designs (Tab. 5.7 and Tab. 5.8).

Tab. 5.7. Experimental and geometric surface areas of bare and NPG modified gold for design 3 of the electrode layout.

Design 3	$A_{geometric}$ (cm^2)	$A_{electrochem}$ (cm^2)	f_r	$\frac{f_r^{NPG}}{f_r^{bare}}$
bare Au	**5.22***	**0.53 ± 0.02**	**0.11 ± 0.04**	**12.8 ± 0.5**
NPG modified Au	**5.22***	**7.34 ± 0.29**	**1.41 ± 0.05**	

Tab. 5.8. Experimental and geometric surface areas of bare and NPG modified gold for design 3 of the electrode layout.

Design 4	$A_{geometric}$ (cm^2)	$A_{electrochem}$ (cm^2)	f_r	$\frac{f_r^{NPG}}{f_r^{bare}}$
bare Au	**5***	**0.34 ± 0.01**	**0.07 ± 0.03**	**7.9 ± 0.3**
NPG modified Au	**5***	**2.74 ± 0.11**	**0.55 ± 0.02**	

**The practical geometric areas of gold electrodes have been estimated to 5.22 cm^2 and 5 cm^2 for designs 3 and 4 respectively, which is less than their theoretical values of 8.97 cm^2 and 7.98 cm^2 accordingly. This was due to the presence of the silver paste extension taking away some of the metal's active surface.*

The electrochemically assisted deposition of Nanoporous Gold Structures resulted in a several fold increase in the active surface areas of gold electrodes, as illustrated in Tab. 5.7 and Tab. 5.8, with a higher value obtained for design 3 (~14 increase as compared to bare Au). Inferior response of electrode of design 4 can be attributed to a number of

factors, primarily the fabrication process resulting in dissimilar quality of deposited metals and their behavior upon electrochemical treatment.

Following the initial CV measurements in sulfuric acid, the response of gold electrodes functionalized with Nanoporous Gold deposits was measured in phosphate buffered solution in the presence of the mediator, 5 mM FCA. 1.384 mM Na_2SO_3 was additionally added into the solution in order to sequester the dissolved oxygen and prevent its diminishing effect on the generated current (Fig. 5.27). Investigation of the redox behavior of the ferrocenecarboxylic acid on NPG electrodes was essential for further implementation of the catalyst, glucose oxidase. Although the enzyme was not present during the preliminary studies, sodium sulphite (Na_2SO_3) was added to the buffer, in order to suppress the possible negative effect of the oxygen on GOX and to mimic the exact conditions when working with the enzyme.

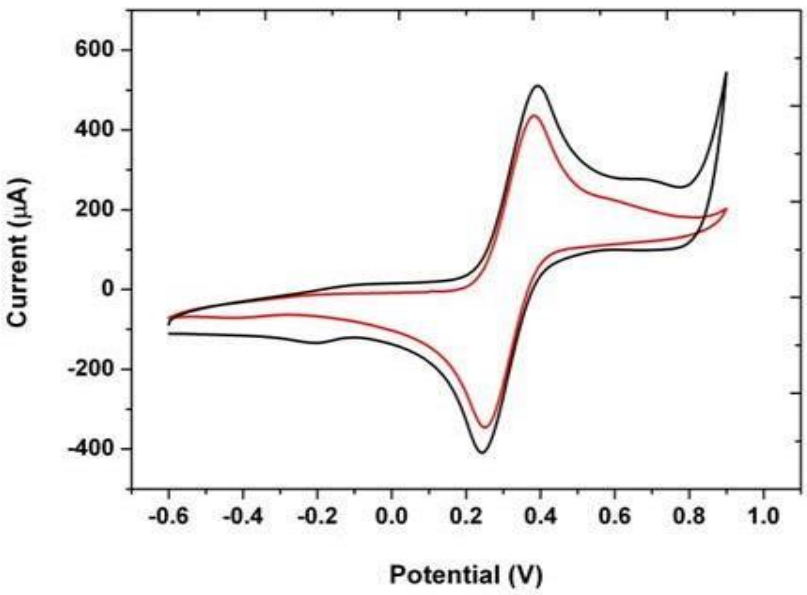


Fig. 5.27. Cyclic Voltammetry measurements of plain (red line) and NPG modified (black line) electrode microfabricated on Zeonor substrate, design 3, in 0.01 M PBS pH 7.0 containing 5 mM FCA and 1.384 mM Na_2SO_3. Potential recorded vs. Ag/AgCl.Scan rate: 20mV s^{-1}.

As depicted in Fig. 5.27, the electrochemical studies on NPG modified electrodes indicated a reversible character of the reaction for ferrocenecarboxylic acid and an approximately 13 % increase in the values obtained for the oxidative and reductive peak

currents, as compared to the bare gold electrode of the same design. This suggests enhanced active surface area of nanoporous gold electrodes and is consistent with the calculated roughness factors for the deposit (Tab. 5.7 and Tab. 5.8). The reversibility of the redox processes for ferrocenecarboxylic acid has been studied based on the potential and current values as described in Appendix A and the results for bare and modified gold electrodes, designs 3 & 4, are summarized in Tab. 5.9 and Tab. 5.10.

Tab. 5.9. Determination of the reversibility of redox reactions for FCA on NPG modified gold electrode, design 3.

NPG design_3 ***0.01M PBS solutions***	***ΔE**(V)*	E_2^1**(V)	$\left\|\frac{i_{reverse}}{i_{forward}}\right\|$
5mM FCA and 1.384mM Na_2SO_4	**0.15**	**0.318**	**0.922**
5mM FCA and 100mM glucose	**0.146**	**0.317**	**0.915**
5mM FCA, 100mM glucose, 1.384mM Na_2SO_4	**0.177**	**0.320**	**0.927**

Tab. 5.10. Determination of the reversibility of redox reactions for FCA on planar gold electrode, design 3.

Planar Au design_3 ***0.01M PBS solutions***	***ΔE**(V)*	E_2^1**(V)	$\left\|\frac{i_{reverse}}{i_{forward}}\right\|$
5mM FCA and 1.384mM Na_2SO_4	**0.132**	**0.316**	**0.974**
5mM FCA and 100mM glucose	**0.123**	**0.317**	**0.963**
5mM FCA, 100mM glucose, 1.384mM Na_2SO_4	**0.162**	**0.319**	**0.993**

*$\Delta E = E_{forward} - E_{reverse}$

** $E_2^1 = \frac{E_{forward} + E_{reverse}}{2}$

The electrochemical studies of planar Au and NPG electrodes in different media confirmed enhanced current values recorded for the latter. The improved electroactive properties were most prominent in 0.1 M H_2SO_4, resulting in a 60 % increase in the oxidative and reductive peak values (Fig. 5.26). Investigation of the behavior of NPG modified electrodes in 0.01 M PBS containing 5 mM FCA and 1.384 mM Na_2SO_3, demonstrated a 25% increase in the electrochemical signal for NPG gold (Fig. 5.27). Additionally, the redox response of 5 mM FCA in 0.01M PBS buffer for planar Au and NPG modified electrodes confirmed a reversible behavior of the mediator based on the measurements of potential and peak currents (Tab. 5.9 and Tab. 5.10).

Preliminary studies on the enzymatic activity of glucose oxidase on NPG functionalized surfaces were carried out for design 3 and 4 of the electrode layouts in 0.01 M PBS buffered solutions containing 100 mM glucose, 5 mM FCA and 1.384 mM Na_2SO_3. Fig. 5.28 compares the electrochemical response of GOX immobilized on nanoporous gold electrodes via drop-coating technique to plain NPG, design 3.

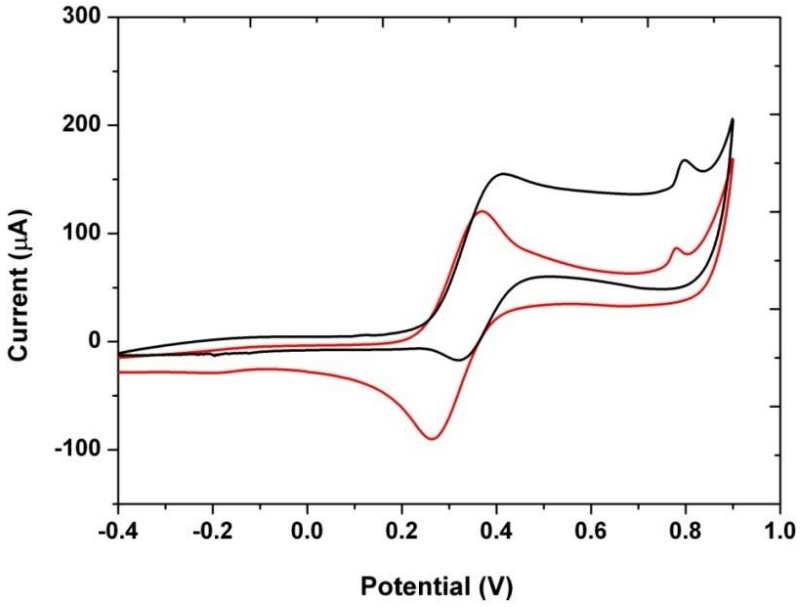


Fig. 5.28. Cyclic Voltammetry measurements of plain NPG (red line) and NPG modified with 1 mg mL^{-1} GOX (black line) electrodes microfabricated on Zeonor substrate, design 3, in 0.01 M PBS containing 100 mM glucose, 5 mM FCA and 1.384 mM Na_2SO_3. Potential recorded vs. Ag/AgCl. Scan rate: 10mV s^{-1}.

The origin of the additional oxidation peak at 0.8 V is the electrode contamination with organic impurities. These were most likely introduced on the NPG fabrication step or due

to a silver residue present as a result of an incomplete etching of Ag component on the dealloying process.

Investigation of NPG electrodes biofunctionalized with glucose oxidase (1 mg mL^{-1} in 0.01 M PBS buffer) indicated retained biological activity of the enzyme and successful catalytic oxidation of glucose in the presence of the mediator species and Na_2SO_3. A significant decline in the reduction current and a 76 % increase in the oxidative peak for modified gold, in the presence of glucose oxidase, have been recorded as can be seen in Fig. 5.28. High current values obtained by the GOX functionalized NPG gold electrode indicates a promising strategy in the preparation of the bioanodes for the future enzymatic biofuel cells with improved performances.

5.7. Design and fabrication of the microfluidic channels.

5.7.1. Selected channel geometries.

The design of the microfluidic channels has been based on the theoretical investigation of the microfluidic system, performed using two numerical software packages: COMSOL *Multiphysics* and *Mathematica*. Optimization of the channel layouts was feasible, due to modelling of the behavior of the flow and the diffusion of species across the anolyte and catholyte compartments of the channel.

Following from the simulation results, a classical Y-shape of the channel layout has been investigated for the development of enzymatic biofuel cells. This design incorporated two types of inlets: well defined, point entries for a vertical supply of the fuel and oxidant (Fig. 5.29 top) or a sideways, horizontal inflow of the species provided in parallel to the channel plane (Fig. 5.29 bottom). Within each design, five different channel and inlet widths have been considered, ranging between 200 μm and 1000 μm (main body of the channel) and 100 μm – 500 μm (inlets). The angle between the inlets has been set for all designs to 45 °. The overall length of the channel compartment is l = 30 mm and it encompasses a number of features: the diameter of the inlet points (d = 3 mm, Fig. 5.29 top), the distance between the inlet points and their intersection with the channel (c = 1.5 mm, Fig. 5.29 top), the gap between the outlet point / inlet junction and the area occupied

by underlying electrodes patterned on top device part (a = 1.15 mm); the separation of the point inlets (Fig. 5.29 top) / outlet from the edge (z = 2.6 mm). Tab. 5.11 presents a complete list of all the dimensions.

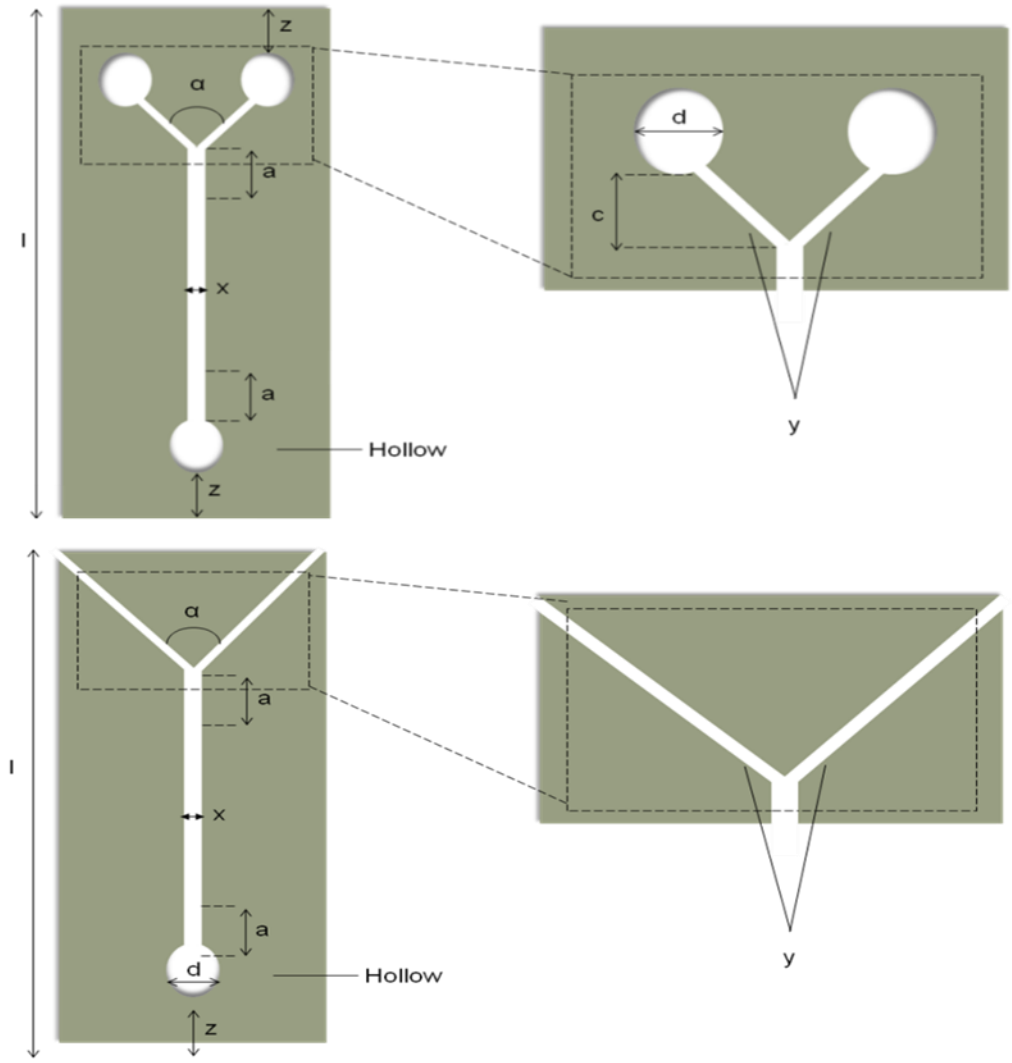


Fig. 5.29. Schematic of the channel designs, classical Y-shape with point inlets for the vertical supply of the fuel and oxidants (top) and sideway entry into the channel for horizontal delivery of the species (bottom).

The considered range of the channel and inlet widths has been selected based on the theoretical investigations of the laminar flow in the microfluidic domain, described in Chapter IV of this thesis. The diameter (d) and the distance between the inlet points (α, c) have been determined by the size of the available tubing connections (Ø 1.6 mm) and the physical requirement for the fuel and oxidant separation. The overall length of the channel

feature and the distance from the inlet junction and outlet point (a), have been governed by the geometries of the underlying electrodes.

Tab. 5.11. Dimensions of the channel patterns for designs 1-5, where x and y are the respective widths of the channel and the inlets.

	x (µm)	***y (mm)***	***z (mm)***	***a (mm)***	***c (mm)***	***l (mm)***	***d (µm)***	***α(°)***
Design 1	200	100	2.6	1.15	1.5	30	3	45
Design 2	400	200	2.6	1.15	1.5	30	3	45
Design 3	600	300	2.6	1.15	1.5	30	3	45
Design 4	800	400	2.6	1.15	1.5	30	3	45
Design 5	1000	500	2.6	1.15	1.5	30	3	45

5.7.2. Fabrication of the microfluidic channels.

Fabrication of the microfluidic features in Zeonor and PDMS substrates has been carried out by imprinting of the channel relief patterns integrated on the silicon stamps onto the polymer materials using common molding techniques: high temperature and pressure hot-embossing in Zeonor and replica molding from a commercial mixture of a liquid PDMS. Silicon stamps have been routinely employed in microfabrication technology as chemically stable and mechanically robust tools for the micro-transfer patterning of small scale features. In this Ph.D. work Si templates with machined reliefs of the channel geometries have been processed based on previously fabricated Chrome-on-Glass (COG) master photomasks. Both templates allow relatively easy and precise transfer of the microscopic patterns onto the respective substrate.

Preparation of the silicon stamps with the channel relief

Fabrication of the channels in polymer materials required two templates: a silicon stamp for direct patterning of the substrates and a COG master to produce the former.

The design of the COG masks was prepared in the Central Fabrication Facility of the Tyndall National Institute using *Mentor Graphics IC Station* software. The processing of photomasks was carried out by Compugraphics Intl. Ltd (Scotland), according to the procedures described in Appendix B. The fabricated COG masks were used as templates for the production of the silicon stamps employed for further engraving of the channel features in the Zeonor and PDMS polymers.

Silicon stamps were prepared by a Deep Reactive Ion Etch (DRIE) of silicon in a mixture of gases. In DRIE, under conditions of low pressure and a strong electrical field, activated ions bombard the surface almost vertically, etching away the underlying material. Silicon etch is typically carried out with sulphur hexafluoride [SF_6] as the main reactive plasma component. In general, stamp fabrication involves the following processing steps: coating the silicon with a thin layer of a photoresist; exposing the surface to UV light through an appropriate COG mask; removal of the resist followed by a deep reactive ion etch of the silicon (areas protected by the photoresist will not be washed away) and finally removing of the remaining resist. The shape and dimensions of the obtained silicon pattern are precisely controlled by the design of the mask. The schematic of the process is illustrated in Fig. 5.30.

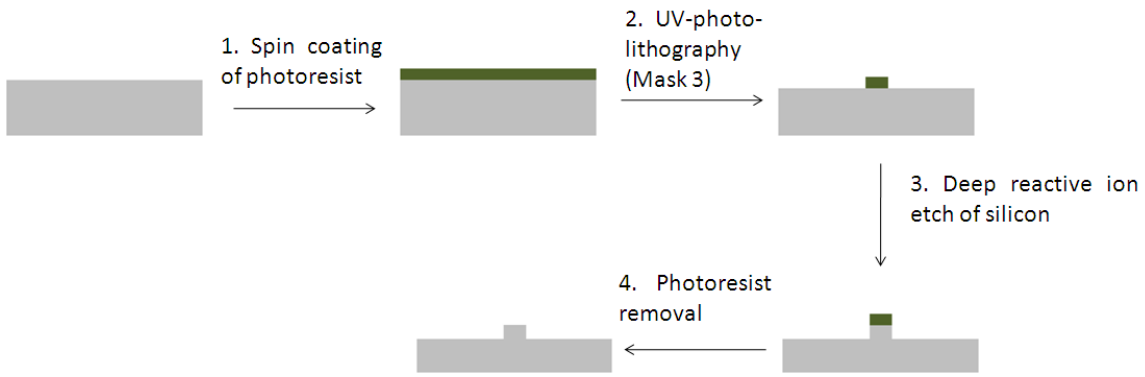


Fig. 5.30. DRIE of silicon masks for the channel fabrication.

Prior to the deep etch, silicon wafers had to undergo a multi-step cleaning protocol, which was carried out in a Silicon Fab at the Tyndall National Institute. The wafers were pre-baked for 40 min at 180 ºC to remove any moisture and an adhesion promoter (hexamethyldisilzane, HDMS) was deposited for 80 s at 150 ºC. The following step involved spin coating of a positive photoresist (OIR 908-35) up to a 3.4 µm thickness (5000 rpm). Wafers were then baked for 90 s at 90 ºC to evaporate off any remaining resist solvent and to enhance the reaction with UV light. Silicon wafers were aligned with the COG masks using a Canon Mask Aligner PLA600 and exposed to UV for 25 s. Post-exposure bake was carried out at 120 ºC for 90 s after which a two stage, "double puddle" development of the resist was performed. Each step involved a 40 s treatment with an OPD 5262 (positive resist developer) and a thorough wash with DI water. Final cleaning of the patterned silicon included: incubation in a H_2SO_4/H_2O_2 bath (5 L of acid: 100 mL of peroxide) at 130 ºC; rinsing with DI water and drying in a semi tool washer-dryer (consecutive DI water wash and drying in a stream of nitrogen).

Silicon wafers were then transferred for Deep Reactive Ion Etch. DRIE is an Aspect Ratio Dependent Etching (ARDE) and its outcome depends highly on the dimensions of the etched features, primarily the depth to width ratio. During the DRIE process reacting gasses have to easily access the structural cavities at the same time allowing the waste products to be efficiently removed. At high aspect ratios (> 5: 1, for very deep and narrow features) the etch rate drops due to gas transport limitations. Another important processing requirement is that for the etch to proceed effectively, at least 30 % of the substrate surface needs to be covered with the photoresist. This prerequisite, governs to a certain extent the ultimate design of the fabricated features. DRIE was carried out in the Fabrication Facility of the Tyndall National Institute using an Advanced Silicon Etcher from (Surface Technology System Plc. UK). Etching of the channel features in silicon was done for 20 min at room temperature using a multiplexed Bosch process. This method involves using alternative etch and passivation steps (typically 9 s etch and 2 s passivation slits) in order to produce a vertical (an-isotropic) feature profile. Reactive ions were produced from a mixture of sulphur hexafluoride (SF_6) and octafluorocyclobutane (C_4F_8). Gasses were provided to the reaction chamber at 200 and 300 sccm flows and at pressures of 54 and 38 mTorr, respectively. Ionization was initiated by applying a radio-frequency (RF) power of 200 W (coil) and 20 W (platen). At the etching step the coil power is inductively coupled into the SF_6 filled upper chamber to produce high density plasma. The silicon wafer sits on a lower chamber (platen) under a

small RF bias and the sulphur hexafluoride plasma chemically etches the exposed silicon. As the etch is an-isotropic, the second part of the Bosch process requires the passivation step. At this stage 200 sccm of octafluorocyclobutane flows into the chamber and the plasma is induced by applying 200 Watts of coil power. The passivation occurs as carbon and fluoride monomers coat the etched silicon surfaces. In the following etch step the SF_6 ions have enough energy to remove the polymer from the bottom surface of the channel but not from the side-walls and therefore the silicon is only etched in the vertical direction. In order to maintain the vertical etch characteristics, it is then crucial to cool down the wafer and the resist. A chiller unit keeps the platen at 20 ºC while helium at the pressure of 10 Torr flows to the back of the wafer providing a good thermal contact between the two. After etch the channel depths were measured with a Tencor Alphastep 200 system (CAE, USA). The schematic representation of the DRIE processing of the silicon stamps with microfluidic channels is depicted in Fig. 5.31.

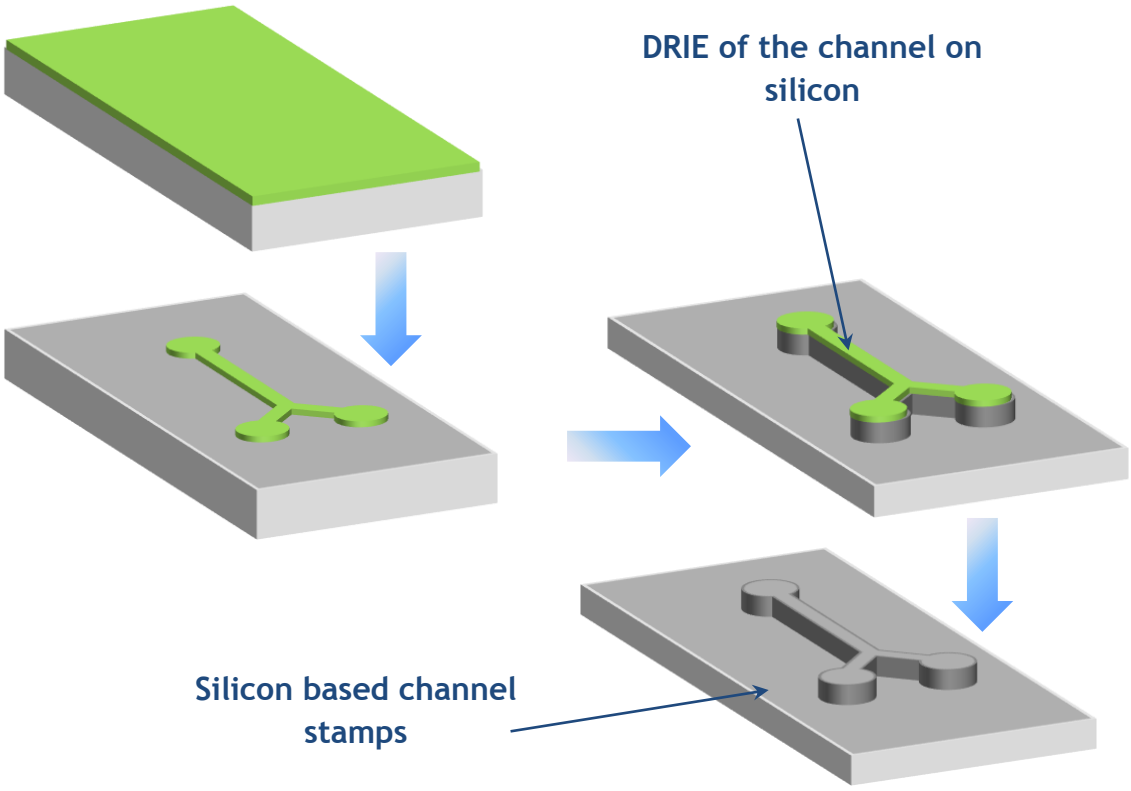


Fig. 5.31. Deep Reactive Ion Etch of silicon for the fabrication of microfluidic channels.

Channel imprinting in PDMS and Zeonor polymers

Patterns of the channels were ultimately transferred to Zeonor and PDMS by respective hot-embossing or simple casting of the liquid PDMS elastomer onto the silicon mask and curing the assembly in the oven until set.

Preparation of the channels in PDMS was carried out by casting a liquid silicon resin solution (Sylgard 184 elastomer kit) onto clean silicon stamp and curing in the oven at 90 ºC for 2 h. PDMS was prepared in disposable plastic container by mixing the two components in a 10:1 base: agent ratio. The curing agent was always added last and mixed vigorously (glass rod used) with the base until numerous air bubbles were formed. Liquid PDMS was then degassed at -20 ºC for 1 h. Silicon stamps were cleaned with copious amounts of IPA and DI water and dried in a stream of nitrogen. A small, circular Pyrex dish was laid out with alumina foil and the clean stamp was placed in it. 11 mL of the silicone mixture (10 mL of the base and 1 mL of the curing agent) was gradually casted on top of the stamp and any remaining air bubbles were removed using a tip of a needle. The stamp was gently pressed to the bottom of the glass dish to ensure no air was trapped in between the Al foil and silicon. Following curing in the oven (1.5 h at 90 ºC) the solidified PDMS and silicone assembly was easily removed from the glass dish, due to the presence of Al, and PDMS cover was carefully peeled off from the Si surface. Silicon stamp was recovered and after cleaning was used for further casting. Channel pattern was cut out from the PDMS bulk and the inlet and outlet points were perforated using a thin hollow metal rod. PDMS channels were rinsed with IPA and DI water and stored in particle-free environment in a closed Petri dish when not in use.

Channel hot-embossing in Zeonor

Zeonor based µ-channels have been prepared by a hot-embossing technique using the fabrication facilities available at the Tyndall National Institute. In this method the silicon stamp bearing the channel features and the polymer substrate were brought together in a hot-embosser (HEX03, Jenoptik Mikrotechnik GmbH, Germany) and a high pressure and temperature were applied to the assembly for a defined period of time.

A series of tests have been performed on a dummy Zeonor slide, in order to optimize the embossing conditions and to provide a set of working parameters (e.g. applied force, temp) for precise transfer of the channel pattern onto the polymer matrix. Fig. 5.32 illustrates two sample channels hot-embossed in Zeonor by applying 140 °C and 9 kN of pressure for 5 min.

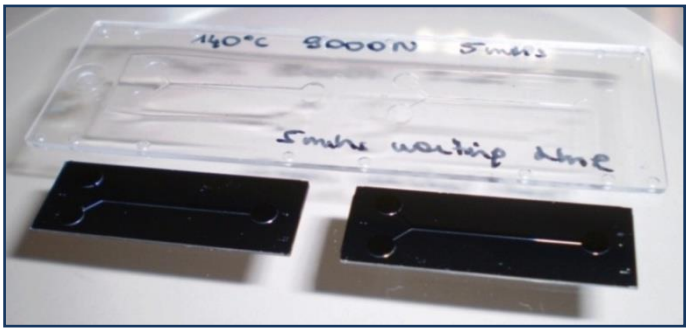


Fig. 5.32. Microfluidic channels hot-embossed in Zeonor by application of 140 ^{o}C and 9 kN for 5 min.

Following the molding step, the quality of imprinted features was visually examined and further assessed by SEM and Tencor measurements. Dimensions of the embossed channels have been investigated using a Zygo optical surface profiler (ZygoLot GmbH, Germany). Based on the analysis of the embossed patterns, the highest accuracy of the channel geometries in Zeonor has been obtained at 145 ºC and 10 kN of applied force, when the processing has been carried out for 360 s. Additionally, a waiting time of 500 s has been employed prior to each thermal molding run. Fig. 5.33 depicts an SEM micrograph of a channel, design 5 (1000 μm wide), hot-embossed in Zeonor and casted in PDMS for better visual examination. The width of the imprinted feature has been determined to 1 mm, confirming a precise tranfer of the channel geometry onto the polyme substrate.

The height of the microfluidic channels, fabricated using the selected embossing parameters (145 °C, 10 kN, 360 s) and determined by Zygo measurements (Fig. 5.34), was in all cases approximately 100 μm, which is in an excellent agreement with the projected height for all channel designs. Fig. 5.34 illustrates Zygo readings recorded at the top view and a cross section of the fabricated channel.

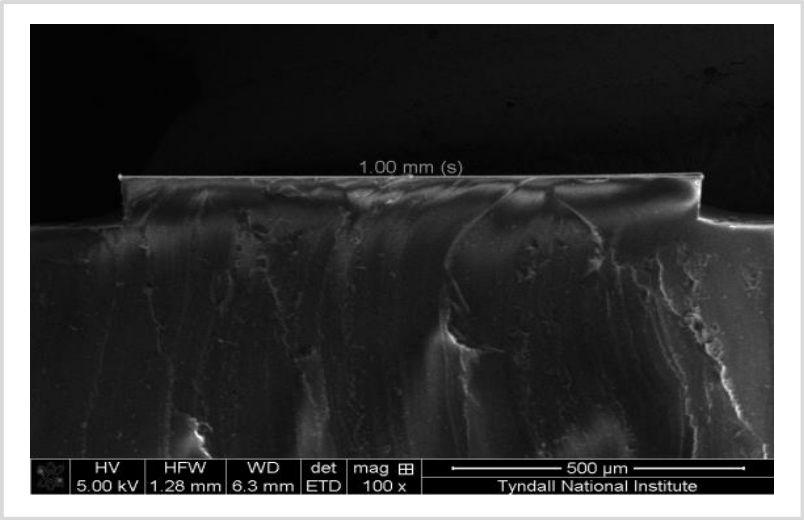


Fig. 5.33. Scanning Electron Micrograph featuring a PDMS cast of a microfluidic channel (design 5) hot-embossed in Zeonor.

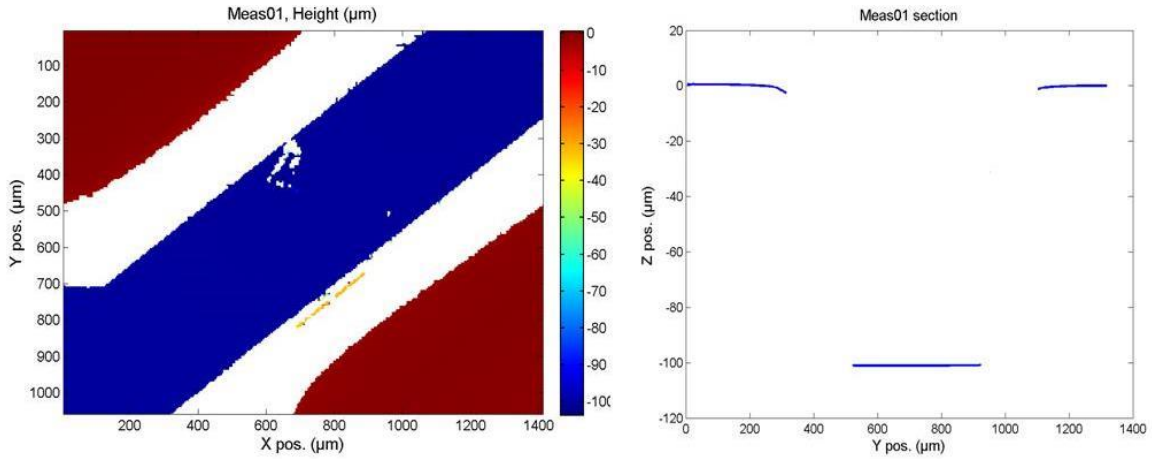
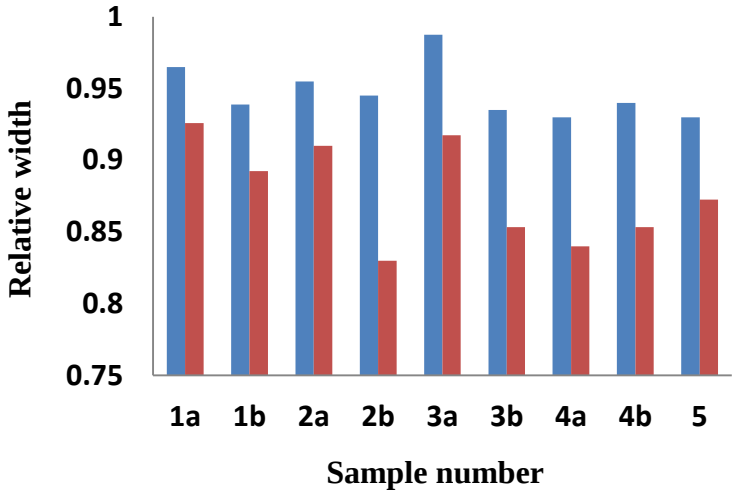


Fig. 5.34. Zygo measurements of the channel's height; top view (left), cross section (right). Indicated as red are walls of the channel, blueis the bottom of the design, white areas are regions inaccessible, due to shadowing effect.

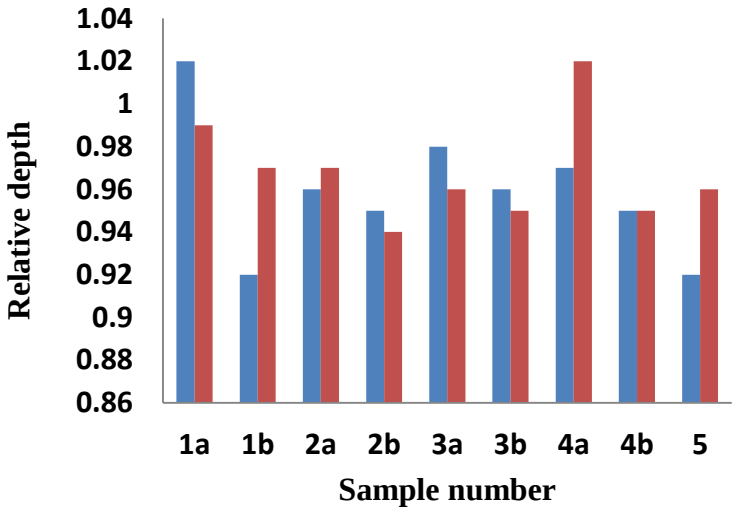
Fig. 5.35 and Fig. 5.36, represent comparison of the hot-embossed channel and inlet dimensions obtained by Tencor measurements with the theoretical values for the width (Fig. 5.35) and the depth (Fig. 5.36). A supplementary table incorporating the ratio

of the experimental (μm) to the theoretical (μm) dimensions (relative, dimensionless values) for the channel and inlets have also been provided.



sample nr	*channel*	*inlet*
1a	0.965	0.926
1b	0.939	0.893
2a	0.955	0.910
2b	0.945	0.830
3a	0.988	0.918
3b	0.935	0.853
4a	0.930	0.840
4b	0.940	0.853
5	0.930	0.873

Fig. 5.35. Ilustrates relative width of the channel (blue) and inlet (red) patterns for a series of hot-embossed Zeonor samples.



sample nr	*channel*	*inlet*
1a	1.020	0.990
1b	0.920	0.970
2a	0.960	0.970
2b	0.950	0.940
3a	0.980	0.960
3b	0.960	0.950
4a	0.970	1.020
4b	1.020	0.990
5	0.920	0.970

Fig. 5.36. Represents relative depth of the channel (blue) and inlet (red) patterns for a series of Zeonor samples hot-embossed at 145 ℃, 10 kN for 360 s.

As indicated in Fig. 5.35 and Fig. 5.36, the relative width and depth of the channel and inlet patterns, calculated as the ratio of the experimental (Tenkor measurements) to the theoretical (design) values, oscilate around 1, indicating a satisfying correspondence of the fabricated patterns with the dimensions implied by the design.

5.7.1. Challenges associated with the channel fabrication.

A number of challenges associated with the manufacturing of the microfluidic channels have been encountered in due course of this fabrication work. The main issue was related with the size of the projected features, ranging from 100 μm up to 1 mm. Investigation of the preliminary batch of the silicon stamps for the channel patterning, revealed the presence of unetched silicon outlayers and undefined inner structures. These can be seen in Fig. 5.37, which represents microscopic images of the areas around the channel and the surrounding of the inlet, obtained with a high resolution Nikon Eclipse LV 150 microscope (Aquilant Scientific, UK).

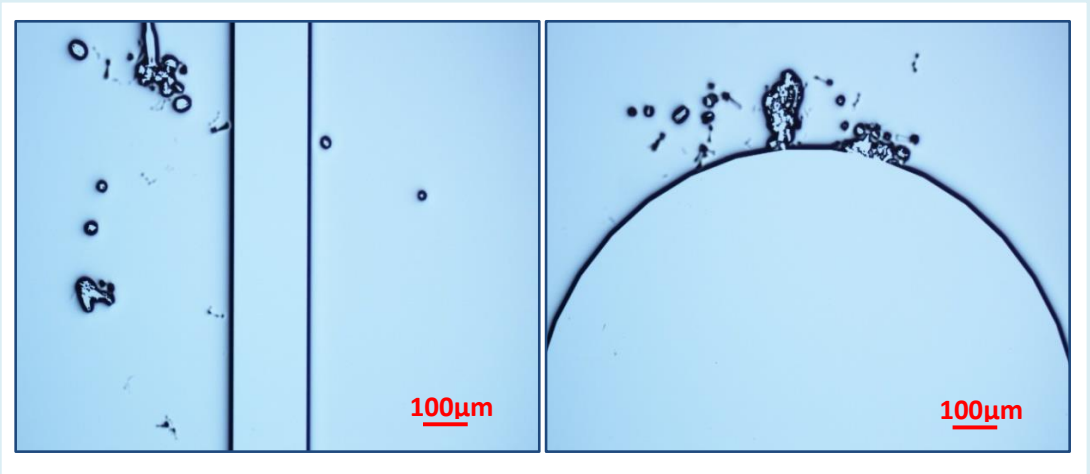


Fig. 5.37. Microscopic images of the silicon masks for the channel fabrication. "Bubbles" of un-etched silicon are visible around the inlet points and the main body of the channel.

Images taken at high magnifications further confirmed the imperfections of the etching technique, when processing the circular features of very small sizes (Fig. 5.38)

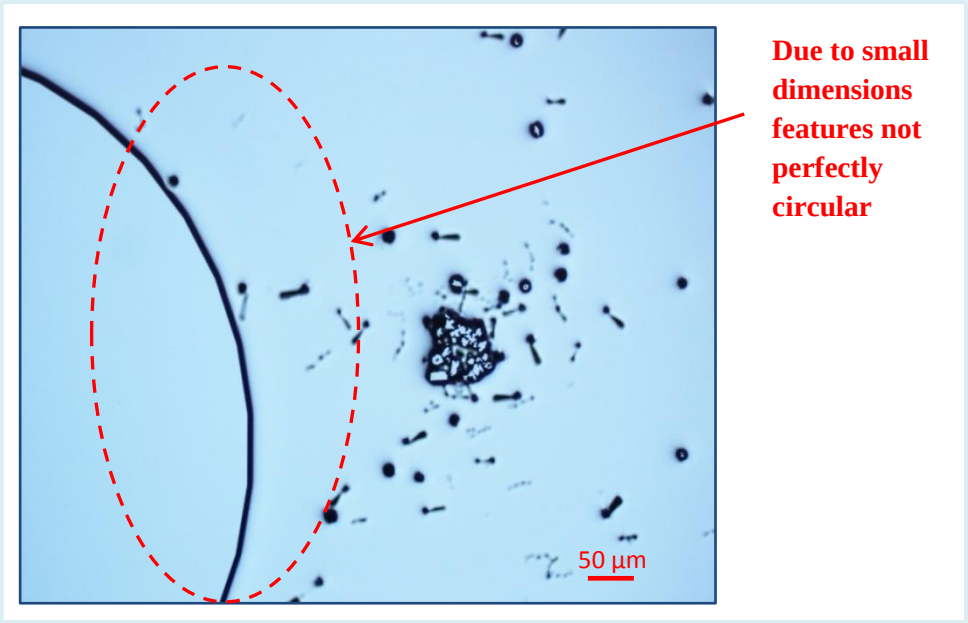


Fig. 5.38. Imperfections of the etching method, due to small dimensions of the inlet features.

The subsequent batch of silicon masks was characterised by much better quality, however the stamps were still very brittle and prone to breaking. In this light, hot-embossing of the channels with the fabricated silicon masters was a challenging task, as it required a perfect alignment of the padding glass slides supporting the Zeonor substrate and the patterned silicon stamp. If not centred, the silicon would crack immediately once the pressure was applied, concurrently damaging the underlying polymer material. Furthermore, the release of the stamps following the hot-embossing step and cutting the channel design out from the rigid Zeonor slides were problematic and required the use of a sharp blade of a knife.

5.8. Assembly of the microfluidic devices.

For a successful operation of the biofuel cell in microfluidic environment, polymer substrates bearing the patterned electrodes and microfabricated channels need to be brought together in a stable, water-tight seal. The integration of the cellular components is schematically illustrated in Fig. 5.39.



Fig. 5.39. Schematic of the electrode and channel assembly.

5.8.1. Bonding of the channels to electrodes in Zeonor.

Bonding of two Zeonor substrates, top channel compartment and bottom electrode unit, has been initially investigated using modified protocols, described in [62, 63]. In this procedure, a thin film of liquid PDMS (10-25 μm) was employed as an adhesive layer, holding the two polymer parts together. Prior to the assembly, the Zeonor substrates have been exposed to the oxygen plasma at 900 mTorr and high power setting for 1 min for three consecutive cleaning cycles. 2 mL of PDMS solution was prepared fresh by mixing the base and the curing agent in a 10:1 (w/w) ratio. The elastomer was degassed at -20 ºC for 40 min and finely coated on a microscopic glass slide. A thin layer of PDMS was then transferred onto the Zeonor substrate with embossed microfluidic channel by pressing the polymer against the glass slide. Following the transfer of PDMS, a Zeonor substrate with patterned electrode was placed on top of the channels and the pressure was applied using a clamp. The assembly was pre-cured at room temperature for 20 hours following which the device was placed in the oven at 90 ºC for 30 min [62]. Additionally, a one-step incubation in the oven at 70 ºC for 1 h [63] has also been considered. The bonding of Zeonor substrates in the presence of a thin layer of PDMS adhesive is illustrated in Fig. 5.40.

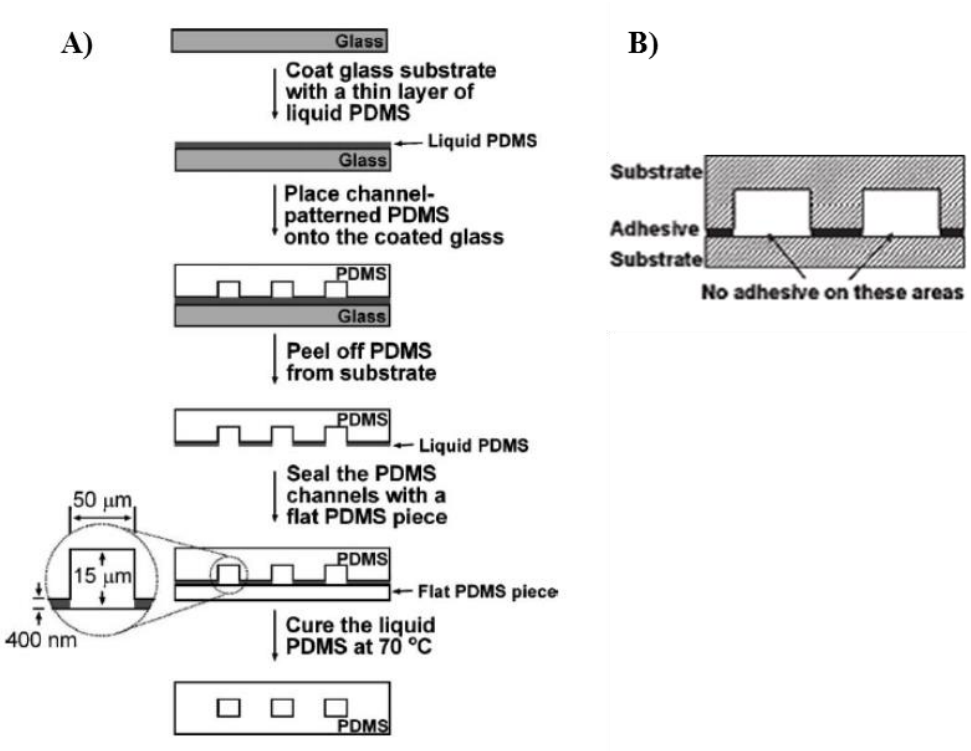


Fig. 5.40. A) Schematic of the bonding protocol using PDMS as the adhesive layer; B) graphical representation of the substrates prior to thermal curing [62].

In order to minimize the risk of blocking the channels with PDMS glue and to provide higher bonding reproducibility, PDMS dilution in toluene was spun-coated onto a clean microscopic glass slide or a glass wafer using a WS-650-15 Spin Coater (Laurell Technologies Corporation, USA). PDMS solution (base: curing agent in 10:1 w/w ratio) was mixed with toluene in 1:4 ratio and deposited on a clean glass wafer in a two-step process (3 s at 500 rpm and 60 s at 1500 rpm). Following the spin coating, Zeonor channels were pressed against the thin coating of PDMS and clamped with Zeonor substrate carrying the electrodes. The device was then cured at room temperature or in the oven. Additionally, bonding of Zeonor slides was also performed using a low temperature UV / ozone treatment, according to the protocol in [49]. In this method, the polymer substrates were thoroughly cleaned in IPA, rinsed with DI and dried in the nitrogen stream. UV / O_3 exposure was carried out in a UV/Ozone Procleaner^{TM} Plus instrument (BioForce Nanosciences, USA) at high power settings for 20 min. Following the treatment, the Zeonor units were manually aligned and assembled in a hot-embosser for 90 s at 60 ºC and an applied force of 10 kN.

The efficiency of the Zeonor - Zeonor assembly was also investigated using organic solvents, according to the protocol described in [64]. The bonding solution was composed of 20 % (by weight) of 1, 2-dichloroethane and 80 % ethanol. Both reagents were of analytical grade. Plain Zeonor slides were cleaned with IPA, immersed in acetone for a period of 10 s and dried in a nitrogen stream. Following the cleaning step, 5 drops of the bonding mixture were applied evenly onto each polymer surface to provide a uniform coating. Zeonor substrates were further clamped in a room temperature for 30 min. Modification of the above protocol employed exposing the polymer to cyclohexane vapors for 10 min prior to bonding. In this method, approximately 20 mL of cyclohexane has been transferred into a glass dish and placed on a hot plate, adjusted to 45 ºC. Zeonor compartment bearing the channel was immobilized at the bottom of a Petri dish and placed over the solvent surface (Fig. 5.41). The substrates were exposed to the vapors for 10 min, following which they were brought together in a clamp.



Fig. 5.41. Solvent bonding of Zeonor substrates using cyclohexane.

Although numerous bonding techniques have been undertaken in the course of this fabrication work, obtaining a permanent assembly of the channels and electrodes patterned in Zeonor was proved to be challenging. UV/ Ozone and organic solvent treatments supported by the application of a pressure in a clamp resulted in a very weak and short - term seal between the two compartments. Additional implementation of a thin PDMS film, manually applied or spun - coated, did not improve the adhesion of Zeonor substrates in the presence of metal electrodes.

5.8.2. Assembly of the Zeonor electrodes to PDMS channels.

Following the preliminary bonding approach, channels in Zeonor have been replaced with PDMS. Many accounts on the successful bonding of PDMS to a variety of substrates have been reported in the literature [63, 65-67]. One of the best known procedures to achieve a permanent attachment to other silicone based materials is plasma activation of the PDMS surface. PDMS is a polymer composed of repeating monomers of silicon oxide and a methyl group- [SiO-(CH_3)]. The intrinsic hydrophobic nature of PDMS prevents an easy adhesion to other materials and can be realized only when the surface is made hydrophilic. In order to make the polymer temporarily hydrophilic, limited exposure to oxygen plasma can be applied. In general, the O_2 plasma acts as an oxidizing agent. It removes the hydrogen atoms from the surface of the PDMS, subsequently creating free carbon radicals, which upon contact with oxygen molecules result in the formation of functional hydroxyl groups. Plasma activation has been found to strongly promote the permanent adhesion of PDMS to glass, silicon and various polymer substrates and hence has been considered as the initial surface treatment employed in the assembly of Zeonor and PDMS based microfluidic devices.

Plasma activation of the PDMS channels

Following preparation, the PDMS surface is hydrophobic and non-reactive. In order to be able to bind it to Zeonor, the surface properties had to be altered in the oxygen plasma. Reactive oxygen species formed in the plasma chamber, attack the methyl groups of silyl (Si-CH_3) and replace them with -OH, producing highly hydrophilic silanol functions (Si-OH) as shown in Fig. 5.42.

Surface modification by plasma treatment is only temporary and after approximately 30 min silanol groups migrate to the PDMS bulk and cross-link with the polymerized entity, restoring the polymer's original hydrophobic character. This process can be effectively impeded by storing PDMS in polar solvents.

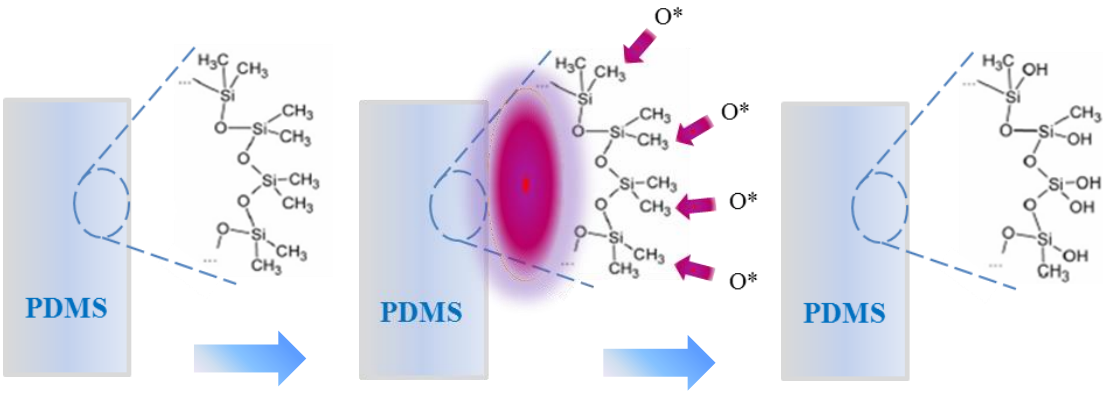


Fig. 5.42. Plasma activation of the PDMS surface.

As demonstrated in the literature [21, 68], the quality of the surface treatment and associated strength of the assembly with other materials depend strongly on the plasma characteristics, with the improved bonding efficiency reported typically at high power (20 Watts RF) and for short periods of time (20 s). Prolonged exposure to high power plasma yields a deep oxidation of PDMS surface and may lead to deactivation of the available chemical groups. Low pressure reactors provide directional bombardment using highly energetic ions, which can effectively disturb the PDMS layer and weaken the interactions at the surface.

PDMS substrates age with time and at a certain point can no longer be activated by the plasma exposure. Although aged PDMS surfaces can be recovered in 5-10 min baths of concentrated HCl acid [21], it is highly recommended to prepare the polymer fresh prior to any experimental work. Successful activation of the PDMS surface can be confirmed by the contact angle measurements, where the reduction in the values recorded following the treatment can be as high as 100 °. In the course of this work, the optimum plasma parameters have been obtained at 900 millitorrs of pressure and high power setting for 1min.

Binding of PDMS channels to metal electrodes on Zeonor

A number of bonding techniques to attach PDMS to various polymer substrates has been described, however by far; the most convenient and hence still the most prevailing approach is plasma activation. In addition, many authors report the use of UV / O_3 treatment in order to activate the siloxane surface prior to bonding [49, 68]. The principle

of the ozone treatment also relies on the formation of highly reactive functional groups through surface oxidation. Depending on the ultimate application, bonding of PDMS to certain substrates can also be achieved using a variety of commercial glues (e.g. Araldite), adhesives of medical grade (e.g. polyimide Tape PPTDE-2, [69]) or biocompatible epoxies (e.g. Adhesive Prime Coat, [11]). A thin layer of PDMS, spun coated onto the substrates and cured in the oven or at a hot press has also been employed by numerous researchers to provide a seal between two samples [70]. Despite the effective binding of the PDMS to glass and silicon materials, several authors demonstrated that a stable bonding with a number of polymer substrates in the presence of metals is often problematic [11].

The initial bonding of PDMS channels and Zeonor based electrodes, performed in due course of this work, involved exposing the PDMS surface to oxygen plasma at 900 mTorr and high power for 1min. Immediately after the treatment, the PDMS cover was placed on the Zeonor electrode part and a pressure was applied manually for 3 min. The assembly was left to cure overnight to increase the efficiency of the bond. The plasma activation approach, although providing a relatively sufficient temporal attachment, unfortunately did not result in a long – term binding of the Zeonor and PDMS substrates, which is an essential prerequisite for successful operation of the biofuel cell in flowing conditions.

Varying the plasma conditions and the application of a number of commercial glues (e.g. Araldite) and biocompatible adhesives have been further considered. Nevertheless, none of the investigated bonding procedures was sufficient to create a strong and long-lasting seal; in certain cases leading to substrate damage (blocked or deformed channels). Elastomeric polymers, such as polydimethylsiloxane, display outstanding non-permanent adhesion to a wide range of substrates [71], which suitable for a number of applications, cannot satisfy the requirements of the microfluidic devices. Yet, only a narrow group of materials including glass, polystyrene and silicon derivatives can create a permanent seal with PDMS upon its surface activation [8]. As demonstrated in due course of this work, bonding in the presence of metal electrodes further inhibits the formation of a long-lasting assembly. In addition, due to limited duration of the plasma activation (<1 min) and the distant location of the Flip Chip bonder, the PDMS and Zeonor could not be aligned automatically using the instrument. For that reason, all devices produced as part of this thesis had to be assembled manually, resulting in human imprecisions and the lack of reproducibility in the alignment of the generated platforms.

A solution to the bonding issue has been found in a form of an Adhesive Sylgard Prime Coat (Dow Corning). As reported in [11], dilutions of the adhesive in heptane (10-100 % by volume), followed by plasma activation, create an irreversible bond between polymer substrates, even in the presence of the metals.

PDMS and Zeonor substrates were cleaned in the oxygen plasma (3 cycles of 1 min at 900 mTorr and high power), rinsed with copious amounts of IPA and deionized water and blow-dried in the nitrogen stream. 10 % concentration of the adhesive was prepared fresh in heptane by mixing 1 mL of the primer with 9 mL of the solvent. A thin layer of the adhesive mixture was then applied evenly on the surface of PDMS channel part avoiding any contact with the channel and exposed to the O_2 plasma for 40 s (900 mTorr and high power). Following the surface activation, the PDMS cover was immediately placed on top of the Zeonor slide bearing Au and Pt electrodes and the pressure was manually applied for 3 min. The assembly was left to cure overnight and the effectiveness of the bond was tested the following morning. Fig. 5.43 represents a Zeonor - PDMS based device assembled using the Adhesive Prime Coat activated in the oxygen plasma, according to the discussed procedure.

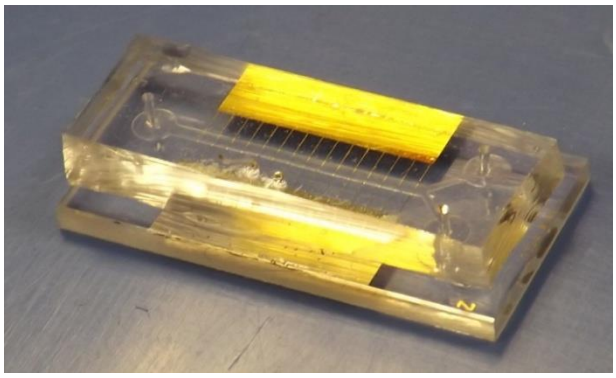


Fig. 5.43. Microfluidic platform composed of top PDMS channel (design 4) and Zeonor bottom compartment with patterned Au and Pt electrodes (design 2) sealed with Adhesive Prime Coat activated in the O_2 plasma.

Tab. 5.12 summarizes the main bonding techniques employed in the assembly of Zeonor to Zeonor and Zeonor to PDMS electrode and channel compartments of the biofuel cell. Despite the number of approaches, the successful binding of the polymer substrates

has been demonstrated only in the presence of 10 % (by volume) Adhesive Sylgard Prime Coat (Dow Corning) in heptane.

Tab. 5.12. Summary of main bonding approaches for Zeonor and PDMS substrates

Zeonor - Zeonor	***Zeonor - PDMS***
PDMS adhesion layer	Oxygen plasma bonding
UV/O_3 bonding	Commercially available glues e.g. Araldite
Solvent bonding with 20 % DCE : 80% EtOH; in the presence of cyclohexane	Adhesive Sylgard Prime Coat in heptane (10 %)

In addition, reversible bonding of PDMS and Zeonor samples was achieved using a microfluidic polycarbonate holder fabricated in the Mechanical Workshop at the Tyndall National Institute, discussed in Chapter II of this Ph.D. thesis.

5.9. Conclusions.

This chapter describes the design and fabrication of microfluidic platforms for the development of enzymatic biofuel cells. The obtained devices are composed of a bottom Zeonor substrate with gold anodes and platinum cathodes and top microfluidic compartment with channels in PDMS. A number of channel and electrode geometries have been obtained for diverse experimental conditions, based on the theoretical investigations of the microfluidic system, discussed in Chapter IV. Corresponding processes for the device fabrication were developed and the components for the biofuel cells have been successfully obtained.

Fabrication of the polymer platforms was carried out in three separate processing steps involving the use of the state – of – the – art microfabrication technologies. Various bonding techniques have been investigated, in order to assemble the electrode and the channel compartments for a future generation of platforms for microfluidic enzymatic biofuel cells. Among the discussed binding approaches, the most successful was the

application of an Adhesive Sylgard Prime Coat (10 % solution in heptane) and hence it is recommended for further studies on the Zeonor and PDMS substrates. A number of fabrication issues have been encountered during the manufacturing step, solutions to which were proposed accordingly. Suggestions for the improvement of the fabrication process, in order to enhance the device performance, have been proposed in each chapter section.

Future work needs to emphasize the need for bonding automation in order to provide reproducibility and high precision alignment by, for instance, using a Flip Chip Bonder (Fig. 5.44). To counteract the challenges related with the component binding, an alternative design encompassing both the channels and the electrodes on a common substrate could be employed. This approach should also minimize any issues with the alignment of the required cellular units. In order to increase the lifetime of the channel stamps, alternatives to silicon should be considered. Hot-embossing of the channel patterns in polymers could be substituted with highly accurate micromachining technologies.

Following successful on-chip fabrication and electrochemical characterization in buffered solutions containing redox species, gold electrodes were modified with NPG structures. The quality of resulted deposits was verified using high resolution SEM instrumentation. The electrochemical response of gold nanostructures was studied in 0.1 M H_2SO_4 and buffered media containing substrate and mediator molecules for GOX, confirming increased electrochemical response of the NPG deposits with respect to bare gold.

Nanoporous Gold Structures exhibit high chemical, mechanical and thermal stability [56]. Unlike typical gold nanoparticles frequently employed in biofuel cells, they do not require carbon support and, as such, can be deposited on metal substrates to form robust and stable modification layers. In theory, porous structure of NPG promotes enhanced mass transfer of reactants towards the active surface of gold and enables efficient release of reaction by-products. Due to their excellent electrical conductivity and unique surface morphology, NPG layers provide an accommodating and stable environment for biocatalyst immobilization. Electronic properties of the porous features favor the intimate contact with the protein, increasing the efficiency of catalysis under

investigation. Although the surface areas of the NPG electrodes are considerably higher with respect to bare Au electrodes, the electrochemical response in static environment is significantly compromised by the diffusion of species in the nanostructures and possible steric hindrance encountered by larger biomolecules [72]. Therefore conducting the same experiments under flowing conditions should significantly enhance the response for NPG electrodes.

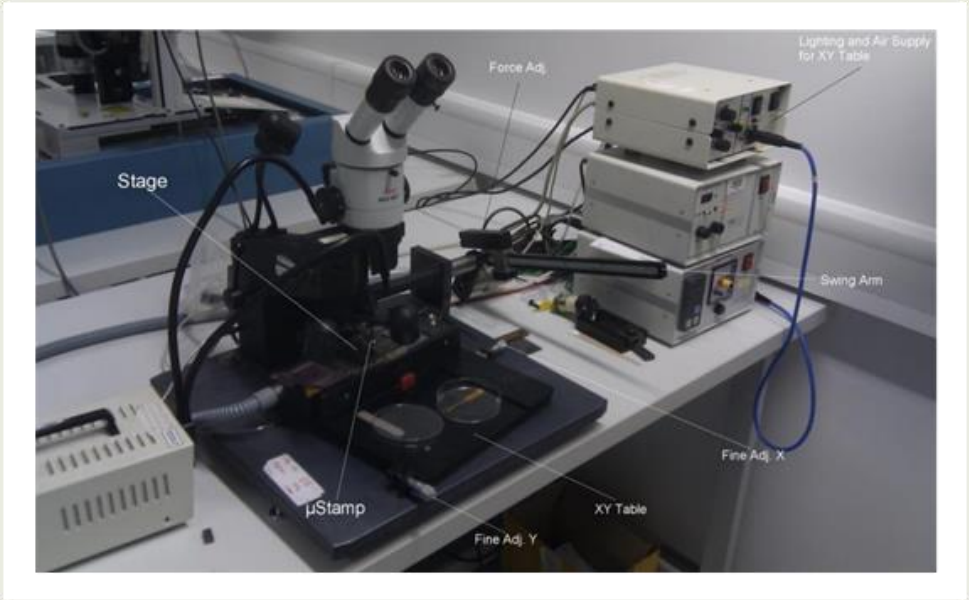


Fig. 5.44. Flip Chip Bonder for the precise alignment of device components; consists of the stage, micro stamp, elements for the adjustment of the substrates and applied force, light source.

5.10. Bibliography.

1. Rincón, R.A., et al., *Enzymatic fuel cells: Integrating flow-through anode and air-breathing cathode into a membrane-less biofuel cell design.* Biosensors and Bioelectronics, 2011. **27**(1): p. 132-136.
2. Becker, H. and L.E. Locascio, *Polymer microfluidic devices.* Talanta, 2002. **56**(2): p. 267-287.
3. Rolland, J.P., et al., *Solvent-resistant photocurable "liquid teflon" for microfluidic device fabrication.* Journal of the American Chemical Society, 2004. **126**(8): p. 2322-2323.
4. Trott, G.R. and A. Shorey. *Glass wafer mechanical properties: A comparison to silicon*. in *Microsystems, Packaging, Assembly and Circuits Technology Conference (IMPACT), 2011 6th International*. 2011. IEEE.
5. Fiorini, G.S. and D.T. Chiu, *Disposable microfluidic devices: fabrication, function, and application.* BioTechniques, 2005. **38**(3): p. 429-446.
6. Barker, S.L., et al. *Fabrication, derivatization, and applications of plastic microfluidic devices*. in *Environmental and Industrial Sensing*. 2001. International Society for Optics and Photonics.
7. Branham, M.L., W.A. MacCrehan, and L.E. Locascio, *Chemical mapping of imprinted plastic microchannel surfaces using group-specific fluorescent probes.* J. Capillary Electrophor. Microchip Technol.,1999. **6**(1/2): p. 43-50.
8. Duffy, D.C., et al., *Rapid prototyping of microfluidic systems in poly (dimethylsiloxane).* Analytical chemistry, 1998. **70**(23): p. 4974-4984.
9. Madou, M.J., *Fundamentals of microfabrication: the science of miniaturization. 2002*. Second Edition, CRC Press LLC, Boca Raton, FL
10. Hufnagel, H., et al., *An integrated cell culture lab on a chip: modular microdevices for cultivation of mammalian cells and delivery into microfluidic microdroplets.* Lab on a Chip, 2009. **9**(11): p. 1576-1582.
11. Kim, L., et al., *A practical guide to microfluidic perfusion culture of adherent mammalian cells.* Lab on a Chip, 2007. **7**(6): p. 681-694.
12. Lee, J.N., C. Park, and G.M. Whitesides, *Solvent compatibility of poly (dimethylsiloxane)-based microfluidic devices.* Analytical Chemistry, 2003. **75**(23): p. 6544-6554.
13. Hierlemann, A., et al., *Microfabrication techniques for chemical/biosensors.* Proceedings of the IEEE, 2003. **91**(6): p. 839-863.
14. VerLee, D., et al., *Solid State Sensor and Actuator Workshop*, 1996, Hilton Head Island, South Carolina.
15. Martynova, L., et al., *Fabrication of plastic microfluid channels by imprinting methods.* Analytical Chemistry, 1997. **69**(23): p. 4783-4789.
16. Becker, H., W. Dietz, and P. Dannberg. *Microfluidic manifolds by polymer hot embossing for μ-TAS applications*. in *Micro Total Analysis Systems' 98*. 1998, Banff, Canada. p. 253-256
17. Locascio, L.E., et al. *Plastic microfluid devices for clinical measurements*. in *Micro Total Analysis Systems' 98*. 1998, Banff, Canada. p. 367-370
18. McCormick, R.M., et al., *Microchannel electrophoretic separations of DNA in injection-molded plastic substrates.* Analytical Chemistry, 1997. **69**(14): p. 2626-2630.
19. Kellogg, G.J., et al. *CENTRlFUGAL MlCROFLUlDlCS: APPLlCATlONS*. in *Micro Total Analysis Systems 2000*. 2000, Enschede, The Netherlands, p. 239-242

20. Hosokawa, K., T. Fujii, and I. Endo. *Hydrophobic Microcapillary Vent for Pneumatic Manipulaiton of Liquid in μtas*. in *Micro Total Analysis Systems' 98*. 1998. Banff, Canada. p. 307-310.
21. Jo, B.-H., et al., *Three-dimensional micro-channel fabrication in polydimethylsiloxane (PDMS) elastomer.* Microelectromechanical Systems, Journal of, 2000. **9**(1): p. 76-81.
22. Roberts, M.A., et al., *UV laser machined polymer substrates for the development of microdiagnostic systems.* Analytical Chemistry, 1997. **69**(11): p. 2035-2042.
23. Lee, L., et al. *Key elements of a transparent teflon® microfluidic system*. in *Micro Total Analysis Systems' 98*. 1998. Banff, Canada. p. 245-248.
24. Debe, M.K., *Electrocatalyst approaches and challenges for automotive fuel cells.* Nature, 2012. **486**(7401): p. 43-51.
25. Koo, J. and C. Kleinstreuer, *Liquid flow in microchannels: experimental observations and computational analyses of microfluidics effects.* Journal of Micromechanics and Microengineering, 2003. **13**(5): p. 568.
26. Sun, M., et al., *Characterization of microfluidic fuel cell based on multiple laminar flow.* Microelectronic Engineering, 2007. **84**(5): p. 1182-1185.
27. Lim, K.G. and G.T.R. Palmore, *Microfluidic biofuel cells: the influence of electrode diffusion layer on performance.* Biosensors and Bioelectronics, 2007. **22**(6): p. 941-947.
28. Liu, J., et al., *High-performance bioanode based on the composite of CNTs-immobilized mediator and silk film-immobilized glucose oxidase for glucose/O_2 biofuel cells.* Biosensors and Bioelectronics, 2012. **31**(1): p. 170-175.
29. Ivanov, I., T. Vidaković-Koch, and K. Sundmacher, *Recent Advances in Enzymatic Fuel Cells: Experiments and Modeling.* Energies, 2010. **3**(4): p. 803-846.
30. Li, X., J. Tian, and W. Shen, *Thread as a versatile material for low-cost microfluidic diagnostics.* ACS Applied Materials & Interfaces, 2009. **2**(1): p. 1-6.
31. Shitanda, I., et al., *Flexible and high-performance paper-based biofuel cells using printed porous carbon electrodes.* Chem. Comm., 2013. **49**(94): p. 11110-11112.
32. van den Berg, A., H.G. Craighead, and P. Yang, *From microfluidic applications to nanofluidic phenomena.* Chemical Society Reviews, 2010. **39**(3): p. 899-900.
33. Manz, A., N. Graber, and H. Widmer, *Miniaturized total chemical analysis systems: a novel concept for chemical sensing.* Sensors and Actuators B: chemical, 1990. **1**(1): p. 244-248.
34. Gravesen, P., J. Branebjerg, and O.S. Jensen, *Microfluidics-a review.* Journal of Micromechanics and Microengineering, 1993. **3**(4): p. 168.
35. Bayraktar, T. and S.B. Pidugu, *Characterization of liquid flows in microfluidic systems.* International Journal of Heat and Mass Transfer, 2006. **49**(5): p. 815-824.
36. Nguyen, N.-T. and S.T. Wereley, *Fundamentals and applications of microfluidics* 2002: Artech House,Inc, Norwood.
37. Tamaki, T., T. Ito, and T. Yamaguchi, *Modelling of Reaction and Diffusion Processes in a High-surface-area Biofuel Cell Electrode Made of Redox Polymer-grafted Carbon.* Fuel Cells, 2009. **9**(1): p. 37-43.
38. Lee, J., et al., *Optimization of microfluidic fuel cells using transport principles.* Analytical Chemistry, 2007. **79**(19): p. 7301-7307.
39. Choban, E.R., et al., *Microfluidic fuel cell based on laminar flow.* Journal of Power Sources, 2004. **128**(1): p. 54-60.
40. Yoon, S.K., G.W. Fichtl, and P.J. Kenis, *Active control of the depletion boundary layers in microfluidic electrochemical reactors.* Lab on a Chip, 2006. **6**(12): p. 1516-1524.

41. Stroock, A.D., et al., *Chaotic mixer for microchannels.* Science, 2002. **295**(5555): p. 647-651.
42. Günther, A. and K.F. Jensen, *Multiphase microfluidics: from flow characteristics to chemical and materials synthesis.* Lab on a Chip, 2006. **6**(12): p. 1487-1503.
43. Becker, H. and C. Gärtner, *Polymer microfabrication technologies for microfluidic systems.* Analytical and Bioanalytical Chemistry, 2008. **390**(1): p. 89-111.
44. Fan, R., et al., *Integrated barcode chips for rapid, multiplexed analysis of proteins in microliter quantities of blood.* Nature Biotechnology, 2008. **26**(12): p. 1373-1378.
45. Saadi, W., et al., *A parallel-gradient microfluidic chamber for quantitative analysis of breast cancer cell chemotaxis.* Biomedical Microdevices, 2006. **8**(2): p. 109-118.
46. Dimov, I.K., et al., *Stand-alone self-powered integrated microfluidic blood analysis system (SIMBAS).* Lab on a Chip, 2011. **11**(5): p. 845-850.
47. Hou, H.W., et al., *Microfluidic devices for blood fractionation.* Micromachines, 2011. **2**(3): p. 319-343.
48. Sun, X. and K.D. Gillis, *On-chip amperometric measurement of quantal catecholamine release using transparent indium tin oxide electrodes.* Analytical Chemistry, 2006. **78**(8): p. 2521-2525.
49. Tsao, C., et al., *Low temperature bonding of PMMA and COC microfluidic substrates using UV/ozone surface treatment.* Lab on a Chip, 2007. **7**(4): p. 499-505.
50. Gooding, J., V. Praig, and E. Hall, *Platinum-catalyzed enzyme electrodes immobilized on gold using self-assembled layers.* Analytical Chemistry, 1998. **70**(11): p. 2396-2402.
51. Stackelberg, M.V., M. Pilgram, and V. Toome, *Bestimmung von diffusionskoeffizienten einiger ionen in wäbriger lösung in gegenwart von fremdelektrolyten. I.* Z. Elektrochem, 1953. **57**: p. 342-350.
52. Xu, C., et al., *Low temperature CO oxidation over unsupported nanoporous gold.* Journal of the American Chemical Society, 2007. **129**(1): p. 42-43.
53. Pattrick, G., et al., *The potential for use of gold in automotive pollution control technologies: a short review.* Topics in Catalysis, 2004. **30**(1-4): p. 273-279.
54. Zielasek, V., et al., *Gold catalysts: nanoporous gold foams.* Angewandte Chemie International Edition, 2006. **45**(48): p. 8241-8244.
55. Qiu, H., et al., *Adsorption of laccase on the surface of nanoporous gold and the direct electron transfer between them.* The Journal of Physical Chemistry C, 2008. **112**(38): p. 14781-14785.
56. Nagle, L.C. and J.F. Rohan, *Nanoporous gold anode catalyst for direct borohydride fuel cell.* International Journal of Hydrogen Energy, 2011. **36**(16): p. 10319-10326.
57. Ji, C. and P.C. Searson, *Synthesis and characterization of nanoporous gold nanowires.* The Journal of Physical Chemistry B, 2003. **107**(19): p. 4494-4499.
58. Liu, Z. and P.C. Searson, *Single nanoporous gold nanowire sensors.* The Journal of Physical Chemistry B, 2006. **110**(9): p. 4318-4322.
59. Molina Concha, B. and M. Chatenet, *Direct oxidation of sodium borohydride on Pt, Ag and alloyed Pt–Ag electrodes in basic media. Part I: Bulk electrodes.* Electrochimica Acta, 2009. **54**(26): p. 6119-6129.
60. Molina Concha, B. and M. Chatenet, *Direct oxidation of sodium borohydride on Pt, Ag and alloyed Pt–Ag electrodes in basic media: Part II. Carbon-supported nanoparticles.* Electrochimica Acta, 2009. **54**(26): p. 6130-6139.

61. Trasatti, S. and O. Petrii, *Real surface area measurements in electrochemistry.* Pure and Applied Chemistry, 1991. **63**(5): p. 711-734.
62. Chow, W.W., et al. *Microfluidic channel fabrication by PDMS-interface bonding*. in *Microelectronics, MEMS, and Nanotechnology*. 2004. International Society for Optics and Photonics.
63. Wu, H., B. Huang, and R.N. Zare, *Construction of microfluidic chips using polydimethylsiloxane for adhesive bonding.* Lab Chip, 2005. **5**(12): p. 1393-1398.
64. Tsao, C.-W. and D.L. DeVoe, *Bonding of thermoplastic polymer microfluidics.* Microfluidics and Nanofluidics, 2009. **6**(1): p. 1-16.
65. Satyanarayana, S., R.N. Karnik, and A. Majumdar, *Stamp-and-stick room-temperature bonding technique for microdevices.* Microelectromechanical Systems, Journal of, 2005. **14**(2): p. 392-399.
66. Lee, K.S. and R.J. Ram, *Plastic–PDMS bonding for high pressure hydrolytically stable active microfluidics.* Lab on a Chip, 2009. **9**(11): p. 1618-1624.
67. Eddings, M.A., M.A. Johnson, and B.K. Gale, *Determining the optimal PDMS–PDMS bonding technique for microfluidic devices.* Journal of Micromechanics and Microengineering, 2008. **18**(6): p. 067001.
68. Kim, J.-H., et al., *A disposable thermopneumatic-actuated microvalve stacked with PDMS layers and ITO-coated glass.* Microelectronic Engineering, 2004. **73**: p. 864-869.
69. Nath, P., et al., *Polymerase chain reaction compatibility of adhesive transfer tape based microfluidic platforms.* Microsystem Technologies: p. 1-7.
70. Zhang, W., G. Ferguson, and S. Tatic-Lucic. *Elastomer-supported cold welding for room temperature wafer-level bonding*. in *Micro Electro Mechanical Systems, 2004. 17th IEEE International Conference on.(MEMS)*. 2004. IEEE.
71. Barker, S.L., et al., *Plastic microfluidic devices modified with polyelectrolyte multilayers.* Analytical Chemistry, 2000. **72**(20): p. 4899-4903.
72. Scanlon, M.D., et al., *Characterization of nanoporous gold electrodes for bioelectrochemical applications.* Langmuir, 2011. **28**(4): p. 2251-2261.

CHAPTER VI

IMMOBILIZATION OF ENZYME CATALYSTS

Research is to see what everybody else has seen, and to think what nobody else has thought.

A discovery is said to be an accident meeting a prepared mind.

Albert Szent- Györgyi

6.1. Introduction.

Enzymatic biofuel cells rely on an efficient communication between bioelectrochemical processes occurring at the anode and the cathode. As the thermodynamic driving force for these enzyme-driven power sources is governed by the electron transfer mechanism, effective electrical connection between the catalyst redox centre and the electrode surface is an essential requirement. Low electron exchange rates, frequently encountered in electrocatalysis, are typically triggered by the three-dimensional structure of the biomolecule, where the active centre is recurrently embedded deeply in the protein shell. In order to circumvent poor charge transfer, a number of solutions have been considered, predominantly the use of mediating molecules and redox polymers. Continuous efforts to achieve direct electrical contact between the active centres and the electrode surface have also been made, as some of the mediators can significantly decrease the operating potential of the cell and introduce certain toxicity. Since the majority of enzyme catalysts are not capable of the direct electron transfer, recent work has focused on the investigation of redox reactive polymers, as both enzyme encapsulation matrices and the facilitators of the electron driven processes. These materials can not only improve the charge transfer between the electrode and the catalyst's active site but can also provide enhanced surface area of the electrode and increased enzyme loading, leading to improved performance of the cell. The reported enzyme stabilisation and retained biological activity

in redox films have been previously employed for enzymatic biofuel cells with extended lifetime and superior operability.

6.1.1. Main objectives.

In order to efficiently carry out bioelectrochemical reactions, a stable and compatible immobilization of enzyme species is required.

In this chapter, the potential of the electrochemically assisted encapsulation of catalysts, providing promising insight into the development of enzymatic biofuel cells, is investigated. This work reviews the state – of – the – art biomolecule immobilization strategies and provides a comprehensive discussion on the selected encapsulation methods, supported by a detailed description of the system components. The immobilization and successful regeneration of cofactor and mediator molecules is also demonstrated and their role in the catalytic performance of modified electrodes validated. Two approaches have been considered as prospective host matrices for various biological catalysts, sol-gel and *o*-phenylenediamine. Electrodeposition of both materials under potential and time controlled conditions, resulted in a subsequent entrapment of the biomolecules suspended in the deposition bath.

Benefits and general conclusions on the performance of the employed encapsulation approaches are presented at the end of the chapter.

6.2. Review of key biomolecule immobilization strategies.

Effective and reproducible immobilization of catalysts onto or in a close proximity of the electrode surface is a vital requisite and one of the key challenges in the development of enzymatic biofuel cells and electrochemical biosensors, in general. In principle, the attachment should provide a reversible but stable incorporation of the species with an overall preservation of its natural biological functions, while ensuring excellent accessibility to the redox centre and defined conformational flexibility of incorporated molecules.

Conventional immobilization protocols are defined based on the degree of interaction with the biomolecule [1] and can be categorized into three main groups: physical adsorption [2, 3], entrapment in a matrix [4, 5] and grafting [5, 6].

Physical adsorption of species to a support

Adsorption of species on the electrode is a physical immobilization method, where by immersing in or casting the solution containing the active component, a reversible assembly is being formed on the surface. Generated films exhibit rather low mechanical strengths and are prone to desorption, a phenomenon frequently occurring upon slight changes in experimental conditions (e.g. pH, ionic strength).

Encapsulation of catalysts in polymer coatings

Entrapment of catalysts in a host matrix (e.g. a polymer) is a method, which gained rapid attention in the area of electrocatalysis in the past few decades. The encapsulation approach was of particular interest in this Ph.D. work, due to the possibility of a precise control of the enzyme layer parameters (e.g. location, thickness), and hence is discussed in detail.

In the early days, catalyst entrapment was carried out by simply mixing the species with a number of components and depositing the suspension on a surface of an appropriate support (e.g. electrode). Currently, in order to accurately control the thickness of the produced films, the encapsulation is typically obtained via electrodeposition under the conditions of a constant potential or current. Due to a large diversity of natural and synthetic organic polymers and inorganic substrates, as well as the simplicity of the preparation step, the method became one of the most extensive routes to enzyme immobilization used at present.

A number of redox, conducting or insulating polymer substrates has been used for immobilization procedures on electrode surfaces. Particular properties of the employed matrices and the specification of coating technique vary depending on the particular application. Electrochemically assisted deposition of polymer materials [7] from the supporting buffer solutions is frequently employed, when a precise control over the film parameters is required. Thickness of the electrogenerated polymer layer is governed by the deposition time and the magnitude of the applied potential. This is of particular consideration in the area of biosensing and power sources, where the diffusion of species across the polymer membrane is a key factor determining the success of the assay.

Unlike, self-assembled monolayers, which are typically formed on gold surfaces, electrogenerated polymer coatings can be obtained on a variety of electrode materials commonly used in electroanalytical chemistry (e.g. glassy carbon, platinum or ITO). Due to the abundance of a wide range of monomer substrates, low cost and simple preparation protocols, polymer electrodeposition has emerged as one of the most efficient and practical modification methods for biosensor and lab-on-chip applications.

Polymer materials can be defined based on their ability to conduct electrical charge and, as such, can be classified as either intrinsically conducting or insulating. Both are organic materials that can be electrodeposited on solid surfaces, once a relevant potential is applied. Conducting polymers, unlike their insulating counterparts, display high electrical conductivity but their mechanical properties differ from the ones offered by other commercial materials. Electrical properties of intrinsically conducting polymers can be fine-tuned through methods developed for organic synthesis. The majority of conducting polymers used up-to-date (polypyrrole, polyaniline etc.) can be generated from aqueous solutions upon mild oxidative conditions, a number of substrates requiring higher potential values (e.g. polythiophenes) or the presence of an acid (e.g. polyanilines).

The ability of polymers to form stable electrode coatings under moderate treatment has been widely reported for the immobilization of biological species [8], such as enzymes [9], antibodies [10] and whole cells [11, 12]. Biofunctionalization of the conductive polymer films can be performed by either entrapment of the species of interest or their attachment to electrochemically generated surfaces [13]. Potential dependent electrolysis of the monomer suspension triggers polymerization of the substrate and subsequent entrapment of the biomolecules in the growing chain of the polymer matrix.

Most organic polymers have highly hydrophobic character and could not be naturally employed for the immobilization of hydrophilic molecules. Modification of the polymer properties with polar functional groups or by simple addition of hydrophilic agents can significantly improve biocompatibility of the matrix and by accommodating the hydration layer retain the biological activity of the incorporated species. Fig. 6.1 illustrates selected applications of biomolecule immobilization in polymer functionalized films.

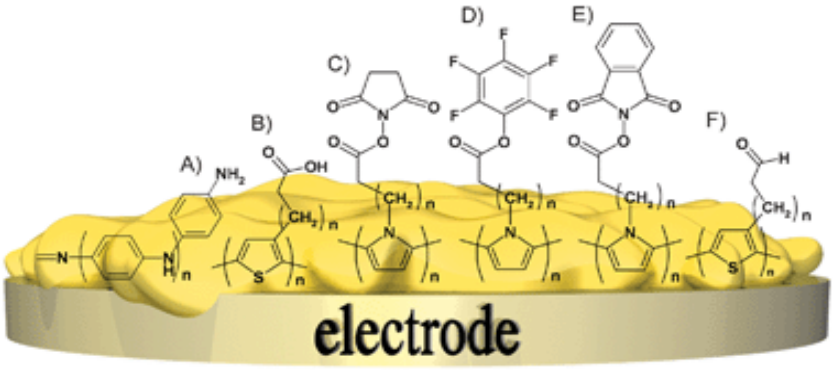


Fig. 6.1. Sample polymer films functionalized with reactive functional groups for covalent attachment of biomolecules A) amines (polyamines); (B) carboxyls (polythiophenes); (C) N-hydroxysuccinimide esters (polypyrroles); (D) pentafluorophenyl esters (polypyrroles); (E) N-hydroxyphthalimide esters (polypyrroles); (F) aldehydes (polythiophenes) [14].

In spite of their diverse advantages, the use of conductive polymers in large-scale applications has a number of limitations, mostly due to relatively high fabrication costs, low exchange rates and non-selective nature. In this light, non-conductive, highly resistant polymers (e.g. polyphenol, poly (*o*-phenylenediamine)) have become emerging matrices for biomolecule immobilization. Insulating films grown by electropolymerization of the monomer suspension are self-limiting and, as such, their thickness is much smaller than what is typically expected for conducting polymers. Thin polymer layers facilitate highly efficient diffusion of analytes across the membrane and provide fast response to molecules of interest which is of a particular consideration in catalytic studies (e.g. enzymatic biofuel cells). Although the substrates and products can rapidly diffuse through the polymer/solution barrier, non-conducting polymers are selectively non-permeable to electroactive species preventing their interfering effect on the sample measurement [15]. Despite numerous advantages, certain polymer materials can potentially introduce undesirable interactions with the matrix and steric strains, resulting in the species deactivation. Development of more potent protocols and highly biocompatible materials is therefore under continuous investigation.

Many contemporary immobilization strategies employ highly conductive carbon nano-materials, in order to increase the active surface area of the electrode and to promote the catalyst attachment. In this method, the confinement of species is achieved by coating

the surface with a CNT suspension, followed by an electropolymerization step, during which the molecules become entrapped in the growing chain of the polymer. Alternatively, the immobilization can be carried out via electrostatic adsorption onto the polymer surface; a covalent binding to the polymer reactive groups or by chemical cross-linking. Fig. 6.2 represents the electrochemical approach to SWCNTs functionalized with β-cyclodextrin-tagged GOX attached to electrogenerated adamantane-pyrrolederivatives [14].

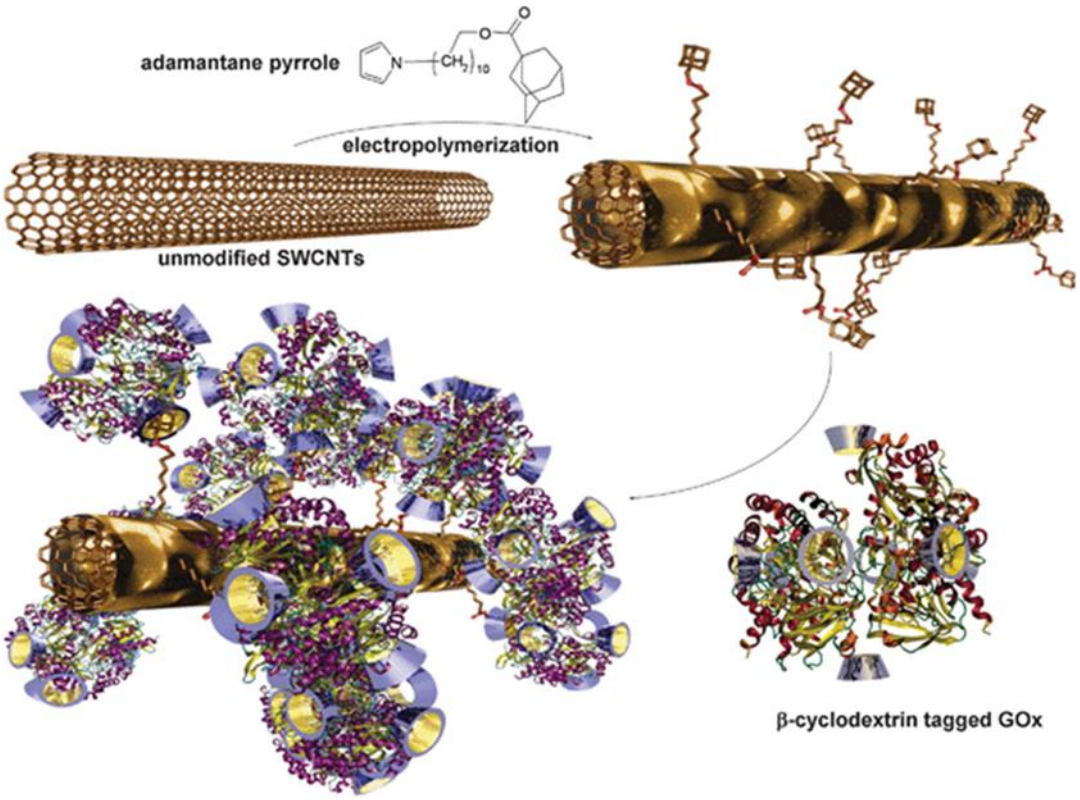


Fig. 6.2. Functionalization of single-walled carbon nanotubes with β-cyclodextrin tagged biomolecules immobilized in electrogenerated adamantane-pyrrole derivatives [14].

Typical methods of biomolecule immobilization are not generic and, in principle, can be employed only for a limited range of biological species and certain research applications. Methods such as non-covalent adsorption or microencapsulation into polymer microspheres and hydrogels pose risks of leaching, enzyme denaturation and do not guarantee the desired spatial orientation of the catalyst [16, 17]. With a significant

diversity and dissimilar nature of existing biomolecules the catalytic systems need to be re-optimized and their components re-adjusted according to the individual requirements of the species incorporated, instigating time consuming and labour intensive protocols. Consequently, a universal immobilization procedure incorporating advanced biocompatible materials, which could successfully accommodate a larger number of catalysts without the necessity for lengthy amendments, is highly desired. In this light, the sol-gel and o-phenylenediamine encapsulation strategies were of particular importance for this Ph.D. work, due to their stabilizing effects on various enzymes and the ability to become selectively electrodeposited at the electrode surfaces.

6.3. Selected methods of enzyme immobilization.

The following section discusses the principles and the advantages of two enzyme immobilization matrices, employed in due course of this Ph.D. work: sol-gel and poly-*o*-phenylenediamine. The benefits of the selected encapsulation strategies in the view of the envisioned biofuel cell concept, supported by the comparison of the polymer materials, are also highlighted.

6.3.1. Sol-gel encapsulation of enzyme catalysts.

The first metal alkoxide was prepared by Ebelman [18] from $SiCl_4$ and alcohol, which upon mixing and exposure to air, condensed into a semi-solid material. Since then, sol-gels have been known as inorganic glasses for over a century [18] but it hasn't been until mid-1950s, when the first encapsulation of biological entities has been initially reported [19]. Following the initial successful entrapment of an enzyme, alkaline phosphatase, reported by Braun and co-workers [20], sol-gel encapsulation became one of the more frequently employed methods for catalyst immobilization [21, 22] in biofuel cells and biosensor devices. Nowadays, the wide range of incorporated species includes proteins, nucleic acids and whole cells, enabling variety of different applications [8, 23]. Application of silicate derived materials as matrices for the encapsulation of biological species expanded the approach to biochemically modified electrodes employed in biosensing and power sources.

Sol-gels offer attractive advantages over other immobilization techniques. They do not swell in aqueous solutions and organic solvents and as such retain the incorporated biomolecules without any risks of leaching and inevitable loss of the active component [24, 25]. Furthermore, as compared to a number of existing immobilization matrices, silica materials display improved mechanical strength and chemical stability and have been largely exploited in the development of robust electrochemical based devices [26, 27].

Electrochemically promoted formation of sol-gel films from sol suspensions of biomolecules leads to a simultaneous encapsulation of biological species in the growing polymer chain on the polycondensation step. Resulting silica coatings are doped with protein molecules, which due to the biocompatible nature of the matrix can successfully sustain their natural catalytic functions. Immobilization of catalysts in the sol-gel has been demonstrated by a number of research groups with a view to various applications [28-30]. In 2007 Nadzhafova and co-workers [28] reported simultaneous encapsulation of haemoglobin and glucose oxidase in silica films electrogenerated on glassy carbon surfaces. Both entrapped enzymes retained their biological properties and were able to carry out direct electron transfer catalysis due to their close proximity with the electrode surface. One-step protocol for the immobilization of GOX in a three dimensional porous silica network has been proposed by Xia *et al.* [29]. The authors reported the use of a bubble template for electrochemically promoted generation of a 3D sol-gel matrix on Pt electrode.

Mentioned properties of the sol-gel matrix overcome the flaws of the existing microencapsulation approach, thus this method has been selected as one of the two techniques considered for the enzyme immobilization with the scope of biofuel cell applications.

A) Biocompatible silane precursors.

While suitable for encapsulation of biomolecules in principle, sol-gel films are not relevant for certain biological applications. Significant efforts have been made towards the optimization of silica derived matrices through a precise control of the gel porosity, adjustment of the chemical surroundings of the encapsulated molecules [24] and incorporation of biocompatible functionalities, such as amino acids and carbohydrates.

Since the alcohol released upon the hydrolysis of silicon alkoxides is a potential denaturing agent, novel biocompatible silane precursors are under continuous investigation. Currently, research has been focused on the replacement of the commonly used tetraethoxysilane, $Si(OC_2H_5)_4$, with a less harmful tetramethoxysilane, $Si(OCH_3)_4$, as methanol has been found less detrimental to the majority of encapsulated biomolecules. Nevertheless, some enzyme catalysts are still prone to deactivation even in the presence of traces of alcohol, hence the conventional two-step alkoxide reaction scheme is not applicable and major adjustments are required. Removal of the denaturant via evaporation under vacuum can overcome this issue by resulting in an alcohol-free hydrolysed solution. Nevertheless, this approach adds an additional step in the sol-gel preparation [31]. Additionally, while the silica framework is gradually formed around the entrapped molecule maintaining its natural biological activity, a certain degree of shrinkage during condensation and drying is inevitable. Since the inflicted stresses can lead to a residual denaturation of the enzymes, a number of polymer additives has been frequently employed, forming a mixture of organic and inorganic gels and acting as 'pore filling' agents. Various supporting materials, such as polyethylene glycol (PEG) or polyvinyl alcohol (PVA), have demonstrated a positive effect on the catalytic properties of the incorporated biotic species [32, 33]. In order to reduce potential unfavourable electrostatic interactions between the silica pores and specific functional groups on the protein surface, enzyme suspensions have been often supplemented with cationic polyelectrolytes. These positively charged macromolecules armour the anionic active sites of enzymes and protect them from silicate sites [34, 35]. Application of biocompatible reagents e.g. polyol-silanes, hydrolysable under mild pH conditions [8] and the use of aqueous silica precursors, such as pure sodium silicate [36] or its suspensions in Ludox [37], greatly improve the catalytic activity and long-term stability of entrapped enzymes. Supplementation with biocompatible glycerol further increases the overall functions of the biomolecules [38]. The implementation of carbohydrates and amino acids to improve the proteins' hydration shell and expand the pores size of the silica support, introducing a favourable chemical environment for incorporated species, has also been reported [39].

B) Principles of the sol-gel process.

A sol is a suspension of solid particles in a liquid phase, where due to very small size (1-100 nm) of the dispersed elements, gravitational forces can be neglected and the predominant interactions between the molecules are weak Van der Waals and electrostatic attractions. Upon hydrolysis and condensation, the sol becomes a colloidal substance composed of a continuous solid backbone encompassing a fluid phase commonly known as gel [40]. The biological entities suspended in the initial silica solution are incorporated into a growing polymer network and become part of the interconnected mesoporous structure. Catalytic activity of embedded molecules is not only retained but in some instances significantly improved, due to a stabilizing effect of the silica against potentially hostile chemical and thermal conditions [41, 42]. During the encapsulation, the sensitive element is gradually captured in a silica cage, individually tailored to its dimensions, providing a chemical environment that favours its biological activity. Subsequent incorporation of the proteins' natural hydration shell preserves their properties and leads to an extended life-span, as compared to soluble enzymes. The highly porous nature of sol-gel films provides a stable medium for large biomolecules with a good permeability to ions and smaller substrates, enabling efficient transport of species to the interior of the matrix [43-45].

Additionally, as silica sol-gels are prepared from mild and non-toxic reagents, under ambient conditions, they provide a physical entrapment without a chemical modification of the incorporated molecules.

Silica films can be synthesised from a variety of hydrophobic and polar entities [42, 46, 47] in the presence of non-protein cofactors and mediators, which are of particular importance for enzyme chemistry. These can be readily incorporated in the silica films by chemical grafting or stabilized by electrostatic interactions and weak physical bonds [46]. Due to the non-conductive nature of sol-gel materials, modification of electrodes with silane derived films is primarily restricted to the applications involving confinement of biological species in compatible materials. The main preparation routes involve either direct deposition of sol-gel films on solid electrodes, using electropolymerization or drop-coating approach, or by dispersion of powdered silane substrates in composite carbon electrodes.

Sol-gels are generated by a complete or partial hydrolysis of an appropriate silane precursor, resulting in a polymerization of the monomer suspension and simultaneous incorporation of the surrounding biomolecules. Preparation of sol-gel films is a multi-step process triggered by hydrolysis of the alkoxysilane solution, followed by the pH dependent condensation of resulting monomer and a gradual growth of the polymer chain.

1. Hydrolysis

The initial step in the preparation of silica derived films involves complete or partial hydrolysis of an appropriate alkoxide monomer (e.g. $Si(OCH_3)_4$; $Si(OC_2H_5)_4$). The process is carried out from an aqueous solution in a mutual solvent and leads to the formation of silanol groups (SiOH), as shown in Fig. 6.3. The presence of H_3O^+ in a form of an inorganic acid has been demonstrated to have a positive effect on the rate of the hydrolysis.

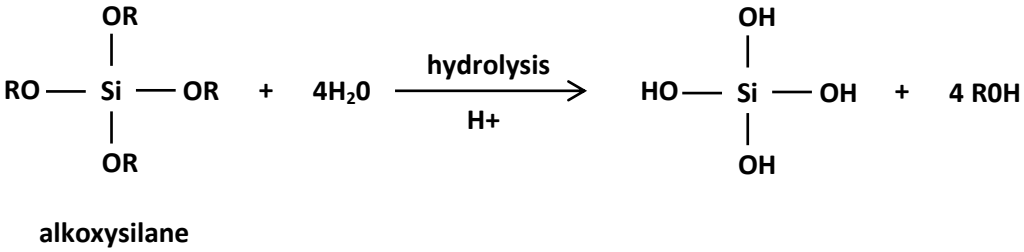


Fig. 6.3. Formation of silanol functions by hydrolysis of an alkoxysilane in acidic medium.

2. Condensation

During the condensation, partially hydrolysed silane molecules join together forming siloxane bonds (Si-O-Si) and generating extended polymer networks (Fig. 6.4). If sufficient time is allowed, the process leads eventually to a pure SiO_2 chain. Water generated as a result of the reaction is captured in the pores of the polymer and can further provide a neutral environment, facilitating the biological activity of incorporated molecules. Gel formation is typically carried out in an electrochemically assisted pH dependent polycondensation of silica precursors at the electrode / solution interface.

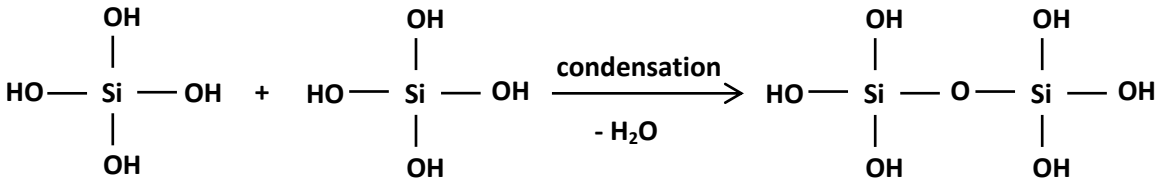


Fig. 6.4. Formation of siloxanes via condensation of silanol bonds in silane molecules.

The morphology of the resulting gels is affected by a number of experimental factors, including the temperature and pH of the silane solution and the concentration of the species, with a particular consideration of the $\frac{[H_2O]}{[Si(OR)_4]}$ ratio. Acid catalysed polymerization yields weakly cross-linked silicon polymers, which upon drying generate microporous xerogel structures of a pore diameter smaller than 2 nm. Neutral and basic pH conditions favour formation of mesoporous xerogels. A complex hierarchical structure of the gels is obtained via acid-base catalysis [40, 48].

3. Aging

Aging is a natural continuation of gelation and leads to an enhanced thickness and decreased porosity of generated silicon based deposits. During aging, the gels undergo additional polycondensation and structural rearrangements, producing strong films resilient to cracking of the subsequent drying.

4. Drying

At the drying stage, water present in the interconnected pores of the silica network is removed under conditions of constant temperature and pressure, causing the gel framework to collapse and re-conform. High density microporous (less than 2 nm) gels develop large capillary stresses, which if not controlled, will ultimately result in the formation of cracks. This phenomenon can be effectively prevented by lowering the surface energy of the remaining liquid through addition of surfactants or via hypercritical evaporation of very small pores. Alternatively, monodisperse pore sizes can be achieved by adjusting the rate of hydrolysis and condensation processes. Depending on the drying conditions, a number of ultimate structures can be obtained. Evaporation of the solvent

under ambient temperature and pressure results in the formation of xerogels ('xero' means dry), where the volume of the polymer is reduced by a factor of up to 10, as compared to the original wet gel [40]. Drying in an autoclave, under supercritical conditions, where relatively little shrinkage and no capillary pressure apply, generates aerogels with a volume fraction of solid as low as 1%.

C) Electrochemically assisted deposition of silica films.

Modification of electrodes with insulating sol-gel materials has been initially restricted to either composite electrode formation (powdered silica materials suspended in carbon paste or in ceramic-carbon) or a direct deposition of thin films onto solid surfaces via spin- or dip-coating. The latter, produced films of controllable thickness (100 nm to few μm), however resulted in a non-selective deposition of silica and could be only applied to flat planes, rather than porous substrates [49]. In principle, diluted concentrations of silica precursors generate highly porous matrices suitable for both enzyme encapsulation and efficient diffusion of reagents (substrates and mediators) to the active component. High concentrations of the starting sol, on the other hand, induce the formation of rather dense membranes, which are not applicable to solutions requiring fast diffusion of species to the electrode.

In the late 90's Schacham and co-workers [50] introduced an innovative method of silica film generation by applying the principles of electrochemistry to a sol-gel process. The protocol employed by the group, relied on a pH dependent electrochemically controlled deposition of silica precursors onto an active surface (Fig. 6.5) and has been used in the formation of silica coatings ever since. In the method established by Schacham, the reduction of protons and water molecules, triggered by the reductive potential applied to the electrode, as illustrated in Fig. 6.5 a), caused a local increase in the OH^- concentration. Alteration of the pH at the electrode/solution interface induced polycondensation of the underlying silica precursors, shown in Fig. 6.5 b), and subsequent deposition of the sol-gel films on the active material independent of its topology [49].

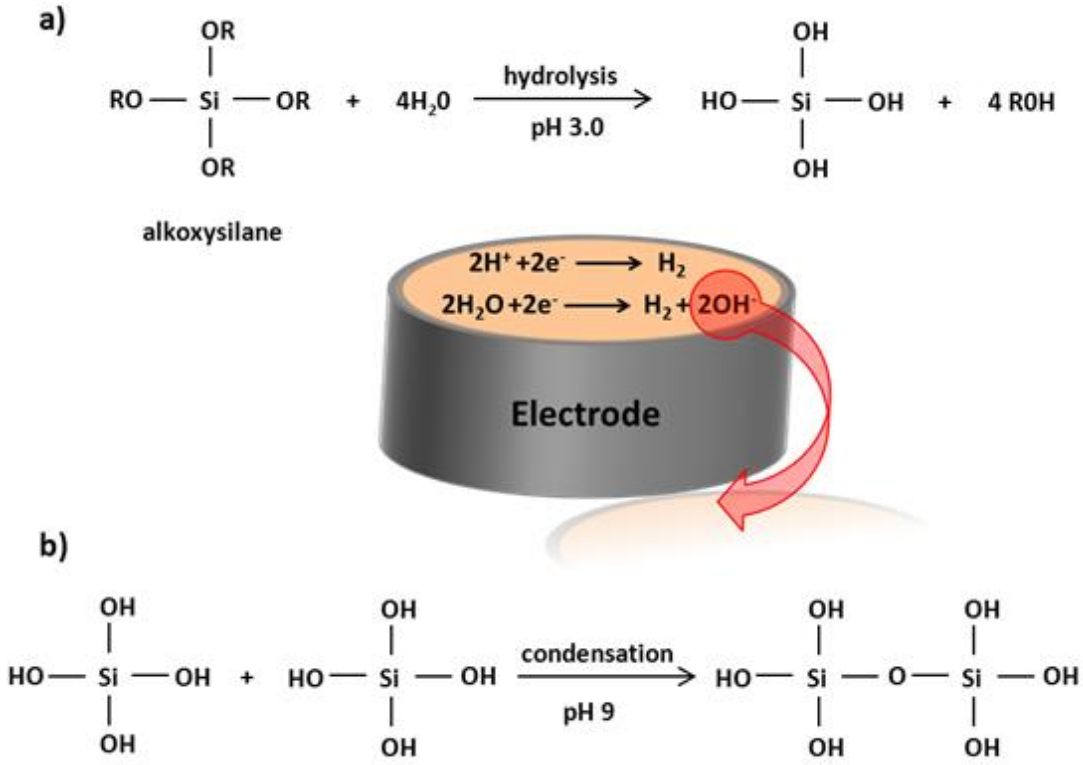


Fig. 6.5. Silica film generation proposed by Schacham [50] involving the: a) hydrolysis of the silane precursor and b) condensation of the generated silanol groups.

The electrodeposition of sol-gel on electrodes offers a number of advantages over traditional methods of surface alteration. By applying a constant potential over a certain time, the thickness and porosity of fabricated films can be precisely controlled and adjusted to the individual applications, while eliminating any issues with overpotential [51].

Electrochemically assisted generation of silica coatings have been originally exploited in the formation of porous deposits and anti-corrosive varnishes [52]. With time, the process gained increased attention in the area of electrochemical sensing [53], in particular in the production of molecularly imprinted films [53] and functionalized silica layers [54]. A recent application of electrogenerated highly ordered silica thin films, as vertically aligned mesochannels, have been reported by Walcarius and co-workers [55] as a tool for mass transport analysis.

6.3.2. Electrodeposition of species in *o*-phenylenediamine.

For many years the use of *o*-phenylenediamine has been primarily devoted to the development of enzyme based glucose, glutamate and lactate biosensors, with an ultimate goal to transpose the sensing elements from the laboratory in vitro systems into devices implantable in a human body [56-58]. Currently, due to the variety of macromolecular structures and multifunctionality, the use of *o*-PD and related amino derivatives is extensively investigated in biomolecule encapsulation, with the application in biofuel cells and biosensors [13, 59]. Since the majority of electrochemical devices employed for power sources and analyte detection, use metal electrodes as their active components, precise confinement of the polymer films within the electrode surface and accurate control of the layer thickness are essential determinants of successful operation

Polymerized *o*-phenylenediamine (P*o*PD) offers great advantages over other immobilization matrices, as the films can be electrochemically synthesised in a reproducible manner, in the presence of various catalysts, resulting in stable thin monolayers of the enzyme-doped polymer. P*o*PD exhibits good conducting properties at its partial reduction state, while acting as an insulator at its high oxidation state. At the electrically inactive region [60], the P*o*PD film is semi permeable to a certain number of neutral small molecules and anions, such as H_2O_2, at the same time preventing the effect of interferences and electrode fouling [61]. Whereas numerous immobilization matrices are prone to catalyst leaching and are susceptible to endogenous electroactive species, *o*-PD polymers block the access of small organic molecules maintaining high sensitivity to reaction substrates and products of their conversion (e.g. H_2O_2).

Stable entrapment of biological catalysts within the polymer network, prevents a physical loss of the active component, while providing selective transport of species at the membrane/solution interface. Furthermore, the ability to generate P*o*PD films via a single-step electro-assisted polymerization on a variety of electrode substrates enables precise control of the deposition area. The produced films are strongly adherent and highly reproducible and, as such, meet the general requirements for robust and reliable electrochemical devices. Unlike the majority of immobilization methods, the protocol for the P*o*PD matrix can be readily applied without further adjustments to successfully encapsulate a wide number of catalysts [62]. This is feasible due to the ability of *o*-PD to form polymeric films upon oxidative electrodeposition from phosphate buffers at a wide

range of pH values and on variety of electrode materials [63]. In particular, the extensive use of electrogenerated poly(*o*-phenylenediamine) thin films has been reported widely for confinement of oxidoreductase enzymes such as glucose oxidase [64, 65], glutamate oxidase [62, 66], lactate oxidase [67, 68], and laccase [69]. Anytime the procedure is not suitable to the individual properties of incorporated biomolecules (e.g. loss of activity of nitrilase reported by 1995 Liu and co-workers [70]), a two-phase immobilization protocol employing the electropolymerization, followed by cross-linking with glutaraldehyde can successfully overcome any stability issues. Furthermore, as the technique is applicable for a wide number of enzyme catalysts and more complex geometry of the electrode surface, a universal immobilization protocol can be established and employed for biofuel cells of different designs and composition.

Encapsulation of glucose oxidase in PoPD

The feasibility to immobilize GOX in "in situ" electrogenerated P*o*PD polymer has been demonstrated for the first time on platinum macroelectrode in the early 90s, by Palmisano and Zambonin [64, 71]. The obtained monolayer of GOX/P*o*PD (10 nm thick) exhibited the fastest ever observed response to glucose (less than 1 s), while radically repelling ascorbate. Excellent stability and recognition properties of the generated film have rapidly attracted the attention for enzyme-modified electrodes, instantly becoming a promising candidate for species encapsulation in biosensors and microfluidic biofuel cells. When Dumont and Fortier compared the behaviour of glucose oxidase in a number of electropolymerization matrices (P*o*PD, PAN, PPY and P*p*PD cross-linked with PPY) [72], they discovered that the GOX/P*o*PD system exhibited the best signal to noise ratio in a 7-10 mM range of glucose. The performance of GOX in numerous polymeric films (e.g. PPY, PAN) has been also investigated by Trojanowicz *et al.*[73], who found that GOX / P*o*PD on Pt and Au electrodes, display the highest sensitivity to glucose and the best durability of all investigated polymer based membranes. An innovative application of P*o*PD membrane has been proposed by Bartlett and co-workers [74]. The authors reported the fabrication of a microelectrochemical enzyme transistor composed of two carbon band electrodes with anodically grown GOX/P*o*PD/PAN bilayer. The change in the conductivity of polyaniline has been determined by reductive properties of the oxidase in

the presence of glucose, switching the PAN between its electrically active and insulating modes.

In 1997, Myler *et al.* used gold coated porous polycarbonate membrane functionalized with GOX and bovine serum albumin in P*o*PD, in order to determine the levels of glucose in the blood. Negatively polarized oxidase provided intrinsic charge repulsion of the anionic interferents, such as ascorbate and urate, facilitating direct measurements of glucose present in physiological fluids. The following year, Ju and co-workers [75], reported successful modification of a nanometer-size (88 nm) microband Au electrode with GOX/P*o*PD coating. The system demonstrated a linear response to a range of glucose concentrations and rejected the interference of numerous aminoacids. An interesting solution to carbohydrate sensing was proposed by Malitesta *et al.* who used poly- (*o*-phenylenediamine) molecularly imprinted by glucose in biomimetic sensors [76]. Wang end co-workers, went a step further in the amperometric detection of glucose in blood, and as the first authors, reported co-encapsulation of heparin to prevent coagulation events and to provide increased biocompatibility of P*o*PD modified electrodes [77]. Simultaneous entrapment of GOX and heparin greatly simplified the preparation process and introduced an attractive route to miniaturized, implantable glucose needle-like sensors.

At the time, several research groups investigated the effect of a multilayer structure on the behaviour of GOX/P*o*PD films. Malinauskas and Garjonyte [78] suggested the best response to glucose by a single coated Pt electrode, with a gradual decline in the enzymatic activity upon the introduction of successive P*o*PD layers. Simultaneously, Yasuzawa *et al.* [79] recommended that the cooperative use of P*o*PD and Nafion results in a better prevention against the amino acid and acetaminophen interferences and provides enhanced performance, thus supporting the findings previously described by Moussy [80]. Recently, Luo and co-workers [81] reported a fabrication of a novel glucose biosensor composed of a palygorskite (Pal)/P*o*PD matrix as a platform for the immobilization of GOX.

Laccase functionalized PoPD films

A number of studies has been carried out on laccase modified electrodes, with potential application in the oxygen sensing [82] and as cathodic systems for biofuel cells

[83]. Although direct electron transfer (DET) has been suggested by several authors [84-87], the majority of work on laccase has been based on mediated electrocatalysis (MET) in the presence of redox reactive species co-encapsulated with the enzyme or soluble in the solution. Unlike the DET systems which primarily rely on the species attached to the electrode by weak physical adsorption or dissolved in the solution [88, 89], The MET approach explores the use of electrochemical techniques to obtain robust and reliable solutions.

Most frequently incorporated laccase mediators include osmium (Os) complexes attached to redox polymers or hydrogel matrix [90-92]. Implementation of Os polymers "wiring" the enzyme to the electrode surface has been found particularly applicable in biofuel cell cathodes, due to the very positive potential values at which the reduction of oxygen occurs. The apparent disadvantage of this approach is however increased toxicity and the relatively high cost of osmium polymers.

It has been reported, that certain conducting polymers, such as, polypyrrole and its certain derivatives, are capable of direct electron exchange with various enzyme catalysts (e.g. glucose oxidase and hydrogen peroxidase) [89, 93]. The exact explanation to why not all non-insulating organic polymers are able to directly catalyse the reduction of O_2 has not yet been elucidated, however the affinity of the monomer unit to the enzyme has been predicted as one of the decisive factors [13]. As the molecular structure of *o*-phenylenediamine resembles some of the natural mediators for laccase, Palys *et al.* suggested that P*o*PD matrix could possibly directly interact with the enzyme and catalyse the 4 e^- reduction of molecular oxygen, without the need for additional mediators [69]. Additionally, it has been showed that the increased catalytic activity of laccase enzymes observed in slightly acidic media corresponds with the pH region of the highest electroactivity of PoPD.

The work on the immobilization of laccase in poly (*o*-phenylenediamine), presented as part of this chapter, has greatly benefited from the comprehensive discussion offered by Rogalski and Palys [69]. The authors investigated the potential role of the P*o*PD matrix as a mediator for the enzyme and studied the influence of the pH on both the electrodeposition and the catalytic activity of the laccase / P*o*PD layer. Additional implementation of quinone (Q) resulted in an observed enhancement in the electrochemical response in the presence of molecular oxygen. This has been attributed to the small size of Q, which enables efficient electron exchange between the enzyme and the electrode. Due to its high affinity in laccase catalysed reaction, quinone has been selected

as a mediator of choice in the experimental work enclosed as part of this dissertation. Entrapment of laccase in P*o*PD films preserved its biological activity and prominently reduced the overpotential of the reaction [69]. The recorded current density was found to be positively dependent on the increasing layer thickness only for very thin laccase / P*o*PD deposits, with a non-linear dependence for thicker films.

According to numerous authors, depending on the pH of the deposition bath, the polymerization of *o*-PD yields two potential products: linear P*o*PD with free $–NH_2$ functional groups or a ladder structure composed of phenazine rings [94, 95]. Infrared reflectance spectra of the laccase/polymer films discussed by Palys *et al.* demonstrated that very acidic solutions (pH less than 2) favour the formation of the linear P*o*PD with prevalent phenazine structures at higher pH [69].

Encapsulation of lactate oxidase in PoPD polymer

Early approach to the immobilization of lactate oxidase (LOX) for catalytic and biosensing purposes, relied primarily on the entrapment of the enzyme behind a semi-permeable membrane [96]. Despite the relative success of this strategy, the method posed a number of limitations, such as a rather low sensitivity and slow response time as well as significant interference issues when operating in physiological solutions.

Numerous scientific reports suggest that electrochemically assisted entrapment of LOX enzymes within an *o*-PD matrix provides simple, highly sensitive and responsive enzymatic films, which can be effectively employed in biofuel cell studies for energy harvesting applications.

Dempsey and Wang were one of the first [68] to demonstrate a one-step electrochemically promoted encapsulation of LOX in a P*o*PD matrix, by applying a constant potential to deaerated and unstirred buffer solutions containing the enzyme and monomer suspension. The authors suggested that thinner polymer films incorporate higher concentrations of the catalyst, resulting in much faster response to L-lactate. Conversely, a thick P*o*PD coating has been found to display slower catalysis and reduced sensitivity to the substrate, due to limited mass transport of species across the membrane. Restricted diffusion of the substrate results in the enzymatic reaction occurring primarily in the outer parts of the polymer layer, where the contact with the solution is not restricted by the membrane, as a consequence not utilizing the enzyme load to its full extent [68]. The

mechanism of P*o*PD synthesis proposed by Wang, relied on a two-step film formation incorporating initial conductive layer of organic polymer (polymerization of generated monocations), followed by an insulating coating generated through the condensation of potentially disproportioned dications. The ability to apply P*o*PD in flowing systems has been shown by Palmisano and co-workers in 1994 [67]. The in-situ electrosynthesised LOX/P*o*PD monolayer layer rejected the interfering agents however a loss of 75 % of its performance has been reported after a week of continuous operation. A layer of polypyrrole placed additionally between the electrode and the poly (*o*-phenylenediamine), improved the stability of the flow-injection system. In 1996, Trojanowicz *et al.* proposed a trilateral detection system composed of LOX/P*o*PD/PPY/polyphenol/Pt [97]. The modified electrode has been successfully used in a flow through determination of lactate in diluted and concentrated human blood serum samples.

Oxidase enzymes, such as LOX, catalyse the oxidation of their respective substrates (e.g. lactate, glucose) subsequently reducing molecular O_2 to H_2O_2 as shown in Eq. 6.1.

$$LOX_{FMN} + L - lactate + O_2 \leftrightarrow LOX_{FMNH_2} + pyruvate + H_2O_2 \qquad Eq.\ 6.1$$

The detection of the catalytic activity of LOX can be thus based in the quantification of the reaction side product, hydrogen peroxide. A typical electrochemical approach to peroxide determination relies on the anodic oxidation on platinum [98, 99] or carbon electrodes [100], however this strategy suffers from significant overpotentials and sensitivity to interfering agents. A solution to overcome this issue is to use a catalytic redox mediator (e.g. Prussian Blue or cobalt hexacyanoferrate [101]).

As the catalytic activity of LOX has been mostly studied based on the amperometric detection of generated H_2O_2, a selective approach to peroxide reduction had to be established. An innovative method to a low-potential, selective detection of hydrogen peroxide has been suggested in 1994, by a group led by Karyakina [102]. The authors demonstrated, that Prussian Blue (PB) polycrystals, deposited in a controlled manner onto the electrode surface, can effectively carry out the electroreduction of H_2O_2 [103]. Since the activity of PB resembles that of biological catalysts, the generated Prussian Blue layer soon became known as an "artificial peroxidase" [104]. A brief description of the PB deposition is enclosed in Chapter II of this thesis.

As oxidase enzymes produce H_2O_2 while decomposing their corresponding substrates, the method can be effectively applied for multiple enzymatic assays. Simultaneous electrochemical determination of a number of organic species (e.g. glucose, lactate, urate) in biological samples is also viable [105] and is an attractive alternative to less precise colorimetric studies (e.g. visual perception issues).

A) Principles of poly (*o*-phenylenediamine) formation.

The mechanism of the phenylenediamine condensation was first proposed in 1958 by Elving and Krivis [106], who suggested the monomer structure and acidity of the deposition solution to be the essential factors determining the success of the electropolymerization process. Although the exact nature of the polymeric film was long unknown [107], early experimental work on pyridine derivatives indicated a formation of a monovalent cation radical as the prime electrolysis product [108]. It was believed that the radical was further involved in a follow-up polymerization reaction with an ultimate generation of an amine-linked polymer. Despite the lack of conclusive evidence, the presence of certain amine linkages was also assumed in P*o*PD. Nowadays, due to advanced research technologies and significantly improved understanding of the underlying chemistry, the structure of the P*o*PD polymer coating can be effectively determined by FT-IR spectroscopy [109], NMR, XPS and UV-Vis techniques [63]. Spectroscopic analysis of the generated PoPD layer, carried out by Kang [110], revealed a head-to-tail (-N-Ph-N-Ph-) arrangements of adjacent *o*-PD units rather than a head-to-head sequence (-Ph-N=N-Ph-). While direct N=N interactions have been reported only under basic and neutral pH conditions, the oxidative product of phenylenediamine in acidic media seems to exhibit primarily the Ph-N arrangement. This phenomenon confirms the dependency of the P*o*PD architecture on the synthetic conditions

In his extensive review [63], Li proposed three potential chemical structures of P*o*PD formed upon electropolymerization of *o*-PD, all presented in Fig. 6.6.

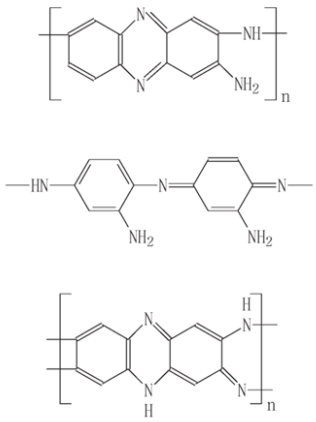


Fig. 6.6. Proposed structures of electropolymerized o-phenylenediamine.

B) Electrochemically assisted deposition of *o*-PD.

The most frequently employed method for the generation of poly-*o*-phenylenediamine films is the electrochemically assisted polymerization. P*o*PD coatings with controllable thickness are generated by applying a suitable potential to the electrochemical bath containing the monomer and the supporting electrolyte, dissolved in a mutual solvent. The electropolymerization of *o*-PD results in higher eletroconductivity of the matrix than if the process was carried out in the presence of chemical oxidants [63]. This has been accredited to higher molecular weight of the produced polymer and greater doping characteristics. In general, the conducting properties of P*o*PD are highly dependent on the polymerization conditions, such as the configuration of the electrochemical set-up and the deposition technique itself [63]. Potentiogalvanostatic and potentiostatic conditions are typically employed in order to produce thin, low conducting phenylenediamine coatings [111], while galvanostatic methods give rise to rather thick polymer membranes with relatively high current density [63, 112]. The insulating properties of thin P*o*PD films self-limiting the deposition process, have been attributed to a lack of charge carriers, which can be due to e.g. protonation of amine sites. The conductivity of the electrogenerated layer can be however significantly improved by functionalization with aniline [113] or an increase in the applied potential and temperature.

The permselectivity of the membrane is a crucial parameter, where the exchange of species is required (e.g. catalytic studies) and it depends strongly on the thickness of the generated films and the pH of the deposition bath. It has been recently demonstrated that

this property is improved when the P*o*PD is obtained from slightly acidic media (e.g. pH 5), a feature attributed to the hydrophobic interactions and effective hydrogen bonding [63].

6.4. Materials and methods.

The following section discusses the preparation methodology of the selected bioanodes and biocathodes and emphasises the importance of the individual redox components on the catalytic performance of the investigated half-cells.

6.4.1. Enzymatic bioanodes.

A) D-Sorbitol dehydrogenase sol-gel based bioanode.

The first catalytic system on bioanode was composed of two enzyme catalysts: D-Sorbitol dehydrogenase (DSDH) and Diaphorase (DI), encapsulated in an electrogenerated sol-gel matrix. DSDH, at a concentration of 10 mg mL^{-1} (100 units / mg), was kindly donated by prof. G.W. Kohring from the Department of Microbiology of the Saarland University, Germany. The enzyme was produced by overexpression in *Escherichia coli* BL21GOLD (DE3) cell culture and purified using a His trap column (GE Healthcare) functionalized with appropriate metal complexes.

The DSDH functionalized bioanode catalysed the oxidative conversion of the substrate, D-Sorbitol, into fructose in the presence of a cofactor molecule, nicotinamide adenine dinucleotide, NAD^+.

Fig. 6.7 illustrates the electrochemically deposited sol-gel matrix employed for the DSDH catalysed oxidation of D-Sorbitol on the bioanode. The electrogenerated films contained both enzymes and the cofactor molecule, while the mediator and the substrate were supplied in the solution and were able to readily diffuse through the membrane/bulk interface. Immersion of the electrode in a D-Sorbitol solution triggered the DSDH catalysed oxidation to fructose, with a simultaneous reduction of NAD^+ to NADH. Cofactor regeneration was carried out by diaphorase. Reduced DI subsequently shuttled the electrons to the mediator molecule, ferrocenedimethanol (FDM), which was in turn regenerated at the surface of the electrode, producing electrical current. The use of FDM

was essential as the direct transfer of charge by diaphorase occurs naturally at a very low rate.

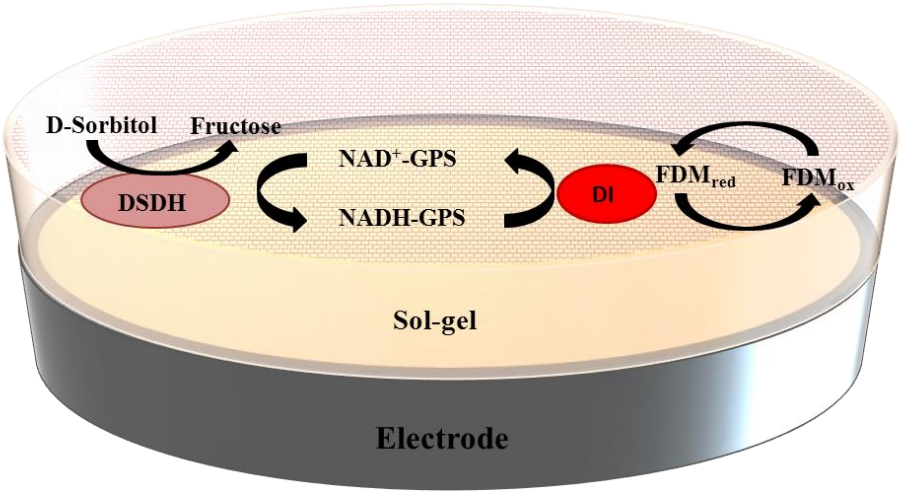


Fig. 6.7. Schematic of the catalytic system applied on bioanode. Sol-gel encapsulation of DSDH and NAD^+-GPS cofactor in the presence of FDM mediator enabled successful oxidation of D-Sorbitol and efficient electron transport to the electrode surface. DI provided means of cofactor regeneration.

The encapsulation of DSDH in a sol-gel matrix was carried out by electrochemically assisted deposition from a solution of 0.25 M hydrolysed Tetraethyl orthosilicate (TEOS), prepared fresh prior to surface alteration based on a modified protocol from [114], as described in Chapter II. A three-electrode system composed of a Au working disc electrode (Ø 4 mm), Pt counter and Ag/AgCl (3 M KCl internal electrolyte) reference has been employed for the electrodeposition of the considered sol-gel films. Prior to the surface modification, the WE has been mechanically polished on wet emery paper (4000) using alumina powder size 0.05 µm and rinsed with copious amounts of deionized water. CE and RE have been washed with DI H_2O and gently dried with tissue paper. Following cleaning, a mixture of 0.25 M TEOS, poly (diallyldimethylammonium chloride) (PDDA); D-Sorbitol Dehydrogenase (DSDH, 10 mg mL^{-1}); diaphorase (DI, 5 mg mL^{-1}); NAD^+-GPS and polyethyleneimine (PEI, 10 % in DI water, pH 9.0) has been swiftly prepared in an Eppendorf tube, accordingly to the protocol enclosed in Chapter II, and 270 µL of the reacting solution has been immediately applied on the working electrode.

The electrogeneration of silica sol-gel films doped with DSDH has been carried out for 60 s at constant potential of -1.2 V applied to the working electrode. The

functionalized electrode has been gently rinsed with deionized water and left at RT for 2 h for drying and aging.

Importance of the cofactor stabilisation and regeneration

Electron transfer properties of dehydrogenases rely strongly on free diffusing species enabling efficient transport of e^- between the enzyme active site and the electrode surface. In order to provide a reliable electrical connection, NAD^+ has been used as a cofactor for DSDH and immobilized in-situ with a glycidoxypropyl trimethoxylsilane (GPS) precursor. GPS is a silane derivative bearing - OCH_3 groups and, as such, can be incorporated into the growing framework of silica at the polycondensation step. It has been previously demonstrated by Liu and co-workers [115], that NAD^+ covalently attached to silica particles can successfully co-operate with entrapped enzyme, enabling efficient electron shuttling and substrate conversion. The epoxy ring, present as part of the glycidoxy group, displays good chemical activity and can interact with NAD^+ through the formation of a covalent bond. Covalent coupling to the cofactor offers enhanced stability of NAD^+ over alternative co-immobilization and encapsulation procedures, however due to a rather elaborate modification process a potential decrease in cofactor's efficiency may be encountered. Since the reaction of the epoxide group with adenine moieties is relatively simple and non-complex, retained redox activity of NAD^+ can be expected.

The electrochemistry of $NAD(P)^+$/ NAD(P)H redox couples on bare electrode surfaces is known to be irreversible and cannot be performed at a potential thermodynamically determined from the half-cell reactions. In order to efficiently recycle enzyme cofactors, while minimizing any potential energetic losses, various organic molecules have been investigated as potential mediators for the electrochemical oxidation of the redox species, such as NADH. Ideal candidates need to undergo a two-electron transfer and need to be able to accept proton ions. In addition, they must be chemically stable, enzymatically active and cannot directly interact with the reaction substrate. Numerous approaches to cofactor regeneration have been proposed up to date including direct, indirect and enzyme-coupled electrochemical routes [116]. Since direct electrochemical detection of NADH on the electrode occurs at high overpotentials, inducing uncontrolled oxidation and rapid deactivation of molecules (e.g. formation of non-active dimers), DI has been employed to regenerate NAD^+ and shuttle the electrons to

the anode. A combined mechanism of the mediated indirect and the enzymatic processes have been however previously investigated by a number of authors. In the sol-gel electrocatalytic oxidation of NADH, a joined application of diaphorase and ferrocene derivatives [117, 118] or osmium polymers [119, 120] has been frequently demonstrated.

Influence of cationic polyelectrolytes

The presence of polyelectrolytes, polydimethyldiallylamonium chloride (PDDA) and polyethyleneminine (PEI), not indicated in Fig.6.9, has been found to have a significant bearing on the biological activity of DSDH. Supplementation of the starting sol with cationic reagents stabilized the negatively charged dehydrogenase and provided an efficient operation of the enzyme.

As has been previously reported by Wang [121], 1-7 % concentrations of PDDA (w/v) result in an improved electrochemical signal of DSDH, with the optimal efficiency observed at 5 % of the PDDA. Since PDDA acts as "macromolecular glue" [121], bringing the catalyst and silica surfaces together, too high or too low concentrations of the electrolyte can have undesirable destabilizing effects. Furthermore, high levels of PDDA (> 10 %) instigate almost immediate gelation of the starting sol and the enzyme suspension, regardless of the applied potential. Although the key role of PDDA is to provide favorable electrostatic interactions between the biomolecule and the matrix, a possible implication in the generation of enlarged silica pores and thus enhanced mass transport of reagents has also been proposed.

The use of PEI in the encapsulation of dehydrogenases has been previously reported for a number of substrates, including glucose [122], D-lactate [123] and alcohol [124]. Similar to PDDA, the stabilizing effect of polyethyleneimine is attributed to the formation of neutral conjugates generated via electrostatic interactions between the cationic surface of the electrolyte and the negatively charged DSDH - NAD^+ complexes. PEI assemblies retain the native conformation of the enzyme by protecting it from uncontrolled unfolding and could potentially enrich the cofactor species available in the active centre.

B) Glucose oxidase modified P*o*PD based bioanode.

The catalytic system for mediated electrooxidation of glucose to gluconolactone was composed of GOX immobilized in electrogenerated poly (*o*-phenylenediamine) film, as illustrated in Fig. 6.8. The mediator, ferrocenecarboxylic acid (FCA), remained soluble in the phosphate buffer solution and facilitated the transfer of electrons generated in the active centre of GOX, as a result of glucose oxidation, to the electrode surface. FCA reduced by the catalytic activity of the enzyme, was further regenerated at the electrode surface, producing electrical current.

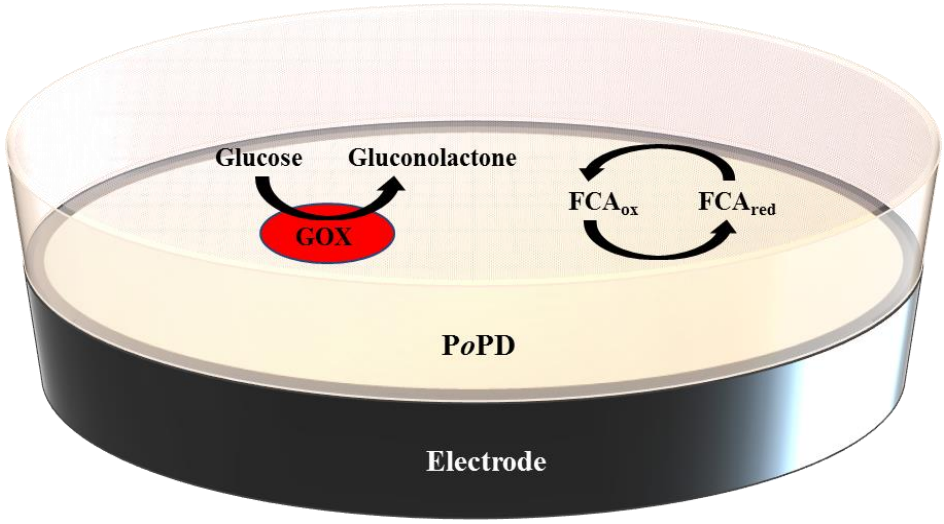


Fig. 6.8. Schematic of the GOX/PoPD bioanode. Mediated electrooxidation of glucose into gluconolactone was carried out in the presence of ferrocenecarboxylic acid (FCA), as the mediator of the electron transfer between GOX and the electrode.

The encapsulation of GOX in *o*-PD matrix has been carried out from deaerated buffered solution of *o*-phenylenediamine, according to [62] and as described in detailed in Chapter II. Sodium sulphite has been further supplied to the deposition bath, in order to prevent the undesirable entrapment of molecular oxygen.

Deposition of *o*-PD films on gold disc (Ø 2 mm) electrodes has been performed at RT in the presence of Pt coil auxiliary and Ag/AgCl reference immersed in 3 M KCl

internal electrolyte. Electrodeposition has been carried out from 10 mL of 0.1 M phosphate buffer, pH 7.4, containing 10 mM *o*-PD, 5 mM Na_2SO_3 and of GOX (10 mg mL^{-1}). The solution was placed in the electrochemical cell and purged with nitrogen (20 mins), in order to remove the oxygen and thereby prevent the consecutive entrapment of O_2 in the matrix. Encapsulation of GOX within the polymer was triggered by applying a potential of 0.75 V for a period of 20 mins, as discussed in Chapter II. Electropolymerization of *o*-PD monomers initiated subsequent encapsulation of GOX and a gradual growth of the film.

Prior to electrochemically promoted deposition of the GOX/P*o*PD composite, illustrated in Fig. 6.9 b), the gold electrode has been mechanically polished with alumina, exposed to O_2 plasma and chemically cleaned in freshly prepared 1 M H_2SO_4 for 3 h, by cycling the electrode potential between 0.4 V and 1.5 V. Fig. 6.9 a) depicts the cyclic voltammetry response of Au disc electrode obtained upon repetitive sweeps in the acid. The CV represents a typical response of gold vs. Ag/AgCl reference, where the metal surface is oxidized at approximately 1.2 V, following which the gold oxide is reduced at around 0.95 V on the reverse potential scan. The electrode was cycled until a reproducible voltammogram has been obtained for the formation and reduction of the gold oxide and the final voltammogram has been presented in Fig. 6.9 a). The drop in the current recorded during the deposition of *o*-PD, indicates a self-limiting character of the process. The additional oxidation and reduction peaks observed at 1.05 V and 0.8 V are due to gold contamination with organic impurities. These are most likely the residues of the previously deposited poly *o*-PD or Prussian Blue, remained at the electrode surface despite the oxygen plasma and the chemical cleaning treatments.

Following the deposition, the electrode was gently rinsed with 0.1 M phosphate buffer (pH 7.4) and the excess moisture was removed with a tissue paper. The catalytic activity of GOX towards mediated glucose oxidation has been monitored immediately after the deposition in substrate solutions of 0.1 M phosphate buffer, pH 7.4, in the presence of FCA. When not in use, GOX-modified electrodes were stored in the buffer (pH 7.4) at 4 ºC.

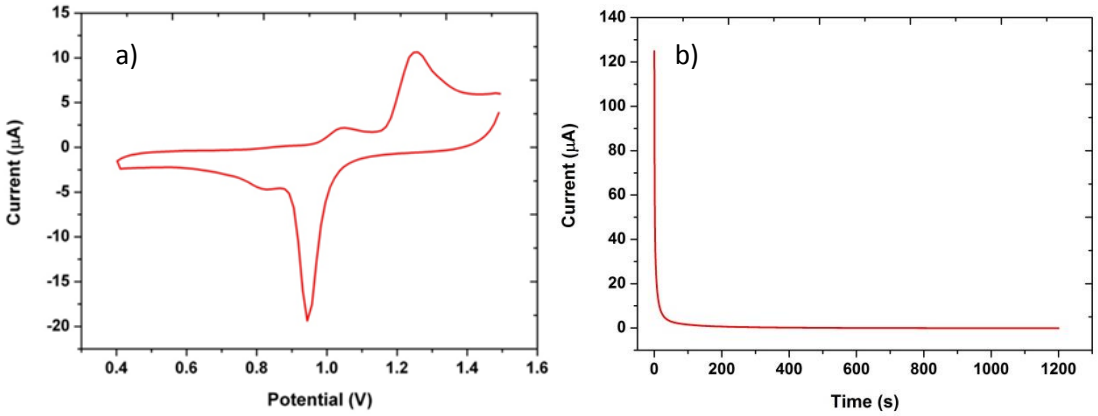


Fig. 6.9 a) Surface cleaning of Au disc electrode in 1 M H_2SO_4; scan rate of 100 mV s^{-1}; b) Electrodeposition of 10 mg mL^{-1} GOX from 10 mM o-PD and 5 mM Na_2SO_3 in 0.1 M phosphate buffer pH 7.4 at 0.75 V for 20 min. Potential recorded vs. Ag/AgCl (3 M KCl).

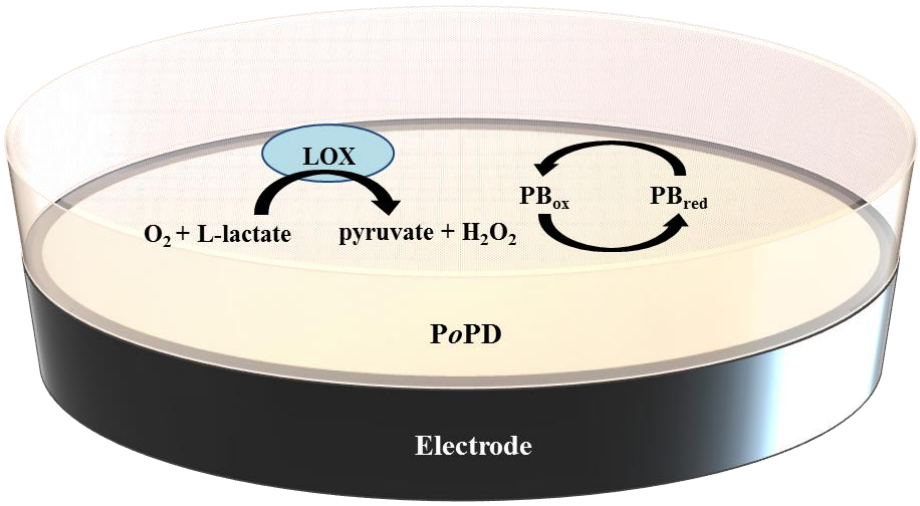


Fig. 6.10. Oxidation of L-lactate by LOX with a simultaneous formation of pyruvate and hydrogen peroxide. The catalytic reduction of peroxide at low potentials was facilitated by a layer of PB.

A) Lactate oxidase functionalized *o*-PD bioanode.

The composition and the operational principle of a lactate oxidase (LOX) based bioanode, constructed as part of this chapter, are illustrated in Fig. 6.10. LOX encapsulated within the P*o*PD polymer catalysed the two-electron oxidation of L-lactate to pyruvate and a subsequent generation of hydrogen peroxide. The catalytic reduction of H_2O_2 was promoted, due to an activate layer of PB pre-deposited onto the electrode surface prior to LOX/P*o*PD deposition, mediating the electron exchange with the electrode.

Encapsulation of lactate oxidase in electrogenerated *o*-phenylenediamine films has been obtained, according to a protocol proposed by Wang [68], from a deaerated, unstirred solution of 5 mM *o*-PD in 0.05 M phosphate buffer, pH 7.4. A potential of 0.65 V has been applied to Au or Pt working electrodes for a period of 20 min in order to initiate the polymerization process.

Prior to LOX encapsulation, illustrated in Fig. 6.11 d), and following the electrode cleaning in 1 M H_2SO_4, depicted in Fig. 6.11 a), a thin layer of Prussian Blue (PB) has been electrodeposited on the electrode [125], as shown in Fig. 6.11 b); electrochemically activated in a supporting electrolyte, accordingly to Fig. 6.11 c); rinsed with DI H_2O and dried in the oven at 90 ºC for 1 h. As previously, Pt coil and Ag/AgCl have been used as the counter and the reference electrodes respectively. Fig. 6.11 a) and Fig. 6.11 d) represent typical electrochemical responses of gold to a sulfuric acid clean and the deposition of the P*o*PD polymer, accordingly. The redox behavior of PB in 0.1 M KCl and HCl solution (reduction and oxidation peaks at ~0.13 V and 0.2 V, respectively) are illustrated in Fig. 6.11 c). The initial rapid increase in the current followed by a gradual plateau, recorded during the electrodeposition of PB layer as presented in Fig. 6.11 b), are indicative of the formation of the electrode coating.

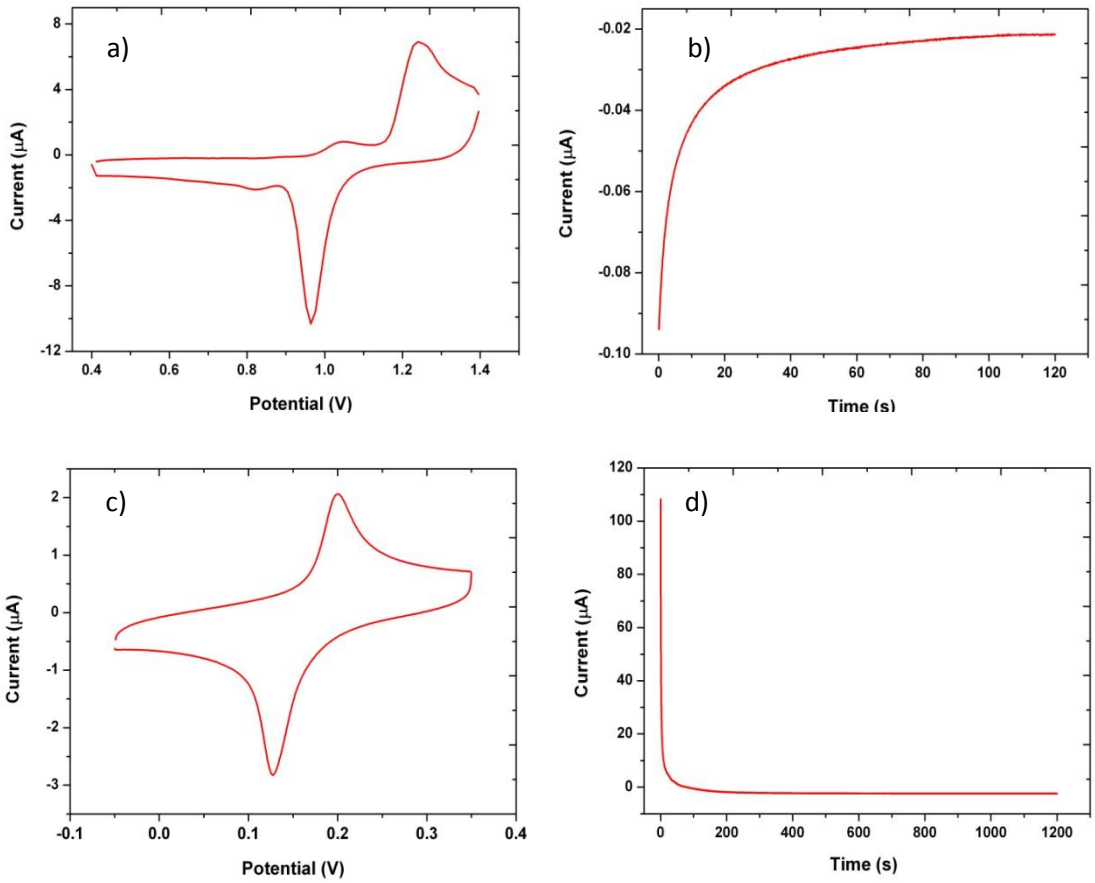


Fig. 6.11 a) Surface cleaning of Au disc electrode in 1 M H_2SO_4; scan rate of 100 mV s^{-1}; b) Electrodeposition of 4 mM PB from 0.1 M KCl and HCl solution at 0.4 V for 120 s; c) Activation of PB in 0.1 M KCl and HCl electrolyte; scan rate of 50 mV s^{-1}; d) Electrodeposition of 0.005 mg mL^{-1} LOX from 5 mM o-PD and 5 mM Na_2SO_3 in 0.05 M phosphate buffer pH 7.4 at 0.65 V for 20 min. Potential recorded vs. Ag/AgCl (3 M KCl).

As previously discussed, the additional oxidation (1.05 V) and reduction (0.8 V) peaks are due to gold contamination with organic impurities, most likely the poly *o*-PD or Prussian Blue residues, which remained at the electrode surface despite the multi-step cleaning procedure.

Following the deposition, the enzyme modified electrode has been submerged in the 0.05 M phosphate buffer (pH 7.4) and stored at 4 ºC, when not in use.

6.4.2. Enzymatic biocathodes.

A) Bilirubin oxidase sol-gel based biocathode.

The enzymatic system of the sol-gel modified biocathode was composed of bilirubin oxidase (BOX), as the catalyst for the reduction of molecular oxygen. While direct electron transfer of BOX has also been investigated as part of this Ph.D. work, the majority of conducted experiments involved the use of osmium (Os) polymer, as the mediator species. Os has been synthesised and kindly donated by prof. Wolfgang Schumann (Bochum, Germany).

Fig. 6.12 is a schematic diagram of the catalytic system employed on the sol-gel modified biocathode. Bilirubin oxidase encapsulated in the sol-gel matrix catalyzed the reduction of molecular oxygen to water. The electrons from the electrode were shuttled through the active redox center of the osmium polymer incorporated in the film at the drop-coating step to the enzyme. The oxygen required for the catalysis was provided by exposing the buffered solutions to air and allowing a passive diffusion of O_2 through silica pores. Reduced Os species were ultimately regenerated at the electrode and the flow of produced electrons was recorded as current.

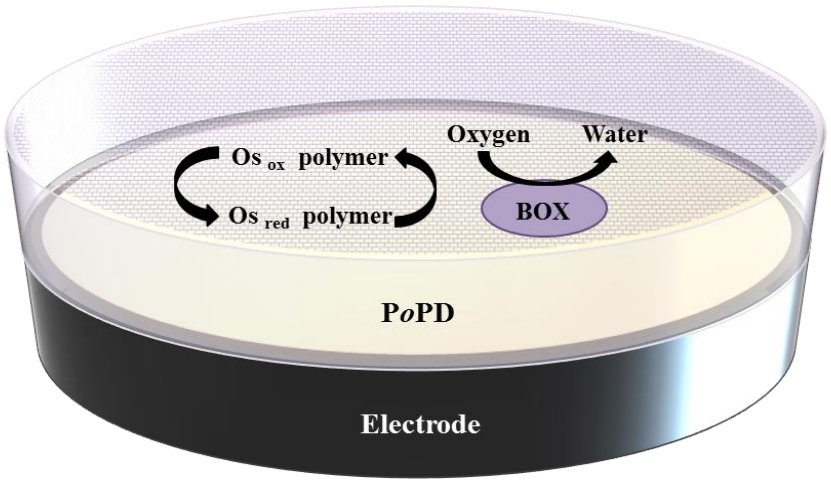


Fig. 6.12. Schematic of the catalytic system selected for biocathode. Sol-gel encapsulation of BOX in the presence of Os polymer as the mediator enabled a successful reduction of molecular oxygen to water and efficient electron transport to the electrode surface.

Osmium complexes have been routinely employed as successful mediators for various oxidoreductase enzymes including glucose [126], lactate [127] and alcohol oxidase [128]. Due to efficient electron shuttling properties and the polymeric nature enabling easy adsorption and stable immobilization of enzyme catalysts [129, 130], the application of flexible osmium redox polymers has offered good prospects in the electrode modification technique and hence has been routinely employed by numerous authors. However due to a rather toxic nature, a number of experimental approaches to replace the osmium with highly conductive carbon nanostructures have been investigated as part of this research work and are discussed in the results section. The use of chitosan as a potential matrix for BOX encapsulation has also been considered.

Encapsulation of BOX in the sol-gel has been carried out, as described in Chapter II, from a 0.25 M hydrolyzed solution of TEOS mixed with the protein suspension (10 mg mL^{-1}) and Os polymer acting as the mediator. As previously described for DSDH bioanode, polyethyleneimine (PEI, 10 % in DI water, pH 9.0) has been added to the starting sol to provide a favorable electrostatic interaction between the cationic polymer and the negatively charged superficial groups on the catalyst. The reacting mixture consisted of 0.25 M TEOS, Os polymer, BOX (10 mg mL^{-1} in deionized H_2O) and polyethyleneimine (PEI, 10 % in DI water, pH 9) rapidly mixed in an Eppendorf tube, as discussed in Chapter II. While DSDH has been encapsulated in the gel via electrochemically assisted deposition, the solution containing BOX has been drop-coated onto the electrode surface and left at RT for 2 h for condensation and aging.

The electrode testing has been carried out using an Autolab PGSTAT-12 potentiostat (Eco Chemie), controlled by the GPES (General Purpose Electrochemical System). A three-electrode cell including a Pt disc auxiliary, Ag/AgCl (3 M KCl internal electrolyte) reference and Pt (Ø 4 mm), Au (Ø 4 mm) or GCE (Ø 3 mm) disc working electrodes have been employed for the electrochemical testing. Prior to drop-coating, the WE has been mechanically polished on wet emery paper (4000) with alumina powder (0.05 µm particle size) and rinsed with deionized water to remove the alumina residues. Following the cleaning, a 5 µL aliquot of a discussed BOX mixture been has been carefully applied on the working electrode, making sure no air bubbles have been introduced in the suspension.

B) Laccase modified sol-gel biocathode.

Laccase functionalized *o*-PD biocathode has been prepared according to [69], as described in Chapter II.

A diagram of the catalytic layer and the reaction scheme for the reduction of molecular oxygen, employed as part of the work on laccase, is depicted in Fig. 6.13. The four electron reduction of molecular O_2 follows from the electrochemical oxidation of the P*o*PD matrix and mediated electron transfer in the presence of quinone (Q), dissolved in the phosphate buffer. The reduced state of the polymer is regenerated by the Nernstian equilibrium [69] and measured as the flow of electrons through the electrode.

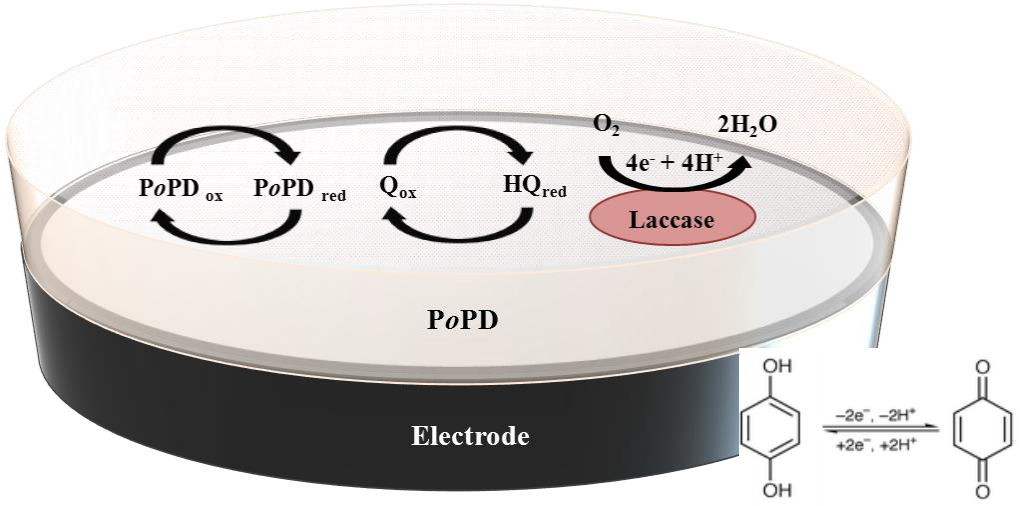


Fig. 6.13. Schematic representation of the biocathode, with laccase entrapped in the PoPD film and catalysing the reduction of molecular oxygen to water in the presence of quinone (Q) dissolved in the buffer solution. The schematic of a 2 e^- redox reactions of HQ is included as an inset.

Electrodeposition of the laccase doped polymer films has been carried out from 10 mL solution of 5 mM *o*-PD and laccase (0.1 mg mL^{-1}) in 0.1 M phosphate buffer, pH 6.0. The solution was placed in a three-electrode electrochemical cell and purged with nitrogen for 20 mins at room temperature. Polymerization of *o*-PD and subsequent incorporation of laccase molecules has been achieved by sweeping the potential of the Pt working electrode (Ø 2 mm) between -0.5 V and 0.9 V for 10 consecutive cycles (20 sweeps), at a scan rate of 20 mV s^{-1}. Pt coil and Ag/AgCl (3 M KCl internal electrolyte) have been used as the

counter and reference electrodes accordingly. The average density of laccase upon two electron oxidation of P*o*PD has been estimated to 12-20 µg per 1 mg of the polymer, as reported by Inzelt *et al.* [131].

Prior to the *o*-PD deposition, illustrated in Fig.6.14 b), the working disc electrode has been mechanically polished and chemically cleaned in 1 M H_2SO_4 for 3 h, by cycling the applied potential between -0.2 V and 1.4 V. Fig.6.14 a) shows a CV response of bare Pt recorded followed the repetitive potential scanning in sulphuric acid. The obtained voltammogram is representative of platinum and provides information on the position of the oxidation and reduction peaks (~ 0.8 V and ~ 0.5 V, respectively) of the metal oxide, as well as the potential range at which the desorption and adsorption of hydrogen occur (-0.2 V – 0 V on both, forward and reverse scans). The CV signal of the Pt in the monomer solution revealed a diminishing oxidation peak of the *o*-PD, indicative of the successful formation of the polymer layer on the electrode surface, as seen in Fig. 6.14 b). Electrodeposited films have been carefully washed with the 0.1 M phosphate buffer pH 6.0 and the excess moisture was adsorbed with a tissue paper.

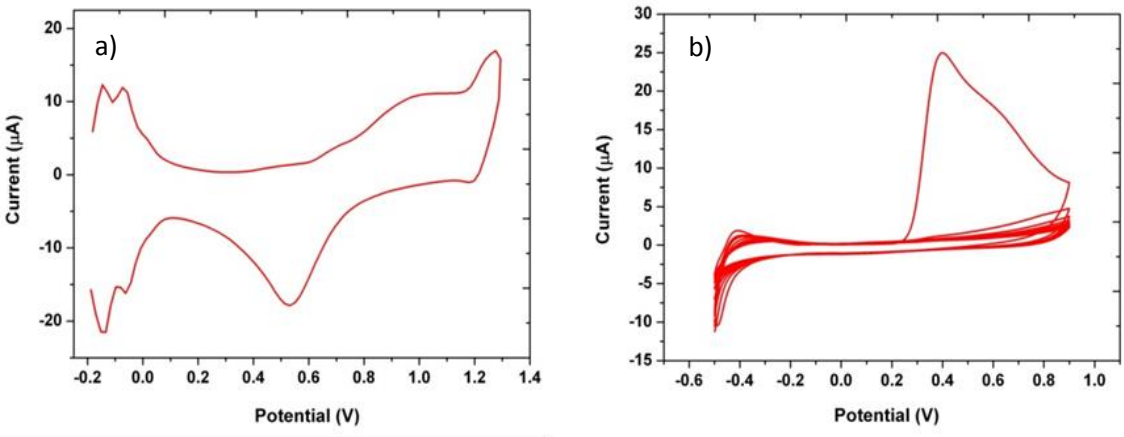


Fig. 6.14 a) Surface cleaning of Pt disc electrode in 1 M H_2SO_4; scan rate of 100 mV s^{-1}; b) Electrodeposition of 0.1 mg mL^{-1} laccase from 5 mM o-PD 0.1 M phosphate buffer pH 6.0 for 20 sweeps at 20 mV s^{-1} scan rate. Potential recorded vs. Ag/AgCl (3M KCl).

Following the modification, the catalytic activity of laccase deposits has been studied in the oxygen deprived and O_2 saturated 0.1 M phosphate buffer solutions, pH 6.0. When not in use, laccase biofunctionalized electrodes were stored in the buffer (pH 6.0) at 4 ^oC.

6.5. Results and discussion.

The following section presents the results of the electrochemical characterization of the constructed bioanodes and biocathodes and discusses the performance of the investigated enzymatic half-cells in terms of their catalytic activity.

6.5.1. Enzymatic bioanodes.

A) D-Sorbitol dehydrogenase sol-gel based bioanode.

Electrochemical studies of DSDH (10 mg mL^{-1}) encapsulated in sol-gel films have been performed via cyclic voltammetry measurements in 0.1 M Tris-HCl buffer, pH 9.0 containing 0.1 mM ferrocenedimethanol (FDM) and in the presence of increasing concentrations of the substrate, D-Sorbitol (2 mM - 8 mM). Although direct oxidation of the substrate has been recently reported for DSDH [132], the use of FDM as the mediator has been shown to have a significant positive effect on the enzymatic activity [114], resulting in much greater current outputs. In the light of these findings, only mediated electron transfer of DSDH has been considered as the scope of this Ph.D. chapter.

Experimental conditions of the set-up were controlled by the Autolab PGSTAT-12 potentiostat (Eco Chemie) and monitored by the GPES (General Purpose Electrochemical System).

The catalytic activity of D-Sorbitol dehydrogenase has been initially studied using silica films containing a 1:1.5 (w/w) ratio of NAD^+ and GPS precursor. Enzymatic oxidation of D-Sorbitol has been investigated on Au disc electrodes modified with DSDH sol-gel deposits and immersed in buffered solutions containing various amounts of the substrate (Fig. 6.15). Successful electrocatalysis would result in increased values of the maximum oxidation current with projected highest activity of the enzyme at a certain concentration of D-Sorbitol. Expected amplification of the oxidative behaviour should be followed by a gradual decline in the reductive current.

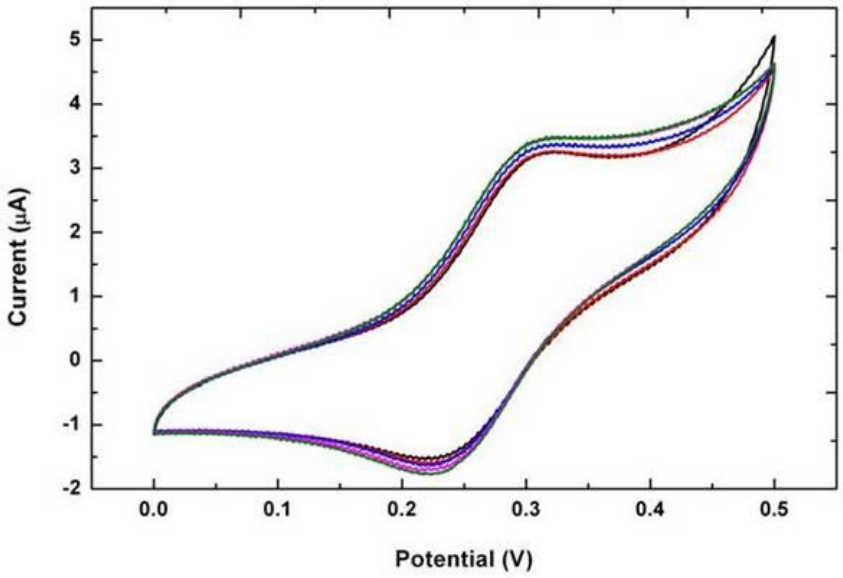


Fig. 6.15. Response of Au disc electrode with electrogenerated DSDH / NAD^+ - GPS / DI / TEOS film to increasing concentrations of substrate in 0.1 M Tris-HCl buffer, pH 9.0, containing 0.1 mM FDM: 0 mM D-Sorbitol (black line); 2 mM D-Sorbitol (red line);4 mM D-Sorbitol (blue line); 6 mM D-Sorbitol (magenta line); 8 mM D-Sorbitol (green line); Scan rate of 20 mV s^{-1}. Potential recorded vs. Ag/AgCl (3M KCl).

As can be seen from Fig. 6.15, cyclic voltammetry analysis of DSDH sol-gel films, obtained with the initial 1:1.5 (w/w) ratio of NAD^+ - GPS, and studied in the presence of increasing concentrations of D-Sorbitol, did not results in a measurable catalysis. This might be due to potential steric hinderance in the electrogenerated silica films preventing efficient electrical contact between the enzyme's redox center and the cofactor.

Due to the absence of detectable enzymatic activity, the solution has been replaced with 5 mL of fresh Tris-HCl buffer supplemented with 1 mM NAD^+, added directly to the medium. The electrode has been further retested in the presence of FDM and increasing concentrations of D-Sorbitol (Fig. 6.16). Increase in the oxidation current would indicate retained catalytic activity of DSDH and successful communication between the catalyst and the cofactor species.

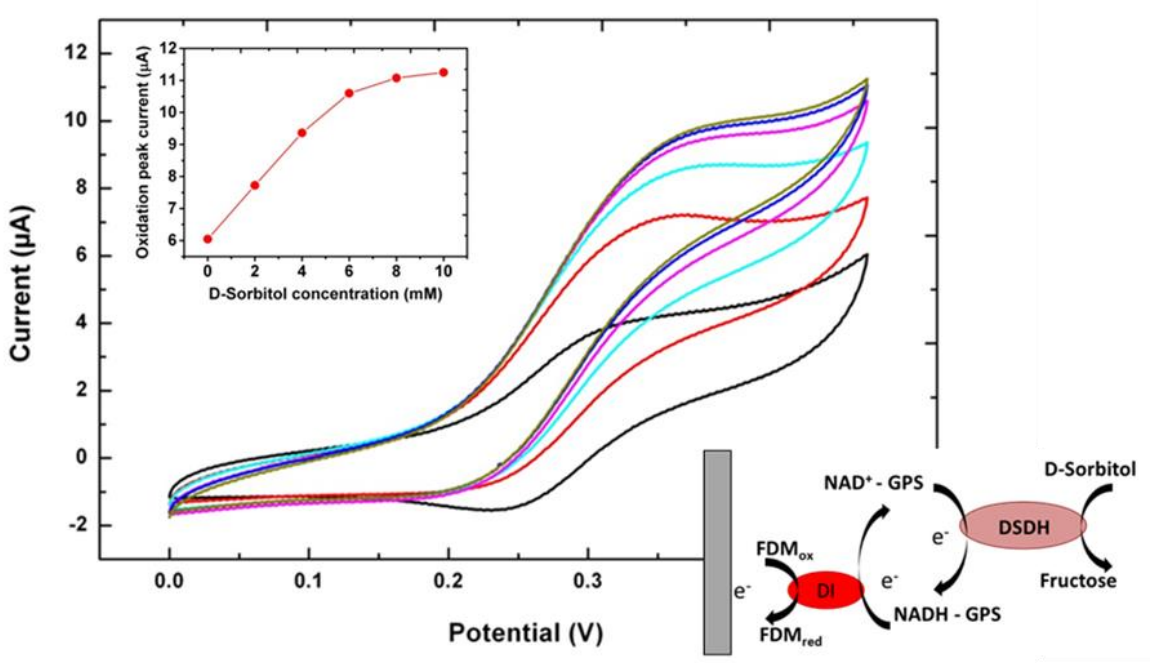


Fig. 6.16. CV of Au disc electrode when 1 mM NAD^+ has been additionally mixed with 0.1 mM FDM, 0.1M Tris-HCl buffer pH 9.0. Response of DSDH to increasing concentrations of D-Sorbitol: 0 mM D-Sorbitol (black line); 2 mM D-Sorbitol (red line);4 mM D-Sorbitol (blue line); 6 mM D-Sorbitol (magenta line); 8 mM D-Sorbitol (green line);10 mM D-Sorbitol (grey line). Scan rate of 20 mV s^{-1}. The maximum oxidation current as a function of D-Sorbitol concentration is shown in the inset. Potential recorded vs. Ag/AgCl (3M KCl).

Following the addition of 1 mM NAD^+ to the buffer solution, the catalytic response of D-Sorbitol dehydrogenase has been recorded with an upsurge in the maximum oxidation current as a function of the substrate concentration (Fig. 6.16). Detectable activity of DSDH, triggered in the presence of soluble cofactor, indicated satisfying biological performance of the enzyme and hence confirmed that the initial lack of response has been due to steric hindrance and limited communication between the enzyme and NAD^+. Significant increase in the produced current has been demonstrated for D-Sorbitol concentrations of up to 4 mM with a gradual saturation of the enzyme from 6 mM onwards. The catalytic efficiency of the DSDH system on bioanode reached a plateau at approximately 8 mM, with the current being only insignificantly larger at 10 mM of the substrate. A schematic representing the reaction is included as an inset.

Following successful determination of DSDH catalytic activity, the original composition of the starting sol has been altered by decreasing the ratio of NAD^+ to GPS to 1: 6.25 (w/w), according to a protocol reported in [133]. Resulting TEOS solution has been then electrodeposited on a clean Au disc electrode, according to the protocol used previously. As formerly, the mediated electron transfer has been studied upon increasing concentrations of D-Sorbitol (Fig. 6.17).

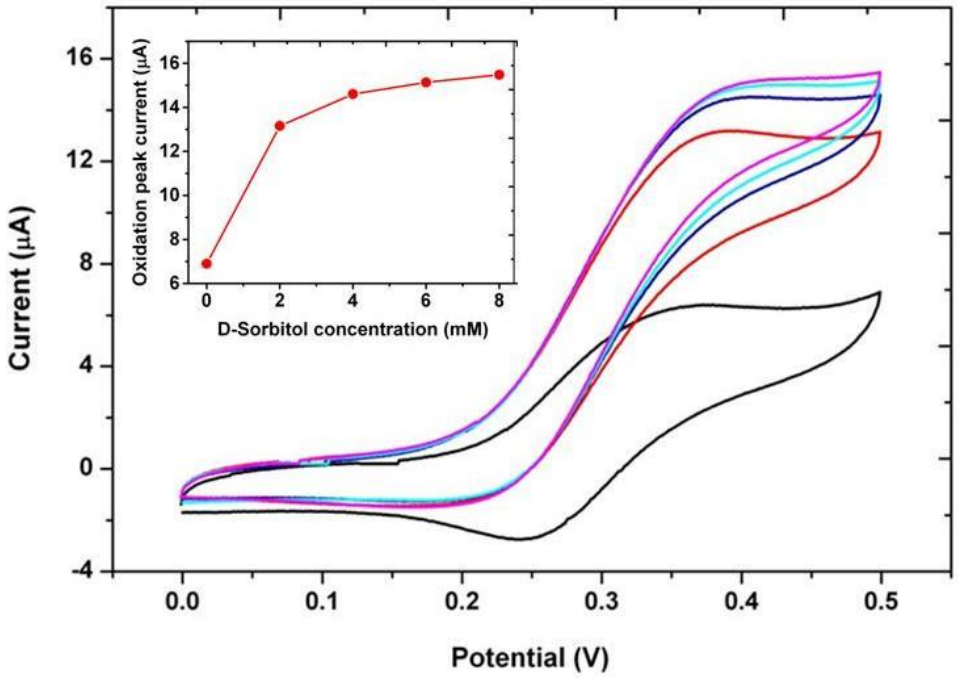


Fig. 6.17. Response of Au disc to increasing concentrations of substrate in 0.1 M Tris-HCl buffer pH 9.0 containing 0.1 mM FDM: 0 mM D-Sorbitol (black line); 2 mM D-Sorbitol (red line); 4 mM D-Sorbitol (navy line); 6 mM D-Sorbitol (cyan line); 8 mM D-Sorbitol (magenta line). Electrode with DSDH/NAD -GPS/DI/TEOS film, containing altered ratio of the NAD^+ to GPS (1: 6.25). Scan rate of 20 mV s^{-1}. The maximum oxidation current as a function of D-Sorbitol concentration is shown in the inset. Potential recorded vs. Ag/AgCl (3M KCl).

As illustrated in Fig. 6.17, alteration of the sol composition, yielded an improved catalysis of DSDH, measured as a 1.2-fold increase in the oxidation current as compared to the plain buffer (no substrate). Decreasing the ratio of NAD^+ to GPS to 1: 6.25 (w/w) provided a less compact matrix structure and much better stabilization of the cofactor

molecule, resulting in an efficient electron exchange with DSDH and higher catalytic currents with the substrate saturation at merely 2 mM (Fig. 6.17) This proves a greater sensitivity of the enzymatic system with high performance obtained at a lower fuel requirement.

Following successful catalysis, the enzymatic response of DSDH to D-Sorbitol has been compared for both systems; with the cofactor freely suspended in the buffer solution, and when it has been co-encapsulated within the TEOS matrix as a NAD-GPS conjugate in a 1: 6.25 (w/w) ratio. Limiting current values for the oxidation reaction have been evaluated as a function of D-Sorbitol concentration and were plotted based on the maximum recorded current (Fig. 6.18).

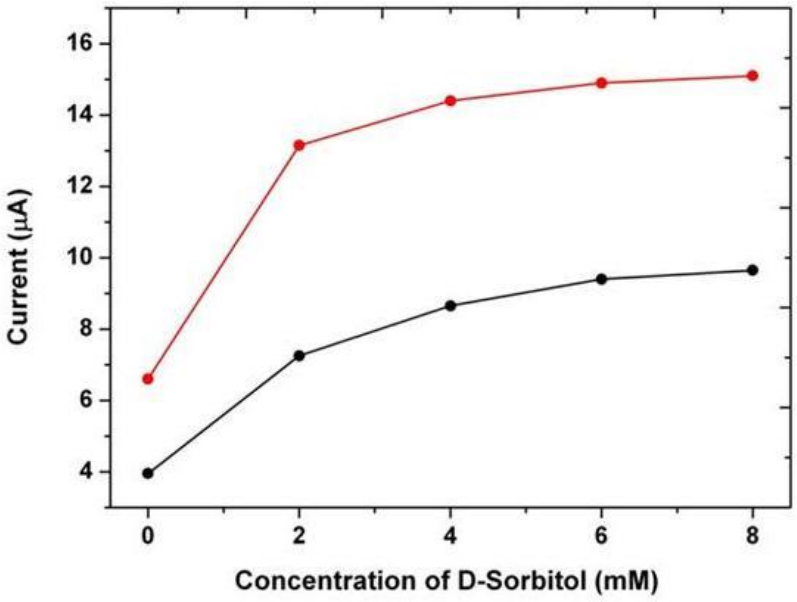


Fig. 6.18. Comparison of the oxidation current for DSDH/NAD^+-GPS/DI/TEOS film electrogenerated on Au with additional 1 mM NAD^+ in the buffer solution (black curve) and when NAD^+ - GPS co-entrapped within the sol-gel matrix (red curve).

As can be seen in Fig. 6.18, an up to 61 % increase in the oxidation current has been recorded when NAD^+ has been co-immobilized within the sol-gel matrix. Rapid increase in the electrode performance has been measured when low concentrations of D-Sorbitol were added to the buffer (2 mM). Higher levels of the substrate resulted in an almost immediate saturation of the enzyme, with a minor change in the current output at

D-Sorbitol concentrations of 5 mM and greater. Nearly a two fold increase in the oxidative current when compared the electron transfer efficiency of immobilized NAD^+ to a soluble cofactor system indicates the favourable effect of cofactor encapsulation on the rate and the frequencey of the electron exchange (Fig. 6.18).

The obtained results emphasize the critical role of the cofactor on the activity of dehydrogenase, highlighting the need to optimize the chemical environment of the sol-gel, according to the intrinsic nature and biological functions of the incorporated species. Only stable entrapment of NAD^+, allowing for its certain mobility within the film, can promote the efficient electron transfer between the redox center of the enzyme and the electrode surface.

B) Glucose oxidase modified P*o*PD based bioanode.

The majority of experimental work on GOX immobilized in poly *o*-PD films has been carried out in 0.1 M phosphate buffer, pH 7.4, in the presence of 50 mM glucose and 7 mM ferrocenecarboxylic acid (FCA). The response of the enzyme has been studied using Cyclic Voltammetry measurements under repetitive cycles.

Initial GOX/*o*-PD films have been prepared by electrodeposition from a 1 mg mL^{-1} suspension of the enzyme in the polymer solution and have been studied in the presence of 1 mM FCA and increasing concentrations of glucose. The buffered substrate has been added gradually to the bulk 0.1 M phosphate buffer (pH 7.4) and the mixture has been thoroughly mixed by pipetting, in order to provide a homogenous solution. The electrochemical signal has been recorded at a 100 mV s^{-1} scan rate under unstirred conditions (Fig. 6.19). All solutions have initially been pre-warmed in the oven at 40 ºC prior to the electrochemical testing, in order to promote the electrocatalysis of GOX. The experiments were however carried out at 30 ºC.

Cyclic voltammetry response of GOX functionalized P*o*PD films deposited on the surface of commercial gold disc (Ø 2 mm) electrodes with an enzyme load of 1 mg mL^{-1}, demonstrated no catalysis of glucose electrooxidation by GOX in the presence of ferrocenecarboxylic acid and increasing concentrations of the substrate (Fig. 6.19). The small rise in the current at the highest electrode potential is most likely due to hydrogen peroxide generation or direct oxidation of glucose on the Pt electrode, not involving the enzyme. The lack of electrocatalytic signal has been attributed to the low concentration of

incorporated GOX and therefore, a higher catalyst load has been recommended for further studies.

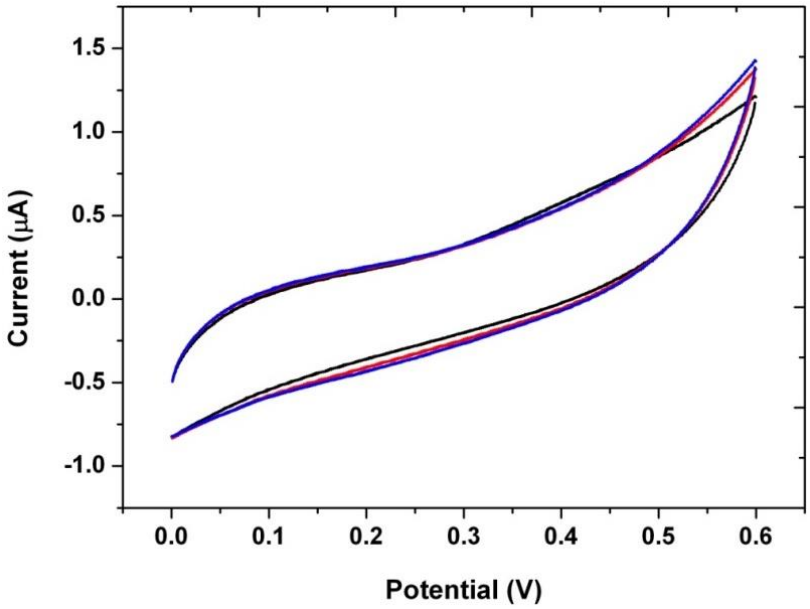


Fig. 6.19. Electrochemical response of 1 mg mL^{-1} GOX in poly o-PD to increasing concentrations of the substrate: no glucose present (black line); 9 mM glucose (magenta line); 16 mM glucose (blue line); signal recorded in 1 mM FCA in 0.1 M phosphate buffer, pH 7.4. Scan rate of 100 mV s^{-1}. Potential recorded vs. Ag/AgCl (3M KCl).

Following an overnight storage in the 0.1 M phosphate buffer (pH 7.4; 4 ºC), the electrode has been re-analysed at higher glucose concentrations in the presence of higher amount of the mediator species (7 mM FCA in 0.1 M phosphate buffer, pH 7.4) and the CV response has been depicted in Fig. 6.20. The sensitivity of GOX to a rapid change in the glucose levels has been measured by diluting the solution with fresh buffer and decreasing the concentration of the substrate by a factor of 5.4 (indicated as a black dashed line).

As indicated by Fig. 6.20, the electrochemical measurements were consistent with the previous results. No significant change in the current has been observed when increasing concentrations of glucose were added or when the working solution was diluted with a fresh buffer (Fig. 6.20, dashed line), suggesting the lack of GOX catalysis. The

minor increase in the maximum recorded current was attributed to H_2O_2 formation or a direct oxidation of glucose on the Pt electrode.

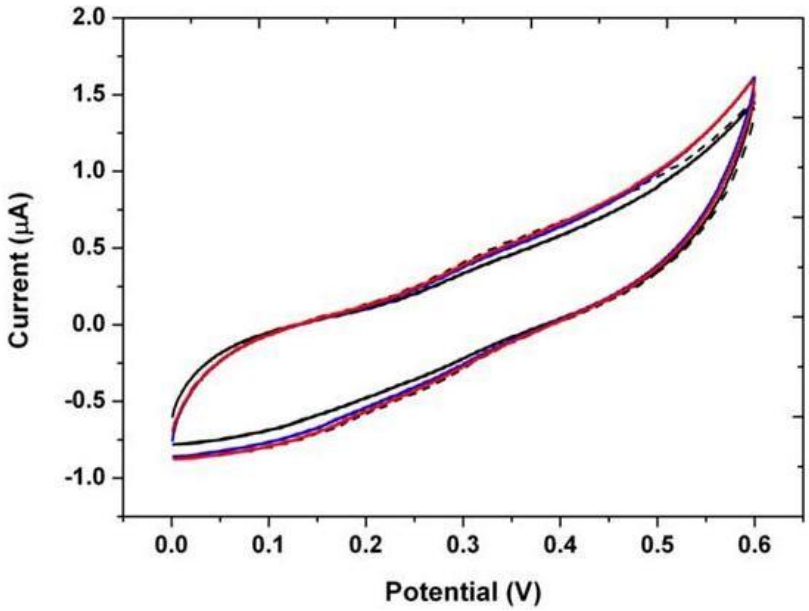


Fig. 6.20. CV of 1 mg mL^{-1} GOX in poly o-PD in the presence of 1 mM FCA and in response to glucose solutions: 0 mM glucose (black solid line); 70 mM glucose (blue line); 124 mM glucose (red line). The signal of GOX to 23 mM glucose, following the dilution with the buffer, is indicated as a black dashed line. Scan rate of 100 mV s^{-1}. Potential recorded vs. Ag/AgCl (3M KCl).

In order to confirm that the change in the response is due to the enzymatic activity of glucose oxidase encapsulated in the polymer film, the electrodeposition has been carried out in the absence of *o*-PD, as shown in Fig. 6.21 a). In this case, a drop in the recorded current has been attributed to the reduction of the o-PD monomer at the electrode / electrolyte interface. The catalysis has been studied in the presence of increasing concentrations of the substrate, according to Fig. 6.21 b), gradually supplied to the solution from a buffered stock of glucose (70 mM) and 1 mM FCA. Upon addition of glucose, the successive increase in the fuel concentrations resulted in decreased redox currents, most likely due to a limited diffusion of mediator molecules in high substrate setting, indicated in Fig. 6.21 b).

CV of the enzymatic layer prepared in the absence of *o*-PD and recorded at increasing amount of buffered glucose, indicated well pronounced oxidation (0.35 V vs. Ag/AgCl) and reduction (0.27 V vs. Ag/AgCl) peaks for FCA; however, no catalysis has been observed, most likely due to the lack of the enzyme at the electrode surface. This result supports the essential role of the matrix, as a physical support for the encapsulation of the catalyst on Au.

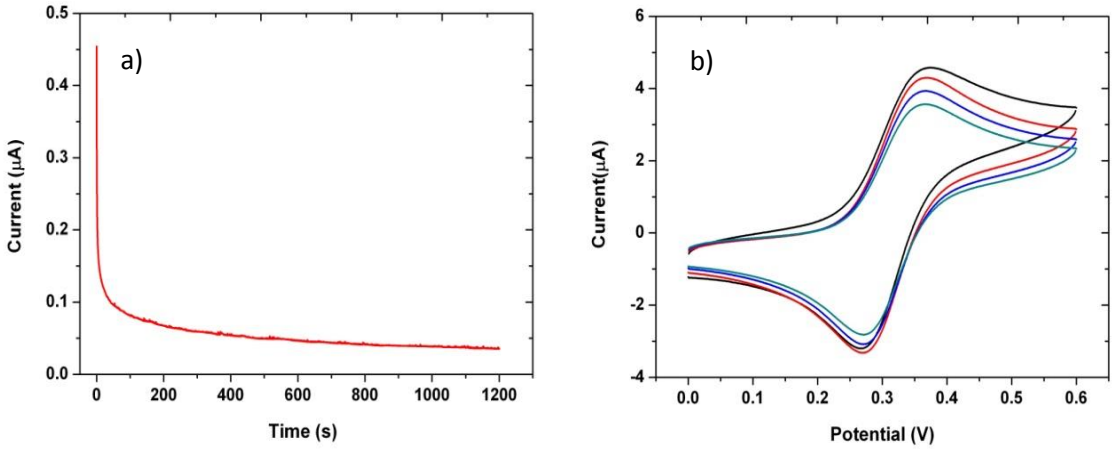


Fig. 6.21 a) Electrodeposition of 1 mg mL^{-1} GOX without poly o-PD matrix from a deaerated phosphate buffer containing 5 mM Na_2SO_3; b) Response of Au disc electrode to glucose solutions in 1 mM FCA in 0.1 M phosphate buffer, pH 7.4: 0 mM glucose (black line); 9 mM glucose (red line); 16 mM glucose (navy blue line); 21 mM glucose (cyan line). Scan rate of 100 mV s^{-1}. Potential recorded vs. Ag/AgCl (3M KCl).

The influence of the concentration of GOX on the intensity of the electrochemical signal has been investigated using deposits obtained from 10 mM *o*-PD suspensions with 10 mg mL^{-1} of the enzyme. The activity of GOX has been evaluated under unstirred conditions, upon a gradual addition of buffered glucose stock of 0.56 M, in the presence of 7 mM FCA (Fig. 6.22).

As can be seen in Fig.6.22, the electrochemical characterization of GOX / P*o*PD films generated from a 10 mg mL^{-1} concentration of the enzyme in the deposition bath, revealed much higher oxidative currents, reaching a value of 3.5 µA when 168 mM of glucose was present in the buffer solution (Fig. 6.22). Unlike for the catalytic system

containing 1 mg mL^{-1} GOX, no saturation of the enzyme has been recorded even for very high concentrations of the substrate.

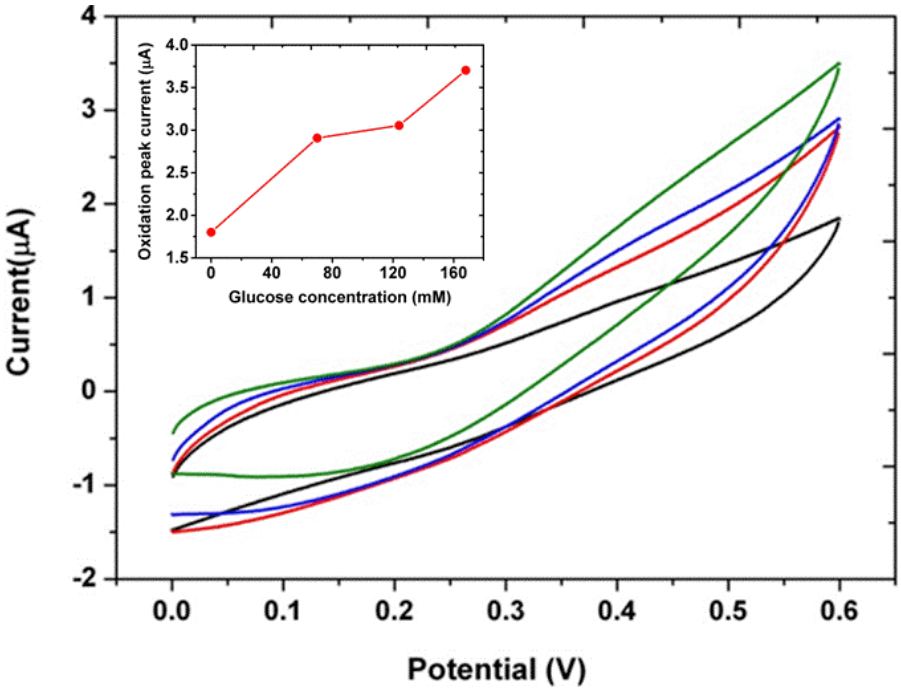


Fig. 6.22. Response of 10 mg mL^{-1} GOX in poly o-PD on Au disc electrode to increasing glucose concentrations recorded in 7 mM FCA in 0.1 M phosphate buffer, pH 7.4: 0 mM glucose (black line); 70 mM glucose (red line); 124 mM glucose (blue line); 168 mM glucose (green line). Scan rate of 100 mV s^{-1}. The dependency of the maximum oxidation current on glucose concentration is depicted in the inset. Potential recorded vs. Ag/AgCl (3M KCl).

The activity of GOX has been re-examined in 0.1 M phosphate buffer (pH 7.4) containing 7 mM FCA and high concentrations of glucose, following an overnight incubation in the air at room temperature (Fig. 6.23). The influence of the storage conditions has been investigated.

As depicted in Fig. 6.23, a 27 % decrease in the current output has been recorded following an overnight air incubation of the enzyme film at room temperature, still resulting in a 36 % higher current output measured at a glucose concentration of 124 mM, as compared to the initial film with a lower enzyme load.

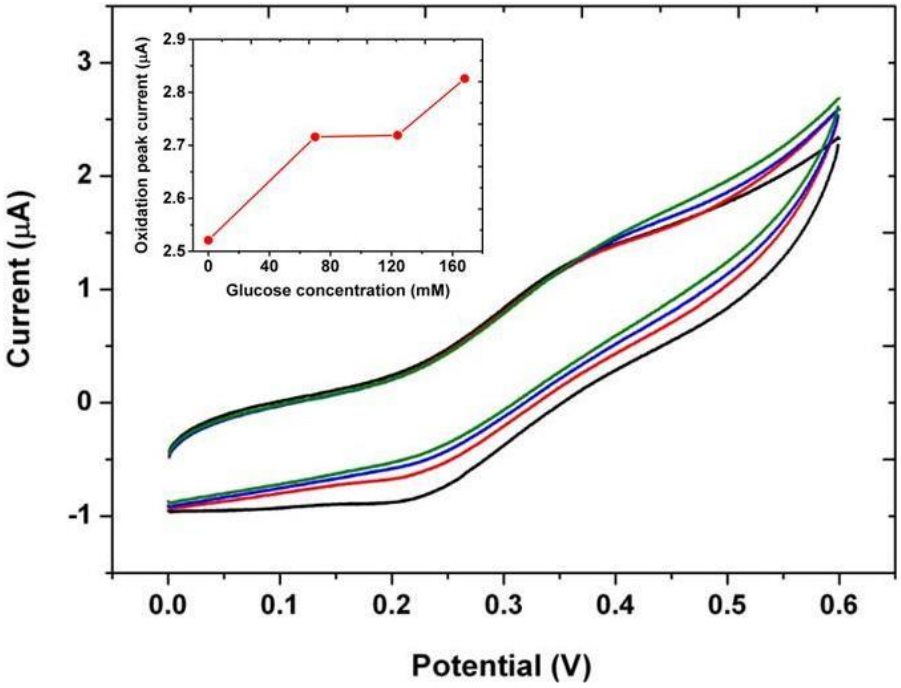


Fig. 6.23. Re-testing the activity of 10 mg mL^{-1} GOX in poly o-PD in the presence of 7 mM FCA and in response to various glucose concentrations: 0 mM glucose (black line); 70 mM glucose (red line); 124 mM glucose (blue line); 168 mM glucose (green line). Scan rate of 100 mV s^{-1}. The dependency of the maximum recorded oxidation current on glucose concentration is depicted in the inset. Potential recorded vs. Ag/AgCl (3M KCl).

In order to study the regeneration of the enzymatic activity of GOX, the electrode has been immersed in the phosphate buffer and stored in the fridge at 4 ºC for 96 h. Following the incubation, the electrocatalytic properties of the film has been determined in buffered glucose solutions (Fig. 6.24). As previously, the sensitivity of the enzyme to a rapid alteration in substrate levels has been measured upon dilution of the working solution by a factor of 5 (indicated as a black dashed line).

As one can see, 96 h period of rehydration of the GOX/P*o*PD layer in 0.1 M phosphate buffer, pH 7.4, resulted in an over 2-fold rise in the catalytic activity, when the electrode was tested in identical working solution. A maximum response of 8.4 μA has been measured for 168 mM of glucose, with 7.85 μA of oxidative current corresponding to 124 mM glucose (Fig. 6.24). These findings not only confirm retained biological functions of GOX encapsulated in the P*o*PD matrix but also suggest a recommended incubation of the deposit in the buffer, prior to the electrochemical testing, in order to obtain catalytically active, highly hydrated enzymatic films.

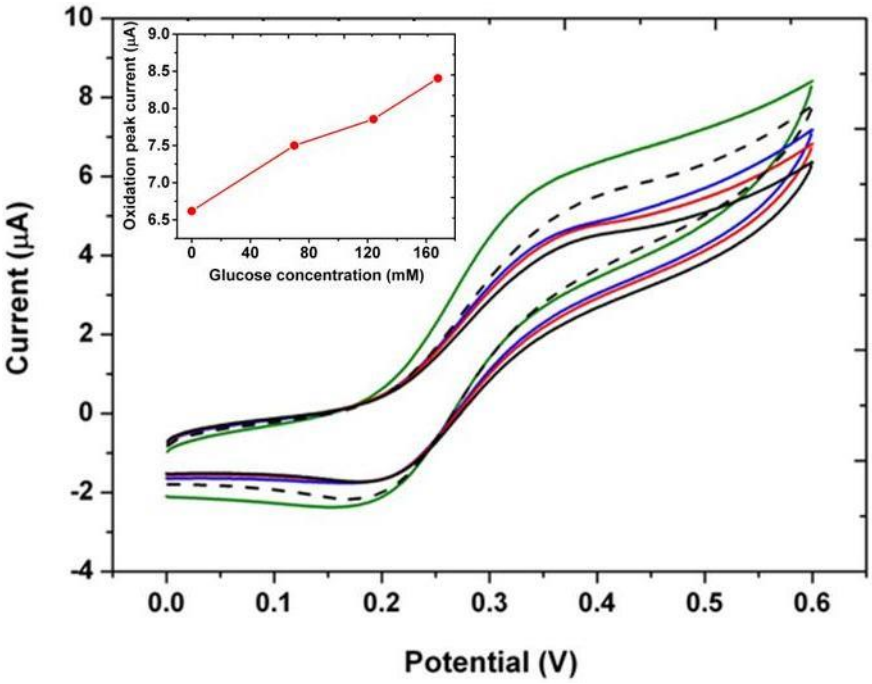


Fig. 6.24. Response of 10 mg mL^{-1} GOX in poly o-PD on Au disc electrode upon 96 h storage in 0.1 M phosphate buffer pH 7.4, 4 ºC. CV signals to varying glucose concentrations recorded in 7mM FCA in 0.1M phosphate buffer, pH 7.4: 0 mM glucose (black solid line); 70 mM glucose (magenta line); 124 mM glucose (blue line); 168 mM glucose (green line); 34 mM glucose following the dilution with the buffer (black dashed line). Scan rate of 100 mV s^{-1}. Potential recorded vs. Ag/AgCl (3M KCl).The dependency of the maximum recorded oxidation current on glucose concentration is depicted in the inset.

The influence of the condition and the duration of the incubation period on the catalytic activity of GOX/poly *o*-PD have been demonstrated in Fig. 6.25, by plotting the electrochemical response recorded in the presence of 168 mM glucose. As can be seen, the 96 h storage of the electrode in the phosphate buffer (pH 7.4, 4°C) not only retained the biological function of the enzyme but yielded a 1.17 fold increase in the catalytic response to glucose (blue line), as compared to the signal recorded directly after the immobilization (black line). Conversely, an overnight incubation of the deposit in air, at RT, resulted in a 25 % decrease in the observed oxidation current. These results suggest the critical effect of the hydration layer on the performance of the catalyst and the regeneration of the solvation shell of the protein following the incubation in the buffer.

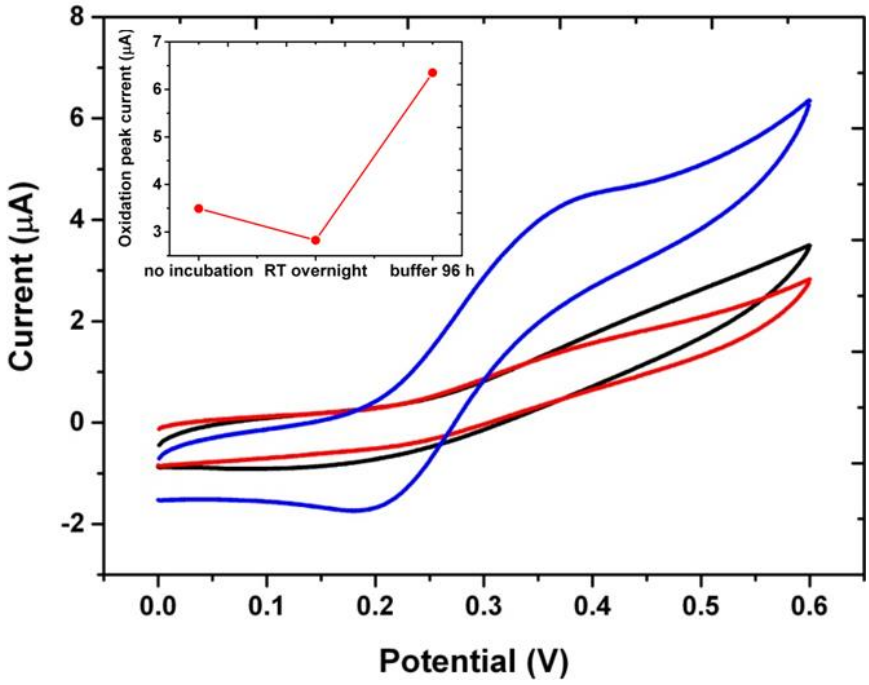


Fig. 6.25. The effect of the incubation on the CV response of 10 mg mL^{-1} GOX in poly o-PD recorded in 0.1 M phosphate buffer pH 7.4 containing 168 mM glucose and 7 mM FCA: no incubation (black line); overnight storage in air at RT (red line); 96 h hour incubation in the buffer at 4 °C (blue line). Scan rate of 100 mV s^{-1}. The effect of the incubation conditions on the maximum recorded oxidation current are illustrated in the inset. Potential recorded vs. Ag/AgCl (3M KCl).

In order to prove that the electrochemical response is due to the electrooxidation of glucose catalyzed by GOX, the signal has been investigated in a buffered FCA solution, in the absence of the substrate and in the plain buffer as a control (Fig. 6.27).

Cyclic voltammograms of the GOX/P*o*PD layer recorded in the plain phosphate buffer and in the presence of 7 mM FCA (Fig. 6.27), demonstrated an identical shape of the electrochemical signal, with a slight increase in the maximum oxidation current for the mediator solution; however, only in the presence of 70 mM glucose the oxidative current reached 6 μA, which is 90 % greater than the signal obtained for FCA.

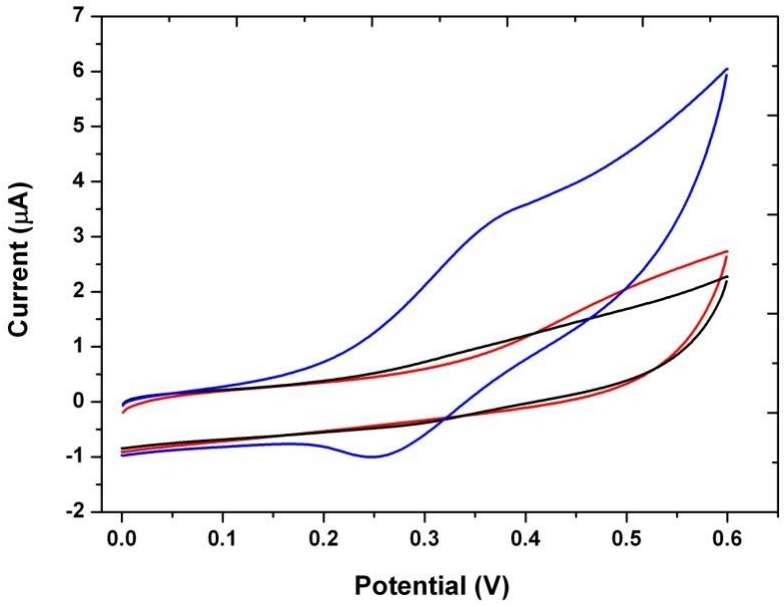


Fig. 6.27. Dependency of the electrochemical response of 10 mg mL^{-1} GOX immobilized in poly o-PD on Au disc electrode on the presence of glucose. CV signals recorded in 0 mM glucose 0.1 M phosphate buffer pH 7.4 (black line); buffer with 7 mM FCA (red line) and buffer with 7 mM FCA and 70 mM glucose (blue line). Scan rate used: 50 mV s^{-1}. Potential recorded vs. Ag/AgCl (3M KCl).

In order to study the effect of buffer composition on the balance of the electrode reactions in the anodic half-cell, the open circuit potential of bare Au disc electrode has been measured for 50 mM buffered glucose solution containing 7 mM FCA and compared against plain 0.1 M phosphate buffer (no glucose), pH 7.4. The immediate OCP readings for the plain buffer and the substrate/mediator medium were 0.6 V and 0.145 V, respectively. Temporal potential measurements, recorded for a period of 600 s, revealed a rather constant OCP value for glucose and FCA solution, consistent with the instant reading. The open circuit potential for the plain buffer did; however; steadily decline in time (Fig. 6.28) reaching a value of approximately 0.425 V after 10 mins. In general, the balance of electrochemical reactions at the electrode surface, which is determined by the OCP, is poorly defined for plain Au, due to the presence of various impurities and dissolved oxygen. In that case, the potential reading for gold electrode in plain buffer drifts in time (Fig, 6.28, black line). On the contrary, the stability of the time dependent OCP reading for the case of the FCA can be explained by a well-defined redox couple (Fig, 6.28, red line). Since the electrochemical reactions at the electrode are dependent on

the mass and charge transfer properties of the electrolyte, as described by Bard in ref. [134], decreased values of measured potential may suggest increased mass and charge exchange rates of the half-cell under investigation.

OCP of bare gold disc electrode measured in phosphate buffer solution (pH 7.4) containing 50 mM glucose and 7 mM FCA, resulted in a lower potential reading, as compared to plain phosphate buffer (Fig. 6.28). An increase in the OCP value indicates improved mass and charge transfer properties at the electrode/solution interface in the mediator solution, suggesting environment favouring the electron exchange processes.

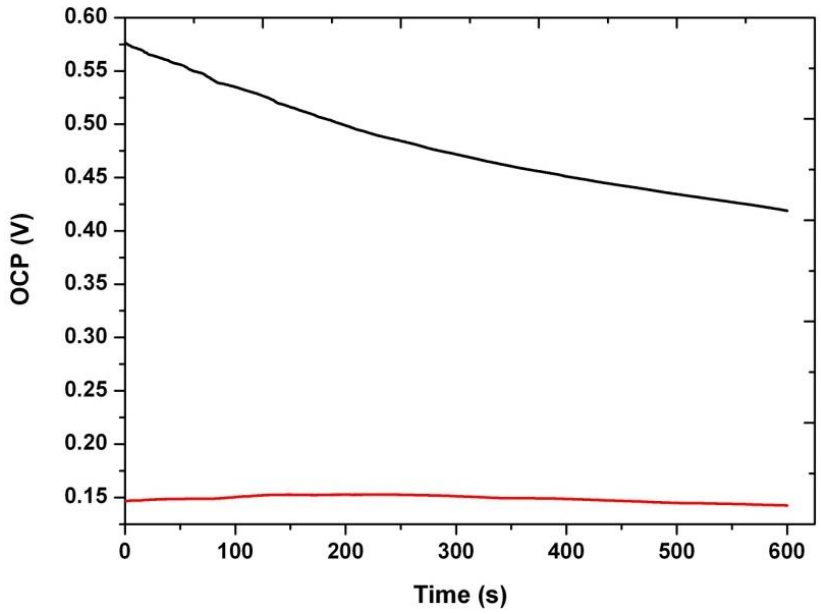


Fig. 6.28. Time-based OCP measurements of bare Au disc electrode in 0 mM glucose (black line) and in 50 mM glucose and 7 mM FCA phosphate buffer pH 7.4 (red line). Potential recorded vs. Ag/AgCl.

The open circuit potential of GOX functionalized poly *o*-PD films on Au disc electrode have been investigated in the presence of glucose and FCA and compared with the potential reading in the plain buffer, as depicted in Fig.6.29. The immediate OCP values for the enzyme doped P*o*PD modified gold, recorded for plain 0.1 M phosphate buffer (pH 7.4) and following the addition of 50 mM glucose and 7 mM FCA, were 0.246 V and 0.211 V accordingly. Time-dependent measurements recorded for 600 s, demonstrated a gradual decline of potential in both solutions, with the same temporal

behavior of the OCP profile reaching the end point value at 0.22 V and 0.186 V for the plain and the substrate/mediator supplemented buffers, respectively. While, the presence of the polymer membrane, should in general, impede the mass and electron exchange at the electrode/solution interface (elevate the measured OCP), the electroactive nature of the mediator promotes the charge transfer mechanisms in the solution more efficient than what is observed for the plain buffer (Fig. 6.29). The nature of the drop in the potential for the GOX/PoPD layer as compared to the bare Au is unclear (Fig. 6.28). Possible explanation might be the intrinsic ability of GOX to carry out the electron transfer processes, which is further facilitated by a relatively high enzyme load (10 mg mL^{-1}). In this light, the presence of the oxidase will result in lower OCP readings (lower half-cell resistance) than what is recorded in the enzyme-free setting.

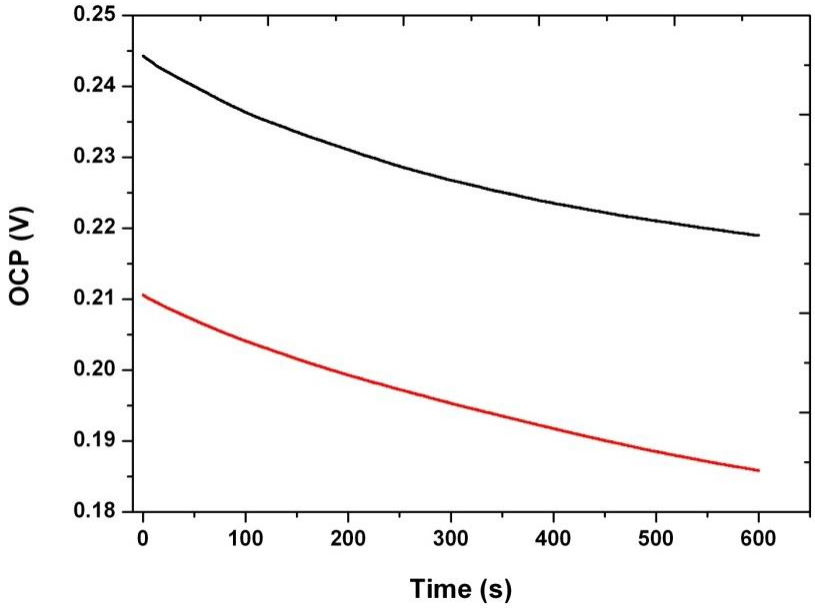


Fig. 6.29. Time - dependent OCP measurements of GOX/PoPD Au disc electrode in 0 mM glucose (black line) and in 50 mM glucose and 7 mM FCA phosphate buffer pH 7.4 (red line). Potential recorded vs. Ag/AgCl.

Following successful preparation of GOX/*o*-PD films and confirmed catalysis of glucose oxidation on the disc electrode, the encapsulation of the oxidase within the polymer matrix has been carried out at gold electrodes plated on Zeonor substrate, as recorded in Fig. 6.30 b). The thin film metal has been chemically cleaned in 1 M H_2SO_4

for 3 h prior to the surface modification, until a reproducible voltammogram for the gold oxide formation (~1.28 V) and reduction (~0.98 V) has been obtained, as depicted in Fig. 6.30 a). The observable drop in the recorded current in Fig. 6.30 b) is indicative of the self-limiting formation of the P*o*PD deposit on the electrode surface. As previously, the additional recurring oxidation and reduction peaks observed at 1.05 V and 0.8 V are most likely the residues of the previously deposited poly *o*-PD or Prussian Blue, which remained at the electrode surface despite the multi-step cleaning treatment.

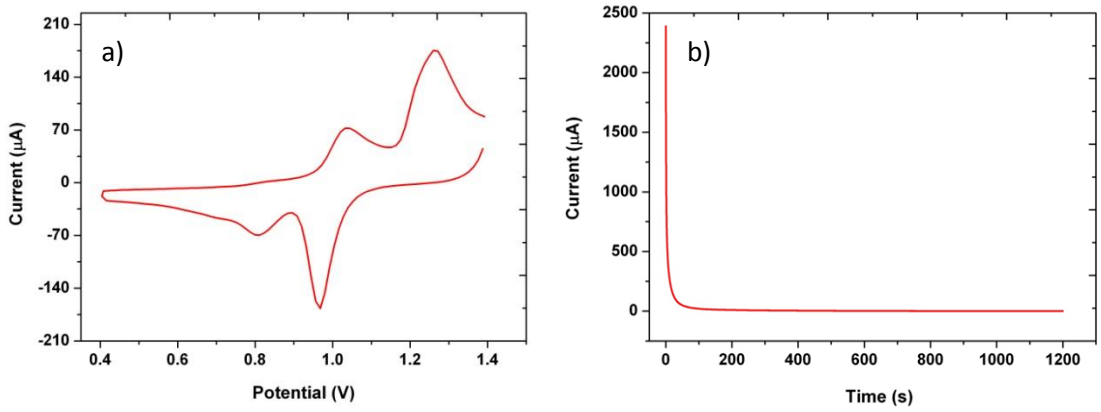


Fig. 6.30 a) Surface cleaning of Au electrode, design 3, in 1 M H_2SO_4; scan rate of 100 mV s^{-1}. Potential recorded vs. Ag/AgCl (3M KCl); b) The electrodeposition of 10 mg mL^{-1} GOX in 10 mM poly o-PD films at 0.75 V for 20 min.

The modified electrode has been prepared from a deaerated suspension of 10 mg mL^{-1} of the enzyme and 10 mM of the monomer in the 0.1 M phosphate buffer, pH 7.4. The electrodeposition has been facilitated by the use of a custom made holder, accommodating the Zeonor platform and the reaction solution, as discussed in Chapter II. The properties of the electrogenerated film have been studied in the presence of 7 mM FCA and increasing concentrations of glucose. The buffered substrate has been added gradually to the bulk 0.1 M phosphate buffer pH 7.4 and the mixture has been thoroughly mixed by pipetting, in order to provide a homogenous solution. The measurements employed the holder as a provisional electrochemical cell, with the Zeonor chip placed at the bottom of the reaction chamber, locating the electrodes horizontally with respect to the redox medium under investigation. The cyclic voltammetry signal has been recorded at a 100 mV s^{-1} scan rate, under unstirred conditions (Fig. 6.31). All solutions have been

initially pre-warmed in the oven at 40 ºC, prior to the electrochemical testing, in order to promote the electrocatalysis by GOX. The experiments were however carried out at 30 ºC.

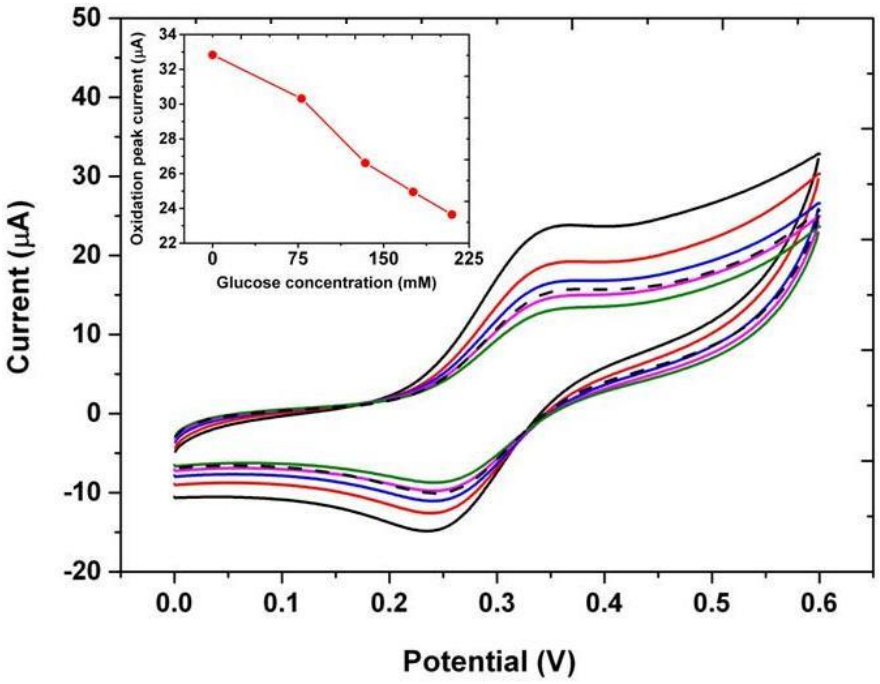


Fig. 6.31. CV signals of 10 mg mL^{-1} GOX in poly o-PD on Au electrode design 3 of the electrode layout. Enzymatic response to varying glucose concentrations recorded in 7 mM FCA in 0.1 M phosphate buffer, pH 7.4: 0 mM glucose (black solid line); 78 mM glucose (red line); 134 mM glucose (blue line); 176 mM glucose (magenta line); 210 mM glucose (green line). Black dashed line represents a concentration of 140 mM glucose following the dilution with the buffer. Scan rate of 100 mV s^{-1}. Potential recorded vs. Ag/AgCl (3M KCl). The maximum observed oxidation current as a function of glucose concentration is shown in the inset.

As can be seen from Fig. 6.31, the investigation of GOX modified poly-*o*-PD, electrodeposited on Zeonor substrate design 3 of the Au electrode layout, revealed no increase in the oxidative current when glucose was added into the solution (Fig. 6.31). Similarly to the response in Fig.6.21 b), the redox peaks of the FCA gradually diminished upon increasing amount of the substrate, indicating diffusion limitations of FCA, possibly due to the effect of the solution viscosity on ferricyanide mobility.

The electrode has been stored in the buffer at 4 ºC overnight and the catalytic response of GOX towards elevated glucose concentrations, determined the following morning (Fig. 6.32). The electrochemical set-up comprised of the holder bearing the horizontally positioned Zeonor chip, has been employed as previously.

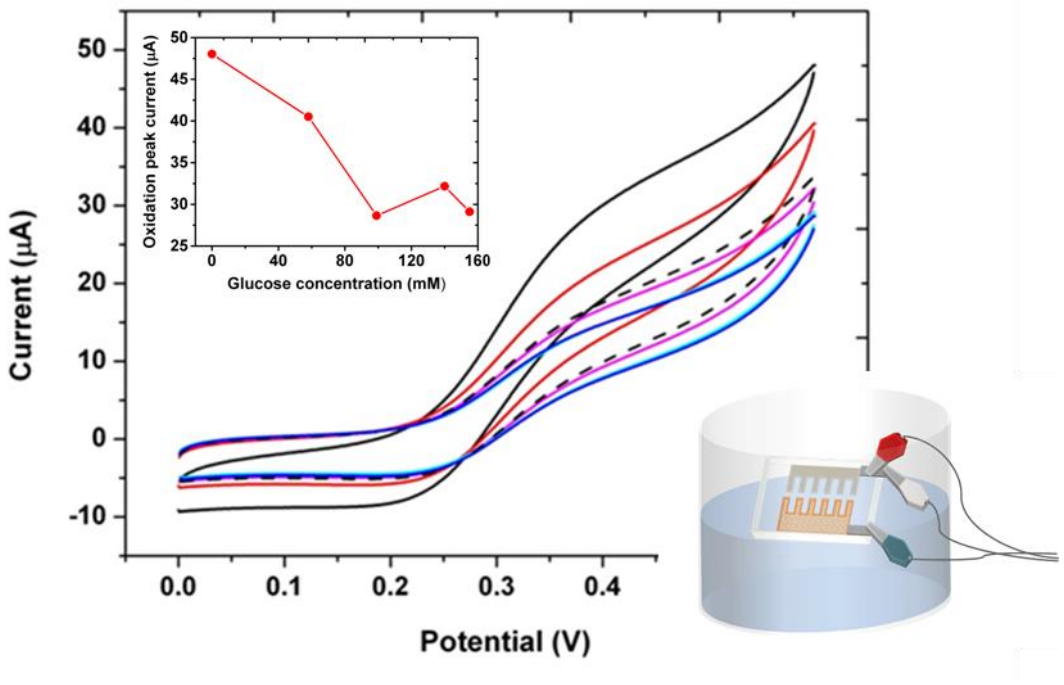


Fig. 6.32. Response of 10 mg mL^{-1} GOX in poly o-PD on Au electrode design 3 of the electrode layout following an overnight incubation in the buffer at 4 ºC. Enzymatic response to increasing glucose concentrations studied in 7 mM FCA in 0.1 M phosphate buffer, pH 7.4: 0 mM glucose (black solid line); 58 mM glucose (red line); 99 mM glucose (navy blue line); 1.4 M glucose (magenta line); 1.55 M glucose (cyan line). Black dashed line represents a concentration of 1.07 M glucose following the dilution with the buffer. Scan rate of 100 mV s^{-1}. Potential recorded vs. Ag/AgCl (3M KCl). The oxidation current vs. glucose concentration dependency and the horizontal position of the electrodes are shown in the insets.

CV measurements, recorded after an overnight incubation in the phosphate buffer, confirmed restricted access of the mediator and lack of catalysis, due to a built up of glucose layer at the electrode/solution interface. This resulted in inhibited exchange of electrons between the mediator molecules and the electrode (Fig. 6.32).

Following a series of ambiguous results, the experimental set-up has been altered by immersing the GOX/*o*-PD modified gold electrodes vertically in the electrochemical cell, containing the redox solution. The catalytic response of the enzyme has been investigated upon addition of glucose, in the presence of FCA as the mediator (Fig. 6.33). For the purpose of this study, a modified gold electrode of design 3 (defined in Chapter V) stored in the buffer for 72 hours, prior to the measurement has been employed, in order to determine the potential catalytic activity of the deposit and the stability of the generated GOX film over time.

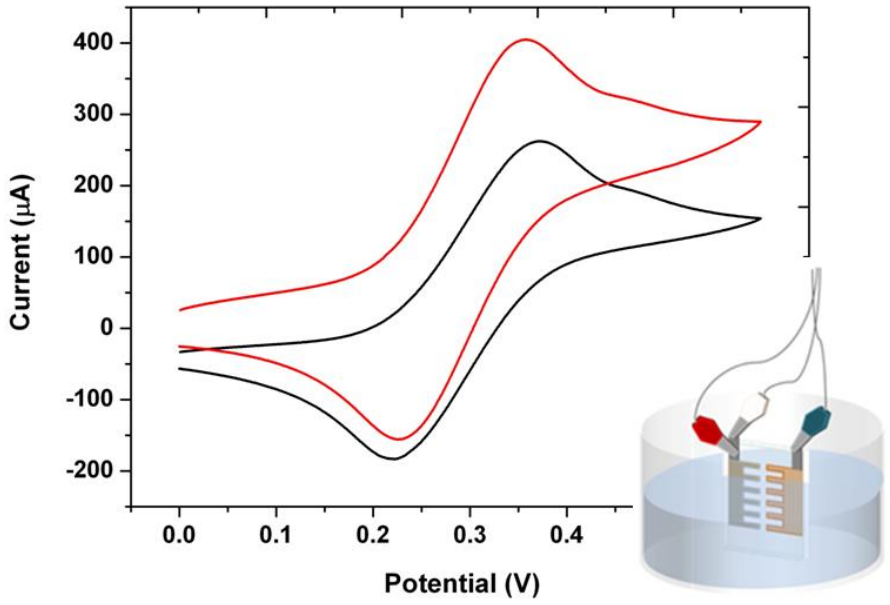


Fig. 6.33. Cyclic voltammetry response of 10 mg mL^{-1} GOX in poly o-PD deposited on Au electrode design 3 of the layout following 72 hour incubation in the buffer at 4 ºC. Catalytic activity of GOX to glucose in 7 mM FCA in 0.1 M phosphate buffer, pH 7.4: 0 mM glucose (black line); in the presence of 70 mM glucose (red line). The electrode was immersed vertically in the electrochemical cell containing the studied solution. Scan rate of 100 m V s^{-1}. Potential recorded vs. Ag/AgCl (3M KCl).The vertical position of the on-chip electrodes is illustrated in the inset.

Altering the configuration of the modified Zeonor platform from horizontal to a vertical resulted in an effective electrooxidation of glucose by GOX (Fig. 6.33), with a 54 % increase in the maximum recorded oxidation current in the presence of glucose (70 mM). In addition, since the investigation has been carried out following a 72 h storage in the phosphate buffer, the stability of electrogenerated film and retained biological activity

of GOX have been simultaneously demonstrated. These results emphasize the importance of an unlimited diffusion of the species towards the polymer film. While the horizontal electrode location results in a built up of a glucose layer at the polymer/solution interface, preventing the access of the mediator, the vertical positioning of the chip impedes substrate accumulation due to gravitational forces. This phenomenon should not; however, be an issue in the case of the mediator being co-immobilized at the electrode surface or in a dynamic system, where the flow of the fuel successfully prevents the local aggregation of the substrate. This is particularly valid for practical applications, where one would like to minimize the preparation of the fuel source and hence maintain all catalytic reagents on the active element.

C) Lactate oxidase functionalized *o*-PD bioanode.

Initial encapsulation of lactate oxidase (LOX) within the *o*-phenylenediamine matrix has been carried out in the absence of Prussian Blue (PB), from buffered solution of 5 mM *o*-PD and 0.005 mg mL^{-1} LOX. The testing involved cathodic detection of the by-product of the enzymatic reaction, H_2O_2, formed upon addition of increasing volumes of the substrate, sodium L-Lactate. The electroreduction of generated H_2O_2 has been studied by posing the electrode at a constant potential of - 0.75 V and recording the resulting current in unstirred conditions over a period of 120 s. Electrochemical decomposition of peroxide enables indirect quantification of L-lactate consumed by the reaction, as such being indicative of the catalytic properties of LOX [68].

The amperometric signal of Au disc electrode modified with LOX / P*o*PD film has been initially recorded in $5 \cdot 10^{-5}$ M sodium L-lactate solution of 0.05 M phosphate buffer pH 7.4. Following the basal signal, the response was measured upon successive 200 µL additions of the initial lactate solution, until a substrate concentration of 27 mM was reached (Fig. 6.34). The solution has been mixed by pipetting after each injection.

The amperometric studies employing LOX/P*o*PD modified Au disc electrodes showed increased current response due to peroxide reduction, upon addition of L-lactate (Fig. 6.34). Due to the minuscule enzyme concentration (0.005 mg mL^{-1}), the current was in the order of nA.

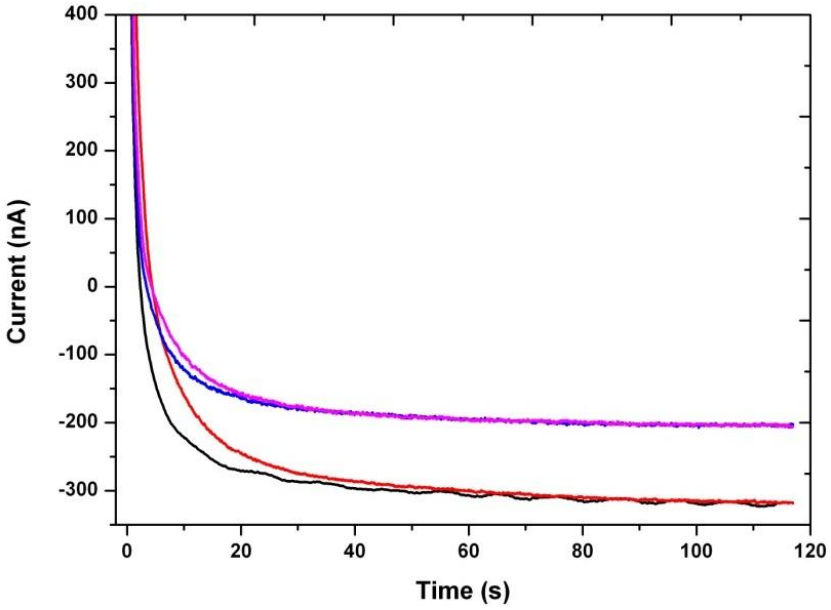


Fig. 6.34. Current-time response of 0.005 mg mL^{-1} LOX/PoPD modified Au disc electrode at -0.75 V to successive additions of $5x10^{-5}$ L-lactate in 0.05 M phosphate buffer, pH 7.4. Signal recorded at 0.75 V for $5x10^{-5}$ L-lactate (magenta line); 10 mM L-lactate (blue line); 19 mM L-lactate (red line) and 27 mM L-lactate (black line).

Sensitivity of the PB modified Au disc macro-electrode to H_2O_2 has been investigated using voltammetry studies in the presence of increasing amounts of H_2O_2, prepared as a solution in 0.05 M phosphate buffer pH 7.4 (Fig. 6.35). The measurement has been performed by cycling the potential of the working electrode within the -0.6 V and 0 V range [135].

The majority of the experimental work on peroxide determination, carried out as part of this chapter, was performed using cyclic voltammetry as the method of choice. Chronoamperometric studies as more sensitive and with long-term applicability [105], are typically employed in electrochemical biosensors where lower detection limits are an essential requirement.

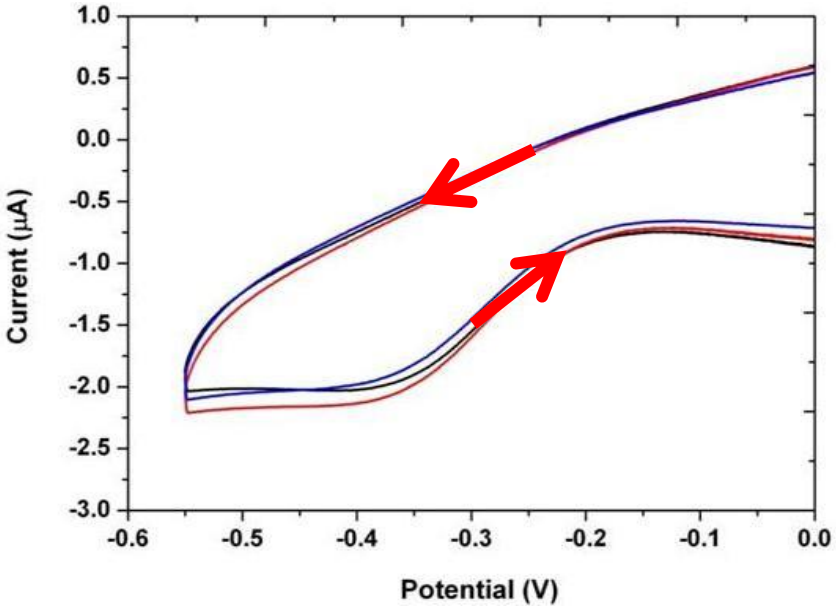


Fig. 6.35. Response of 4 mM PB modified Au disc electrode to successive increase in peroxide concentration. Signal recorded in 0.05 M phosphate buffer pH 7.4 with 6.66 ppb of H_2O_2 (black line); 22 ppb H_2O_2 (blue line) and 36 ppb H_2O_2 (red line). Scan rate of 100 mV s^{-1}. Potential recorded vs. Ag/AgCl (3M KCl).

As depicted in Fig. 6.35, the slightly elevated reduction currents for the electrodeposited PB polycrystals were consistent with the small rise in the peroxide concentration. The peak onset for the electrochemical reduction of H_2O_2 by PB was recorded at -0.2 V.

For the comparison purpose, the response of PB has been also analyzed using a commercial Au micro-electrode (Ø 12.5 μm), provided by Dr. Alan O'Riordan from the Nanotechnology Group of the Tyndall National Institute. The investigation was carried out in order to study the properties of the system transposed onto a different electrode configuration (Fig. 6.36).

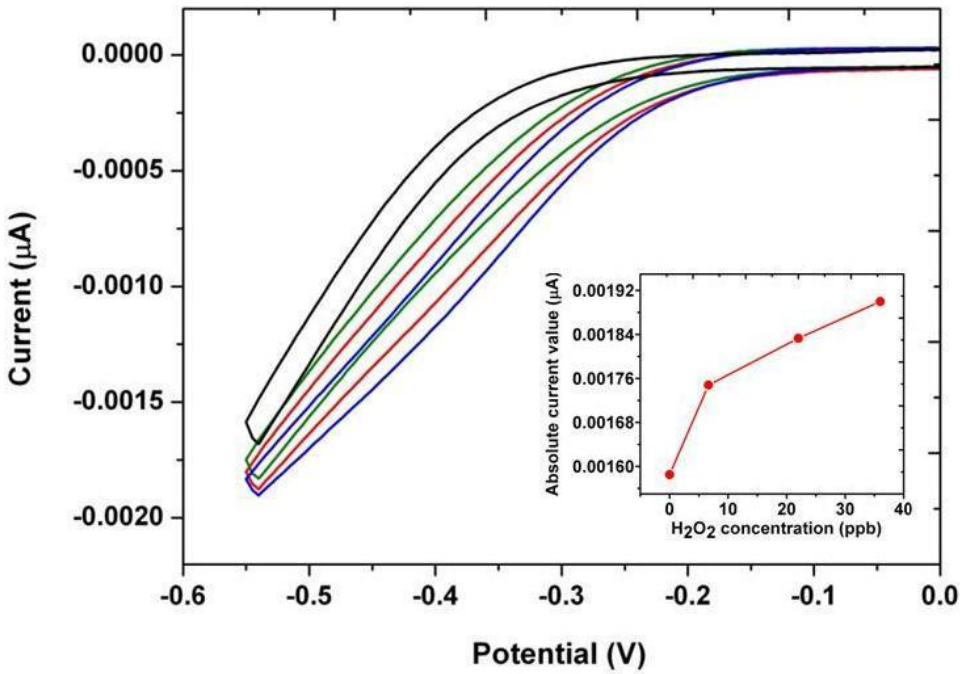


Fig. 6.36. Electrochemical reduction of hydrogen peroxide catalysed by 4 mM PB modified Au micro-electrode. CV recorded in 0.05 M phosphate buffer at pH 7.4 (black line) as a control and in the presence of: 6.66 ppb of H_2O_2 (green line); 22 ppb H_2O_2 (red line) and 36 ppb H_2O_2 (blue line). Scan rate of 100 mV s^{-1}. Potential recorded vs. Ag/AgCl (3M KCl).The plot of an absolute value of current as a function of peroxide concentration is presented in the inset.

PB supported reduction of the peroxide on a commercial gold micro electrode (Ø 12.5 µm), conducted in order to study the reproducibility of the method, revealed small increase in the peak values with a potential onset for the reductive current at -0.2 V vs. Ag/AgCl (Fig. 6.36). The dependency of the current on the amount of H_2O_2, illustrated as the inset of Fig, 6.37, indicates a steady increase in the response within the investigated range of peroxide concentrations.

The magnitude and the shape of the electrochemical signal of Au have been further evaluated following the electrodeposition of *o*-PD on a macro-electrode, previously modified with PB. The electroreduction of peroxide has been recorded as formerly, by measuring the CV response at various H_2O_2 concentrations, as shown in Fig. 6.37.

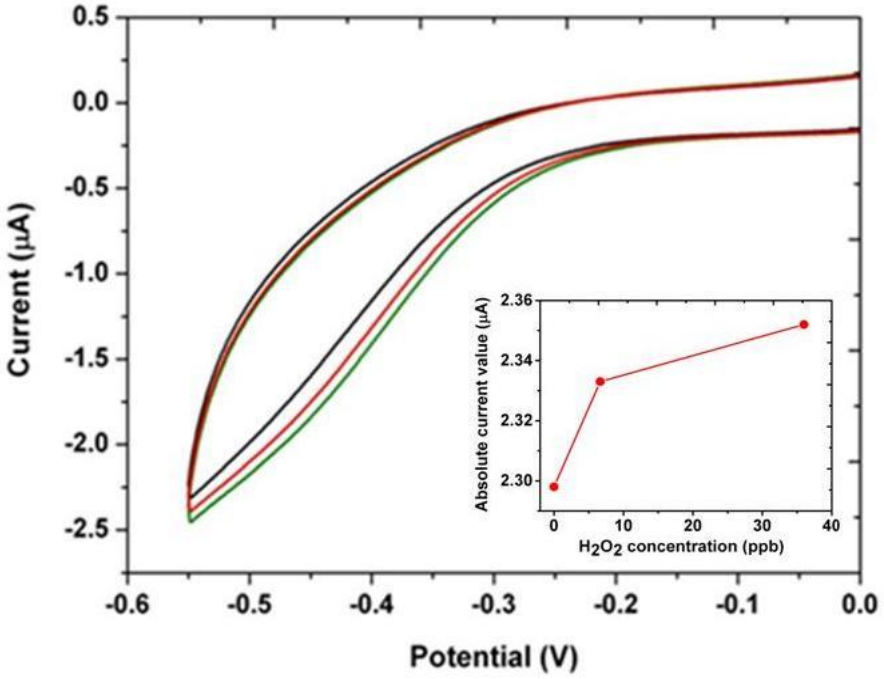


Fig. 6.37. Electroreduction of hydrogen peroxide by PoPD/PB modified Au disc macro-electrode. CV recorded in 0.05 M phosphate buffer pH 7.4 (black line) as a control and in the presence of: 6.66 ppb of H_2O_2 (red line) and 36 ppb H_2O_2 (green line). Scan rate of 100 mV s^{-1}. Potential recorded vs. Ag/AgCl (3M KCl). The dependency of the absolute reduction current as a function of peroxide concentration is depicted in the inset.

Cyclic voltammetry measurements of P*o*PD/PB modified Au disc macro-electrode (Fig. 6.37) suggested enhanced electrocatalytic activity of PB towards peroxide reduction, as compared to PB alone (Fig.6.36), a phenomenon which has been ascribed to the stabilizing effect of the polymer layer.

Following successful detection of H_2O_2 by P*o*PD / PB deposits, the activity of LOX (0.005 mg mL^{-1}) modified polymer films has been determined via CV measurements of generated peroxide, when increasing concentrations of L-lactate have been added to the buffer solution (Fig. 6.38). The potential of the working electrode has been cycled between -0.8 V and 0.2 V.

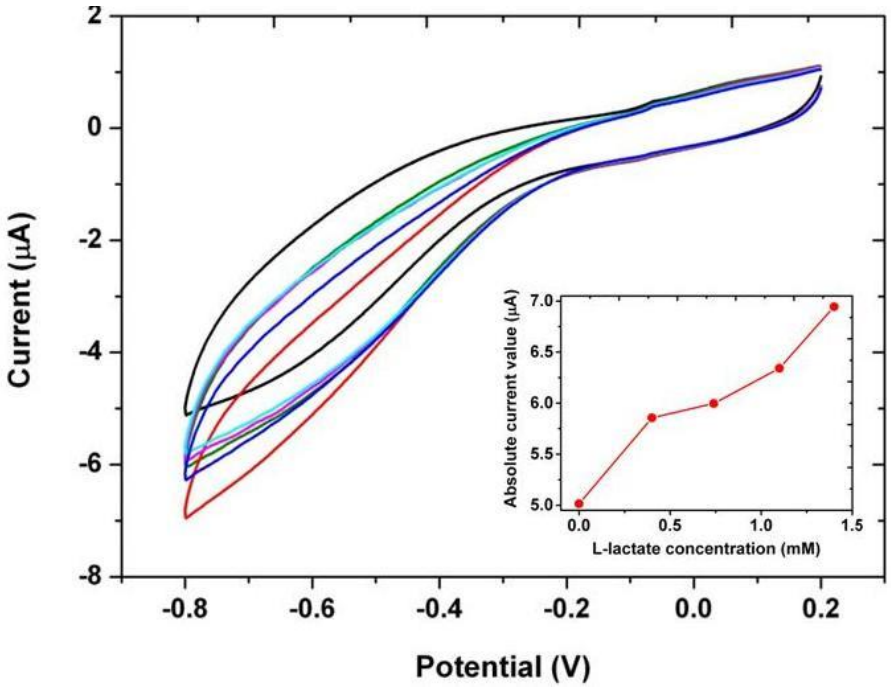


Fig. 6.38. Response of LOX/PoPD/PB modified Au disc macro-electrode to H_2O_2 electroreduction. CV recorded in plain 0.05 M phosphate buffer pH 7.4 (black line) and in the presence of: 0.4 mM L-lactate (cyan line); 0.74 mM L-lactate (magenta line); 1.1 mM L-lactate (green line); 1.4 mM L-lactate (navy blue line); 1.7 mM L-lactate (red line). Scan rate of 100 mV s^{-1}. Potential recorded vs. Ag/AgCl (3M KCl). The dependency of H_2O_2 reduction current (absolute value) on the concentration of L-lactate is illustrated in the inset.

The encapsulation of LOX in the polymer film and a consecutive addition of the L-lactate demonstrated successful catalysis by enzyme at increasing concentrations of the substrate (Fig. 6.38). As the reaction has been followed by voltammetric detection of its by-product, peroxide, a gradual rise in the reduction peak of H_2O_2 commencing at -0.2 V has been detected upon addition of the lactate.

As previously, the response of the enzyme modified PoPD / PB double layer to the presence of lactate has been also confirmed on Au micro-electrode (Ø 12.5 μm) and is presented in Fig. 6.39.

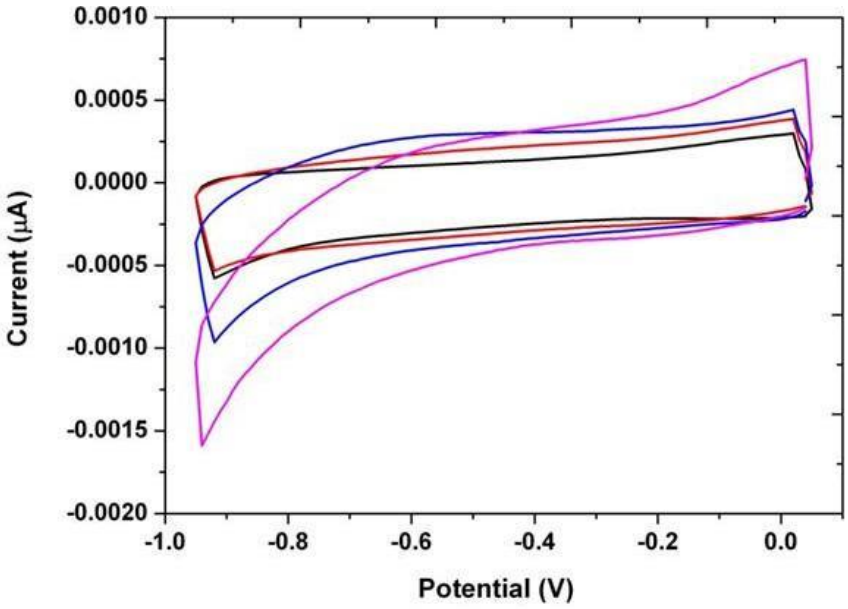


Fig. 6.39. Electrochemical detection of H_2O_2 by LOX/PoPD/PB modified Au microelectrode. CV recorded in plain 0.05 M phosphate buffer pH 7.4 (red line) and in the presence of: 2 mM L-lactate (black line); 4 mM L-lactate (blue line) and 6 mM L-lactate (magenta line). Scan rate of 100 mV s^{-1}. Potential recorded vs. Ag/AgCl (3M KCl).

As can be seen from Fig. 6.39, a sudden increase in the current has been recorded at 4 mM of L-lactate, resulting in a 40 % enhancement in the electrochemical response as compared to the signal in plain 0.05 M phosphate buffer pH 7.4. Implementation of the catalytic system on the commercial Au micro-electrode confirmed that the immobilization protocol can be successfully applied in both macro- and micro-scale metal supports.

6.5.2. Enzymatic biocathodes.

A) Bilirubin oxidase sol-gel based biocathode.

The electrochemical response of BOX (10 mg mL^{-1} in DI H_2O) biofunctionalized sol-gel films containing the Os polymer to O_2 has been recorded in 0.1 M Phosphate Buffer Saline (PBS), pH 7.0, via cyclic voltammetry measurements. The enzymatic activity has been studied in the presence of atmospheric oxygen in aerated buffers, following a 30 mins exposure to air.

A number of strategies have been undertaken in the attempt to immobilize BOX in the polymer matrix, while maintaining its biological activity and providing efficient catalysis. Tetraethyl orthosilicate (TEOS) and chitosan have been considered as potential host materials for the enzyme encapsulation, with glassy carbon, platinum and gold selected as the solid supports for the surface treatment. Although carbon materials are routinely employed in catalytic studies due to their excellent electrical properties, the immobilization of oxidase on metal surfaces was of particular interest in the development of biocathodes, envisaged as part of this chapter. This is due to the fact that the electrodes microfabricated on Zeonor substrates, as discoursed in Chapter V, are platinum and gold based and therefore in order to transpose the constructed half-cell into a microfluidic setting, the enzymatic system for BOX needs to be compatible with Pt and Au. For this reason, numerous efforts have been directed towards the adaptation of the surface properties of the metals. The effects of carbon nanotubes and polyelectrolytes have been also investigated, in order to improve the electron transfer properties within produced films and to stimulate the electrocatalysis of BOX in the presence of oxygen.

Influence of the redox mediator

The catalytic reduction of molecular oxygen by BOX sol-gel films has been investigated on commercial glassy carbon (GCE) disc electrodes, in the presence of the polyelectrolyte, PEI (Fig. 6.40). 5 µL of the 0.25 M hydrolysed TEOS mixture containing the enzyme and polyethyleneimine in 4:1 (v/v) ratio has been drop-coated onto a clean GCE electrode and left at RT for 2 h to polymerise and dry. Following the matrix polymerization, the film has been immersed in the 0.1 M PBS buffer pH 7.0 and the electrochemical signal in the aerated and oxygen-free solutions has been analyzed by cyclic voltammetry measurements. The analysis has been performed in absence, Fig. 6.40 b), and in the presence, Fig. 6.40 a), of the mediator, Os polymer, co-encapsulated in the sol-gel matrix. Successful electrocatalysis would result in an increase in the maximum recorded reduction current, followed by a rapid decline in the oxidative current. Direct electron transfer properties of BOX, reported by a number of authors [136, 137], have been evaluated when no Os has been added to the starting sol.

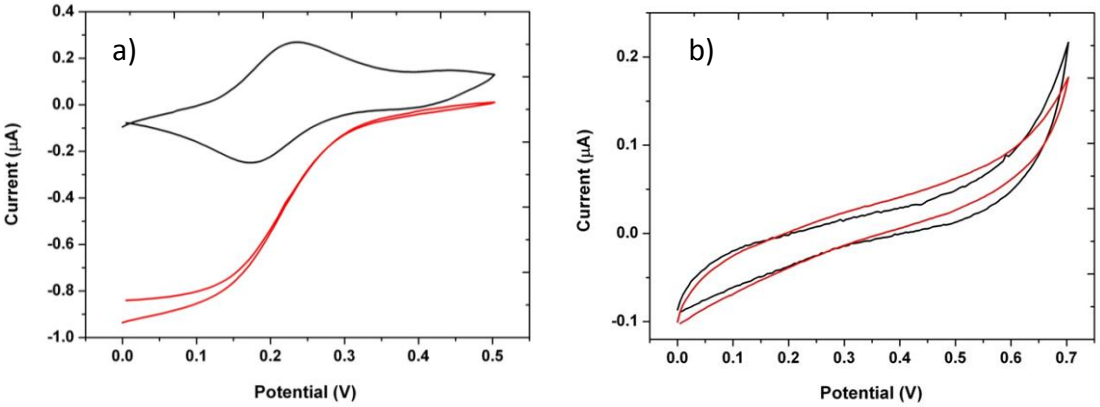


Fig. 6.40. Cyclic voltammograms of 10 mg mL^{-1} BOX in 0.25 M TEOS containing PEI, drop-coated on GCE disc electrode, recorded in 0.1 M PBS buffer pH 7.0: a) Mediated electron transfer in the presence of osmium polymer; detectable oxidation and reduction peaks of Os recorded at 0.23 V and 0.16 V accordingly in oxygen-free solution (black line); reduction of molecular oxygen by BOX in aerated buffer (red line); b) Direct electron transfer of BOX in oxygen-free solution (black line) and in the presence of molecular oxygen (red line). Scan rate of 20 mV s^{-1}. Potential recorded vs. Ag/AgCl (3M KCl).

Electrochemical studies of the electroreduction of oxygen by BOX functionalized sol-gel films indicate the dependency of the catalysis on the Os species. As can be seen from the Fig. 6.40 b), the enzyme did not exhibit direct electron transfer and the effective reduction of oxygen has been demonstrated only in the presence of osmium polymer co-encapsulated in the in sol-gel film, as shown in Fig. 6.40 a). The oxidation and reduction peaks recorded at 0.16 V and 0.23 V accordingly, represented in Fig. 6.40 a) by a black line, correspond to the steady and reproducible response of the Os mediator measured in nitrogen purged buffer solutions.

The catalytic behavior of the enzyme and efficient electrical communication between the active components have been established upon effective mediated electroreduction of oxygen. The modified GCE electrode exhibited a continuous catalytic response under multiple CV scans.

Influence of the polymer additives

In order to investigate the role of the polyelectrolyte on the catalytic properties of BOX, the electrochemical response of the oxidase has been studied in the absence of PEI, as seen in Fig. 6.41 b), and compared with the response in the presence of polyethyleneimine, depicted in Fig. 6.41 a). 5 µL of the enzyme and Os suspension in 2:1 (v/v) ratio, prepared in 0.25 M hydrolysed TEOS, has been applied onto a clean GCE surface and the film was left at RT for 2 h to age and dry. Following the matrix condensation, the electrode has been immersed in the 0.1 M PBS buffer pH 7.0 and the CV signal has been recorded in aerated and oxygen-free solutions, obtained according to a previously used protocol.

As illustrated in Fig. 6.41, the successful catalysis of the O_2 electroreduction by BOX, co-immobilized within the sol-gel with Os polymer, was only possible in the presence of positively charged polyethyleneimine, PEI, illustrated by a) in Fig. 6.41. No response has been recorded in the absence of the polyelectrolyte, as demonstrated in Fig. 6.41 b.

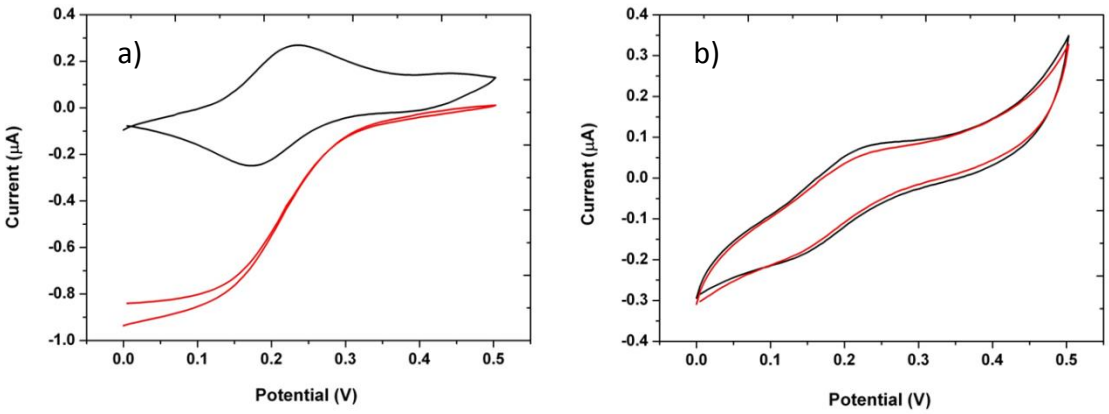


Fig. 6.41. Cyclic voltammograms of 10 mg mL^{-1} BOX in 0.25 M TEOS, containing Os polymer and drop-coated on GCE disc electrode; signal recorded in 0.1 M PBS buffer pH 7.0: a) Response in the presence of PEI; oxidation and reduction peaks of Os recorded at 0.23 V and 0.16 V accordingly in oxygen-free solution (black line); reduction of molecular oxygen by BOX in aerated buffer (red line); b) CV of BOX in the absence of PEI, in oxygen-free solution (black line) and in aerated buffer (red line); oxidation and reduction peaks of Os detectable at 0.23 V and 0.16 V respectively. Scan rate of 20 mV s^{-1}. Potential recorded vs. Ag/AgCl (3M KCl).

Influence of the electrode material

The enzymatic conversion of molecular oxygen to water has been additionally studied on Au and Pt disc electrodes modified with 10 mg mL^{-1} BOX sol-gel films containing both PEI and the Os polymer as the mediator for the reduction reaction. The deposits have been obtained as previously, by casting the hydrolysed TEOS suspension of the enzyme onto a mechanically polished electrode material. Cyclic voltammetry measurements have been performed in 0.1 M PBS buffer pH 7.0, in the presence of O_2. CV response in the deaerated solutions has been used as a control. Fig. 6.42 represents the response of BOX/Os/PEI functionalized sol-gel film on gold, denoted in a), and platinum, as shown in b), disc macro-electrodes when the buffer was exposed to air or purged with nitrogen. In order to provide a durable attachment of drop-coated silica films and promote the response of BOX, Au and Pt electrodes have been pre-treated with 3-mercaptopropyl trimethoxysilane (MPTMS) self-assembly monolayer. The electrochemical signal on GCE is presented in Fig. 6.42 c) for comparison.

Surface modification of Au and Pt has been carried out by incubating the electrode with a 100 μL aliquot of a 20 mM MPTMS in EtOH mixture for 10 minutes, according to a protocol described in [138]. The electrode was rinsed in a 1:1 water/ethanol mixture and the TEOS solution containing BOX, PEI and Os polymer has been subsequently applied. MPTMS is an organosilane and, as such, is likely to interact with the electrode surface. The application of mercaptopropyl silane derivative has been successfully demonstrated on gold [139-143], where it acted as a "nanoglue" holding the succeeding silica film and the electrode together, while providing an efficient exchange of species with the external solution.

As can be seen from Fig. 6.42, the electrochemical behaviour of bilirubin oxidase immobilized in drop-coated silica films indicated a significant dependency of the enzymatic activity on the electrode material. Successful catalysis has been recorded only on glassy carbon, as shown in Fig. 6.42 c), with a rather poor response on MPTMS modified platinum, reported in Fig. 6.42 b). No measurable signal for the electroreduction of oxygen has been detected on gold, pre-treated with MPTMS, as indicated in Fig. 6.42 a). The maximum observed redox currents for Os, at 0.23 V and 0.16 V vs. Ag/AgCl, are however evident in deaerated buffer scans for both metals. The efforts to improve the adhesion of sol-gel films onto gold and platinum by surface treatment with MPTMPS,

although provided a stable attachment of succeeding silica layer, did not result in a successful catalysis, as reported in Fig. 6.42 a) and b).

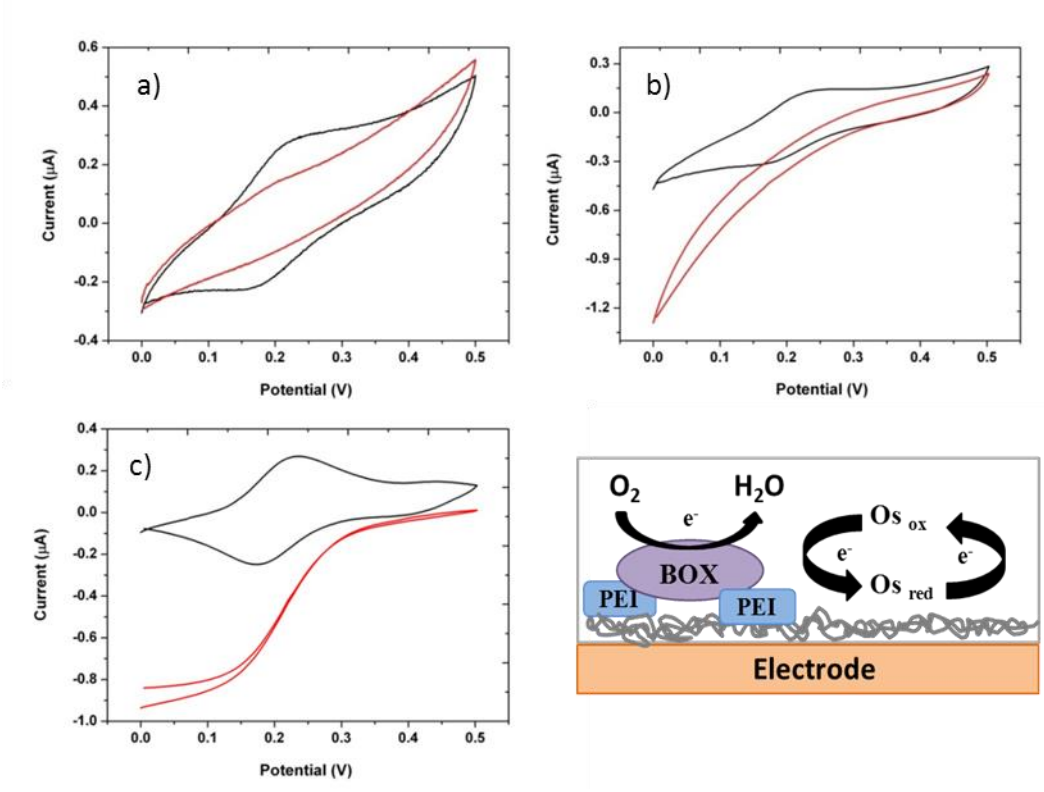


Fig. 6.42. Electrochemical response of BOX (10 mg mL^{-1})/Os/PEI sol-gel films drop-coated on various electrode materials recorded in 0.1 M PBS buffer, pH 7.0 for: a) Au disc electrode previously treated with 20 mM MPTMS, in the presence of molecular oxygen (red line) and in the oxygen-free solution (black line); b) Pt disc electrode treated with MPTMS, signal in the aerated (red line) and oxygen-free (black line); c) MPTMS-untreated GCE in oxygen-free solution (black line); reduction of molecular oxygen by BOX in aerated buffer (red line); Oxidation and reduction peaks of Os in deaerated buffer have been recorded at 0.23 V and 0.16 V vs. Ag/AgCl, accordingly. Scan rate of 20 mV s^{-1}. Potential recorded vs. Ag/AgCl (3 M KCl).Cartoon of the catalytic mechanism is also included.

Influence of the MWCNTs

Since no catalytic activity has been detected on metal electrodes, the surface of gold has been modified with Multi Walled Carbon Nanotubes functionalized with Os (MWCNT-Os), in order to promote the electron transfer between the active site of BOX and the electrode. MWCNT-Os has been prepared by sonicating the solution containing the nanostructures for 1 h and successive incubation with the osmium polymer for a period of 12 h, as described in [144]. The treatment leads to a stable attachment of the positively charged polymer to the sidewalls surface of MWCNT. Simple mixing of MWCNTs with Os-polymer suspension did not result in a stable functionalization.

Sol-gel films have been obtained in a two-step protocol with a MWCNT-Os / TEOS bottom layer applied on a clean electrode and subsequent top coating of the enzyme and PEI suspension in 0.25 M TEOS. Fig. 6.43 illustrates schematically the double-layer catalytic system formed in silica sol-gel by drop-coating. Application of the highly conductive carbon nanotubes has been reported [145] to successfully promote the direct electron transfer catalysis of BOX and, as such, should lead to elevated reduction current, even in the absence of Os polymer.

Cyclic voltammetry measurements of gold disc electrode modified with a sandwich assembly of MWCNT-Os/TEOS and BOX/PEI/TEOS (0.25 M) have been performed as previously in 0.1 M PBS buffer (pH 7.0). The solution has been purged with nitrogen or aerated for 20 mins and the electrochemical signal of BOX has been recorded for Au disc electrode in Fig. 6.44 a). In order to validate the potential mediating properties of MWCNT-Os, the modification protocol has also been applied to GCE and the electrochemical response was recorded in oxygen-free and aerated buffer solution, as shown in Fig. 6.44 b).

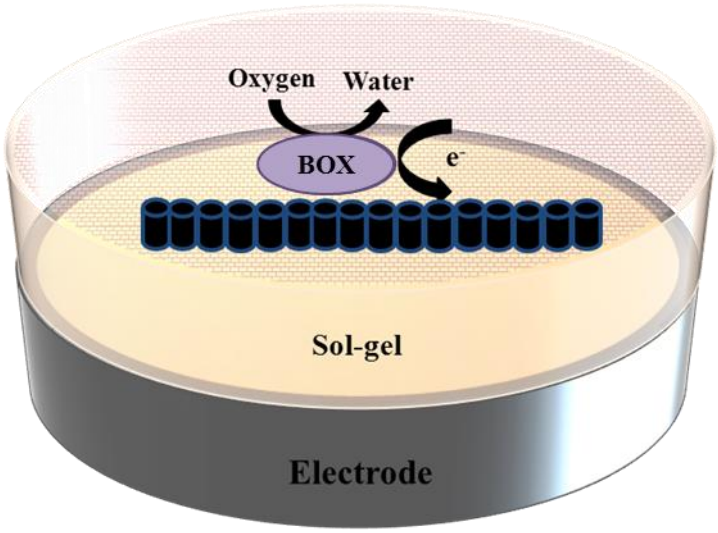


Fig. 6.43. Schematic of the BOX / PEI sol-gel modified electrode pre-treated with MWCNT-Os layer.

Electrically conductive Multi Walled Carbon Nanotubes functionalized with Os, directly applied as a separate layer on the electrode surface, did not promote the direct electroreduction of oxygen on Au, as can be seen in Fig.6.44 a). Additionally, the transposition of the system onto glassy carbon, performed as a control experiment, did not demonstrate the enzymatic activity of BOX in the presence of Os conjugates with MWCNT, see Fig. 6.44 b), suggesting a lack of communication between the catalyst and carbon-mediator species.

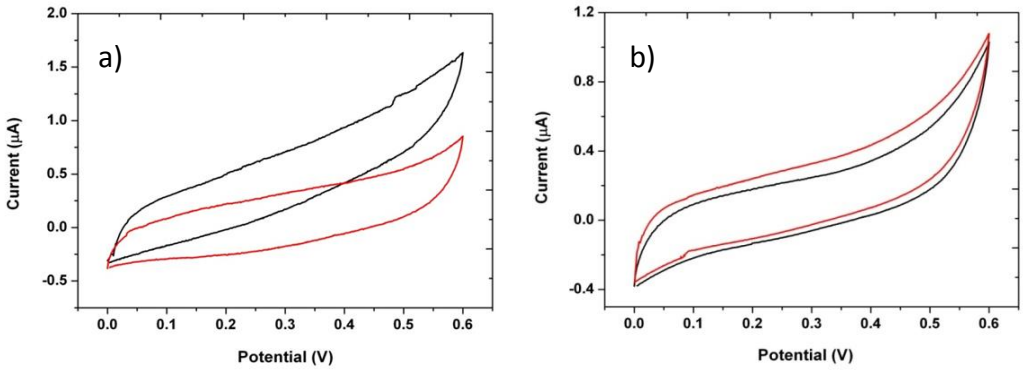


Fig. 6.44. Electrochemical response of 10 mg mL^{-1} BOX/PEI sol-gel modified disc electrode previously treated with MWCNT-Os/TEOS the air (red line) and after 20 mins purge with the nitrogen (black line) for: a) Au; b) GCE. Signals recorded in 0.1 M PBS, pH 7.0. Scan rate of 20 mV s^{-1}. Potential recorded vs. Ag/AgCl (3M KCl).

Influence of chitosan

The selection of chitosan as an alternative matrix for the immobilization of BOX has been determined by the literature reviews, indicating that the polar groups within the polymer provide a favourable chemical environment for the biomolecule entrapment. The positive influence of chitosan on the stability of incorporated species has been previously demonstrated in particular when in combination with silica gels and, hence the material has been widely exploited in electrocatalytic studies [146, 147]. As reported in [121], the encapsulation matrices incorporating polymers with protonated amine or ammonium functions, significantly improve the enzymatic activity of certain catalysts, such as DSDH.

The preliminary studies investigated the influence of chitosan as a potential matrix for MWCNT-Os encapsulation on gold disc electrode. The oxidase was not present in the initial analysis. The modification solution was prepared from 0.5 % chitosan (medium molecular weight), according to the protocol enclosed in Chapter II, by mixing the powdered polymer with 1 % acetic acid and sonicating the suspension for 1 h. The resulting solution was further mixed with MWCNT-Os, and applied on the electrode by drop-coating. Following the drying, the electrochemical behaviour of the film has been studied in 0.1 M PBS buffer, pH 7.0 and compared to the response of 0.25 M hydrolysed TEOS (Fig. 6.45).

The application of 0.5% chitosan suspension in acetic acid, as a potential matrix for species encapsulation, revealed good redox behaviour of Os polymer (Fig. 6.45). The cyclic voltammetry measurements of the polysaccharide entrapped MWCNT-Os have shown improved electrochemical response, as compared to the silica gel (Fig. 6.45). Nevertheless, the mechanical stability of drop-coated chitosan films was not satisfactory.

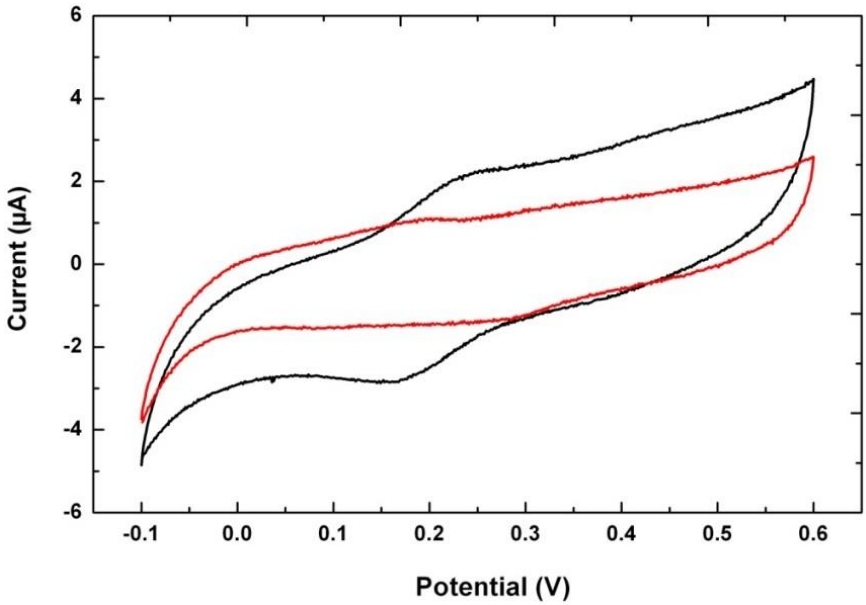


Fig. 6.45. Electrochemical response of MWCNT-Os polymer drop-coated on Au disc electrode in 0.5 % chitosan (black line) and in 0.25 M TEOS (red line); signal measured in 0.1 M PBS buffer pH 7.0. Scan rate of 20 mV s^{-1}. Potential vs. Ag/AgCl.

In order to minimize potential unfavorable effects of the working buffer on the biological activity of BOX, the electrochemical response of 10 mg mL^{-1} BOX has been studied on Pt working electrode at pH 5.5 and pH 7.0. Direct electron transfer properties of the enzyme encapsulated in the chitosan matrix (5% in acetic acid) have been explored in the presence of the substrate, oxygen, and in deaerated buffer solutions. The shape and the onset of the reduction peak of modified electrodes have been compared to the signal of bare Pt (Fig. 6.46).

The electrochemical characterization of BOX / chitosan modified and bare platinum, studied in the absence of Os and PEI, revealed a dependency of the reduction peak shape upon the pH of the buffer (Fig. 6.46) with approximately 36 % increase in the maximum recorded reduction current at pH 7.0. Prolonged exposure to air resulted in a greater response of chitosan films, however when compared to the signal of bare Pt, much lower current has been obtained, regardless of the pH, as depicted in Fig. 6.46 a) and b). One explanation to these findings is a possible compact structure of the film, preventing efficient diffusion of oxygen towards Pt. The lack of the enzymatic catalysis can be attributed to the absence of Os and PEI, confirming the polyelectrolyte requisite and no direct electron transfer of BOX in chitosan matrix.

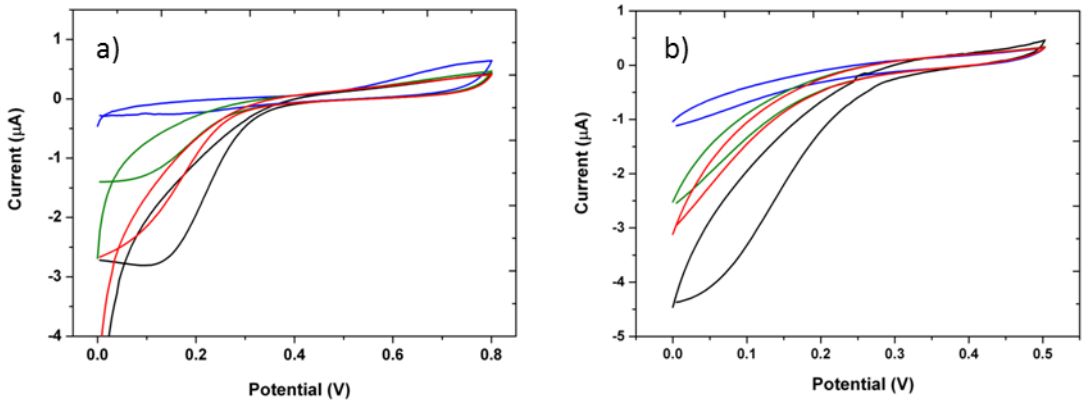


Fig. 6.46. Influence of the pH of the studied solution on the biological response of 10 mg mL^{-1} BOX in 5 % chitosan at bare Pt, 20 mins in air (black line); BOX/chitosan/Pt, 20 mins in air (red line); BOX/chitosan/Pt, 10 mins in air (green line); BOX/chitosan/Pt, 20 mins in nitrogen (blue line) for a) pH 5.5 and b) pH 7.0. Scan rate of 20 mV s^{-1}. Potential recorded vs. Ag/AgCl (3M KCl).

Tab. 6.1. recapitulates the experimental approaches undertaken in the development of a sustainable and electrochemically active BOX/sol-gel biocathode. As discussed previously, the work employed a number of electrode materials (GCE and metals), supplementation of the host matrix with chitosan and the investigation of the mediator effect on the catalytic activity of the enzyme. Despite the rather simple configuration of the catalytic layer, in particular when compared with the multi-component bioanodic system for DSDH, successful catalysis of BOX has only been demonstrated on GCE and in the presence of Os and the PEI polyelectrolyte. The functionalization of the metal electrodes with MWCNT, in order to mimic the properties of carbon materials, as well as surface modification with MPTMS, described in the results section, did not result in a detectable catalytic activity of the oxidase.

Tab. 6.1. Summary of the sol-gel immobilization strategies for the development of BOX based bioanode.

Biocathode	Electrode material	Matrix	Stabilizer	Electron transfer	SWCNTs	Catalytic activity
1	GCE	TEOS	PEI	DET	No	—
2	GCE	TEOS	No	MET (Os polymer)	No	—
3	GCE	TEOS	PEI	MET (Os polymer)	No	+
4	Au,Pt	TEOS	PEI	MET (Os polymer)	No	—
5	GCE	chitosan	PEI	DET	Yes	—
6	GCE	chitosan	PEI	MET (Os polymer)	No	—
7	Au,Pt	TEOS	PEI	MET (Os polymer)	Yes	—

B) Laccase modified sol-gel biocathode.

The electrochemical characterization of laccase biofunctionalized *o*-PD films has been carried out in 0.1 M phosphate buffer pH 6.0, in the presence and absence of the substrate, molecular oxygen. As the initial attempts to use ABTS to facilitate mediated electron transfer of the enzyme were unsuccessful, quinone (Q) has been further selected as the mediator for the catalytic activity of laccase, as reported in ref. [69]. The response of the enzyme and stability of generated deposits have been studied using cyclic voltammetry measurements under repetitive potential cycles.

The initial laccase/P*o*PD modified films have been obtained by electrodeposition from 0.1 M acetate buffer at pH 6.0 containing 0.1 mg mL^{-1} of the enzyme and 5 mM of the polymer solution. The activity of laccase towards mediated electroreduction of molecular O_2 has been studied in oxygen purged phosphate buffer (0.1 M, pH 6.0), containing 3 mM Q. The gas was let to vigorously bubble through the medium for 30 mins

prior to the CV measurement being taken and gently flow over the solution surface throughout the experiment. The catalytic activity of the enzyme in deoxygenated solution has been recorded as a control (Fig. 6.47). All solutions have been initially pre-warmed in the oven at 40 ºC, prior to the electrochemical testing, in order to promote the electrocatalysis of laccase. The experiments were however carried out at 30 ºC.

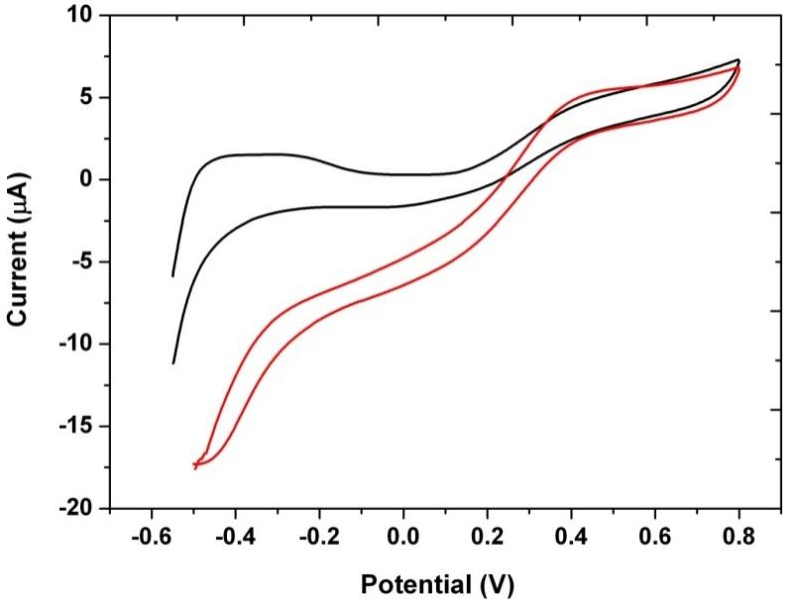


Fig. 6.47. Cyclic voltammetry response of 0.1 mg mL^{-1} laccase in 5mM poly o-PD deposited on Pt disc electrode from 0.1 M phosphate buffer pH 6.0. Response in 3 mM Q in 0.1 M phosphate buffer pH 6.0 following a 40 mins nitrogen purge (black line) and 20 mins oxygen purge (red line). Scan rate of 10 mV s^{-1}. Potential recorded vs. Ag/AgCl (3M KCl).

When studied the catalysis of laccase following a 20 mins purge of the buffer (pH 6.0) with pure oxygen, a 60% rise in the reductive current has been recorded as compared to the signal in deaerated buffer (Fig. 6.47).

The dependency of the shape and the intensity of the electrochemical signal on the availability of the substrate and the mediator species have been investigated and is illustrated in Fig. 6.48. The cyclic voltammetry response of laccase/P*o*PD film electrodeposited on Pt disc electrode has been studied in 0.1 M phosphate buffer (pH 6.0) containing 3 mM Q, in the presence (blue line) and in the absence (red line) of molecular

oxygen. The signal of the enzyme in a plain buffer has been recorded as a control measurement.

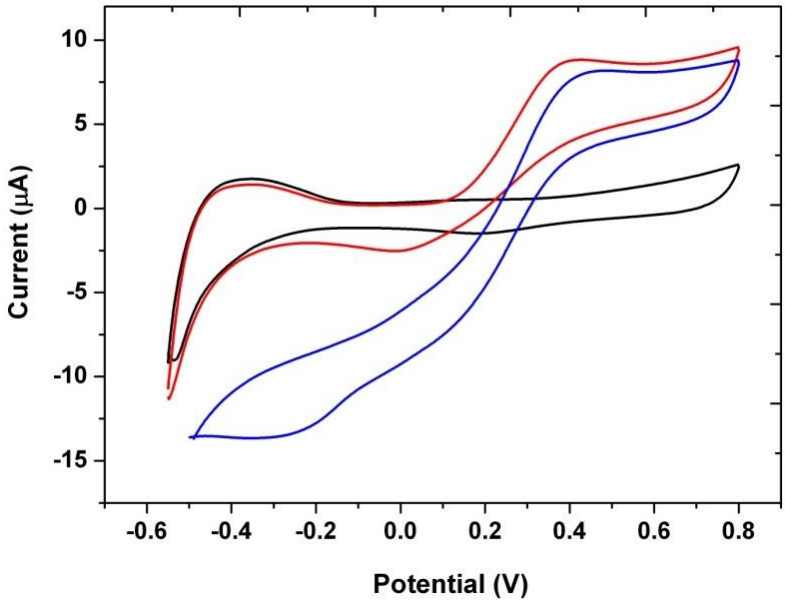


Fig. 6.48. Response of 0.1 mg mL^{-1} laccase in 5mM poly o-PD deposited on Pt disc from 0.1 M phosphate buffer, pH 6.0. CV signals in: pure 0.1 M phosphate buffer pH 6.0 following a 30 mins nitrogen purge (black line); buffer containing 3 mM Q purged with nitrogen for 30 mins (red line) and buffer with 3 mM Q purged with oxygen for 20 mins (blue line). Scan rate of 10 mV s^{-1}. Potential vs. Ag/AgCl (3M KCl).

In order to investigate the stability of the generated laccase film, the electrode has been stored in the phosphate buffer (pH 6.0) at 4 ºC for 10 days and re-tested under the same principal working conditions (Fig. 6.49).

The investigation of the electrochemical signal in the presence and absence of molecular oxygen confirmed that the increase and the characteristic shape of the produced current peak is attributed to the electroreduction of O_2 only (Fig. 6.48 & Fig. 6.49). Cyclic voltammograms of a laccase/P*o*PD film stored at 4 ºC in the phosphate buffer at pH 6.0 for 10 consecutive days, not only did not show any signs of biological deterioration but demonstrated a 30% increase in the maximum observed current prior to incubation (Fig. 6.49), indicating excellent stability of generated membranes. Additionally, while the peak response suggested diffusion controlled process (Fig. 6.49), the plateau signal of laccase prior to storage is limited by the rate of the electrocatalytic reaction [69]. This implies that

if the diffusion of oxygen was not the rate limiting factor, the current drawn from the reaction catalysed by laccase could possibly be even higher.

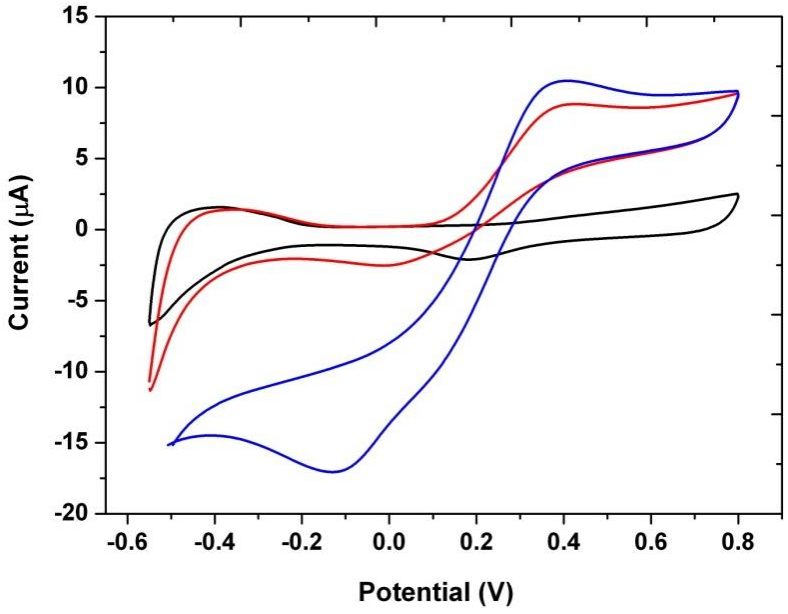


Fig. 6.49. Signal of 0.1 mg mL^{-1} laccase in 5mM poly o-PD film deposited on Pt disc from 0.1 M phosphate buffer pH 6.0, following 10 days of storage in the buffer. CV recorded in: plain 0.1 M phosphate buffer pH 6.0 purged with nitrogen for 40 mins (black line); buffer with 3 mM Q, 40 mins nitrogen purge (red line) and 40 mins oxygen purge (blue line). Scan rate of 10 mV s^{-1}. Potential vs. Ag/AgCl (3 M KCl).

The potential role of poly *o*-phenylenediamine, as the mediator for laccase, has been determined on Pt disc electrode in the presence of pure molecular oxygen, at pH 6.0. The signal of the laccase/P*o*PD layer in oxygen-free environment has been recorded as a control measurement (Fig. 6.50).

The electrochemical investigation of the potential role of the P*o*PD matrix as a mediator for laccase, illustrated in Fig. 6.50, was in an excellent agreement with the results reported by Palys and Rogalski [69]. The 3-fold increase in the reductive current recorded in the presence of molecular O_2 (40 mins exposure), visible in a Fig. 6.50 in a form of the characteristic peak shape, confirms electron transfer properties of the polymer matrix. As discussed in [69], the polymer could successfully act as the mediator for the laccase.

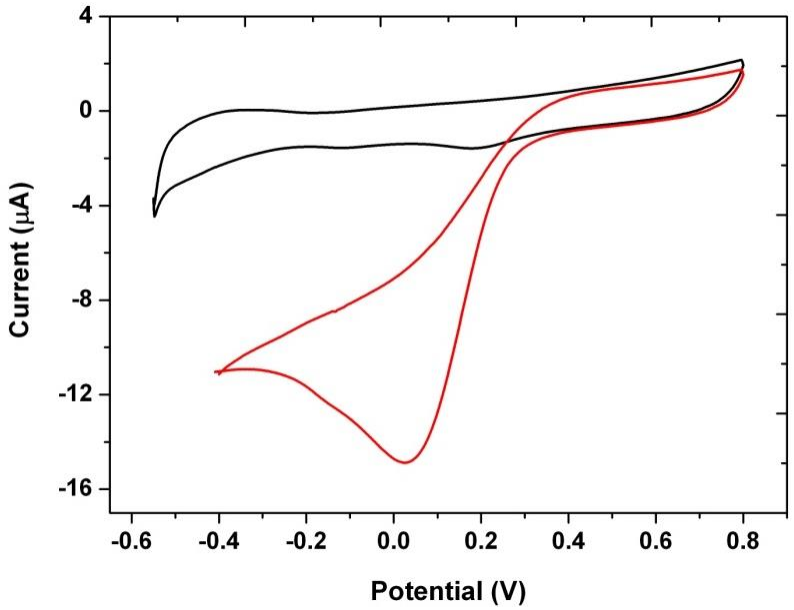


Fig. 6.50. Mediator-less response of 0.1 mg mL^{-1} laccase/poly o-PD film, deposited on Pt disc from 0.1 M phosphate buffer pH 6.0. CV recorded in: plain 0.1 M phosphate buffer pH 6.0 purged with nitrogen for 40 mins (black line); plain 0.1 M phosphate buffer pH 6.0 purged with oxygen for 40 mins (red line). Scan rate of 10 mV s^{-1}. Potential recorded vs. Ag/AgCl (3M KCl).

The direct catalysis of the oxygen reduction and the electrochemical behaviour of P*o*PD matrix in laccase deficient polymer films have been also evaluated in both, oxygen saturated and deaerated buffer solution, as shown in Fig. 6.51.

Investigation of the direct electrocatalysis of the oxygen reduction in the absence of the enzyme (Fig. 6.51) revealed a considerable difference in the P*o*PD response between the deaerated (black curve) and oxygen purged (red curve) phosphate buffer solutions. An approximately 14-fold increase in the recorded reductive current, with a potential onset at 0.45 V vs. Ag/AgCl (Fig. 6.51), indicates electrocatalytic activity of the poly (*o*-phenylenediamine) towards O_2. As the potential wave of the laccase-free polymer is shifted by 0.1 V towards more positive values when compared to the enzyme functionalized films (Fig. 6.50), the electrochemical signals of the catalyst and P*o*PD alone can be readily distinguishable. Moreover, the location and the intensity of the maximum recorded currents for the laccase/P*o*PD and P*o*PD in oxygen saturated buffer also vary, with -15 μA at 0.05 V (Fig. 6.50) and -13 μA at -0.3 V (Fig. 6.51) accordingly. While P*o*PD alone can, in principle, catalyse the reduction of molecular oxygen, the theoretical

current output in the presence of laccase is expected to be twice as high, due to a four-electron transfer carried out by the enzyme as opposed to a two-electron polymer process.

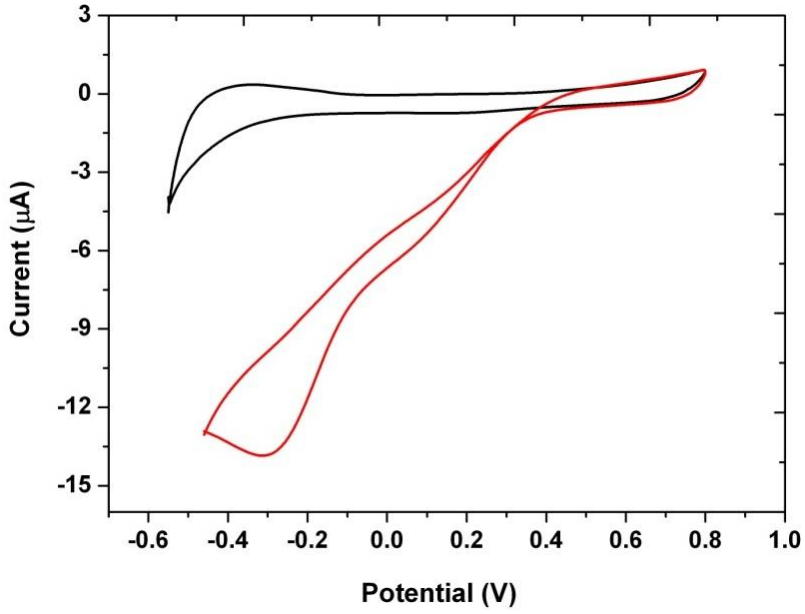


Fig. 6.51. Direct catalysis of oxygen reduction by 5 mM PoPD film deposited on Pt disc from 0.1 M phosphate buffer pH 6.0. CV in plain 0.1 M phosphate buffer pH 6.0 purged with nitrogen for 40 mins (black line) and plain 0.1 M phosphate buffer pH 6.0 oxygenated for 40 mins (red line). Scan rate of 10 mV s^{-1}. Potential recorded vs. Ag/AgCl (3 M KCl).

Following a successful modification of commercial Pt disc electrode, laccase doped poly *o*-PD films have been reproduced on platinum in-house microfabricated on Zeonor platforms. Electrochemically assisted deposition has been carried out for design 3 of the electrode layout from deaerated solution of laccase (0.1 mg mL^{-1}) and *o*-PD monomer (5 mM), in the absence of Na_2SO_3, as shown in Fig. 6.52 b), after chemical cycling in 1 M H_2SO_4. Fig. 6.52 a) represents the CV response of Pt upon repetitive potential sweeping in sulphuric acid. The voltammogram demonstrates typical redox behaviour of the metal in H_2SO_4. The gradual decline in the oxidation peak in Fig. 6.52 b) is indicative of a successful condensation of the *o*-PD monomer and formation of the polymer layer on the electrode surface.

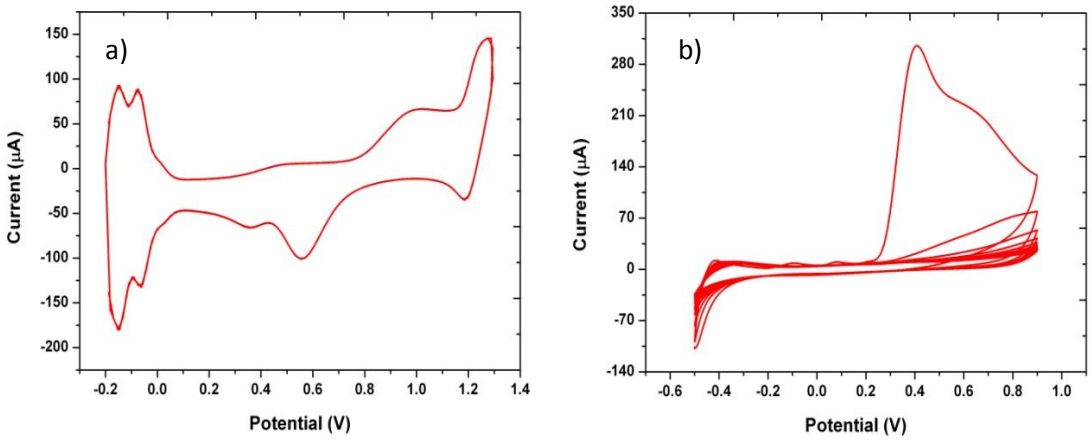


Fig. 6.52 a) Sulphuric acid clean of Pt disc electrodes, design 3; scan rate of 100 mV s^{-1}; b) Electrodeposition of 0.1 mg mL^{-1} laccase in 5 mM poly o-PD for 10 consecutive cycles (20 sweeps) at -0.5 V and 0.9 V at 20 mV s^{-1} scan rate. Potential recorded vs. Ag/AgCl (3 M KCl).

As previously, the process has been facilitated by the use of a custom made holder designed explicitly to accommodate the Zeonor chip during chemical treatment and testing of modified electrode surfaces. The catalytic behaviour of laccase films has been evaluated in the phosphate buffer (pH 6.0) solutions supplemented with Q and molecular oxygen (Fig. 6.53).

As depicted in Fig. 6.53, the presence of molecular oxygen, which is a natural substrate for laccase, resulted in an increase in the recorded reduction current, as compared with the control measurement in the N_2 purged buffer. This suggests successful catalysis of the O_2 reduction by the enzyme functionalized P*o*PD film in the presence of the mediator, Q.

The influence of the presence of the mediator and the substrate for laccase, on the shape and magnitude of the electrochemical response has been also studied as shown in Fig. 6.54.

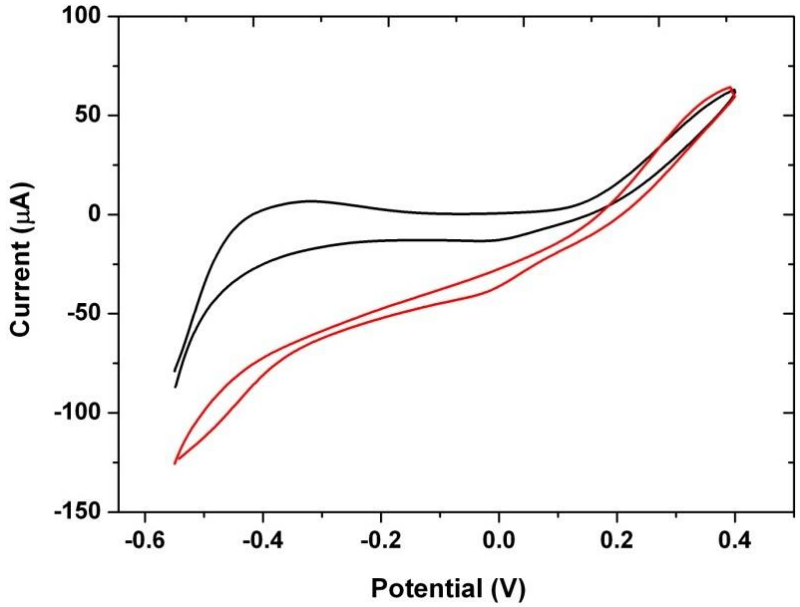


Fig. 6.53. Response of 0.1 mg mL^{-1} laccase/PoPD (5mM) modified Pt, design 3 of the electrode layout in 3 mM Q 0.1 M phosphate buffer, pH 6.0, purged for 20 mins with nitrogen (black line) or oxygen (red line). Scan rate of 10 mV s^{-1}. Potential recorded vs. Ag/AgCl (3 M KCl).

Electrochemically assisted deposition of 0.1 mg mL^{-1} laccase/PoPD on Pt electrodes, design 3 of the Zeonor chip, resulted in an effective enzymatic reduction of O_2 as presented in Fig. 6.53 and Fig. 6.54. Following a 20 mins exposure to oxygen, a 67 % increase in the produced current (Fig. 6.53) has been recorded as compared with the signal in the oxygen-free buffer, with the potential onset for the reaction at 0.25 V being in agreement with the results obtained on the Pt disc. The nearly 10 fold rise in the current output has been attributed to a nearly 8-fold surface enhancement of the in-house fabricated on-chip electrodes. Extending the O_2 purge to 40 mins resulted in a 4-fold increase in the maximum observed reduction current, as shown in Fig. 6.54, indicating much higher reaction turn over. Additionally, the investigation of the effect of the mediator and substrate on the enzymatic activity of laccase, confirmed that the catalysis is only observed in the presence of O_2 and according to a mediated electron transfer mechanism (Fig. 6.54). The observed decline in the reduction peak can therefore be attributed solely to the activity of the enzyme.

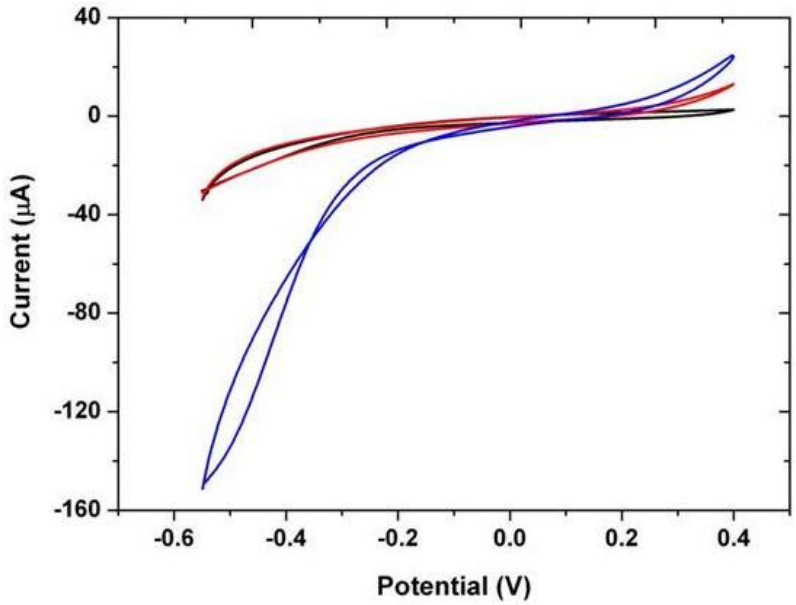


Fig. 6.54. Cyclic voltammogram of 0.1 mg mL^{-1} laccase/ PoPD (5mM) modified Pt electrode, design 3, in 0.1 M phosphate buffer, pH 6.0. Signal recorded in plain buffer purged with nitrogen for 40 mins (black line); 3 mM Q buffered solution, deaerated (blue line) and oxygenated (blur line) for 40 mins. Scan rate of 10 mV s^{-1}. Potential recorded vs. Ag/AgCl (3 M KCl).

The OCP measurements of the bare Pt disc electrode have been recorded in the oxygenated phosphate buffer, pH 6.0, containing 3 mM HQ and in the oxygen-free plain buffered solution (pH 6.0). The immediate OCP readings, following a 30 mins purge with either O_2 or N_2 were 0.249 V and 0.623 V accordingly. Time-based potential measurements, recorded for a period of 600 s, indicated a highly stable OCP value in both case studies, closely comparable to the instant reading (Fig. 6.55). The Open Circuit Potential for the O_2 and Q supplemented phosphate buffer, gradually reached a value of approximately 0.25 V, which when compared to 0.628 V obtained for deaerated plain medium, suggested facilitated electrode reactions due to improved mass and charge transfer properties of the buffered solution in the presence of the mediator and molecular oxygen.

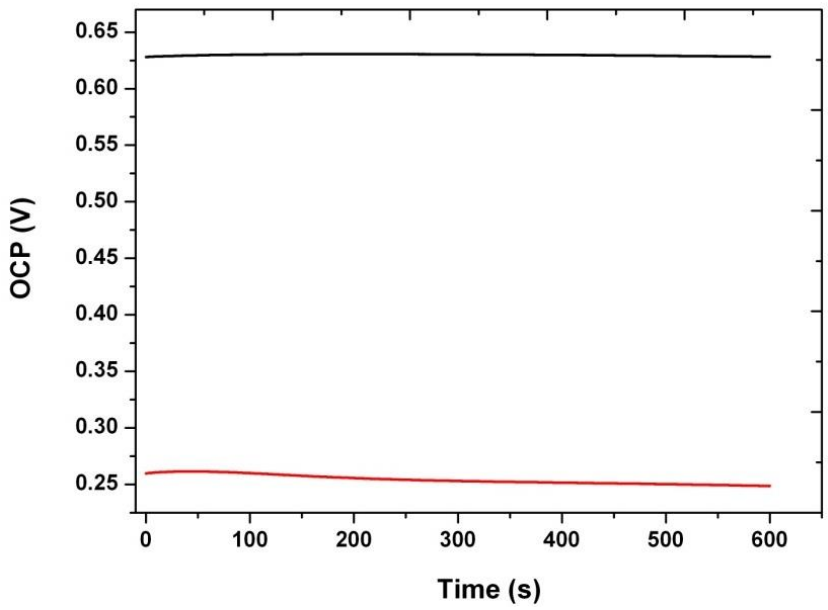


Fig. 6.55.Open Circuit Potential of bare Pt disc electrode recorded in deaerated, mediator-free (black line) and oxygen purged (red line) 0.1 M phosphate buffer pH 6.0 containing 3 mM HQ. Potential recorded vs. Ag/AgCl.

The OCP of the Pt disc electrode modified with laccase (0.1 mg mL^{-1})/PoPD film has been studied in the oxygenated and oxygen-free 3 mM Q phosphate buffer pH 6.0. The immediate potential readings following a 30 mins purge with either N_2 or O_2 were - 0.258 V and 0.258 V accordingly. Time-based potential measurements, recorded for a period of 600s, indicated a relatively stable OCP value in the presence of oxygen, closely comparable to the instant reading (Fig. 6.56). The Open Circuit Potential for the deaerated buffer gradually stabilized in time to a value of approximately 0.085 V, indicating more favourable mass and transfer properties for 3 mM Q buffer solution in the absence of molecular oxygen.

Open circuit potential measurements of bare Pt disc electrode indicate an improvement in the charge exchange rates at the electrode/solution interface, in the presence of molecular oxygen (30 mins purge) and the mediator, Q (Fig. 6.55). Since both species are natural substrates for the reactions occurring at the platinum, they facilitate a mutual transport of electrons to the metal surface, improving the e^- exchange rates. Conversely, the OCP measurements of laccase/P*o*PD modified Pt disc electrode in phosphate buffer (pH 6.0) containing 3 mM Q, demonstrated higher potential reading in the presence of molecular O_2 (30 mins purge). An increase in the OCP value indicated

lower mass and charge exchange rates at the electrode contained in an oxygen saturated solution (Fig. 6.56). Impeded mass and charge transfer properties of Pt modified half-cell corresponds to the presence of laccase doped polymer layer. Additionally, the limited enzyme concentration, results in a potential competitive effect of the mediator and O_2 species in their electron accepting properties from the active site of the catalyst. The transient behaviour of the OCP in the deaerated buffer solution (black line) has been attributed to the residual presence of O_2, remained in the porous structure of the P*o*PD polymer, despite the N_2 purge.

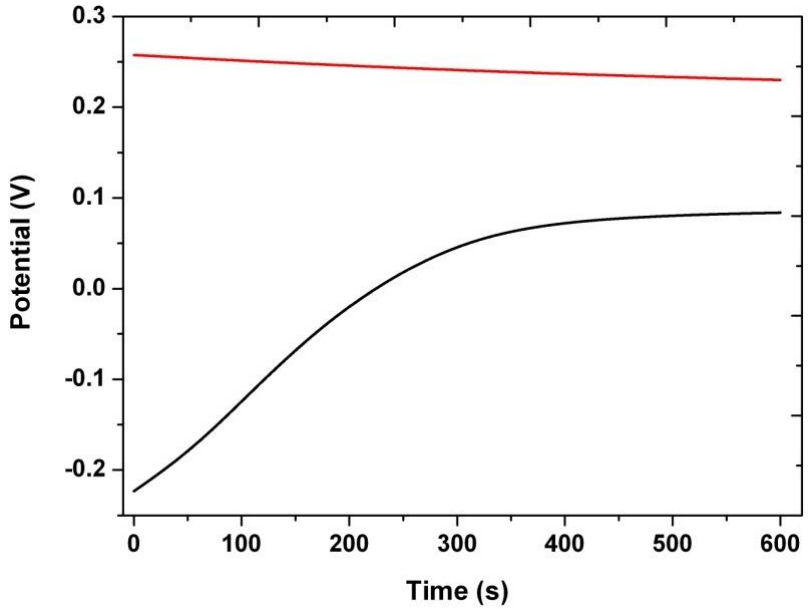


Fig. 6.56. Open Circuit Potential of laccase/PoPD modified Pt disc electrode recorded in deaerated (black line) and oxygen purged (red line) 0.1 M phosphate buffer pH 6.0 containing 3 mM Q. Potential recorded vs. Ag/AgCl.

6.6. Enzymatic biofuel cell in static conditions. Preliminary studies.

The applicability of the poly (*o*-phenylenediamine) encapsulation matrix has been examined in the construction of an enzymatic biofuel cell (EBF) utilizing GOX and laccase as the respective anodic and cathodic catalysts. The composition and operational principle of the cell were based on the design proposed and discussed in detail in Chapter III. As described previously, the set-up consisted of Au (Ø 2 mm) and Pt disc (Ø 2 mm) electrodes immersed in respective buffered substrate solutions containing suitable mediator species. While the original strategy to enzyme confinement relied on a simple

drop-coating of buffered GOX and laccase solutions, the second generation of the in-house built EBFC employed the species electrochemically deposited within a P*o*PD matrix. It has been envisaged that the encapsulation of the enzymes within the polymer film should, in principle, improve the current and power densities drawn from the cell. The anolyte was composed of 50 mM glucose and 7 mM FCA dissolved in 0.1 M phosphate buffer pH 7.4, while the catholyte contained 3 mM Q in 0.1 M phosphate buffer pH 6.0 purged with O_2 for 30 mins. The half-cells were separated by an appropriate insulating membrane, attached via biocompatible glue to the upper Eppendorf acting as the top cellular compartment. The graphical representation of the enzymatic reactions in the constructed biofuel cell is depicted in Fig. 6.57.

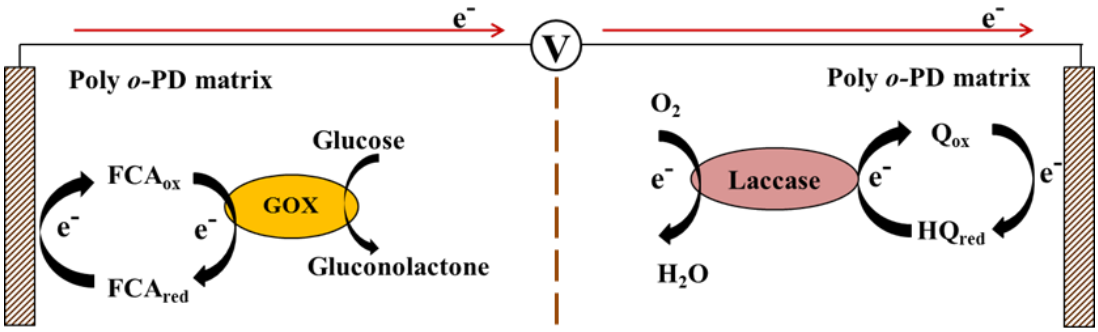


Fig. 6.57. Schematic of the glucose/O_2 biofuel cell utilizing GOX and laccase as the anodic and cathodic catalysts, accordingly.

All solutions have been initially pre-warmed in the oven (40 ºC) prior to any investigation.The experiments were however carried out at 30 ºC. Electrochemical measurements have been carried out in a two-electrode configuration, where GOX/P*o*PD/Au was connected to the potentiostat as the counter and reference, while laccase/P*o*PD/Pt was used as the working electrode respectively. The current drawn from the cell has been measured amperometrically for a series of applied potentials, from which power output has been calculated and plotted as a function of V.

A) Enzymatic biofuel cell with an Al Anodisc membrane.

The current density for the enzymatic biofuel cell, utilizing the Ø 0.2 µm Anodisc membrane as the separator of the anodic and cathodic reactions, has been recorded as a function of the applied potential and presented in Fig. 6.58.

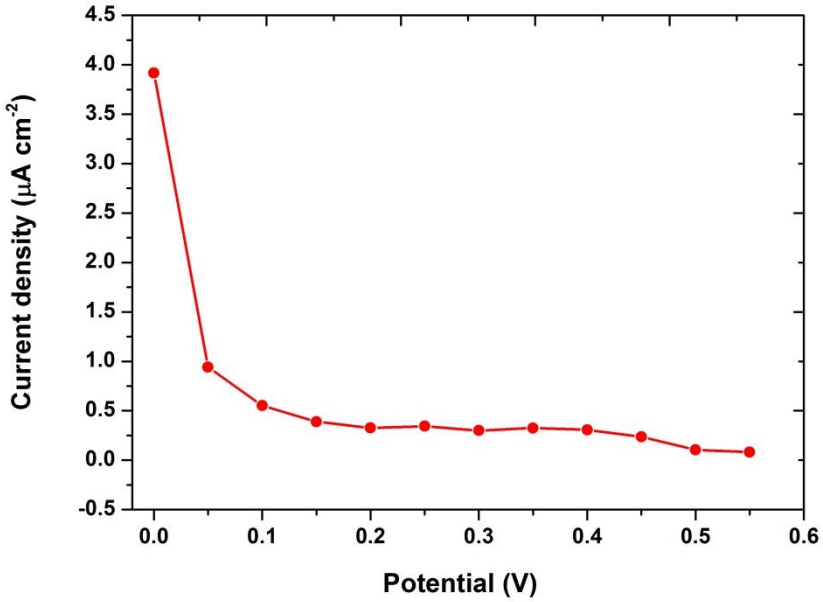


Fig. 6.58. Current density as a function of the potential (vs. Ag/AgCl) for the glucose/O_2 biofuel cell composed of GOX/PoPD/Au anode and laccase/PoPD/Pt cathode; immersed in 50 mM glucose, 7 mM FCA in 0.1 M phosphate buffer pH 7.4 and oxygen saturated (30 mins), 3 mM Q in 0.1 M phosphate buffer pH 6.0 anolyte and catholyte solutions respectively. Half-cell separation was established by a Whatman Al Anodisc membrane.

The observed decline in the current with increased potential values is consistent with the expected I vs. V profile for a fuel cell in operation.

The dependency of the power density on the applied potential for the constructed glucose/oxygen biofuel cell is illustrated in Fig. 6.59. The maximum obtained power density of 0.123 µW cm^{-2} has been recorded when a potential of 0.4 V was applied to the cell.

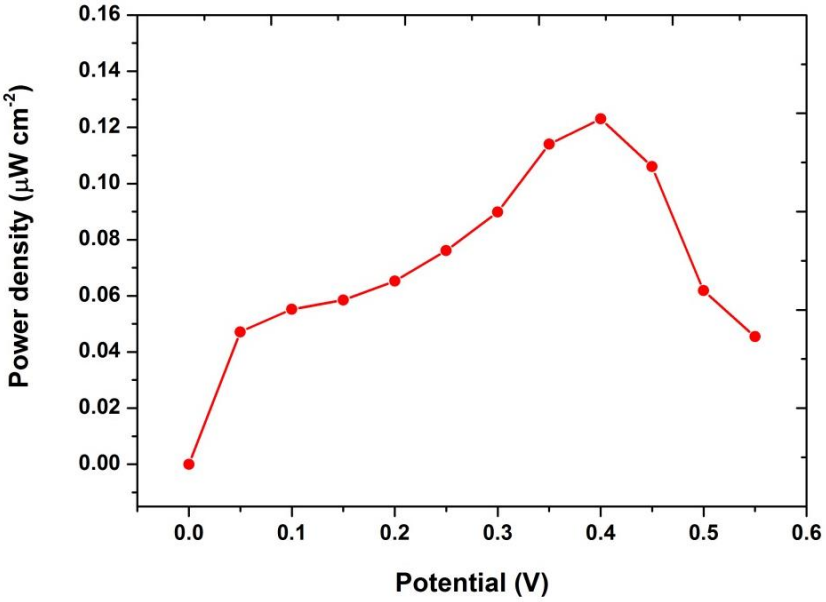


Fig. 6.59. Dependency of the power density on the potential (vs. Ag/AgCl), measured for glucose and O_2 biofuel cell composed of GOX/PoPD/Au anode and laccase/PoPD/Pt cathode; immersed in 50 mM glucose, 7 mM FCA in 0.1 M phosphate buffer pH 7.4 and oxygen saturated (30 mins), 3 mM Q in 0.1 M phosphate buffer pH 6.0 anolyte and catholyte solutions respectively. Half-cell separation was established by a Whatman Al Anodisc membrane.

B) Biofuel cell with Nafion perfluorinated membrane.

The dependency of the current density on the potential for the glucose/oxygen biofuel cell, when the half-cell separation was achieved by Nafion perfluorinated membrane, is depicted in Fig. 6.60. The cell was operating under identical working conditions as reported for Al Anodisc case study.

As previously, an inversely proportional relationship between the current and applied potential has been demonstrated, a characteristic feature of the fuel cells response.

The power density has been plotted as a function of the potential and is presented in Fig. 6.61.

As formerly, the highest power has been observed when the cell was posed at a potential of 0.4 V. The power output for Nafion perfluorinated film was 0.105 μW cm^{-2}.

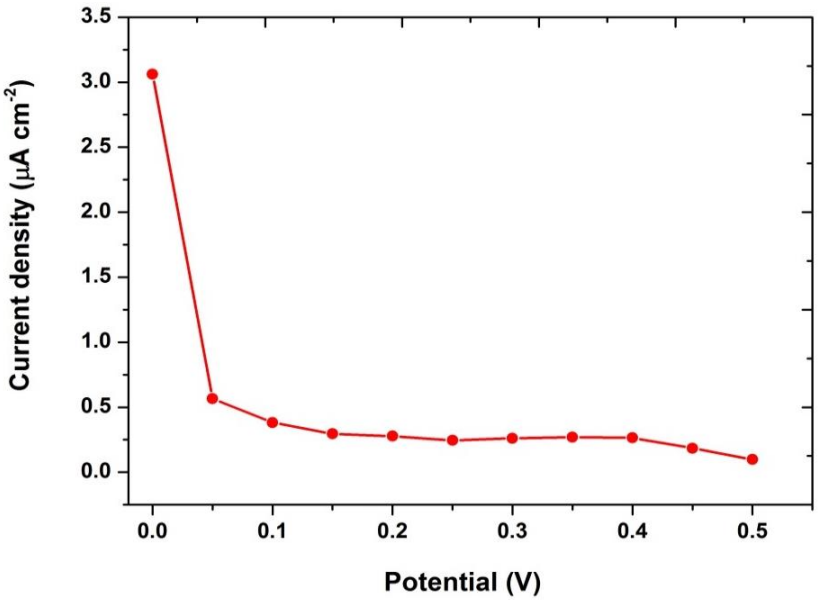


Fig. 6.60. Current density vs. potential (vs. Ag/AgCl) for glucose and O_2 biofuel cell composed of GOX/PoPD/Au anode and laccase/PoPD/Pt cathode; immersed in 50 mM glucose, 7 mM FCA in 0.1 M phosphate buffer pH 7.4 and oxygen saturated (30 mins), 3 mM Q in 0.1 M phosphate buffer pH 6.0 anolyte and catholyte solutions respectively. Half-cell separation has been established by a Nafion perfluorinated membrane.

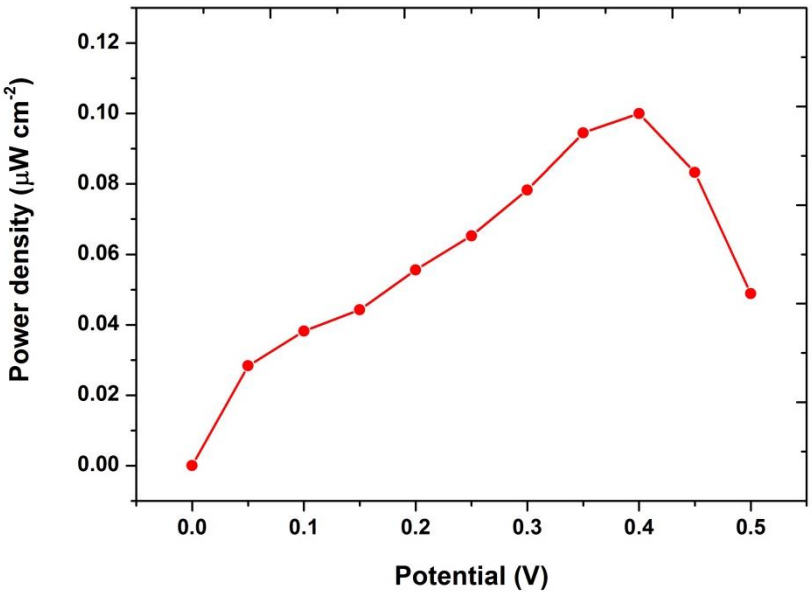


Fig. 6.61. P vs. V (vs. Ag/AgCl) curve for glucose and O_2 biofuel cell composed of GOX/PoPD/Au anode and laccase/PoPD/Pt cathode. The anolyte comprised of 50 mM glucose, 7 mM FCA in 0.1 M phosphate buffer pH 7.4 and oxygen saturated (30 mins), 3 mM HQ in 0.1M phosphate buffer pH 6.0 catholyte solution were separated by commercial Nafion perfluorinated membrane.

Although the recorded P vs. V functions diverge from the typical parabolic behaviour for fuel cells, they enable the determination of the maximum power and optimum potential couple. The reason behind atypical response is most likely due to a limited stability of the bioelectrochemical system and the interfering effect of the background signal associated with the electronic equipment. The power densities obtained from the enzymatic biofuel cell, with both catalysts immobilized within the P*o*PD polymer, are approximately two times lower in comparison with the results obtained for the initial set-up, where GOX and laccase were physically adsorbed on the electrode surface (Chapter III). A plausible explanation to the lower performance of the cell could be an insufficient enzyme or mediator load. In this regards, it would be recommended to investigate the effect of higher catalyst concentrations and an increased amount of the fuel and, if possible, the oxidant. Impeded transport of the H^+ through the Nafion and Al Anodisc membranes and the application of dissimilar mediator molecules, with less suitable redox potentials, are other potential reasons for decreased efficiency of the catalytic conversions. As discussed in Chapter III, the use of Nafion did not result in a substantial performance of the cell. While it would be recommended to perform the testing in the presence of previously characterized silicon based membranes, due to the high costs associated with their fabrication, more affordable, commercially available material alternatives had to be employed instead.

In principle, the power output from the device depends on the driving force for the reaction which is represented by the voltage measured between the oxidation and reduction processes occurring at each half-cell. These are very often determined by the formal potential of the employed mediators. In general, the more significant the potential difference at which the two redox reactions occur, the better the performance of the cell. Typically, one would like to work at the lowest possible anodic and the highest cathodic potentials in order to obtain the maximum [148]. Future investigation into optimum catalyst and mediator couples offering attractive electrodynamics should be considered.

6.7. Conclusions.

A) Sol-gel immobilization approach.

Successful immobilization of DSDH, NAD^+-GPS and DI in the silica sol-gel films has been reported on gold, via electrochemically assisted deposition from a hydrolyzed TEOS sol. The catalytic behavior of the enzyme and efficient electrical communication between the active components have been confirmed by effective electrooxidation of D-Sorbitol in the presence of the mediator, FDM. The modified Au electrode displayed a steady response under repetitive cyclic voltammetry scans. Although direct oxidation of the substrate has been recently reported for DSDH [132], the use of FDM as the mediator has been shown to have a significant positive effect on the enzymatic activity [114], resulting in much greater current outputs. In the light of these findings, only mediated electron transfer of DSDH has been considered as the scope of this Ph.D. chapter.

Previous attempts to co-immobilize FDM within electrogenerated sol-gel film by Wang *et al.* [149], revealed no detectable catalysis, which has been atttributed to the limitations associated with mediator incorporation. The authors proposed that operational communication between the electrode and FDM could be established by a uniform distribution of the species through drop-coating of the solution on the electrode surface rather than by electrodeposition.

Effective encapsulation of BOX, Os polymer and PEI in the silica sol-gel films has been reported on glassy carbon via simple casting of the hydrolysed sol suspension. The catalytic behavior of the enzyme and efficient electrical communication between the active components have been established upon mediated electroreduction of oxygen. The modified GCE electrode exhibited a continuous catalytic response under multiple CV scans.

The electrochemically assisted deposition of DSDH and encapsulation via drop-coating of BOX in silica sol-gels retained the biological activity of both enzymes and promoted efficient electrocatalysis in the presence of appropriate substrate and mediator molecules as well as polyelectrolytes. The proposed single step all-in-one immobilization protocol provides an effective way of stable entrapment of biological species. Once adjusted to individual properties of incorporated biomolecules, the sol-gel matrix can yield excellent enzymatic turnover.

B) Poly (*o*-phenylenediamine) encapsulation technique.

The electrochemically assisted deposition of GOX, laccase and LOX in poly (*o*-phenylenediamine) matrix retained the biological functions of the enzymes and promoted efficient electrocatalysis in the presence of appropriate substrate and mediator molecules. The electrogenerated films exhibited excellent stability upon long-term storage in the buffer solutions, with enhanced catalytic properties of the entrapped biomolecules following the storage. The polymer layer was able to sustain the activity of GOX during exposure to dry-air conditions for several hours and following rehydration in the buffer the enzyme demonstrated its natural functions for a number of days. Furthermore, it has been reported that the P*o*PD can act as a mediator for laccase and can also substitute the enzyme in effective catalysis of the two-electron reduction of oxygen. The demonstrated one-step universal immobilization protocol provides an effective way of stable entrapment of various biological species. As discussed previously, the encapsulation method is suitable for a wide range of oxidoreductase enzymes and can yield excellent enzymatic turnover even for residual enzyme quantities.

The selective electrodeposition of catalysts on gold and platinum electrodes microfabricated as part of this Ph.D. work, supported by their confirmed biological activity in the P*o*PD matrix, offers a promising strategy in the development of catalytic systems operating in the environment of a flow channel.

C) Comparison of the sol-gel and *o*-PD methods.

Among the numerous procedures for enzyme encapsulation, many authors report the use of sol-gel [27, 29] and *o*-PD [69, 81] as successful encapsulation matrices for a variety of enzyme catalysts, hence the reasoning behind the particular choice of polymer materials.

Biomolecules entrapped within sol-gels are contained within cage-shaped silica structures and exposed to little or no interactions with the matrix. As the hydration state of the gel is primarily controlled by the aging and drying conditions, the amount of water within the silica pores is typically sufficient to maintain the supportive layer of H_2O in the protein solvation shell. Nevertheless it is possible that the shrinkage of the gel on the

maturation step can introduce film deterioration and negatively affect the catalyst. Although the sol-gel process in principle does not involve the use of harsh and hazardous agents, the acid or base required for the hydrolysis of the starting sol, can potentially denature biomolecules. Furthermore, the alcohol released upon hydrolysis of the alkoxide, if not removed prior to the polymerization, can have a negative impact on the enzyme activity. Some authors report the substitution of TEOS with TMOS as methanol released in the silicate hydrolysis is less harmful for the catalysts than ethanol. A key challenge with the sol-gel protocol is however the necessity to adjust the composition of the deposition solution and the exact parameters of the process, in order to meet the individual requirements of incorporated species. As the nature and properties vary greatly between seemingly congenial catalysts, it is not feasible to obtain an all-purpose sol-gel encapsulation procedure. Re-adjustment of the electrodeposition conditions can be a particularly challenging task for more complex systems requiring cofactors and additional molecules mediating their regeneration, a good example being the discussed DSDH/sol-gel films.

O-phenylenediamine exhibits all the properties of a desirable encapsulation matrix and unlike sol-gel it can be successfully employed in the confinement of a variety of different oxidoreductase enzymes without the preconditioning requisite.

Encapsulation of enzymes in poly (*o*-phenylenediamine) presents an elegant and simple approach to catalyst immobilization, which does not require or produce any potentially harmful chemicals. The insulating character of the P*o*PD self-limits the electrodeposition process, producing thin polymer composites with high catalyst load, facilitating efficient exchange of species at the membrane/solution interface and effective catalysis. Moreover the P*o*PD polymer imparts remarkable permselectivity to the reaction substrates, while excluding any co-existing electroactive interferences (e.g. ascorbate, acetaminophen) and proteins naturally present in physiological samples [62, 150]. Despite the peculiar discriminating nature of poly (*o*-phenylenediamine), the response time and very good sensitivity are not compromised and as such the material can be successfully applied in the development of enzyme modified electrodes. In addition, generated P*o*PD films exhibit excellent stability when stored in buffer solutions and provide a long-term support for the incorporated biological species, offering a versatile and powerful strategy in the fabrication of catalytic systems with a view to biofuel cell applications.

D) Challenges associated with enzyme immobilization.

Due to the fragile nature of enzyme catalysts, the encapsulation of biomolecules poses a number of challenges. While, in principle, the immobilization significantly extends the life-span of species, prolonging the operability of the corresponding biofunctionalized component, the vitality of the molecules depends greatly on the choice of the host matrix and encapsulation method. Retained catalytic activity and long-term stability of catalysts, efficient electrical contact with the underlying electrode due to correct spatial arrangement of the molecule and enzyme's active centre easily accessible to the substrate are only some of the essential factors affecting the overall performance of the immobilized enzyme. A number of organic and synthetic materials along with various encapsulation techniques have been established and employed throughout the years in order to confine the molecules within the electrode area. In an ideal scenario, the majority of biological species or at least those of similar biotic functions and structures would be confineable via a small number of rapid one-step immobilization procedures. Unfortunately, this is not the case in real life applications as most organic catalysts require slightly different conditions and the procedure needs to be adjusted to their individual properties. Furthermore, each protocol must be specific to a particular research application, whether it is a low-detection limit biosensor or power sources with a fast diffusion of reaction reagents and a rapid, continuous catalytic response. For instance, enzymatic biofuel cells which are the scope of this PhD thesis typically require a balance between the amount of incorporated catalyst and the thickness of the catalytic layer. Whereas higher concentrations of the active component, in principle, improve the substrate turn-over, thick impermeable coatings of the enzymatic support may prevent efficient exchange of the reaction reagents. Furthermore, in some instances, elevated enzyme concentrations result in oversaturation and undesirable interactions between individual biological particles.

While precise control of the thickness and the location of the enzymatic system are nowadays facilitated by the electrochemically-assisted deposition route, not all catalysts can undergo the electrodeposition process. Since the electrochemically induced generation of enzyme/polymer composites enables efficient coating of electroactive surfaces with complex geometry, the inapplicability of this technique to certain species impedes the deposition on non-planar electrodes, restricting the number of potential applications.

Another essential factor is the homogeneity of generated films, which although is accurately controlled in electrolytic approach, cannot be regulated by simple casting and immersing techniques.

The two main challenges encountered while conducting the work as part of this experimental chapter were the stability of the produced enzyme doped films (sol-gel) and the inability to effectively co-encapsulate the mediator molecules. Rapid deterioration of the enzymatic activity, although not experienced here, can be also induced on the immobilization step by small alterations in the pH or addition of necessary denaturing chemicals. While these may be required for the matrix formation, they might lead to an undesired catalyst deactivation thus need also to be carefully considered.

6.8. Bibliography.

1. Fouletier, J. and P. Fabry, *Chemical Sensors: Development and Industrial Requirements.* Chemical and Biological Microsensors: Applications in Liquid Media. ISTE Ltd and John Wiley & Sons, Inc.,UK, 2010: p. 25-44.
2. Wollenberger, U., et al., *Enzyme electrodes using bioelectrocatalytic reduction of hydrogen peroxide.* Analytical Letters, 1990. **23**(10): p. 1795-1808.
3. Topoglidis, E., et al., *Protein adsorption on nanocrystalline TiO_2 films: an immobilization strategy for bioanalytical devices.* Analytical Chemistry, 1998. **70**(23): p. 5111-5113.
4. Zhang, Z., H. Liu, and J. Deng, *A glucose biosensor based on immobilization of glucose oxidase in electropolymerized o-aminophenol film on platinized glassy carbon electrode.* Analytical Chemistry, 1996. **68**(9): p. 1632-1638.
5. Adeloju, S.B. and A.N. Moline, *Fabrication of ultra-thin polypyrrole–glucose oxidase film from supporting electrolyte-free monomer solution for potentiometric biosensing of glucose.* Biosensors and Bioelectronics, 2001. **16**(3): p. 133-139.
6. Zhang, G., et al., *A chemiluminescence fiber-optic biosensor for detection of DNA hybridization.* Analytical Letters, 1999. **32**(14): p. 2725-2736.
7. Brewer, G.E., *Electrodeposition of Polymers.* Coatings technology handbook, Second Edition, 2001. Marcel Dekker, Inc., NY: p. 181.
8. Gill, I. and A. Ballesteros, *Encapsulation of biologicals within silicate, siloxane, and hybrid sol-gel polymers: an efficient and generic approach.* Journal of the American Chemical Society, 1998. **120**(34): p. 8587-8598.
9. Caruso, F., et al., *Enzyme encapsulation in layer-by-layer engineered polymer multilayer capsules.* Langmuir, 2000. **16**(4): p. 1485-1488.
10. Viswanathan, S., et al., *Electrochemical immunosensor for cholera toxin using liposomes and poly (3, 4-ethylenedioxythiophene)-coated carbon nanotubes.* Analytical Chemistry, 2006. **78**(4): p. 1115-1121.
11. Sagot, Y., et al., *Polymer encapsulated cell lines genetically engineered to release ciliary neurotrophic factor can slow down progressive motor neuronopathy in the mouse.* European Journal of Neuroscience, 1995. **7**(6): p. 1313-1322.
12. Nie, Z. and E. Kumacheva, *Patterning surfaces with functional polymers.* Nature Materials, 2008. **7**(4): p. 277-290.
13. Cosnier, S., *Biomolecule immobilization on electrode surfaces by entrapment or attachment to electrochemically polymerized films. A review.* Biosensors and Bioelectronics, 1999. **14**(5): p. 443-456.
14. Cosnier, S. and M. Holzinger, *Electrosynthesized polymers for biosensing.* Chemical Society Reviews, 2011. **40**(5): p. 2146-2156.
15. Yuqing, M., C. Jianrong, and W. Xiaohua, *Using electropolymerized non-conducting polymers to develop enzyme amperometric biosensors.* TRENDS in Biotechnology, 2004. **22**(5): p. 227-231.
16. Mosbach, K., *Immobilized enzymes.* Methods in enzymology, 1976. **44**: p. 3.
17. Mullis, K.B. and F.A. Faloona, *Specific synthesis of DNA in vitro via a polymerase-catalyzed chain reaction.* Methods in Enzymology, 1987. **155**: p. 335.
18. Ebelmen, J., *Untersuchungen über die Verbindungen der Borsäure und Kieselsäure mit Aether.* Liebigs Ann. Chem, 1846. **57**: p. 319-355.
19. Dickey, F.H., *Specific adsorption.* The Journal of Physical Chemistry, 1955. **59**(8): p. 695-707.

20. Braun, S., et al., *Biochemically active sol-gel glasses: the trapping of enzymes.* Materials Letters, 1990. **10**(1): p. 1-5.
21. Lim, J., et al., *Nanostructured sol-gel electrodes for biofuel cells.* Journal of the Electrochemical Society, 2007. **154**(2): p. A140-A145.
22. Moehlenbrock, M.J. and S.D. Minteer, *Extended lifetime biofuel cells.* Chemical Society Reviews, 2008. **37**(6): p. 1188-1196.
23. Gill, I. and A. Ballesteros, *Bioencapsulation within synthetic polymers (Part 1): sol–gel encapsulated biologicals.* TRENDS in Biotechnology, 2000. **18**(7): p. 282-296.
24. Avnir, D., et al., *Recent bio-applications of sol–gel materials.* Journal of Materials Chemistry, 2006. **16**(11): p. 1013-1030.
25. Livage, J., T. Coradin, and C. Roux, *Encapsulation of biomolecules in silica gels.* Journal of Physics: Condensed Matter, 2001. **13**(33): p. R673.
26. Zhou, M. and S. Dong, *Bioelectrochemical interface engineering: toward the fabrication of electrochemical biosensors, biofuel cells, and self-powered logic biosensors.* Accounts of Chemical Research, 2011. **44**(11): p. 1232-1243.
27. Urbanová, V., M. Etienne, and A. Walcarius, *One Step Deposition of Sol-Gel Carbon Nanotubes Biocomposite for Reagentless Electrochemical Devices.* Electroanalysis, 2013. **25**(1): p. 85-93.
28. Nadzhafova, O., M. Etienne, and A. Walcarius, *Direct electrochemistry of hemoglobin and glucose oxidase in electrodeposited sol–gel silica thin films on glassy carbon.* Electrochemistry Communications, 2007. **9**(5): p. 1189-1195.
29. Jia, W.-Z., et al., *One-step immobilization of glucose oxidase in a silica matrix on a Pt electrode by an electrochemically induced sol-gel process.* Langmuir, 2007. **23**(23): p. 11896-11900.
30. Tian, F., E. Llaudet, and N. Dale, *Ruthenium purple-mediated microelectrode biosensors based on sol-gel film.* Analytical Chemistry, 2007. **79**(17): p. 6760-6766.
31. Ferrer, M.L., F. del Monte, and D. Levy, *A novel and simple alcohol-free sol-gel route for encapsulation of labile proteins.* Chemistry of Materials, 2002. **14**(9): p. 3619-3621.
32. Reetz, M.T., *Entrapment of biocatalysts in hydrophobic sol-gel materials for use in organic chemistry.* Advanced Materials, 1997. **9**(12): p. 943-954.
33. Pierre, A. and P. Buisson, *Influence of the porous texture of silica gels on the enzymatic activity of lipases in esterification reactions.* Journal of Molecular Catalysis B: Enzymatic, 2001. **11**(4): p. 639-647.
34. Chen, Q., G.L. Kenausis, and A. Heller, *Stability of oxidases immobilized in silica gels.* Journal of the American Chemical Society, 1998. **120**(19): p. 4582-4585.
35. Heller, J. and A. Heller, *Loss of activity or gain in stability of oxidases upon their immobilization in hydrated silica: significance of the electrostatic interactions of surface arginine residues at the entrances of the reaction channels.* Journal of the American Chemical Society, 1998. **120**(19): p. 4586-4590.
36. Bhatia, R.B., et al., *Aqueous sol-gel process for protein encapsulation.* Chemistry of Materials, 2000. **12**(8): p. 2434-2441.
37. Odile, M., *Bacteria quorum sensing in silica matrices.* Journal of Materials Chemistry, 2004. **14**(14): p. 2264-2268.
38. Besanger, T.R., et al., *Screening of inhibitors using enzymes entrapped in sol-gel-derived materials.* Analytical Chemistry, 2003. **75**(10): p. 2382-2391.
39. Brennan, J.D., et al., *Using sugar and amino acid additives to stabilize enzymes within sol-gel derived silica.* Chemistry of Materials, 2003. **15**(3): p. 737-745.

40. Brinker, C.J. and G.W. Scherer, *Sol-gel science: the physics and chemistry of sol-gel processing.* Academic Press, Boston, 1990: p.908.
41. Besanger, T.R. and J.D. Brennan, *Entrapment of membrane proteins in sol-gel derived silica.* Journal of Sol-gel Science and Technology, 2006. **40**(2-3): p. 209-225.
42. Lan, E.H., B. Dunn, and J.I. Zink, *Nanostructured systems for biological materials*, in Protein Nanotechnology, Protocols, Instrumentation, and Applications. Humana Press Inc., Totowa, NJ, 2005. **300**: p. 53-79.
43. Polska, K. and S. Radzki, *Spectral and AFM characterization of trimethylammoniophenylporphyrin and concanavalin A associate in solution and monolithic SiO_2 gels obtained by the sol–gel method.* Optical Materials, 2008. **30**(10): p. 1644-1654.
44. Gupta, R. and N. Chaudhury, *Entrapment of biomolecules in sol–gel matrix for applications in biosensors: problems and future prospects.* Biosensors and Bioelectronics, 2007. **22**(11): p. 2387-2399.
45. Xu, Z., X. Chen, and S. Dong, *Electrochemical biosensors based on advanced bioimmobilization matrices.* TrAC Trends in Analytical Chemistry, 2006. **25**(9): p. 899-908.
46. Pierre, A., *Sol-Gel Immobilization of Catalytic Molecules and Applications: A Review.* Advances in Science and Technology, 2006. **45**: p. 2127-2136.
47. Kandimalla, V.B., V.S. Tripathi, and H. Ju, *Immobilization of biomolecules in sol–gels: biological and analytical applications.* Critical Reviews in Analytical Chemistry, 2006. **36**(2): p. 73-106.
48. Brinker, C.J., D.E. Clark, and D.R. Ulrich, *Better ceramics through chemistry: symposium held February 1984 in Albuquerque, New Mexico, USA*1984: North-Holland.
49. Sibottier, E., et al., *Factors affecting the preparation and properties of electrodeposited silica thin films functionalized with amine or thiol groups.* Langmuir, 2006. **22**(20): p. 8366-8373.
50. Shacham, R., D. Avnir, and D. Mandler, *Electrodeposition of Methylated Sol-Gel Films on Conducting Surfaces.* Advanced Materials, 1999. **11**(5): p. 384-388.
51. Goux, A.l., et al., *Oriented mesoporous silica films obtained by electro-assisted self-assembly (EASA).* Chemistry of Materials, 2009. **21**(4): p. 731-741.
52. Sheffer, M., A. Groysman, and D. Mandler, *Electrodeposition of sol–gel films on Al for corrosion protection.* Corrosion Science, 2003. **45**(12): p. 2893-2904.
53. Zhang, Z., L. Nie, and S. Yao, *Electrodeposited sol–gel-imprinted sensing film for cytidine recognition on Au-electrode surface.* Talanta, 2006. **69**(2): p. 435-442.
54. Sayen, S. and A. Walcarius, *Electro-assisted generation of functionalized silica films on gold.* Electrochemistry Communications, 2003. **5**(4): p. 341-348.
55. Guillemin, Y., et al., *Electrogeneration of highly methylated mesoporous silica thin films with vertically-aligned mesochannels and electrochemical monitoring of mass transport issues.* Journal of Materials Chemistry, 2010. **20**(32): p. 6799-6807.
56. Dixon, B.M., J.P. Lowry, and R.D. O'Neill, *Characterization in vitro and in vivo of the oxygen dependence of an enzyme/polymer biosensor for monitoring brain glucose.* Journal of Neuroscience Methods, 2002. **119**(2): p. 135-142.
57. O'Neill, R.D., et al., *Comparisons of platinum, gold, palladium and glassy carbon as electrode materials in the design of biosensors for glutamate.* Biosensors and Bioelectronics, 2004. **19**(11): p. 1521-1528.

58. Garjonyte, R., et al., *Prussian Blue-and lactate oxidase-based amperometric biosensor for lactic acid.* Sensors and Actuators B: Chemical, 2001. **79**(1): p. 33-38.
59. Cosnier, S., *Recent advances in biological sensors based on electrogenerated polymers: a review.* Analytical Letters, 2007. **40**(7): p. 1260-1279.
60. Yano, J., A. Shimoyama, and K. Ogura, *Poly (o-phenylenediamine)-film-coated electrode having a permselective response to halogenide ions.* Journal of the Electrochemical Society, 1992. **139**(5): p. L52-L53.
61. Geise, R.J., et al., *Electropolymerized films to prevent interferences and electrode fouling in biosensors.* Biosensors and Bioelectronics, 1991. **6**(2): p. 151-160.
62. Windmiller, J.R., et al., *Bicomponent microneedle array biosensor for minimally-invasive glutamate monitoring.* Electroanalysis, 2011. **23**(10): p. 2302-2309.
63. Li, X.-G., et al., *Novel multifunctional polymers from aromatic diamines by oxidative polymerizations.* Chemical Reviews, 2002. **102**(9): p. 2925-3030.
64. Malitesta, C., et al., *Glucose fast-response amperometric sensor based on glucose oxidase immobilized in an electropolymerized poly (o-phenylenediamine) film.* Analytical Chemistry, 1990. **62**(24): p. 2735-2740.
65. Lowry, J.P., et al., *Characterization of glucose oxidase-modified poly (phenylenediamine)-coated electrodes in vitro and in vivo: homogeneous interference by ascorbic acid in hydrogen peroxide detection.* Analytical Chemistry, 1994. **66**(10): p. 1754-1761.
66. Cooper, J., et al., *Glutamate oxidase enzyme electrodes: microsensors for neurotransmitter determination using electrochemically polymerized permselective films.* Journal of Electroanalytical Chemistry, 1995. **388**(1): p. 143-149.
67. Palmisano, F., D. Centonze, and P. Zambonin, *An in situ electrosynthesized amperometric biosensor based on lactate oxidase immobilized in a poly-o-phenylenediamine film: determination of lactate in serum by flow injection analysis.* Biosensors and Bioelectronics, 1994. **9**(7): p. 471-479.
68. Dempsey, E., J. Wang, and M.R. Smyth, *Electropolymerised o-phenylenediamine film as means of immobilising lactate oxidase for a L-lactate biosensor.* Talanta, 1993. **40**(3): p. 445-451.
69. Palys, B., A. Bokun, and J. Rogalski, *Poly-o-phenylenediamine as redox mediator for laccase.* Electrochimica Acta, 2007. **52**(24): p. 7075-7082.
70. Liu, T.Z., et al., *Determination of organonitriles using enzyme-based selectivity mechanisms. 2. A nitrilase-modified glassy carbon microelectrode sensor for benzonitrile.* Analytical Chemistry, 1995. **67**(10): p. 1679-1683.
71. Centonze, D., et al., *An in situ electrosynthesized poly-ortho-phenylenediamine glucose-oxidase amperometric biosensor for flow-injection determination of glucose in serum*. Annali di Chimica, 1992. **82**(5-6): p. 219-234.
72. Dumont, J. and G. Fortier, *Behavior of glucose oxidase immobilized in various electropolymerized thin films.* Biotechnology and Bioengineering, 1996. **49**(5): p. 544-552.
73. Trojanowicz, M., et al., *Biosensors based on oxidases immobilized in various conducting polymers.* Sensors and Actuators B: Chemical, 1995. **28**(3): p. 191-199.
74. Bartlett, P. and P. Birkin, *A microelectrochemical enzyme transistor responsive to glucose.* Analytical Chemistry, 1994. **66**(9): p. 1552-1559.
75. Ju, H., et al., *Amperometric biosensor for glucose based on a nanometer-sized microband gold electrode coimmobilized with glucose oxidase and poly (o-phenylenediamide).* Electroanalysis, 1998. **10**(8): p. 541-545.

76. Malitesta, C., I. Losito, and P.G. Zambonin, *Molecularly imprinted electrosynthesized polymers: new materials for biomimetic sensors.* Analytical Chemistry, 1999. **71**(7): p. 1366-1370.
77. Wang, J., et al., *One-step electropolymeric co-immobilization of glucose oxidase and heparin for amperometric biosensing of glucose.* Analyst, 2000. **125**(8): p. 1431-1434.
78. Garjonyte, R. and A. Malinauskas, *Glucose biosensor based on glucose oxidase immobilized in electropolymerized polypyrrole and poly (o-phenylenediamine) films on a Prussian Blue-modified electrode.* Sensors and Actuators B: Chemical, 2000. **63**(1): p. 122-128.
79. Yasuzawa, M., et al., *Characterization of glucose sensor prepared with the electropolymerized pyrrole containing a saccharide unit.* Electrochemistry Tokyo, 2000. **68**(11): p. 920-923.
80. Moussy, F., et al., *Performance of subcutaneously implanted needle-type glucose sensors employing a novel trilayer coating.* Analytical Chemistry, 1993. **65**(15): p. 2072-2077.
81. Luo, S., et al., *Palygorskite-poly (o-phenylenediamine) nanocomposite: An enhanced electrochemical platform for glucose biosensing.* Applied Clay Science, 2013. **86**: p. 59-63.
82. Rowinski, P., et al., *Electrodes modified with monoolein cubic phases hosting laccases for the catalytic reduction of dioxygen.* Analytical Chemistry, 2004. **76**(2): p. 283-291.
83. Bartlett, P. and J. Cooper, *A review of the immobilization of enzymes in electropolymerized films.* Journal of Electroanalytical Chemistry, 1993. **362**(1): p. 1-12.
84. Shleev, S., et al., *Direct electron transfer reactions of laccases from different origins on carbon electrodes.* Bioelectrochemistry, 2005. **67**(1): p. 115-124.
85. Shleev, S., et al., *Direct electron transfer between copper-containing proteins and electrodes.* Biosensors and Bioelectronics, 2005. **20**(12): p. 2517-2554.
86. Qiu, H., et al., *Adsorption of laccase on the surface of nanoporous gold and the direct electron transfer between them.* The Journal of Physical Chemistry C, 2008. **112**(38): p. 14781-14785.
87. Stolarczyk, K., et al., *Nanostructured carbon electrodes for laccase-catalyzed oxygen reduction without added mediators.* Electrochimica Acta, 2008. **53**(11): p. 3983-3990.
88. Ghindilis, A., *Direct electron transfer catalysed by enzymes: application for biosensor development.* Biochemical Society Transactions, 2000. **28**(2): p. 84.
89. Bogdanovskaya, V., et al., *Structure and properties of polymer biocomposite materials.* Russian Journal of Electrochemistry, 2004. **40**(3): p. 311-316.
90. Trudeau, F., F. Daigle, and D. Leech, *Reagentless mediated laccase electrode for the detection of enzyme modulators.* Analytical Chemistry, 1997. **69**(5): p. 882-886.
91. Barton, S.C., et al., *Electroreduction of O_2 to water on the "wired" laccase cathode.* The Journal of Physical Chemistry B, 2001. **105**(47): p. 11917-11921.
92. Barton, S.C., et al., *The "Wired" laccase cathode: high current density electroreduction of O_2 to water at + 0.7 V (NHE) at pH 5.* Journal of the American Chemical Society, 2001. **123**(24): p. 5802-5803.
93. Yabuki, S.-i., H. Shinohara, and M. Aizawa, *Electro-conductive enzyme membrane.* Journal of the Chemical Society, Chemical Communications, 1989(14): p. 945-946.

94. Chiba, K., et al., *Electrochemical preparation of a ladder polymer containing phenazine rings.* Journal of Electroanalytical Chemistry and Interfacial Electrochemistry, 1987. **219**(1): p. 117-124.
95. Yano, J., *Electrochemical and structural studies on soluble and conducting polymer from o-phenylenediamine.* Journal of Polymer Science Part A: Polymer Chemistry, 1995. **33**(14): p. 2435-2441.
96. Blaedel, W. and R.A. Jenkins, *Study of a reagentless lactate electrode.* Analytical chemistry, 1976. **48**(8): p. 1240-1247.
97. Trojanowicz, M., A. Lewenstam, and A. Moszczynska, *Lactate solid-state biosensor with multilayer of electrodeposited polymers for flow-injection clinical analysis.* Biosensors and Bioelectronics, 1996. **11**(11): p. 1155-1165.
98. Kawakami, M., H. Koya, and S. Gondo, *Immobilization of enzyme to platinum electrode and its use as enzyme electrode.* Applied Biochemistry and Biotechnology, 1991. **28**(1): p. 211-219.
99. Miyashita, M., et al., *Development of urine glucose meter based on micro-planer amperometric biosensor and its clinical application for self-monitoring of urine glucose.* Biosensors and Bioelectronics, 2009. **24**(5): p. 1336-1340.
100. Hu, T., et al., *A screen-printed disposable enzyme electrode system for simultaneous determination of sucrose and glucose.* Electroanalysis, 2000. **12**(11): p. 868-870.
101. Pauliukaite, R., M. Florescu, and C.M. Brett, *Characterization of cobalt-and copper hexacyanoferrate-modified carbon film electrodes for redox-mediated biosensors.* Journal of Solid State Electrochemistry, 2005. **9**(5): p. 354-362.
102. Karyakin, A.A., O.V. Gitelmacher, and E.E. Karyakina, *A high-sensitive glucose amperometric biosensor based on Prussian Blue modified electrodes.* Analytical Letters, 1994. **27**(15): p. 2861-2869.
103. Karyakin, A.A., E.E. Karyakina, and L. Gorton, *Prussian-Blue-based amperometric biosensors in flow-injection analysis.* Talanta, 1996. **43**(9): p. 1597-1606.
104. Karyakin, A.A., E.E. Karyakina, and L. Gorton, *The electrocatalytic activity of Prussian blue in hydrogen peroxide reduction studied using a wall-jet electrode with continuous flow.* Journal of Electroanalytical Chemistry, 1998. **456**(1): p. 97-104.
105. Dungchai, W., O. Chailapakul, and C.S. Henry, *Electrochemical detection for paper-based microfluidics.* Analytical Chemistry, 2009. **81**(14): p. 5821-5826.
106. Elving, P. and A. Krivis, *Voltammetric studies with graphite indicating electrode.* Analytical Chemistry, 1958. **30**(10): p. 1645-1648.
107. Desideri, P.G., D. Heimler, and L. Lepri, *Electrochemical behavior of 3-amino-pyridine, 2, 3-diamino-pyridine and 2, 6-diamino-pyridine in aqueous solutions.* Journal of Electroanalytical Chemistry and Interfacial Electrochemistry, 1978. **88**(3): p. 407-416.
108. Lee, H. and R. Adams, *Anodic Voltammetry and EPR studies of isomeric phenylenediamines.* Analytical Chemistry, 1962. **34**(12): p. 1587-1590.
109. Han, J., et al., *Poly (o-phenylenediamine) submicrosphere-supported gold nanocatalysts: synthesis, characterization, and application in selective oxidation of benzyl alcohol.* Langmuir, 2009. **25**(18): p. 11054-11060.
110. Kang, E., K. Neoh, and K. Tan, *Polyaniline: a polymer with many interesting intrinsic redox states.* Progress in Polymer Science, 1998. **23**(2): p. 277-324.
111. White, H.S., H.D. Abruna, and A.J. Bard, *Semiconductor Electrodes XLI. Improvement of Performance of Electrodes by Electrochemical Polymerization of*

o-Phenylenediamine at Surface Imperfections. Journal of the Electrochemical Society, 1982. **129**(2): p. 265-271.
112. Deshpande, M. and D. Amalnerkar, *Biosensors prepared from electrochemically-synthesized conducting polymers.* Progress in Polymer Science, 1993. **18**(4): p. 623-649.
113. Prokeš, J., et al., *Aniline-phenylenediamine copolymers.* Synthetic Metals, 1999. **102**(1): p. 1205-1206.
114. Wang, Z., et al., *Electrochemically assisted deposition of sol–gel bio-composite with co-immobilized dehydrogenase and diaphorase.* Electrochimica Acta, 2011. **56**(25): p. 9032-9040.
115. Liu, W., S. Zhang, and P. Wang, *Nanoparticle-supported multi-enzyme biocatalysis with in situ cofactor regeneration.* Journal of Biotechnology, 2009. **139**(1): p. 102-107.
116. Kohlmann, C., W. Märkle, and S. Lütz, *Electroenzymatic synthesis.* Journal of Molecular Catalysis B: Enzymatic, 2008. **51**(3): p. 57-72.
117. Kashiwagi, Y. and T. Osa, *Electrocatalytic oxidation of NADH on thin poly (acrylic acid) film coated graphite felt electrode coimmobilizing ferrocene and diaphorase.* Chemistry Letters, 1993. **22**(4): p. 677-680.
118. Osa, T., Y. Kashiwagi, and Y. Yanagisawa, *Electroenzymatic oxidation of alcohols on a poly (acrylic acid)-coated graphite felt electrode terimmobilizing ferrocene, diaphorase and alcohol dehydrogenase.* Chemistry Letters, 1994. **23**(2): p. 367-370.
119. Nikitina, O., et al., *Bi-enzyme biosensor based on NAD^+-and glutathione-dependent recombinant formaldehyde dehydrogenase and diaphorase for formaldehyde assay.* Sensors and Actuators B: Chemical, 2007. **125**(1): p. 1-9.
120. Antiochia, R. and L. Gorton, *Development of a carbon nanotube paste electrode osmium polymer-mediated biosensor for determination of glucose in alcoholic beverages.* Biosensors and Bioelectronics, 2007. **22**(11): p. 2611-2617.
121. Wang, Z., et al., *Critical effect of polyelectrolytes on the electrochemical response of dehydrogenases entrapped in sol-gel thin films.* Electroanalysis, 2010. **22**(17-18): p. 2092-2100.
122. Teramoto, M., et al., *Effect of addition of polyethyleneimine on thermal stability and activity of glucose dehydrogenase.* Applied Microbiology and Biotechnology, 1992. **38**(2): p. 203-208.
123. Shu, H.C., et al., *A reagentless amperometric electrode based on carbon paste, chemically modified with D-lactate dehydrogenase, NAD^+, and mediator containing polymer for D-lactic acid analysis. I. Construction, composition, and characterization.* Biotechnology and Bioengineering, 1995. **46**(3): p. 270-279.
124. Dominguez, E., et al., *A carbon paste electrode chemically modified with a phenothiazine polymer derivative for electrocatalytic oxidation of NADH. Preliminary study.* Biosensors and Bioelectronics, 1993. **8**(3): p. 167-175.
125. Karyakin, A.A. and E.E. Karyakina, *Prussian Blue-basedartificial peroxidase'as a transducer for hydrogen peroxide detection. Application to biosensors.* Sensors and Actuators B: Chemical, 1999. **57**(1): p. 268-273.
126. Park, T.-M., et al., *Sol–gel-based amperometric glucose biosensor incorporating an osmium redox polymer as mediator.* Analytical Communications, 1996. **33**(8): p. 271-273.
127. Park, T.-M., et al., *Sol-gel based amperometric biosensor incorporating an osmium redox polymer as mediator for detection of L-lactate.* Talanta, 1997. **44**(6): p. 973-978.

128. Alpeeva, I.S., et al., *Bi-enzyme alcohol biosensors based on genetically engineered alcohol oxidase and different peroxidases.* Microchimica Acta, 2005. **152**(1-2): p. 21-27.
129. Heller, A., *Electron-conducting redox hydrogels: design, characteristics and synthesis.* Current Opinion in Chemical Biology, 2006. **10**(6): p. 664-672.
130. Heller, A. and B. Feldman, *Electrochemical glucose sensors and their applications in diabetes management.* Chemical Reviews, 2008. **108**(7): p. 2482-2505.
131. Martinusz, K., E. Czirok, and G. Inzelt, *Studies of the formation and redox transformation of poly (o-phenylenediamine) films using a quartz crystal microbalance.* Journal of Electroanalytical Chemistry, 1994. **379**(1): p. 437-444.
132. Wang, Z., et al., *Reagentless d-sorbitol biosensor based on d-sorbitol dehydrogenase immobilized in a sol–gel carbon nanotubes–poly (methylene green) composite.* Analytical and Bioanalytical Chemistry, 2013: p. 1-8.
133. Urbanová, V., et al., *Functionalized carbon nanotubes for bioelectrochemical applications: Critical influence of the linker.* Journal of Electroanalytical Chemistry, 2013. **707**: p. 129-133.
134. Bard, A.J. and L.R. Faulkner, *Electrochemical methods: fundamentals and applications*. Vol. 2. 1980: Wiley New York.
135. Li, Z.-H., et al., *Optimization of Hydrogen Peroxide Detection for a Methyl Mercaptan Biosensor.* Sensors, 2013. **13**(4): p. 5028-5039.
136. Lim, J., et al., *Direct electron transfer in nanostructured sol–gel electrodes containing bilirubin oxidase.* Physical Chemistry Chemical Physics, 2007. **9**(15): p. 1809-1814.
137. Gupta, G., et al., *Direct electron transfer catalyzed by bilirubin oxidase for air breathing gas-diffusion electrodes.* Electrochemistry Communications, 2011. **13**(3): p. 247-249.
138. Walcarius, A. and E. Sibottier, *Electrochemically-induced deposition of amine-functionalized silica films on gold electrodes and application to Cu (II) detection in (hydro) alcoholic medium.* Electroanalysis, 2005. **17**(19): p. 1716-1726.
139. Che, G. and C.R. Cabrera, *Molecular recognition based on (3-mercaptopropyl) trimethoxysilane modified gold electrodes.* Journal of Electroanalytical Chemistry, 1996. **417**(1): p. 155-161.
140. Thompson, W.R., et al., *Hydrolysis and condensation of self-assembled monolayers of (3-mercaptopropyl) trimethoxysilane on Ag and Au surfaces.* Langmuir, 1997. **13**(8): p. 2291-2302.
141. Shankaran, D.R. and Y.B. Shim, *An Amperometric Sensor for Hydrogen Peroxide Based on a (3-Mercaptopropyl) trimethoxysilane Self-Assembled Layer Containing Hydrazine.* Electroanalysis, 2002. **14**(10): p. 704-707.
142. Shen, Y., et al., *Comparison of two-typed (3-mercaptopropyl) trimethoxysilane-based networks on Au substrates.* Talanta, 2005. **65**(2): p. 481-488.
143. Niedziolka, J., et al., *Characterisation of gold electrodes modified with methyltrimethoxysilane and (3-mercaptopropyl) trimethoxysilane sol–gel processed films.* Journal of Electroanalytical Chemistry, 2005. **578**(2): p. 239-245.
144. Wang, Z., et al., *Dehydrogenase-based reagentless biosensors: electrochemically assisted deposition of sol-gel thin films on functionalized carbon nanotubes.* Electroanalysis, 2012. **24**(2): p. 376-385.
145. Weigel, M.C., E. Tritscher, and F. Lisdat, *Direct electrochemical conversion of bilirubin oxidase at carbon nanotube-modified glassy carbon electrodes.* Electrochemistry Communications, 2007. **9**(4): p. 689-693.

146. Yang, Y., J. Wang, and R. Tan, *Immobilization of glucose oxidase on chitosan–SiO_2 gel.* Enzyme and Microbial technology, 2004. **34**(2): p. 126-131.
147. Dai, H., et al., *A highly performing electrochemiluminescent biosensor for glucose based on a polyelectrolyte-chitosan modified electrode.* Electrochimica Acta, 2009. **54**(19): p. 4582-4586.
148. Rincón, R.A., et al., *Enzymatic fuel cells: Integrating flow-through anode and air-breathing cathode into a membrane-less biofuel cell design.* Biosensors and Bioelectronics, 2011. **27**(1): p. 132-136.
149. Wang, Z., et al., *Durable cofactor immobilization in sol–gel bio-composite thin films for reagentless biosensors and bioreactors using dehydrogenases.* Biosensors and Bioelectronics, 2012. **32**(1): p. 111-117.
150. O'Neill, R.D., *Strategies for decreasing ascorbate interference at glucose oxidase-modified poly (o-phenylenediamine)-coated electrodes.* Analyst, 1996. **121**(6): p. 773-777.

CHAPTER VII

CONCLUSIONS AND FUTURE WORK

The original intent of this Ph.D. work was to develop a state-of-the-art, commercially viable, microfluidic enzymatic biofuel cell which could operate on environmental and physiological fluids. The intended devices were cost-effective, robust and highly reproducible electrochemical systems for effective extraction of electrical energy from the organic resources abundant in waste water. Ideally, the basic cell design would be adaptable to different fuels by changing the catalytic reagents with potential prospects in biomedical applications and as nature deployed energy harvesting devices.

In the course of the theoretical and experimental studies, it became apparent that this is no easy task. In order to establish such a device, a detailed analysis of each individual subcomponent of the cell must be carried out. The integration of biological activity with microfabrication technology requires an extensive analysis of the available fabrication techniques, the compatible micro-scale device design components and applicable enzyme incorporation strategies. Overall, this project presents a comprehensive and challenging research task. In this light, the focus of this thesis has been on component level investigations on the way toward a final assembled device.

The work flow of such a process is comprised of three essential aspects: theoretical studies of the microfluidic environment and catalytic reaction; fabrication of the cell components using cutting edge microfabrication technologies and a characterisation of the enzyme chemistry and component responses.

The results of this work are broken into four main sections: the feasibility of the biofuel cell concept in a small-scale format (Chapter III); design and optimization studies (Chapter IV); device fabrication, electrochemical characterization and modification of patterned electrodes (Chapter V) as well as enzyme immobilization (Chapter VI).

The viability of a small scale enzymatic biofuel cell was examined using a simple custom-made set-up composed of commercial Au and Pt disc electrodes and operating in

static conditions at room temperature, Chapter III. The design incorporated two enzyme catalysts: glucose oxidase and laccase so that glucose and oxygen could be used as the respective substrates. Successful conversion of the fuel and oxidant was investigated in the presence of mediator species with a silicon dioxide or nitride membrane separating the anodic and cathodic reactions. The electrochemical studies indicated increased electrical output in the presence of biological catalysts. The cell produced the maximum current and power densities of 1.97 $\mu A\ cm^{-2}$ and 0.197 $\mu W\ cm^{-2}$, recorded at 0.1 V, a value greater than some existing biofuel cell solutions [1]. While the initial prototype relied on a simple enzyme adsorption technique and the use of various silicon based membranes, in order to separate the anolyte and catholyte reactions, the fundamental concept of an energy harvesting device powered by biological catalysts has been successfully validated. The knowledge gained here was leveraged in the development of micro-scale devices.

The microfluidic approach to the biofuel cell design has been driven by an envisioned reduction of the device complexity, associated production and operating costs and an efficiently performing cell. In order to develop a functional catalytic microsystem, detailed studies of the flow on a micro scale including the properties of the enzymatic reaction needed to be carried out. These studies are discussed in Chapter IV and result in recommended device design and working conditions and offer a starting point for experimental work. The numerical studies examined the effects of the channel geometry and flow velocity on the mass transport of fuels. While, the majority of contemporary biofuel cell solutions report the use of a single macro-electrode design, this work focused on spatially distributed electrodes. Further work looked at the reaction kinetics occurring within a polymer membrane on top of these electrodes. Concentration profiles for an isolated and diffusion controlled system indicate gradients across the membrane dependent on the system parameters.

Additional studies on the rate constants, the thickness of the membrane and the initial concentration of the substrate contribute to the design rules for the cells. Computed cyclic voltammograms which incorporate the cell potential through the Nernst equation at the electrode boundary condition reproduced redox processes controlled by enzyme kinetics. One output of this thesis is a mathematical framework within which a range of biological species could be investigated provided catalytic rates for these species are known.

The fabrication and characterisation of components for the microfluidic enzymatic biofuel cells was discussed in Chapter V. The channel and electrode components have been obtained from common polymers, Zeonor (COC) and PDMS. The motivation behind the material choice was a selection of cost-effective, environmentally friendly, chemically inert and disposable plastic substrates. The original design plan used Zeonor for both structural parts of the device, namely the bottom electrode and the top channel, which would be then permanently attached to form a water tight seal using a combined chemical and mechanical assembly step. Due to a number of challenges associated with the patterning of the channel in COC and its subsequent attachment to the metal electrode unit, the final fabrication scheme employed Au and Pt electrodes deposited on Zeonor and a PDMS based channel.

Fabrication of the cell components has been carried out in separate processing steps involving the use of the state-of-the-art microfabrication techniques available at the facilities of the Tyndall National Institute, University College Cork, Ireland. Five channel and four electrode layouts with various numbers and dimensions of the patterned features were created. In the course of the fabrication work, a number of issues arose at both the components and the integration stages. Whereas the former was with the small feature size (μm range), the task of realizing a complete device with long-lasting operability in aqueous media requires a high level of process control which is resource intensive. While various accessible chemical and physical bonding approaches have been investigated, the assembly via oxygen plasma activated prime coat adhesive produced the most promising results in terms of the stability and sustainability of the generated seal under the flowing conditions. The techniques employed in the development of the individual physical components of the device as well as the work on the cell integration offer good groundwork for prospective large-scale, commercial fuel cell platforms.

The electrochemical characterization of microfabricated electrodes and a recommended method for modification of gold surfaces have also been presented in Chapter V. The investigation of the deposited metals confirmed the electroactive character of Au anodes and Pt cathodes. Cyclic voltammetry measurements of microelectrode designs 1 and 2 revealed a sigmoidal shape of the electrochemical response indicative of a radial influx of species and affected by the electrode kinetic limitations. Conversely, the studies of macroelectrode designs 3 and 4, displayed a peak shape behaviour suggesting a diffusion controlled process. This suggests current limitations, due to the concentration

gradient and the redox reaction being governed by species diffusion rather than limited kinetics of the electron transfer. In this case, it was reasonable to assume that layout 1 and 2 of the microelectrodes, due to high mass transport of species, are suitable for diluted fuels, while geometries 3 and 4 characterized by slower rate of species replenishment can be applied for high concentrations of analytes.

Additionally, modification of gold anodes with Nanoporous Gold (NPG) structures, in order to increase the electrochemically active area of the metal and to introduce surface porosity enabling improved catalyst immobilization is discussed. Scanning Electron Microscopy analysis of electrochemically deposited nanoporous gold features, confirmed the presence of a 200 nm layer of high density nanostructures. Cyclic voltammetry measurements of modified Au in 0.1M H_2SO_4 indicated enhanced current output consistent with an up to 14-fold increase in the active surface area as compared to bare gold. The catalytic response of glucose oxidase drop-coated on the NPG gold electrode retained biological activity of the catalyst and showed a 76% increase in output current at the oxidation peak potential in the presence of glucose, as compared to bare Au. Since static solutions often suffer from diffusion-limitations and uncompensated resistance of the supporting electrolyte, it is expected that conducting the experiments in flowing conditions should further enhance the response of NPG modified electrodes to electroactive species in the solution due to an improved access of the latter to the openings of the pores.

Enzyme immobilization is an important requirement for biofuel cells and is the focus of Chapter VI. While a variety of applicable techniques have been reported in the literature, only strategies enabling precise confinement of catalysts at the electrode surface have been considered within the scope of this work. Sol-gel (TEOS) and *o*-phenylenediamine (*o*-PD) have been selected as host matrices for encapsulation of a number of enzymes as both methods rely on an electrochemically assisted deposition of given biological species from the bulk solution containing an electroactive monomer. Application of a suitable potential to a working electrode immersed in an aqueous solution of TEOS or *o*-PD triggers the electropolymerization of the starting material at the surface of working electrode and subsequent incorporation of the available enzyme molecules. The studies on electrogenerated and drop-coated sol-gel films focused on the use of D-sorbitol dehydrogenase and bilirubin oxidase as respective anodic and cathodic catalysts. The deposits exhibited excellent electrochemical response to the substrate in the presence

of respective mediator species, however laborious optimization of the system components and the application of cationic additives were necessary to maintain the catalytic activity of DSDH and BOX. Further work was therefore carried out using *o*-phenylenediamine (o-PD) which exhibits properties desirable for an encapsulation matrix but unlike sol-gel can be successfully employed in the confinement of a range of oxidoreductase enzymes without the need for prior preconditioning. In this work, poly-*o*-phenylenediamine generated coatings have been used for efficient encapsulation of glucose oxidase, laccase and lactate oxidase. Following the initial successful immobilization of the species on commercial disc electrodes, the method has been applied in the modification of gold and platinum microfabricated on-chip electrodes. In both cases, the encapsulation approach resulted in a significant increase in the generated current response in the presence of respective substrate and mediator molecules. High stability of generated poly *o*-PD films, retained functionality of encapsulated biomolecules and selective discrimination of interfering agents enable successful implementation of the polymer in the preparation of enzyme electrodes paving the way for future device developments.

There are multiple avenues of investigation which could be explored to continue this work. For instance, the mathematical framework could be extended to use potential dependent rate coefficients and the boundary conditions for the computational fluid dynamics simulations could incorporate those of the enzyme kinetics. Simultaneous analysis of the anodic and cathodic dynamics should also be considered. Modelling of the time-dependent performance of the biofuel cell under flowing conditions for a time varying potential could be done. Feedback from experimental data could refine the model.

Challenges related to the assembly of the microfluidic platforms remain. An alternative approach to a permanent seal between the channel and the electrode units needs to be developed. Ideally, the bonding technique should be automated in a way to provide reproducible and highly precise alignment of the physical components. One approach would be to form the channel and the electrode features on a single substrate to eliminate the need for alignment and bonding altogether. Using micromachining technologies should surpass the hot-embossing techniques in terms of quality and reproducibility of obtained structures and be more large-scale production friendly. Furthermore, easily manufacturable silicon alternatives with enhanced durability should be considered as materials for the fabrication of stamps. Designs of the microfluidic devices using multiple inlet and outlet points for enhanced fuel and oxidant utilization would also be within scope

of future work as would parallel process and stacking of several biofuel cell units to increase fuel turnover and improve overall efficiencies. Fabrication processing developed as part of this thesis could be employed in a generation of on-chip catalytic systems containing numerous distinct electrode/channel features for simultaneous entry and consumption of diverse biological species. These multipurpose platforms could also seed the development of versatile tools for biosensing purposes. While the NPG structures, discussed in Chapter V, offer significant increase in the active area of the gold electrodes due to their highly porous character, in order to benefit from the enhanced metal surface, experimental characterisation should be carried out in flowing conditions where there would be improved mass transport of species into the pores. Immobilization of various enzyme catalysts on the NPG structures should also be investigated. Challenges associated with the fouling of active catalytic surfaces and the loss of enzymatic activities could be resolved by incorporating other highly catalytic electrode materials.

Investigation of the viability of poly *o*-PD as the host matrix for the encapsulation of diverse oxioreductase enzymes for prospective use with alternative organic fuels would also be worthwhile. The open circuit potential of the cell, determined by the potential separation of the anodic and cathodic processes, is the driving force for the enzymatic reaction and since one would like to work at the lowest anode potential in order to obtain the highest cell voltage, the use of NAD^+-dependent catalysts is highly desirable [8]. The combination of NAD^+-dependent alcohol dehydrogenase coupled with poly-methylene green (poly-MG) and laccase as anodic and cathodic enzymes provided a theoretical maximum cell voltage of 0.63V, and indicated a minimum loss of enzymatic activity [8]. The work on enzymatic biofuel cells operating in a microfluidic setting originated in this thesis should greatly benefit from the application of the suggested catalyst couple. High energy density substrates, such as glycerol or ethanol should be considered as fuels for the enzymatic reactions in order to meet the large energy demand of certain applications (e.g. micro-electronics).

The financial support of the Irish Environmental Protection Agency (EPA) through grant number 2009-ET-MS-10-S2 is sincerely appreciated.

7.1. Bibliography.

1. Beneyton, T., et al., *Membraneless glucose/O_2 microfluidic biofuel cells using covalently bound enzymes.* Chemical Communications, 2013. **49**(11): p. 1094-1096.
2. Feofilova, E., Y.E. Sergeeva, and A. Ivashechkin, *Biodiesel-fuel: Content, production, producers, contemporary biotechnology (Review).* Applied Biochemistry and Microbiology, 2010. **46**(4): p. 369-378.
3. Arechederra, R. and S. Minteer, *Complete oxidation of glycerol in an enzymatic biofuel cell.* Fuel Cells, 2009. **9**(1): p. 63-69.
4. Deng, L., et al., *A membraneless biofuel cell powered by ethanol and alcoholic beverage.* Biosensors and Bioelectronics, 2010. **26**(1): p. 70-73.
5. Chen, K.-I., A.G. McEwan, and P.V. Bernhardt, *Mediated electrochemistry of dimethyl sulfoxide reductase from Rhodobacter capsulatus.* JBIC Journal of Biological Inorganic Chemistry, 2009. **14**(3): p. 409-419.
6. Abo, M., et al., *Amperometric dimethyl sulfoxide sensor using dimethyl sulfoxide reductase from Rhodobacter sphaeroides.* Biosensors and Bioelectronics, 2003. **18**(5): p. 735-739.
7. Creevey, N.L., A.G. McEwan, and P.V. Bernhardt, *A mechanistic and electrochemical study of the interaction between dimethyl sulfide dehydrogenase and its electron transfer partner cytochrome c 2.* JBIC Journal of Biological Inorganic Chemistry, 2008. **13**(8): p. 1231-1238.
8. Rincón, R.A., et al., *Enzymatic fuel cells: Integrating flow-through anode and air-breathing cathode into a membrane-less biofuel cell design.* Biosensors and Bioelectronics, 2011. **27**(1): p. 132-136.

PUBLICATION LIST

Oral presentations:

1. Eirelec'11 Conference (Adare, Ireland, 16-18 May 2011): "*Microfabricated electrochemical devices for sensing and energy applications*". Grégoire Herzog, Monika Żygowska

2. Guardian Angels workshop (Helsinki, Finland, 15-16 September 2011): "*Energy harvesting from glucose and oxygen. Can biofuel cells power up smart autonomous systems*? ". G. Herzog, Monika Żygowska

3. Tyndall Technology / Analog Devices Forum (Limerick, 20 October 2011): "*Wireless Sensors and Energy Harvesting*". Cian O'Mathuna, Grégoire Herzog, Monika Żygowska

4. 12th Topical Meeting of the International Society of Electrochemistry & XXII International Symposium on Bioelectrochemistry and Bioenergetics of the Bioelectrochemical Society (Bochum, Germany, 17-21 March 2013): "*Electrochemically-assisted deposition of chitosan and sol-gel enzyme bio-composites for microfluidic biofuel cell applications*". Monika Żygowska, Veronika Urbanova, Mathieu Etienne, Grégoire Herzog, Vladimir Ogurtsov.

5. Tyndall Internal Conference (Cork, Ireland, 25 April 2013): "From doughnuts to energy. Miniature enzyme driven biofuel cells". Monika Żygowska, Grégoire Herzog, Vladimir Ogurtsov.

Poster presentations:

1. EPA National Conference (Croke Park, Dublin, Ireland, 23 June 2010): "*Design and fabrication of microfluidic systems for efficient energy bioconversion*" Monika Żygowska, Grégoire Herzog.

1. 8th EPA Postgraduate Conference (Dublin, Ireland 11 November 2010): "*Simulation studies for the optimization of microfluidic designs for biofuel cell applications*". Monika Żygowska, Grégoire Herzog.

2. Tyndall Postgraduate Poster Competition (Tyndall National Institute, Cork, 23 July 2010): "*Microfluidic systems for efficient energy bioconversion*" (poster number 23, page 7 of the Book of Abstracts). Monika Żygowska, Grégoire Herzog.

3. XXI International Symposium on Bioelectrochemistry and Bioenergetics (Krakow, Poland, 8-12 May 2011): "*Fabrication and characterisation of microfluidic devices for efficient energy bioconversion*" (poster number PS3-17, page 33 of the Conference Programme). Monika Żygowska, Grégoire Herzog.

4. NanoBio-Europe (Cork, Ireland, 21-23 June 2011):*"Fabrication and characterisation of microfluidic devices for efficient energy bioconversion*" (poster number 67, page 112 of the Book of Abstracts). Monika Żygowska, Grégoire Herzog.

5. Tyndall Postgraduate Poster Competition (Tyndall National Institute, Cork, 22 July 2011): "*Fabrication and characterisation of microfluidic devices for Biofuel Cell applications"*. Monika Żygowska, Grégoire Herzog.

6. 9th EPA Postgraduate Conference (Dublin, Ireland, 17 November 2011): "*Fabrication, characterisation and modelling of microfluidic devices for efficient energy bioconversion*" – 2nd Prize for poster presentation (page 8 of Book of Abstracts). Monika Żygowska, Grégoire Herzog, Vladimir Ogurtsov.

7. ADI meeting: "*Electrochemical Energy*". James Rohan, Grégoire Herzog, Monika Żygowska,, Vladimir Ogurtsov

8. ENVIRON 2012 conference (Dublin, Ireland, 7-9 March 2012) "Our Environment: Integrating Today's Research with Tomorrow's Actions" The 22nd Irish Environmental Researcher's Colloquium: "*Microfluidic devices for Enzymatic Biofuel Cell applications. Fabrication, characterisation and modelling studies*" (page 148 of the Book of Abstracts). Monika Żygowska, Vladimir Ogurtsov, Grégoire Herzog.

9. Lab-On-A-Chip conference (Edinburgh, Scotland, 28-29 March 2012): "*Enzymatic Biofuel Cells on chip*: *Fabrication, characterisation and modelling studies".* Monika Żygowska, Vladimir Ogurtsov, Grégoire Herzog.

10. 2012 Postgraduate Student Poster Competition (Tyndall National Institute, Ireland, 20 July2012): "*Mathematical model for the catalytic system of the Enzymatic Biofuel Cells"*. Monika Żygowska, Aidan Daly, Grégoire Herzog, Vladimir Ogurtsov.

11. Conference on Analytical Sciences in Ireland, CASi (Devere Hall, University College Cork, Ireland, 1-2 July 2013): "*Development and Investigation of Miniature Enzyme Driven Biofuel Cells* ". Monika Żygowska, Aidan Daly, Grégoire Herzog, Vladimir Ogurtsov.

Additional contributions:

1. Section on Enzymatic Biofuel Cells in the Guardian Angels " *Energy Benchmarking & Roadmaps"* proposal

Journal publications in preparation:

1. "*Fluid flow and catalytic reactions in a microfluidic enzymatic biofuel cell*" - Energies
2. "*Development and characterization of electrodeposited enzymatic microfluidic biofuel cells*" - Journal of the Electrochemical Society
3. "*Miniature glucose/O_2 enzymatic biofuel cell*" - Bioelectrochemistry
4. "*Electrogeneration of meso- and nanoporous materials for the modification of microelectrode arrays*" - Journal of the Electrochemical Society

APPENDIX A

METHODS OF ELECTROCHEMICAL CHARACTERIZATION

The following supplementary information encompasses a concise description of the fundamental concepts of electrochemistry and provides a brief discussion on the experimental techniques employed in this Ph.D. work.

A.1 Principles of electrochemistry.

The field of electrochemistry emerged in the first half of the XIX century from chemistry and the science of electricity. Nowadays, electrochemistry is a rigorous research area investigating the quantitative relations between the chemical, electrical and surface properties of various systems, with a strong consideration of diverse biological processes [1].

Electrochemical methods study the production of current generated as a result of chemical reactions at the electrode/solution interface or the chemical processess instigated by the application of external electrical energy [2]. Several types of electrochemical reactions exist including: simple electron transfer, electron transfer coupled with a chemical reaction, formation of an oxide layer, metal deposition or gas evolution [3] however only the two former were of interest in this work.

A) Electrochemical cells.

The principle of electrochemical systems relies on the transport of charge between the *electrode* (an electronic conductor) and the *electrolyte* (an ionic conductor) as a result of unprompted or enforced redox reactions occurring in the electrochemical cells. While the charge transfer in the electrode is facilitated by the movement of electrons, the carriers of electrical energy in the electrolyte are ionic species (e.g. H^+, Na^+, Cl^-) present in liquid

(aqueous or organic) solutions [2]. Electrode materials typically employed in the electrochemical measurements include solid (e.g. Au, Pt, glassy carbon) or liquid (e.g. Hg, Gal, In) metals, carbon (e.g. graphite, graphene, carbon nanostructures) or semiconductors.

Electrochemical cells can be divided into electrolytic and galvanic [2, 4]. The principal difference between these two electrical systems is that in the latter the reactions at the electrodes happen spontaneously once the electrodes are connected to an external conductor. Galvanic devices include bio- and fuel cells and commercially available primary (non-rechargeable) and secondary (rechargeable) cells and hence are of particular interest in this Ph.D. work. In the electrolytic cells, on the other hand, the electrochemical conversion is promoted only if a voltage greater than the reversible potential of the cell is applied (Fig. A.1). Electrolytic devices are routinely employed where the energy consumption is the requirement such as in electrolytic synthesis, electroplating or electrorefining [2].

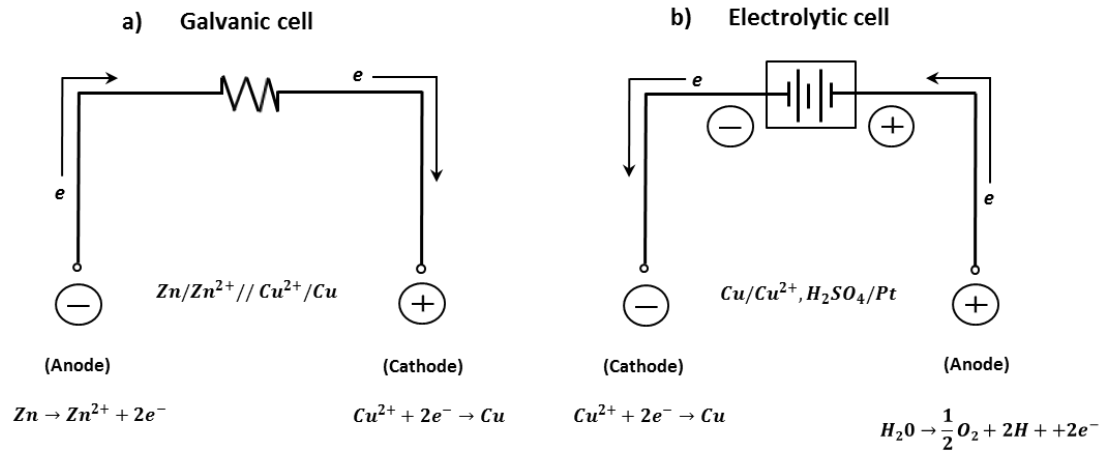


Fig. A.1. Schematic of galvanic (a) and electrolytic (b) cells. Adapted from [2].

B) Electrochemical reactions.

In principle, the application of a negative potential to the electrode yields an increased energy of electrons at the vicinity of the electrode/bulk interface. Once the energetic levels are satisfied, a transfer of e^- to the lowest unoccupied molecular orbital (LUMO) of species involved occurs, producing a so called *reducing current*, flowing outwards from the electrode. By convention, the reduction current associated with the cathodic processes, is considered to be negative. Correspondingly, positive potential

values lead to the electron transfer from the highest occupied molecular orbital (HOMO) of reactive species present at the electrode/solution boundary producing an *oxidative current* [1, 2], which by definition is a positive quantity [5]. A schematic of the electronic transitions during electrochemical processess occurring is illustrated in Fig. A.2.

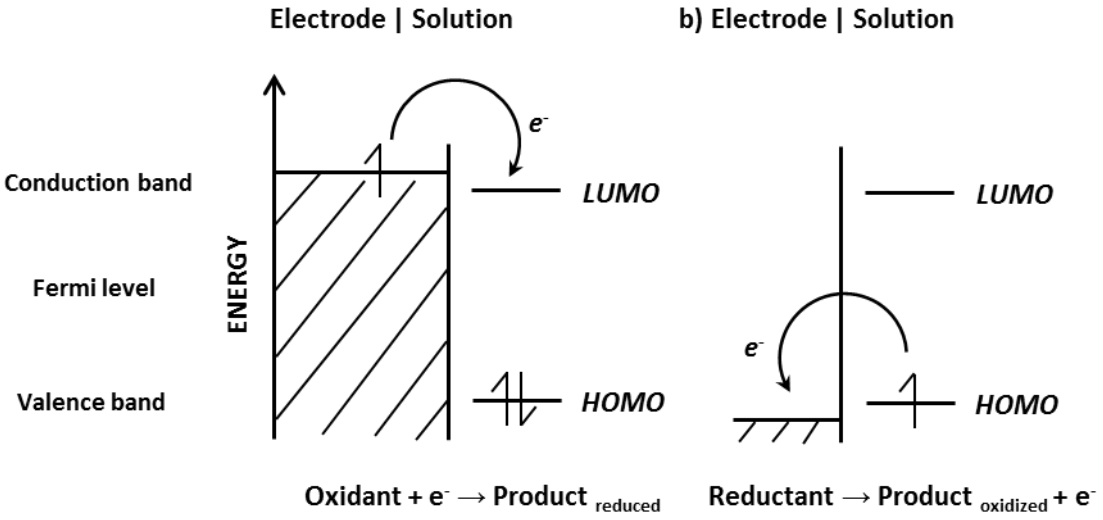


Fig. A.2. Diagram of the direction of the electron transfer during reduction (a) and oxidation (b) of species at the electrode/bulk interface. LUMO and HOMO represent the respective lowest unoccupied and the highest occupied molecular orbitals of the species involved in the reactions.

In principle, in an electrolytic cell, the *reducing (cathodic) current* is associated with the electrochemical reactions taking place on the negative *cathode*, while the *oxidative (anodic) current* is generated on a positive *anode*. In galvanic cells however, where the redox processes occur spontaneously, the *cathode* is positive with respect to the *anode*.

C) Faradaic and non-faradaic processes.

The redox reactions occurring in classical electrochemical cells can be categorized based on the type of processes involved, into *faradaic* and *non - faradaic*. The former, involve electron transfer at the electrode/solution interface and obey Faraday's law

(Eq.A.1) which defines a direct relationship between the charge passed through the cell and the number of moles of species involved in the reaction.

$$Q = nNF \qquad Eq.\ A.1$$

Here, Q is the charge in Coulombs (C), n and N represent the respective numbers of exchanged electrons and moles of the redox species (mol) involved in the reaction and *F* is a Faraday constant (F = 96485 C).

Electrodes at which faradaic processes occur are often called *charge-transfer electrodes.*

Non-faradaic electrochemical reactions include adsorption and desorption effects and need to be accounted for when investigating the faradaic processes. In this case, the electrode/bulk boundary acts as a capacitor (electrical element composed of two metal plates facing each other, [2]), which stores the charge upon the application of a suitable potential with accordance to Eq.A.2.

$$\frac{Q}{E} = C \qquad Eq.\ A.2$$

Where, Q is the charge accumulated in the capacitor (in Coulombs, C), E is the potential across the capacitor in volts (V) and *C* stands for the capacitance in Farads (F).

As a result of the interface charging, a *charging current* flows in the system.

D) The electrical double layer effect.

When a potential is applied to the working electrode, the net interactions between the electrode surface and the species in the solution result in the formation of an electrical double layer [4, 6, 7], which is characterized by a double layer capacitance [2]. The electrical models, routinely adopted for the double layer rely on the existence of multiple stratums, with the inner layer, closest to the electrode, containing solvent molecules and specifically adsorbed species.

In a simple classical *Helmholtz double layer* model, two layers of opposite charge separated by atomic distance, form at the electrode/solution boundary (Fig. A.3a). The *diffusive layer*, introduced later by Gouy and Chapman considered a more complex approach by incorporating a continuous distribution of the electrolyte ions (cations and anions) in the bulk solution, driven by thermal motion (Fig. A.3b). Due to very high

capacitance arising from the latter, Stern proposed a combined effect of Helmholtz and Gouy-Chapman models to explicitly recognize two regions of ion distribution, the inner layer known currently as compact or Stern and the outer diffusive layer (Fig. A.3c). The former contains often highly hydrated ions, which are strongly adsorbed at electrode surface, generating a compact coating. Furthermore, the Stern layer also consists of specifically adsorbed ions (mostly anions) and non-specifically adsorbed solvated counter-ions [8]. As the ionic composition of Stern layer varies with the distance from the electrode, the inner and outer Helmholtz planes are typically used in order to distinguish between the closest specific (IHP) and solvated non-specific ionic interactions (OHP).

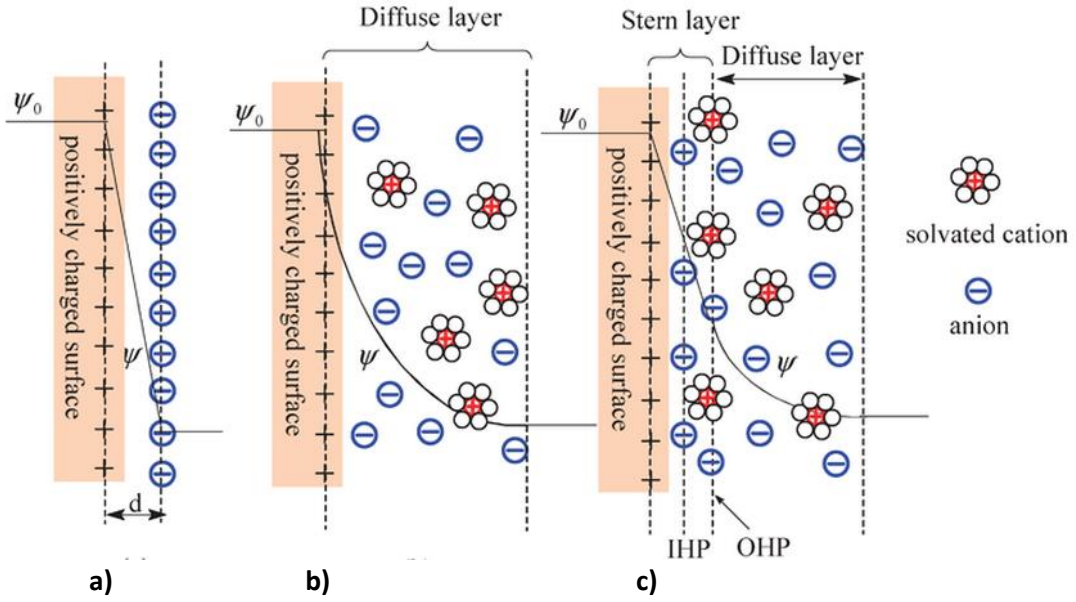


Fig. A.3. Models of the electrical double layer formed at the positively charged electrode surface: a) the Helmholtz model, b) the Gouy-Chapman model, and c) the Stern model with indicated IHP and OHP plane, where the diffuse layer begins. Here, d is the double layer distance described by the Helmholtz model, φ_0 and φ represent the potentials at the electrode and the electrode/bulk interface, respectively [8].

The thickness and composition of the double-layer depends strongly on the total ionic concentration in the solution. While in general, the charging current generated by the double-layer is negligible with respect to the faradaic current; at low quantities of electroactive species it may interfere with the measurement of faradaic processes, essential for the study of fast electrochemical or chemical reactions [9].

E) Mass transport in electrolytes.

Mass transport considerations are essential for *reversible* or *nernstian* electrode reactions as they obey the thermodynamic relationships and rely on the movement of species in the electrochemical systems [2]. Provided fast kinetics of the heterogeneous charge transfer and reversible, homogenous chemical reactions, one can assume the electrochemical processess occurring in the system to be at equilibrium and the concentrations of the species at the electrode surface to be dependent on the applied potential and dominated by the Nernst law. As a result, the rate of the electrode reaction, v, is governed by v_{mt}, reliant on the mass transport of species to the reaction zone (Eq. A.3).

$$v = v_{mt} = \frac{i}{nFA} \qquad Eq.\ A.3$$

Mass transfer of species, responsible for the material balance in the electrochemical systems, is defined as an organised movement of matter induced by ion migration, diffusion or convection. Although each has a different origin (gradients: of electrical potential, concentration or pressure), mixed transport mechanisms are quite common in electrochemical systems [9].

Diffusion - In multicomponent systems, such as solutions, diffusion is promoted by concentration gradients, when at least one of the components (ionic or neutral solute) is not uniformly distributed. The diffusional flux is always consistent with the direction of the decreasing concentrations (from high to low) and the rate at which the mass transfer occurs is directly proportional to the slope of the concentration differential [4, 7], as described in Fick's First Law (Eq. A.4)

$$j(x,t) = -D\,\frac{\partial c(x,t)}{\partial x} \qquad Eq.\ A.4$$

Here, j denotes the flux in mol cm^{-2} s^{-1} and it corresponds to the number of moles of a component passing through a unit area in a unit time; D denotes the proportionality factor, known as the diffusion coefficient (cm^2 s^{-1}) and $\frac{\partial c(x,t)}{\partial x}$ represents the local concentration gradient in an isolated point in space, x. Although the values for diffusion coefficient are

typically within a range 10^{-6}-10^{-5} cm^2 s^{-1}, D is dependent on the temperature and varies with the size of the molecule, with bigger components having slower proportionality factor. While Eq. is valid for diluted species, it is not obeyed in highly concentrated solutions, where the relationship between the flux and the concentration gradient is no longer represented by the proportionality constant (D varies with the concentration). In this case, as the diffusion process balances the chemical potentials, the formula for the flux can be represented using thermodynamic activities rather than the concentrations of the species [1] as shown in Eq. A.5.

$$j(x,t) = -D\frac{\partial a(x,t)}{\partial x} \qquad Eq.\ A.5$$

Where $\frac{\partial a(x,t)}{\partial x}$ denotes the gradient of the thermodynamic activities. Even in the modified form, the equation however still does not accurately represent the experimental behaviour of the solution.

Migration is a transport mechanism of ionic particles when a potential is applied to the electrode. As a result a gradient of the electrical potential is being formed at the interface with the solution, driving the movement of the charged molecules accordingly to the electrostatic force (e.g. repulsion of cations and attraction of anions) [7].

Convection - While the mass transfer mechanism in *diffusion* and *ionic migration* relies on an active movement of suspended matter through the solvent, the solute in the *convection* is carried by the solvent, moving as a whole upon the influence of a pressure gradient [9]. Convection can be categorised as natural or forced. The former, results from a density gradient in the solution, caused by e.g. localised thermal variations, and induces the flow of matter towards less dense regions. Since the natural convection is usually undesirable and irreproducible, the electrochemical experiments are typically designed in order to minimize their effects. Forced convection, on the contrary, is instigated by a deliberate action of mechanical stirring or agitation of the solution by e.g. bubbling gasses, rotating disk electrodes and may be characterized by stagnant regions and laminar or turbulent regimes [2].

In general, convection is a more efficient mass transfer process than diffusion or migration and when forced, leads to a rapid and an almost complete homogenization of the

solution [9]. In this light, it is often designed as part of the experimental set-up, to govern the mass transport of species in the electrochemical systems. Certain electroanalytical techniques, such as hydrodynamic voltammetry, are based on controlled convective flux to the working electrode [10].

Considering the aforementioned mechanisms, the net rate of the mass transfer for a one-dimensional case (along x-axis, towards the electrode surface), can be described by the Nernst-Planck formula (Eq. A.6), where the individual terms represents contributions of diffusion, migration and convection [2].

$$J_i(x) = \underbrace{-D_i \frac{\partial C_i(x)}{\partial x}}_{\textit{diffusion}} \underbrace{- \frac{z_i F}{RT} D_i C_i \frac{\partial \Phi(x)}{\partial x}}_{\textit{migration}} + \underbrace{C_i v(x)}_{\textit{convection}} \qquad Eq.\ A.6$$

Here, $J_i(x)$ represents the flux of species *i* (mol sec^{-1} cm^{-2}) at a distance x from the electrode surface, D_i is the diffusion coefficient (cm^2 sec^{-1}), $\frac{\partial C_i(x)}{\partial x}$ stands for the concentration gradient at a distance x, z_i and C_i (mol cm^{-3}) are the respective charge and concentration of species *i*, *F*, *R* and *T* are Faraday constant (96485 C), the real gas constant (8.314 J K^{-1} mol^{-1}) and the temperature (K) accordingly, $\frac{\partial \Phi(x)}{\partial x}$ represents the potential gradient at x and $v(x)$ is the velocity (cm s^{-1}) at which a particle moves towards the electrode (along x-axis).

Since the equation for the flux becomes intricate when all three mechanisms contribute concurrently, the electrochemical systems are often simplified in order to neglect one or more of the mass transfer contributions. As such, in the presence of a strong electrolyte and in still, unstirred solutions, the diffusional effects dominate the system and both migration and convection can be neglected.

A.2. Electrochemical techniques.

Electrochemical detection is typically categorized depending on the physical parameter being measured, into *current*, *potential* and *impedance* based methods.

The majority of detection and catalytic studies employ electrochemical techniques as the reactions under investigation can be effectively monitored by measurable currents

(amperometry), potential (potentiometry) or charge accumulation (chronocoulometry) or variations in the conductive properties of the medium between the electrodes (conductometry) [11]. As the oxidation and reduction potentials are characteristic to the individual species, the electrochemical approach provides additional means of selectivity in the analysis. Since the experimental methods applied as part of this Ph.D. work focused primarily on temporal current and potentiometric measurements, conductometry and impedance will not be discussed.

A) Amperometric and voltammetric measurements.

Amperometric and voltammetric studies rely on the measurement of the current generated as a result of a potential being applied to the working electrode (or an indicator) *versus* the reference electrode [12]. The current, produced by electrolytic oxidation or reduction processess occurring at the electrode/solution interface, is dependent on the rate of the mass transfer of species to the working electrode [12].

In principle, if the current is measured during controlled variations of the potential (scanning the potential over a set range) the method is referred to as *voltammetry*. The current response in voltammetric techniques is proportional to the concentration of the redox species and is typically represented by a peak or a plateau. Voltammetry includes a number of methods with a wide dynamic range such as linear sweep voltammetry, hydrodynamic voltammetry, differential pulse voltammetry, square wave voltammetry, polarography, stripping voltammetry and the most frequently employed, cyclic voltammetry [11].

In contrast, in *amperometry*, the current generated as a result of electrochemical redox reactions is recorded in time, while a constant potential is maintained at the working electrode with respect to the reference [13]. Unlike voltammetry, in this technique the potential is directly stepped to or held at the desired value during the current measurement. The amount of electrical energy drawn from the sample is however also proportional to the concentration of electroactive species. One of the prime advantages of a fixed potential employed in the amperometric techniques is the negligible charging current, which is typically required to apply a potential to a system. This in turn reduces the background signal, which has a negative impact on the performance of the electrochemical detection. Furthermore, the hydrodynamic amperometric methods in the presence of e.g. rotating

working electrode or in flowing conditions [14, 15] can significantly improve mass transport of particles to the electrode surface.

Amperometric and voltammetric techniques are typically carried out in a two- or three-electrode configuration, with gold, platinum and carbon based materials as the working electrode and in the presence of a reference, which if the currents are low (10^{-9} - 10^{-6} A) can also act as the auxiliary. The current drawn from the sample is proportional to the rate of the mass transfer and the bulk concentration of species [11].

1. Cyclic voltammetry (CV).

Cyclic voltammetry (CV) is an analytical technique widely employed to study the behavior of electrochemical systems and can be used to obtain useful information on the kinetics of the electrode reactions and the degree of their reversibility. The CV method is carried out by applying a variable triangular potential waveform (Fig. A.4) to a working electrode and measuring the current in response to the applied voltage.

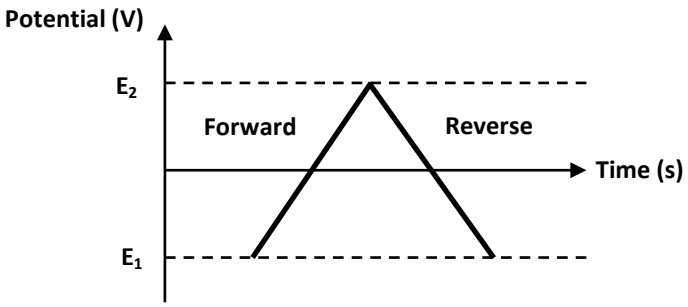


Fig. A.4.The triangular potential waveform applied to the working electrode in a cyclic voltammetry measurement.

As depicted in Fig. A.4, the potential of the electrode is swept between two chosen E limits at a constant rate, known as a *scan rate*. The potential of the working electrode begins originally with E_1 and is swept in a linear manner to a vertex potential of E_2 in a so called forward scan. At this point, the direction of the scan is reversed and the electrode returns back to E_1, which is the final potential for most CV measurements. This process generates a cyclic effect and is typically repeated multiple times, depending on the number

of sweeps. The generated I vs. E relationship is commonly known as a 'cyclic voltammogram'.

In a simple reversible one-component (*R*) redox reaction, illustrated in Eq.A.7, the current response of the forward scan is the linear potential sweep voltammogram as *R* is oxidised to *O*, producing an anodic peak. On the reverse scan, the reduction of *O* to *R* occurs, resulting in a cathodic peak. A plot of an applied potential versus current is used to depict such generated cyclic voltammograms (Fig. A.5).

$$O + ne^{-} \leftrightarrow R \qquad Eq.\ A.7$$

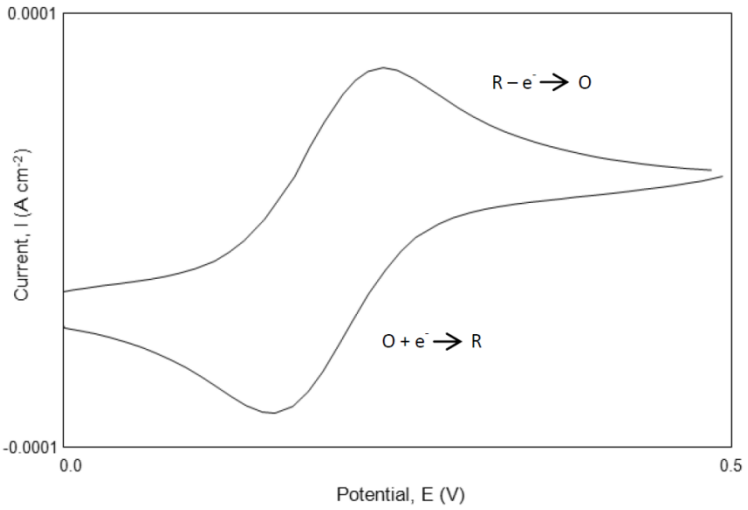


Fig. A.5.Current-potential dependency of a cyclic voltammogram for a reversible redox species [16].

The potential interval ($\Delta E_p = E_{pc} - E_{pa}$) and the current peak ratio ($\frac{i_{pc}}{i_{pa}}$) obtained from cyclic voltammograms (Fig. A.6) provide useful information on the reversibility of the redox system [10].

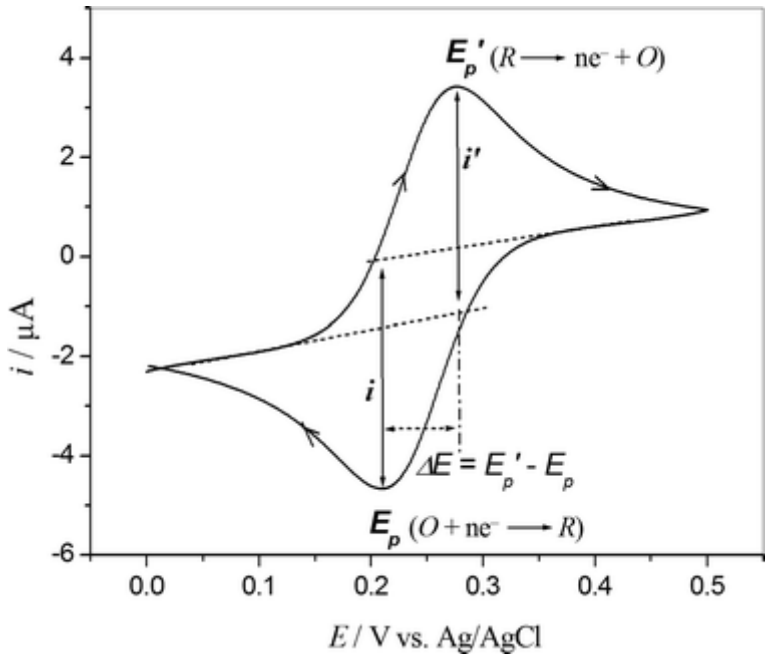


Fig. A.6. Typical cyclic voltammogram for a reversible redox reaction with indicated oxidation (E_p') and reduction (E_p) peak potentials; anodic (i') and cathodic (i) peak currents as well as the peak separation, ΔE [17].

- **Kinetic analysis based on CV.**

As indicated previously, the cyclic voltammogram response recorded at varied scan rates can reveal useful kinetic information regarding the electrocatalytic processes occurring at the electrode/bulk interface. This primarily includes the diffusion and adsorption effects as well as the determination of the degree of reversibility represented by a given redox system.

In principle, the factors which influence the shape of the response and the magnitude of the peak current for a typical reversible reaction at 25 ºC can be described by the Randles-Sevcik equation presented in Eq. A.8. Generally, the reversibility of the cyclic voltammogram will be solely observed when the oxidized and reduced species are uniquely stable and provided that the electron transfer occurs at a sufficient rate [18].

$$i_p = 2.69 \cdot 10^5 \cdot n^{\frac{3}{2}} \cdot A \cdot C \cdot D^{\frac{1}{2}} \cdot v^{\frac{1}{2}} \qquad Eq.\ A.8$$

Where n is the number of electrons involved in the reaction, A represents the electrode surface area in cm^2, C and D are the bulk concentration (mol cm^{-3}) and the diffusion coefficient (cm^2 s^{-1}) of the redox species and v is the scan rate (V s^{-1}).

As determined from the Randles-Sevcik equation, the peak current (i_p) should be directly proportional to the square root of the scan rate $(v^{\frac{1}{2}})$ used and parameters associated with the electroactive species: its bulk concentration and the diffusion coefficient (D). Accordingly, a linear dependency of the measured current on the square root of the scan rate indicates that a given redox reaction conforms to the Randles-Sevcik relationship and is therefore governed to a certain extent by a diffusion-controlled behaviour. Consequently, the redox reaction process can be considered adsorption free. Furthermore, if the peak current (i_p) plotted against the $(v^{\frac{1}{2}})$ results in a straight line, the diffusion coefficient (D) can be calculated from the slope of the linear function, assuming fast kinetics and reversibility of the reaction and provided that the electron stoichiometry, the concentration of species and the surface area of the electrode are known.

The Randles-Sevcik equation has been used in Chapters III and VI in order to determine the D of electron shuttling mediators, potassium ferricyanide ($K_3[Fe(CN)_6]$), ferrocenecarboxylic acid (FCA) and 2, 2'-azino-bis (3-ethylbenzothiazoline-6-sulphonic acid) (ABTS) on Au and Pt disk electrodes (Ø2mm).

For i_p vs. $v^{\frac{1}{2}}$ dependency, which is defined by a standard Randles-Sevcik formula, it is anticipated that the electrochemical system will also follow other patterns. A number of tests can be applied to the sample which, in principle, should be fulfilled over a wide range of potential sweeps provided the reversible character of the reaction. In general, these are based on the ratio of the forward and reverse peak currents $\frac{i_p^A}{i_p^C}$ and the peak separation ΔE_p . For any reversible electrochemical system at 25 ºC, the magnitude of the $\frac{i_p^A}{i_p^C}$ should be equal to unity and independent of the scan rate used, as shown in Eq. A.9. Furthermore, the peak separation should satisfy Eq. A.10 and the difference in the peak potentials and the half-wave peak potentials should comply with Eq. A.11. If any of these requirements are not satisfied, the electron transfer process is not reversible under the conditions of the experiment and the process is considered to be more complex [19].

$$\frac{i_p^A}{i_p^C} = 1 \qquad Eq.\ A.9$$

$$\Delta E_p = E_p^A - E_p^C \ = \frac{59}{n} mV \qquad Eq.\ A.10$$

$$\Delta E_p = E_p - \ E_{\frac{p}{2}} \ = \frac{59}{n} mV \qquad Eq.\ A.11$$

Where i_p^A and i_p^C are the respective oxidation and reduction peak currents expressed in A, E_p^A and E_p^C represent peak potentials of the anodic (oxidation) and cathodic (reduction) waves (mV), $E_{p/2}$ stands for the half-wave potential (mV) and *n* is the number of electrons exchanged in the redox reaction [16, 19].

If the electron transfer does not occur within the projected timescale of the experiment, which is indicative of slow exchange rates, the system can be considered irreversible. The irreversibility of a given redox reaction is determined by the lack of a reverse peak in the recorded cyclic voltammogram. The peak current in this case can be described by a modified Randles-Sevcik equation, which holds at 25 ºC and incorporates the number of electrons transferred up to the rate-determining electrochemical step ($n_\propto$) and the charge-transfer coefficient of the reverse reaction ($\propto_C$), depicted in Eq. A.12.

$$i_p = 2.99 \cdot 10^5 \cdot n(\propto_C n_\propto)^{\frac{1}{2}} \cdot A \cdot C \cdot D^{\frac{1}{2}} \cdot v^{\frac{1}{2}} \qquad Eq.\ A.12$$

Furthermore, while the oxidation peak currents for an irreversible system are proportional to the square root of the scan rate, each decade change in *v* yields in a $\frac{30}{\propto_C n_\propto} mV$ shift in the peak potentials. In addition, the difference in the peak potentials and the half-wave peak potential at 25 ºC can be described according to Eq. A.13 [16].

$$E_p - E_{\frac{p}{2}} = \frac{48}{\propto_C n_\propto} mV \qquad Eq.\ A.13$$

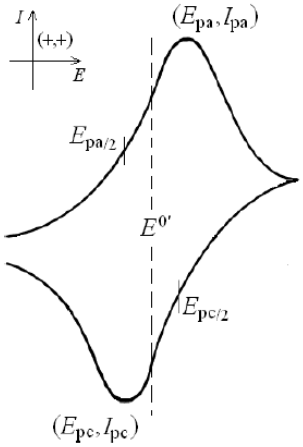
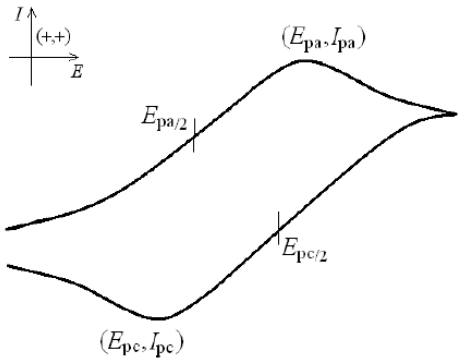
For transitional systems, which do not fully comply with either the reversible or irreversible electron mechanisms and rather exist between the two extremes, a quasi-reversible behaviour is assumed. The kinetics of a quasi-reversible system are not very fast or very slow and both the forward and reverse reactions contribute to the peak current, which increases with the square root of the scan rate, as indicated in the Randles-Sevcik equation (Eq. A.12). Nevertheless, at high scan rate values, where the kinetic equilibrium

of the redox couple is attained slowly (small standard rate constant, k^{θ}), the peak current is no longer proportional to the square root of the scan rate [16].

Provided that $\propto_C$ and $n_{\propto}$ are equal to 0.5, the peak oxidation and reduction currents for the quasi-reversible system should be even (the ratio equals unity), analogously to the fully reversible redox case. The separation of the anodic and cathodic peaks is typically larger than $\frac{59}{n} mV$ and increases with higher scan rates, as the peak potential shifts [19].

The properties of the reversible and quasi-reversible redox systems are summarized in Tab. A.1.

Tab. A.1. Comparison of reversible and quasi-reversible redox systems [16].

Reversible	Quasi-reversible
	
$I_p \propto \upsilon^{1/2}$	I_p not always proportional to $\upsilon^{1/2}$ as υ increases
E_p independent of υ	$\lvert E_p \rvert$ increases as υ increases
$\Delta E_p = 59/n$ mV	$\Delta E_p > 59/n$ mV

One of the prime applications of cyclic voltammetry is a qualitative analysis of homogenous chemical reactions which precede or follow the heterogeneous electrochemical processes at the electrode/electrolyte solution in e.g. amperometric enzyme-electrodes for catalytic studies [17].

2. Chronoamperometry.

Chronoamperometry is, after cyclic voltammetry, the second most employed electrochemical technique widely used to gain information about the kinetics and mechanisms of redox reactions. In this method, the potential applied to the working electrode is stepped from an initial nil-current condition at which no faradaic reactions occur, to a value corresponding to a zero surface concentration of the electroactive species. With no current being drawn at the start of the measurement, the mass transport under the final potential is governed merely by diffusion [17]. While, chronoamperometric studies typically employ a single potential step, additional potential switches can be introduced if required.

The current-time dependency generated from chronoamperometric detection, commonly known as an amperometric i-t curve, reflects the change in the concentration gradient of species at the vicinity of the electrode/solution interface.

In general, the current recorded for a planar electrode, decays with time according to the Cottrell equation (Eq. A.14).

$$i(t) = \frac{nFACD^{\frac{1}{2}}}{\pi^{\frac{1}{2}}t^{\frac{1}{2}}} \qquad Eq.\ A.14$$

Where *n* is the number of electrons exchanged in the redox reaction, *A c*orresponds to the electrode area in cm^2, *C* (mol cm^{-3}) and *D* (cm^2 s^{-1}) are the bulk concentration and the diffusion coefficient of the electroactive species respectively, F is a Faraday constant (96485 C mol^{-1}) and *t* is the time of the potentiostatic measurement in s.

Although the classical Cottrell equation is relevant solely to planar electrodes, it can be appropriately adapted for spherical, cylindrical or rectangular geometries by applying a suitable laplace operator and corresponding boundary conditions in conjunction with Fick's second law of diffusion [2, 4]. The formula is often simplified to Eq. A.15 by introducing a factor *k*, which is a collection of constants for a given electrochemical system.

$$i(t) = kt^{-\frac{1}{2}} \qquad Eq.\ A.15$$

Here, *k* represents the electrochemical constants (*n*, *F*, *A*, *C* and *D*).

In general, the current drawn from the electrochemical reaction in the short amperometric measurements corresponds to a monodimensional diffusion of the analyte; while at prolonged times a steady state is reached. This phenomenon is prominent in potentiostatic deposition of polymer films, which was of particular interest for this Ph.D. work and its practical application in the encapsulation of enzyme catalysts is discussed in Chapter VII. In polymer deposition, a constant potential is applied for a certain period of time to the working electrode in a monomer containing electrolyte solution in order to enable the formation of a desired film thickness. Fig. A.7 represents a sample amperometric i-t curve obtained for the deposition of glucose oxidase in *o*-phenylenediamine polymer. Initial rapid decrease in the observed current followed by a steady-state behavior arise from the early charging of the double layer and ultimate self-limitation of the electrochemical process at longer deposition times. The magnitude of the charging current decay is governed by the RC time constant (time required to charge a capacitor) which is associated with the size of the electrode and the conductivity of the investigated solution [6] .

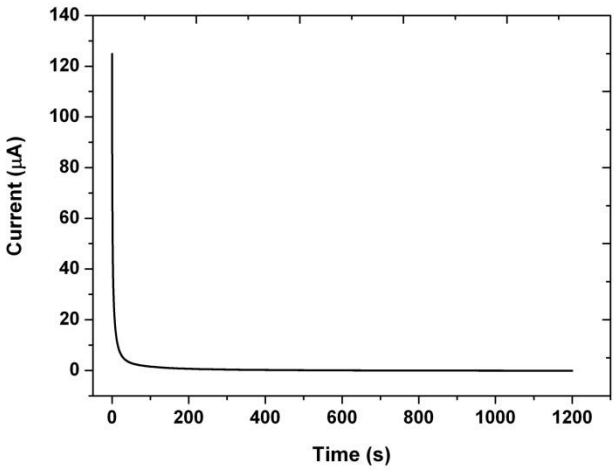


Fig. A.7. I-t curve obtained during potentiostatic deposition of 10 mg ml $^{-1}$ GOX in 10 mM o-PD polymer at 0.75V vs. Ag/AgCl for 1200 s.

Although CV has been routinely employed in the electrogeneration of polymer films due to the smooth nature of formed deposits, generally stated in the literature [20], numerous authors report the preferred use of potentiostatic techniques [21, 22] as resulting in more adherent, uniform and stable polymer coatings.

B) Potentiometric analysis.

Potentiometry is a technique employed to measure the potential of the electrochemical solution between two electrodes at a negligible current, usually referred to as a zero-current state. The method provides useful information about the ionic activity in the electroactive sample. Potentiometric studies employ electrodes appropriate to certain charged species, such as ion-selective (ISE) and glass-membrane pH electrodes for the discriminatory detection of F^-, K^+, Cl^-, H^+ [4, 11, 23]. In order to record the potential (typically across a membrane that reacts with the ions of interest), two electrodes are required in the electrochemical cell, an *indicator* and a reference.

In potentiometric studies, the potential of the cell (E_{cell}), also referred to as the electromotive force (EMF) is governed by the Nernst formula presented in Eq. A.16 The observed E_{cell}, recorded at a zero current, is dependent on the composition of the electrolyte and other phases of variable concentrations and as indicated from the equation, logarithmically proportional to the specific ion concentrations.

$$E_{cell} = E^0_{cell} + \frac{RT}{nF} lnQ \qquad Eq.\ A.16$$

where, E^0_{cell} is a constant that depends on the nature of the electrode reaction and represents the potential of the cell at a standard state (1mol dm^{-3} of solute concentration, 1 atm pressure and 297K), R is the universal gas constant, T stands for the absolute temperature (K), n is the number of electrons exchanged in the reaction, F is a Faraday constant and Q is the ratio of the concentration of anodic and cathodic ions. Since the correction term for the concentrations, is relatively small, the value of the electrode potential is predominantly reliant on the E^0_{cell} constant. As follows from the Nernst equation, raising the concentration of the oxidizing agent, shifts the potential in the positive direction, with the opposite result with increased amount of the reducing component [1].

Although potentiometric devices have been predominantly applied in the field of biosensing [24], systems able to generate sufficient electrical current, may also be adopted in the development of energy-harvesting biofuel cells [85] and nano-size bioelectronics devices operating in physiological fluids [25]. In principle, these chemical based sensors can be coated with a biological element, such as an enzyme, capable of catalyzing biochemical reactions and generating ions which can be further detected by the

underlying electrode. Alternatively, by products of the enzymatic reaction may alter the pH of the studied solution, which can be indirectly recorded as a change in the potential.

A.3 Bibliography.

1. Bagotsky, V.S., *Fundamentals of electrochemistry*. Vol. 44. 2005: Wiley & Sons, Inc.
2. Bard, A.J. and L.R. Faulkner, *Electrochemical methods: fundamentals and applications*. Second Edition. 2001: Wiley & Sons, Inc.
3. Herzog, G.J.A., *Underpotential Deposition at Modified Sensor Surfaces*, Electrochemistry, 2004.
4. Wang, J., *Analytical electrochemistry* 2006: Wiley & Sons, Inc.
5. Pletcher, D., *Instrumental methods in electrochemistry* 2001: Horwood Publishing Limited, Chemical Science Series.
6. Myland, J.C. and K.B. Oldham, *How does the double layer at a disk electrode charge?* Journal of Electroanalytical Chemistry, 2005. **575**(1): p. 81-93.
7. Bond, A.A.M. and F. Scholz, *Electroanalytical methods: guide to experiments and applications* 2010: Springer - Verlag Berlin Heidelberg
8. Zhang, L.L. and X. Zhao, *Carbon-based materials as supercapacitor electrodes.* Chemical Society Reviews, 2009. **38**(9): p. 2520-2531.
9. Oldham, K. and J. Myland, *Fundamentals of electrochemical science* 1993: Academic Press, Inc.
10. Compton, R.G. and C.E. Banks, *Understanding voltammetry* 2007. Imperial College Press, London.
11. Ronkainen, N.J., H.B. Halsall, and W.R. Heineman, *Electrochemical biosensors.* Chemical Society Reviews, 2010. **39**(5): p. 1747-1763.
12. Kissinger, P.T. and W.R. Heineman, *Laboratory techniques in electroanalytical chemistry* 1996: Marcel Dekker, Inc.
13. Bartlett, P.N., *Bioelectrochemistry: fundamentals, experimental techniques and applications* 2008: Wiley & Sons Inc.
14. Von Sturm, F. and G. Richter, *Pacemaker with biofuel cell*, 1976, US Patent 3941135 A.
15. Trojanowicz, M., M. Szewczynska, and M. Wcislo, *Electroanalytical flow measurements–recent advances.* Electroanalysis, 2003. **15**(5-6): p. 347-365.
16. Hamilton, A., *The Formation and Characterisation of a Polypyrrole Based Sensor for the Detection of Urea*, 2012, PhD thesis, National University of Ireland Maynooth.
17. Zhao, F.,Slade, R.C.T. and Varcoe, J.R., *Techniques for the study and development of microbial fuel cells:an electrochemical perspective.* Chem.Soc.Rev., 2009. **38**: p. 1926-1939.
18. Zhao, G.-C., et al., *Voltammetric studies of the interaction of methylene blue with DNA by means of β-cyclodextrin.* Analytica Chimica Acta, 1999. **394**(2): p. 337-344.
19. Greef, R., et al., *Electrocatalysis.* Instrumental Methods of Electrochemistry (Chichester, England: Ellis Horwood Limited, 1985), 1985.
20. Palys, B., A. Bokun, and J. Rogalski, *Poly-o-phenylenediamine as redox mediator for laccase.* Electrochimica Acta, 2007. **52**(24): p. 7075-7082.
21. Sazou, D., M. Kourouzidou, and E. Pavlidou, *Potentiodynamic and potentiostatic deposition of polyaniline on stainless steel: Electrochemical and structural studies for a potential application to corrosion control.* Electrochimica Acta, 2007. **52**(13): p. 4385-4397.

22. Dempsey, E., J. Wang, and M.R. Smyth, *Electropolymerised-o-phenylenediamine film as means of immobilising lactate oxidase for a L-lactate biosensor.* Talanta, 1993. **40**(3): p. 445-451.
23. Thévenot, D.R., et al., *Electrochemical biosensors: recommended definitions and classification.* Biosensors and Bioelectronics, 2001. **16**(1): p. 121-131.
24. Ramanavicius, A., A. Kausaite, and A. Ramanaviciene, *Potentiometric study of quinohemoprotein alcohol dehydrogenase immobilized on the carbon rod electrode.* Sensors and Actuators B: Chemical, 2006. **113**(1): p. 435-444.
25. Mano, N., F. Mao, and A. Heller, *A miniature biofuel cell operating in a physiological buffer.* Journal of the American Chemical Society, 2002. **124**(44): p. 12962-12963.

APPENDIX B

MICROFABRICATION TECHNOLOGY

Appendix B discusses the state-of-the-art microfabrication techniques and their application in the development of microfluidic platforms for enzymatic biofuel cells. Additionally, section B.2 focuses explicitly on the processing of the Chrome-on-Glass (COG) masks for the photolithographic deposition of gold and platinum electrodes as well as the fabrication of microfluidic channels.

B.1 Review on the fabrication processes.

Fabrication of microfluidic devices emerged, and is still reliant, on the technologies developed for the integrated circuit (IC) industry and as such, facilitates the manufacturing of a large volume of identical devices at a low cost and with feasible prospects for mass production. Basic IC technology incorporates a number of fabrication steps with deposition of thin films (by evaporation or sputtering), 3D structuring of the device (by wet and dry etching techniques) and back-end processing (dicing, wiring and packaging) being the prime manufacturing stages. Fabrication of microfluidic systems ascended from these techniques to ultimately develop as an independent research field. Depending on the applications, various materials can be considered for the fabrication of the micro-scale devices, primarily silicon, glass and plastic. At the early stage of development, the majority of microfluidic devices were fabricated in silicon, since the micromaching in Si was the leading technology at the time. Relatively high material and processing costs as well as poor yield rate (fewer microfluidic to electronic devices can be placed on a silicon wafer), made silicon too expensive to be considered as a viable and sustainable substrate for disposable miniature systems. Since mid-90s, microfabrication technology has been continuously moving towards polymer materials as more economical alternatives whose

manufacturing is time-efficient, cost-effective and does not require intense labor contributions.

Among a wide number of available plastics, three types of polymeric substrates have been frequently employed in device microfabrication nowadays [1]:

- photodefinable polymers such as SU-8, widely employed in microelectronics;
- thermoplastic materials e.g. poly-methylmethacrylate (PMMA) and cyclic olefin copolymers (COC), due to their unique optical properties, high degree of mouldability and low water intake;
- elastomers among which the most popular is poly-dimethylsiloxane (PDMS);

PDMS, belonging to a group of polymeric organosilicons, is a viscoelastic material with low chemical reactivity and a non-toxic nature. It possesses a unique flexural and dielectric strength, high gas permeability and compressibility as well as usability over a wide range of temperatures. Furthermore PDMS is biocompatible and can be applied together with enzymes or microbial cells, without the risk of losing their activities. As an optically transparent material, it is very suitable for the prototyping of microfluidic devices and academic use.

A) Generic microfabrication techniques for microfluidic chip production.

There are four basic microtechniques originally applied for microelectronics and MEMS applications, which have been frequently employed in the fabrication of microfluidic devices for various purposes [2].

1. Photolithography.

Photolithography is a derivative of lithography, a technique extensively used for patterning of microscale structures in the microelectronics industry [3]. The method uses a photosensitive emulsion layer known as a *resist*, which allows the transfer of desired features from a transparent mask onto the given substrate. The mask can be an either

transparent glass plate with metal patterns on its surface or a low-cost, disposable thin film of plastic produced by a high-resolution imagesetter. A typical photolithographic process consists of three steps:

- *Positioning*: Alignment of the resist pre-coated substrate and the mask containing the transferrable features including the adjustment of the optimal position and distance;
- *Exposure*: Transfer of the patterns to the photoresist layer via exposure to UV or X-ray;
- *Development*: Depending on the origin of the resist, pattern development is obtained by dissolution (for negative resists) or etching (for positive resists) in an appropriate developer solutions.

Thick resist coatings, which are employed in microfluidic devices as functional layers or as templates for polymer moulding, can be achieved by repetitive spin-coating steps or by using viscous resist at a slower spinning velocity.

2. Additive Techniques.

a) Chemical Vapour Deposition (CVD).

CVD is a technique employed to coat substrates with films of solid material generated as a result of a reaction between gaseous components [3] taking place on heated substrate surfaces in specially designated reaction chambers. While certain desirable compounds adsorb onto the substrate, remaining gaseous products leave the chamber without any interference with the substrate. Depending on the conditions under which the reaction occurs, three types of CVD processing can be distinguished:

- Atmospheric Pressure Chemical Vapor Deposition (APCVD);
- Low-pressure Chemical Vapor Deposition (LPCVD);
- Plasma-enhanced Chemical Vapor Deposition (PECVD).

Both APCVD and LPCVD require elevated temperatures, which makes them suitable only for metals with high eutectic temperatures with silicon e.g. tungsten. For the

PECVD, lower temperatures can be applied since the energy derives partially from plasma.

b) Thermal oxidation.

Thermal oxidation is the simplest method of depositing silicon dioxide layer onto a silicon substrate. In Si-based microfluidic devices, thermal oxidation is used primarily in order to adjust the width of the channel and the size of filter pores if applicable [3]. Two main type of oxidation exist, dry and wet, depending on the nature of the reagent used. While the former relies on pure oxygen reacting with silicon in high temperatures and generating silicon dioxide, in wet oxidation, silicon is subjected to a water vapor producing dioxide as the product.

c) Spin Coating.

Spin coating is considered to be one of the simplest and most efficient methods of casting the substrates with films of controlled thickness. The technique is predominantly employed in the deposition of pre-polymers and protective resist layers for photolithography. In this method, the coating material is dissolved in suitable organic solvent and applied on the substrate surface, prior to the deposition step. The sample is then spun at an elevated speed for a certain period of time, generating relatively planar films of precise thickness. While most of the solvent dissipates upon spin-coating, a certain amount of solvent remains after the spinning process and can be evaporated by baking the sample at high temperatures [3].

3. Subtractive Techniques.

a) Wet Etching.

Refers to an etching process of solid materials in chemical solutions, whereby the substrate is either immersed in the reaction bath or sprayed with the applicable etchant [3]. The technique is highly selective and repeatable, with the etch rate being controlled by the concentration of the active component and yielding relatively planar imprinted surfaces. The performance of wet etching is reliant on the dynamics of the system and is dependent on the stirring rate as the reaction products can interfere with the etchants and the surface of the substrate. Chemical etching is often employed to deliberately remove thin layers of

the substrate or film coatings. Tab. B.1 illustrates examples of chemical reagents used in thin film etching of functional materials.

Tab. B.1. Sample wet etchants for thin films of functional materials.

Material	Chemical etchants	Selective to:
Si	HF, HNO_3, CH_3COOH	SiO_2
Si	KOH	SiO_2
SiO_2	NH_4, HF	Si
SiO_2	HF, HNO_3, H_2O	Si
SiO_2	H_3PO_4, HNO_3, H_2O	Si
Si_3N_4	H_3PO_4	SiO_2

b) Dry Etching.

- ***Chemical Dry Etching (CDE).***

The principle of Chemical Dry Etching is the use of collisional interactions between gaseous reagents to strip off atomic layers from the material surface under investigation. It is a technique comparable in its selectivity to wet etching with an extensive practical applications in wafers cleaning [3]. Tab. B.2 lists examples of dry etchants commonly employed in microfabrication in functional materials.

- ***Physical Dry Etching (PDE).***

Unlike CDE, Physical Dry Etching utilizes the kinetic energy derived from electrons, photons or beams of ions to attack the surface of the sample. The released material is subsequently removed due to the high energy of the beam. Although PDE can be applied to diverse materials, several shortcomings have been associated with this technique. As the ions generated in the reaction chamber display poor selectivity, the method is typically non-specific and results in undifferentiated processing of the material.

Slow rates of etching and trench effects of ions reflected from the sample surface pose additional limitations of the PDE.

Tab. B.2. Sample gaseous etchants for thin films of functional materials.

Material	Gaseous etchants	Selective to:
Si	BCl_3/Cl_2, BCl_3/CF4, BCl_3/CHF_3, Cl_2/CF_4, Cl_2/He, Cl_2/CHF_4, HBr, HBr/Cl_2/He/O_2, HBr/SiF_4/NF_3/HCl/CF_4	SiO_2
SiO_2	CF_4/H_2, C_2F_6, C_3F_8, CHF_3,CHF_3/O_2, CHF_3/CF_4	Si(Al)
Si_3N_4	CF_4/H_2, C_2H_6, CHF_3, CF_4/CHF_3/He	Si(SiO_2)
Al	BCl_3, BCl_3/Cl_2, BCl_3/Cl_3/He, $BCl_3/Cl_2/CHF_3$, HJ, HBr/Cl_2 etc.	SiO_2
Organics	O_2, O_2/CF_4, O_2/SF_6	_

4. Pattern Transfer Techniques.

a) Subtractive Transfer.

Subtractive transfer is a four step process used to transpose the features engraved in a mask onto a sample previously pre-coated with a layer of a functional material , such as an adhesive layer of titanium [3]. Following the initial varnish with the functional layer, the substrate is spin-coated with a photoresist (positive or negative) and a mask bearing the patterned structures is applied (dark mask for positive and clear for negative resist). The features are then selectively etched and the remaining photoresist is washed away in a suitable developer.

b) Additive Transfer.

- ***Lift-off technique.***

The most frequently employed additive technique is a *lift-off* method in which the functional material (e.g. Ti or Pt) is deposited directly on the post-baked patterned photoresist layer, pre-coating the substrate, Fig. B.1 a) – d). The resist is subsequently resolved with acetone and removed together with the overlying active material. The remaining functional layer forms the desired structure, Fig. B. 1 e). *Lift-off* is a technique which has an immense application in microfluidics, where direct wet etching process poses a risk of undesirable alteration of the properties of polymers and catalytic metals (e.g. Pt or Pd) [3].

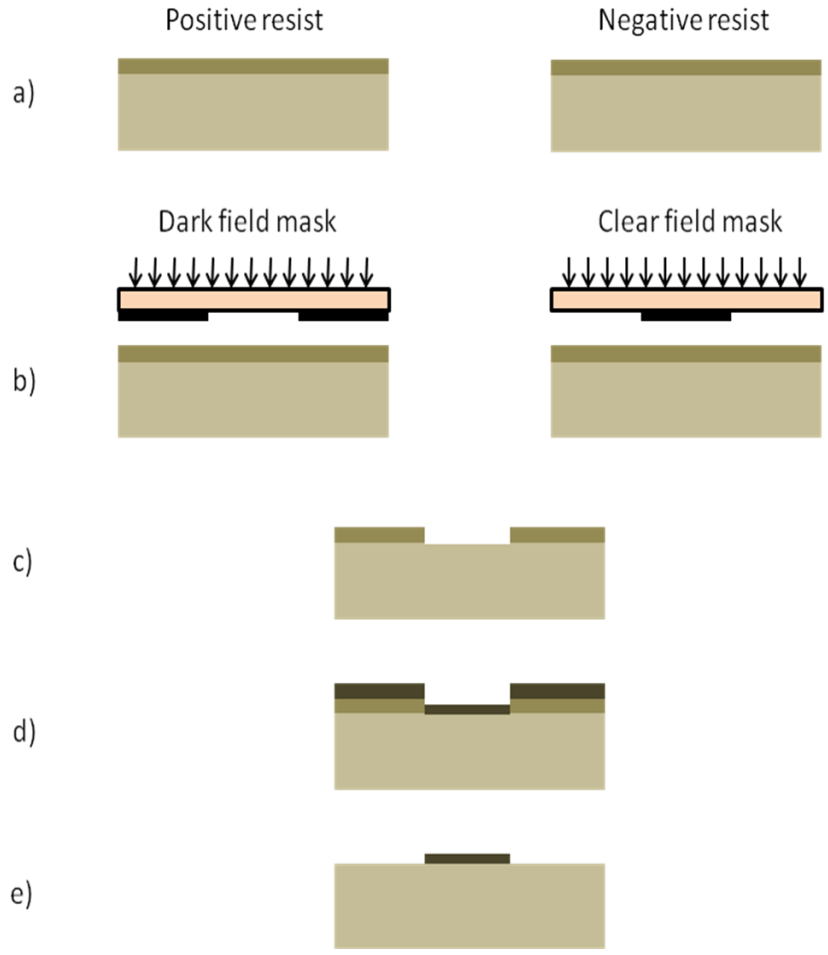


Fig. B.1. Pattern transfer with the lift-off technique: (a) spin-coating of a photoresist (negative or positive); (b) photolithography through a patterned mask (dark or clear) dark; (c) photoresist development; (d) deposition of the functional layer (e.g. Ti or Pt) and

(e) removal of the photoresist and the overlaying functional material, the transferred structure remains.

- ***Selective electroplating.***

In the selective electroplating a metal seed layer is initially deposited on the substrate, spun-coated and shielded with a thick layer of a photoresist, which is then subsequently electroplated with e.g. a metal as schematically illustrated. Electroplating is a process in which ions from the solution are deposited on a conductive substrate due to the applied electric current. The rate of plating is strongly reliant on the current density and a such the accurate control of the uniformity of the electrodeposited layer may be challenging [3].

In general, selective electroplating is used to obtain high aspect ratio structures for microfluidic devices with thick photoresist layers, which can be then employed as molds for the preparation of micro-sized features (e.g. microchannels, microvalves and micropumps). Fig. B.2 illustrates a microfabrication process including lithography and both, the additive and subtractive techniques.

Continuous expansion of the commercial and research applications results in a growing demand for alternative materials such as stainless steel or ceramics. Examples of less conventional fabrication techniques employing alternate substrates include microcutting, laser machining, microelectrodischarge machining or laminating.

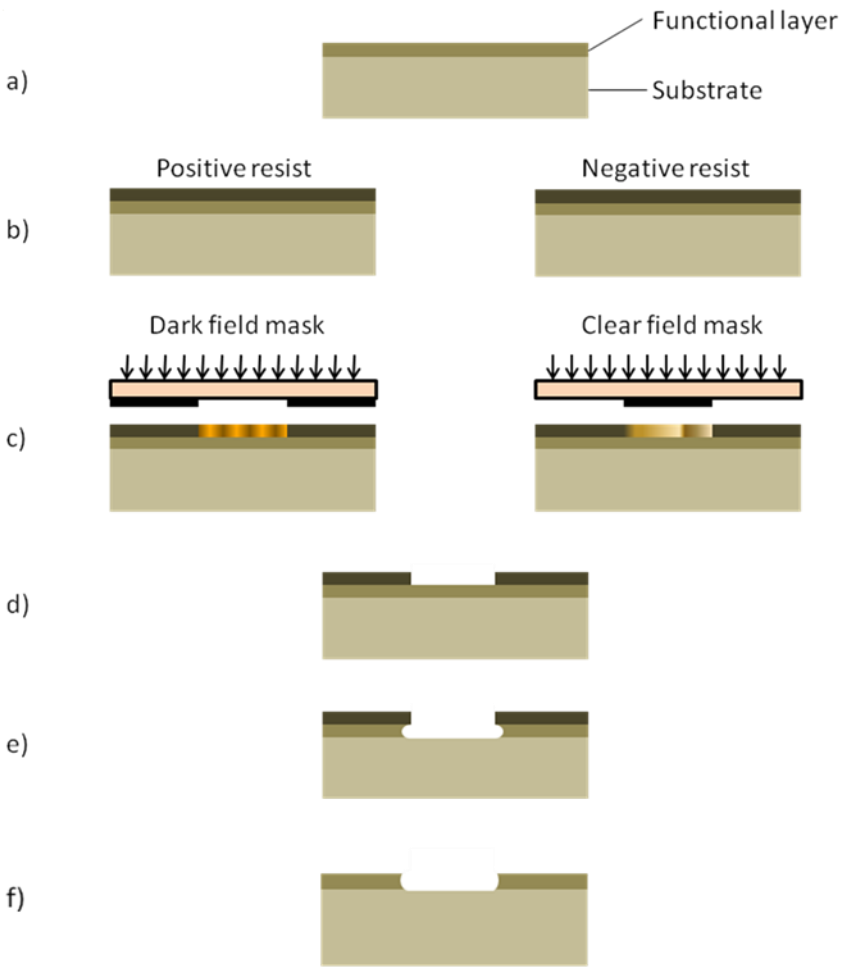


Fig. B.2. Pattern transfer with additive technique, lithography and subtractive technique: (a) deposition of the functional layer; (b) photoresist coating (positive or negative); (c) photolithography with a patterned mask (dark or clear field); (d) photoresist removal; (e) selective etching of the functional layer (photoresist is not attacked); and (f) structure is transferred to the functional material.

B) Polymer based micromachining techniques.

While conventional polymer based techniques employ an extensive number of methods (e.g. laser micromachining), the most frequently used is LIGA. LIGA, is a German acronym to ***L****ithographie,* ***G****alvanoformung,* ***A****bformung,* and is a fabrication technology which relies on thick resist photolithography, electroplating and micromolding processes to produce high-aspect-ratio microstructures. X-Ray LIGA and UV LIGA are two main fabrication strategies derived from the mainstream technology for respective

processing of features with high and low aspect ratios. Despite the existing differences in the machining protocols, the structural substrate has to be a polymer [3].

The growing number of alternative micromachining techniques for high output polymeric microstructures, includes several fabrication strategies however only three are within the scope of this Ph.D. thesis and hence will be discussed herein: thick resist lithography, soft lithography and micromolding.

1. Thick resist lithography.

a) Polymethylmethacrylate (PMMA) Resist.

Polymethylmethacrylate commonly known as *Plexiglas,* was initially used as a resist material in LIGA techniques [4]. Nowadays is has been extensively employed in the fabrication of microfluidic devices for various biochemical and electrochemical applications. It can be applied on a substrate by a number of methods, such as multiple spin coating, simple casting or through plasma condensation [5]. Since multilayer coating of PMMA is often associated with high interfacial stress, in some instances it may lead to the introduction of cracks in the resist layer. In order to avoid his phenomena, a prefabricated PMMA sheet bonded to the substrate [6] or polymerization in situ with a casting resin [7] are frequently employed instead. As a monomer, methyl methacrylate has been regularly used as an adhesive for bonding processes [8].

Structuring of PMMA in the LIGA technology, requires a collimated X-ray source with a specified range of wavelengths (0.2 nm - 2 nm), available only in synchrotron facilities, which is one of the prime shortcomings of the method. Additionally, it has been demonstrated that this type of electromagnetic radiation irreversibly alters the properties of PMMA in the exposed area, which is chemically etched during the process. Furthermore, in order to obtain high resolution of patterning, a suitable beryllium or titanium mask needs to be applied on the substrate, further increasing the fabrication cost. In general, the thicker the mask the higher the applied X-ray energy, which yields an increased aspect ratio of produced PMMA microstructures [3]. Limited access to the synchrotron facilities and additional costs associated with LIGA micromachining in PMMA, in particular, led to increased consideration of alternative thick resist films, such as SU-8.

b) SU-8 Resist.

SU-8 is a cost-effective alternative to a PMMA resist. Developed originally by IBM [9, 10] and soon adapted for MEMS applications, it is an EPON SU-8 epoxy based negative photoresist for the near UV-wavelengths (365 nm to 436 nm).The material is commercially available with a variety of viscosities, an essential factor controlling the thickness of the film during the spin coating of the substrate. As an epoxy (composed of O bridged atoms) resin, during the curing process SU-8 is converted into a thermoset form of a three-dimensional structural network. In order to promote the curing upon UV exposure, the typical SU-8 consists of three primary components: the resin (e.g. EPON SU-8), the photoinitiator, such as triarylium-sulfonium salts and the mutual solvent (e.g. Γ-butyrolactone).

A typical SU-8 process is composed of a multi-step protocol consisting of:

- *Spin coating* – The structural height and the film thickness is reliant on the viscosity of the used photoresist, with thicker resist films being favored by lower spin velocities or higher viscosities.

- *Soft baking* – Used to remove the solvent following the spin coating step, either on a level hot plate or in a convection oven [11, 12].

- *Exposure* – SU-8 can be exposed using mercury lamp with a near - UV wavelength with the thickness of the film co-related with the exposure dose. Since the optical absorption of SU-8 increases significantly below 350 nm, longer UV wavelengths are typically recommended.

- *Post exposure baking* – Used for a selective cross-linking of the previously exposed SU-8 area. In order to prevent cracking effects associated with high cross-linking stress, a two-step sequence and a slow cooling procedure are usually implemented [13, 14].

- *Resist development* – Immersion or spray processes, utilizing solvent-based developers, such as diacetone alcohol, are typically used to remove non-polymerized areas of SU-8.

- *Hard baking* – Applied optionally if additional baking at elevated temperatures (150ºC - 200ºC) is required [15]. At very high temperatures hard baking can cause increased thermal stress and lead to structural cracks which need to be accounted for.

- *Resist removal* – It is considered as the most difficult step due to high degree of polymerized SU-8 cross-linking. A number of methods is available however the removal of SU-8 is typically obtained by an acidic etch, RIE (reactive ion etch) or laser ablation [16].

Due to its labor-efficient processing and rather attractive mechanical properties, SU-8 has been widely used as the prime material for the fabrication of microfluidic devices. Despite a number of possible microfabrication techniques, the simplest strategy of forming a microchannel in the SU-8 layer is to use it as a spacer. In this method, both top and bottom walls of the channel are originally made of materials other than SU-8, primarily from silicon or glass wafer. A metal seed layer is initially applied on the wafer; a photoresist is subsequently spun-coated and structured on top. The microchannel is later etched in SU-8 film via oxygen plasma treatment through an aluminum mask. The last step involves assembling the etched structure with a glass plate [17]. Three-dimensional microchannel structures can also be patterned using conventional photolithography techniques, relying on a multilayer exposure (Fig. B.3). In the lithographic processing SU-8 is spin-coated and exposed on a silicon substrate, onto which a secondary resist layer is later applied. In order to avoid double exposure, the mask for the ancillary SU-8 film needs to completely cover all the unexposed areas of the first layer. Following the exposure, the double resist is developed to ultimately form a channel structure. In the next fabrication steps a fully developed microfluidic feature is formed due to cross-linking effect between the exposed SU-8 layer and a glass plate coated with a thin unexposed photoresist sheet [18].

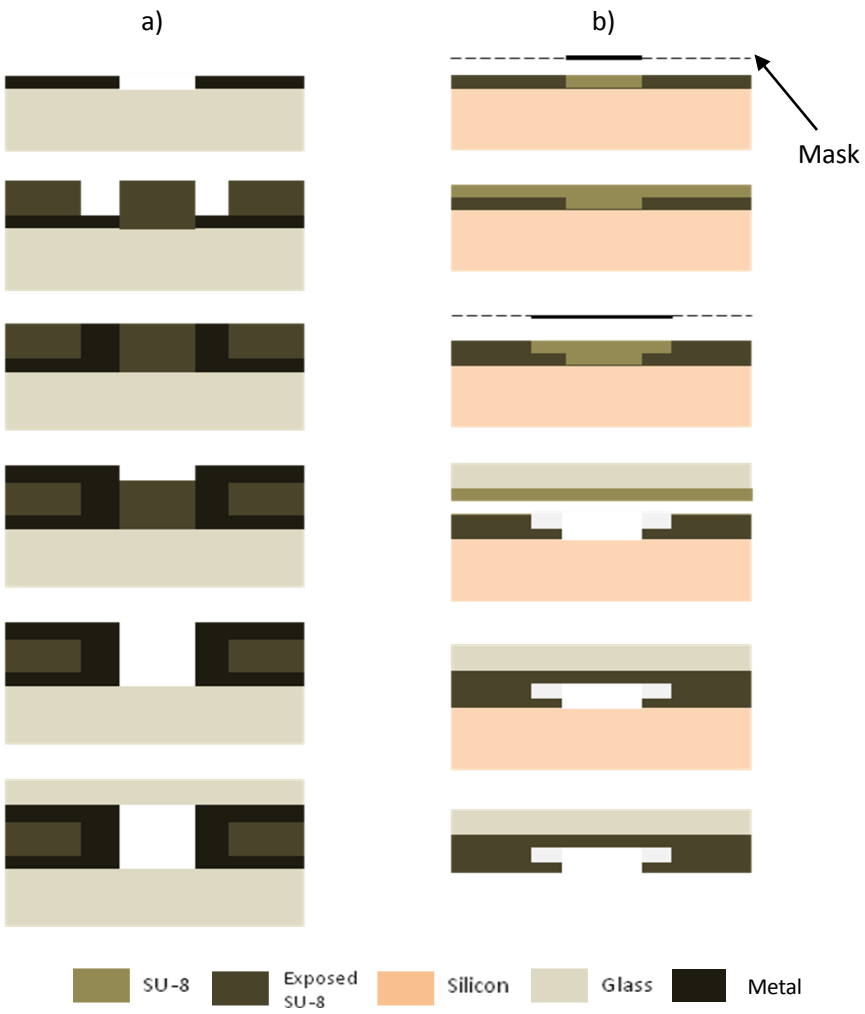


Fig. B.3. Fabrication of microchannels in SU-8: (a) single layer with electroplating (b) multiple layers.

Although standard micromachining in SU-8 results in good resolution of features of 2 mm high with an aspect ratio greater than 20 and is based on a low-cost UV-exposure, the height and the aspect ratio of fabricated structures cannot compete with those of LIGA-X-Ray processing in PMMA.

2. Soft lithography.

Unlike thick resist lithography, its soft equivalent is not an optical transfer technique and it requires a 'soft' elastomeric stamp to transfer the relief features patterned on its surface onto the substrate via *microcontact printing* or *replica micromolding* [19]. A

variety of elastomers can be used for the fabrication of the stamp but the most common for this purpose is polydimethylsiloxane (PDMS). The motivation behind the extensive use of PDMS relies in its unique physicochemical properties associated with its interesting, mixed chemical structure. As an example of an organosilicon, PDMS is composed of an inorganic siloxane backbone with organic methyl groups attached to it as shown in Fig. B.4.

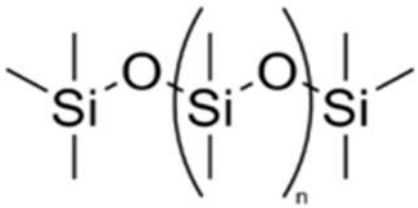


Fig. B.4.Chemical structure of PDMS.

Polydimethylsiloxane is an economical, non-toxic and optically transparent polymer and as such is an ideal candidate for the fabrication of low cost microfluidic components and comprehensive lab-on chip miniature devices. Due to its low interfacial free energy, PDMS exhibits chemical inertness and does not stick nor react with the substrate it has been applied to. In addition, it is resistant to humidity and elevated temperatures and as an elastomer it can readily attach to nonplanar surfaces. Furthermore, due to its mechanical durability and the susceptibility to UV exposure, PDMS can be successfully applied in soft lithography techniques.

Some of the major shortcomings of PDMS include volume change (e.g. shrinking effect) and elastic deformations upon solvents swelling and curing. The latter influences the aspect ratio of the designed polydimethylsiloxane structure, causing either pairing effect (when high aspect ratio) or sagging of the noncontact regions (when low aspect ratio), which in consequence block further processing steps of the soft lithography. Ideally, the optimal PDMS structures are obtained when mixing prepolymer and the curing agent in the aspect ratio ranging between 0.2 and 2 [19].

a) Fabrication of microfluidic devices in PDMS.

The stamp for the soft lithography patterning in PDMS can be fabricated from various different substrates e.g. glass, silicon or SU-8 using traditional micromachining technologies. Once manufactured and chemically clean, most masters do not require further treatment with an exception of silicon, which needs to be initially silanised by exposure to $CF_3\,(CF_2)_6\,(CH_2)\,SiCl_3$ vapors [20]. The siloxane prepolymer is applied onto the master bearing the relief of desired patterns and cured at elevated temperatures (Fig.B.4 A). Once set, the polymer layer can be easily peeled off and attached to a substrate plate (e.g. glass) following its surface activation in e.g. oxygen plasma. In a similar approach, various 3D structured PDMS layers can be laminated together to create a final polymer product.

b) Microcontact printing with a PDMS stamp.

The PDMS features can be used as stamps themselves in order to transfer the relief patterns of self-assembled monolayers (SAMs) in a contact-based technique called *microcontact printing* (Fig. B.4 B). In this method, the PDMS substrate is immersed in the $Y\,(CH_2)_n\,X$ SAM precursor solution, where X and Y are respective head and anchoring groups, and pressed against the surface of the ultimate structural material, transferring the SAM pattern. The self-assembly monolayer can later act as a resist coating protecting the underlying material during imprinting in a chemical etching step and can be applied as a mask for the Reactive Ion Etching (RIE). Due to its small thicknesses, SAM deposits are, in general, very fragile and can be easily damaged by ion bombardment.

Surface properties of SAM, determined by the X group type of the ligand, allow these structures to be applied as templates for selective and controlled deposition of other materials, such as metals and ceramics.

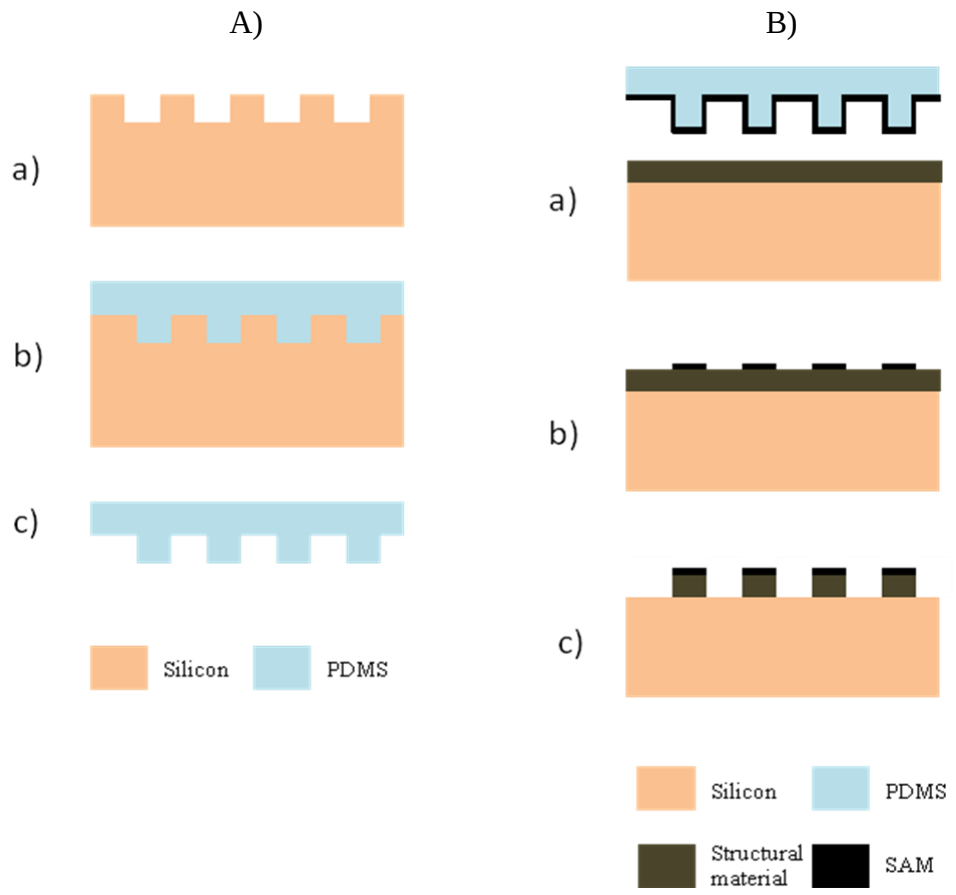


Fig. B.4 (A) Fabrication of a PDMS stamp: a) DRIE of silicon master, b) application of liquid PDMS, c) stamp release; (B) Microcontact printing with PDMS stamp: a) immersion of the PDMS master in the ligand solution e.g. SAM; b) transfer of the features; c) etching of the underlying structural material.

c) Micromolding with a PDMS Replica Master.

As proposed by Xia and co-workers [19], the general field of micromolding with a PDMS replica master can be subdivided into four main categories: *replica molding, microtransfer molding, micromolding in capillaries and solvent-assisted micromolding* out of which three, most relevant to this Ph.D. work has been briefly discussed below.

Replica molding allows structures smaller than 10 nm to be produced using the PDMS stamp as a replica for the suitable prepolymer. The final pattern is obtained by thermal curing of the assembly or upon UV exposure for a certain period of time (Fig. B.5).

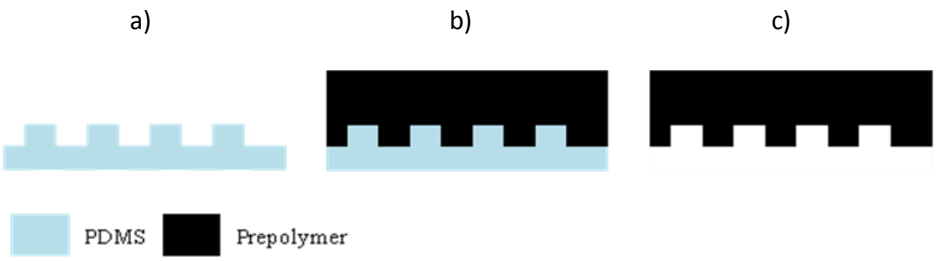


Fig. B.5. Schematic of a replica molding with a PDMS master. Curing of the PDMS and prepolymer assembly (b) results in a pattern transfer into the substrate (c).

In *microtransfer molding* liquid prepolymer is applied on the elastomer stamp filling the gaps within the PDMS structure. Following the removal of the excess material, a planar substrate (e.g. glass or a polymer slide) is then placed on top and the assembly is cured thermally or by exposure to the UV light. The PDMS master is later peeled off revealing the desired pattern on the surface of the substrate (Fig. B.6). The key disadvantage of this technique is that one cannot completely remove the excess prepolymer and thus a thin layer the order of 100 nm remains on top of the structural polymer and the master and needs to be etched away in the oxygen plasma prior to any further microfabrication steps [19].

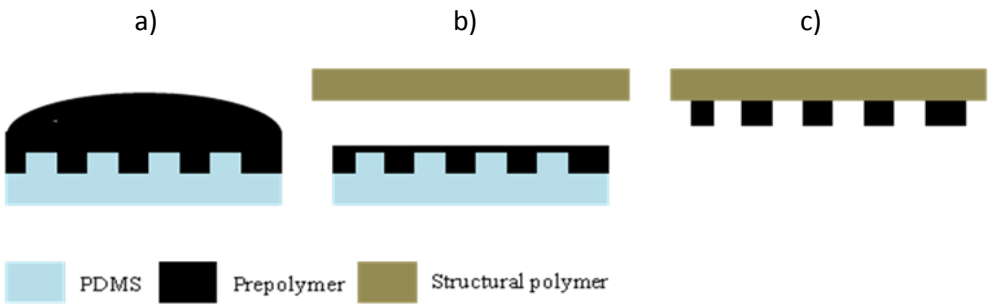


Fig. B.6. Graphical representation of the microtransfer molding technique using a PDMS master comprised of prepolymer casting (a), removal of the excess material and application of the planar substrate (b), and structure transfer following thermal or UV curing (c).

Solvent-assisted micromolding is a modified version of the classical embossing approach, whereby instead of heat and pressure, the patterning relies on the application of a suitable solvent at the interface between the PDMS stamp and the structural polymer. The solvent wets the master and softens the underlying polymeric substrate living the PDMS intact. When the elastomer is pressed against the structural polymer it dissolves it and fills the gaps in between the PDMS structure. The final pattern is obtained after the removal of PDMS relief and solvent evaporation (Fig. B.7).

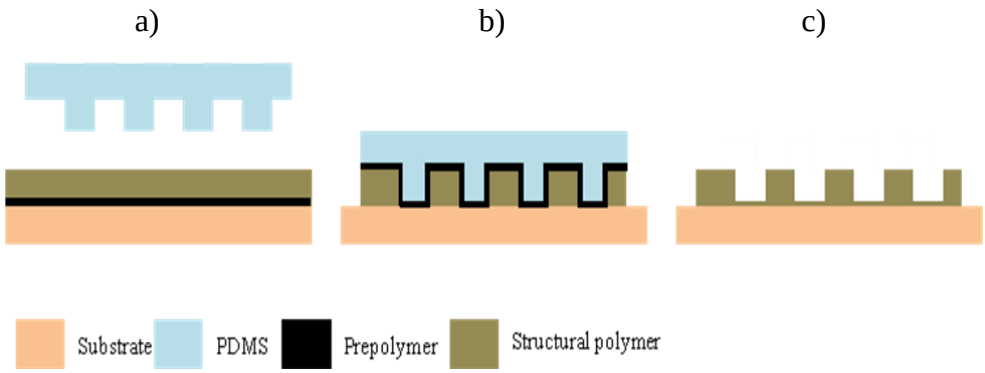


Fig. B.7. Schematic of a solvent-assisted micro molding with PDMS stamp including substrate coating with structural polymer and a solvent layer (a), assembly of the PDMS stamp and the substrate (b), pattern release following dissipation and solvent evaporation (c).

d) Microchannel fabrication using Soft Lithography technique.

Soft lithography using PDMS as a structural material has been extensively employed in the rapid prototyping of microfluidic devices for over two decades now [19, 21-23]. The widespread use of PDMS is primarily due to its easy micromachining and a number of suitable properties including low toxicity, high optical transparency from visible into the near UV wavelengths and chemical inertness.

Liquid PDMS for the channel molding is typically prepared by mixing the polymer base and the curing agent in a recommended 10:1 or 5:1weight ratio. The stamp is usually fabricated from SU-8 with defined inlet and outlet points, spun-coated onto a silicon wafer. The prepolymer mixture is poured into a solid master and let to self-level for

several minutes. The assembly is then thermally cured at temperatures ranging between 60-100°C for a defined period of time, following which the solidified PDMS can be easily peeled off and the access points introduced. Low-temperature oxygen plasma treatment activates the surface of the PDMS layer and enables its bonding to clean glass, silica or another surface activated PDMS substrate (Fig. B.8).

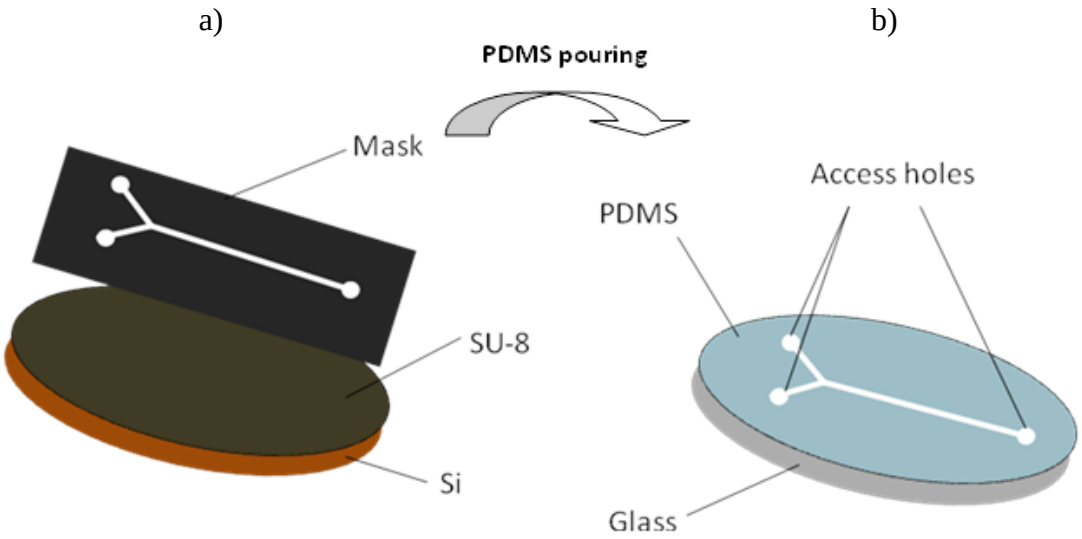


Fig. B.8. Summary of the fabrication of microchannels in a PDMS substrate via soft lithography. Spin-coating of a silicon wafer with a thin layer of SU-8, UV exposure through a patterned mask and SU-8 development (a), pouring of the liquid PDMS on the SU-8 mold, curing and surface activation prior to glass bonding (b).

Although plasma oxidation of the PDMS surface is essential in order to obtain permanent attachment (up to 5 bars of pressure) to a number of substrates (glass, silicon, PDMS), certain applications require reversible, watertight seals for detachable fluidic devices and hence the activation step is neglected. Furthermore, it has been suggested that plasma oxidation of the polymer substrate can be temporarily inhibited by methanol, which impedes instant bonding between multiple layers of PDMS following the exposure [24].

The vast majority of microfluidic fuel cells reported up to date have been fabricated on glass supports pre-coated with metal or carbon based electrodes and a PDMS cover carrying the microfluidic channel [25-28]. While, the conventional fabrication strategy is suitable for small-scale lab-based research, it is not applicable in large demand commercial markets, where a high degree of automation and low manufacturing costs are

the main prerequisite. In this light, cost effective, easy to fabricate and disposable plastic miniature devices seem to be an attractive alternative to the classical approach using glass or silicon substrates. In addition, replacing expensive patterning of noble metal electrodes with economically-friendly conducting materials such as indium tin oxide (used in the field of electrochemical and optical sensing) has a potential to significantly lower manufacturing expenses and the complexity of the existing microfluidic systems. Substituting the platinum cathode with an oxidant reducing enzyme-based biocathode, alongside a 'green' bioanode for the pollutant-free oxidation of the given fuel can ultimately remove the need for precious metal catalysts in the microfluidic environment. Such innovative designs of polymer microfluidic chips would help to overcome problems related with the diffusion layer thickness at the interface between anodic and cathodic compartments of the cell as well as the issues associated with the depletion of fuel in the microfluidic channel. Furthermore, miniaturization of the biofuel cells and their fabrication from economical polymer substrates would enable cost-efficient stacking of numerous devices in order to reduce the total volume occupied by the system and enhance the current and power outputs drawn from the cells.

B.2. Fabrication of the COG masks for the electrode and channel preparation.

A) COG masks for the electrode patterning.

In order to deposit gold and platinum on Zeonor substrate a detailed design of the electrode layouts had to be put in place. Electrode patterns were prepared in the Central Fabrication Facility of the Tyndall National Institute using *Mentor Graphics IC Station* software and the designs were sent to Compugraphics Intl. Ltd (Scotland) for the fabrication of Chrome-on-Glass (COG) photolithographic masks. Due to separate deposition steps for Au and Pt, two sets of master layouts had to be fabricated. Each mask contained five different electrode patterns. Fig. B.9 is a graphical representation of the designed COG masks.

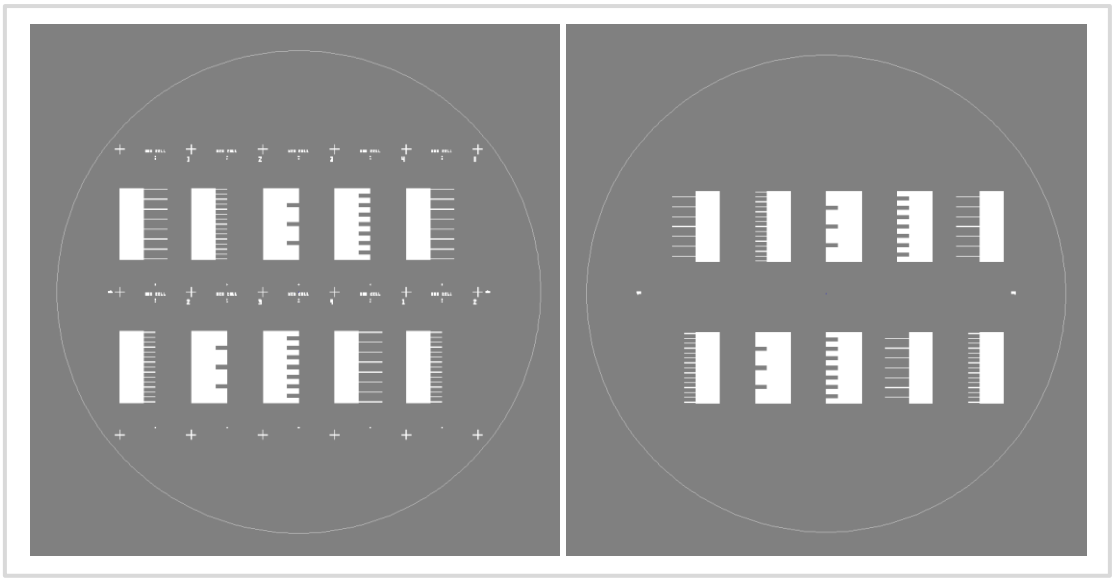


Fig. B.9. Designs of the electrode layouts for the fabrication of Chrome-on-Glass masks

Photomasks provide templates for semiconductor components, the universal element in almost all modern electronics. They are plates typically made from high quality quartz or glass, carrying precise and detailed images of integrated circuits. With the significant development in the area of bioelectroanalysis photomasks have gained increased interest as tools for fabrication of electrochemical devices and, as such, are frequently used for patterning of micro- and nano-features for lab-on-chip applications. Transcription of the pattern is carried out by shining a UV light through the photomask onto a thin wafer of the substrate (silicon, polymer etc.). The wafer acts as a foundation for the device manufacturing and is coated with a photo-sensitive material that reacts with the light shone through the mask. After the etch step and stripping off the resist a detailed layout of the miniature features (electrodes, channels etc.) is formed on the wafer.

Exact specifications of the photomask are determined by the customer requirements. Layout of the required patterns is sent to the company in a form of a technical drawing via email or a FTP server (GDSII, AutoCAD, MEBES, Gerber or CIF data formats are accepted). The design provides records about the features, polarity, mirroring and the mask title. Information is encoded in a specialized language operating the fabrication tools and ready-to-write data is sent back to the customer for a final quality check prior to manufacture. Once approved, the mask substrate is coated with thin layers of chrome and photoresist and exposed to laser tools which transfer the pattern onto the

resist. Following exposure the underlying chrome is chemically etched (wet etch) and the remaining photoresist removed (Fig. B.10). After fabrication the mask undergoes a series of visual and automatic inspections including die-to-die, die-to-mask and die-to-database checks.

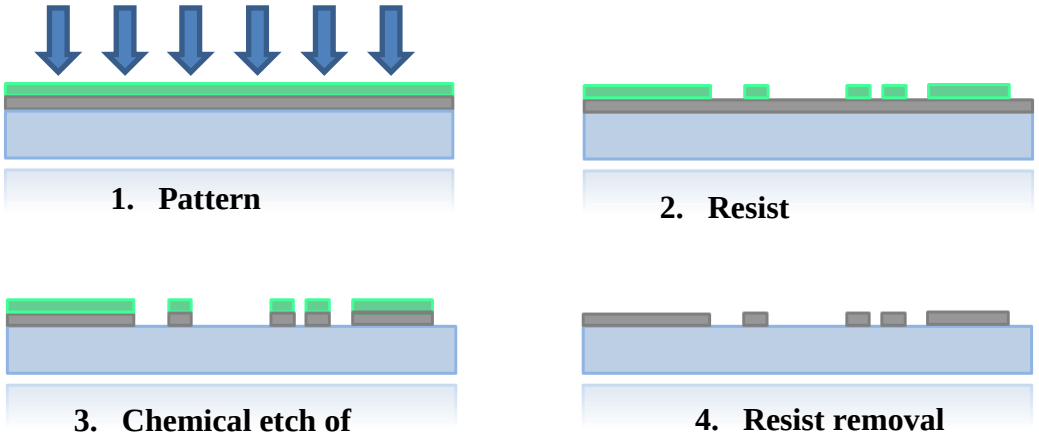


Fig. B.10. Diagram representing laser fabrication of the Chrome on Glass photomasks (Compugraphics Ltd, Scotland)

B) COG mask for the microfluidic channel layouts.

Chrome-on-Glass (COG) photomasks for the fabrication of the microfluidic channels have been designed at the Central Fabrication Facility of the Tyndall National Institute, using *Mentor Graphics IC Station* software, and manufactured by Compugraphics Intl. Ltd (Scotland). Fig. B.11. illustrates the schematic design of the mask alongside with the produced mask.

The fabrication process is based on a wet etching technique, in which a thin film of chrome is coated onto a glass substrate, following which a layer of positive photoresist is applied. After UV exposure, the resist is developed leaving behind the desired pattern of the channel, as illustrated in Fig. B.12.

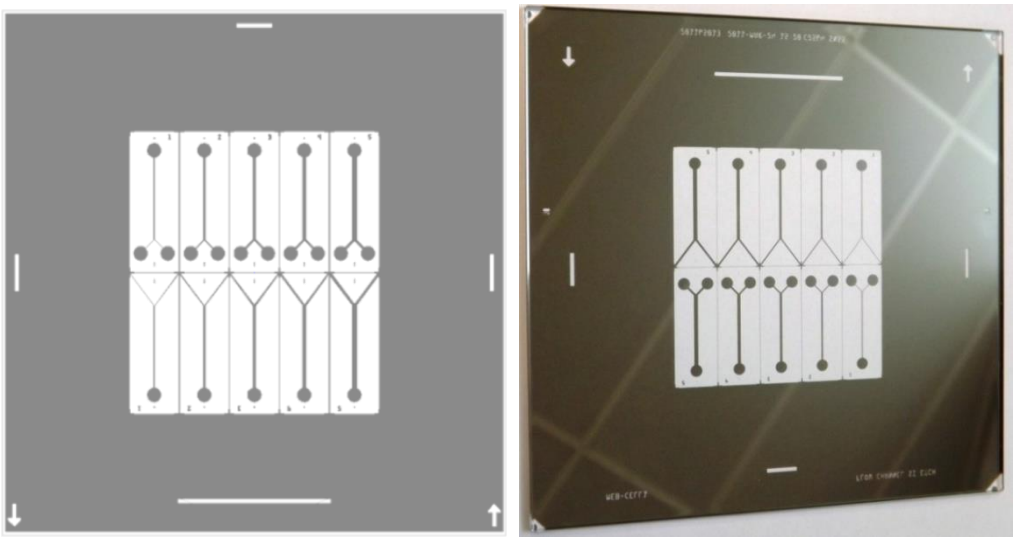


Fig. B.11 Images of the Chrome-on-Glass masks for the fabrication of channel layouts, technical drawings (left), fabricated mask (right).

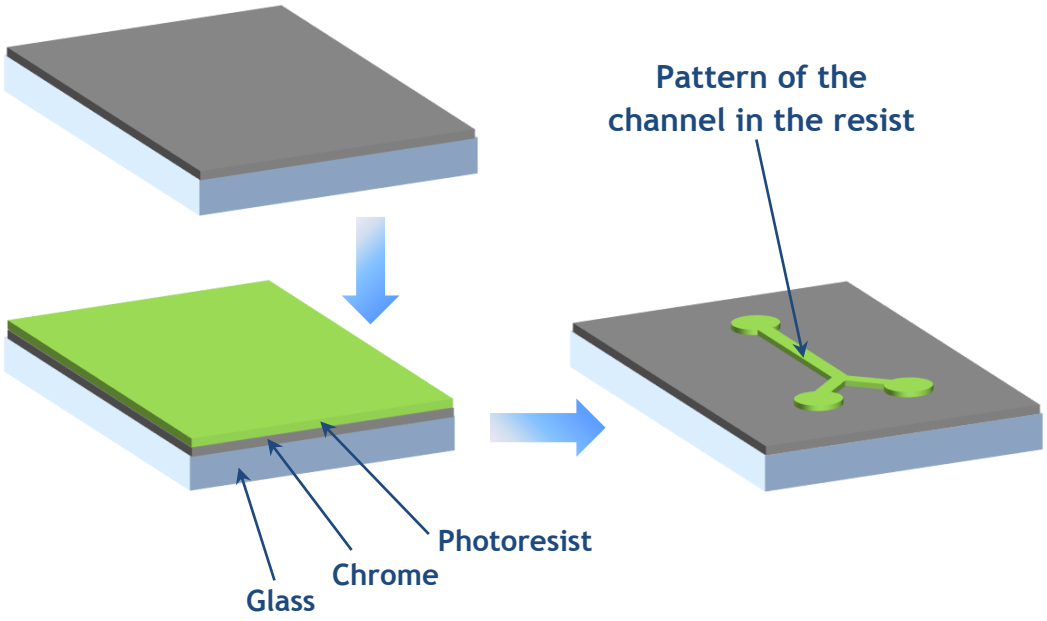


Fig. B.12. UV pattern exposure and photoresist development in the fabrication of COG masks.

Following resist development, the underlying chrome is etched away in a mixture of gases (dry etch) and the remaining photoresist is removed via acid treatment (Fig. B.13).

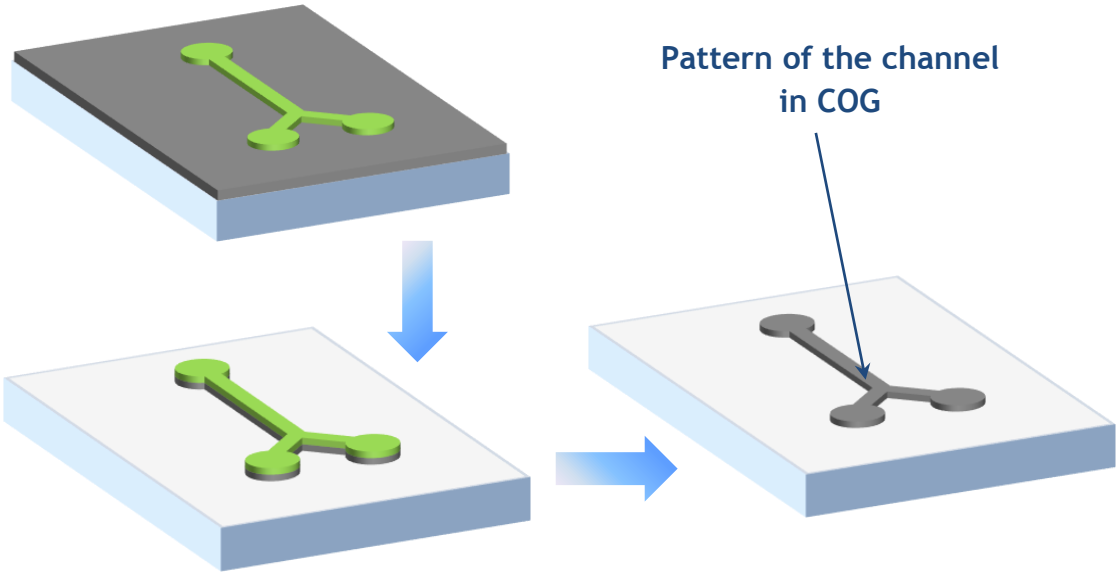


Fig. B.13. UV pattern exposure and photoresist development in the fabrication of COG masks.

B.3. Bibliography.

1. Madou, M.J., *Fundamentals of Microfabrication: The Science of Miniaturization. 2002*. CRC Press LLC, Boca Raton, FL
2. Whitesides, G.M., *The origins and the future of microfluidics*. Nature, 2006. **442**(7101): p. 368-373.
3. Nguyen, N.-T. and S.T. Wereley, *Fundamentals and applications of microfluidics* 2002. Artech House, Inc. MEMS Series
4. Becker, E., et al., *Fabrication of microstructures with high aspect ratios and great structural heights by synchrotron radiation lithography, galvanoforming, and plastic moulding (LIGA process).* Microelectronic engineering, 1986. **4**(1): p. 35-56.
5. Muller, R.S., et al., *Solid-State Sensor and Actuator Workshop Held at Hilton Head Island, South Carolina on June 6-9, 1988*, 1988, DTIC Document.
6. Ehrfeld, W., et al., *Progress in deep-etch synchrotron radiation lithography.* Journal of Vacuum Science & Technology B: Microelectronics and Nanometer Structures, 1988. **6**(1): p. 178-182.
7. Guckel, H., T.R. Christenson, and K. Skrobis, *Formation of microstructures using a preformed photoresist sheet*, 1995, Google Patents.
8. Chaudhuri, B., et al., *Photoresist application for the LIGA process.* Microsystem Technologies, 1998. **4**(4): p. 159-162.
9. Lee, K., et al., *Micromachining applications of a high resolution ultrathick photoresist.* Journal of Vacuum Science & Technology B: Microelectronics and Nanometer Structures, 1995. **13**(6): p. 3012-3016.
10. Shaw, J.M., et al., *Negative photoresists for optical lithography*. IBM Journal of Research and Development, 1997. **41**(1.2): p. 81-94.
11. Mata, A., A.J. Fleischman, and S. Roy, *Fabrication of multi-layer SU-8 microstructures.* Journal of Micromechanics and Microengineering, 2006. **16**(2): p. 276.
12. Ho, C.-H., et al., *Ultrathick SU-8 mold formation and removal, and its application to the fabrication of LIGA-like micromotors with embedded roots.* Sensors and Actuators A: Physical, 2002. **102**(1): p. 130-138.
13. Dykes, J.M., et al. *Creation of embedded structures in SU-8*. in *MOEMS-MEMS 2007 Micro and Nanofabrication*. 2007. International Society for Optics and Photonics.
14. Westwood, S.M., et al. *Thick SU-8 and PDMS three-dimensional enclosed channels for free-standing polymer microfluidic systems*. in *Electrical and Computer Engineering, 2007. CCECE 2007. Canadian Conference on*. 2007. IEEE.
15. Chang, H.-K. and Y.-K. Kim, *UV-LIGA process for high aspect ratio structure using stress barrier and C-shaped etch hole.* Sensors and Actuators A: Physical, 2000. **84**(3): p. 342-350.
16. Ghantasala, M.K., et al., *Patterning, electroplating and removal of SU-8 moulds by excimer laser micromachining.* Journal of Micromechanics and Microengineering, 2001. **11**(2): p. 133.
17. Ayliffe, H.E., A.B. Frazier, and R. Rabbitt, *Electric impedance spectroscopy using microchannels with integrated metal electrodes.* Microelectromechanical Systems, Journal of, 1999. **8**(1): p. 50-57.

18. Jackman, R.J., et al., *Microfluidic systems with on-line UV detection fabricated in photodefinable epoxy.* Journal of Micromechanics and Microengineering, 2001. **11**(3): p. 263.
19. Xia, Y. and G.M. Whitesides, *Soft lithography.* Annual Review of Materials Science, 1998. **28**(1): p. 153-184.
20. Man, P., D. Jones, and C. Mastrangelo. *Microfluidic plastic capillaries on silicon substrates: a new inexpensive technology for bioanalysis chips*. in *Micro Electro Mechanical Systems, 1997. MEMS'97, Proceedings, IEEE., Tenth Annual International Workshop on*. 1997. IEEE.
21. Kim, P., et al., *Soft lithography for microfluidics: a review.* Biochip Journal, 2008. **2**(1):p. 1-11.
22. Qin, D., Y. Xia, and G.M. Whitesides, *Soft lithography for micro-and nanoscale patterning.* Nature Protocols, 2010. **5**(3): p. 491-502.
23. Devaraju, N.S.G.K. and M.A. Unger, *Pressure driven digital logic in PDMS based microfluidic devices fabricated by multilayer soft lithography.* Lab on a Chip, 2012. **12**(22): p. 4809-4815.
24. Jo, B.-H., et al., *Three-dimensional micro-channel fabrication in polydimethylsiloxane (PDMS) elastomer.* Microelectromechanical Systems, Journal of, 2000. **9**(1): p. 76-81.
25. Moore, C.M., S.D. Minteer, and R.S. Martin, *Microchip-based ethanol/oxygen biofuel cell.* Lab on a Chip, 2005. **5**(2): p. 218-225.
26. Togo, M., et al., *An enzyme-based microfluidic biofuel cell using vitamin K_3-mediated glucose oxidation.* Electrochimica Acta, 2007. **52**(14): p. 4669-4674.
27. Zebda, A., et al., *Enzyme-Based Microfluidic Biofuel Cell to Generate Micropower.* Enzyme, 2011. **2**: p. O2.
28. Beneyton, T., et al., *Membraneless glucose/O_2 microfluidic biofuel cells using covalently bound enzymes.* Chemical Communications, 2013. **49**(11): p. 1094-1096.

APPENDIX C

MATHEMATICA CODE

Define Constants

```
Ds = 2.7 × 10^-5;
De = 4 × 10^-4;
Dp = 2.7 × 10^-5;
Dem = 0;
kespos =  10 000;
kesneg =  400;
kcat = 12 500;
kemneg = 8.4 × 10^4;
kempos =  2.1 × 10^6;
km = 1250;(*1150*)
ke = 2.075 × 10^6;
E0 = 5 × 10^-3;
M0 = 5 × 10^-3;
S0 = 150 × 10^-3;
time = 1.5;
l = 5 × 10^-3;
Kem = (kemneg + km)/kempos;
Kes = (kesneg + kcat)/kespos;
Ecell = 0.6;
Eformal = 3.33;
Const = 0.0591;
```

Generate space-time profiles of the various species

```
rateeqns = {(*These are the rate equations,
   there 8 of them altogether. Each species is a function of x and t *)
   D[S[x, t], {t, 1}] == Ds D[S[x, t], {x, 2}] + kesneg ES[x, t] - kespos S[x, t] Eox[x, t],
   D[Eox[x, t], {t, 1}] ==
    De D[Eox[x, t], {x, 2}] + kesneg ES[x, t] - kespos S[x, t] Eox[x, t] + km EM[x, t],
   D[ES[x, t], {t, 1}] == Dem D[ES[x, t], {x, 2}] -
     (kesneg + kcat) ES[x, t] + kespos S[x, t] Eox[x, t],
   D[P[x, t], {t, 1}] == Dp D[P[x, t], {x, 2}] + kcat ES[x, t],
   D[Ered[x, t], {t, 1}] == De D[Ered[x, t], {x, 2}] +
     kcat ES[x, t] - kempos Ered[x, t] Mox[x, t] + kemneg EM[x, t],
   D[Mox[x, t], {t, 1}] == De D[Mox[x, t], {x, 2}] + kemneg EM[x, t] -
     kempos Ered[x, t] Mox[x, t],
   D[EM[x, t], {t, 1}] == Dem D[EM[x, t], {x, 2}] - (kemneg + km) EM[x, t] +
```

```
      kempos Ered[x, t] Mox[x, t],
    D[Mred[x, t], {t, 1}] == De D[Mred[x, t], {x, 2}] + km EM[x, t]};

initialcons = {(*These are the initial and boundary conditions. For each species
     there are two boundary conditions and one initial condition. The *)
    S[0, t] == S0, (D[S[x, t], {x, 1}] /. x → l) == 0, S[x, 0] == S0,

    (D[Ered[x, t], {x, 1}] /. x → 0) == 0,
    (D[Ered[x, t], {x, 1}] /. x → l) == 0, Ered[x, 0] == 0,

    (D[Mred[x, t], {x, 1}] /. x → 0) == 0,
    Mred[l, t] == M0 / (1 + e^((Ecell-Eformal)/Const)), Mred[x, 0] == M0 / (1 + e^((Ecell-Eformal)/Const)),

    (*(D[EM[x,t],{x,1}]/.x→0)==0,(D[EM[x,t],{x,1}]/.x→l)==0*)EM[x, 0] == 0,

    (*(D[ES[x,t],{x,1}]/.x→0)==0,(D[ES[x,t],{x,1}]/.x→l)==0*)ES[x, 0] == 0,

    (D[Eox[x, t], {x, 1}] /. x → 0) == 0,
    (D[Eox[x, t], {x, 1}] /. x → l) == 0, Eox[x, 0] == E0,

    (D[Mox[x, t], {x, 1}] /. x → 0) == 0,
    Mox[l, t] == M0 / (1 + e^((Eformal-Ecell)/Const)), Mox[x, 0] == M0 / (1 + e^((Eformal-Ecell)/Const)),

    (D[P[x, t], {x, 1}] /. x → 0) == 50 P[0, t],
    P[x, 0] == 0, (D[P[x, t], {x, 1}] /. x → l) == 0};
fulleqns = Flatten[Join[rateeqns, initialcons]];
solsdf = NDSolve[fulleqns, {S, Eox, ES, P, Ered, Mox, EM, Mred},
    {x, 0, l}, {t, 0, time}, MaxSteps → ∞, MaxStepSize → 10^-2];
p1 = Plot3D[S[x, t] /. solsdf[[1]], {t, 0, time}, {x, 0, l},
    PlotLabel → "S[t]", PlotRange → All];
p2 = Plot3D[Ered[x, t] /. solsdf[[1]], {t, 0, time}, {x, 0, l},
    PlotLabel → "Ered[t]", PlotRange → All];
p3 = Plot3D[Eox[x, t] /. solsdf[[1]], {t, 0, time}, {x, 0, l},
    PlotLabel → "Eox[t]", PlotRange → All];
p4 = Plot3D[Mox[x, t] /. solsdf[[1]], {t, 0, time}, {x, 0, l},
    PlotLabel → "Mox[t]", PlotRange → All];
p5 = Plot3D[Mred[x, t] /. solsdf[[1]], {t, 0, time}, {x, 0, l},
    PlotLabel → "Mred[t]", PlotRange → All];
p6 = Plot3D[ES[x, t] /. solsdf[[1]], {t, 0, time}, {x, 0, l},
    PlotLabel → "ES[t]", PlotRange → All];
p7 = Plot3D[EM[x, t] /. solsdf[[1]], {t, 0, time}, {x, 0, l},
    PlotLabel → "EM[t]", PlotRange → All];
p8 = Plot3D[P[x, t] /. solsdf[[1]], {t, 0, time}, {x, 0, l},
    PlotLabel → "P[t]", PlotRange → All];
plotlist = {p1, p2, p3, p4, p5, p6, p7, p8};
GraphicsGrid[Partition[plotlist, 4]]

SetDirectory["C:\\Users\\Monika"]

Mred3Dexportdata =
  Table[{x, t, Mred[x, t] /. solsdf[[1]]}, {t, 0, time, time / 150}, {x, 0, l, l / 100}];
```

```
Export["Mred_full_3d_part" <> ToString[#] <> ".dat", Mred3Dexportdata[[#, All, 3]]] & /@
 Range[Length[Mred3Dexportdata]]
```

CV curve generation at a single scan rate (evaluation time length)

```
Estart = -2;
Estop = 3;
Estep = 0.1;
elist = Table[i, {i, Estart, Estop, Estep}];
potentials = Join[elist, Drop[Reverse[elist], 1]];

potentials

tramp = 0.05;
time = 0.15;

data = {};
(*Preparation step at first potential*)
Ecell = potentials[[1]];
initialconsPREP = {
   S[0, t] == S0, (D[S[x, t], {x, 1}] /. x → l) == 0, S[x, 0] == S0,

   (D[Ered[x, t], {x, 1}] /. x → 0) == 0,
   (D[Ered[x, t], {x, 1}] /. x → l) == 0, Ered[x, 0] == 0,

   (D[Mred[x, t], {x, 1}] /. x → 0) == 0,
   Mred[l, t] == M0/(1 + e^((Ecell-Eformal)/Const)), Mred[x, 0] == M0/(1 + e^((Ecell-Eformal)/Const)),

   (*(D[EM[x,t],{x,1}]/.x→0)==0,(D[EM[x,t],{x,1}]/.x→l)==0*)EM[x, 0] == 0,

   (*(D[ES[x,t],{x,1}]/.x→0)==0,(D[ES[x,t],{x,1}]/.x→l)==0*)ES[x, 0] == 0,

   (D[Eox[x, t], {x, 1}] /. x → 0) == 0,
   (D[Eox[x, t], {x, 1}] /. x → l) == 0, Eox[x, 0] == E0,

   (D[Mox[x, t], {x, 1}] /. x → 0) == 0,
   Mox[l, t] == M0/(1 + e^((Eformal-Ecell)/Const)), Mox[x, 0] == M0/(1 + e^((Eformal-Ecell)/Const)),

   (D[P[x, t], {x, 1}] /. x → 0) == 0, (D[P[x, t], {x, 1}] /. x → l) == 0, P[x, 0] == 0};
fulleqns = Flatten[Join[rateeqns, initialconsPREP]];
solsloop = NDSolve[fulleqns, {S, Eox, ES, P, Ered, Mox, EM, Mred},
  {x, 0, l}, {t, 0, time}, MaxSteps → ∞, MaxStepSize → 10^-2];
(*Loop over potentials*)
For[r = 1, r ≤ Length[potentials], r++, {
  Ecell = potentials[[r]];
  Clear[moxpiece]; Clear[mredpiece];

  mredpiece[t_ /; 0 ≤ t ≤ tramp] :=
   1/tramp (M0/(1 + e^((Ecell-Eformal)/Const)) - (Mred[l, time] /. solsloop[[1]])) t +
    (Mred[l, time] /. solsloop[[1]]);
```

```
mredpiece[t_ /; t > tramp] := M0 / (1 + e^((Ecell - Eformal)/Const)); Mreddata =
 Table[{t, mredpiece[t]}, {t, 0, time, time/1000}]; newMred = Interpolation[Mreddata];

moxpiece[t_ /; 0 ≤ t ≤ tramp] := 1/tramp (M0/(1 + e^((Eformal - Ecell)/Const)) - (Mox[l, time] /. solsloop[[1]])) t +
  (Mox[l, time] /. solsloop[[1]]);
moxpiece[t_ /; t > tramp] := M0 / (1 + e^((Eformal - Ecell)/Const)); Moxdata =
 Table[{t, moxpiece[t]}, {t, 0, time, time/1000}]; newMox = Interpolation[Moxdata];

initialcons = {

  S[0, t] == S0, (D[S[x, t], {x, 1}] /. x → l) == 0,
  S[x, 0] == (S[x, time] /. solsloop[[1]]),


  (D[Ered[x, t], {x, 1}] /. x → 0) == 0,
  (D[Ered[x, t], {x, 1}] /. x → l) == 0, Ered[x, 0] == (Ered[x, time] /. solsloop[[1]]),


  (D[Mred[x, t], {x, 1}] /. x → 0) == 0,
  Mred[l, t] == newMred[t], Mred[x, 0] == (Mred[x, time] /. solsloop[[1]]),


  EM[x, 0] == (EM[x, time] /. solsloop[[1]]), ES[x, 0] == (ES[x, time] /. solsloop[[1]]),


  (D[Eox[x, t], {x, 1}] /. x → 0) == 0,
  (D[Eox[x, t], {x, 1}] /. x → l) == 0, Eox[x, 0] == (Eox[x, time] /. solsloop[[1]]),


  (D[Mox[x, t], {x, 1}] /. x → 0) == 0,
  Mox[l, t] == newMox[t], Mox[x, 0] == (Mox[x, time] /. solsloop[[1]]),


  (D[P[x, t], {x, 1}] /. x → 0) == 0,
  (D[P[x, t], {x, 1}] /. x → l) == 0, P[x, 0] == (P[x, time] /. solsloop[[1]])},

 fulleqns = Flatten[Join[rateeqns, initialcons]],
 solsloop = NDSolve[fulleqns, {S, Eox, ES, P, Ered, Mox, EM, Mred},
   {x, 0, l}, {t, 0, time}, MaxSteps → ∞, MaxStepSize → 10^-2],
 fluxS = D[S[x, t] /. solsloop[[1]], x] /. {x → 0, t → time}, curr = Ds fluxS,
 AppendTo[data, {Ecell, Abs[curr]}], PrintTemporary[Ecell]}]
ListPlot[data, Joined → True, PlotRange → All]
```

CV curve generation at a multiple scan rates (evaluation time lengths)

```
Estart = -3;
Estop = 3;
Estep = 0.05;
elist = Table[i, {i, Estart, Estop, Estep}];
potentials = Join[elist, Drop[Reverse[elist], 1]];
```

```
potentials
```

$$\{-3.,\ -2.8,\ -2.6,\ -2.4,\ -2.2,\ -2.,\ -1.8,\ -1.6,\ -1.4,\ -1.2,\ -1.,\ -0.8,\ -0.6,\ -0.4,\ -0.2,\ 1.66533\times10^{-16},\ 0.2,\ 0.4,\ 0.6,\ 0.8,\ 1.,\ 1.2,\ 1.4,\ 1.6,\ 1.8,\ 2.,\ 2.2,\ 2.4,\ 2.6,\ 2.8,\ 3.,\ 2.8,\ 2.6,\ 2.4,\ 2.2,\ 2.,\ 1.8,\ 1.6,\ 1.4,\ 1.2,\ 1.,\ 0.8,\ 0.6,\ 0.4,\ 0.2,\ 1.66533\times10^{-16},\ -0.2,\ -0.4,\ -0.6,\ -0.8,\ -1.,\ -1.2,\ -1.4,\ -1.6,\ -1.8,\ -2.,\ -2.2,\ -2.4,\ -2.6,\ -2.8,\ -3.\}$$

```
tstart = 0.1; (*0.1*)tstop = 0.25; (*0.5*)tstep = 0.15; (*0.15*)
tlist = Table[i, {i, tstart, tstop, tstep}]
```

```
tramp = 0.05; time = 0.15;
```

```
data = {}; {time = tlist[[#]]; dataloop = {};

   Ecell = potentials[[1]];
   initialconsPREP = {
     S[0, t] == S0, (D[S[x, t], {x, 1}] /. x → l) == 0, S[x, 0] == S0,

     (D[Ered[x, t], {x, 1}] /. x → 0) == 0,
     (D[Ered[x, t], {x, 1}] /. x → l) == 0, Ered[x, 0] == 0,

     (D[Mred[x, t], {x, 1}] /. x → 0) == 0,
     Mred[l, t] == M0/(1 + e^((Ecell-Eformal)/Const)), Mred[x, 0] == M0/(1 + e^((Ecell-Eformal)/Const)),

     (*(D[EM[x,t],{x,1}]/.x→0)==0,(D[EM[x,t],{x,1}]/.x→l)==0*)EM[x, 0] == 0,

     (*(D[ES[x,t],{x,1}]/.x→0)==0,(D[ES[x,t],{x,1}]/.x→l)==0*)ES[x, 0] == 0,

     (D[Eox[x, t], {x, 1}] /. x → 0) == 0,
     (D[Eox[x, t], {x, 1}] /. x → l) == 0, Eox[x, 0] == E0,

     (D[Mox[x, t], {x, 1}] /. x → 0) == 0,
     Mox[l, t] == M0/(1 + e^((Eformal-Ecell)/Const)), Mox[x, 0] == M0/(1 + e^((Eformal-Ecell)/Const)),

     (D[P[x, t], {x, 1}] /. x → 0) == 0, (D[P[x, t], {x, 1}] /. x → l) == 0, P[x, 0] == 0};
   fulleqns = Flatten[Join[rateeqns, initialconsPREP]];
   solsloop = NDSolve[fulleqns, {S, Eox, ES, P, Ered, Mox, EM, Mred},
     {x, 0, l}, {t, 0, time}, MaxSteps → ∞, MaxStepSize → 10^-2];
   (*Loop over potentials*)
   For[r = 1, r ≤ Length[potentials], r++, {
     Ecell = potentials[[r]];
     Clear[moxpiece]; Clear[mredpiece];
```

```
mredpiece[t_ /; 0 ≤ t ≤ tramp] :=
  1/tramp (M0/(1 + e^((Ecell-Eformal)/Const)) - (Mred[l, time] /. solsloop[[1]])) t +
   (Mred[l, time] /. solsloop[[1]]);
mredpiece[t_ /; t > tramp] := M0/(1 + e^((Ecell-Eformal)/Const));
Mreddata = Table[{t, mredpiece[t]}, {t, 0, time, time/1000}];
newMred = Interpolation[Mreddata];


moxpiece[t_ /; 0 ≤ t ≤ tramp] :=
  1/tramp (M0/(1 + e^((Eformal-Ecell)/Const)) - (Mox[l, time] /. solsloop[[1]])) t +
   (Mox[l, time] /. solsloop[[1]]);
moxpiece[t_ /; t > tramp] := M0/(1 + e^((Eformal-Ecell)/Const));
Moxdata = Table[{t, moxpiece[t]}, {t, 0, time, time/1000}];
 newMox = Interpolation[Moxdata];


initialcons = {

  S[0, t] == S0,
  (D[S[x, t], {x, 1}] /. x → l) == 0, S[x, 0] == (S[x, time] /. solsloop[[1]]),


  (D[Ered[x, t], {x, 1}] /. x → 0) == 0, (D[Ered[x, t], {x, 1}] /. x → l) == 0,
  Ered[x, 0] == (Ered[x, time] /. solsloop[[1]]),


  (D[Mred[x, t], {x, 1}] /. x → 0) == 0,
  Mred[l, t] == newMred[t], Mred[x, 0] == (Mred[x, time] /. solsloop[[1]]),


  EM[x, 0] == (EM[x, time] /. solsloop[[1]]),
  ES[x, 0] == (ES[x, time] /. solsloop[[1]]),


  (D[Eox[x, t], {x, 1}] /. x → 0) == 0,
  (D[Eox[x, t], {x, 1}] /. x → l) == 0, Eox[x, 0] == (Eox[x, time] /. solsloop[[1]]),


  (D[Mox[x, t], {x, 1}] /. x → 0) == 0,
  Mox[l, t] == newMox[t], Mox[x, 0] == (Mox[x, time] /. solsloop[[1]]),


  (D[P[x, t], {x, 1}] /. x → 0) == 0,
  (D[P[x, t], {x, 1}] /. x → l) == 0, P[x, 0] == (P[x, time] /. solsloop[[1]])},
```

```
    fulleqns = Flatten[Join[rateeqns, initialcons]],
    solsloop = NDSolve[fulleqns, {S, Eox, ES, P, Ered, Mox, EM, Mred},
      {x, 0, l}, {t, 0, time}, MaxSteps → ∞, MaxStepSize → 10^-2],
    fluxS = D[S[x, t] /. solsloop[[1]], x] /. {x → 0, t → time}, curr = Ds fluxS,
    AppendTo[dataloop, {Ecell, Abs[curr]}], PrintTemporary[Ecell]}],
  AppendTo[data, {time, dataloop}], PrintTemporary[
   "solver time = " <> ToString[time]]} & /@ Range[Length[tlist]];

ListPlot[data[[All, 2]]]
```

Export the CV data

```
SetDirectory["C:\\Users\\Monika"]
```

```
Export["CV_Evaltime=" <> ToString[#[[1]]] <> "s_.dat", #[[2]], "CSV"] & /@ data
```

```
{CV_Evaltime=0.1s_.dat, CV_Evaltime=0.25s_.dat}
```

Some interactive plots

```
Manipulate[ListPlot[data[[fg, 2]], Joined → True,
  PlotLabel → "Eval Time = " <> ToString[data[[fg, 1]]],
  PlotRange → {{-0.8, 1.2}, {0, 0.0011}}], {fg, 1, Length[data], 1}]
```